DOT/FAA/TC-15/21

Federal Aviation Administration
William J. Hughes Technical Center
Aviation Research Division
Atlantic City International Airport
New Jersey 08405

Experimental Flow Characterization and Computational Model Development of Aqueous Film Forming Foam Firefighting Jets

June 2015

Final Report

U.S. Department of Transportation
Federal Aviation Administration

NOTICE

This report is available at the Federal Aviation Administration William J. Hughes Technical Center's Full-Text Technical Reports page: actlibrary.tc.faa.gov in Adobe Acrobat portable document format (PDF).

Technical Report Documentation Page

1. Report No.	2. Government Accession No.	3. Recipient's Catalog No.
DOT/FAA/TC-15/21		

4. Title and Subtitle	5. Report Date
EXPERIMENTAL FLOW CHARACTERIZATION AND COMPUTATIONAL MODEL DEVELOPMENT OF AQUEOUS FILM FORMING FOAM FIREFIGHTING JETS	June 2015
	6. Performing Organization Code

7. Author(s)	8. Performing Organization Report No.
Christopher P. Menchini, Gary J. Morris, and Wade W. Huebsch	

9. Performing Organization Name and Address	10. Work Unit No. (TRAIS)
West Virginia University Mechanical & Aerospace Engineering Department PO Box 6106 Morgantown, WV 26506-6106	11. Contract or Grant No. FA4819-10-C-0013

12. Sponsoring Agency Name and Address	13. Type of Report and Period Covered
Federal Aviation Administration Airport Safety and Operations Division (AAS-300) 800 Independence Avenue SW Washington, DC 20591	Final Report
	14. Sponsoring Agency Code AAS-300

15. Supplementary Notes

The FAA Airport Technology Research and Development Branch COR was Mr. Keith Bagot.

16. Abstract

Over the past few decades, aircraft rescue and firefighting (ARFF) research has made technical strides on multiple fronts. Continuing efforts have helped develop computer-aided engineering tools to quantify risk assessment for a variety of ARFF aspects such as aircraft pool fire combustion and dynamic crash-related events. A study was conducted to characterize firefighting agent application behavior and to quantify the flow characteristics that differentiate water and aqueous film forming foam (AFFF) jets.

An aqueous firefighting agent application laboratory was specially constructed to carry out experiments on firefighting jets ranging from 1 to 11 MPa (150 to 1550 lb·in.$^{-2}$) and 4 to 25 l·min^{-1} (1 to 6.4 gal·min^{-1}) at AFFF concentration levels ranging from 0% (pure water) to 12% by volume. Experimental flow characterization consisted of flow visualization, agent ground pattern distribution analysis, and two-dimensional phase Doppler particle analysis (PDPA). Flow visualization results depicted minimal qualitative differences in terms of overall jet structure between AFFF and water jets. However, PDPA results showed AFFF enhanced jet breakup and generated droplet sizes 7% to 38% less in diameter compared to water jets with AFFF jets lagging water jet velocities by as much as 10% in certain cases. Agent ground pattern results confirmed flow performance factors, such as ground coverage area, reach, and maximum span, all benefit from an increase in nozzle pressure-flow rate.

An Euler-Lagrange, large eddy simulation computational fluid dynamic (CFD) strategy accounting for droplet collision and breakup was employed to predict firefighting jet flow dynamics with and without the addition of AFFF. AFFF influence was handled computationally via material property variation from pure water in terms of density, viscosity, and surface tension effects. CFD model results were agreeable with flow visualization and phase Doppler data as they reproduced global trends in both droplet velocity and size data, particularly with respect to the influence of AFFF. However, oversimplified nozzle injection conditions led to greater differences than expected. CFD model result errors were difficult to quantify entirely due to PDPA upper particle size range limitations and complexities associated with direct comparisons to data.

This work describes the first known, comprehensive effort to quantify flow characteristics and properties that differentiate water and AFFF firefighting jets using high-fidelity experimental techniques. This work also includes the first known iteration of a firefighting agent application CFD model designed for use in the ARFF industry that takes into account the influence of AFFF.

17. Key Words	18. Distribution Statement
Phase Doppler particle analysis, Jet structure, Computational fluid dynamics, Aqueous film forming foam, Water jet	This document is available to the U.S. public through the National Technical Information Service (NTIS), Springfield, Virginia 22161. This document is also available from the Federal Aviation Administration William J. Hughes Technical Center at actlibrary.tc.faa.gov.

19. Security Classif. (of this report)	20. Security Classif. (of this page)	21. No. of Pages	22. Price
Unclassified	Unclassified	263	

TABLE OF CONTENTS

LIST OF FIGURES

LIST OF TABLES

LIST OF ACRONYMS AND ABBREVIATIONS

1-D	One-dimensional
2-D	Two-dimensional
3-D	Three-dimensional
AFCEC	Air Force Civil Engineer Center
AFFF	Aqueous film forming foam
ARFF	Aircraft rescue and firefighting
CFD	Computational fluid dynamic
CPU	Central processing unit
DoD	Department of Defense
DPM	Discrete phase model
DNS	Direct Numerical Simulation
DSLR	Digital single-lens reflex
EPA	Environmental Protection Agency
FAA	Federal Aviation Administration
FFT	Fast Fourier transform
LES	Large eddy simulation
MIL-SPEC	Military specification
MPa	Megapascal
NFPA	National Fire Protection Association
PDPA	Phase Doppler particle analysis
PFOA	Perfluorooctanoic acid
PFOS	Perfluorooctane sulfonate
pH	Power of hydrogen
RMS	Root mean square
RPM	Revolutions per minute
SSD	Stochastic secondary droplet
TAB	Taylor Analogy Breakup
VOF	Volume of fluid
WALE	Wall-adapting local eddy-viscosity subgrid scale model
WVU	West Virginia University

LIST OF SYMBOLS

Symbol	Definition	Units
β	Damping coefficient	$kg \cdot s^{-1}$
γ_{SG}	Specific gravity	--
Δt	Simulation time step	s
δ	Fringe spacing	μm
ε	Gas to liquid density ratio	--
η_0	Initial liquid jet disturbance wavelength	m^{-1}
θ	PDPA laser beam intersection angle	degrees (°)
ϕ	PDPA phase shift angle	degrees (°)
Φ	Raw data signal	--
λ	Wavelength	m^{-1}
μ	Dynamic viscosity	Pa·s
μ_G	Gaseous dynamic viscosity	Pa·s
μ_L	Liquid dynamic viscosity	Pa·s
ν	Kinematic viscosity	$m^2 \cdot s^{-1}$
ρ	Density	$kg \cdot m^{-3}$
ρ_G	Gaseous density	$kg \cdot m^{-3}$
ρ_L	Liquid density	$kg \cdot m^{-3}$
σ	Surface tension	$mN \cdot m^{-1}$
σ_{AFFF}	Surface tension of AFFF	$mN \cdot m^{-1}$
σ_C	Surface tension of cyclohexane	$mN \cdot m^{-1}$
σ_I	Interfacial tension between cyclohexane and AFFF	$mN \cdot m^{-1}$
$\sigma_{L/G}$	Surface tension between a liquid and surrounding gas	$mN \cdot m^{-1}$
σ_S	Spreading coefficient due to surfaced tension	$mN \cdot m^{-1}$
φ	PDPA scattering angle	degrees (°)
ψ	PDPA receiving angle	degrees (°)
ω	Droplet oscillation frequency	Hz
A	Amplitude of an undamped oscillation	m
C	Solution concentration	% by volume
C_β	TAB model constant	--
C_b	TAB model constant	--
C_{Drag}	Drag coefficient	--
$C_{Drag,Sphere}$	Drag coefficient of a sphere	--
C_F	TAB model constant	--
C_k	TAB model constant	--
d	Droplet diameter	μm
d_{MIN}	Minimum droplet diameter	μm
d_{MAX}	Maximum droplet diameter	μm
D	Liquid jet or nozzle diameter	mm
$D10$	Mean droplet diameter	μm
$D32$	Sauter mean droplet diameter	μm
D_{RMS}	Root mean square diameter	μm

E	Estimated deviation between the true mean and calculated mean in a measured flow parameter	$m \cdot s^{-1}$ or μm
$f_{Doppler}$	Doppler frequency	Hz
F_{Ext}	External Force	N
F_{Drag}	Drag force	N
F_{Other}	Other force	N
g	Acceleration due to gravity	$m \cdot s^{-2}$
k	Spring stiffness constant	$N \cdot m^{-1}$
m_d	Droplet mass	kg
$\dot{m}_d$	Droplet mass flow rate	$kg \cdot s^{-1}$
M	PDPA phase-diameter slope	--
Oh	Ohnesorge or stability number	--
N	Number of samples	--
N_{decorr}	Number of decorrelated samples	--
r	Droplet radius	μm
R	Nozzle radius	m
Re_d	Relative Reynolds number base on droplet diameter	
Re_L	Reynolds number based on liquid jet characteristics	--
s	TAB model droplet distortion	m
t	Simulation time	s
t_d	Droplet life time	s
T	Temperature	K
V_d	Droplet velocity	$m \cdot s^{-1}$
$V_{c,rel}$	Relative velocity between colliding droplets	$m \cdot s^{-1}$
$V_{d,rel}$	Relative velocity between a droplet and the surrounding gas phase	$m \cdot s^{-1}$
$V_{d,X}$	Axial droplet velocity	$m \cdot s^{-1}$
$V_{d,Z}$	Vertical droplet velocity	$m \cdot s^{-1}$
$V_{G,X}$	Axial gaseous (air) velocity	$m \cdot s^{-1}$
$V_{G,Z}$	Vertical gaseous (air) velocity	$m \cdot s^{-1}$
V_J	Jet velocity	$m \cdot s^{-1}$
We_d	Gaseous Weber number based on liquid droplet characteristics	--
We_L	Weber number based on liquid jet characteristics	--
We_T	Weber number based on Taylor's analogy	--
x	Axial direction	--
x_e	TAB model droplet equator location	m
y	Horizontal direction	--
z	Vertical direction	--
Z	Jet breakup length	m

EXECUTIVE SUMMARY

In recent decades, aircraft rescue and firefighting (ARFF) research has made large technical strides on multiple fronts. Continuing efforts have helped develop computational engineering tools to quantify risk assessment for a variety of ARFF aspects such as aircraft pool fire combustion and dynamic crash-related events. To supplement this work, an experimental study was conducted to quantify flow characteristics that differentiated water and aqueous film forming foam (AFFF) jets and to provide a first known attempt at developing a firefighting agent application model that included the effects of AFFF. Progress in this area hopefully will lead to further simulation capability, including a combined aircraft crash-fire-suppression application risk assessment model.

An aqueous firefighting agent application laboratory at West Virginia University was constructed to conduct experiments on firefighting agent application jets ranging from 1 to 12 MPa and 4 to 25 $L \cdot min^{-1}$ at AFFF concentration levels ranging from 0% to 12% by volume mixed with water. Experimental efforts were met with challenges due to the lack of firefighting nozzles available that are capable of producing adequate foam quality at low flow rates for fire suppression while covering the pressure range of interest. The Stoneage Waterblast Tools® AP4™ family of nozzles was selected because it provided the best compromise among all of the aforementioned criteria. Laser sheet, conventional, macro, and high-speed photography methods were used to conduct flow visualization on different firefighting jet configurations. One-dimensional and two-dimensional (2-D) agent ground pattern analyses were conducted to measure accumulation and foam expansion ratio. Firefighting jet 2-D velocity, droplet size distribution, and spray concentration measurements were recorded using phase Doppler particle analysis (PDPA). Afterwards, experimental work and support from the literature were used to develop a computational fluid dynamic (CFD) simulation strategy to predict firefighting jet transport characteristics including the effects of AFFF.

Firefighting jet flow visualization showed unremarkable differences between water and AFFF jets in terms of overall shape and structure. However, AFFF jets exhibited a greater opacity and appeared more dispersive compared to water jets due to an increase in the amount of visible scattered light. Conventional firefighting jets were categorized via the literature in the atomization breakup regime and were characterized by a discontinuous liquid jet core, which was verified during flow visualization. This attribute was observed to amplify as jet pressure increased and dampen as jet flow rate increased. This implies overall firefighting jet flow dynamics were driven by droplet transport, their interaction with the surrounding air, as well as themselves in terms of collision, coalescence, and breakup. Although multiple high-fidelity flow visualization techniques were performed, few were very successful due to poor lighting, the high-speed nature of the subject, and inconsistent focal planes in key downstream jet locations. For low-pressure jets, near-field imagery captured the existence of sporadic foam bubbles whereas medium- and high-pressure jets maintained appearances very similar to that of water jets. Certain firefighting jet configurations exhibited periodic oscillations or pulsations during delivery. These were traced back to pump mechanics and did not significantly affect the analysis.

All firefighting jet performance factors in terms of foam quality, ground coverage area, reach, and maximum span were aided by an increase in flow rate. The results were similar for nozzle

pressure, except changes in foam quality were shown to be inconclusive for laboratory-scale conditions. For full-scale flow rate conditions examined at Tyndall Air Force Base, Florida, an increase in nozzle pressure was shown to definitively decrease foam quality. An AFFF concentration sensitivity study showed foam quality strongly increased as AFFF concentration increased.

PDPA revealed near-field mean jet velocity expectedly increased with increasing nozzle pressure, and mean droplet size expectedly increased as flow rate was increased. It was also shown that downstream mean droplet velocity dropped significantly faster for medium- to high-pressure jets compared to low-pressure jets, which incurred relatively less breakup during transport. AFFF jets exhibited mean droplet diameters 7% to 38% smaller compared to that of water jets, indicating AFFF enhances droplet breakup through the use of its surface tension-lowering surfactants. Although agent ground pattern foam quality results exhibited a strong positive, proportional dependence on AFFF concentrate up to the maximum tested concentration of 12%, PDPA droplet size distribution results became nearly independent of AFFF concentration between 6% and 9%. All firefighting jets exhibited log-normal droplet distribution behavior consistent with pressure atomizer nozzles. The best log-normal fit for all firefighting jet settings came from the Nukiyama-Tanasawa fit. PDPA droplet concentrations were generally inconclusive due to mixed trends in the data and the dependency the measurement could have on signal quality.

A CFD modeling framework was generated using the commercial CFD software code ANSYS Fluent v14.5® based on measurement details from the PDPA and support from the literature. An Euler-Lagrange simulation strategy using discrete phase model trajectory tracking of agent droplets through a gaseous Eulerian atmosphere was chosen, which best accommodates the atomization breakup phenomena mentioned earlier. Firefighting jet initial conditions were derived from the firefighting agent delivery system flow meter, nozzle geometry, and the mean droplet size distribution measured from the near-field PDPA measurement plane. The CFD model accounted for droplet collision and coalescence stochastically. Because a low (< 100) gaseous Weber number range was identified based on the firefighting jet configuration and confirmed by experimental results, the Taylor Analogy Breakup model was used to model droplet disintegration, which is best suited for the low Weber number regime. AFFF effects were accounted for in the material properties primarily by surface tension and less significantly by density and viscosity, which already exhibit strong similarity to tap water.

CFD results showed good agreement with velocity magnitudes with error often less than 10% in most firefighting jet configurations considered. The largest discrepancies were due to an oversimplification of firefighting jet injection conditions that affected the firefighting nozzle near field the most, and proportionally less the further downstream each jet developed. Although bulk CFD and PDPA mean droplet diameter well resembled magnitudes and trends from PDPA data, precise model performance was difficult to judge based on the challenge of comparing identical sampling locations. Further uncertainty stemmed from the PDPA having a finite droplet size measurement range, whereas the CFD model enforced no such boundaries. The downstream jet containment bed had minor influence on experimental flow patterns that were not accounted for in the simulation.

A combination of experimental and computational work has led to the quantification of firefighting jet transport in terms of ground pattern and in-flight flow characterization for both water and AFFF jets. Although far-field inspection revealed little novel information, near-field PDPA measurements confirmed highly atomized AFFF jets behave similar to water jets with the added characteristic of enhanced breakup, reducing mean downstream droplet sizes. Experimental results aided construction of a CFD model capable of predicting primary jet flow features with sensitivity to AFFF effects.

This work describes the first known, comprehensive effort to quantify flow characteristics and properties that differentiate water and AFFF firefighting jets using high-fidelity experimental techniques. This work also includes the first known iteration of a firefighting agent application CFD model designed for use in the ARFF industry that takes into account the influence of AFFF. Data collected from this study can be used to develop future, more eco-friendly alternatives to AFFF, optimize current AFFF compositions and application techniques for greater effectiveness, and aid the on-going construction of a simulation framework to provide scientifically based risk assessment for aircraft-crash-fire suppression scenarios of interest.

1. INTRODUCTION.

1.1 BACKGROUND.

In recent decades, aircraft rescue and firefighting (ARFF) research as a metrological science has evolved largely due to the advancement of applicable engineering tools. Government civil and defense sectors, in conjunction with academic institutions, have established programs investigating all aspects of accidental fire phenomenology, including combustion mechanisms, fire mitigation strategies, and emergency response tactics. Innovation fostered in fields other than the ARFF industry has also played a major role through technology transfer. However, most fundamental research is still rooted in the principal sciences.

ARFF research is primarily driven by changes in threat level posed by technological advances in other aspects of the aircraft industry. Novel materials, fuel compositions, airport or airbase logistics, layouts, structures, and the evolution of aircraft shape and size provide unique challenges fire safety planners must continuously address. Research efforts are chiefly supported by the Department of Transportation Federal Aviation Administration (FAA) and the Department of Defense (DoD), including relationships with national laboratories.

As part of an interagency agreement with the Air Force Civil Engineer Center (AFCEC) Fire Research Group, the FAA has supported a multitude of research efforts to investigate risk assessment metrics for aircraft crash fire environments. These programs have included a combination of engineering approaches that have historically relied on the AFCEC multiscale live fire facilities located at Tyndall Air Force Base, Florida. Figures 1 through 3 illustrate various research programs including characterization of combustion environments, fire suppression techniques, and emergency vehicle performance.

Figure 1. A Large-Frame Aircraft Mockup Engulfed by a JP-8 Pool Fire

Figure 2. An ARFF Vehicle Undergoing a Mobility Performance Trial

Figure 3. Firefighting Agent Evaluation on a Two-Dimensional Pool Fire

Although full-scale testing is critical to aviation fire research, it harbors some disadvantages. Fuel, firefighting agent, equipment, and manpower costs can be prohibitive. Outdoor studies must contend with uncontrolled and often chaotic atmospheric influences typically resulting in significant variance between repeated trials that are important to study but difficult to quantify. In addition, the destructive combustion spray environment results in reduced life expectancy for both fabricated test and data acquisition equipment. Constantly increasing pressure from environmental regulators also threatens full-scale experimental sustainability. Efforts are further complicated by historically unreported or inexact statistics recorded for aviation fire mishaps. This makes fire emergency service readiness difficult to analyze. Experimental aviation crash data are also scarce due to expense and practicality.

To supplement testing efforts, computational methods are under investigation to further characterize the comprehensive aircraft-crash-fire-suppression event. The results from the present work are intended to provide further quantitative insight into the complex environment,

as well as provide an additional set of engineering tools to predict mishap scenarios that are too expensive or impractical to reproduce experimentally. A collaborative effort has been established on four distinct but interrelated fronts: (1) a dynamic aircraft crash analysis, (2) fuel spread analysis, (3) pool fire combustion analysis, and (4) an agent application fire suppression analysis. Each module presents a distinct set of modeling challenges that represent varying degrees of difficulty and progress level in their respective field. Each sector also requires a specific level of fidelity to adequately represent the bulk physical characteristics necessary for fire risk assessment. Figure 4 depicts the framework under investigation.

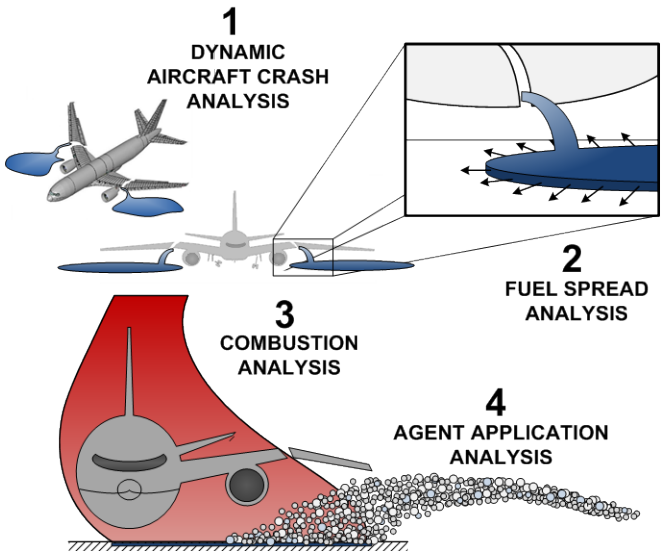

Figure 4. The AFCEC Computational Aircraft-Crash-Fire-Suppression Methodology

1.2 TERMINOLOGY.

This document assumes the reader has familiarity with basic terms commonly used in the academic field of fluid mechanics and the ARFF industry. The phrase "aqueous film-forming foam (AFFF) concentrate" strictly refers to the nondiluted composition direct from the manufacturer. The term "AFFF" refers to a solution of AFFF concentrate mixed with water. The term "*n*-percent AFFF" denotes the specific percent *n* amount of AFFF concentrate that is mixed by volume with water. The term "firefighting jet" generically refers to both AFFF and water jets. Unless otherwise specified, "water" refers to tap water. All results are reported in the metric-based Système Internationale units for consistency, with dual reference to English units in some instances for added clarity.

1.3 SCOPE.

The goal of the present study was to provide a better understanding of the firefighting agent application process. Its mission was to experimentally quantify the flow characteristics that differentiate water and AFFF jets and to provide the first known attempt at developing a firefighting agent application delivery model that included the influence of AFFF. Experimental efforts focused on measuring jet droplet velocity and size in addition to ground accumulation behavior. Although AFFF has served as the mainstay agent for aviation class B liquid fire

suppression for several decades, its applicability in its current composition moving forward has been brought into question due to evolving environmental regulations. Even though its emulsified foam state has been well characterized, especially in the presence of a hydrocarbon-fuel-air interface, very little is known about the fluid dynamics of AFFF in the turbulent liquid jet breakup flow regime en route to the flame front. Once the fire has been breached by spray impingement, AFFF acts to form a layer of insulating foam between the liquid hydrocarbon fuel surface and heated fuel vapor in order to prevent re-ignition. Of particular interest was studying the effect varying pressure, flow rate, and AFFF concentration had on the jetting process. Agent fluid dynamics altered by the presence of fire were neglected for the present study, which only focused on firefighting jet flow characterization within an adiabatic environment. Research efforts were focused on analyzing the in-flight portion of firefighting jet flows up until initial contact with the ground is made. Post airborne interactions, such as liquid-liquid (i.e., agent-fuel surface) or agent surface-spreading parameters, were not considered. The long-term goal is to integrate the firefighting jet modeling approach developed in the present study with the global aircraft-crash-fire-suppression simulation methodology depicted in figure 4.

The following technical objectives were identified as key milestones necessary to achieve the aforementioned goals.

- Apply experimental flow visualization techniques to provide graphical details of the in-flight firefighting jet transport process.

- Conduct experimental agent ground pattern analysis to quantify firefighting jet performance characteristics such as resultant firefighting foam quality (AFFF jets only), agent accumulation rates, and agent distribution.

- Apply experimental phase Doppler particle analysis (PDPA) to measure in-flight firefighting jet droplet velocity and droplet size distribution.

- Develop a computational fluid dynamic (CFD) modeling strategy to predict the in-flight firefighting jet characteristics measured and qualitatively corroborated by PDPA and flow visualization, respectively.

A literature review is presented in section 2 to discuss the physical characteristics of AFFF in both liquid and emulsified foam forms. An introduction to turbulent round liquid jets entering still air with an extension to firefighting applications is then discussed from both an experimental and computational perspective. The aqueous firefighting agent application laboratory constructed for experimental work is overviewed in section 3. Section 4 explains the experimental approach taken, including the flow visualization process, agent ground pattern analysis, PDPA, and measurement and uncertainty analysis. Section 5 discusses the implementation of an Euler-Lagrange CFD modeling strategy using ANSYS Fluent® v14.5 to model the firefighting jet configurations tested in the laboratory. Key results are summarized in section 6 followed by conclusions and references in sections 7 and 8, respectively. An overall case summary is listed in appendix A. AFFF material property data to support the aforementioned objectives is presented in appendix B. Auxiliary PDPA data are depicted in

appendix C, and an overview on the PDPA calibration procedure carried out by the instrument's manufacturer is summarized in appendix D.

2. LITERATURE REVIEW.

2.1 OVERVIEW.

With current work investigating the effect AFFF has on conventional firefighting jet transport, a background on AFFF including its molecular composition and physical traits as both a liquid and foam is reported. Very little, if any, research exists on characterizing the role AFFF plays in influencing firefighting jet breakup. Most conventional firefighting jets are a subset of a broader phenomenology of round, turbulent, pressure-atomized liquid jets discharging into still air. Due to this, an introduction to the fundamental principles governing liquid jet instability and breakup is discussed with a look at pioneering work followed by a modern-day perspective. Analysis of the fluid transport mechanisms and liquid jet breakup regimes are described highlighting regions specific to firefighting jets. Because AFFF is a surface active agent, studies examining the role surfactants play in primary liquid jet disintegration and secondary droplet breakup are also considered. Relevant analytical, experimental, as well as computational modeling methods used to characterize turbulent liquid jet breakup behavior are then discussed with extension to firefighting jet applications where available. Most firefighting jet research dating back to the 1960s is generally limited to nozzle design and delivery improvements to water jets. The majority of contemporary fire suppression spray research focuses on sprinkler system designs for fighting class A fires in buildings, which is outside the scope of the present effort.

2.2 PHYSICAL CHARACTERISTICS OF AQUEOUS FILM FORMING FOAM.

2.2.1 Background.

AFFF is a highly effective, water-based, class B liquid fire suppression agent initially developed for military purposes by the Naval Research Laboratory in cooperation with the fluorochemical manufacturer 3M in the early 1960s. During the same time period, commercial airline passenger service and military airpower demands increased significantly, and an alternate synthetic option was desired. The synthetic option needed to be capable of doubling fire suppression performance in terms of reduced foam requirements over older, less efficient, protein-based foams. AFFF adoption became widespread and made its way into the civilian firefighting industry by the late 1970s. It has emerged as the firefighting agent of choice for fighting pool fires at domestic airports, military bases, oil refineries, and other outlets where operations rely heavily on hydrocarbon consumption [1 and 2].

Originally referred to as "light water," AFFF has the ability to cover a low-density liquid hydrocarbon fuel surface with a foam layer to act as both thermal and evaporative barriers to hinder and ultimately extinguish combustion. Water is typically unsuccessful at extinguishing hydrocarbon fires because it is high density, and it sinks below the low-density fuel providing negligible firefighting benefit. Figure 5 depicts AFCEC personnel applying AFFF to an aircraft JP-8 pool fire at Tyndall Air Force Base, Florida.

Figure 5. The AFFF Being Applied to an Aircraft JP-8 Pool Fire

AFFF's film-forming properties are derived from its ability to sustain a thin film along the hydrocarbon fuel surface after the foam layer has collapsed, exhibiting a unique capacity to self-heal if penetrated by debris [1]. Previous research has characterized AFFF-based firefighting foam compositions in terms of agent delivery proportioning characteristics, minimum AFFF concentration needs, and nozzle discharge requirements for effective fire suppression. Foam rheological properties, such as yield stress, density, and viscosity, have also been investigated to develop AFFF composition guidelines for use in delivery systems designed for protein foams that by comparison are heavier, more viscous, less stable, and have faster drain rates [1 and 3-8]. Continued research has led to the development of a minimum set of performance standards for agent quality as well as firefighting agent delivery systems that are recognized by several key agencies, including the DoD, FAA, International Civil Aviation Organization, and the National Fire Protection Agency (NFPA). Military Specification (MIL-SPEC) AFFF used by the DoD must conform to performance provisions outlined by Mll-F-24385 current revision F [9]. Civilian firefighting practices are governed by the FAA and follow standards in NFPA 403: Standard for Aircraft Rescue and Fire-Fighting Services at Airports and NFPA 412: Standard for Evaluating Aircraft Rescue and Fire-Fighting Foam Equipment [10 and 11]. Military firefighting standards often adhere to the same or similar standards as those defined by NFPA.

2.2.2 Molecular Composition and Behavior.

MIL-SPEC C301MS 3% AFFF manufactured by Chemguard and Williams®, a subsidiary of Tyco International, was the AFFF concentrate used exclusively for the present study. Its constituents and fluid properties are typical of most MIL-SPEC AFFF formulations. MIL-SPEC AFFF is manufactured and distributed in concentrate form in either 3% or 6% formulas. The percentage denotes the volumetric proportion at which AFFF concentrate must be mixed with water to generate a firefighting agent solution capable of meeting MIL-SPEC (or NFPA) performance criteria. Specifically, 3% AFFF concentrate must be mixed 3 parts concentrate with 97 parts water, and a 6% AFFF concentrate must be mixed with 6 parts concentrate and 94 parts water for both solutions to achieve the same minimum required level of firefighting effectiveness. In practice, most modern firefighting agent delivery systems allow for variable water-AFFF concentrate proportioning to suit specific needs. Table 1 lists the known chemical

constituents that make up the AFFF concentrate used in the present study [12]. Approximate AFFF concentrate compositions developed by other manufacturers are in references [2] and [13-16].

Table 1. Reported AFFF Concentrate Chemical Constituents Used in the Present Study [12]

Chemical Name	Percentage
Diethylene glycol mono butyl ether (Butyl Carbitol™)	0% – 8%
Magnesium sulfate	0.5% – 1.5%
Ethylenediane tetra acetic acid	0.5% – 1.5%
Hydrocarbon surfactant	Proprietary
Fluorocarbon surfactant	Proprietary

AFFF concentrate is primarily made up of an active blend of hydrocarbon and fluorocarbon surfactants, also referred to as surface active agents, in percentages known exclusively to the manufacturer. Modern synthesis of fluorocarbon surfactants is typically the most expensive manufacturing stage based on telomerization. Older techniques used by manufacturers like 3M relied on electrochemical fluorination. Because highly favorable firefighting foam properties can be achieved from a relatively low concentration of fluorocarbon surfactants, their expense is off-set when mixed with more of the less expensive hydrocarbon surfactants. Both types of surfactant exhibit enhanced firefighting performance when mixed together as opposed to when used separately. AFFF concentrate also contains secondary viscosity enhancers (such as Butyl Carbitol™) along with minor additives (such as insoluble salts, thickeners, corrosion inhibitors, and stabilizers) to optimize the final physical state of the foam. Unfortunately, an exact explanation on the complex role each ingredient plays is publicly unavailable due to the proprietary nature of the AFFF concentrate formulation. AFFF concentrate compositions may also vary significantly from batch to batch as long as industry-specific performance requirements, such as the MIL-SPEC standard, are met [2].

The surfactants in AFFF concentrate are made up of long anionic and amphoteric molecular chains of hydrophilic, hydrophobic, and oleophobic components that are barely miscible in water. These components are used to lower the surface energy of the aqueous solution, generate foam, and improve spread efficiency across the fuel surface. Water-soluble surfactants are typically modeled as having a hydrophilic ionic or polarized “head” along with an organic hydrophobic or oleophobic “tail.” Anionic surfactants are a common subfamily of surfactants displaying properties characteristic of most soaps and detergents. These surfactants generate complicated electrical interactions in head groups along water-oil interfaces that are capable of creating regions of unbalanced charge. These intermolecular forces, largely based on the dissolved ionic concentration, can significantly affect interfacial rheology. Amphoteric surfactants are less commonly used industrially and can exhibit a positive, negative, or dual charge, depending on the solution power of hydrogen (pH) or acidity level [17]. Figure 6 illustrates two telomerization-based fluorocarbon surfactants identified in AFFF concentrate specific to this study [18].

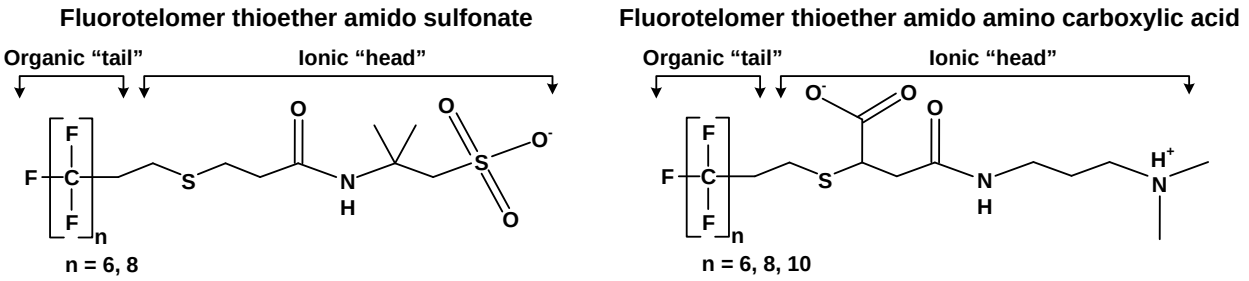

Figure 6. Examples of Fluorocarbon Surfactants Identified in AFFF [18]

AFFF surfactant molecules prefer to align along a free surface, such that their hydrophilic heads migrate toward water, and their hydrophobic and oleophobic tails migrate toward the fuel surface and air, respectively. Although fluorocarbon and hydrocarbon surfactant polar head groups can exhibit strong similarities, fluorocarbon surfactant tails are both hydrophobic and oleophobic by nature, whereas hydrocarbon surfactant tails are only hydrophobic [13]. Figure 7 illustrates the favorable orientation of surfactant molecules when AFFF is situated between a fuel-air interface.

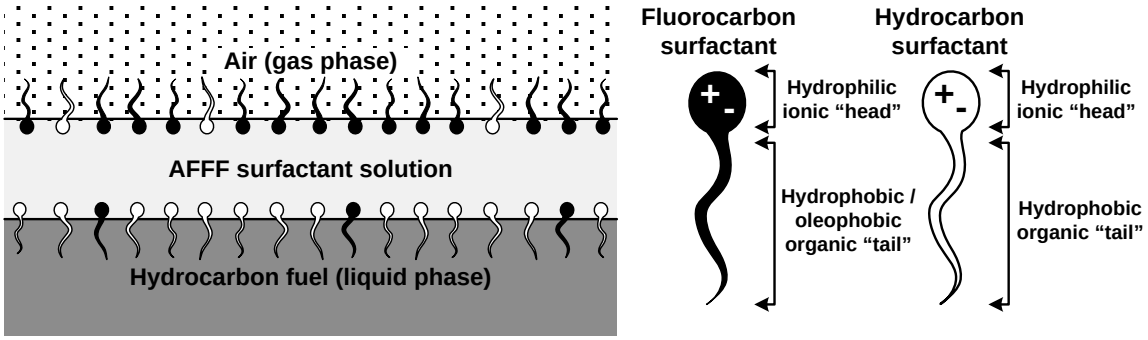

Figure 7. The Conceptual Alignment of Surfactants in an Air-Water-Fuel Environment [2 and 13]

Fluorocarbon surfactants are generally characterized by outstanding film-forming traits that help lower the surface tension of AFFF. Fluorocarbon surfactants also provide stronger thermal resistance and stability compared to hydrocarbon surfactants that are known for having greater foam-forming capability and lowering the overall interfacial tension between AFFF and the fuel surface [17].

In dynamic scenarios, such as firefighting jets where AFFF is injected into the atmosphere from a nozzle breaking up into droplets, the surfactant's preference to self-orient becomes a time-dependent process based on molecular diffusion. In the initial stages of injection into air, surfactants are randomly distributed throughout the AFFF. As time progresses, the surfactant molecules undergo preferential alignment to create a monolayer based upon the same rules as those illustrated in figure 7. The level of organization the surfactants reach increases as surface age increases. This molecular process helps define an instantaneous surface tension at a finite rate, better known as the dynamic surface tension of the fluid. Figure 8 depicts this morphology using the cross-section of a single airborne droplet of AFFF aging with time [2].

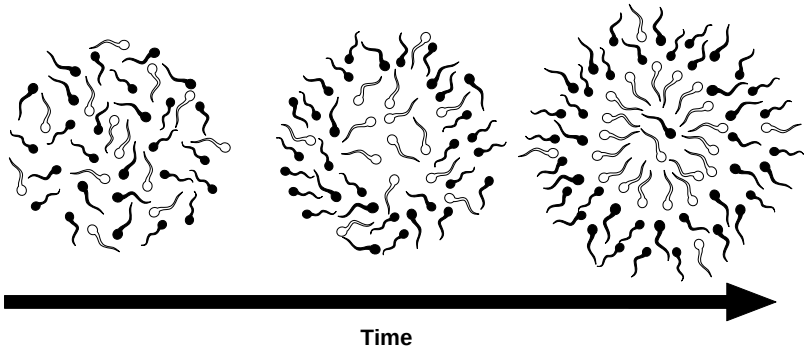

Figure 8. An Illustration Depicting the Tendency of Surfactant Molecules to Self-Align Within an Airborne Droplet of AFFF as Surface Age Increases [2]

In the absence of a free surface, surfactants are inclined to self-organize if their concentration is adequately high; this is referred to as the critical micelle concentration. Beyond the critical micelle concentration, surfactants freely combine to form spherical structures called micelles to reduce the contact between the hydrophobic tail of the molecule and the aqueous solution. Solution concentrations above the critical micelle concentration allow minimum surface and interfacial tensions to be achieved in shorter time periods that scale with an increase in concentration. However, an increase in surfactant concentration does not significantly alter the minimum values of either surface or interfacial tension. Figure 9(a) illustrates the shape of a standard water-soluble micelle. This shape can evolve into complex structures, such as double, cylindrical, and multilayered sheet micelles, if the surfactant concentration increases significantly beyond the critical micelle concentration. Figure 9(b) depicts the relationship between the surfactant's interfacial tension and the surfactant concentration (*C*) denoting the location of the critical micelle concentration [17].

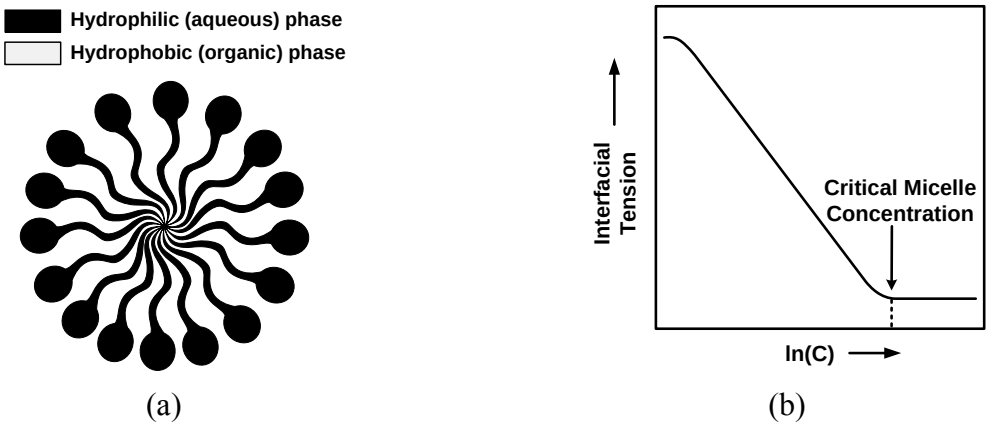

Figure 9. (a) Illustration of a Standard Micelle and (b) Interfacial Tension vs Surfactant Concentration [17]

Although fluorocarbon surfactants are oxidatively stable, they have been found to appear in surface and ground water near military firefighting training sites [14]. In the late 1990s, perfluorooctyl sulfonate (PFOS)-based surfactants used in early 3M-based AFFF compositions

were found to be bioaccumulative, environmentally persistent, slightly toxic, and classified as an emerging contaminant by the United States Environmental Protection Agency (EPA). PFOS was subsequently replaced by presumably more environmentally friendly surfactants like perfluorooctanoic acid (PFOA) in the early 2000s. In 2012, however, PFOA was also recognized as an emerging contaminant, jeopardizing the long-term viability of current AFFF compositions. In response to the negative effect PFOS and PFOA have on human health and the environment, by 2010 the EPA's PFOA stewardship program committed eight major manufacturers to reduce PFOA and its related chemical production by 95%. All PFOA production is to be eliminated by 2015. These concerns over current AFFF concentrate compositions highlight the pressing need for firefighting agent research to identify and preserve key performance characteristics for next generation agents that will be subject to even more rigorous environmental regulations [13 and 19].

2.2.3 Liquid Continuum Characteristics.

AFFF concentrate exhibits many of the same fluid state properties as water, most notably density with others like boiling and freezing point. These properties approach the properties of water even more so once AFFF concentrate is diluted at typical proportions with water to form firefighting agent solution. AFFF concentrate tends to be slightly alkaline at approximately 7.9 pH, but it falls within the acceptable range for tap water between 6.5 and 8.5 pH. Besides its slightly yellow to amber appearance, viscosity and more so surface tension properties differentiate AFFF concentrate from water the most, as alluded to in the previous section. These intrinsic properties are typically used to quantify the influence AFFF has on firefighting jet performance, especially on the continuum scale. Table 2 lists the equilibrium fluid properties of AFFF compared to water at standard conditions.

Table 2. Equilibrium Fluid Properties of Water and AFFF at Standard Conditions

Fluid Property	Water	AFFF
Density ($kg \cdot m^{-3}$)	997.0 [20]	1079 [12]
Dynamic viscosity ($kg \cdot m^{-1}s^{-1}$)	8.9×10^{-4} [20]	7.0×10^{-3} [12]
Equilibrium surface tension ($mN \cdot m^{-1}$)	72.1 [20]	17.4 [12]

Because firefighting jets represent a dynamic process, variation of fluid properties, when exposed to transient conditions or to a range of applied stresses, is of further interest. Although the non-Newtonian behavior of AFFF in its emulsified foam state is well documented, details on the viscous nature of any MIL-SPEC AFFF over a range of applied shear rates was not found. AFFF concentrate derivatives, such as alcohol-resistant AFFF, are known to exhibit strong non-Newtonian behavior. They demonstrate pseudoplastic, shear-thinning, and thixotropic properties due to the addition of rheological modifiers such as xanthan gum resins or Carbopol® [21]. However, these derivatives are beyond the scope of the current study.

Dynamic surface tension data exist for several AFFF compositions, some of which are reproduced to illustrate the property's sensitivity to various controlled conditions [22 and 23]. Dynamic surface tension is strongly dependent on factors such as surfactant concentration, molecular diffusion rates, fluid temperature, and salinity, along with other variables that may affect the surfactant's relationship with the aqueous solution and surrounding atmosphere. For

very low surface ages without surfactant additives, dynamic surface tension approaches the value of the solution (i.e., water). Equilibrium surface tension values are approached for high surface ages. In the case of pure liquids, such as water, surface tension is independent of surface age [22].

Hyland and Williams used a model Kruss BP2 maximum bubble pressure tensiometer to measure dynamic surface tension with sensitivity to AFFF composition, dilution, salinity, and temperature. These relationships are illustrated in figures 10(a) and (b) and 11(a) and (b), respectively [22]. Figure 10(a) shows that MIL-SPEC AFFF formulations behave similarly as expected due to the common equilibrium surface tension values all MIL-SPEC compositions must meet. Figure 10(b) illustrates that as AFFF concentration is increased, dynamic surface tension approaches its equilibrium value more rapidly; a concept illustrated previously on the molecular level in figure 9(b).

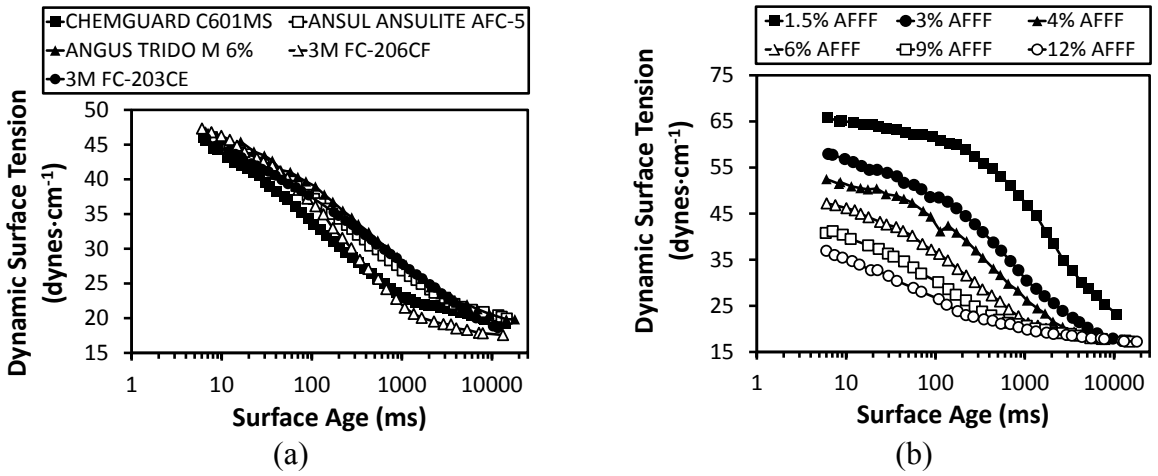

Figure 10. Dynamic Surface Tension vs Surface Age for (a) Various MIL-SPEC AFFF Formulations and (b) Different Concentration Levels [22]

Figure 11(a) shows that for certain MIL-SPEC AFFF formulations, water salinity can significantly affect dynamic surface tension, whereas in others, it plays a negligible role, owing to the diverse secondary (i.e., nonsurfactant) constituents some makers use in the manufacturing process. The salt water solution used represents the effect of ocean water composed of 41.2 g of sea salt (as defined by the ASTM D-1141-52 standard) mixed with 1 L of distilled water [24]. Figure 11(b) illustrates the dynamic surface tension's dependency on temperature as it lowers with increasing temperature, similar to typical viscosity trends. In figures 10 and 11, it should be noted the dynamic surface tension magnitudes of MIL-SPEC AFFF start off almost 50% from one another. But, by a surface age of approximately 10 s, all values are within 25% or significantly less of one another along with the AFFF equilibrium surface tension value listed in table 2.

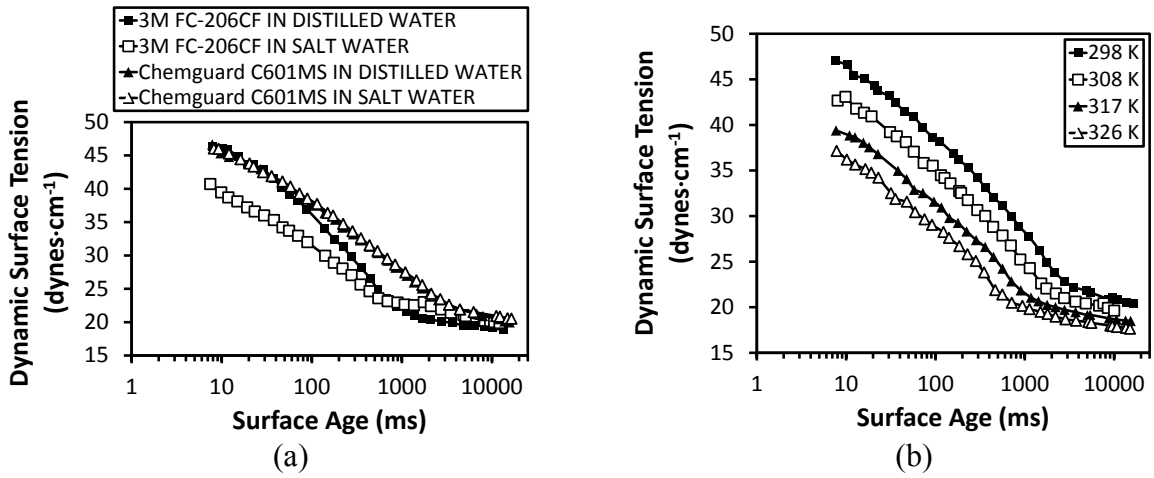

(a) (b)

Figure 11. Dynamic Surface Tension vs Surface Age for (a) Various Salinities and (b) Various Solution Temperatures [22]

2.2.4 Foam Continuum Characteristics.

AFFF fluid dynamics have been analyzed on multiple spatial levels spanning molecular to continuum length scales. Most literature is dedicated to AFFF's state as homogenous, stabilized foam slowly spreading over top fuel layers where interacting fluid surface and interfacial molecular tension forces help drive bulk motion [25]. Very little information is available on the state of foam or foam solution during the jetting process. Specific work has focused on foam stability, rheology, viscosity, as well as its fire suppression capability [5-8, 15, 19, 23, and 26-30].

Nonequilibrium foam behavior is important due to AFFF's thermodynamically unstable, time-dependent life. With temporal scales on the order of a few seconds or less during the jetting process, fluid properties (i.e., surface tension, viscosity, and concentration) help shape downstream foam formation characteristics. The influential degree of each property is still unknown, as is the physical state of AFFF during the firefighting jet transport process. Increases in AFFF concentration typically shorten the nonequilibrium time scale and encourage foam growth to occur more rapidly compared to more diluted AFFF compositions [26]. This trend is shown in figure 10(b) [22]. Some researchers have inferred that quasi-equilibrium conditions can be assumed considering conventional foam evolutionary time scales are on the order of several seconds to approaching minutes. This would hold true for particularly high-speed liquid jets made up of smaller agent droplets that travel relatively short distances. Overall, this would result in the suppression of foam growth [31].

Table 3 lists some of the key chemical and physical performance requirements MIL-SPEC AFFF must meet either in concentration or solution form with water. Some performance characteristics not relevant to the present study, such as corrosion rate, biodegradability, and toxicity, have been omitted from this table.

Table 3. The MIL-SPEC AFFF Chemical and Physical Minimum Performance Criteria [9]

Requirement	Values		Applicable Publication
	Type 3%	Type 6%	
Refractive index (minimum)	1.3630	1.3580	--
Viscosity, centistokes Maximum at 278.15 K Minimum at 298.15 K	 20 2	 20 2	ASTM D445.74
Hydrogen ion concentration (pH)	7.0 to 8.5	7.0 to 8.5	--
Spreading coefficient (minimum)	3	3	--
Foamability Minimum foam expansion Maximum 25% drainage time, minutes (minimum)	 5.0 2.5	 5.0 2.5	 NFPA 412 NFPA 412
Dry chemical compatibility, burn back, resistance time, seconds (minimum)	360	360	--

The spreading coefficient refers to the rate at which AFFF can cover a fuel surface. The spreading coefficient must be positive if spontaneous spreading is to occur. The spreading coefficient (σ_S) due to surface tension is defined by the following relationship:

$$\sigma_S = \sigma_C - \sigma_{AFFF} - \sigma_I \tag{1}$$

where σ_C is the surface tension of cyclohexane, σ_{AFFF} is the surface tension of the AFFF, and σ_I is the interfacial tension between the cyclohexane and AFFF. Foam expansion is determined from one of two methods from NFPA 412. The most common method uses a foam-sampling apparatus to collect foam from a firefighting jet in 1000-mL graduated cylinders positioned below a collecting back board. Foam expansion is calculated in equation 2.

$$Expansion = \frac{volume\ of\ foam}{volume\ of\ solution} \tag{2}$$

Foam 25% drainage time is calculated by monitoring the amount of time it takes for 25% of the agent solution to be drained from the foam captured downstream of a firefighting jet in a similar fashion to the foam expansion test mentioned above. For details on 25% foam drainage time testing and other AFFF foam-testing procedures listed in table 3, refer to either the MIL-SPEC [9] or NFPA 412 standard [11].

2.3 TURBULENT ROUND LIQUID JETS ENTERING STILL AIR.

2.3.1 Early Work on Liquid Jet Instability and Breakup Entering Still Air.

Although the study of liquid jet instability and disintegration when injected into a stagnant gaseous atmosphere has been documented since the early 1800s, the problem of liquid jet breakup, particularly in the turbulent flow regime, is still not fully understood [32-36]. McCarthy and Malloy summarized that early observations on low-speed, laminar jet flows

conducted by Savart followed by theoretical perspectives offered by Plateau resulted in some of the first impressions regarding this complex physical phenomenon. Further contributions by Bidone, Magnus, Buff, and Boussinesq helped pave the way for laminar instability theory substantiated by Rayleigh and Weber, which sets up the discussion for examining turbulent liquid jet breakup behavior. (All of the aforementioned authors are cited by McCarthy and Malloy in reference 33.) Work by Grant, Phinney, Chen and Davis, Hoyt and Taylor, and Ruff et al. have provided the most useful theoretical and empirical perspectives specific to the turbulent liquid jet breakup regime leading into the 1980s [32, 35, and 37-39]. Detailed reviews by Grant, McCarthy and Malloy, Lin and Reitz, Faeth et al., and most recently Birouk and Lekic in 2009, summarize the general physical mechanisms believed to be responsible for liquid jet disintegration into still air, highlighting areas where further work is still needed [32-34, 36, and 40].

Rayleigh proposed that a laminar-free jet surface near the nozzle in a vacuum represents a wide range of infinitesimal, symmetrical disturbances that could be represented mathematically as sinusoidal waves, a basis rooted in small perturbation theory. Through an energy balance between a disturbed and undisturbed water column and extrapolating the surface disturbance growth rate, Rayleigh derived a linearized relationship describing the breakup length for an inviscid laminar liquid jet in air as a sole function of surface tension and inertial forces, expressed as:

$$\frac{Z}{D} = 1.03\left(ln\frac{R}{\eta_0}\right)We_L^{0.5} \tag{3}$$

where Z is the continuous jet breakup length, D is the liquid jet diameter, R is the liquid jet radius, η_0 is the infinitesimal disturbance, and We_L is the Weber number based on liquid jet characteristics. The Weber number is generally defined as the ratio between inertial and surface tension forces, and specifically defined in equation 3 as:

$$We_L = \frac{\rho_L V_J^2 D}{\sigma_{L/G}} \tag{4}$$

where ρ_L is the density of the jet liquid, V_J is the jet nozzle velocity, and $\sigma_{L/G}$ is the surface tension between the liquid jet and the surrounding ambient gas. Rayleigh postulated that liquid jet breakup occurs because infinitesimal axisymmetric disturbances near the nozzle exit grow exponentially until they reach the same length scale of the liquid jet radius causing destabilization, what he referred to as varicose breakup (now referred to as Rayleigh breakup). Equation 3 can also be derived in a similar format using similitude analysis [32 and 33].

Weber extended Rayleigh's efforts with the inclusion of viscous effects by assuming the liquid jet maintains a mean flow with surface disturbances imparted upon it. After developing a characteristic equation for the disturbance growth rate in terms of surface tension and simplifying through an order of magnitude analysis, Weber was able to expand equation 3 to include viscosity [32 and 33]:

$$\frac{Z}{D} = ln\frac{R}{\eta_0}\left\{We_L^{0.5} + \frac{3We_L}{Re_L}\right\} \tag{5}$$

where Re_L is the Reynolds number defined as the ratio of inertial to viscous forces, and specifically in equation 5 with respect to liquid jet characteristics as:

$$Re_L = \frac{\rho_L V_J D}{\mu_L} \tag{6}$$

where μ_L is the dynamic viscosity of the jet liquid. Equation 5 provides a good approximation for the breakup length for limiting cases in which the physical assumptions of an axisymmetric, low-speed laminar Newtonian viscous jet apply, except in peculiar situations, such as for a mercury liquid jet, where the linear slope $ln(R/\eta_0)$ was approximately four times larger compared to other liquids in experiments conducted by Smith and Moss (cited in reference 33). Alternatively, Grant and Middleman (cited in reference 33) state the slope in equation 3 is better represented by the following relation,

$$ln\frac{R}{\eta_0} = -2.66\, ln(Oh) + 7.68 \tag{7}$$

where *Oh*, referred to as the Ohnesorge or stability number, is defined as a combination of the Weber and Reynolds number:

$$Oh = We_L^{0.5} Re_L^{-1} = \frac{\mu_L}{\left(\rho_L D\, \sigma_{L/G}\right)^{0.5}} \tag{8}$$

where dependence on the characteristic velocity (V_J) is removed through a combination of the Weber and Reynolds number. With the addition of equation 8, Grant and Middleman recast equation 5 with modified coefficients from their own experimental work based on a wide range of liquid viscosities but minor changes in surface tension and density [33]:

$$\frac{Z}{D} = 19.5\left\{We_L^{0.5} + \frac{3We_L}{Re_L}\right\}^{0.85} \tag{9}$$

Although linear instability theory forged a mathematical argument for laminar liquid jet breakup, it has since been repudiated by more recent experimental observations identifying irregular surface waves near the nozzle, even in the case of low Reynolds number laminar jets [36]. Phinney among others has brought attention to the lack of a theoretical framework governing turbulent liquid jet flows, exhibiting minor success in extending linearized laminar theory into the turbulent flow regime [35 and 36]. The majority of early turbulent liquid jet stability studies have resulted in empirical correlations, which prove useful in a few limiting situations [33]. Owing to the physical complexities involved with describing liquid jet breakup behavior, especially in the case of transitional to fully turbulent flow, contemporary views recommend more sophisticated aerodynamic theories that also take into account nonlinear interactions associated with the liquid jet's surroundings [36].

2.3.2 Modern Methods of Classifying Jet Breakup.

Modern liquid jet breakup classification is based on regimes that reflect qualitative differences in appearance as the operating conditions are modified. Characteristics such as surface tension, liquid inertia, and aerodynamic forces are the measurable criteria used to quantify these regimes that are absorbed in dimensionless parameters like the Reynolds, Weber, and Ohnesorge numbers [34]. Fundamental principles of primary and secondary atomization are introduced followed by a more rigorous classification of each breakup regime.

Birouk and Lekic define a liquid jet as a "beam of liquid emerging from a nozzle into a quiescent, gaseous atmosphere," and specifically for the current study as a firefighting jet consisting of either an AFFF or water jet discharging into still air [36]. After exiting the nozzle, the liquid disintegrates in either a one- or two-stage process. Primary breakup takes place when the liquid jet core is torn into ligaments and other irregular shapes as its surface interacts in close proximity with the surrounding air to form a multiphase mixing layer. As ligament strands peel away from the liquid jet core, they morph or break off into individual droplets. Primary breakup governs the liquid jet breakup length, starts the atomization process, and facilitates initial conditions for secondary breakup to occur in the dispersed downstream region of the flow [40]. Primary breakup is also heavily dependent upon internal liquid forces derived from surface tension, velocity profile relaxation, and turbulence [33]. Secondary breakup occurs if shed satellite droplets further disintegrate into smaller droplets resulting from an even stronger influence from the surrounding air. Figure 12(a) illustrates near-field representations of primary breakup from the liquid jet surface adapted from shadowgraph photography recorded by Sallam and Faeth [36]. Figure 12(b) depicts both primary and secondary breakup with respect to the liquid jet breakup length.

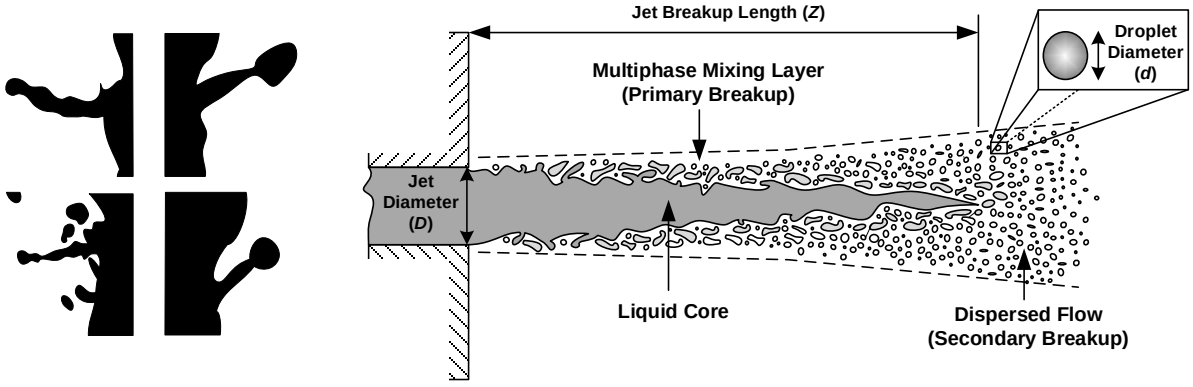

Figure 12. (a) Shadowgraphs of Ligaments Peeling Away From an Intact Liquid Jet Core [36] and (b) An Illustration of the Nozzle Exit Region Depicting Primary and Secondary Breakup [40]

As illustrated in figure 13, liquid atomization can be further resolved into four liquid jet breakup regimes: the Rayleigh (varicose) breakup regime I, the first wind-induced (sinuous) breakup regime II, the second wind-induced breakup regime III, and the atomization breakup regime IV. The physical characteristics that define each regime are discussed after figure 13.

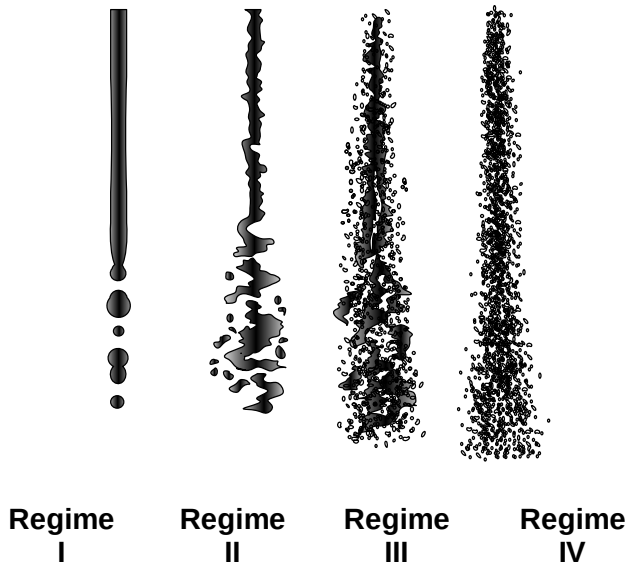

Figure 13. The Four Regimes of Liquid Jet Breakup [41]

- The Rayleigh Liquid Jet Breakup Regime I—The Rayleigh (or varicose) regime is characteristic of laminar, low-velocity inviscid liquid jets with long wavelengths and small, symmetric surface perturbations dominated by the interaction between surface tension (capillary) and inertial forces. Aerodynamic effects are considered insignificant in the Rayleigh breakup regime where surrounding air entrainment is negligible. Drop diameters that form downstream are sized slightly larger than that of the liquid jet diameter, exclusively characterized by primary break-up mechanisms [34 and 36].

- The First Wind-Induced Liquid Jet Breakup Regime II—The first wind-induced, sinuous, or wavy regime are common referral names that involve slightly higher relative velocities compared to the Rayleigh regime. Liquid jet dynamics are identified by sinusoidal (or transverse) vibrations that are still dilatational by nature but slightly amplified by the surrounding ambient air. Similar to the Rayleigh regime, primary breakup dominates this regime as well. The resulting droplet formation is sized on the order of the liquid jet diameter [34 and 36].

- The Second Wind-Induced Liquid Jet Breakup Regime III—The second wind-induced regime has a more pronounced aerodynamic interdependency with atmosphere conditions compared to lower regimes causing more liquid jet surface irregularity to form. Primary and secondary breakups are easily visible in this regime, forcing downstream droplet formation much smaller compared to the jet diameter [34 and 36].

- The Atomization Liquid Jet Breakup Regime IV—The atomization regime represents liquid jets with the highest velocities and consequently the highest kinetic energy. This regime is distinguished by the formation of a dense, fully dispersed liquid jet that breaks down into fine droplets very close to the nozzle exit resulting almost exclusively in secondary breakup, often the result of cavitating nozzle conditions. The existence of a coherent liquid core is widely debated in this regime, and those that do believe in its existence agree it is very short and ends close to the nozzle exit [34 and 36].

Historically, each breakup regime has been graphically defined using two different approaches: Ohnesorge's classification and the liquid jet stability curve. Depicted in figure 14, Ohnesorge's classification provides the most reliable approach by identifying each regime within a logarithmic plot of Ohnesorge versus Reynolds number. Most conventional firefighting jets are characterized by pressure-atomized nozzle conditions that fall within the atomization liquid breakup regime IV highlighted in figure 14. Ohnesorge's classification can be similarly defined via the liquid and ambient gas Weber number, We_L and We_G, respectively, listed in table 4. The ambient gas Weber number is defined as follows with ρ_G denoting the ambient gas density [36].

$$We_G = \frac{\rho_G V_J^2 D}{\sigma_{L/G}} \tag{10}$$

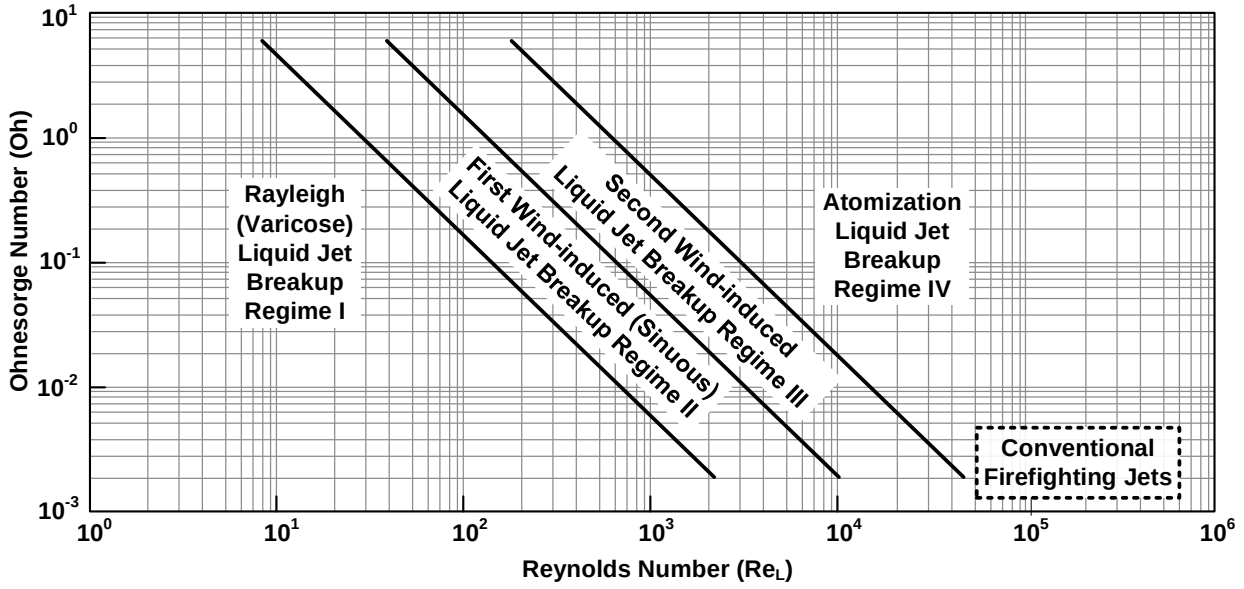

Figure 14. Liquid Jet Breakup Regime Classification in Quiescent Air With Respect to Reynolds Number and Ohnesorge Number [36]

Table 4. Ohnesorge's Classification of Various Liquid Jet Breakup Regimes Using Liquid and Ambient Gas Weber Number [36]

Liquid Jet Breakup Regime	Range
Rayleigh Liquid Jet Breakup Regime I	$We_L > 8$, $We_G < 0.4$
First Wind-Induced Liquid Jet Breakup Regime II	$0.4 < We_G < 13$
Second Wind-Induced Liquid Jet Breakup Regime III	$13 < We_G < 40$
Atomization Liquid Jet Breakup Regime IV*	We_G ~> 40

*Conventional firefighting liquid jet breakup regime.

An alternate approach to classifying the liquid breakup regimes is by analyzing the ambient gas-to-liquid jet to ambient-air density ratio (ε) as a function of Reynolds number, defined as:

$$\varepsilon = \rho_G \cdot \rho_L^{-1} \tag{11}$$

Figure 15 depicts the nonlinear sensitivity the gaseous Weber number has on defining the breakup regimes as this ratio approaches zero. With a ratio of about 0.001 for water ejecting into still air, the conventional firefighting liquid jet breakup regime is again highlighted in its respective location within the atomization liquid breakup regime. Further information on the gaseous Weber number correlation shown in figure 15 separating breakup regime I from regime II are in the associated figure reference.

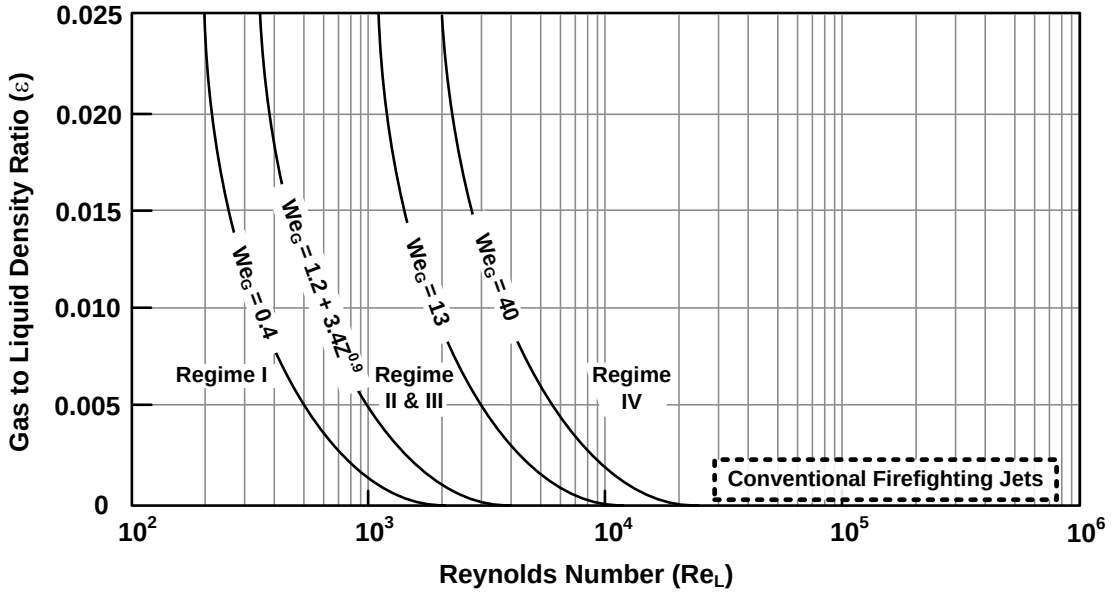

Figure 15. Liquid Jet Breakup Regimes Classification in Still Air With Respect to Weber Number, Reynolds Number, and the Gas-to-Liquid Density Ratio [36]

The liquid jet stability curve shown in figure 16 provides an alternate interpretation of the liquid jet breakup regimes depicting liquid jet breakup length as a function of jet efflux (flow) velocity. Although qualitative trends of the liquid jet stability curve are well accepted, precise numerical bounds on the data remain a point of contention due to data collection inconsistencies among

researchers. The conventional firefighting liquid jet breakup regime in figure 16 is estimated based upon values defined in figures 14 and 15.

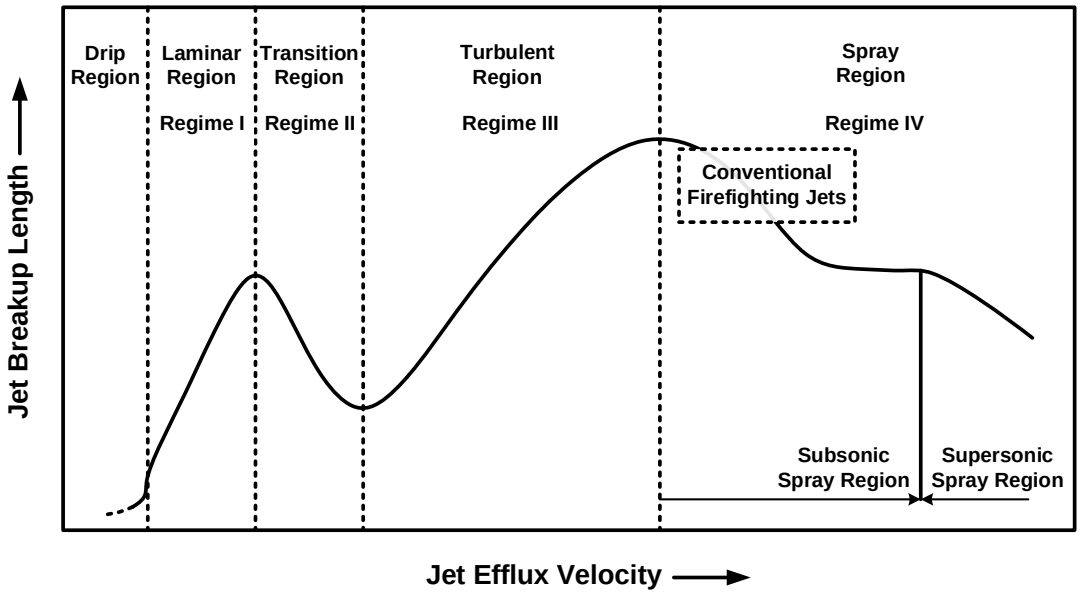

Figure 16. The Jet Stability Curve for Liquid Jets Entering a Gaseous Atmosphere [36]

The liquid jet stability curve is broken down into five subsequent, interconnected regions with reference to the four liquid jet breakup regimes already mentioned for comparison: the drip region, the laminar region, the transition region, the turbulent region, and the fully developed spray region. The laminar flow region is reflective of the Rayleigh breakup regime I depicting a constant increase in the liquid jet breakup length as velocity increases, and graphically representative of the classic linear instability analysis referred to earlier. The preceding drip region has a sporadic, inconsistent breakup length due to almost negligible flow velocity and is ignored for breakup regime classification. The transition region (also referred to as the wavy jet region) is representative of Ohnesorge's first wind-induced liquid jet breakup regime II characterized by the production of surface transverse as opposed to symmetrical waves to dissipate energy more rapidly, but with no significant aerodynamic interactions present. The first influential nonlinear interactions with the surrounding environment emerge here, and overall breakup length begins to decrease with increasing velocity [36]. Grant proposed an empirical correlation for this regime based upon fully developed parabolic profiles emanating from long tubes, expressed as:

$$Re_L = 3.25(Oh)^{-0.28} \tag{12}$$

which corresponds well with equation 7, but only for liquid jets interacting with standard atmospheric conditions [32, 33, and 36]. As inertial forces continue to increase with increasing jet velocity, transition to a fully turbulent flow causes shearing aerodynamic forces to dominate the liquid-stagnant air interface indicative of the second wind-induced breakup regime III. This restabilizes the flow field causing the liquid jet breakup length to increase again. The interaction of liquid jet turbulence and atmospheric effects play a paramount role in the turbulent breakup

regime because ambient air properties like pressure and density can amplify or dampen surface perturbations and three-dimensional (3-D) turbulent structures resulting in drastically different breakup lengths and overall jet behavior. The physics in the fully developed subsonic spray regime are analogous to the atomization breakup regime IV. Liquid jet breakup in the supersonic spray regime introduces more complex nonlinearities and is beyond the scope of inquiry for conventional firefighting jets and the present study [36].

Key elements known to significantly influence liquid jet breakup discharged into still air, especially in the turbulent flow regime, are summarized [34-37, 39, and 42]:

- Aerodynamic and hydrodynamic force interactions between the coherent liquid jet surface, expelled droplets, and ambient air interface
- Thermodynamic and physical states of both the liquid and ambient air
- Upstream delivery disturbances such as supply line pressure vibration and unsteady electromechanical disruption
- Nozzle internal flow characteristics such as flow separation and cavitation
- Liquid jet velocity profile attributes at the nozzle exit
- Liquid jet vorticity, liquid turbulence, and ambient-air turbulence magnitudes

2.3.3 Secondary Breakup of Liquid Droplets in Still Air.

Because conventional firefighting jets are principally characterized by atomization via secondary breakup, further attention must be paid to the physical mechanisms responsible for satellite droplet disintegration due to interactions with the surrounding air. Based on figures 14 and 15, liquid jet disintegration is enhanced for higher Reynolds numbers ($Re_D > 10^3$) and lower Ohnesorge number flows ($Oh < 1$), or for when viscous effects are minimal. Five droplet breakup regimes have been identified: vibrational, bag, multimode, sheet-thinning, and catastrophic. These breakup regimes are well defined via the gaseous Weber number based on droplet diameter d, defined as:

$$We_d = \frac{\rho_G V_J^2 d}{\sigma_{L/G}} \tag{13}$$

The gaseous Weber number loses its dependence on Ohnesorge number for conventional firefighting jet flow regimes, or more generally for liquid jets entering gaseous atmospheres that exhibit Ohnesorge numbers less than 0.1 [36]. The five droplet breakup regimes are shown in figure 17 with their respective gaseous Weber number ranges presented in table 5. Each droplet breakup regime is described after table 5.

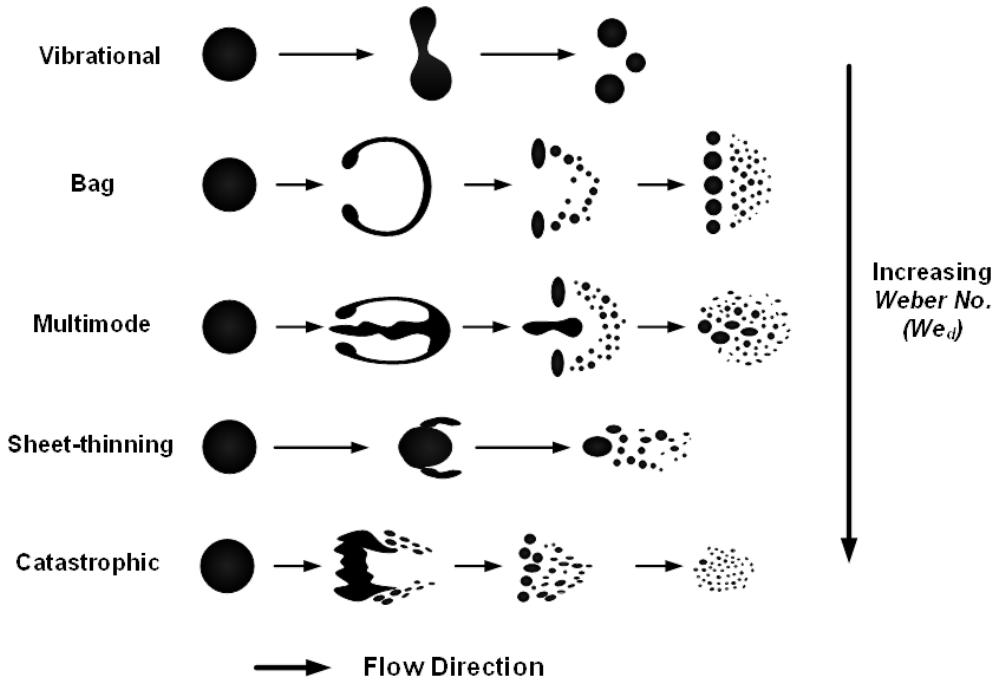

Figure 17. The Five Droplet Breakup Regimes [43]

Table 5. The Five Droplet Breakup Regimes Based on Weber Number [43]

Breakup Regime	We_d Range
Vibrational	We_d <~ 12
Bag	~ 12 < We_d <~ 35
Multimode	~ 35 < We_d <~ 80
Sheet-Thinning	~ 80 < We_d <~ 350
Catastrophic	~350 > We_d

- The Vibrational Droplet Breakup Regime—The vibrational breakup regime is characterized by negligible aerodynamic stripping forces and droplet fragmentation due to destabilizing oscillations generated at the natural frequency of the parent droplet. Vibrational droplet deformation typically morphs into an oblate spheroid resulting in child droplets sized on the order of the parent droplet. This breakup regime requires longer breakup times compared to other breakup regimes, and it is often overlooked, even though deformation originates here and significantly affects secondary breakup drag and trajectory.

- The Bag Droplet Breakup Regime—The bag droplet breakup regime is best described in four stages where aerodynamic forces have become elevated: (1) initial deformation where spherical droplets become oblate spheroids, (2) bag growth where the drop center expands downstream from a ring opening into a balloon-like shape, (3) bag breakup where the bag ruptures into a large number of small droplets, and (4) ring breakup where, finally, the bag ring bursts into further satellite droplets forming several smaller fragments. Although the physical mechanisms that govern bag growth are still not well

understood, most believe dynamics and overall breakup structure are guided by capillary instabilities as well as local air and liquid disturbances due to turbulence and particulate impurities.

- The Multimode Droplet Breakup Regime—The multimode breakup regime, also known as the bag-and-stamen or dual bag breakup regime, is a transitional regime that exhibits characteristics of both bag and sheet-thinning droplet breakup due to further increased aerodynamic influence. This regime acts similar to bag breakup, except the central core is maintained further downstream resulting in the existence of a sustained internal plume where drops are continuously stripped, reflecting sheet-thinning behavior.

- The Sheet-Thinning Droplet Breakup Regime—Sheet-thinning droplet breakup exhibits rapid shear droplet deformation due to high relative velocity gradients induced between the droplet surface and the surrounding air. Ligament stripping occurs along the droplet edge until the droplet has completely disintegrated. The physical processes responsible for this regime are generally disputed with accepted theories driving severe fragmentation based on boundary layer stripping or shear-stripping mechanisms observed along the liquid-air interface.

- The Catastrophic Droplet Breakup Regime—Catastrophic droplet breakup is characteristic of low-density liquid jets with droplets at extremely high relative velocities to that of the surrounding air. This regime is dominated by the growth of unstable surface waves along the liquid-air interface that eventually penetrate the droplet, causing catastrophic shattering. Both Rayleigh-Taylor and Kelvin-Helmholtz instabilities are well represented in this breakup regime. Alternative breakup theories are offered based on shear-induced entrainment and boundary layer stripping mechanisms mentioned earlier, except droplet surface disturbances play a stronger role in determining wave propagation and final droplet fragmentation.

Experimental efforts have shown that for liquid-to-ambient gas density ratios over 500 (e.g., firefighting jets), primary breakup is governed mainly by upstream liquid turbulent conditions and velocity profiles dictated by nozzle entrance and geometric conditions. Velocity profile relaxation, or the act of momentum transfer between layers normal to the direction of flow, imposes relative motion on the jet velocity profile as it expands from the confines of the nozzle. These redistributive forces are destabilizing, enhance mixing rates, and add to surface disturbances already present along the liquid-air interface. Thus, fully developed uniform or plug profiles characteristic of turbulent jets are naturally more stable compared to laminar jets represented by more rounded, parabolic profiles. Secondary breakup is more dependent on the surrounding air turbulence and its aerodynamic interaction with individual liquid droplets [32, 33, 36, and 44-46].

2.3.4 Experimental Flow Characterization With Extension to Firefighting Jets.

Most modern, experimental, fire suppression research involves characterizing and enhancing water mist systems for indoor fire protection, which is beyond the scope of the present study. However, earlier work specific to firefighting jets examined the delivery process of high-flow, turbulent water jets. Few mathematical correlations exist for firefighting streams because large

characteristic, turbulent-length scales are not accounted for in traditional breakup theories based on surface tension effects. Aspects such as nozzle discharge coefficient tuning, methods to reduce turbulence, and trajectory analysis are the major emphases in this area of research, with more recent developments dedicated to investigating the role droplet size and distribution play. The average consensus from most researchers is that maximum jet throw distance is achieved by delivery mechanisms that sustain a uniform velocity profile, remove swirl, and reduce turbulence at the nozzle entrance [47]. Although flow characterization of chemical additives to alter liquid jet breakup behavior has been well documented from a variety of industries, little information is available regarding the application of foaming surfactant additives such as AFFF.

The study of firefighting jets has been an on-going effort since the late 1800s with Freeman's pioneering work analyzing the hydraulics of firefighting agent delivery systems, focusing primarily on the optimization of nozzle discharge coefficients [48]. Freeman's investigation into the physical fundamentals of firefighting streams not only helped give birth to the fire research community, but served as a keystone reference for decades to come. Rouse, Howe, and Metzler examined the role of turbulence nearly 70 years later through a comprehensive evaluation of high-flow water jets for naval firefighting [49]. The work of Rouse et al. provided the first detailed description of turbulent flow structures within firefighting jets by analyzing their negative impact on agent delivery efficacy in three major areas: (1) a reduction in internal flow efficiency as the agent navigates the delivery system and nozzle geometry, (2) the transverse growth of turbulent eddies interacting with the air orthogonal to the firefighting jet's trajectory, and (3) entrainment of the surrounding atmosphere forming a surge of air in the direction of the flame front. Rouse et al.'s work elevated the current state-of-the-art nozzle design by applying turbulent flow fundamentals to address practical firefighting suppression needs. Murakami and Katayama also examined losses in firefighting jets due to turbulence, providing a detailed review of discharge coefficient theory studying performance affecting factors such as nozzle geometry, surface roughness, and flow straighteners [50].

Rouse et al.'s work included the construction of an indoor 100- by 10- by 14-ft test facility where flow visualization and jet concentration measurements were conducted catching the agent normal to the oncoming flow along with full-scale trajectory experiments. Firefighting jet disintegration was studied indoors using high-speed photography in conjunction with a specialized profilometer using a high-intensity horizontal beam of light. Figure 18 depicts the experimental gallery outlining the relative location of the pumping system, monitor station, and spray capture zone. Figure 19(a) shows a sample firefighting jet concentration plot, and figure 19(b) illustrates the sampler apparatus used to record the measurements. A typical concentration plot consisted of over 900 data acquisition points [49].

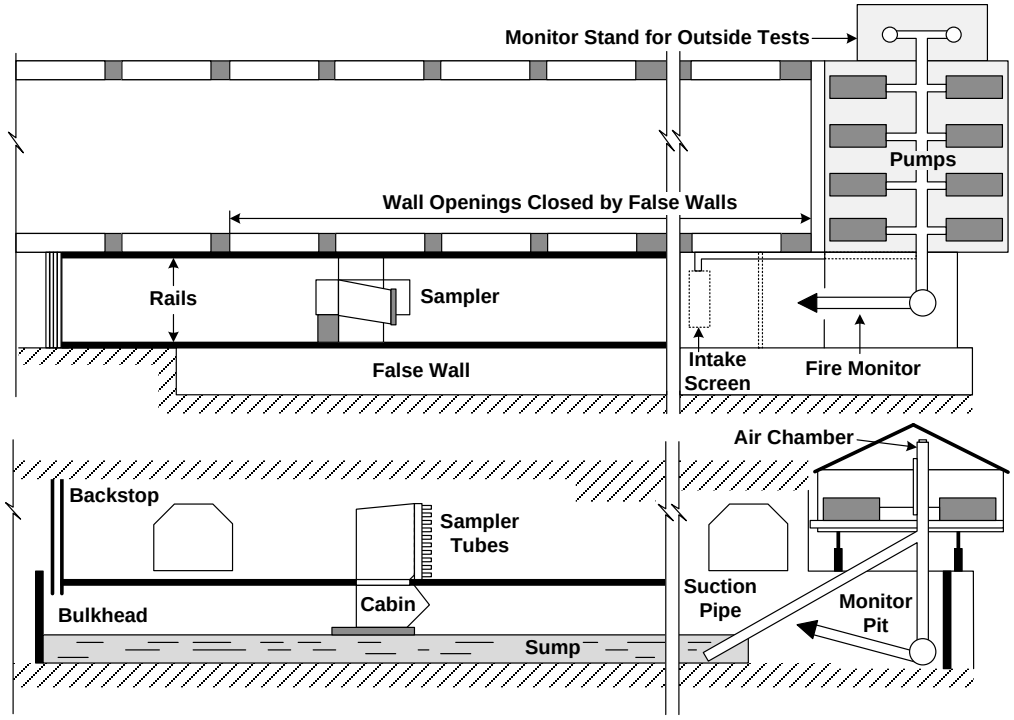

Figure 18. The Indoor Firefighting Jet Test Facility Layout [49]

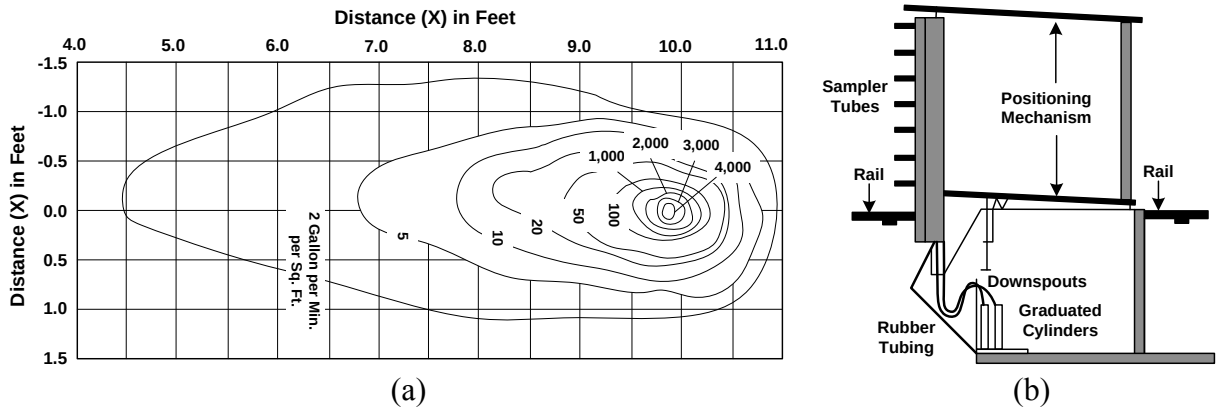

Figure 19. (a) A Sample Firefighting Jet Concentration Plot 27 m From a 30° Inclined Nozzle and (b) The Sampler Tube Apparatus Used to Record the Jet Concentration Plot [49]

Testing higher-flow rate firefighting jets required an exterior target stand designed similar in stature to the sampler apparatus, but instead having a general open capture area on the order of 10 m^2 (100 ft^2). Exterior trajectory measurements proved quite challenging with favorable atmospheric conditions present about 1% of the time [49]. Analogous water jet capture efforts were conducted later by Theobald to optimize nozzle design in terms of maximizing agent delivery quantities at particular downstream locations [51]. Figures 20 and 21 illustrate Theobald's methodology.

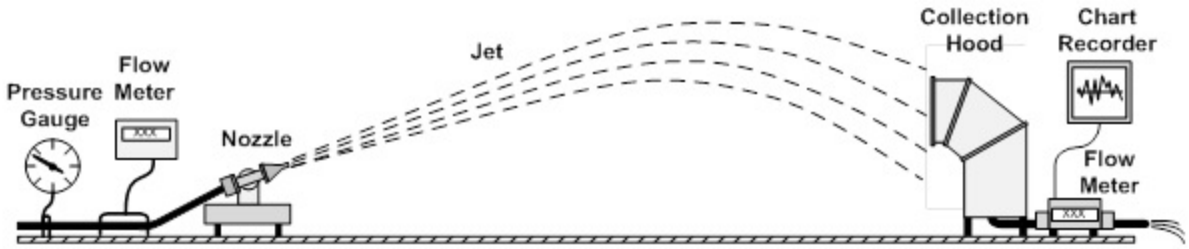

Figure 20. Theobald's Test Configuration for Measuring Downstream Nozzle Delivery Efficiency [51]

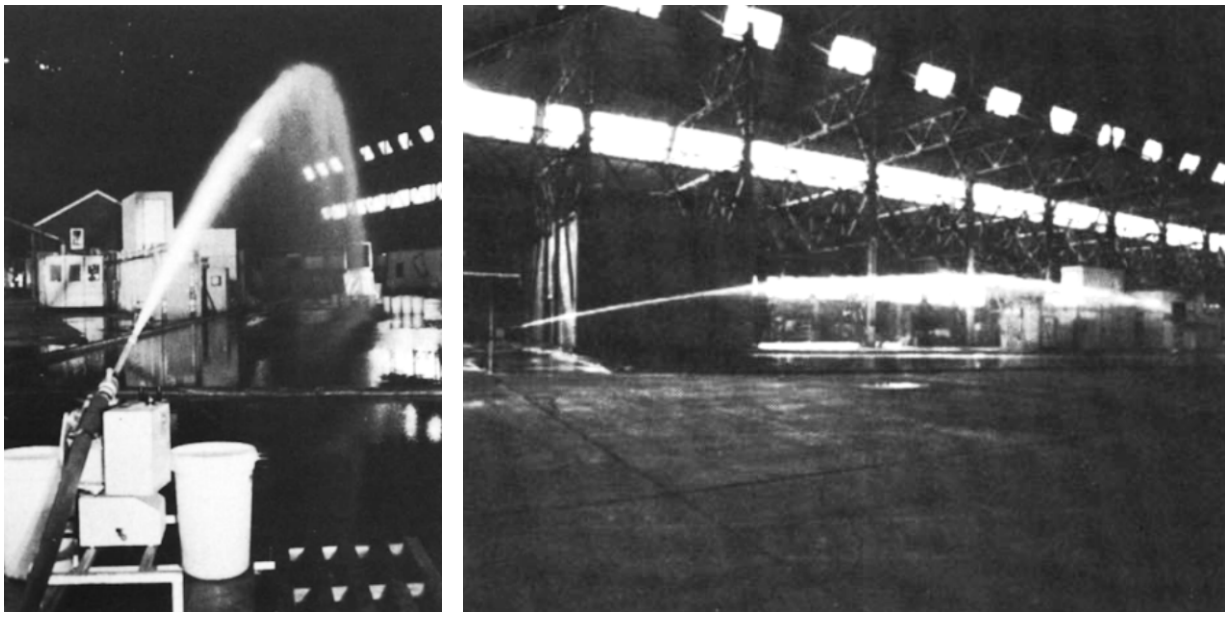

(a) (b)

Figure 21. Theobald's Test Configuration for Measuring Downstream Nozzle Delivery Efficiency (a) Axial View and (b) Horizontal View [51]

In a different study, Theobald determined the range and distribution of firefighting jets using what he referred to as a "continuous bucket" approach to analyze agent accumulation as a function of pressures ranging from approximately 200 to 400 kPa (2 to 4 bar) [51]. Figure 22 depicts the results from his analysis showing, as pressure increases, accumulation disperses over a wider area while the deliver area increases.

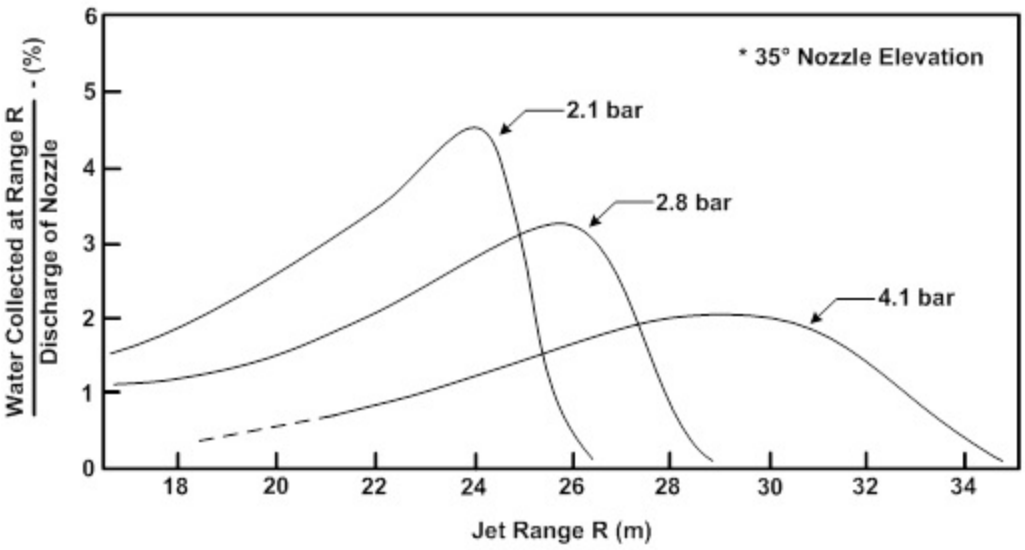

Figure 22. Theobald's "Continuous Bucket" Results Depicting Dispersion Variation With Nozzle Pressure [51]

Geyer conducted one of the first known studies on AFFF characterization to determine its firefighting compatibility with protein foams and prospective value to aviation fire suppression. The scope of his work involved quantifying full-scale fire suppression, fire containment, and foam characteristics from various AFFF manufacturers. Geyer measured foam quality among other bulk fluid properties, fire suppression effectiveness, as well as provided full ground pattern estimates for different nozzle designs. His work also outlined the first working guidelines for AFFF [5].

Multiple authors have used various methods to quantify turbulent liquid jet breakup and better define the stability curve, particularly for firefighting jet applications. The most common experimental techniques are based on monitoring the change of electrical resistance of a conductive substrate placed normal to the oncoming firefighting jet at various axial locations downstream of the nozzle, a practice applied by Phinney, Hiroyasu, and Theobald [35, 42, and 52]. Figure 23(a) illustrates Theobald's measurement concept, and figure 23(b) depicts the firefighting jet stability's sensitivity to nozzle design. Theobald's work developing firefighting jet stability curves for a variety of firefighting nozzles proved considerably sensitive to nozzle geometry reaffirming conclusions presented earlier [52].

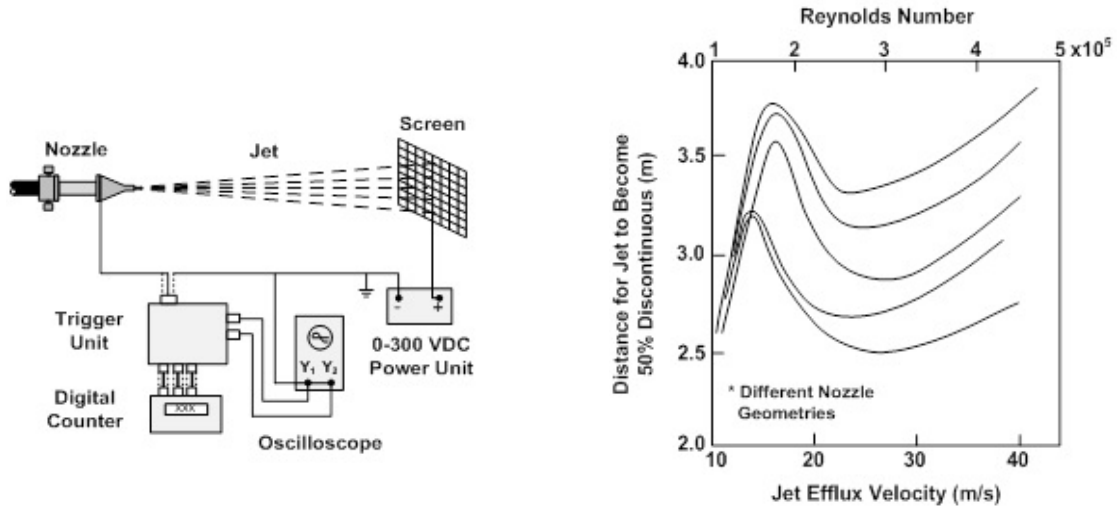

(a) (b)

Figure 23. (a) A Schematic of the Firefighting Jet Continuity Measurement Apparatus and (b) A Plot Illustrating the Dependence of Firefighting Jet Stability on Nozzle Design [52]

Theobald also formed regressions correlating factors such as maximum firefighting jet height and range based upon nozzle pressure and nozzle diameter, concluding primary breakup and trajectory could be approximated by the projectile equations of motion up to apogee (or maximum height) of the firefighting jet. Once secondary breakup occurs due to increased aerodynamic effects, range becomes a stronger function of droplet size [52].

2.3.5 Computational Modeling Methods With Extension to Firefighting Jets.

Little CFD work has been conducted specific to firefighting jets. Most modeling progress in the field of turbulent liquid jets entering still air has been with respect to fuel spray model development to enhance internal combustion engine performance. Computational firefighting jet research has its roots in the late 1970s when Hatton and Osborne developed a numerical technique to predict water jet trajectories exposed to various operating conditions such as efflux velocity, flow rate, nozzle elevation, along with head and tail wind effects [47]. They solved seven simultaneous projectile equations of motion explicitly, and simulations were validated with experimental data from Rouse et al. [49]. The results affirmed that for very large firefighting jet streams operating at moderately low nozzle pressures, the flow path can be adequately modeled with first order accuracy [47 and 52]. Although Hatton and Osborne did not report results for higher-nozzle pressures, it is speculated this approach would be less accurate and loses applicability because of secondary breakup domination less representative of slug or projectile-like jet flow. Figure 24 illustrates example results from Hatton and Osborne's work.

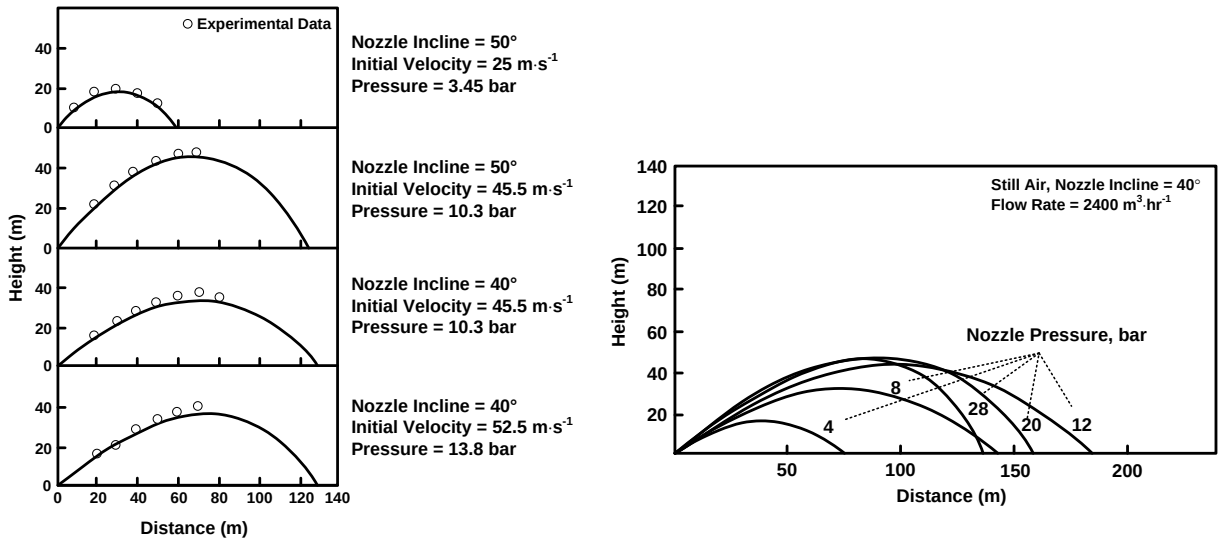

(a) (b)

Figure 24. Numerical Solutions of Large-Scale Firefighting Jet Trajectories [47]

Modern CFD methods have approached the challenge of predicting liquid jet breakup using a wide range of sophisticated numerical techniques. Several extensive reviews on computational gas-liquid, two-phase jet flows have been conducted, including works by Jiang et al., Gorokhovski and Herrmann and, most recently, Archambault in 2010 [53-55]. Most CFD multiphase jet modeling flow classifications fall into one of three main categories: stochastic, Euler-Euler, or Euler-Lagrange. Stochastic or probabilistic modeling methods are often based on a probability density function that describes the indiscriminate evolution of a droplet property interacting with the gaseous phase capable of gathering a wide range of statistics at every point in the flow. They are often advantageous for modeling highly atomized, dispersed liquid jet flows that result in a very random motion [56].

Euler-Euler or dual-continuum techniques govern droplet transport by a set of conservation equations assigned to each phase whereby coupling is achieved through each phase's respective source terms [56]. Dual-continuum techniques are generally not well suited for modeling firefighting jets because the discrete droplet phase is treated as a continuous medium not indicative of the firefighting jet atomization flow regime classification noted earlier. However, application may exist for very high-flow, low-pressure jets where local droplet number densities are high enough such that most of the liquid jet core stays intact so that it can be assumed continuous with negligible dependence on secondary breakup. Volume of fluid (VOF) modeling is a popular industrial Euler-Euler technique suitable for this type of modeling. However, VOF modeling is highly reliant on the mesh resolution interface between the two fluid mediums and not computationally efficient for modeling large-scale firefighting jets that are dominated by secondary droplet breakup mechanisms [56]. Figure 25 depicts a high-fidelity direct numerical simulation (DNS) using VOF modeling techniques conducted by Menard, Tanguy, and Berlement [57]. The figure shows the details of a 3-D turbulent liquid jet atomization process including a close-up of primary ligament and droplet breakup.

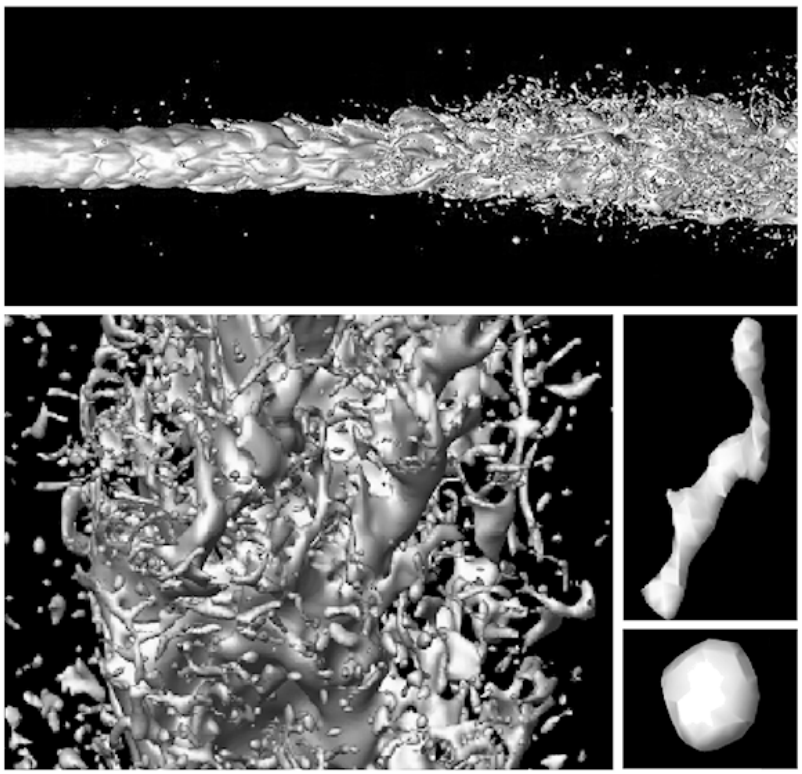

Figure 25. A 3-D Model of Liquid Jet Surface and Breakup Near the Nozzle Using VOF Techniques [57]

Euler-Lagrange methods describe liquid jets by injecting discrete droplets into the continuous gas phase. Droplet time-accurate trajectories are calculated by numerically integrating the Lagrangian equations of motion. Reynolds-Averaged Navier-Stokes modeling is often unwisely chosen to govern the gas phase due to a conflicting time-accurate versus time-averaged description of the interacting discrete and continuous phases, respectively. However, its implementation is often the rule rather than the exception due to computational resource limitations. A more appropriate physical treatment of the Eulerian phase is to use an inherently unsteady method such as large eddy simulation (LES) or DNS to match the unsteady nature of the Lagrangian phase. For most time and length scales associated with industrial engineering problems, DNS computational costs are too prohibitive. Thus, LES methods with well-described spatial filters provide a workable compromise. The common limiting factor with Euler-Lagrange techniques is the number of droplet trajectories required to resolve a typical firefighting jet, especially for large-length scales indicative of real-world firefighting agent delivery systems. To reduce computational overhead, success has been shown grouping droplets into parcels, each of which are tracked separately. However, accurate coupling of the interphase exchange terms and submodeling of the discrete phase interaction with itself can be critical, depending on the dominating flow physics within the problem [55]. It should be noted that several hybrid methods of the three aforementioned classes exist whereby detailed exchange must occur between primary and secondary breakup mechanisms. Most of these methods are still relatively novel and have yet to make their way into commercial codes for interaction with other submodeling methods such as combustion modeling [56]. Figure 26 shows the evolution of a high-velocity

turbulent liquid jet injected into still air using the Euler-Lagrange approach from a simulation conducted by Shi and Kleinstreuer [58]. The figure shows the change in overall liquid jet shape and droplet diameter over time.

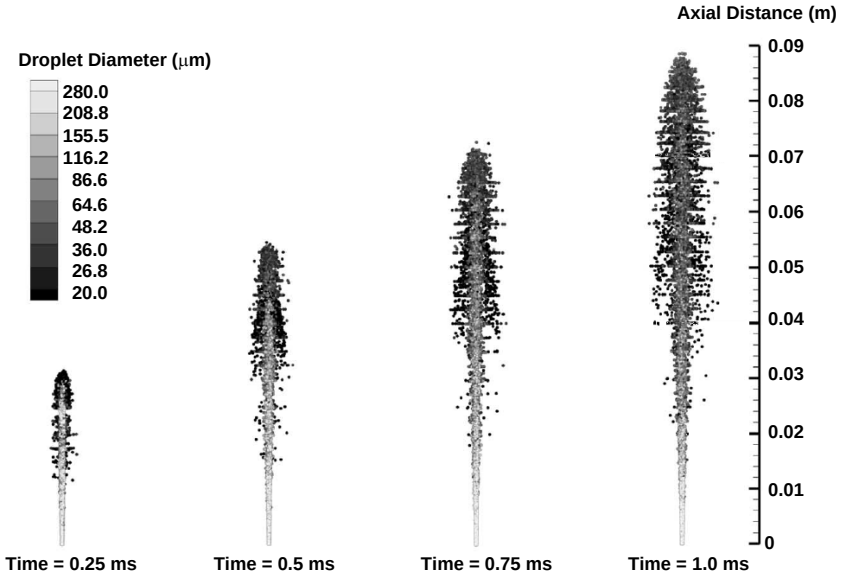

Figure 26. Time-Evolved CFD Results From an Euler-Lagrange Liquid Jet Flow Model [58]

Similar to experimental research, little work exists on the general application of CFD modeling of large-scale water jets, particularly those designed for fire suppression or interaction with other combustion submodeling techniques. Most work in this area involves modeling sprinkler sprays for the use inside of residential buildings to quantify aspects such as nozzle discharge coefficients, water mist spray optimization, and to address the general problem of predicting the amount of fire suppression agent required to suppress a unique indoor fire threat. The majority of these approaches apply Euler-Lagrange techniques in commercial CFD packages referred to as either discrete phase model (DPM) or particle tracking model methods [59-63]. High-fidelity fire suppression applications used to model firefighting jet interactions with larger, outdoor fire environments have been successfully implemented by DesJardin and Gritzo on the SANDIA in-house CFD (code named VULCAN) for simulating cooling jet interaction with LES fires [64].

3. AQUEOUS FIREFIGHTING AGENT APPLICATION LABORATORY.

3.1 OVERVIEW.

To experimentally characterize firefighting jets, a flow parameter envelope was selected to accommodate practical, small-scale experimental conditions while not significantly sacrificing relational validity to a full-scale firefighting jet environment. To accomplish this task, an indoor test facility was constructed to maximize firefighting jet dimension while eliminating outdoor atmospheric influences. A 25- by 9-m (80- by 30-ft) mezzanine storage space in the West Virginia University (WVU) hangar at the Morgantown, West Virginia, Municipal Airport (Hart Field) was converted into an aqueous firefighting agent application laboratory for the experimental phase of this study. Figure 27 shows most of the major laboratory features.

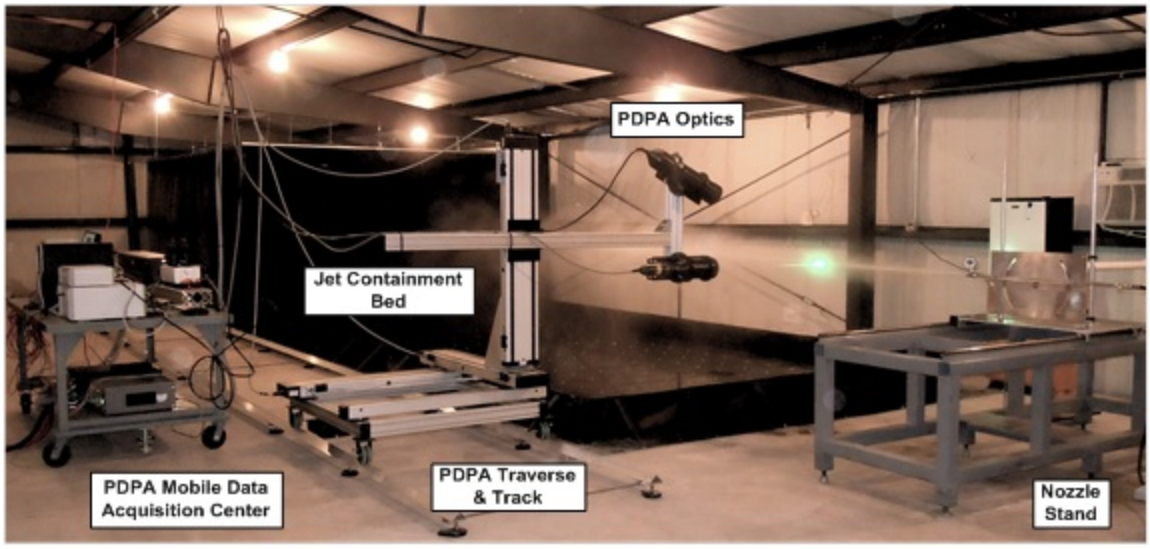

Figure 27. Key Components of the Aqueous Firefighting Agent Application Laboratory

Besides essential features required for wet-laboratory operation, a custom firefighting agent delivery system, nozzle apparatus, firefighting jet containment bed, backdrop curtain for flow visualization, and mobile PDPA were key additions to the transformation. All components were custom fabricated unless otherwise noted. To manage spray drift, dilute AFFF droplet emissions, and help maintain a constant relative humidity, a 221-$m^3 \cdot min^{-1}$ (7800-$ft^3 \cdot min^{-1}$) exhaust fan was installed to exchange laboratory air about every 3.5 minutes. A 51/34-mJ (48,000/32,000-Btu) heating and cooling system was added to air condition the space. Standard 110-V electrical service was also installed throughout the laboratory along with 208 and 480 V to power the air conditioning units, 5-Watt PDPA laser, and firefighting jet delivery system. Figure 28 shows a schematic of the laboratory depicting the overall layout including all critical components. Figure 29 depicts key laboratory dimensions including the origin and orientation of the coordinate system employed throughout this effort.

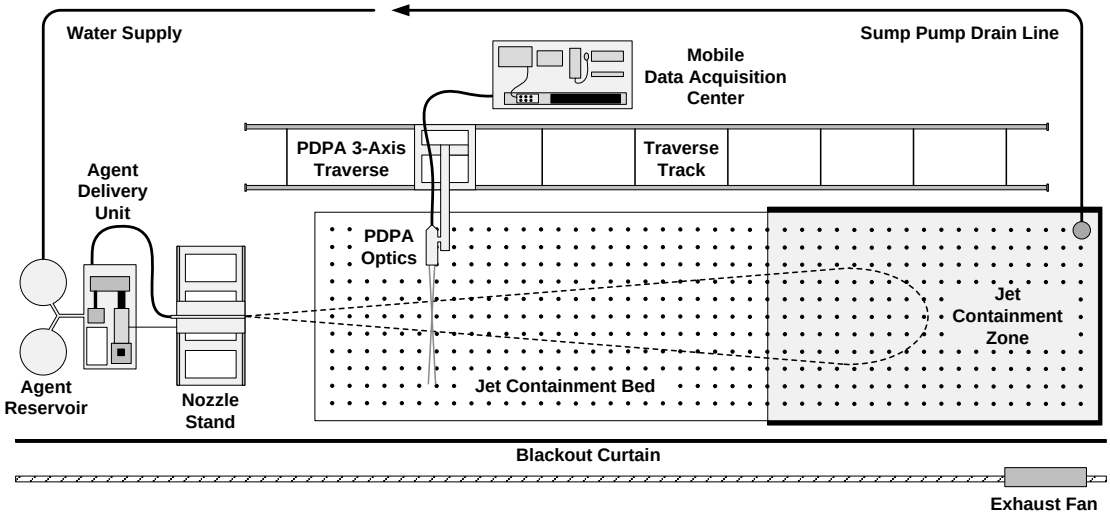

Figure 28. Schematic of the Aqueous Firefighting Agent Application Laboratory

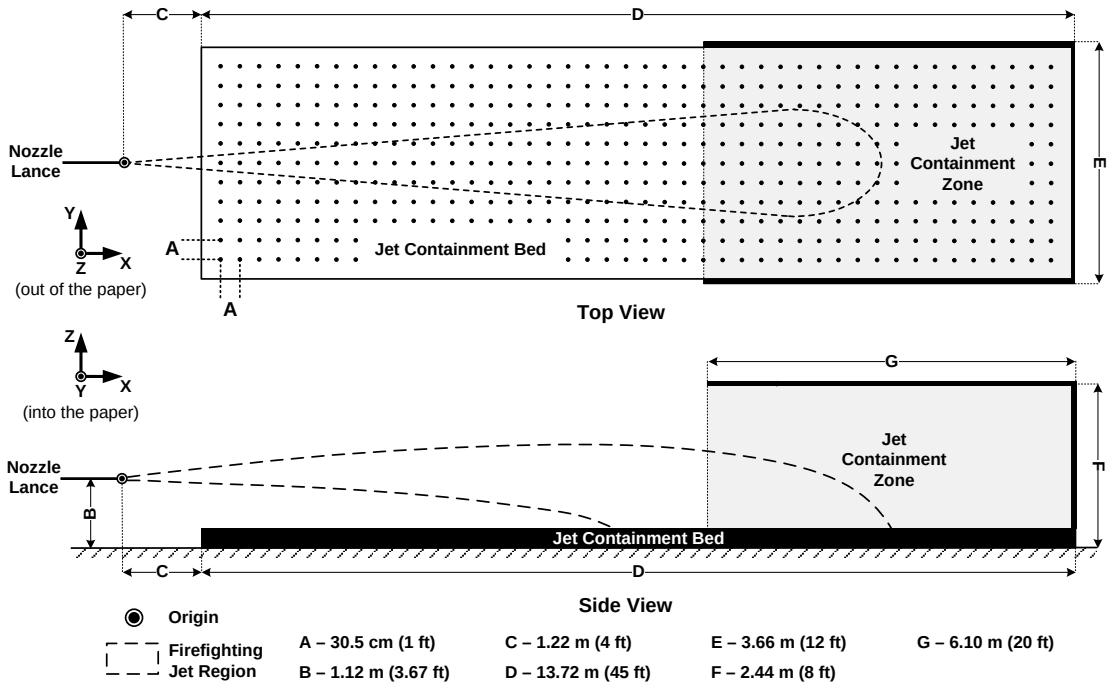

Figure 29. The Aqueous Firefighting Agent Application Laboratory Identifying Key Dimensions

3.2 FIREFIGHTING AGENT DELIVERY SYSTEM.

The firefighting agent delivery system was designed and fabricated by AFCEC personnel. The firefighting jet was generated using a small-scale, variable-speed agent delivery system capable of dispensing approximately 4 to 25 $L \cdot min^{-1}$ (1 to 6 $gal \cdot min^{-1}$) of agent from 0 to 21 MPa (0 to 3000 $lbf \cdot in^{-2}$). Due to laboratory electrical power constraints, nozzle pressures were limited to half the aforementioned range at maximum flow rate. Maximum axial throw and horizontal span, based on conventional nozzles of about 15 and 3 m (50 and 10 ft), respectively, were achievable within the bounds of the test facility. The system was powered by a reciprocating piston pump directly driven through a 1.5:1 gear ratio by a 480-V AC 3.7-kW (5-hp) electric motor to maintain highly repeatable nozzle entrance conditions. A digital interface provided manual or automatic control through variable frequency regulation while reporting current draw, voltage, and motor speed in revolutions per minute (RPM). Figure 30 illustrates the torque and power curves as a function of shaft motor speed for the electric motor. Because available power beyond the motor speed midpoint range began to decay with increasing speed, nozzle performance envelopes were nonuniform and limited in high-flow, high-pressure regimes requiring maximum power. Peak performance was also a function of other variables such as plumbing configuration, pump resistance due to temperature-dependent lubricating oil, and thermal losses incurred by the electric motor during operation.

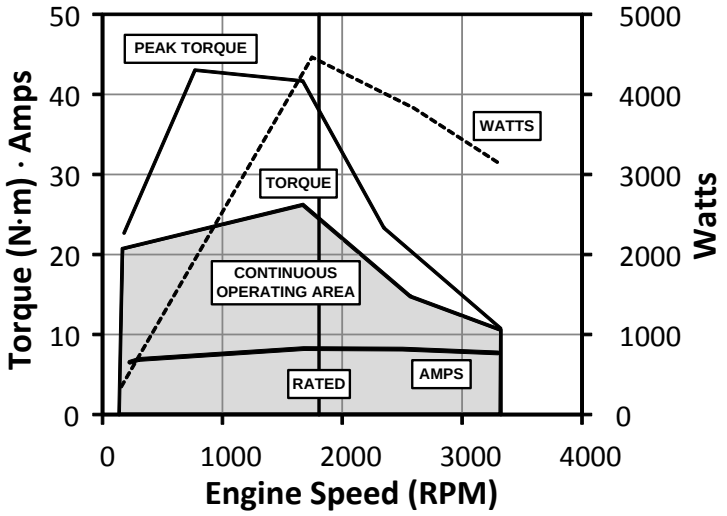

Figure 30. Firefighting Agent Delivery System Electric Motor Performance [65]

The firefighting agent delivery system was fitted with a supplemental agent reservoir designed to provide 757-L (200-gal) capacity for sustained periods of low-flow rate testing, voiding the use of an original 132-L (35-gal) onboard tank. Agent was fed individually or simultaneously from two separate 379-L (100-gal) tanks through a wye valve connected to a small centrifugal pump priming the main reciprocating pump. A 3.79 to 37.9 ±0.76-L·min^{-1} (1 to 10 ±0.2-gal·min^{-1}) turbine flow meter with digital display was installed between the two pumps to report agent flow rate. For the present work, one tank exclusively held tap water, and the other tank held premixed AFFF to reduce firefighting jet contamination from leftover residue. An accumulator was installed downstream of the main pump to dampen high-frequency acoustics due to periodic pulsations induced by pump operation. A 6-m (20-ft), high-pressure rubber hose delivered agent to a 1-m- (3-ft-) long, 0.25-in.-diameter pipe. The 1-m entrance pipe was followed by a pipe cross to accommodate static pressure measurements using a 0 to 21 ±0.05-MPa (0 to 3000 ±7.5-lbf·in.$^{-2}$) digital display pressure gauge and 0 to 14 ±0.06-MPa (0 to 2000 ±8-lbf·in.$^{-2}$) pressure transducer for data acquisition. A multipurpose high-speed USB dual data acquisition and analog control module capable of recording and function generation at a rate up to one million samples·s^{-1} was used to capture the signal output from the pressure transducer. A low-pressure loss Swagelok® fitting immediately downstream of the pipe cross allowed for easy nozzle exchange. Although the nozzle entrance length was not perfectly conditioned to achieve fully-developed flow according to academic standards because of the pipe cross fitting, the firefighting agent delivery system was typical of fire suppression field units exhibiting flow discontinuities typically all the way up to the nozzle entrance. This is generally due to design compromises based on competing factors such as multiple delivery technologies feeding a single nozzle or configuration conflicts with other platform subsystems, especially with respect to deployable fire suppression systems where weight and space are at a premium.

A ball valve installed on the low-pressure side of the reciprocating pump controlled recirculation back to the AFFF tank to unload system pressure. It also provided flow logic to premix the AFFF before testing. A pressure relief valve pre-set to 24 MPa (3500 lbf·in.$^{-2}$) was installed for

safety, and an analog 0 to 35 ±0.34-MPa (0 to 5000 ±50-lbf·in.$^{-2}$) Bourdon-style gauge was stationed on the high-pressure side of the reciprocating pump to monitor pump exit pressure. All plumbing hardware was made of high-grade stainless steel to withstand high-pressure agent flows and to avoid corrosion. All low-pressure hardware and agent storage tanks were forged from polypropylene derivatives to also resist corrosion. Figure 31(a) depicts the firefighting agent delivery system highlighting the major features discussed, and figure 31(b) shows the system accompanied by the agent reservoir addition. Figure 32 illustrates the firefighting agent delivery system's flow control schematic.

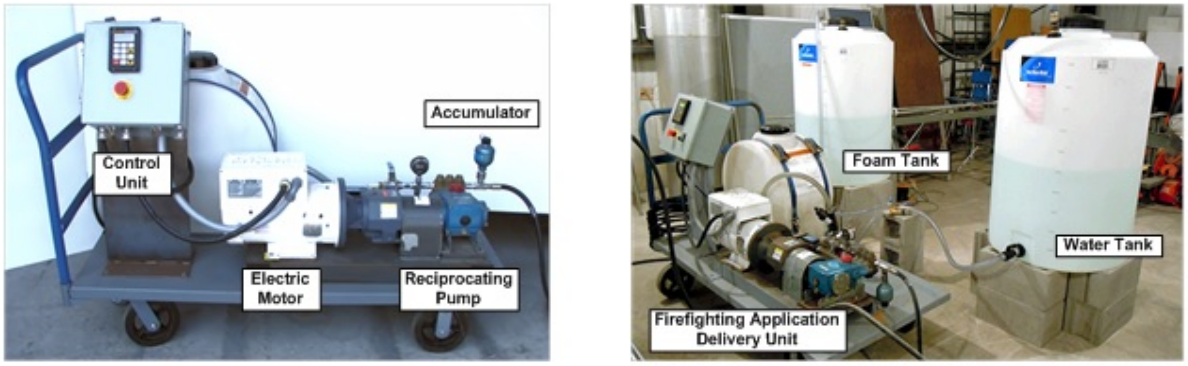

(a) (b)

Figure 31. The Firefighting Agent Delivery System

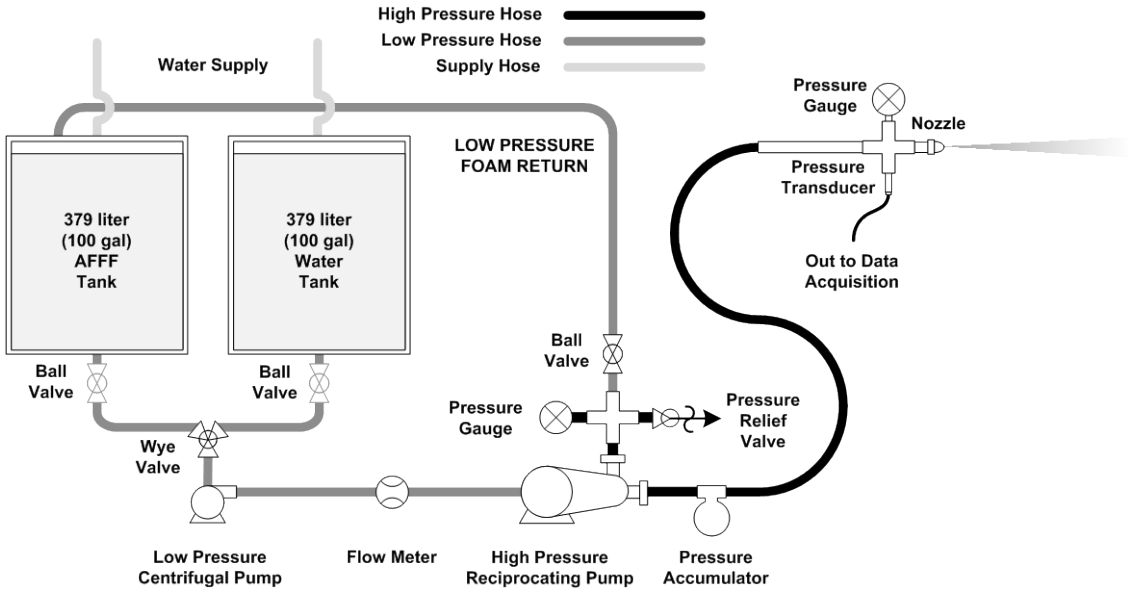

Figure 32. The Firefighting Agent Delivery Flow Control Schematic

The nozzle stand consisted of a 2.4- by 1.2- by 0.9-m (8- by 4- by 3-ft) linear rail table, which allowed the nozzle to be swept horizontally parallel with the firefighting jet containment bed. The nozzle lance (1-m- (3.3-ft-) long entrance pipe) was supported by a rectangular platform

resting on four linear bearing pillow blocks riding the table rails. The platform hosted two masts, with the forward one fixed and the rear one free to rotate for fine adjustment in the transverse plane. The nozzle lance rested directly on a subplatform attached to a vertical plate supported by the two masts allowing for rotation and fine adjustment in the vertical plane. Nozzle platform adjustment along with the linear motion table provided three degrees of freedom for nozzle positioning. Figure 33 illustrates various aspects of the nozzle stand and surrounding accessories.

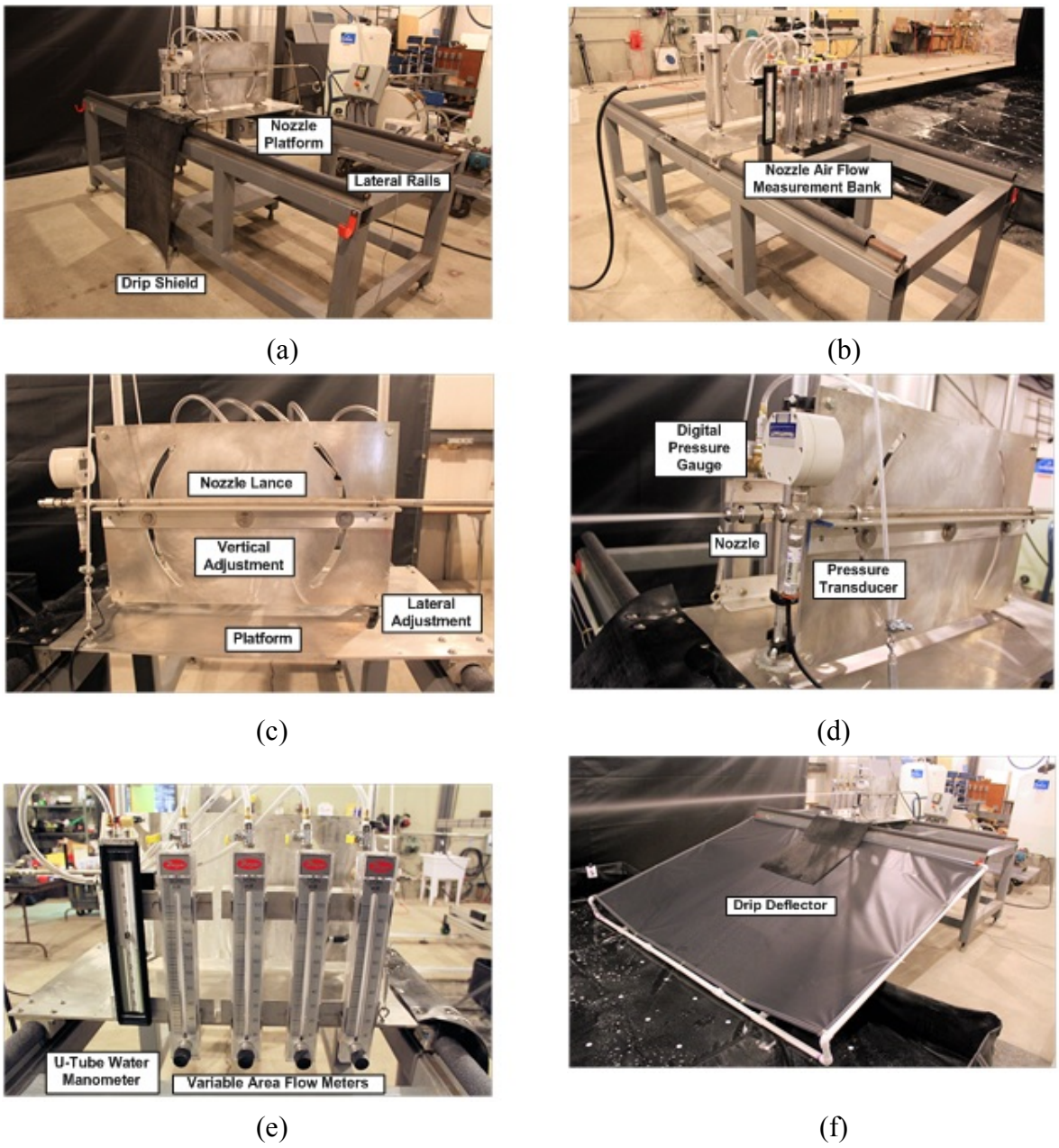

Figure 33. The Nozzle Stand and Accompanying Accessories

Although not used in the present study, the nozzle platform was also fitted with a nozzle air flow measurement bank consisting of a U-tube water manometer and a series of variable area flow

meters to monitor air ingestion pressure and flow for air aspirating nozzles. To contain drip run-off generated by the firefighting jet during sustained test periods, a drip shield and deflector were installed to bridge the gap between the nozzle stand and firefighting jet containment bed.

3.3 FIREFIGHTING JET CONTAINMENT BED.

The firefighting jet containment bed consisted of a floor-anchored, vinyl-coated, polyester 13.7- by 3.7- by 0.3-m (45- by 12- by 1-ft) spill berm manufactured by Seattle Tarp and used traditionally as a protective environmental barrier for heavy-duty trucks undergoing maintenance. With minor runoff handled by the drip deflector, it was stationed 1.2 m (4 ft) away and parallel to the nozzle stand yielding an effective longitudinal capture zone of about 15 m (50 ft). Although the containment bed was designed to hold up to 15,142 L (4,000 gal) of liquid, agent levels seldom surpass a few hundred gallons at a time due to an on-demand 34-L·min^{-1} (9-gal·min^{-1}) sump pump that was installed to continuously drain the bed while the test was in progress. The bed floor was outfitted with painted 2.5-cm- (1-in.-) diameter white dots orthogonally spaced 30.5 cm (1 ft) apart throughout the floor to form a Cartesian grid that served as a location reference for agent ground pattern analysis.

A 6.1- by 3.7- by 2.4-m (20- by 12- by 8-ft) jet containment zone riding a U-shaped, galvanized curtain track suspended from the ceiling protected the rear laboratory walls from jet drift. The vertical containment curtain was made of similar corrosion-resistant material to that of the bed, and the curtain was weighted and stiffened by metallic chain sewn into its base to reduce flapping. The rear containment zone was completed using similar material to form a roof over the track centrally supported by a tent-like suspension system from structural ceiling beams. Containment zone roof edges were secured through industrial grade Velcro® along the track and canvas periphery. Roller track, as opposed to a more permanent fixture, was installed to easily alter the containment zone wall configuration for jet interaction studies and add optical access for flow visualization and PDPA. Figure 34(a) shows the firefighting jet containment bed in standard deployment, and figure 34(b) shows the rear containment zone with its curtain sides drawn demonstrating its versatility.

(a) (b)

Figure 34. Various Views of the Firefighting Jet Containment Bed

3.4 FLOW VISUALIZATION SYSTEM.

Firefighting jet flow visualization was available using a variety of capture techniques involving high-speed videography, standard digital photography with laser sheeting, as well as stroboscopic lighting techniques. A stowable, backdrop curtain that ran along the jet containment bed lip opposite the PDPA traverse track was used with the jet containment zone track to alter the optical access for different photographic conditions. Firefighting jet high-speed video was available with the aid of a Photron SA5 color camera capable of 7500 frames·s^{-1} at 1-megapixel resolution. Although the camera could reach recording speeds up to 1 million frames·s^{-1} at a reduced resolution, indoor lighting limited recording speeds to between 5000 and 7500 frames·s^{-1}. Figure 35(a) depicts the camera, and figure 35(b) shows it in operation with industrial work lighting.

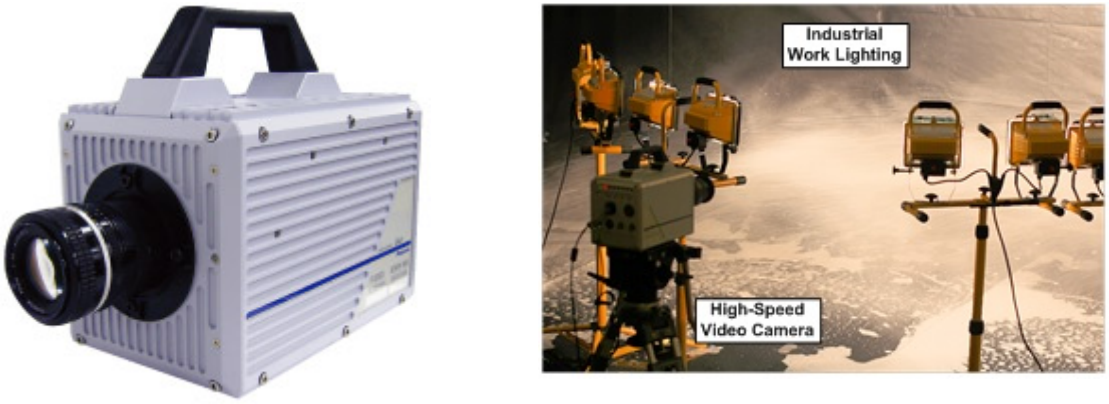

(a) (b)

Figure 35. The High-Speed Video Camera in Operation

Laser sheet photography was accomplished using an XY galvanometer scanner employing the laser light from the 5-Watt PDPA argon-ion laser. Its key components were supplied by Cambridge Technology with system integration executed in-house. The galvanometer scanner was mounted on the optical bench, which intercepted the laser beam before entering the beam separator used for PDPA. By oscillating one mirror (i.e., using a sine wave voltage signal applied to the galvanometer scanner and holding the opposing mirror at a constant deflection angle), the galvanometer scanner, operating at speeds on the order of 500 Hz, was able to produce a uniform intensity horizontal or vertical laser sheet at a maximum 40° angular excursion. Both mirrors were driven by a function generator powered through the high-speed multipurpose USB module also used for pressure transducer data acquisition. Figure 36(a) shows the galvanometer scanner mounted on the PDPA optical bench in operation. It was outfitted with a heat sink to dissipate heat away from the galvanometer scanner's mirror drive. Figure 36(b) shows the galvanometer scanner creating a vertical laser sheet.

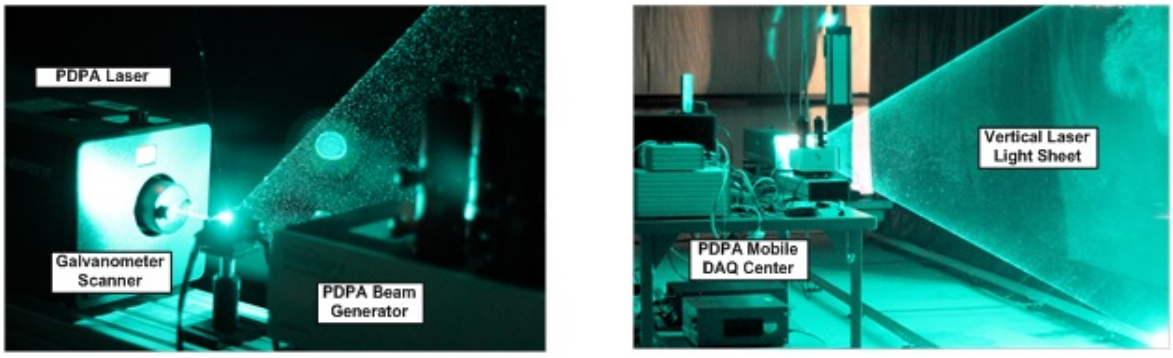

(a) (b)

Figure 36. The XY Galvanometer Scanner in Operation

For firefighting jets that exhibited strong periodicity, a stroboscope can be used to highlight the pulsation frequency to allow conventional photography techniques to capture flow details. An 18.1-megapixel Canon® EOS Rebel T3i, digital single-lens reflex (DSLR) camera with an 18- to 55-mm image stabilizer lens and a 50-mm fixed focal length lens was available to take standard still photographs and low-speed, high-definition (1080p) video. A 60-mm macro (zoom) lens was also used to resolve small-scale breakup dynamics at a safe distance from the jet.

3.5 PHASE DOPPLER PARTICLE ANALYZER.

To quantify firefighting jet spray characteristics, a PDPA manufactured by TSI, Inc. was used to measure the axial (*x*-direction) velocity, vertical (*z*-direction) velocity, and droplet size distribution. PDPA is a high-fidelity experimental flow characterization tool based on similar operating principles to that of laser Doppler velocimetry with the ability to record particle size. By assuming the particles (or droplets/small bubbles) are small, on the order of microns to submillimeter in size and spherical in shape, PDPA was used to quantify their velocity and size by measuring the scattered light off of them. The PDPA data acquisition process is explained as follows. The intersection of two laser beams for each velocity component generates a probe (or measuring) volume. Each probe volume is composed of a bright and dark fringe pattern. When a droplet passes through the probe volume, light scattered from crossing a bright fringe is collected by a photo detector via optics. The droplet velocity is determined from this data collection process and knowledge of the fringe geometry and laser beam wavelength (λ). The axial droplet velocity component ($V_{d,x}$), for example, is calculated by the following linear relationship [66]:

$$V_{d,X} = \delta f_{Doppler} \tag{14}$$

where δ is the fringe spacing and $f_{Doppler}$ is the Doppler frequency, also known as the temporal frequency, for that velocity component measured by the PDPA. Fringe spacing is calculated in equation 15.

$$\delta = \frac{\lambda}{2\sin(\theta/2)} \tag{15}$$

where θ is the laser beam intersection angle [66]. Figure 37 shows the geometric relationship between the intersecting beam angle and the measuring volume [67].

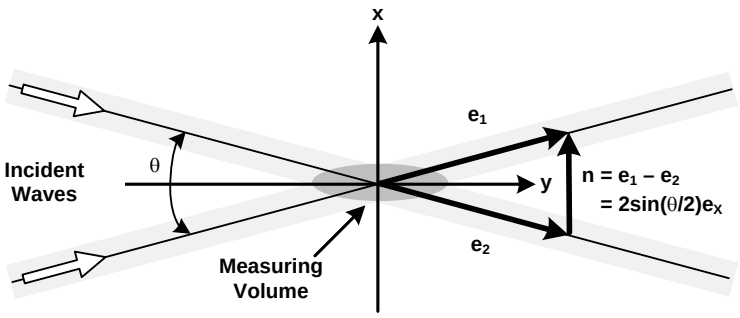

Figure 37. Relevant Vector Relations for Determining Droplet Velocity [67]

To discern flow direction and measure droplets at or near zero velocity, one of the two intersecting beams for each velocity component is frequency shifted by a Bragg cell, which effectively generates moving fringes at 40 MHz. If a droplet is moving against the fringe pattern motion, its frequency is 40 MHz minus the Doppler frequency. If a droplet is moving with the fringe pattern, its frequency is 40 MHz plus the Doppler frequency. Photomultiplier tubes convert collected scattered light from the fringes in the probe volume to electrical current pulses. Figure 38 depicts a typical light-scattering pattern recorded by a droplet passing through the laser beam intersection or measuring volume. Its envelope shape is Gaussian in nature due to laser beam Gaussian light intensity across the beam width [66].

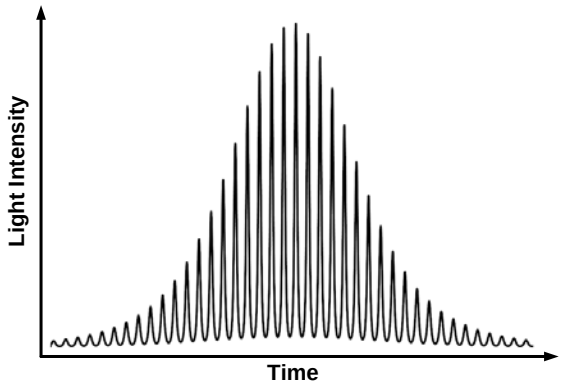

Figure 38. Light Intensity Scattered by a Particle Passing Through the Probe Volume [66]

The photomultiplier tube electrical output is passed through a high-pass filter to remove the low frequency from the signal generating the low-frequency envelope, or what is commonly referred to as the pedestal. The signal is then further filtered through a series of band pass filters and amplified [66].

Whereas particle velocity is proportionally based on a temporal frequency and particle size is proportionally based on the spatial frequency of the scattered light fringe pattern. Scattered light rays are composed primarily of reflection and refraction. An exact description of scattered light by a homogeneous sphere for the case of wavelength comparable to or much smaller than the particle size is given by a solution based on the Mie theory to Maxwell's equations. In addition to the intersection angle of the two laser beams and their wavelength, scattered light measurements that calculate particle size are also dependent on particle liquid index of refraction, the receiving angle (ψ), and the scattering angle (φ). Particle diameter measurements are also reliant on the polarization or scattering plane orientation with respect to the photo detector as well as the shape and size of the photo detector aperture. As a particle scatters light from the two incident laser beams, two different photo detectors receive the scattered light ray, resulting in a measurement of the shifted Doppler phase. Each phase is defined by the scattered light's optical path length. The phase shift angle (ϕ) between these two signals is proportional to the particle surface curvature, which effectively is a measure of particle diameter based on the assumption that the particles are perfectly spherical. Figure 39(a) illustrates how incident laser beam light reflects and refracts off a particle, and figure 39(b) depicts the orientation of each optical parameter involved with measuring the phase shift. The particle or droplet diameter (d) is derived from its relationship with the phase shift from equation 16:

$$\frac{\phi}{360} = M \times \frac{Photo\ Detector\ Separation}{Receiver\ Focal\ Length} \times \frac{d}{\delta} \tag{16}$$

where M is the slope of the phase-diameter relationship estimated based on the Mie theory and constants defined by the PDPA optics and the droplet fluid medium [66 and 67].

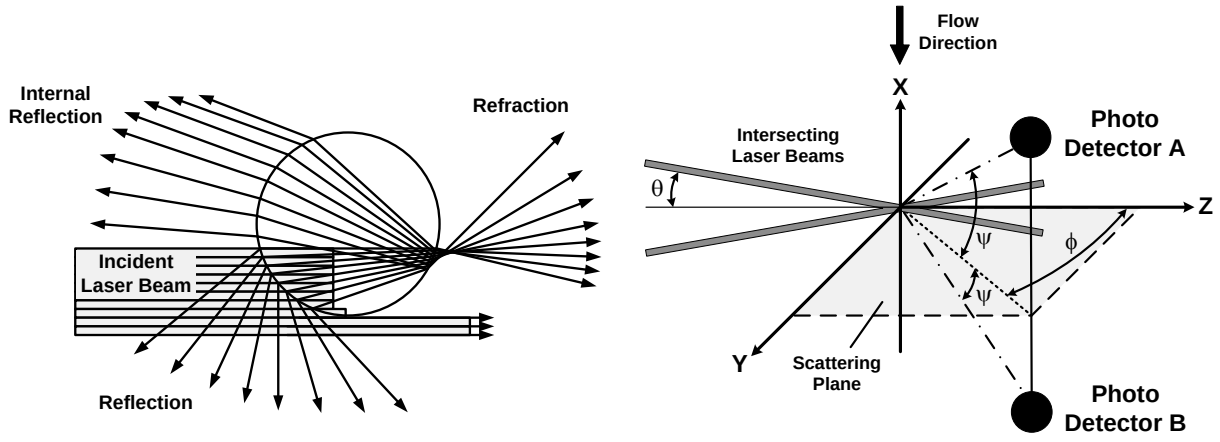

Figure 39. (a) Methods of Light Scatter off a Particle Based on the Mie Theory [66] and (b) The Orientation of Each Optical Parameter Involved in Measuring Phase Shift [68]

To improve measurement confidence, three photo detectors were used to generate a correlation based upon two independent droplet size measurements. Both Fast Fourier Transform (FFT) and autocorrelation techniques were employed to obtain the droplet temporal frequency (velocity) and phase (diameter) measurement [66]. Error in both the velocity and droplet size measurement

is difficult to determine precisely, as it is a function of not only hardware resolution but also system spatial alignment. Taking these factors into account, velocity measurement uncertainty is typically less than 0.50% of the measured velocity. Droplet diameter measurement uncertainty has similar dependencies and is generally less than 1% of the maximum measurable droplet diameter plus 1% of the actual measured droplet diameter [69].

A software-compatible, tri-axis traverse was installed to translate the PDPA optics with submillimeter resolution over one metric volume. The traverse could be controlled automatically through PDPA data acquisition software or positioned manually using a hand-controlled unit. The traverse was customized with a V-groove wheel base to travel along a 13.7-m- (45-ft-) long, 1-m- (3.3-ft-) wide aluminum linear V-track fabricated in-house to run adjacent against the jet containment bed. The track was supported in approximate 1.8-m (6-ft) intervals with adjustable floor levelers to make up for known sag in the suspended laboratory floor.

The rest of the PDPA components trail the traverse on a nearby mobile table accommodating a water-cooled, 5-Watt, argon-ion continuous laser and multicolor beam separator aligned on an optical bench. The beam separator was responsible for splitting the primary laser beam into different wavelengths for each velocity component, as well as creating a shifted and unshifted beam per wavelength via an internal Bragg cell (green – 514.5 nm for the axial or *x*-direction velocity component and blue – 488 nm for the vertical or *z*-direction velocity component). Although the beam separator could accommodate three component velocity measurements, the configuration used for the current study was only set up for two. To complete the system, the table also housed a photo detector module containing the photomultiplier tubes and 175-MHz signal analyzer to interpret droplet velocity and size, a desktop computer to command the PDPA data acquisition software, the laser power supply, and traverse controller. The FSA 4000 signal analyzer was chosen based on its ability to resolve high-speed velocities expected near the nozzle for high-pressure firefighting jets with exit velocities in excess of 100 $m \cdot s^{-1}$. The signal analyzer had a maximum sampling rate of 800 MHz. Signals were digitized at numerous sampling rates to allow automatic dynamic selection of the appropriate sampling rate to measure droplet size and velocity accurately. A digital, high-speed oscilloscope was also available to conduct independent PDPA diagnostics.

The PDPA transmitter probe and optical receiver were mounted on the traverse to communicate transmitted and reflected laser light via fiber optic cable from the beam separator and to the photo detector module, respectively. Fiber optic and traverse axis power cables were suspended from the ceiling to reduce floor hazards. Figure 40 shows the main PDPA components in forward-scatter mode along with their associated connectivity.

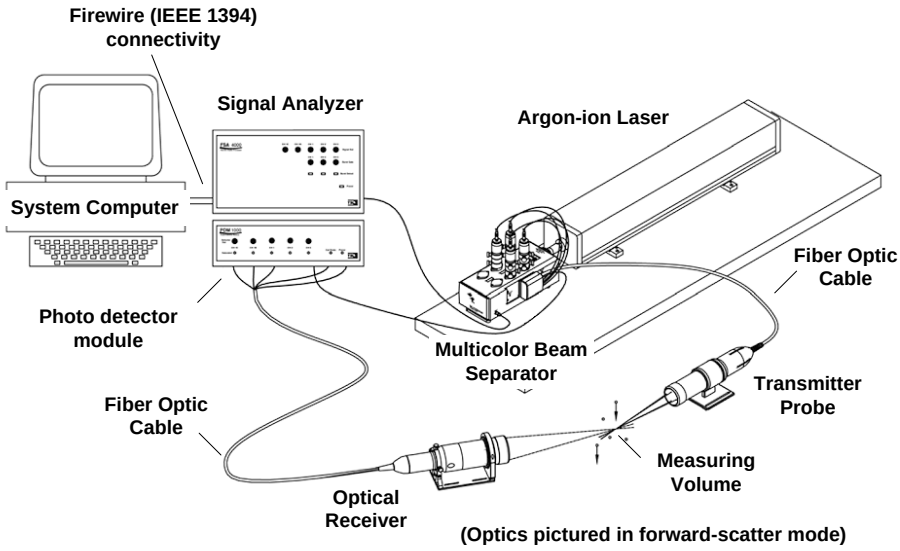

Figure 40. The PDPA Components in Forward-Scatter Mode [70]

To accommodate the horizontal expanse of the jet containment bed, PDPA optics were arranged in backward-scatter mode, positioning the optical receiver on the same side of the measuring volume as the horizontal transmitter probe. Following figure 39(a) as an orientation guide with respect to the incident laser beam and light scatter direction, forward-scatter mode measures light scattered due to refraction, and back-scatter mode measures light scattered due to internal reflection. The optical receiver was stationed about 30 degrees off axis from the transmitting probe to optimize the reception of scattered light reflected back from the jet droplets. A 2-m (6.6-ft) T-rail supported the optics secured against the vertical traverse axis. Due to the substantial moment arm imposed by the cantilevered configuration, the traverse base was counterweighted opposite the optics to reestablish stability. Using a 1-m focal length lens on the transmitter probe and receiver, from traverse (track) center, measurements were taken approximately 2.6 m (8.5 ft) away, just beyond the containment bed longitudinal centerline. Alternate optical configurations were available, but this layout accommodated the laboratory design the best. Figure 41 shows the major PDPA system components while in operation.

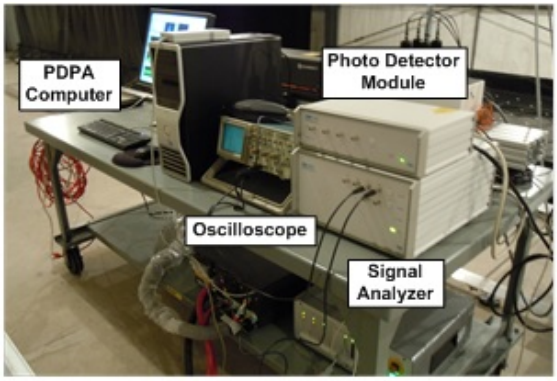

(a)

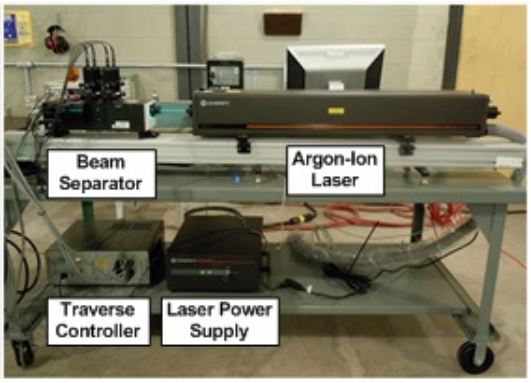

(b)

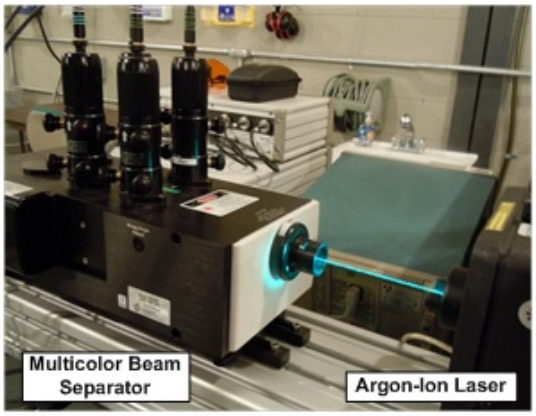

(c)

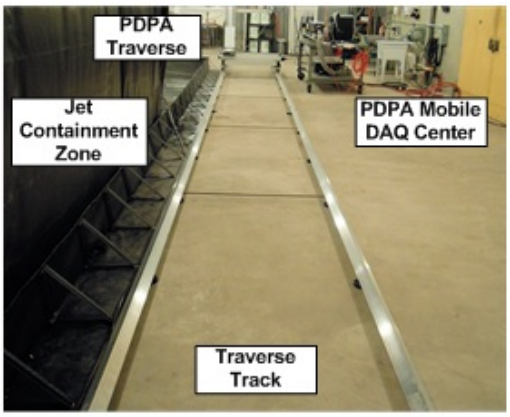

(d)

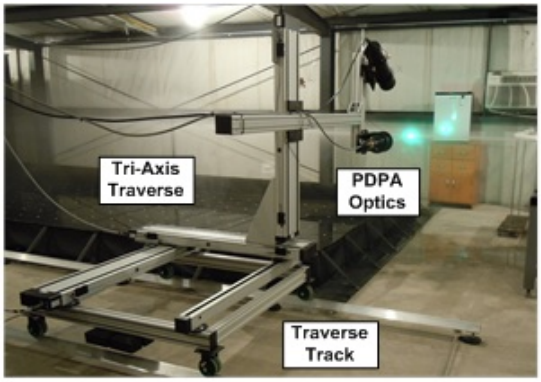

(e)

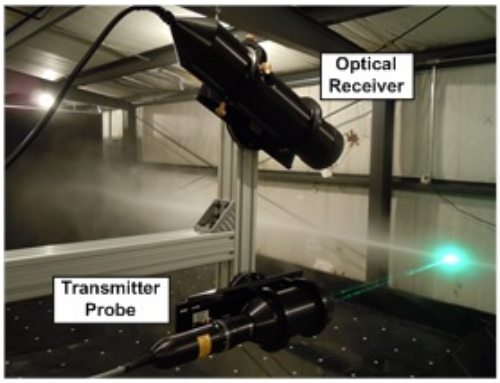

(f)

Figure 41. Overview of the PDPA System

4. EXPERIMENTAL APPROACH.

4.1 OVERVIEW.

Experiments were conducted in the aqueous firefighting agent application laboratory to characterize firefighting jet performance with respect to changes in nozzle pressure, flow rate, and AFFF concentration. Measured output parameters included jet velocity, droplet size, ground accumulation pattern, and foam quality. Initial strides were taken to characterize a commercial firefighting nozzle designed to operate within the firefighting agent delivery system performance envelope while meeting minimum foam quality standards as outlined by the NFPA [11]. Further constraints on nozzle selection dictated the use of conventional channel flow nozzle profiles to reduce geometric complexity to simplify the translation process to a CFD model environment. A firefighting nozzle meeting all these criteria did not exist during the time of testing. All commercially available firefighting nozzles designed for 37.8 $L \cdot min^{-1}$ (10 $gal \cdot min^{-1}$) or lower operation reported a maximum foam expansion of approximately 3:1, which is below the minimum accepted NFPA value of 5:1 for ARFF use [11]. Several nozzles designed for alternative applications, such as industrial cleaning, were examined. Each nozzle failed at least one of the aforementioned criteria. In following the tendency of most manufacturers, high foam quality was forfeited to meet the other requirements in this study. The 6.4-mm (0.25-in.) AP4™ Attack Tip (AP4) developed by Stoneage Waterblast Tools® was chosen due to (1) its precise manufacturing standards; (2) the availability of its family of self-similar, simple nozzle designs to span the entire firefighting agent delivery system performance envelope; and (3) its capacity to produce reasonable foam quality. The AP4 nozzle is a single-bore nozzle with a step-reducing channel. Figure 42 shows various views of the AP4 nozzle, with *D* denoting nozzle diameter.

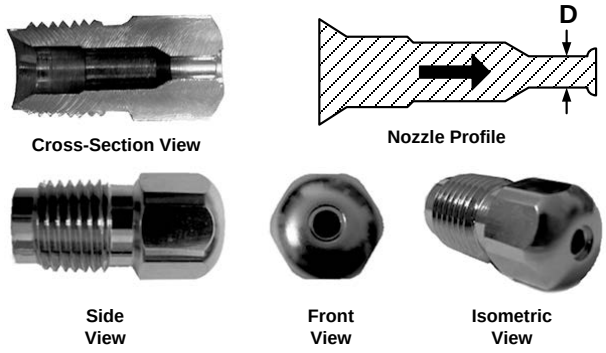

Figure 42. The Stoneage Waterblast Tools AP4 Nozzle

Figure 43 provides a visual overview of all experiments conducted in the laboratory using the AP4 nozzle family in terms of nozzle exit pressure and flow rate combinations. Each of the 18 dotted lines represents the performance of an individual AP4 nozzle with a unique exit diameter. All nozzle performance profiles were measured using only water because the addition of AFFF negligibly affected nozzle pressure and flow rate measurements. Firefighting jet flow rates were chosen to fill out the firefighting agent delivery performance envelope with respect to nozzle pressures regimes commonly applied in the ARFF industry. Three nozzle pressure and flow rate magnitudes were chosen and spaced equally to designate a low, medium, and high condition for

pressure and flow rate. Studies that involved varying AFFF concentration were carried out in 3% increments, ranging from only water up to a maximum of 12% AFFF concentrate by volume mixed with water.

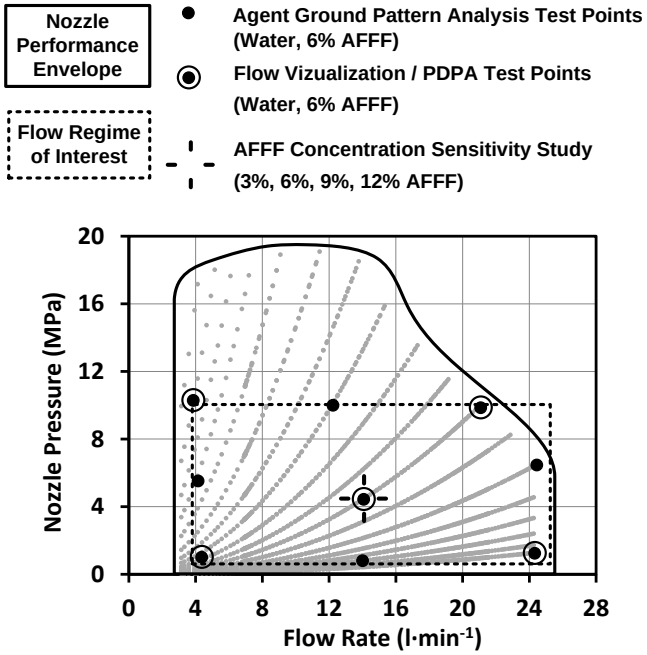

Figure 43. The Firefighting Agent Delivery System Performance Envelope and Associated Firefighting Jet Experiments

A two-dimensional (2-D) agent ground pattern analysis was conducted using water and 6% AFFF at the nine pressure-flow rate combinations shown in figure 43. Due to the expense and high consumption rate of AFFF during testing, the number of experimental conditions conducted for flow visualization and phase Doppler measurements were reduced from nine to five by removing the pressure-flow rate border midpoints. PDPA as well as flow visualization was conducted using water and 6% AFFF at the five reduced pressure-flow rate combinations highlighted in figure 43. Presampled flow visualization results ranging from 3% to 12% AFFF also showed negligible difference to warrant a more thorough study. A one-dimensional (1-D) AFFF concentration sensitivity study was conducted at the pressure-flow rate center point for both the agent ground pattern analysis and PDPA, ranging from 3% to 9% AFFF and 3% to 12% AFFF, respectively. The 12% AFFF was removed from the PDPA concentration sensitivity study because a negligible change in results was observed beyond 6% AFFF.

Ten tests were conducted for flow visualization, twenty for agent ground pattern analysis, and thirteen for PDPA. Table 6 summarizes all the aforementioned experiments that were carried out in the aqueous firefighting agent application laboratory.

Table 6. Firefighting Jet Test Case Summary in the Aqueous Firefighting Agent Application Laboratory

	Water Jet			AFFF Jet		
Flow Visualization	Nozzle Flow Rate			Nozzle Flow Rate		
Nozzle Pressure	Low	Medium	High	Low	Medium	High
Low	•		•	o		o
Medium		•			o	
High	•		•	o		o
Agent Ground Pattern Analysis	Nozzle Flow Rate			Nozzle Flow Rate		
Nozzle Pressure	Low	Medium	High	Low	Medium	High
Low	•	•	•	o	o	o
Medium	•	•	•	o	□	o
High	•	•	•	o	o	o
Phase Doppler Particle Analysis	Nozzle Flow Rate			Nozzle Flow Rate		
Nozzle Pressure	Low	Medium	High	Low	Medium	High
Low	•		•	o		o
Medium		•			◊	
High	•		•	o		o

• Water; o 6% AFFF; ◊ 3%, 6%, and 9% AFFF; □ 3%, 6%, 9%, and 12% AFFF

The key operating conditions for the test cases presented in figure 43 and table 6 are in appendix A. It should be noted that Reynolds, Weber, and Ohnesorge numbers reported in appendix A are consistent with firefighting jet regimes highlighted in section 2.3.2.

Additional 1-D jet centerline ground pattern measurements were also recorded at similar laboratory pressures, but at full-scale flow rates approximately three times larger than the laboratory high flow rate condition. The results from this particular analysis are presented in section 6.2.6 separately from the core experiments conducted in the aqueous firefighting agent application laboratory.

In an ancillary effort, several AFFF material properties were quantified due to insufficient data available in the literature. Vital to nearly all phases of research, their collection focused on the classification of Chemguard C301MS 3% AFFF in various dilutions with water for which all experimental work was conducted. Density, dynamic viscosity, equilibrium, and dynamic surface tension, in addition to index of refraction, were either recorded or extrapolated from relationships to measurements of other properties. Details of each property characterization effort are summarized in appendix B.

Proper proportioning of AFFF concentrate with water was critical for producing consistent foam quality and for ensuring repeatability throughout the experimental phase. All experimental AFFF solutions were premixed in storage tanks via a closed-loop feedback to the firefighting agent delivery pumps with dilution levels adjusted based on test condition requirements. The firefighting agent delivery system was flushed prior to testing whenever AFFF proportion levels

had to be modified between experiments. The output from the AFFF jets was periodically sampled to ensure the AFFF concentrate was proportioned within ±0.25% of the specified value. AFFF proportion levels were calibrated and monitored using refractive techniques. Details of this process are in appendix B-4, where the AFFF index of refraction results are presented. All results from the experimental effort, including flow visualization, agent ground pattern analysis, and PDPA, are presented in sections 6.2, 6.3, and 6.4, respectively.

4.2 FLOW VISUALIZATION.

Flow visualization was conducted on five pressure-flow rate combinations using water and 6% AFFF to record a total of ten unique firefighting jet configurations. As mentioned earlier, 6% AFFF was used solely for flow visualization because variation in AFFF concentration was qualitatively difficult to perceive. Conventional photography with standard lighting, as well as laser sheet lighting, high-speed photography, and stroboscopic (pulsed lit) photography techniques were all used to characterize various aspects of the firefighting jet environment. The details of these flow visualization methods are discussed in section 3.4. Standard, wide, and macro (zoom) lenses were used, depending on the subject size and relative range to the camera. Figure 44 depicts the three main focal planes from a top view where far-field flow visualization was recorded along with the approximate location of the camera. Each plane is defined based on the direction it is normal to via the coordinate system. The *x*-plane refers to x = 6.09-m (20-ft) downstream of the nozzle running vertically upward in the *z*-direction and was chosen as an approximate mid plane for all firefighting jets investigated. The *y*-plane refers to the y = 0-m plane intersecting the nozzle vertically along the *z*-direction, and the *z*-plane refers to the z = 0-m plane intersecting the nozzle horizontally along the *x*-direction. The blackout curtain adjacent to the laboratory wall was dropped to provide contrast for the photographs. The jet containment zone walls were partially exposed to allow extended optical access for *y*-plane, far-field photography. Near-field imagery was taken at various locations along the *y*-plane. All results from flow visualization are presented in section 6.2.

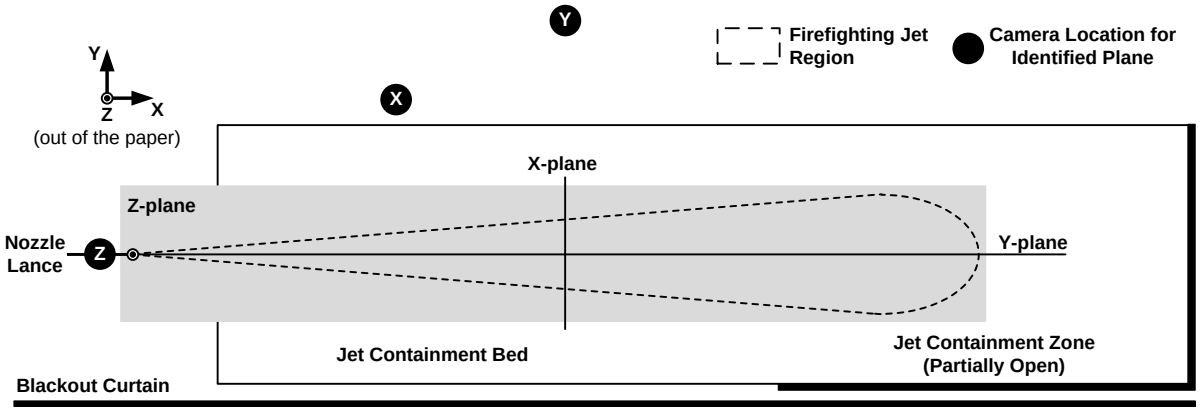

Figure 44. The Main Focal Planes Used for Firefighting Jet Flow Visualization

4.3 AGENT GROUND PATTERN ANALYSIS.

An agent ground pattern analysis was conducted to describe agent accumulation, foam quality, ground coverage area, reach, and maximum span. Using the containment bed's floor reference system, modified 100 ±2-mL graduated cylinders were placed along the footprint of the jet to measure agent accumulation. The adapted capture device consisted of a standard polypropylene cylinder outfitted with a 127-mm- (5-in.-) diameter funnel attached to the cylinder mouth via a holed rubber stopper slightly bored out to friction fit the funnel's neck. The funnel was necessary to extend the effective agent capture rate range without compromising measurement resolution. A steel puck was fixed to the cylinder's underside to add extra weight and keep the device upright when exposed to the oncoming force of the jet. The entire base was dipped in a plasticizer to avoid corrosion. Agent accumulation was recorded by manually reading the agent height within the cylinder. Foam quality, or foam expansion ratio, defined by equation 2 as the volumetric ratio of the emulsified foam relative to the same quantity collapsed to a pure liquid, was determined by a more involved method. Once the agent volume was read, the capture device was weighed and recorded using a 1000 ±0.2-g scale. Knowing the dry weight of each capture device beforehand via prenumbered identification, the expansion ratio was calculated by dividing the difference in the capture base's wet and dry weight into the agent volume. This process was justified irrespective of foam concentration percentage because the density of AFFF is similar to that of water (1 $g \cdot mL^{-1}$) as noted in appendix B-1.

A standard agent ground pattern test was conducted by operating the firefighting agent delivery system at one of the jet conditions illustrated in figure 43 and listed in table 6. To avoid transience during developing jet conditions prior to each experiment, a flow deflector was positioned in front of the jet to divert the flow away from the path of the floor capture devices to a location near the corner of the containment bed. Once the firefighting agent delivery system reached steady-state operation, the deflector was removed and the agent capture devices were allowed to fill up. Firefighting jet delivery periods were determined based on the observed time it took for at least one capture device in the entire footprint to consistently become 90% full over repeated trials. Due to different nozzle and agent composition conditions affecting jet trajectory, accumulation times were optimized for each case. This method was enforced to maximize measurement accuracy for each configuration. The results were reported nondimensionally for consistent comparison and to reduce nozzle condition dependence. This method was reminiscent of Theobald's more simplified testing of high-flow firefighting jets discussed in section 2.3.4 [51 and 52]. Because there were 454 grid floor locations and only 150 capture devices, most full 2-D agent ground pattern investigations were completed using multiple runs to populate the entire floor pattern. For large foam ground patterns generated by medium- and high-flow rate and medium- and high-pressure AFFF jets, a staggered measurement pattern was enforced everywhere but along the centerline. Skipped measurement locations were interpolated from surrounding measurement locations. Three replicated measurements were taken and averaged for each location due to the laborious nature of the data acquisition process. Although foam drainage was on the order of minutes, it did not strongly influence measurement accuracy because the foam's dry cell structure was still visibly resident in the same suspended cylinder location even hours after testing. Sample agent ground pattern tests were conducted using 1000-mL graduated cylinders to confirm foam accumulation was not dependent upon capture vessel design or scale. For highly expanded (dryer) foams, funnel drain size could become a

limiting factor for this particular design as the drainage rate into the graduated cylinder may be slower than the rate at which the funnel fills up with foam.

A jet containment zone sensitivity study was initially performed to quantify the curtain's effect on agent ground pattern measurements. The high-flow, high-pressure jet was selected because it was the largest sized jet and presumed to have the most interdependency with the curtains and other local surroundings. Agent ground coverage area was calculated by summing all agent capture devices that recorded at least 2 mL of agent. A 1-D ground centerline AFFF concentration sensitivity study, ranging from 3% to 12% AFFF, was conducted at the medium-flow, medium-pressure jet condition illustrated in figure 43 and listed in table 6. A 1-D agent ground pattern test was approached similar to the 2-D test, except data were recorded exclusively along the jet centerline. Figure 45(a) depicts the capture device, and figure 45(b) through (d) shows various aspects of a conventional ground pattern test conducted in the laboratory. Figure 46 shows the coverage area for a typical ground pattern measurement based upon the firefighting jet spray region.

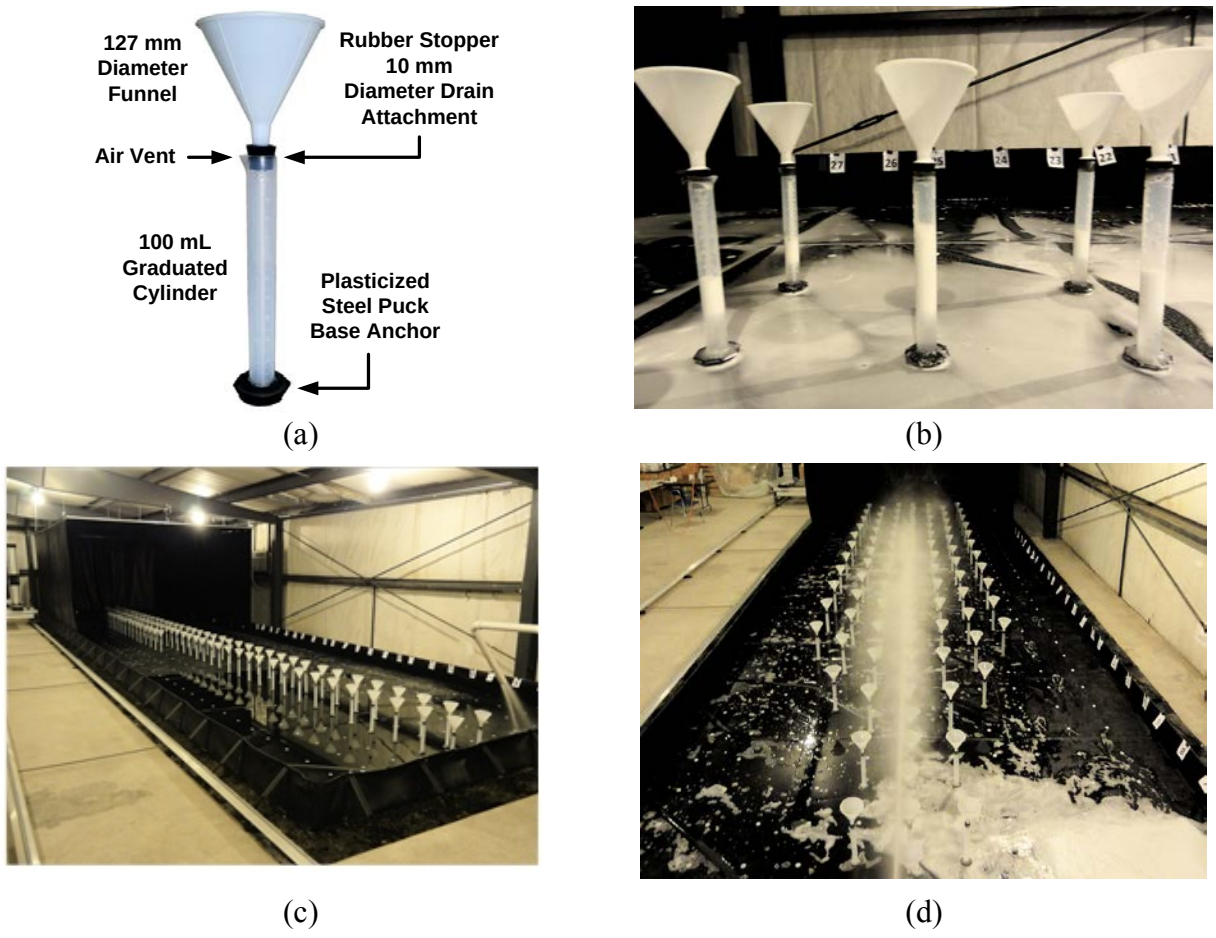

Figure 45. (a) The Agent Ground Pattern Capture Device, (b) A Near-Field View of the Agent Ground Pattern Capture Device Array After Testing, (c) A Water Pattern Test Using the Flow Deflector During Startup, and (d) A Semi-Aerial View of an AFFF Jet Test in Progress

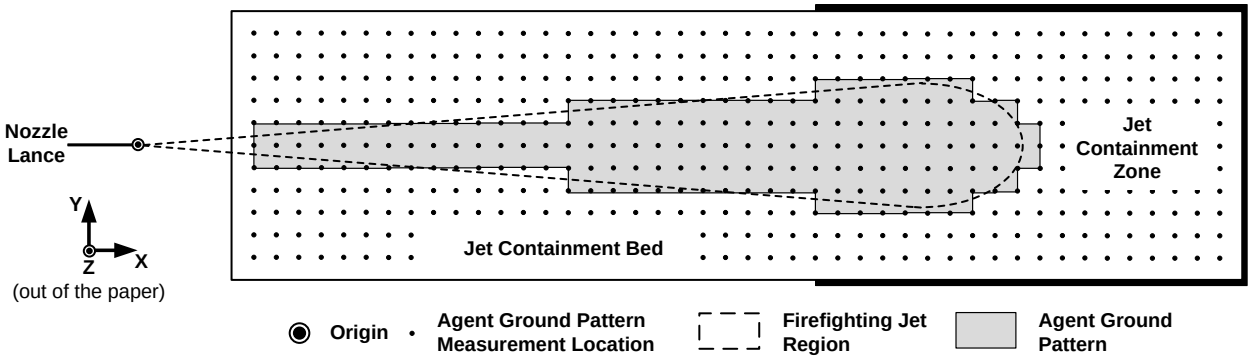

Figure 46. An Example Agent Capture Device Footprint Based on Firefighting Jet Delivery Geometry

Full-scale, 1-D jet centerline agent ground pattern experiments were conducted in the Sky X Hangar test facility located at Tyndall Air Force Base, Florida, with the aid of AFCEC personnel to supplement laboratory testing. Water accumulation and 6% AFFF foam expansion ratio patterns were recorded using the same AP4 nozzle family. The nozzles were modified to support a flow rate of 75.7 $L \cdot min^{-1}$ (20 $gal \cdot min^{-1}$), representative of a full-scale firefighting hand line. Nozzle pressures were tested at the same approximate low-, medium-, and high-pressure magnitudes as those in the laboratory. Full-scale test procedures were analogous to laboratory tests, except all aspects were scaled upwards to accommodate larger jets including agent capture device volume (100 to 1000 mL), distance between capture devices (30 to 60 cm or 1 to 2 ft), and overall measurement length (15.2 to 23.2 m or 50 to 76 ft). Figure 47 illustrates the full-scale nozzle stand, a water jet and AFFF jet test in progress, and representative agent capture devices filled with foam after an AFFF jet test was completed, respectively.

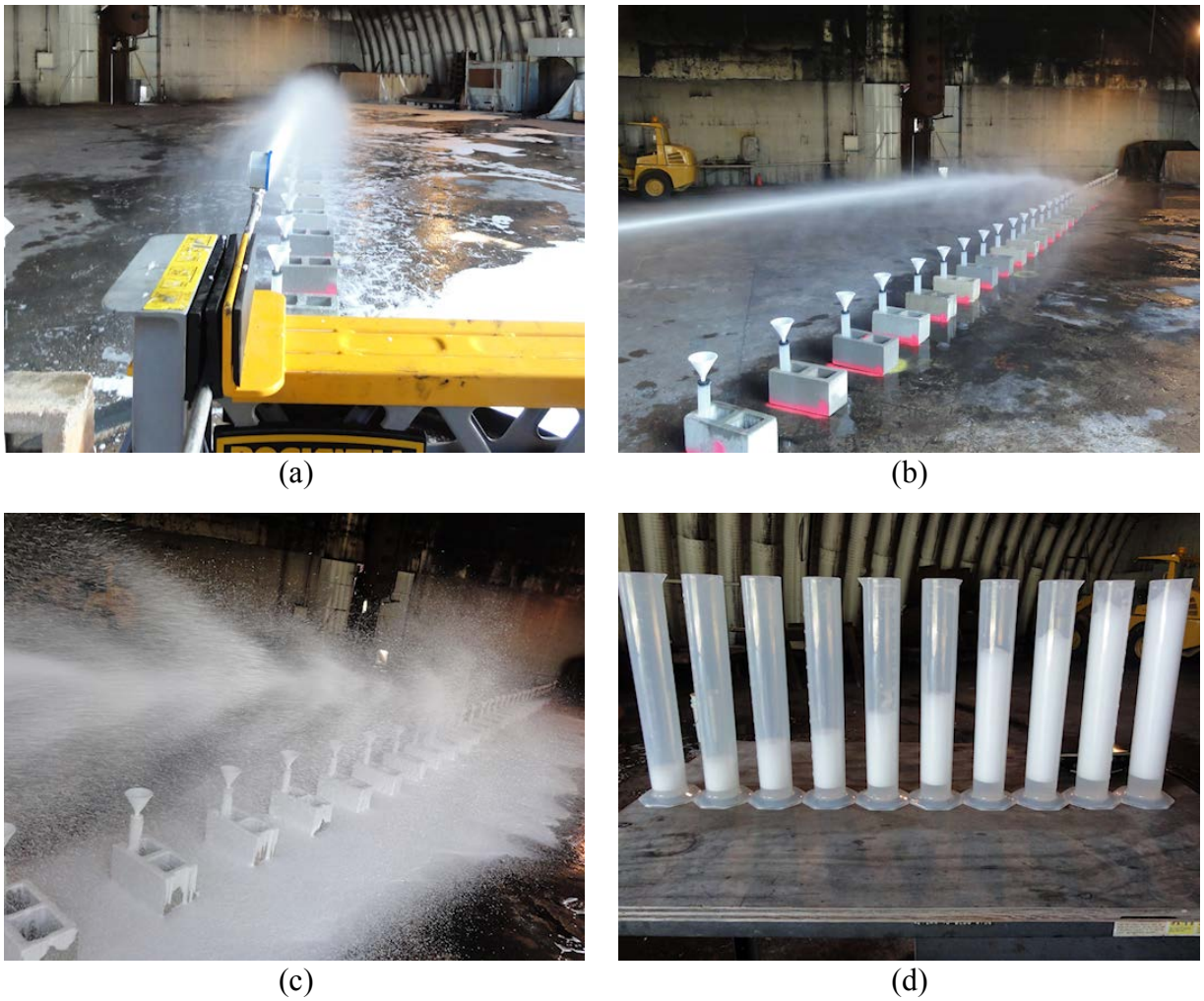

Figure 47. Full-Scale, 1-D Agent Ground Pattern Test

4.4 PHASE DOPPLER PARTICLE ANALYSIS.

PDPA was used to measure 2-D (axial *x*-direction and vertical *z*-direction) droplet velocity and droplet size of the firefighting jet configurations illustrated in figure 43 and listed in table 6. PDPA data acquisition details are discussed in section 3.5. For each firefighting jet configuration, nine to eleven 1-D vertical (*z*-direction) profiles were recorded, depending on jet reach. For the medium-flow, medium-pressure jet, an additional reduced set of 1-D horizontal (*y*-direction) profiles was also recorded. PDPA profile data were collected first at a specific location on a fully developed water jet. Once complete, the firefighting agent delivery system was manually transitioned to dispense AFFF while maintaining pump RPM. While the AFFF jet was fully developing, the PDPA traverse retraced its steps in space to repeat the measurement process for the AFFF jet at the same discrete point locations where the water jet data were just recorded. The tri-axis traverse in tandem with the traverse track allowed profiles to be measured from the nozzle exit to a distance of about 13.7 m (45 ft) downstream. However, the maximum range of all firefighting jet configurations considered for the present study ended at approximately x = 9.14 m (30 ft), so PDPA data acquisition ceased at that location. Twenty-five

discrete points were recorded for each 1-D profile. The points were located close together near the jet axial centerline to resolve steep velocity gradients and then rapidly expanded outward to measure as much of the jet profile as possible within the range of the traverse stationed on the track. Uneven, time-sampled data were recorded for 20 seconds at each point or a combined 50,000 valid droplet velocity and diameter measurement count, whichever limit was reached first. Vertical profiles were spaced in close proximity to the nozzle to capture large jet velocity gradients and expanded further downstream to increments of about 1.5 m (5 ft) beyond the x = 1.5-m (5-ft) location where changes in jet velocity were less drastic. Vertical profiles were also subject to variation in relative distance from the ground due to profile relaxation from droplet dispersion and overall jet sag due to gravity. These aspects varied for each pressure-flow rate combination. To characterize the horizontal expanse of the medium-flow, medium-pressure jet, horizontal profiles were measured at four axial locations that coincided with the vertical profile locations. These same four axial stations were also chosen to conduct an AFFF solution concentration sensitivity study on medium-flow, medium-pressure jet conditions from 3% to 9% AFFF. Figure 48 shows the location of each PDPA profile, and table 7 lists the x-axis location of each profile shown along with the agent composition recorded.

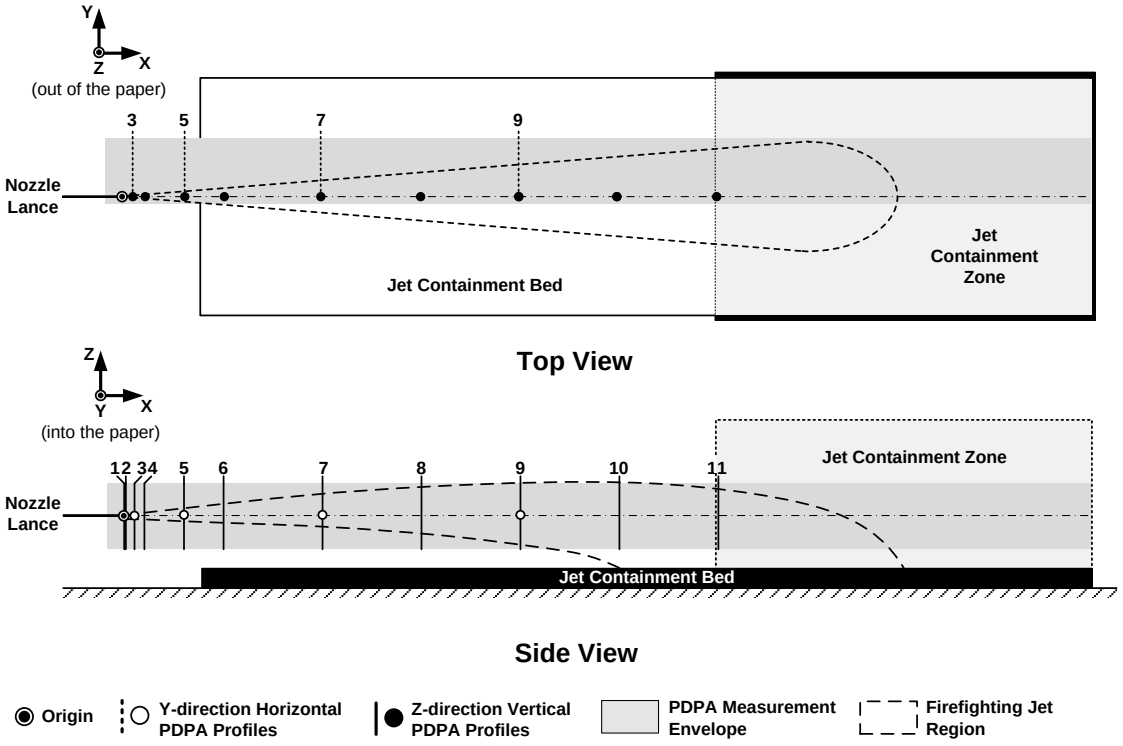

Figure 48. The PDPA Profile Measurement Locations

Table 7. Summary of the PDPA Profile Measurement Locations

		Water Jet		AFFF Jet	
Station No.	X-Axis Location	1-D Vertical Z-Axis Profile	1-D Horizontal Y-Axis Profile	1-D Vertical Z-Axis Profile	1-D Horizontal Y-Axis Profile
1	6.4 mm (0.25 in.)	•		o	
2	25.4 mm (1 in.)	•		o	
3	0.152 m (6 in.)	•	•	◊	o
4	0.305 m (1 ft)	•		o	
5	0.914 m (3 ft)	•	•	◊	o
6	1.52 m (5 ft)	•		o	
7	3.05 m (10 ft)	•	•	◊	o
8	4.57 m (15 ft)	•		o	
9	6.10 m (20 ft)	•	•	◊	o
10	7.62 m (25 ft)	•		o	
11	9.14 m (30 ft)	•		o	

• Water; **o** 6% AFFF; ◊ 3%, 6%, and 9% AFFF

PDPA data acquisition was a challenge in peripheral areas of the jet where droplet concentrations were sparse, making it difficult to record a large number of samples. Special care was required in conserving AFFF to keep operating costs manageable. Even-time data sampling considerations were universally abandoned because of severely limited data acquisition rates in sparsely populated droplet locations in the flow. Firefighting jet unsteadiness, particularly for low-pressure jets where droplet velocities were significantly lower in the far downstream reach of the jet, provided the additional challenge of recording consistent, repeatable data.

Figure 49(a) and (b) show the PDPA recording an automated vertical far-field profile of both a water and AFFF jet, respectively.

(a) (b)

Figure 49. The PDPA on a Low-Flow, Low-Pressure (a) Water Jet and (b) AFFF Jet

4.5 MEASUREMENT AND UNCERTAINTY ANALYSIS.

Measurement error and uncertainty analysis for all quantitative data are addressed in section 6 in context with the results presented. Supplemental commentary on PDPA measurement error and uncertainty is generalized in section 3.5 using methods developed by the manufacturer, and information regarding measurement uncertainty and instrument calibration specific to the PDPA system used in the current study is in appendix D.

5. COMPUTATIONAL MODELING APPROACH.

5.1 OVERVIEW.

CFD models were developed to predict general firefighting jet transport behavior with special attention paid to the influence AFFF has on droplet dynamics. An overall simulation strategy was shaped by the firefighting jet breakup atomization regime classification coupled with data analysis from experiments. Developing a set of consistent modeling techniques for all flow regimes examined proved challenging due to the wide range of time and length scales associated with each nozzle condition. Other goals included developing a computational method that was compatible with combustion models to eventually examine scenarios involving aircraft fire and firefighting jet interaction. Model dependence on parameters (such as certain CFD physical submodels and the modeling environment) and on temporal and spatial mesh resolution were also investigated. Solidworks® 2012 and Pointwise® v17.0 were used for solid modeling of the flow environment and mesh generation, respectively [71 and 72]. ANSYS Fluent® v14.5 was chosen as the CFD modeling software due to its extensive array of multiphase modeling tools and their ease of integration with combustion modeling methods already in use for aircraft hydrocarbon pool fires [56]. ANSYS Fluent® was also used for flow visualization and postprocessing. The CFD simulation strategy and technical details of each CFD submodel selected, construction of the physical modeling environment, boundary and initial conditions, numerical methods, and overall solution strategy are discussed in sections 5.2 through 5.7. Table 8 lists the CFD case results reported, which reflects key PDPA results used for model development and comparison. For further details on any CFD submodels presented, refer to the associated reference.

Table 8. The Computational Matrix Summarizing Firefighting Jet Simulation Conditions

	Water Jet Models			AFFF Jet Models		
CFD	Nozzle Flow Rate			Nozzle Flow Rate		
Nozzle Pressure	Low	Medium	High	Low	Medium	High
Low	•		•	o		o
Medium		•			o	
High	•		•	o		o

• Water; **o** 6% AFFF

5.2 PHYSICAL SUBMODELS.

5.2.1 Multiphase Flow.

Conventional firefighting jet transport for the flow regimes under investigation is principally dominated by secondary droplet disintegration mechanisms with little evidence to suggest the existence of a continuous liquid core. This infers firefighting jet flow dynamics are governed primarily by droplet trajectories interacting with the surrounding air as well as themselves in terms of collision and breakup. An Euler-Lagrange multiphase modeling architecture best supports these assumptions by treating the atmosphere as a continuum (Eulerian) field by solving the Navier-Stokes equations while tracking firefighting jet droplets as a dispersed (Lagrangian) phase through the calculated flow field. Referred to as DPM in ANSYS Fluent®, limitations on this computational approach exist when the local volume of dispersed droplets approaches the volume of the discretized continuum field (i.e., local mesh cell volume is significantly less than local droplet volume, or about 10% to 12% droplet-to-cell volume). However, large droplet-to-air mass ratios are acceptable and still allow for numerically robust simulations. Similar modeling approaches, such as dense DPM, remove the limitation of secondary phase, high-volume loading and may be more accurate for simulating higher-flow rates where near-nozzle jet disintegration is not as distinct. However, this method is currently incompatible with combustion models actively used to predict aircraft fire behavior and thus was not considered for the present study [56].

Discrete droplet trajectories were predicted by a force balance integration equating the droplet inertia with the surrounding forces acting on the droplet from the continuous gas phase such as gravity, atmospheric pressure gradients, and aerodynamic drag. The general force balance can be written as follows [56].

$$\frac{dV_d}{dt} = F_{Drag} \cdot V_{d,rel} + \frac{g\left(\rho_L - \rho_G\right)}{\rho_L} + F \tag{17}$$

where V_d is the droplet velocity, $V_{d,rel}$ is the relative velocity between the droplet and gas phase, g is the acceleration due to gravity, t is the simulation time, and $F_{Drag} \cdot V_{d,rel}$ is the drag force per unit particle mass. The F term is a general acceleration per unit mass term that accounts for additional forces such as flow field pressure gradients and virtual mass effects. The drag force is defined as [56]:

$$F_{Drag} = \frac{18\mu_G}{\rho_L d^2}\frac{C_{Drag}Re_d}{24} \tag{18}$$

where μ_G is the gas phase dynamic viscosity. The C_{Drag} term is the drag coefficient, and Re_d is the relative Reynolds number based on the droplet diameter, defined as [56]:

$$Re_d = \frac{\rho_G d\left|V_{d,rel}\right|}{\mu_G} \tag{19}$$

Droplets were modeled in the present study as adiabatic (nonevaporating) inert particles undergoing collision and breakup due to two-way coupled momentum exchange with the surrounding environment. Momentum exchange was calculated by inspecting the forces imposed on the droplet as it passed through each mesh cell, or control volume, computed as:

$$F = \sum \left(\frac{18\mu_G C_{Drag} Re_d}{\rho_L d^2 24} V_{d,rel} + F_{Other} \right) \dot{m}_d \Delta t \tag{20}$$

where $\dot{m}_d$ is the mass flow rate of the droplets and Δt is the simulation time step. The F_{Other} term represents per unit mass forces generated from other CFD submodels, such as turbulence, which can play a significant role in altering overall droplet momentum. Mass and heat exchange effects were assumed negligible primarily due to relative humidity measurements approaching 100%, particularly in the local jet flow region in the laboratory. This simplification was further supported based on expectedly short in-flight droplet lifetimes coupled with larger droplet diameters with relatively low evaporation rates. Unsteady droplet trajectory calculations were resolved coincidentally with the transient continuous phase solution. If droplets collided, they either bounced off one another or coalesced to form a single droplet. Solution time step size was limited primarily by numerical stability requirements from two-phase solution coupling and secondarily by accuracy requirements induced by droplet collision and breakup submodels. Too coarse of a time step or mesh resolution caused collision and breakup models to falsely steer the solution. Time step size also affected trajectory accuracy by controlling the accuracy of the direction and distance a droplet must travel with respect to its velocity [56].

Droplet drag estimation was approximated using a dynamic drag law that accounted for the effects of droplet distortion observed to be significant in certain circumstances from near-field flow visualization photography. Distortion effects are important because drastic changes in droplet shape can affect drag values by as much as 50% or more. The dynamic drag law varies the drag between the value for a sphere ($C_{Drag,Sphere}$) and a value of 1.54 corresponding to the shape of a disk parallel to the oncoming flow. The drag coefficient is derived through empirical correlation and defined by [56]:

$$C_{Drag} = C_{Drag,Sphere}(1 + 2.632s) \tag{21}$$

where $C_{Drag,Sphere}$ is determined by:

$$C_{Drag,Sphere} = \begin{cases} 0.424 & Re_d > 1000 \\ \frac{24}{Re_d}\left(1 + \frac{1}{6} Re_d^{2/3}\right) & Re_d \leq 1000 \end{cases} \tag{22}$$

The s term is droplet distortion derived from the solution of:

$$\frac{d^2 s}{dt^2} = \frac{C_F}{C_b} \frac{\rho_G}{\rho_L} \frac{V_{d,rel}{}^2}{r^2} - \frac{C_k \sigma_{L/G}}{\rho_L r^3} s - \frac{C_\beta \mu_L}{\rho_L r^2} \frac{ds}{dt} \tag{23}$$

where C_F, C_b, C_k, and C_β terms are dimensionless model constants associated with Taylor's analogy. The r term represents the droplet radius. At maximum distortion (s = 1), the drag

coefficient asymptotes to a disk. In the limit of no distortion ($s = 0$), the drag coefficient of a sphere is recovered [56].

Droplet breakup model selection was governed by the jet's characteristic gaseous Weber number regime. Firefighting jets exhibit gaseous Weber numbers typically less than 100, indicating a low gaseous Weber number model was best suited for this study. Vibrational and bag breakup typically govern low gaseous Weber number jet disintegration. The classic Taylor Analogy Breakup (TAB) model was selected due to model implementation simplicity, acceptable accuracy for a wide range of industrial flows including the firefighting jets presently studied, as well as numerical speed to achieve a solution compared to alternate breakup models. The TAB model is based on Taylor's analogy between a distorting and oscillating droplet and a spring mass system. The equation governing a damped, forced oscillator is:

$$F_{Ext} - kx_e - \beta\frac{dx_e}{dt} = m_d\frac{d^2x_e}{dt^2} \tag{24}$$

where x_e is the droplet equator placement from its spherical or undisturbed position, β is a damping coefficient, and m_d is the mass of the droplet. Model coefficients are derived from Taylor's analogy:

$$\frac{F_{Ext}}{m_d} = C_F\frac{\rho_G V_{d,rel}^2}{\rho_L r} \tag{25}$$

$$\frac{k}{m_d} = C_k\frac{\sigma_{L/G}}{\rho_L r^3} \tag{26}$$

$$\frac{\beta}{m_d} = C_\beta\frac{\mu_L}{\rho_L r^2} \tag{27}$$

where droplet drag, surface tension, and viscosity forces are analogous to the restoration of an externally applied aerodynamic force (F_{Ext}), a spring force defined via a spring stiffness constant (k), and a damping force. The droplet is assumed to break up if the distortion grows to a critical ratio of the droplet radius defined by:

$$x_e > C_b r \tag{28}$$

where C_b is a constant equal to 0.5, indicating breakup occurs when droplet distortion is equal to half the droplet radius. This approach assumes the droplet undergoes a single or fundamental oscillation mode. Once the amplitude (A) for an undamped oscillation is calculated using equation 29,

$$A = \left[(s - We_T)^2 + \left(\frac{ds \cdot dt^{-1}}{\omega}\right)^2\right]^{0.5} \tag{29}$$

a solution for determining droplet breakup can be found. By nondimensionalizing the droplet distortion term $s = x_e \cdot C_b r^{-1}$, substituting back into equation 23 and solving for s yields:

$$\begin{aligned} s(t) \;=\; & We_T \\ & + e^{-(t \cdot t_d^{-1})} \left[(s(0) - We_T) cos(\omega t) \right. \\ & \left. + \frac{1}{\omega} \left(\frac{ds(0)}{dt} + \frac{s(0) - We_T}{t_d} \right) sin(\omega t) \right] \end{aligned} \tag{30}$$

For $s > 1$, droplet breakup occurs. The term We_T is the modified gaseous Weber number based on droplet radius and TAB model coefficients are defined as:

$$We_T = \frac{C_F}{C_k C_b} \frac{\rho_g V_{d,rel}^2 r}{\sigma_{L/G}} \tag{31}$$

where droplet lifetime (t_d) and oscillation frequency (ω) are defined, respectively, as:

$$t_d = \frac{2}{C_\beta} \frac{\rho_L r^2}{\mu_L} \tag{32}$$

$$\omega = \left(C_k \frac{\sigma_{L/G}}{\rho_L r^3} - \frac{1}{t_d^2} \right)^{0.5} \tag{33}$$

The model constants C_k, C_β, and C_F are a combination of both empirically and theoretically derived terms taken to be 8, 5, and 0.33, respectively [56].

As droplet oscillations grow toward a critical value, the parent droplet breaks into a number of smaller child droplets. As droplets distort from a spherical shape, the dynamic drag law accounts for modifications to the drag coefficient. The child droplet's size is determined by equating the total energy of the parent drop due to distortion and oscillation to the combined energy of the child droplets, all while enforcing mass conservation. The TAB model is customized to the jet in terms of child droplet resolution when breakup does occur, and it can become a limiting factor in terms of defining a smooth child droplet diameter distribution [56].

An alternative breakup model, referred to as the Stochastic Secondary Droplet (SSD) model, also applicable to low gaseous Weber number flows was also available within ANSYS Fluent®. It treats breakup as a discrete random event resulting in a distribution of diameter scales over a range independent of parent droplet size. The SSD model is sampled from an analytical solution to the Fokker-Planck equation for the probability distribution of breakup with droplet size distribution based on local conditions. The SSD model provided nearly identical results to that of the TAB model, but it was not selected due to reduced computational efficiency [56].

Because firefighting jets consist of billions of droplets, the computational cost to explicitly calculate droplet collision from first principles with respect to the large-length scales specifically involved with this study was still prohibitive. To circumvent this issue, parcels or a statistical representation of a number of individual droplets, were used to simulate droplet collision as well as breakup mechanisms. A second-order accurate collision algorithm, developed by O'Rourke

(cited in reference 56), was employed. Its implementation was based on the relationship between a pair of parcels located within the same computational mesh cell. Collision stemmed from a probability distribution based on a Poisson distribution. Collision estimates were calculated with respect to the parcel containing the larger-diameter droplet. If both parcels were on a head-on collision or approaching one another at an obtuse angle, the collision tended to result in coalescence. If the collision angle was acute, parcels tended to deflect or bounce off one another. Once parcels impacted one another, trajectory was altered regardless of collision type. Collision calculations were based on the collisional Weber number (We_C), defined as follows [56]:

$$We_C = \frac{\rho_G V_{c,rel}^2 D10}{\sigma} \tag{34}$$

where $V_{c,rel}$ is the relative velocity between colliding parcels and $D10$ is the mean droplet diameter of the involved parcel groups [56].

5.2.2 Turbulence.

All jet configurations investigated were high Reynolds number flows consistent with conventional firefighting jet classification, thus the role of turbulence was considered. The LES turbulent model was selected for its ability to explicitly resolve large-scale eddies primarily dependent on boundary conditions, simulation geometry, and droplet-air interactions. Small-scale eddies were mathematically modeled, which tended to be geometrically independent, more isotropic, and therefore more universal. However, complex multiphase fluid interactions between the liquid jet and surrounding air can be viable sources of anisotropic turbulence. LES models typically demand more refined meshing requirements due to near-wall effects often limiting their industrial application by substantially increasing computational overhead. However, most wall effects were neutralized in the present work because the physical domain of interest had minimal relative wall influence in critical areas of the flow [56].

LES models use a subgrid scale model to mathematically represent the finer, small-scale turbulent eddies in the continuous phase. It should be noted that the effect of droplets have not been included in the subgrid scale model, which can be significant for the flow regimes in the present study. The Wall-Adapting Local Eddy-Viscosity (WALE) subgrid scale model was employed due to its wide applicability to an assortment of jet flows. The WALE model provided further advantage by returning zero turbulent viscosity in pure laminar areas of the flow field. Alternative subgrid scale modeling options were incapable of approaching exclusive laminar flow behavior. The WALE model also provided greater numerical stability when solving the firefighting jet flow field compared to other subgrid scale models [56].

5.3 PHYSICAL DOMAIN.

The physical domain was modeled to represent the extent of the jet containment bed and nozzle stand region. Geometries were kept simple to maintain high grid quality and to focus refinement in areas exposed to high jet shear flow rates, particularly local and axially downstream from the nozzle. The nozzle, its stand, and downstream jet containment zone were not explicitly modeled. This approach resulted in a fully orthogonal structured mesh topology, as shown in figure 50.

The mesh consisted of approximately 411,000 cells ranging in size from 2 cm near the nozzle to 10 cm in far downstream reaches. The origin, located at the nozzle exit, along with directional orientation was kept consistent with the experimental study. Details on the firefighting jet injection settings into the physical domain are discussed with boundary conditions in section 5.4.

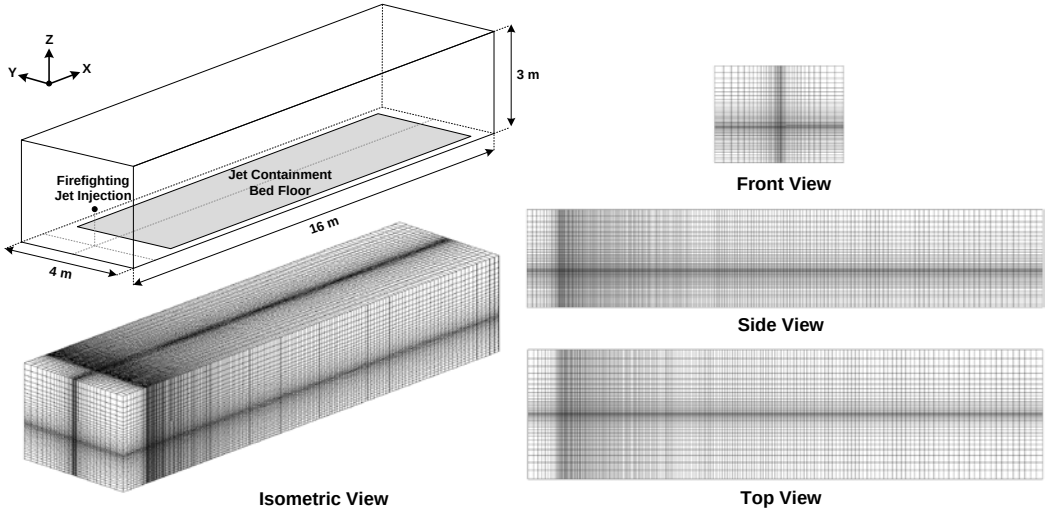

Figure 50. The Physical Model Flow Domain

5.4 BOUNDARY CONDITIONS.

Individual boundary conditions were assigned for the continuous (Eulerian) phase representing the atmosphere as well as the discrete (Lagrangian) phase representing firefighting jet droplet dispersion. The continuous phase ceiling and sides were defined as subsonic pressure outlet boundaries, and the continuous phase floor was defined as a no-slip wall with respect to the air. With air expected to flow in and out of the domain due to jet entrainment, the pressure outlet boundary was selected because the flow direction was allowed to float either inward or outward based on local changes in total pressure. The boundary static pressure was set to 101.3 kPa. Figure 51 depicts boundary condition assignments for the continuous phase.

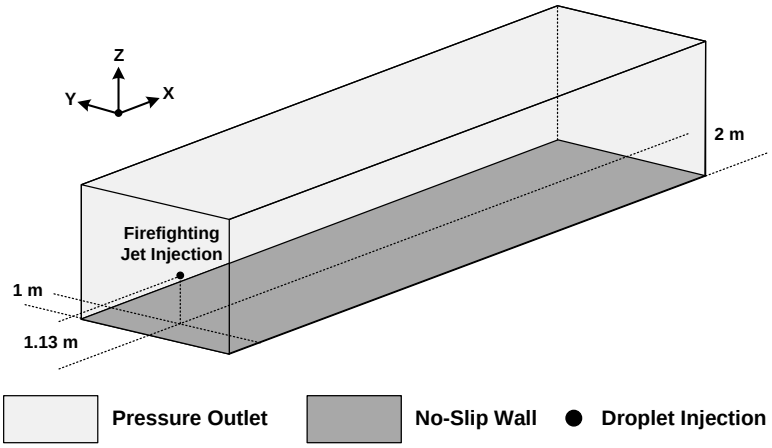

Figure 51. Continuum Phase Model Boundary Conditions

Although the experimental setup included a containment zone along the back half of the firefighting jet containment bed, it was not integrated into the final model results. Its influence was estimated to be minimal based on agent ground pattern tests in comparing the results with and without containment zone curtains. These results are reported in section 6.2.1. A CFD model sensitivity study, with and without the presence of the rear jet containment zone, was conducted to further examine this issue.

An escape condition was applied for the discrete phase to all domain boundaries. Although in reality the droplets landing on the floor either formed a liquid pool or foam pattern, depending on agent composition, this detail was disregarded, as the goal of this modeling effort was to analyze the flow dynamics of the firefighting jetting process only. No significant coupling between the firefighting jet and ground pooling behavior was observed experimentally during flow visualization.

Firefighting jet entry into the domain was defined in terms of a single point DPM injection where the nozzle was located in space, similar to how the experiments were conducted. Unique injection conditions were defined for each firefighting jet condition listed in table 8. Phase Doppler, 1-D vertical profile data recorded closest to the nozzle exit (x = 6.4-mm (0.25-in.) plane) was used to define constant injection conditions. Near-nozzle exit perturbation effects were not considered. Droplet injection velocity for all diameter bins was approximated by the maximum profile, mean axial droplet velocity from the x = 6.4-mm (0.25-in.) plane, which was typically located at the central point of where phase Doppler data were collected. Droplet size distribution was approximated using measurements from the same profile point discretized over 25 equal width diameter bins. Mean axial droplet velocities recorded by the PDPA were corroborated by readings from the firefighting agent delivery system flow meter and knowledge of the nozzle diameter for each test case. The flow meter results were also used to define the firefighting jet total mass flow injection rate.

5.5 MATERIAL PROPERTIES.

Although all CFD simulations were adiabatic, material properties were defined at 298 K, consistent with the approximate mean laboratory temperature during the phase Doppler tests. Compressibility effects were negligible as air flow velocities stayed well below Mach 0.3, and the liquid firefighting agent density was assumed to be constant. All material properties were defined as constant values for both the continuous air phase as well as the discrete phase representing the liquid droplets. Material properties were defined uniquely for both water and AFFF, including parameters such as density, dynamic viscosity, and surface tension. The differences in these properties, particularly with regard to surface tension, provided the distinguishing influence of AFFF in the computational study. Although AFFF surface tension varies as a function of surface age due to current CFD submodeling software incompatibilities, this property was defined as its equilibrium constant. This was considered a reasonable simplification given the average firefighting jet droplet spent most of its in-flight lifetime, which was determined to be on the order of 1 s near its equilibrium surface tension value. For low-pressure firefighting jets with low nozzle exit velocities, this argument is strengthened, and vice versa for high-pressure firefighting jets with high nozzle exit velocities. All AFFF material properties used in the present study are in appendix B.

5.6 NUMERICS.

All simulations were solved using the semi-implicit method for pressure-linked equations (SIMPLE) pressure-velocity coupling algorithm for the continuous phase. DPM droplet trajectories were solved using the default automated tracking scheme and employed both a highorder trapezoidal and low order implicit discretization method. This approach was favored over alternatives because it handled non-equilibrium flow conditions with greater accuracy. This method also maintained compatibility with the largest number of CFD submodels capable of imparting forces on droplet parcels likely to be employed in future stages of model development. By default, the CFD software applies the influence of the DPM parcel only to the control volume or mesh cell containing the parcel. As an alternative approach, a high order Gaussian node-based averaging scheme was used to incorporate the influence of surrounding mesh cells on the droplet parcel. This method which employed default scheme values also helped reduce mesh dependence particularly on collision and breakup calculations [56].

Spatial discretization of gradients, pressure, and momentum were enforced using least squares cell-based, second order, and bounded central differencing methods, respectively. Transient formulations were carried out using bounded second order implicit techniques. Bounded methods are preferred over unbounded methods due to their added numerical stability. Under-relaxation factors were kept at default software values. See reference 55 for additional details regarding aspects of the numerical strategy.

5.7 SOLUTION STRATEGY.

Preprocessing, preliminary CFD calculations, and postprocessing were conducted on a 3.46-GHz Intel Xeon® Westmere-EP 12-core Linux server with 48 GB of shared memory located in the WVU Engineering Data Center. Final production computations were carried out at the U.S. Army Engineering Research and Development Center DOD Supercomputing Resource Center on a SGI Altix Ice 8200. The SGI is capable of 172 teraflops operating 1,920 2.8-GHz Intel Xeon® (Nehalem-EP) nodes, 8 cores per node, with 48 GB of shared memory per node. The SGI uses 4X DDR Infiniband for distributed (parallel) computing across nodes.

The physical domain was initialized to static pressure and zero velocity conditions. For each firefighting jet configuration, droplets were injected at each time step to match the total mass flow rate of the jet at the firefighting jet injection location shown in figure 51. After a temporal sensitivity study was conducted, a 1-ms fixed time step was chosen for all firefighting jet simulation cases with the continuous and discrete phase coupled after every time step. Inner temporal iterations were limited to 30 with convergence set at the scaled residual default of 0.001. Conservation of the coupled droplet-air mass and momentum convergence was achieved on most occasions but not for every single time step. However, residuals dropped a minimum of three orders of magnitude every time step, exhibiting excellent convergence consistency and numerical stability. Simulations were solved for 10 s in physical time to ensure each firefighting jet was fully developed. Droplet velocity and size data were tabulated as they passed through virtual planes positioned normal to the jet centerline axis defined in the same axial location as phase Doppler vertical profiles. Solutions took about 375 central processing unit (CPU) hours to complete. Sixty-four CPUs per simulation on DOD SGI resources were used, which equated to about 4 to 6 hours of real time, based on machine load, to solve each CFD model case.

6. RESULTS.

6.1 EXPERIMENTAL FIREFIGHTING JET FLOW VISUALIZATION RESULTS.

Flow visualization was recorded on the ten firefighting jet configurations presented in section 4.1. Each configuration is illustrated in figure 43 and listed in table 6. Details on the experimental approach are in section 4.2. The ten configurations represented five nozzle pressure-flow rate combinations using water and 6% AFFF as the agent. Images were recorded at far-, middle-, and near-field points of observation. All photographs were converted to gray scale with their brightness and contrast optimized to better distinguish firefighting jet features from their surroundings. Standard photographs taken of middle- and high-pressure jets were slightly blurry compared to low-pressure jets at the expense of camera shutter speed to allow for great illumination of the subject matter. Although laser sheet lighting methods alleviated most of these issues, this process was limited by the maximum sweep speed achievable by the galvanometer scanner generating the laser sheet, which was still lower than jet speeds reached near the nozzle for medium- and high-pressure jets. However, further downstream, galvanometer scanner speeds were adequate for all firefighting jet flow visualizations.

6.1.1 Far-Field Flow Visualization Results.

Figures 52 through 61 illustrate the firefighting jet far field in the axial direction using standard photography methods. White square makers were stationed every 1.5 m (5 ft) for reference. Pictures were recorded with an 18-mm focal length for wide-angle capture of the jet parallel to the y = 0-m plane. The camera was positioned against the opposing laboratory wall to maximize viewing area. The effective reach of all firefighting jets fell within the bounds of the frame, except for high-flow rate, low-pressure jets, which extended 1 to 2 m (3.3 to 6.6 ft) beyond.

Based on these photographs, low-pressure jets stayed intact, demonstrating a more cohesive stream compared to medium- and high-pressure jets, which exhibited enhanced breakup and relatively larger-scale turbulent eddy formation and dispersion due to an increase in jet Reynolds number. As flow rate was increased, an increase in jet reach was observed due to an increase in axial momentum. High-pressure jets were less affected by gravity and exhibited more axial symmetry transporting smaller, less massive droplets at higher axial velocities compared to low-pressure droplets composed of larger, more massive droplets at lower axial velocities.

Qualitative structural differences between water and AFFF jets were difficult to perceive because AFFF jets were significantly more opaque, even when nozzle conditions (i.e., pressure and flow rate) were held constant. The blackout curtain, providing background contrast, remedied this issue somewhat, but improvements were marginal. AFFF jets appeared fuller or thicker, which was assumed to be due to a larger concentration of droplets forming downstream compared to water jets. Figures 62 through 66 illustrate the firefighting jet far field in the axial direction, which were photographs taken at an oblique angle from behind and above the nozzle focused on the z = 0-m plane and illuminated by a horizontal laser light sheet. Figures 67 through 71 depict an oblique horizontal view across the y-direction of each firefighting jet along the x = 6.1-m (20-ft) plane, which were also illuminated by a vertical laser light sheet. This plane approximates the axial midpoint for medium- and high-flow rate jets. Figures 62 through 71 support the same observations as those stated for figures 52 through 61.

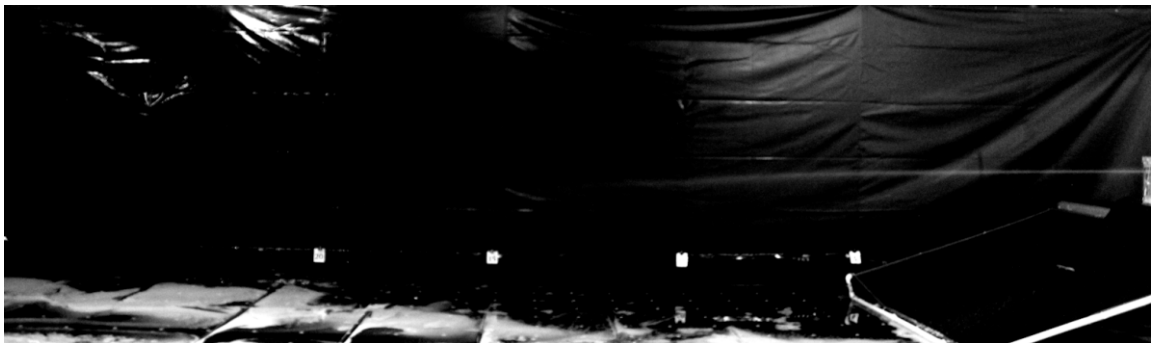

Figure 52. Standard Far-Field Flow Visualization Parallel to the y = 0-m Plane: Low-Flow, Low-Pressure Water Jet (Flow is from right to left.)

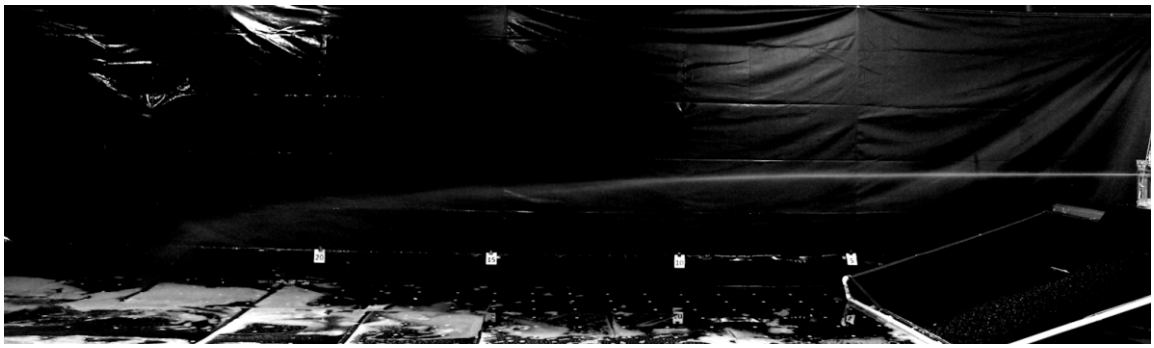

Figure 53. Standard Far-Field Flow Visualization Parallel to the y = 0-m Plane: Low-Flow, Low-Pressure AFFF Jet (Flow is from right to left.)

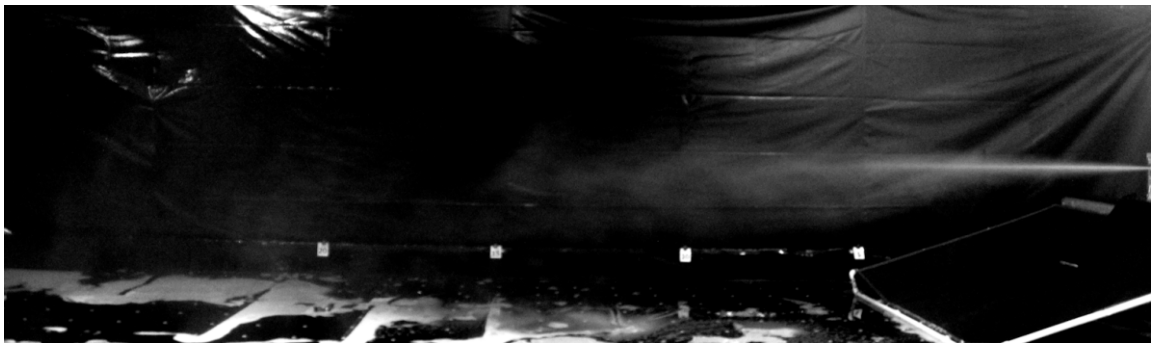

Figure 54. Standard Far-Field Flow Visualization Parallel to the y = 0-m Plane: Low-Flow, High-Pressure Water Jet (Flow is from right to left.)

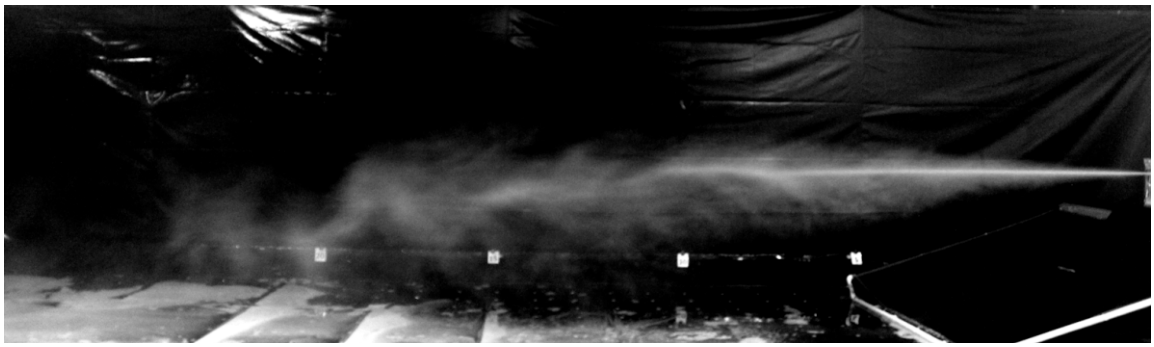

Figure 55. Standard Far-Field Flow Visualization Parallel to the y = 0-m Plane: Low-Flow, High-Pressure AFFF Jet (Flow is from right to left.)

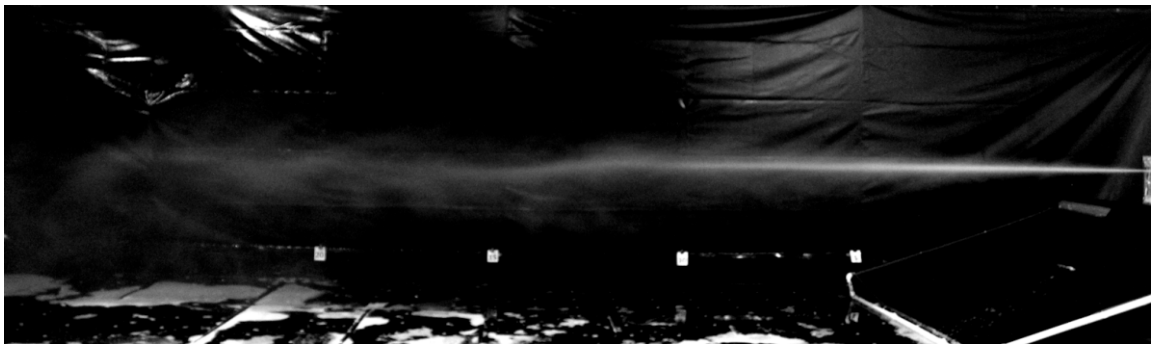

Figure 56. Standard Far-Field Flow Visualization Parallel to the y = 0-m Plane: Medium-Flow, Medium-Pressure Water Jet (Flow is from Right to Left)

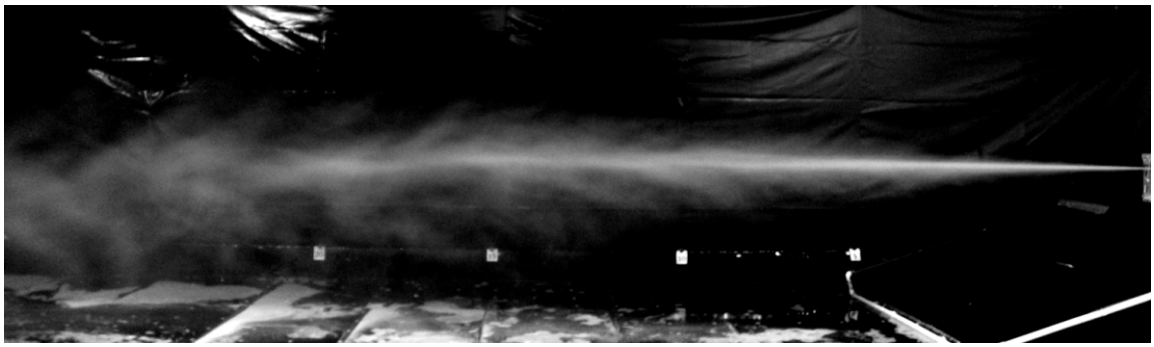

Figure 57. Standard Far-Field Flow Visualization Parallel to the y = 0-m Plane: Medium-Flow, Medium-Pressure AFFF Jet (Flow is from right to left.)

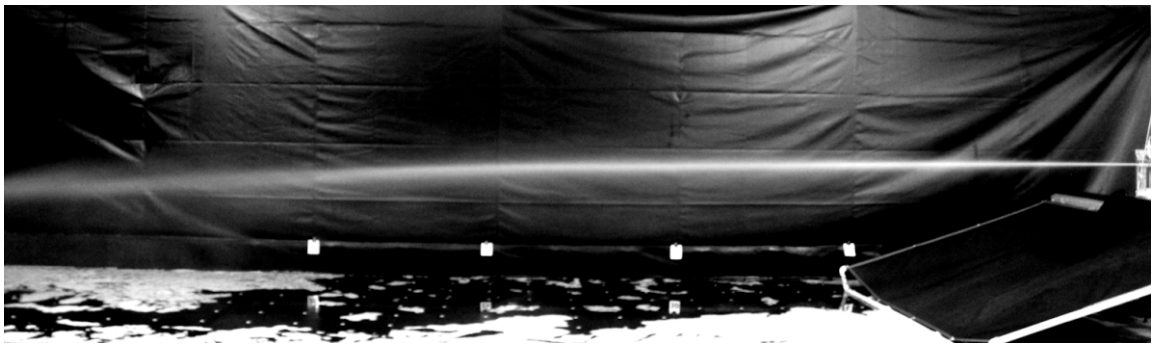

Figure 58. Standard Far-Field Flow Visualization Parallel to the y = 0-m Plane: High-Flow, Low-Pressure Water Jet (Flow is from right to left.)

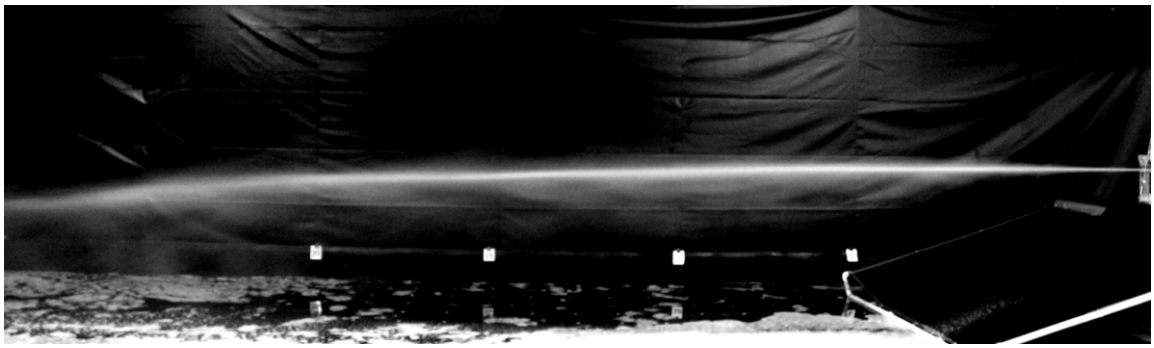

Figure 59. Standard Far-Field Flow Visualization Parallel to the y = 0-m Plane: High-Flow, Low-Pressure AFFF Jet (Flow is from right to left.)

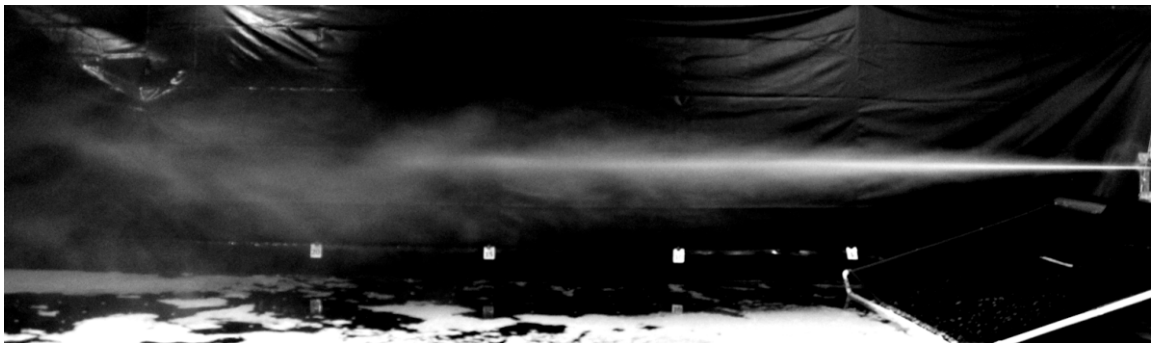

Figure 60. Standard Far-Field Flow Visualization Parallel to the y = 0-m Plane: High-Flow, High-Pressure Water Jet (Flow is from right to left.)

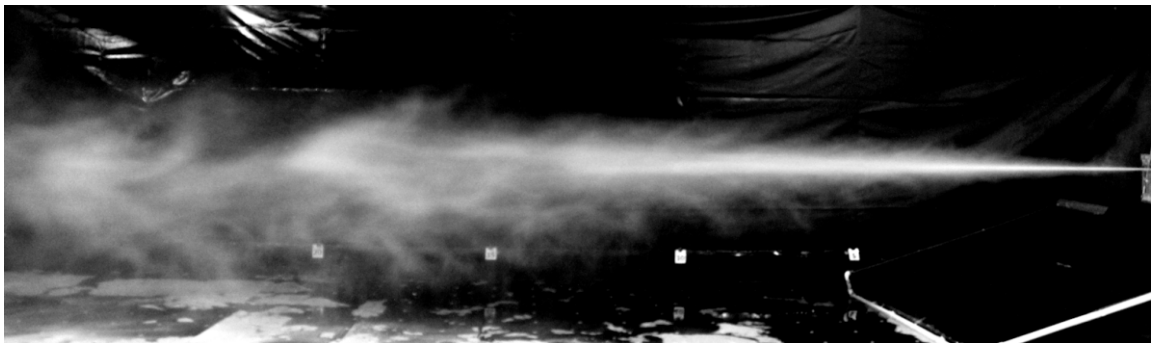

Figure 61. Standard Far-Field Flow Visualization Parallel to the y = 0-m Plane: High-Flow, High-Pressure AFFF Jet (Flow is from right to left.)

(a) (b)

Figure 62. Laser Sheet Far-Field Flow Visualization Oblique to the z = 0-m Plane (a) Low-Flow, Low-Pressure Water Jet and (b) Low-Flow, Low-Pressure AFFF Jet (Flow is from bottom to top.)

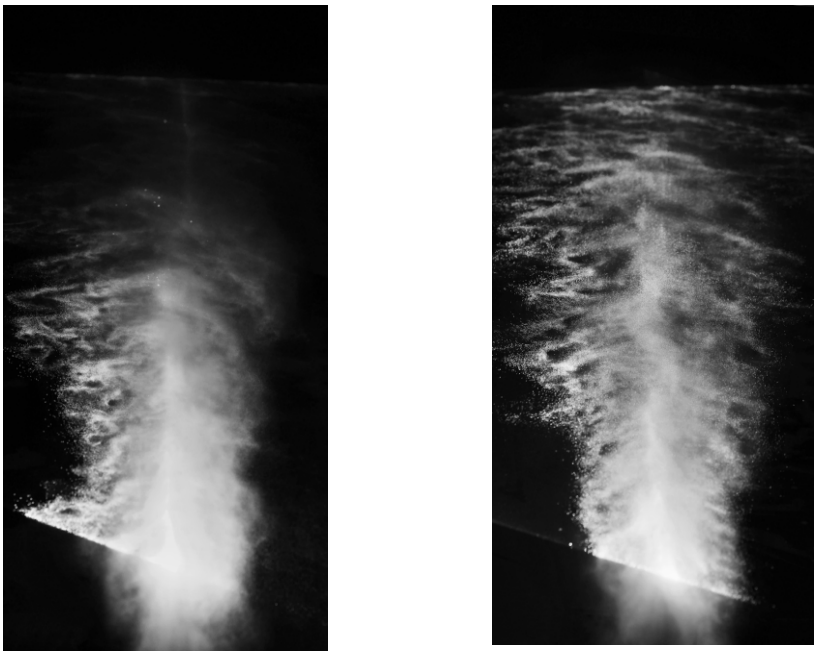

(a) (b)

Figure 63. Laser Sheet Far-Field Flow Visualization Oblique to the z = 0-m Plane (a) Low-Flow, High-Pressure Water Jet and (b) Low-Flow, High-Pressure AFFF Jet (Flow is from bottom to top.)

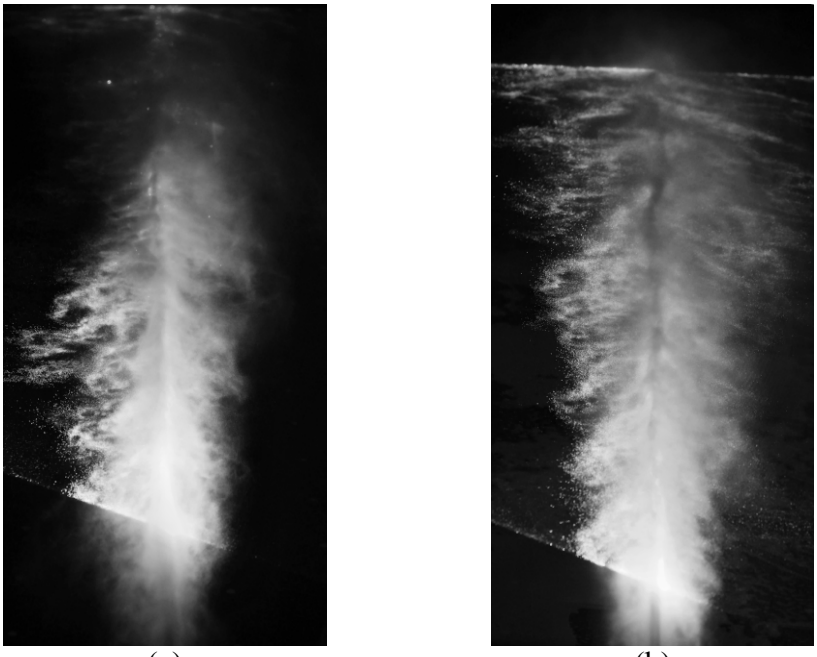

(a) (b)

Figure 64. Laser Sheet Far-Field Flow Visualization Oblique to the z = 0-m Plane (a) Medium-Flow, Medium-Pressure Water Jet and (b) Medium-Flow, Medium-Pressure AFFF Jet (Flow is from bottom to top.)

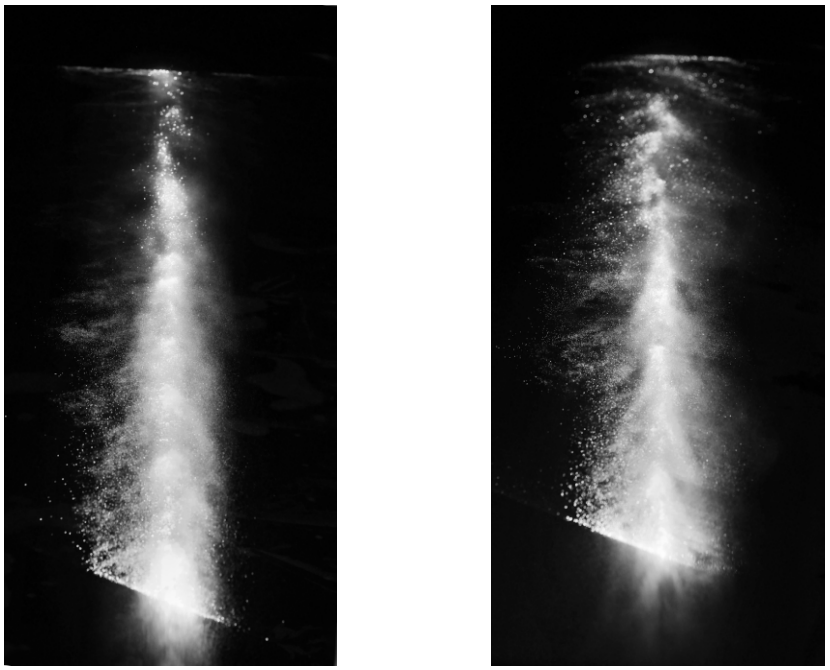

(a) (b)

Figure 65. Laser Sheet Far-Field Flow Visualization Oblique to the z = 0-m Plane (a) High-Flow, Low-Pressure Water Jet and (b) High-Flow, Low-Pressure AFFF Jet (Flow is from bottom to top.)

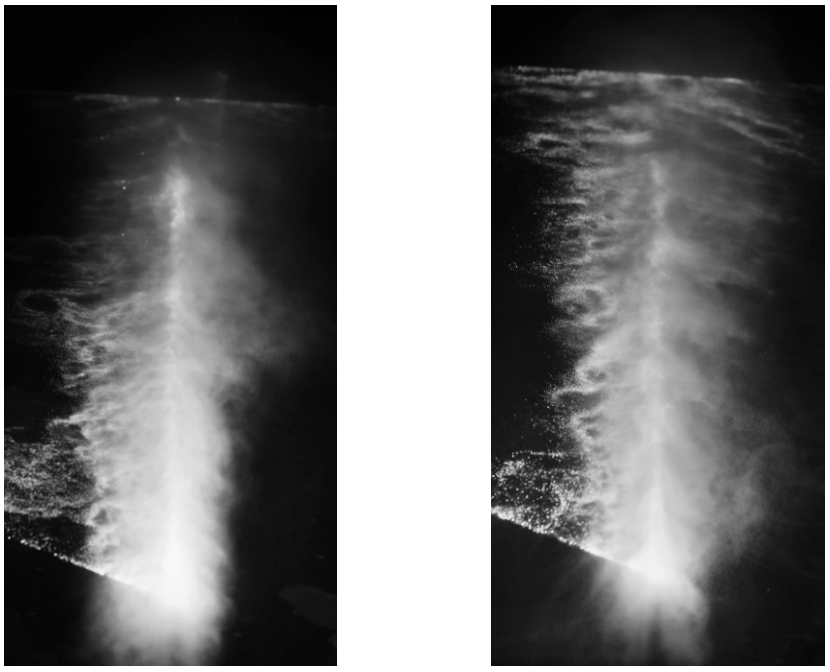

(a) (b)

Figure 66. Laser Sheet Far-Field Flow Visualization Oblique to the z = 0-m Plane (a) High-Flow, High-Pressure Water Jet and (b) High-Flow, High-Pressure AFFF Jet (Flow is from bottom to top.)

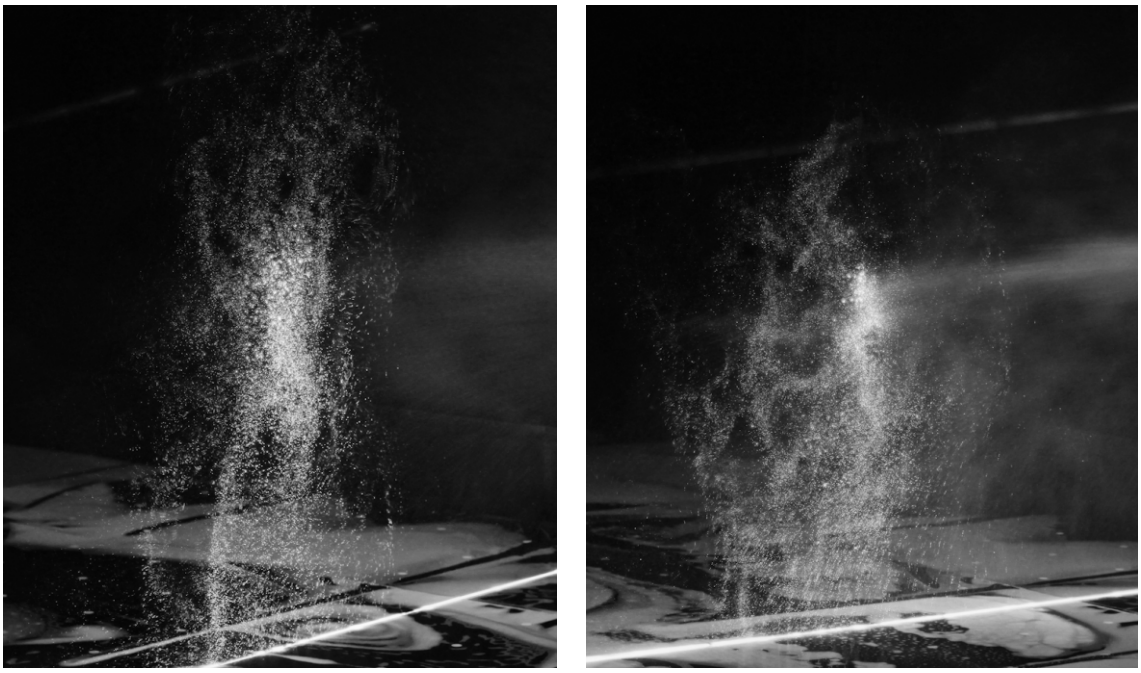

(a) (b)

Figure 67. Laser Sheet Far-Field Flow Visualization Oblique to the x = 6.1-m (20-ft) Plane (a) Low-Flow, Low-Pressure Water Jet and (b) Low-Flow, Low-Pressure AFFF Jet (Flow is from bottom to top.)

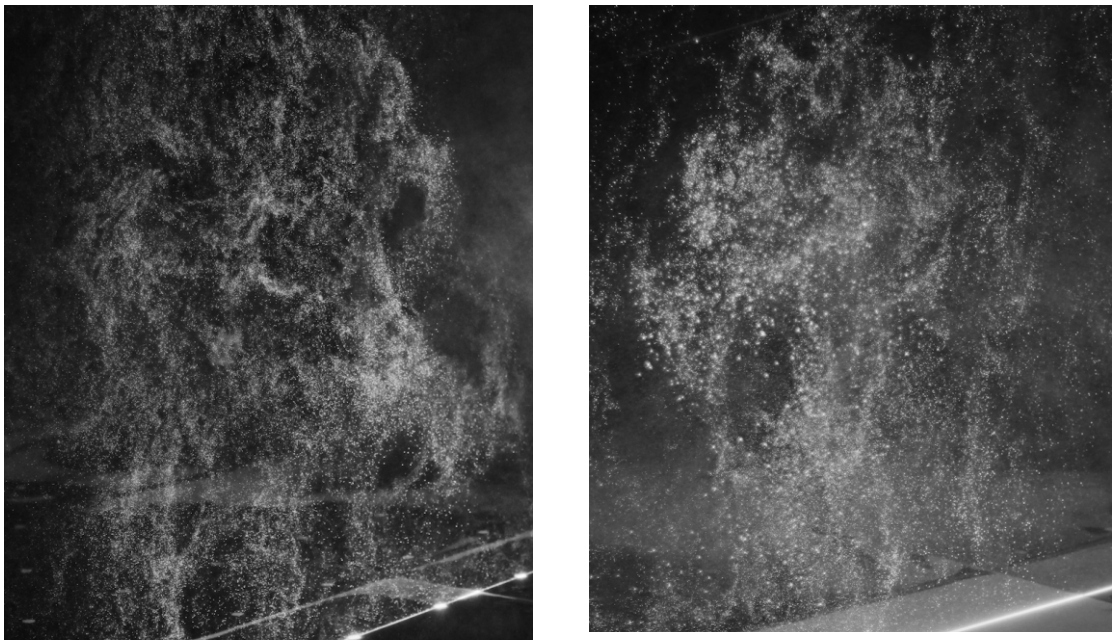

(a) (b)

Figure 68. Laser Sheet Far-Field Flow Visualization Oblique to the x = 6.1-m (20-ft) Plane (a) Low-Flow, High-Pressure Water Jet and (b) Low-Flow, High-Pressure AFFF Jet (Flow is from right to left.)

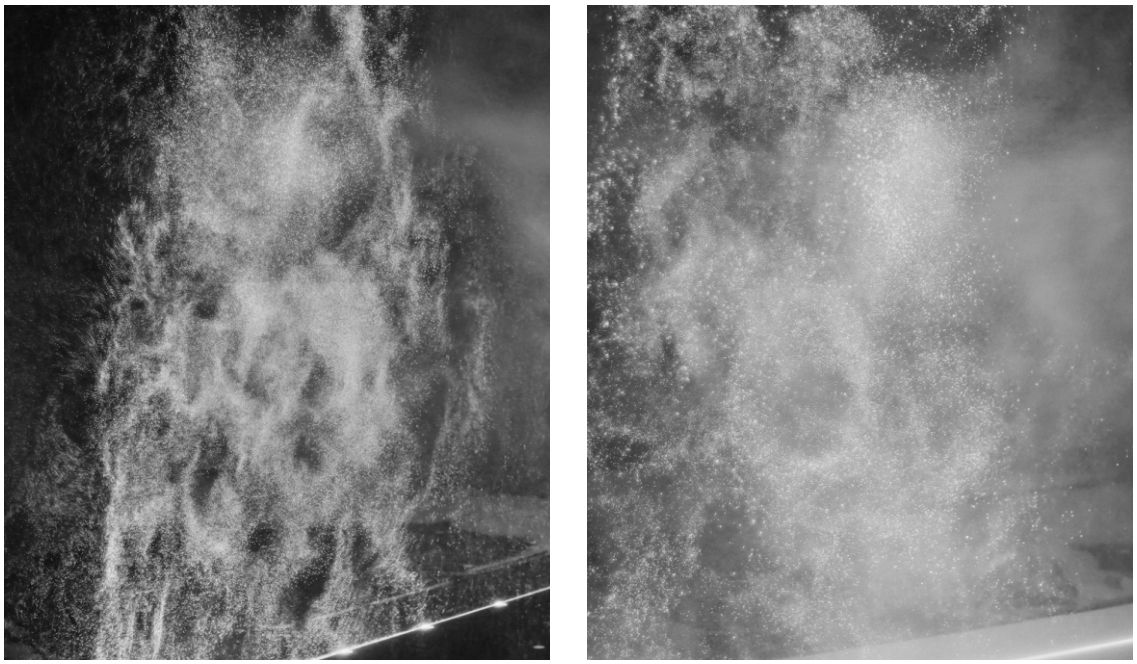

(a) (b)

Figure 69. Laser Sheet Far-Field Flow Visualization Oblique to the x = 6.1-m (20-ft) Plane (a) Medium-Flow, Medium-Pressure Water Jet and (b) Medium-Flow, Medium-Pressure AFFF Jet (Flow is from right to left.)

(a) (b)

Figure 70. Laser Sheet Far-Field Flow Visualization Oblique to the x = 6.1-m (20-ft) Plane (a) High-Flow, Low-Pressure Water Jet and (b) High-Flow, Low-Pressure AFFF Jet (Flow is from right to left.)

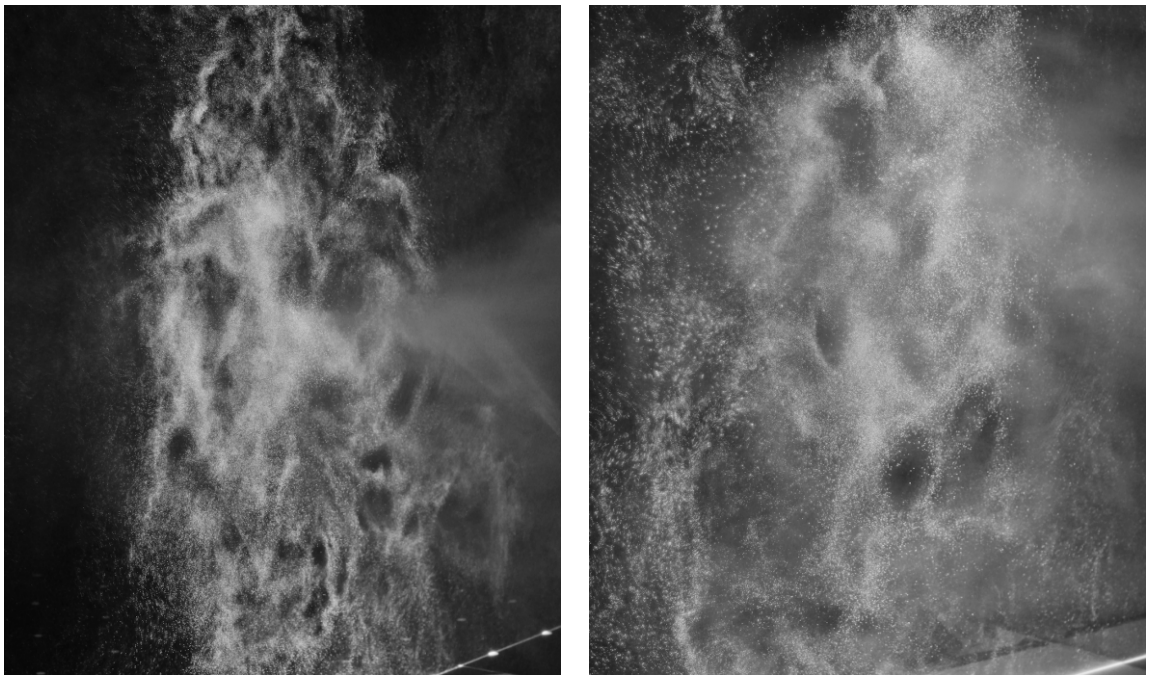

(a) (b)

Figure 71. Laser Sheet Far-Field Flow Visualization Oblique to the x = 6.1-m (20-ft) Plane (a) High-Flow, High-Pressure Water Jet and (b) High-Flow, High-Pressure AFFF Jet (Flow is from right to left.)

6.1.2 Mid-Field Flow Visualization Results.

The mid-field flow visualization illustrated the relationship between overall jet flow dynamics and near-field droplet interactions. The mid-field image capture was a challenge compared to far-field capture due to the 3-D downstream jet spread. This made focal plane alignment sporadic and difficult, thus limiting most imagery to areas close to the nozzle near the y = 0-m plane where the jet path was more reliable. High-quality, mid- and near-field image captures were mostly restricted to low-pressure jets when the camera shutter speed was not a limiting factor, especially for standard photographic techniques. High-speed video was recorded, and still images were extracted for presentation. However, frame rates were limited to a maximum of 7500 frames·s^{-1} due to poor subject illumination even after adding significant lighting. With a DSLR camera shutter speed of 4000 frames·s^{-1}, high-speed video results were marginally better compared to conventional methods for high-pressure jets. Electrical safety and water damage risk to photography equipment was an equal concern that limited access to downstream medium- and high-pressure jets where agent dispersion was the greatest.

Figure 72 depicts various evolutionary stages of the high-flow, low-pressure water jet near the nozzle using stroboscopic photography techniques. High-quality images were possible due to the strong periodic nature observed with this particular pressure-flow rate combination. The second strongest periodicity was witnessed from the medium-flow, medium-pressure water jet with photographs of its mid field shown in figure 73. The other jets exhibited some, but much less definitive, periodicity. The qualitative difference between the water and AFFF jets was unremarkable using stroboscopic techniques due to the saturated lighting conditions masking

fine-droplet details. The strobe flash was set at 2350 and 5100 Hz for the high-flow, low-pressure and medium-flow, medium-pressure water jets, respectively. The high-flow, low-pressure water jet pulsation frequency corresponded to the oscillation frequency of the three pump pistons based on the firefighting agent delivery system's motor speed. The medium-flow, medium-pressure water jet pulsation frequency was more difficult to associate with mechanical pump oscillation, although motor speeds were operating at almost half the RPM of the high-flow, low-pressure water jet, indicating a possible shared harmonic. The medium-flow, medium-pressure water jet pulsation frequency could have also been influenced by the accumulator located immediately downstream of the pump. It was configured to suppress higher-frequency (i.e., higher-pressure) pulsations for which the firefighting agent delivery system was originally designed.

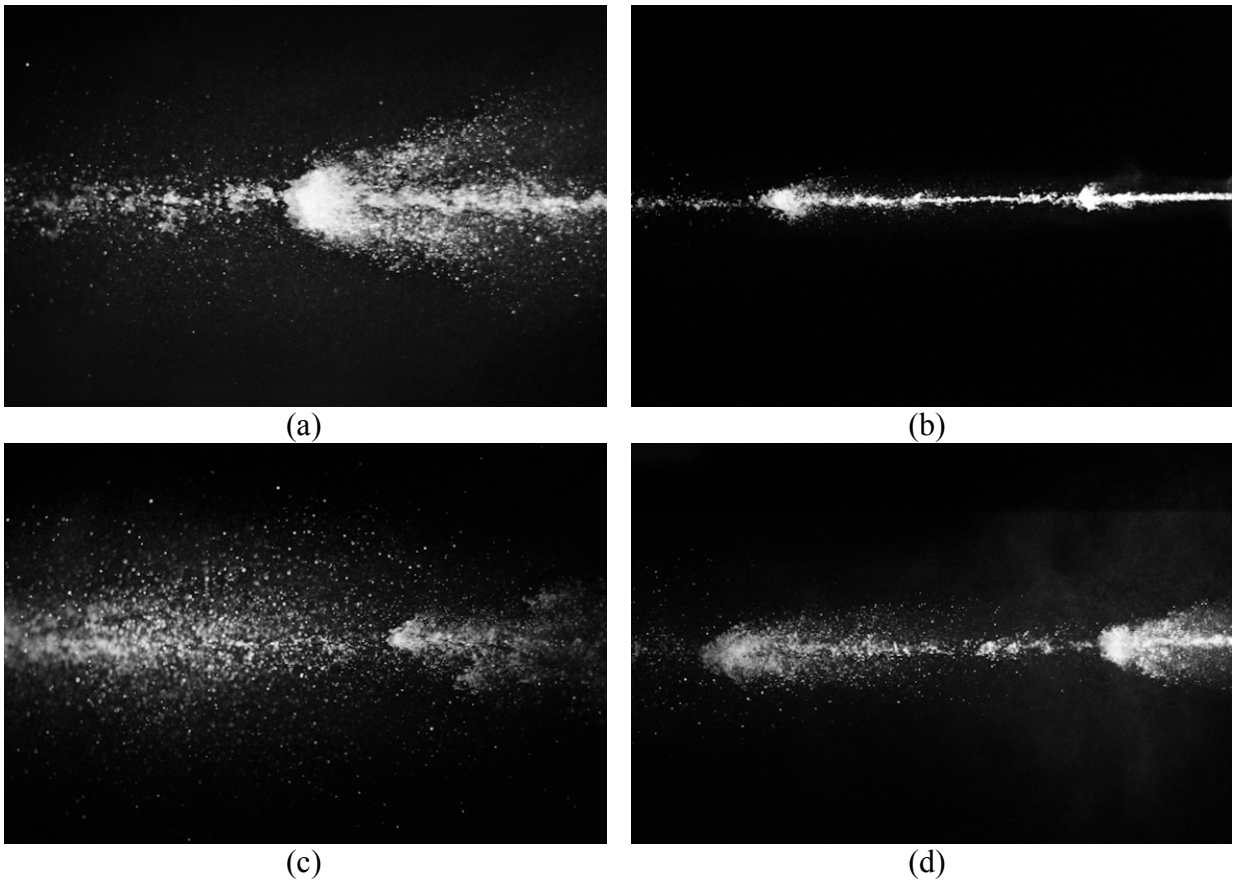

Figure 72. Stroboscopic Mid-Field Flow Visualization of the High-Flow, Low-Pressure Water Jet at Different Stages of Evolution: (a) Magnification of a Pulsation, (b) Pulsation Growth Near the Nozzle Exit, (c) Pulsation Fully Dispersing, and (d) Two Pulsations in Succession (Flow is from right to left.)

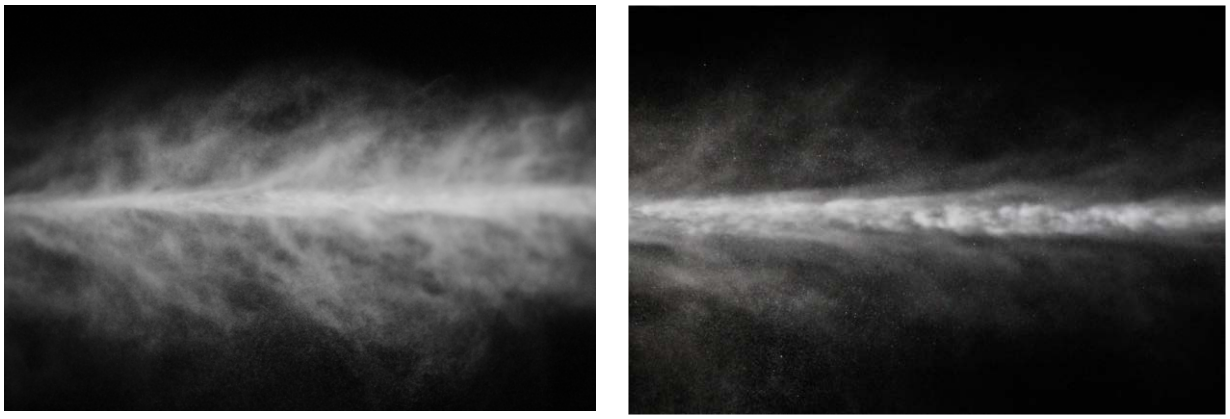

(a) (b)

Figure 73. Stroboscopic Mid-Field Flow Visualization Focused on the y = 0-m Plane of the Medium-Flow, Medium-Pressure Water Jet (a) Downstream of the Nozzle and (b) Near the Nozzle (Flow is from right to left.)

Figures 74 and 75 depict a normalized FFT spectral analysis on pressure data recorded by the nozzle pressure transducer for the high-flow, low-pressure and medium-flow, medium-pressure water jet configurations, respectively. The FFT analysis indicates a dominant frequency mode at about 124 Hz corresponding to the pump piston oscillation frequency for the high-flow, low-pressure water jet, with a less dominant but similar frequency at about 122 Hz for the medium-flow, medium-pressure water jet. Stronger frequencies in the vicinity of the dominant mode in the medium-flow, medium-pressure water jet may indicate why stroboscopic pulsations were not as well-defined for the high-flow, low-pressure water jet.

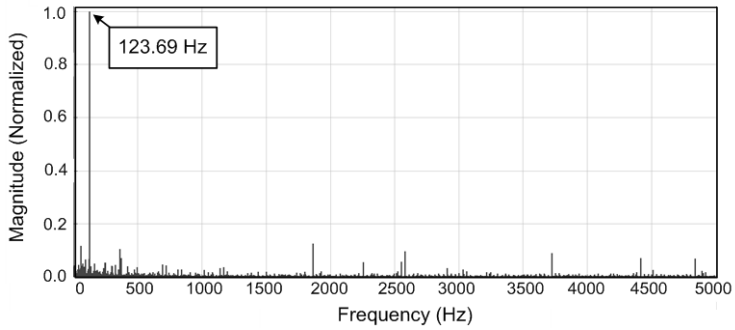

Figure 74. The FFT Analysis of Nozzle Pressure Recorded on the High-Flow, Low-Pressure Water Jet

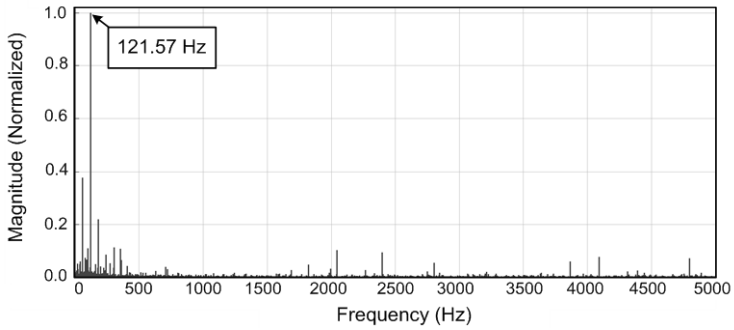

Figure 75. The FFT Analysis of Nozzle Pressure Recorded on the Medium-Flow, Medium-Pressure Water Jet

Figure 76 compares conventional images of the high-flow, low-pressure and medium-flow, medium-pressure water jets recorded at a shutter speed of 4000^{-1} s. High-flow, low-pressure pulsations were easily identified at these camera speeds, but became less apparent for the medium-flow, medium-pressure water jet. Figure 77 depicts high-speed photographic stills from the high-speed video recorded using a 24-mm lens for both water and AFFF jets from the mid field near the nozzle along the y = 0-m plane. The images depict similar trends as those taken with conventional photography techniques, except the elevated high-speed camera frame rate was able to resolve a few extra lower-frequency modes.

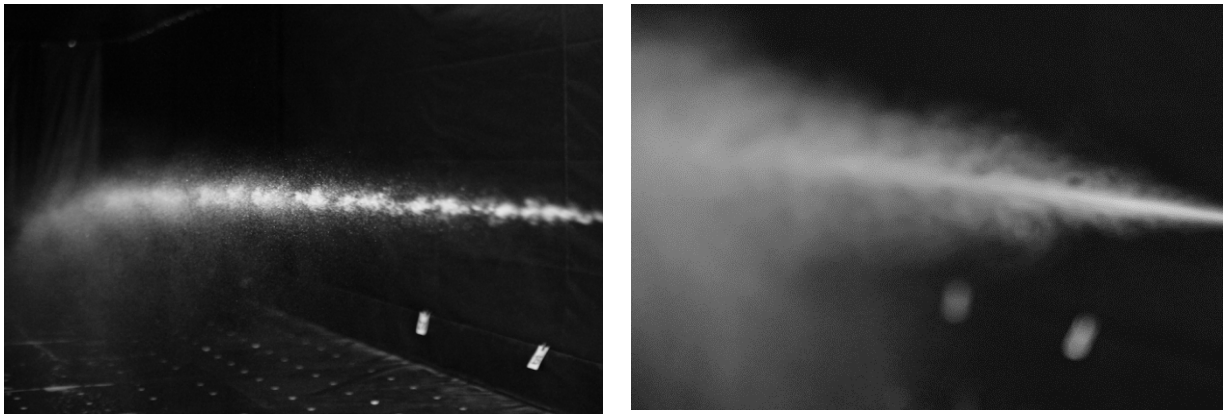

(a) (b)

Figure 76. Standard Mid-Field Flow Visualization Focused Oblique to the y = 0-m Plane for the (a) High-Flow, Low-Pressure Water Jet and (b) Medium-Flow, Medium-Pressure Water Jet (Flow is from right to left.)

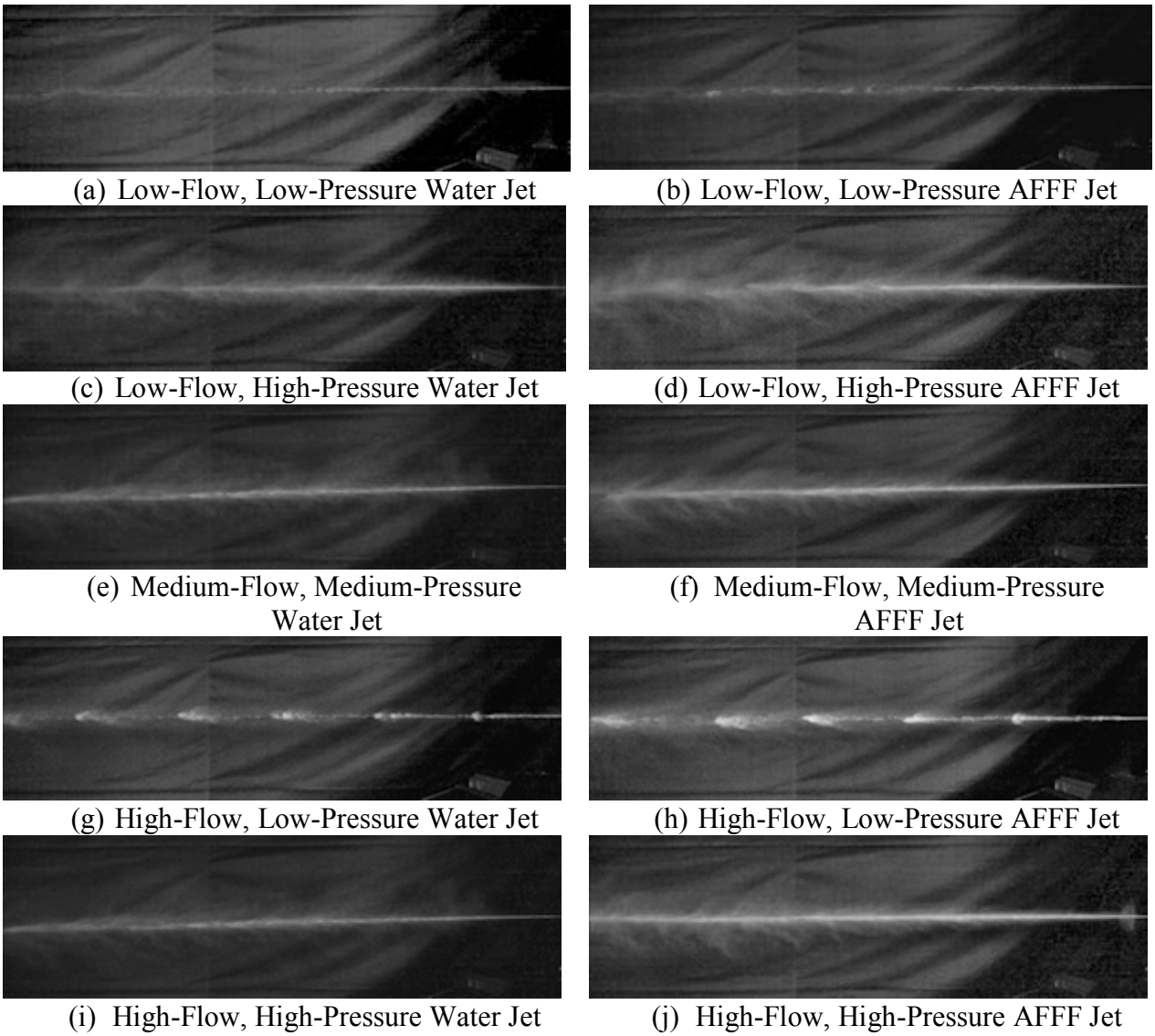

(a) Low-Flow, Low-Pressure Water Jet
(b) Low-Flow, Low-Pressure AFFF Jet
(c) Low-Flow, High-Pressure Water Jet
(d) Low-Flow, High-Pressure AFFF Jet
(e) Medium-Flow, Medium-Pressure Water Jet
(f) Medium-Flow, Medium-Pressure AFFF Jet
(g) High-Flow, Low-Pressure Water Jet
(h) High-Flow, Low-Pressure AFFF Jet
(i) High-Flow, High-Pressure Water Jet
(j) High-Flow, High-Pressure AFFF Jet

Figure 77. High-Speed, Mid-Field Flow Visualization of Each Jet Configuration Focused on the y = 0-m Plane (Flow is from right to left.)

6.1.3 Near-Field Flow Visualization Results.

The near-field photography of droplet breakup posed similar challenges to those encountered while recording mid-field imagery, except the issues were amplified due to the relatively smaller length scales involved. Macro or zoom lenses ranging from 100 to 180 mm in focal length were used. High-quality images were restricted to low-pressure jets as the required combination of high-intensity lighting and camera speeds made fine droplet flow visualization details from medium- to high-pressure jets unfeasible, especially near the nozzle where jet velocities were the greatest.

Figure 78 illustrates the standard evolution of a droplet emanating from the nozzle of a high-flow, low-pressure water jet at incremental distances downstream. Secondary jet breakup was

detected throughout the entire flow field leading up to the nozzle exit plane. This phenomenon was similarly witnessed for the low-flow, low-pressure water jet and was more readily apparent for higher-pressure jets, both using water and AFFF as the agent. This observation supports the validity that the Reynolds, Weber, and Ohnesorge classification of firefighting jets illustrated in figures 14 and 15 largely inhabits the atomization breakup regime.

Qualitative differences between low-flow, low-pressure water and AFFF jet breakup were easiest to discern at 3 m (10 ft) downstream shown in figure 78(a) and (b), respectively. Figure 79 shows that a higher concentration of satellite droplets formed for the AFFF jet compared to the water jet; however, the primary flow structures making up most of the jet mass did not significantly change. This trend held for higher-pressure jet configurations; although, overall droplet size tended to decrease from visual inspection.

Contrary to other jet configurations, near-field imagery of the high-flow, low-pressure AFFF jet identified unique multiscale bubble formations along the leeward side of decaying droplet groupings from the pulsations found approximately halfway downstream from the nozzle. Figure 80(a) through (c) illustrates various examples of this phenomenon, i.e., significant bubble growth in areas associated with the largest concentration of droplets. These bubble growth structures appear similar to droplet multimode breakup and bag breakup discussed in section 2.3.3 and illustrated in figure 17. Figure 80(d) illustrates the more common occurrence of sparse sporadic bubble formation found throughout the jet.

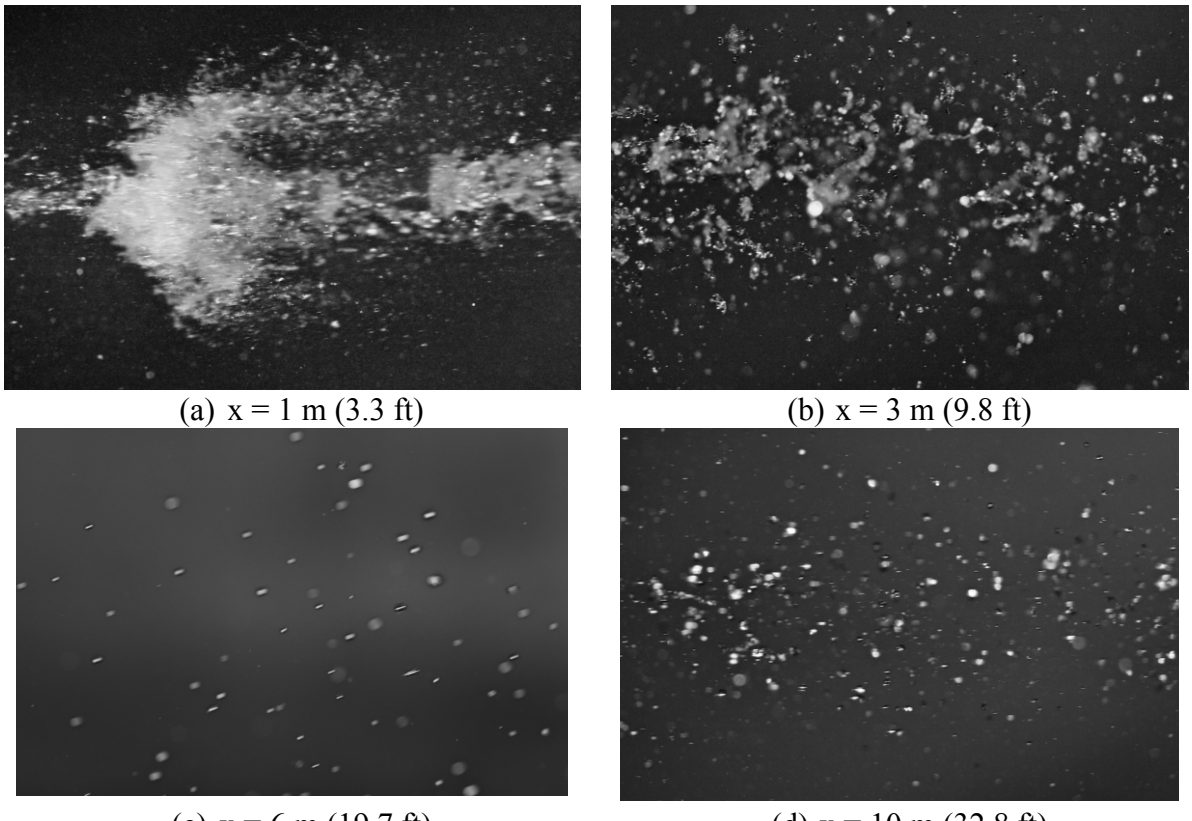

(a) x = 1 m (3.3 ft) (b) x = 3 m (9.8 ft)

(c) x = 6 m (19.7 ft) (d) x = 10 m (32.8 ft)

Figure 78. Near-Field View of the High-Flow, Low-Pressure Water Jet at Select Downstream Nozzle Locations (Flow is from right to left.)

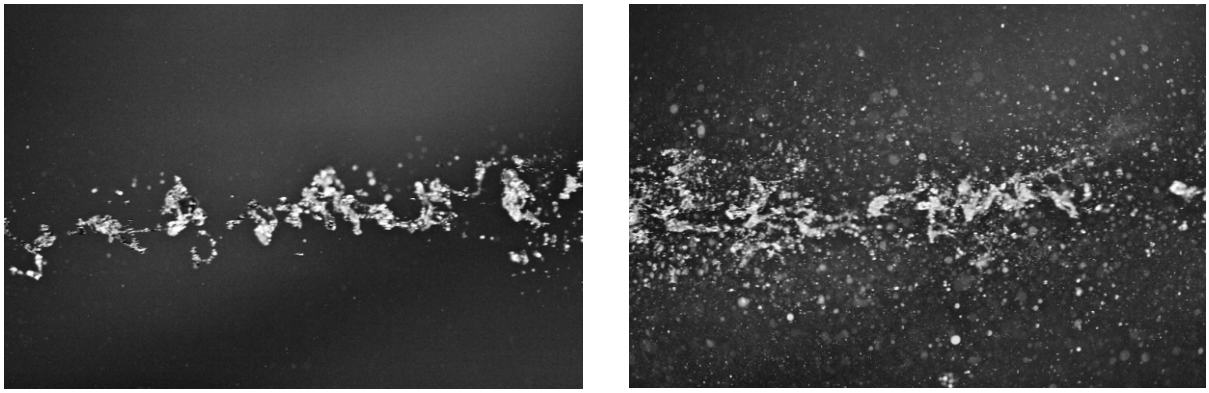

(a) (b)

Figure 79. Near-Field View of Jet Breakup Approximately 3 m (9.8 ft) Downstream From the Nozzle for the (a) Low-Flow, Low-Pressure Water Jet and (b) Low-Flow, Low-Pressure AFFF Jet (Flow is from right to left.)

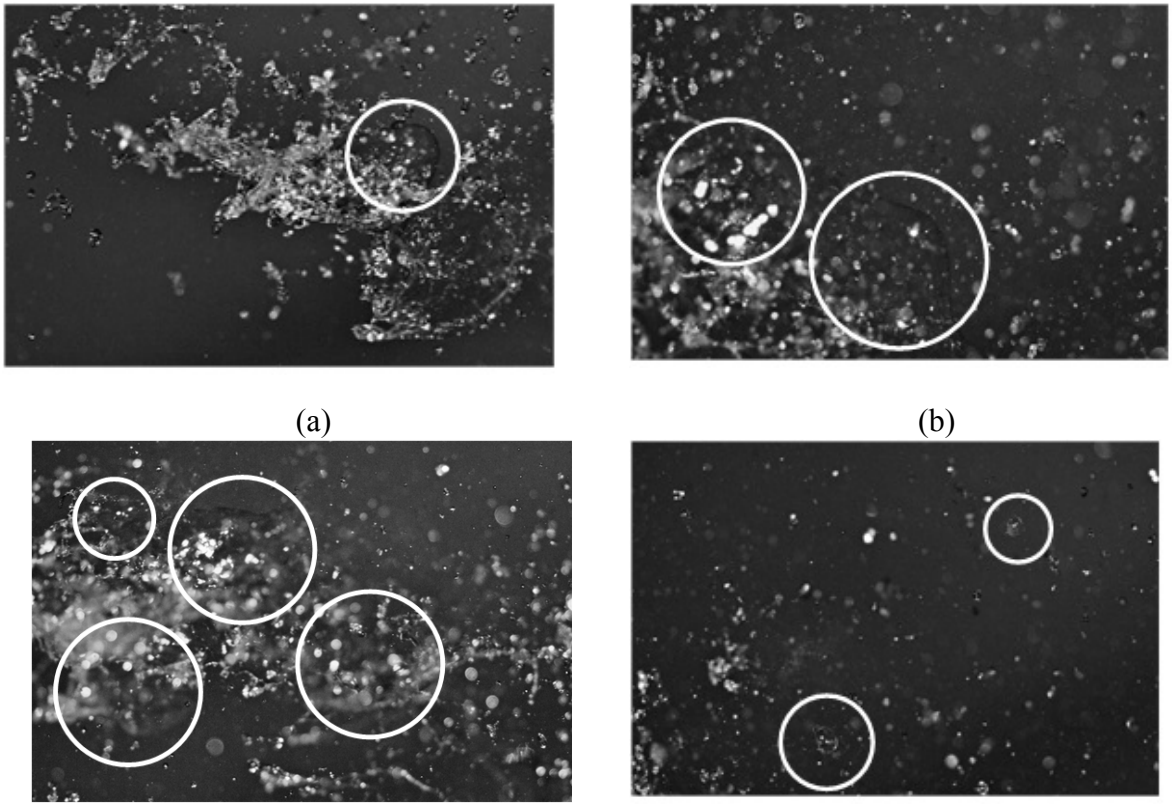

(a) (b)

(c) (d)

Figure 80. Near-Field Flow Visualization of the High-Flow, Low-Pressure AFFF Jet Highlighting Multiscale Bubble Masses at Different Downstream Locations (Flow is from right to left.)

6.2 EXPERIMENTAL FIREFIGHTING JET GROUND PATTERN RESULTS.

An agent ground pattern analysis was conducted on the 21 different firefighting jet configurations overviewed in section 4.1. Each configuration is illustrated in figure 43 and listed in table 6. Details of the experimental approach are in section 4.3. Two-dimensional agent ground pattern measurements are presented on nine pressure-flow rate combinations using water and 6% AFFF as the agent. A brief study was also conducted to examine the influence the firefighting jet containment zone had on the results. One-dimensional, centerline, agent ground pattern measurements were also recorded on the medium-flow, medium-pressure jet to determine the agent ground pattern sensitivity to AFFF concentration ranging from 3% to 12% AFFF. Agent ground pattern reach, coverage area, and span results for all 2-D firefighting jet work were then summarized, followed by a mass conservation analysis. In addition, six 1-D, centerline, agent ground pattern experiments were recorded to examine how full-scale flow rates alter the agent ground pattern compared to those tested at a smaller scale in the laboratory.

6.2.1 The 2-D Water Jet Containment Zone Sensitivity Ground Pattern Results.

A 2-D water ground pattern sensitivity analysis was conducted to determine the jet containment zone's influence on firefighting jet flow behavior. For spatial reference, figure 46 illustrates the relative size and location of a medium-sized firefighting jet with respect to the downstream containment zone. Agent ground pattern 2-D accumulation studies were conducted on the largest (high-flow, high-pressure) water jet tested with and without the curtains drawn in the downstream portion of the jet containment bed. The tests were not carried out with AFFF jets for this particular study. Figure 81 compares the agent ground pattern results for both circumstances. The results are presented nondimensionally as a percentage of the total agent dispensed for all agent ground pattern studies to remove the dependency on jet flow rate. The dimensions shown in figure 81 reflect those of the firefighting jet containment bed with the inclusion of an additional 1.2 m (4 ft) between the nozzle and containment bed boundary where accumulation was negligible.

The test case with containment zone curtains open shows the firefighting jet body tapering slightly towards the negative *y*-direction, indicating interaction with the adjacent laboratory wall parallel to the bed. The proximity of this wall generated a lower-pressure region, which caused the firefighting jet to bend toward it resulting in asymmetric flow along the *x*-axis or axial centerline of the jet. The test case with containment zone curtains closed depicts a more axisymmetric jet from the pseudo wall effect imposed by the curtains located equidistant from the axial jet centerline. Firefighting jet characteristics were slightly affected by the presence of the containment curtains by limiting reach about 5% and inflating the coverage area by 8%. This was determined to be an acceptable consequence, as protecting the laboratory environment from daily moisture deposition and potential mildew growth was paramount.

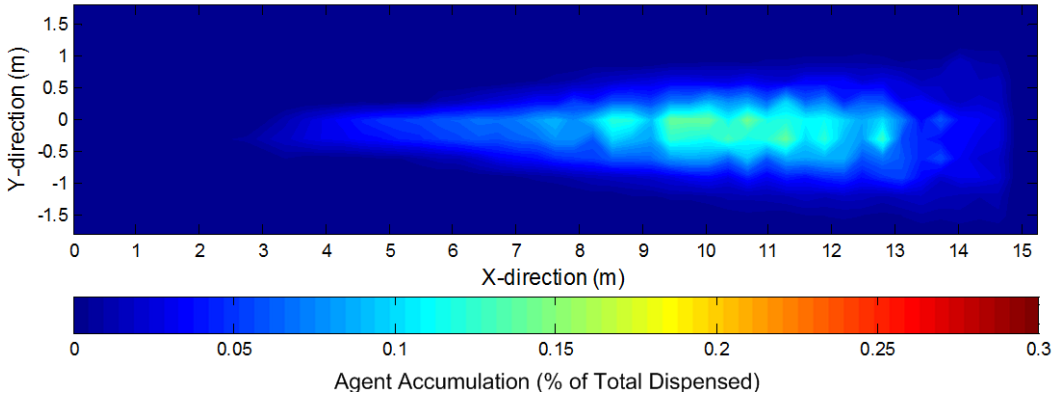

(a) Containment Zone Curtains Open

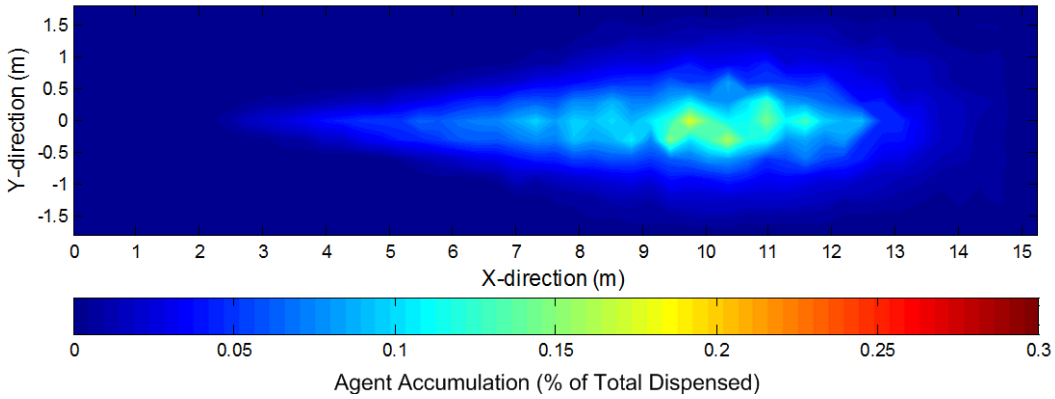

(b) Containment Zone Curtains Closed

Figure 81. The 2-D Agent Ground Pattern Water Accumulation Contour Plots Illustrating Firefighting Jet Dependence on the Firefighting Jet Containment Zone Curtains

6.2.2 The 2-D Water Jet Ground Pattern Results.

The 2-D water ground pattern accumulation results were recorded on nine firefighting jet pressure-flow rate combinations. Figures 82 through 84 depict 2-D water accumulation contour plots grouped by nozzle pressure to show trends based on increasing flow rate from (a) to (c) for each figure. The results are presented similar to figure 81. Accumulation levels were greatest for low-pressure jets because they exhibited the least amount of jet dispersion with a peak of 1.8% of total agent dispensed, whereas high-pressure jets exhibited the most spread peaking at 0.3%. All ground pattern results showed that most accumulation fell along the jet centerline and downstream, following the airborne jet trajectory. An increase in ground reach was shown to be strongly dependent on an increase in jet flow rate with less of an impact on maximum ground span, which was dominated by nozzle pressure similar to coverage area.

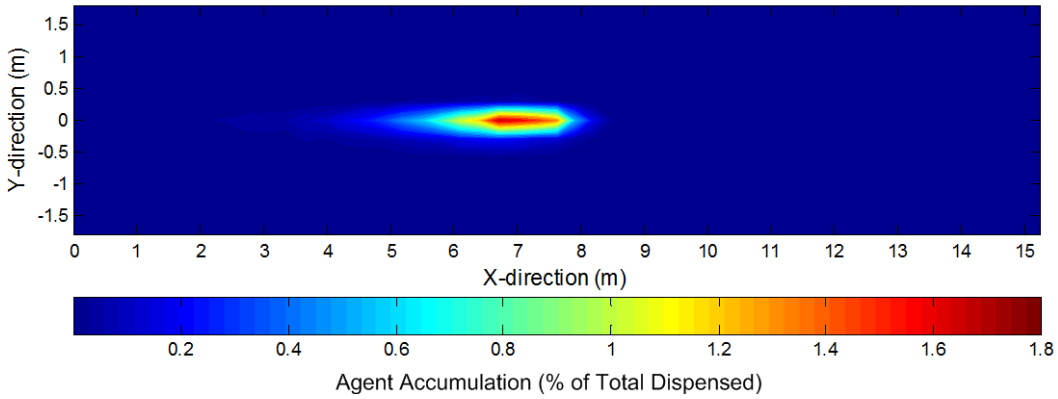

(a) Low-Flow, Low-Pressure Water Jet

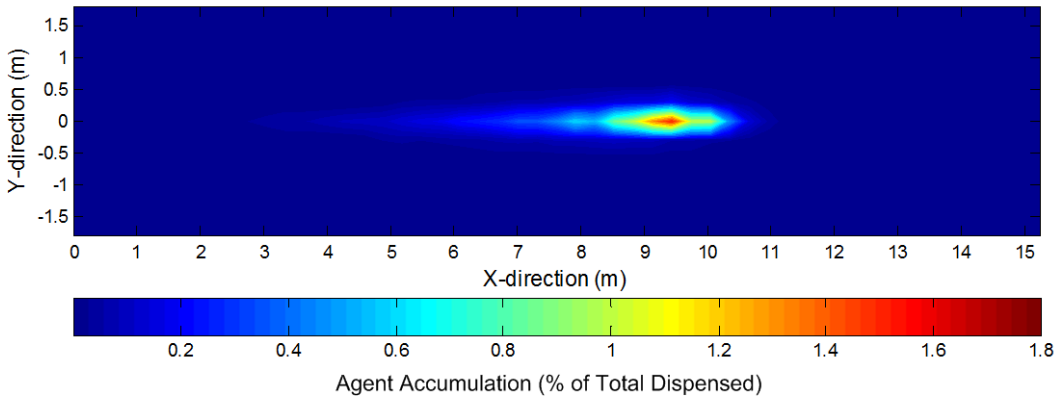

(b) Medium-Flow, Low-Pressure Water Jet

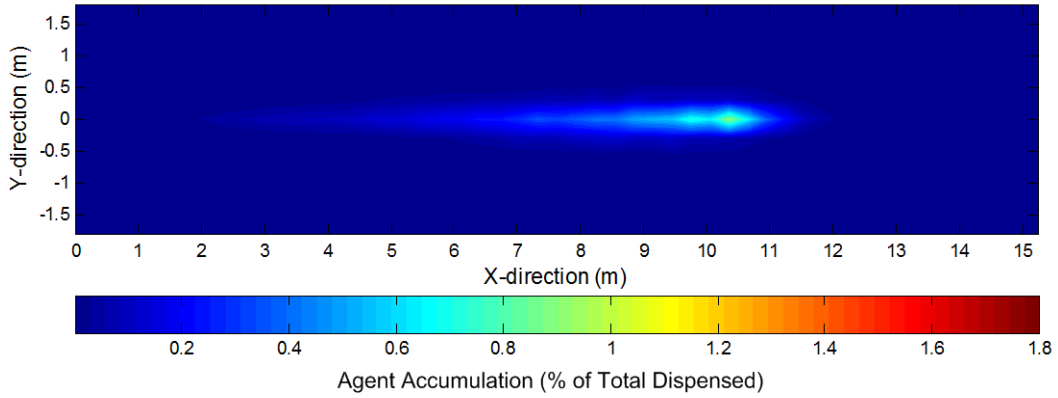

(c) High-Flow, Low-Pressure Water Jet

Figure 82. The 2-D Agent Ground Pattern Contour Plots of Low-Pressure Water Jets

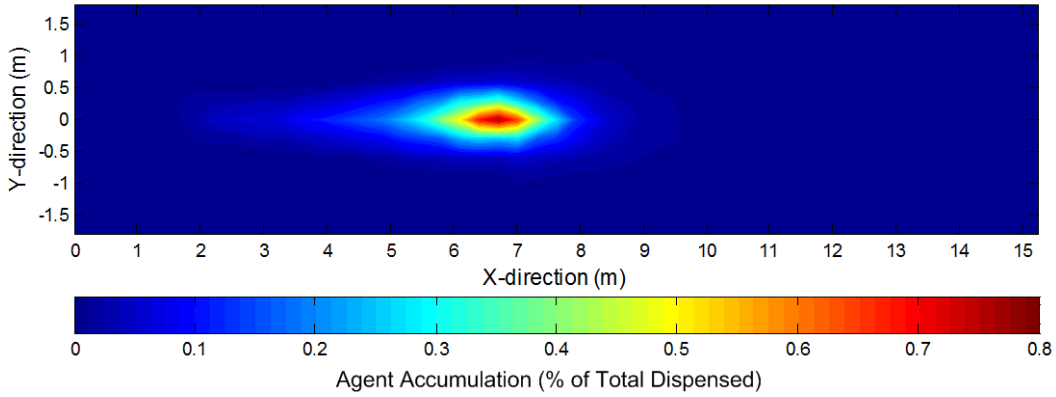

(a) Low-Flow, Medium-Pressure Water Jet

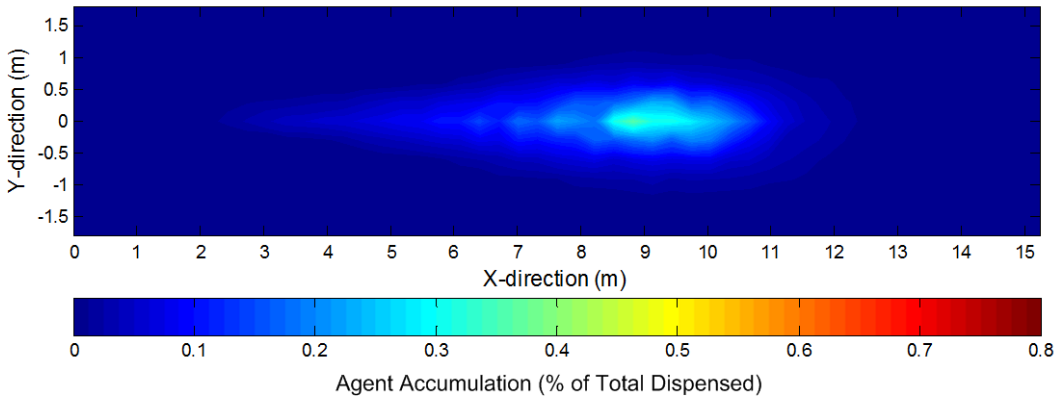

(b) Medium-Flow, Medium-Pressure Water Jet

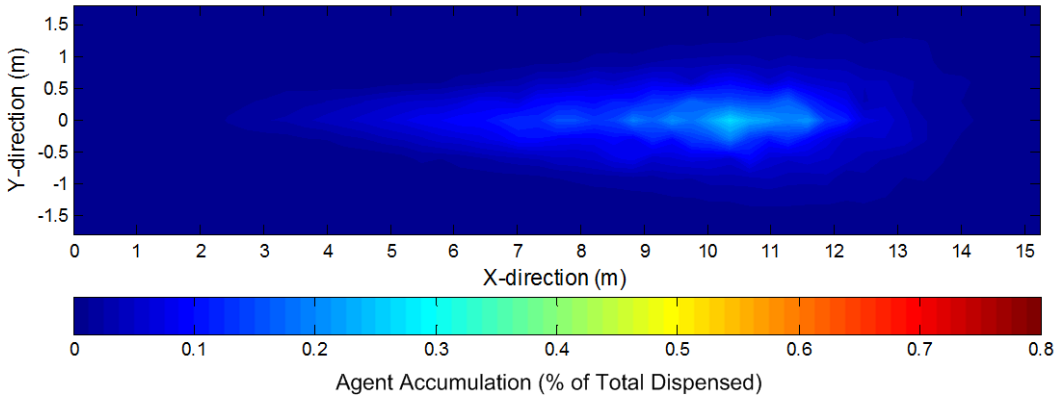

(c) High-Flow, Medium-Pressure Water Jet

Figure 83. The 2-D Agent Ground Pattern Contour Plots of Medium-Pressure Water Jets

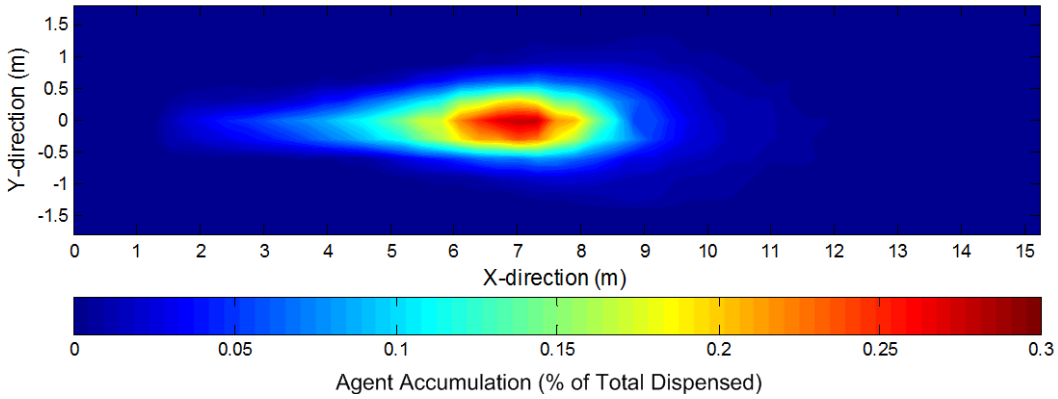

(a) Low-Flow, High-Pressure Water Jet

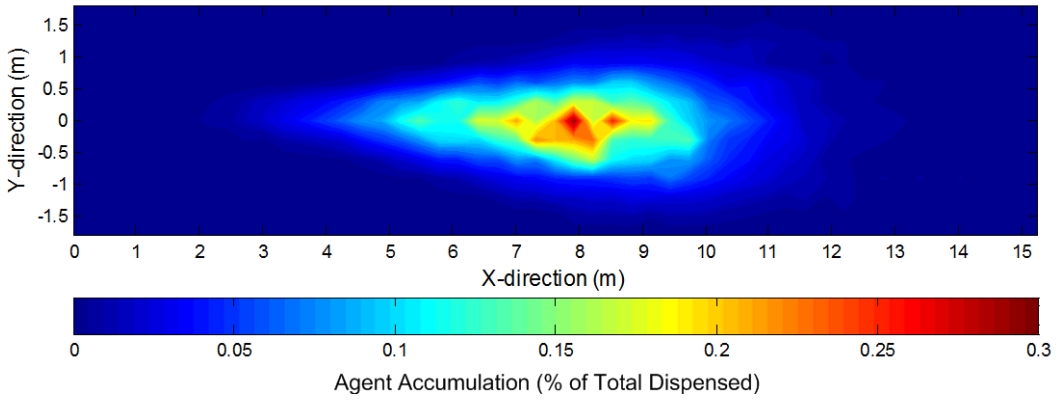

(b) Medium-Flow, High-Pressure Water Jet

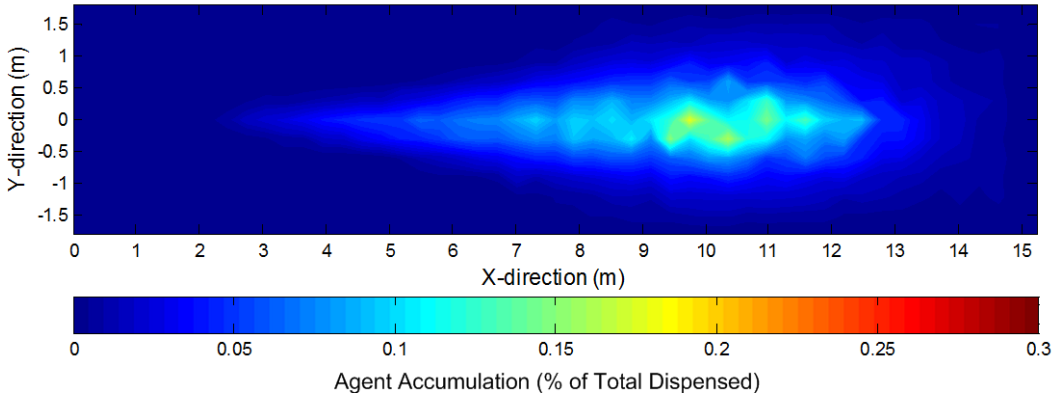

(c) High-Flow, High-Pressure Water Jet

Figure 84. The 2-D Agent Ground Pattern Contour Maps of High-Pressure Water Jets

6.2.3 The 2-D AFFF Jet Ground Pattern Results.

The 2-D AFFF ground pattern accumulation results were recorded on the same nine firefighting jet pressure-flow rate combinations as those conducted with water. Figures 85 through 87 depict 2-D foam expansion ratio (or foam quality) contour plots grouped by flow rate. Six-percent AFFF was used for all results shown. Trends based on an increase in nozzle pressure are shown from (a) to (c) for each respective figure. AFFF was not collected in zones showing a foam expansion ratio of zero. Low-flow rate and medium-flow rate AFFF jets peaked with foam qualities of about 2.5:1. Foam expansion ratio increased for the high-flow rate AFFF jet peaking at a foam quality of approximately 3:1. For low-flow rate AFFF jets, foam quality increased as nozzle pressure increased. However, this trend was not consistent for medium- and high-flow rate AFFF jets as the foam expansion ratio maintained a constant value across all nozzle pressure settings resulting in an inconclusive relationship between the two factors, at least for the parameter space examined in the laboratory.

The ground pattern shapes generated by AFFF mostly resembled those of the water ground patterns discussed in section 6.2.2, except with a minor inflation in coverage area and span along with a minor reduction in jet reach. In general, this suggests foam expansion ratio may be dependent on local agent accumulation. The largest pattern discrepancy was observed to be in areas closer to the nozzle where AFFF jet distribution appeared more dispersive as evidenced by flow visualization results reported in section 6.1.3 and specifically illustrated in figure 79.

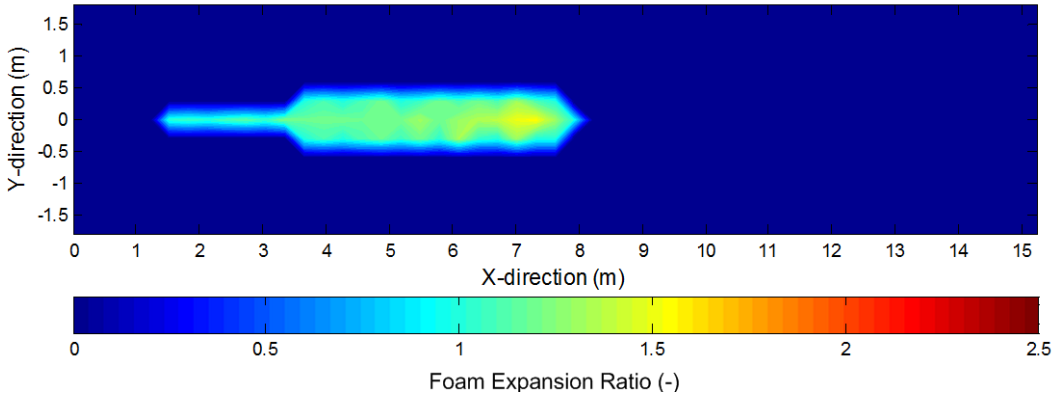

(a) Low-Flow, Low-Pressure AFFF Jet

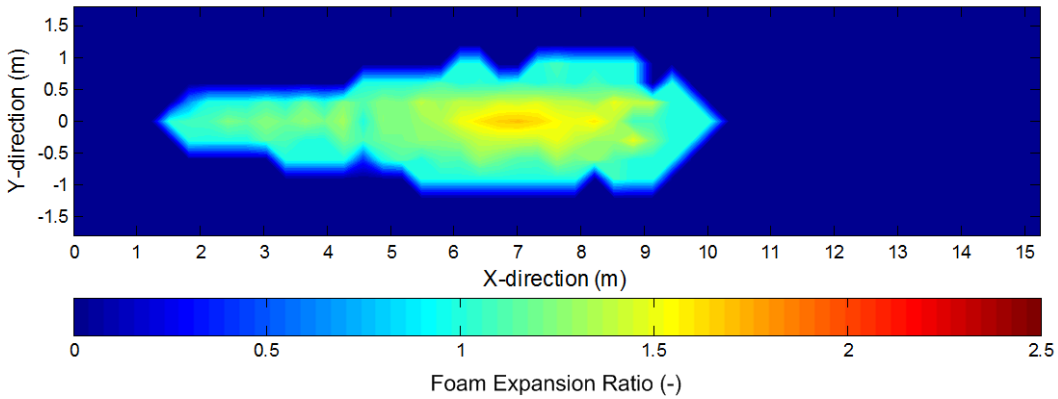

(b) Low-Flow, Medium-Pressure AFFF Jet

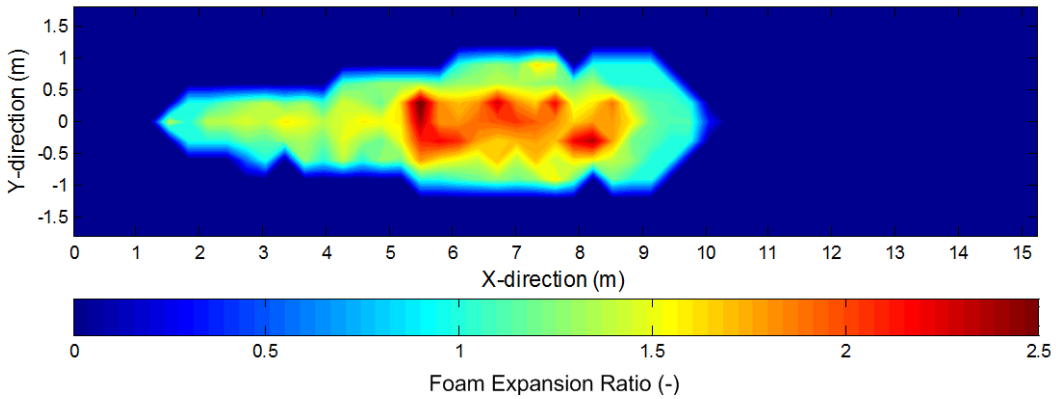

(c) Low-Flow, High-Pressure AFFF Jet

Figure 85. The 2-D Agent Ground Pattern Contour Plots of Low-Flow AFFF Jets

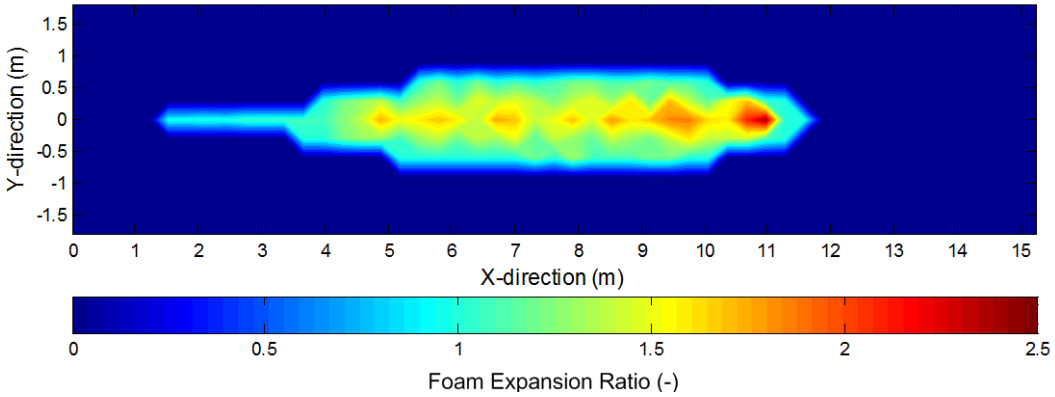

(a) Medium-Flow, Low-Pressure AFFF Jet

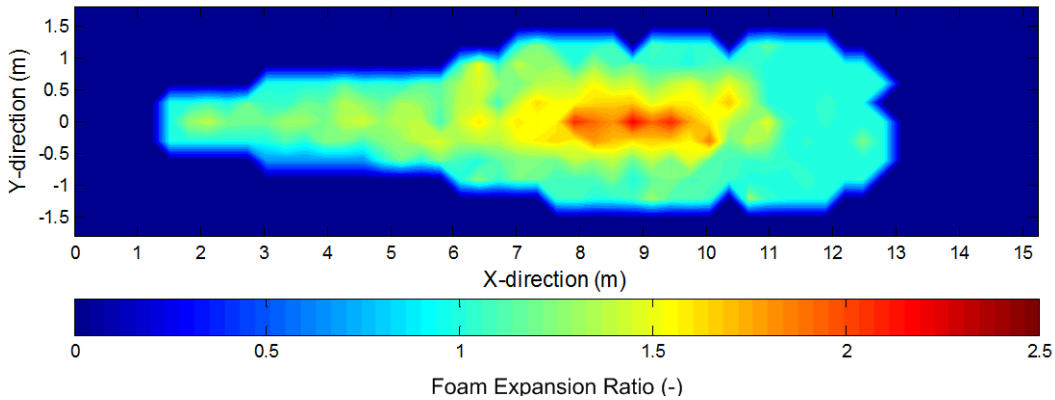

(b) Medium-Flow, Medium-Pressure AFFF Jet

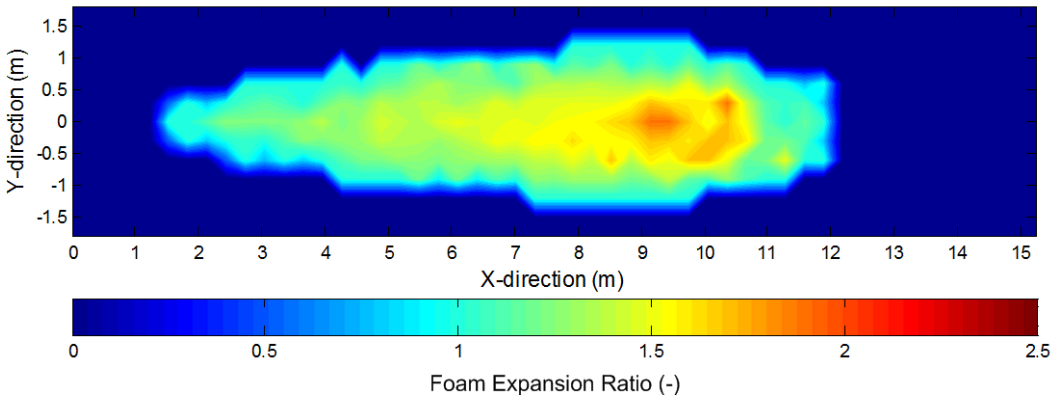

(c) Medium-Flow, High-Pressure AFFF Jet

Figure 86. The 2-D Agent Ground Pattern Contour Plots of Medium-Flow AFFF Jets

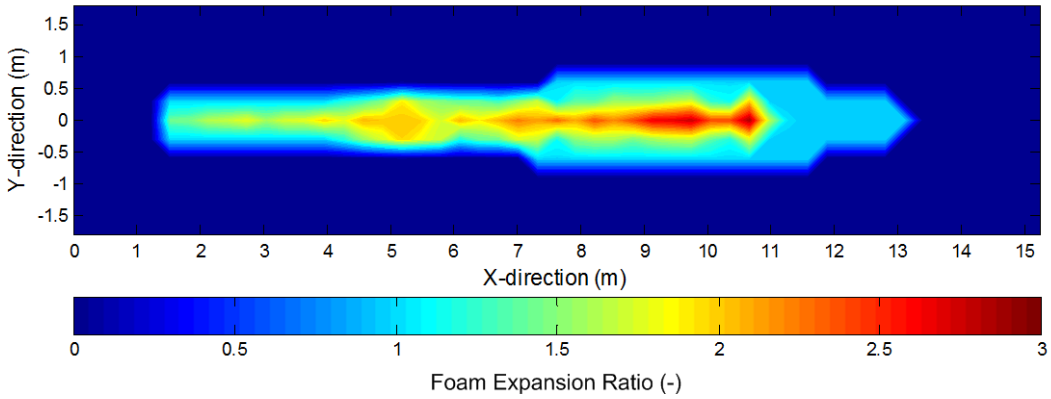

(a) High-Flow, Low-Pressure AFFF Jet

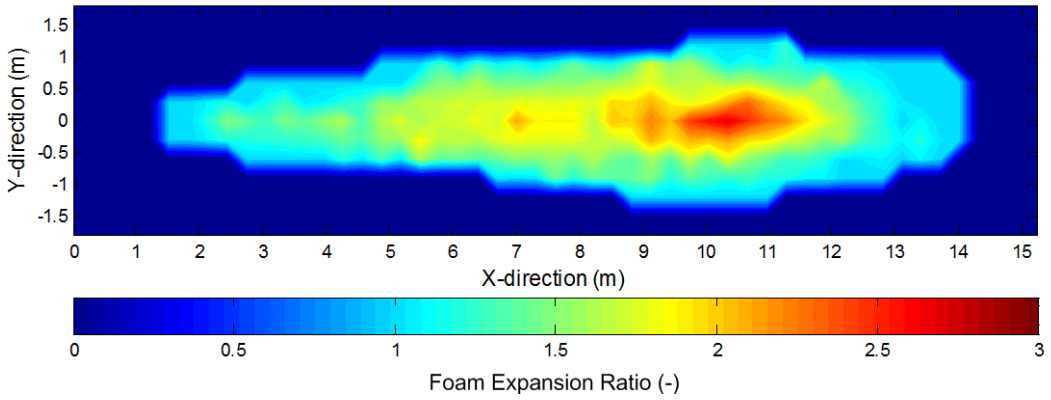

(b) High-Flow, Medium-Pressure AFFF Jet

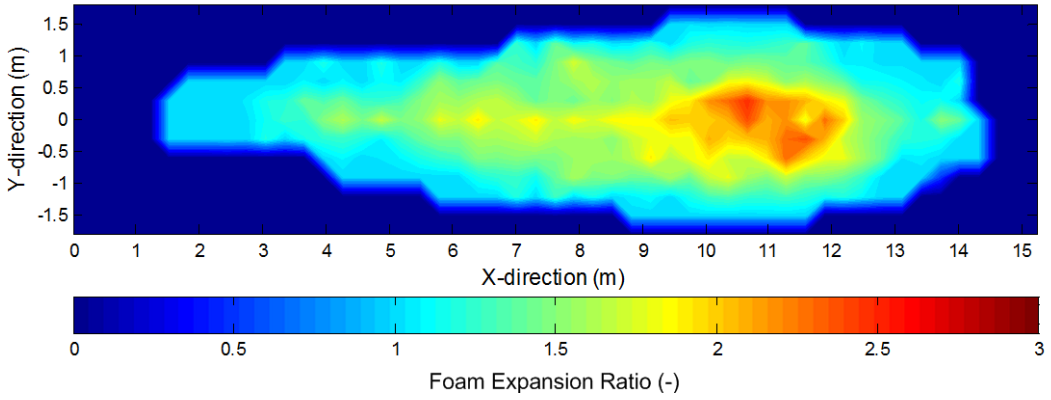

(c) High-Flow, High-Pressure AFFF Jet

Figure 87. The 2-D Agent Ground Pattern Contour Plots of High-Flow AFFF Jets

6.2.4 The 2-D Firefighting Jet Ground Pattern Results Summary.

Figure 88 summarizes all 2-D agent ground pattern test results presented in sections 6.2.2 and 6.2.3 for water and 6% AFFF jets, respectively. Firefighting jet performance parameters are presented in terms of total ground coverage area, maximum reach, and maximum span as a function of flow rate. The data are grouped illustrating linear trends based on nozzle pressure. AFFF jets exhibited a mean 3.3% increase in coverage area efficiency and a mean 0.08% decrease in maximum reach efficiency per unit increase in flow rate compared to water jets. AFFF jets demonstrated a mean 1.5% gain in maximum span efficiency per unit increase in flow rate compared to water jets. These subtle distinctions are attributed to enhanced AFFF droplet breakup generating slightly greater jet dispersion. Droplet dynamics and their influence on global jet behavior are explored further in section 6.3 as part of the PDPA. Error estimates are not shown in figure 88 because agent capture devices remained in a static position for each flow configuration measured. This was due to little change between each firefighting jet ground pattern measurement coupled with the coarseness of the floor grid. Firefighting jet agent ground pattern uncertainty is addressed in sections 6.2.5 and 6.2.6.

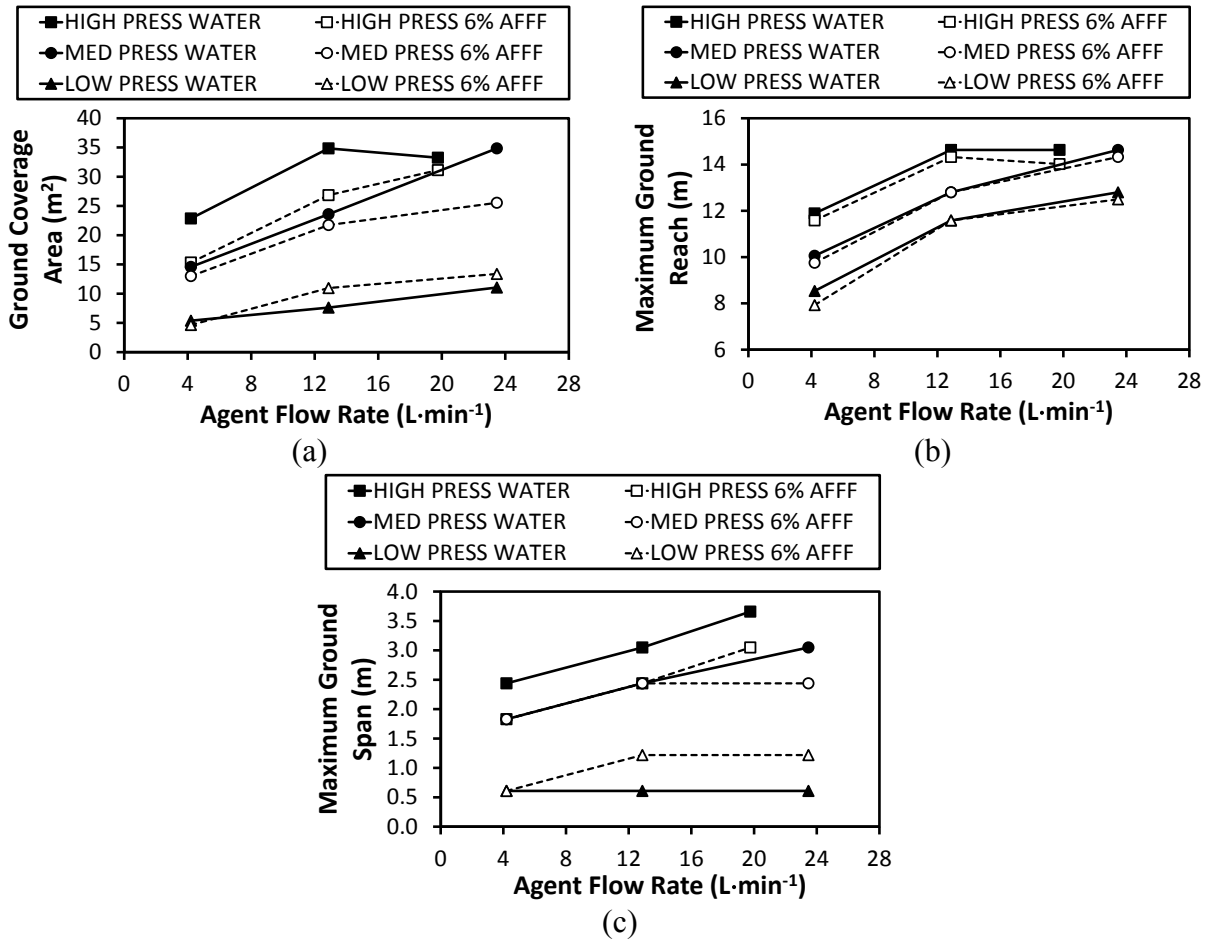

Figure 88. Agent Ground Pattern Firefighting Jet Performance Summary

Ground pattern data were used in conjunction with agent capture assumptions to estimate the amount of firefighting jet mass conserved between the nozzle and the jet containment bed. Assuming each firefighting jet uniformly distributed agent across the containment bed floor, the ideal agent captured was about 13.63%. This value is based on the percent area all agent capture devices occupied with respect to the entire containment bed floor area. The method neglects loss due to evaporation and droplets transported outside the containment bed. Table 9 lists the mean actual agent captured for all ten 2-D agent ground pattern tests recorded along with their associated differences compared to ideal settings. An overprediction as high as 6.60% was recorded for the low-flow, low-pressure water jet, and an underprediction as low as 19.44% was recorded for the low-flow, low-pressure jet for all cases considered. Overpredictions occurred for low-pressure jets as the majority of agent landed along the axial centerline where agent capture devices were located, leaving less agent to fall on the remaining floor area. Conversely, medium- and high-pressure jets were underpredicted because of their much greater horizontal spread couples with excess mass loss due to evaporation and/or drift out of the jet containment bed. Medium- and high-pressure jets were prone to increased evaporation due to the generation of smaller, more concentrated droplets compared to a lesser number of larger droplets created from low-pressure jets. In general, AFFF jets demonstrated increased mass loss compared to water jets due to the enhanced secondary droplet formation caused by the surfactants in AFFF.

Table 9. Agent Ground Pattern Mass Conservation Analysis

Nozzle Flow Setting	Ideal Agent Captured (%)	Actual Water Captured (%)	Actual Water Difference (%)	Actual AFFF Captured (%)	Actual AFFF Difference (%)
Low Flow, Low Pressure	13.63	14.53	6.60	13.89	1.91
Low Flow, Medium Pressure	13.63	12.40	-9.02	11.76	-13.72
Low Flow, High Pressure	13.63	11.13	-18.34	10.98	-19.44
Medium Flow, Low Pressure	13.63	14.80	8.58	13.97	2.49
Medium Flow, Medium Pressure	13.63	13.55	-0.59	12.74	-6.53
Medium Flow, High Pressure	13.63	13.01	-4.55	13.03	-4.40
High Flow, Low Pressure	13.63	14.67	7.63	13.94	2.27
High Flow, Medium Pressure	13.63	13.40	-1.69	12.89	-5.43
High Flow, High Pressure	13.63	11.88	-12.84	11.93	-12.47

6.2.5 The 1-D Firefighting Jet Ground Pattern AFFF Sensitivity Results.

A 1-D AFFF concentration sensitivity ground pattern analysis was conducted using medium-flow, medium-pressure nozzle settings to examine how foam expansion ratio changed with respect to AFFF solution concentration. Figure 89 shows the results from this study comparing foam quality distribution from 3% to 12% AFFF in 3% increments as a function of jet axial (x) location downstream nondimensionalized in terms of nozzle diameter D. The two vertical bars

shown for each AFFF concentration plotted in figure 89 represent the minimum and maximum uncertainty based on two standard deviations, or a 95.5% confidence level, that the data falls within that range. Per 3% increase in AFFF concentration, the AFFF jet foam expansion ratio proportionally increased by about 25%. These results followed the same accumulation trend as the 2-D AFFF jet ground pattern results presented in section 6.2.3 by generating peak foam expansion ratio magnitudes where maximum agent also accumulated along the centerline.

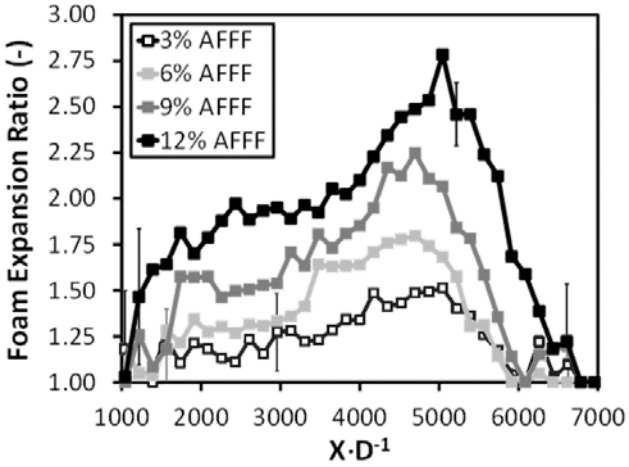

Figure 89. Foam Expansion Ratio vs Axial Location of the Medium-Flow, Medium-Pressure AFFF Jet With Respect to Variation in AFFF Solution Concentration

6.2.6 Full-Scale, 1-D Firefighting Jet Ground Pattern Results.

Full-scale, 1-D firefighting jet ground pattern experiments were conducted at Tyndall Air Force Base, Florida, using the AP4 nozzle family at higher flow rates but similar low-, medium-, and high-pressure settings as those tested in the aqueous firefighting agent application laboratory. Details on the experimental approach are shown in figure 47. Data were recorded for water and 6% AFFF jets at a flow rate applicable to real-world firefighting conditions of 75.7 $L \cdot min^{-1}$ (20 $gal \cdot min^{-1}$). Figure 90(a) and (b) report water accumulation and foam expansion ratio magnitudes, respectively, as a function of axial (x) downstream location similar to figure 89. The vertical bars represent the same uncertainty conditions as those in figure 89. Figure 90(a) shows that water jet accumulation peaks at low pressure and decreases as nozzle pressure is increased. This is expected as an increase in nozzle pressure enhances jet spread, which causes droplets to disperse more widely and thus reduce centerline accumulation. Figure 90(a) also shows how water jet reach is significantly increased as nozzle pressure is increased across the test range by about a factor of two. Figure 90(b) confirms a similar effect on jet reach as figure 90(a) but for the AFFF jet instead. The foam expansion ratio measurements illustrate that foam quality has a stronger dependence on nozzle pressure at full-scale flow rates compared to lower flow rates measured in the laboratory. Peak foam expansion ratios of 4.8:1 were recorded, resulting in an approximate 50% increase over laboratory measurements at the same pressure. It is also shown by comparison with small-scale laboratory results that the foam expansion ratio increased as flow rate increased. The results further confirm foam quality is significantly dependent on agent accumulation as both figures depict a similar trend between the two parameters.

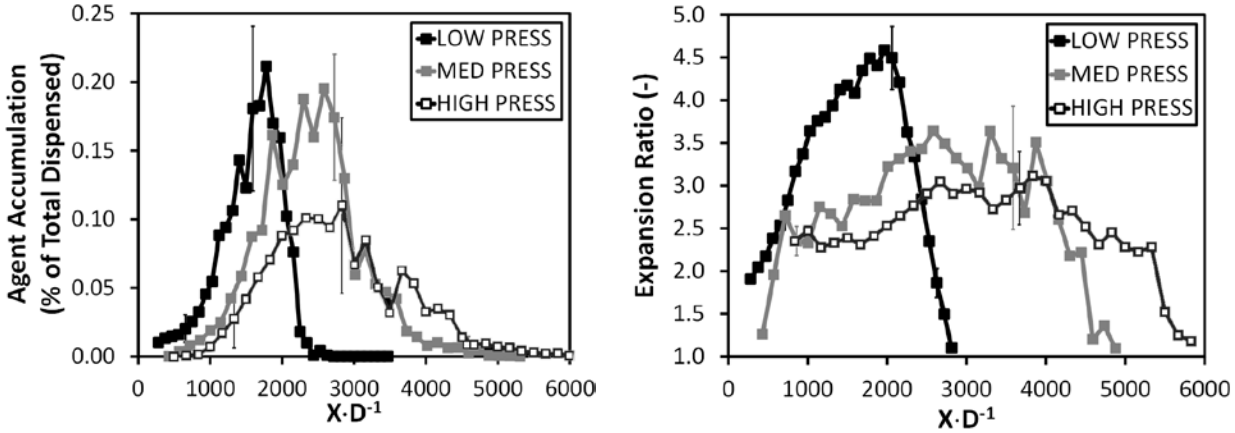

(a) Water Jets (b) 6% AFFF Jets

Figure 90. Full-Scale, 1-D Agent Ground Pattern Results Illustrating (a) Agent Accumulation vs Axial Location and (b) Foam Expansion Ratio vs Axial Location

6.3 EXPERIMENTAL FIREFIGHTING JET PHASE DOPPLER RESULTS.

PDPA was conducted on 12 firefighting jet configurations presented in section 4.1. Each configuration is depicted in figure 43 and listed in table 6. Details on the experimental approach are in section 4.4. The 12 configurations represented 5 nozzle pressure-flow rate combinations using water and 6% AFFF as the agent. Additional phase Doppler data were recorded for 3% and 9% AFFF at the pressure-flow rate center point, namely the medium-flow, medium-pressure jet, to examine the sensitivity of phase Doppler results on AFFF concentration. Characteristic droplet size distribution results and their characteristic relationship to droplet velocity are presented initially. Substantial amounts of phase Doppler data were recorded resulting in approximately 300 figures to represent all firefighting jet flow conditions tested. Select firefighting jet phase Doppler results from the central nozzle configuration are shown to introduce all the flow parameters measured, outline the presentation style of the data, and to discuss trends common to all firefighting jet conditions. The full catalog of phase Doppler results is in appendix C. All phase Doppler profile data listed in appendix C is averaged and summarized into what are referred to as firefighting jet mean profile results to analyze global trends in the phase Doppler data in a condensed format.

6.3.1 Firefighting Jet Phase Doppler Droplet Size Distribution Results.

Consistent with spray types involving hole-type fuel injectors or pressure atomizers, the AP4 nozzle family was best represented by Gaussian or normal drop size distribution laws that employed the logarithm of the droplet diameter as part of the fitting function. This class of droplet size distribution is referred to as the log normal distribution. Of the log normal-based fitting functions available in the phase Doppler data acquisition software, Flowsizer™, the Nukiyama-Tanasawa distribution function provided the best fit for all phase Doppler firefighting jet points measured. The Nukiyama-Tanasawa distribution is defined as follows:

$$f(d) = d^2 exp - (bd)^q \tag{35}$$

where $f(d)$ is a number distribution function describing the number of droplets of a given diameter d. The parameters b and q are fit variables. The characteristic droplet size distribution measured is illustrated in figure 91 showing the fit comparison for both water and a 6% AFFF jet over a range of 25 discrete, equal width droplet size bins. The results represent the droplet size distribution of a measurement point that recorded about 50,000 measurements. The water and AFFF jets have similar distributions, except the water jets exhibited larger mean droplet diameters. This pattern was consistent for all firefighting jet pressure-flow rate combinations considered. More droplet size distribution data presented similarly to figure 91 are in appendix C.

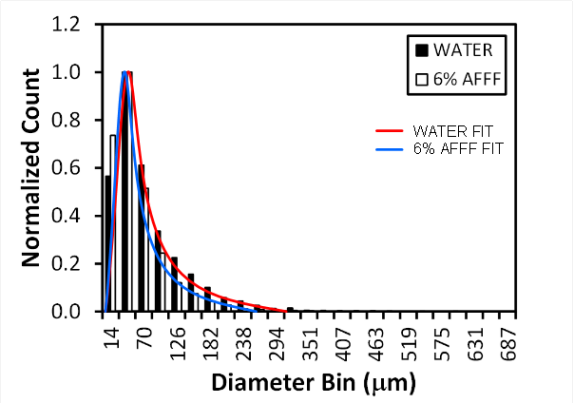

Figure 91. A Characteristic Firefighting Jet Droplet Size Distribution Measurement

Phase Doppler data of the mean axial droplet velocity ($V_{d,X}$) as a function of droplet diameter d were examined for both the water and 6% AFFF jets to analyze the sample distribution. Five locations spread across a 25-point, 1-D profile were chosen for each firefighting jet. A downstream location from the central nozzle configuration was selected for presentation, which demonstrates the characteristic trends of most data acquired. The ten locations are highlighted in figure 92, illustrating the mean axial droplet velocity and mean droplet diameter ($D10$) as a function of vertical location, respectively, based on approximately 50,000 recorded samples.

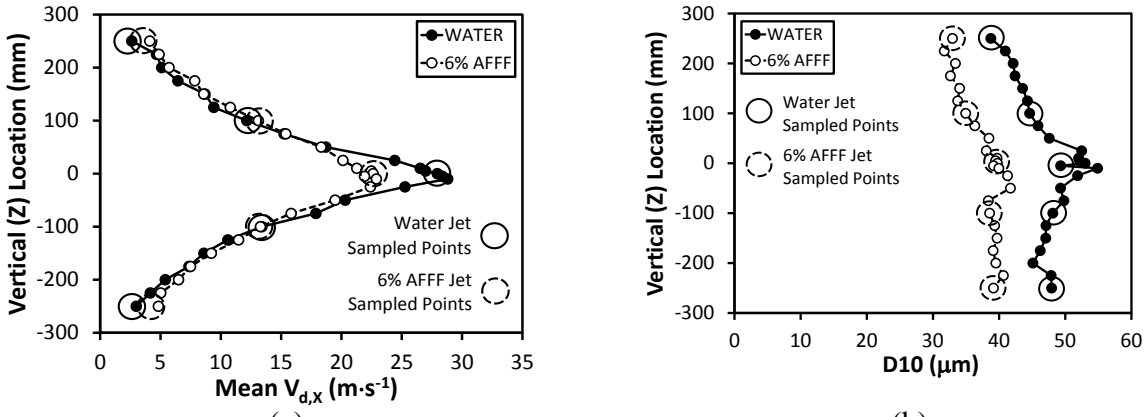

Figure 92. Phase Doppler Profile Measurement Locations Selected to Depict Mean Axial Droplet Velocity and Mean Droplet Diameter Sample Distribution at x = 3.05 m (10 ft)

Figure 93 illustrates the sample distribution for each point shown in figure 92. The most significant observation is the reduction in droplet size with the addition of AFFF. A minor degree of velocity spread between AFFF and water is also shown.

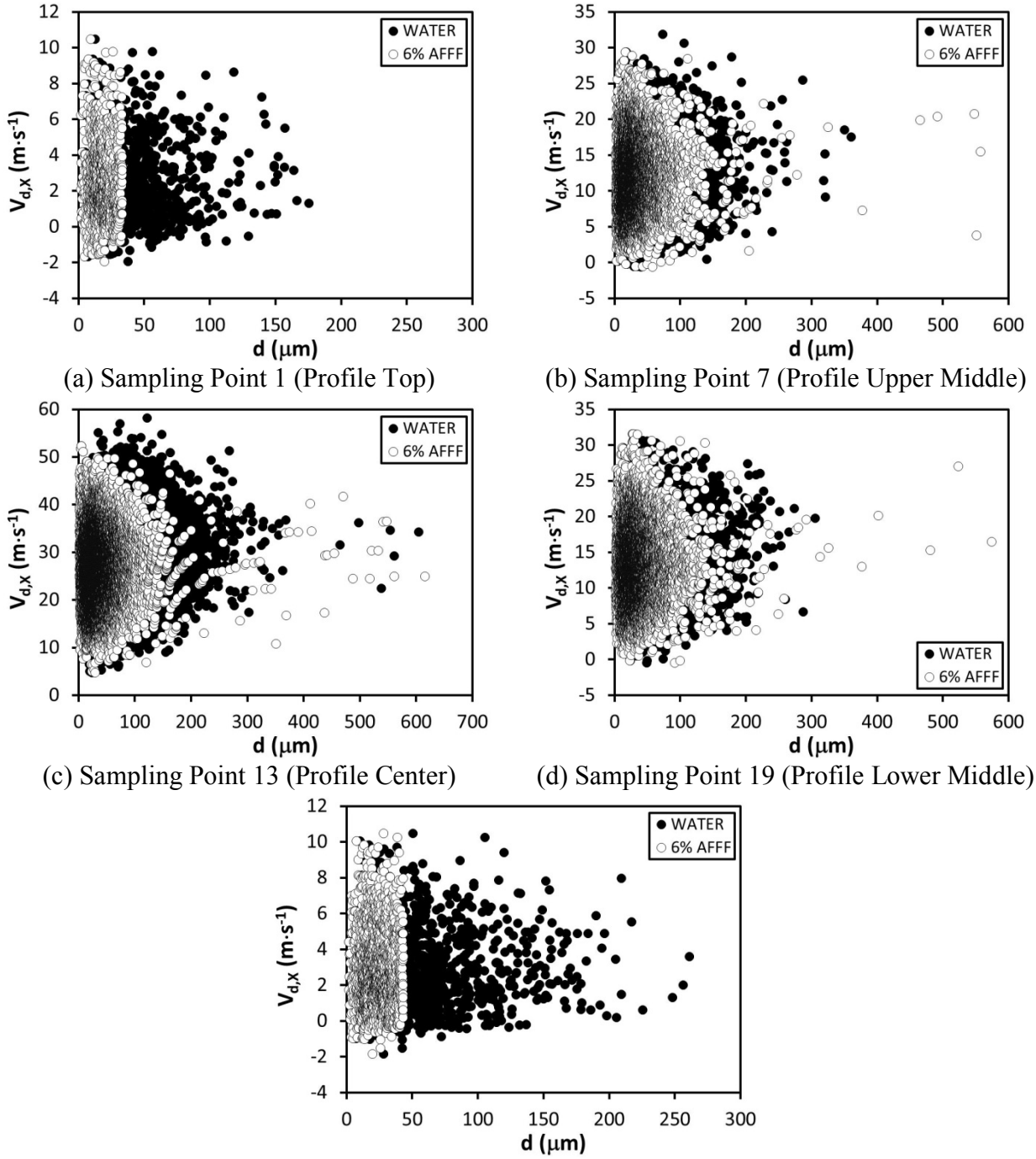

(a) Sampling Point 1 (Profile Top)

(b) Sampling Point 7 (Profile Upper Middle)

(c) Sampling Point 13 (Profile Center)

(d) Sampling Point 19 (Profile Lower Middle)

(e) Sampling Point 25 (Profile Bottom)

Figure 93. Select Sampling Data of Axial Droplet Velocity vs Droplet Diameter of the Medium-Flow, Medium-Pressure Jet at x = 3.05 m (10 ft)

No major clipping was observed due to PDPA hardware limitations. Edge profile locations shown in figure 93(a) and (e) exhibited a minor asymmetric distribution of 75- to 100-μm-sized droplets moving at lower velocities compared to other points of observation.

6.3.2 Select Firefighting Jet Phase Doppler Results.

The main phase Doppler results are presented using the following five flow parameters:

Mean Axial Droplet Velocity: $$V_{d,X} = \frac{1}{N}\sum_{i=1}^{N} v_{d,X_i} \quad (36)$$

Mean Vertical Droplet Velocity: $$V_{d,Z} = \frac{1}{N}\sum_{i=1}^{N} v_{d,Z_i} \quad (37)$$

Mean Droplet Diameter: $$D10 = \frac{1}{N}\sum_{i=1}^{N} d_i \quad (38)$$

Root Mean Square Droplet Diameter: $$D_{RMS} = \sqrt{\frac{1}{N}\sum_{i=1}^{N} d_i^2} \quad (39)$$

Sauter Mean Droplet Diameter: $$D32 = \left[\frac{\sum_{i=1}^{N} N_i d_i^3}{\sum_{i=1}^{N} N_i\, d_i^2}\right] \quad (40)$$

where N is the total number of samples recorded, and v_{d,X_i}, v_{d,Z_i}, and d_i are the instantaneous axial droplet velocity, vertical droplet velocity, and droplet diameter, respectively. The mean droplet diameter is the standard method for comparing the relative difference between two droplet samples. The root mean square (RMS) droplet diameter is a measure of diameter spread about the mean. Mean axial and vertical droplet velocity is reported with minimum and maximum ±RMS velocity for each profile shown via two horizontal bars. These bars are a visual characterization of the level of variability that occurs versus time due to the turbulence and not due to error bias. The Sauter mean droplet diameter represents the volume-to-surface ratio of the mean droplet diameter and typically defines the fineness of the jet spray. It is commonly used in efficiency studies involving mass transfer and chemical reactions making it a popular metric for characterizing firefighting agent application and combustion-related events.

In all the phase Doppler plots, the filled (black) symbols and solid lines refer to the water jet data, and the open (white) symbols and dashed lines refer to the AFFF jet data. A statistically unbiased, order of magnitude estimate (E) of the deviation between the calculated mean droplet velocity and diameter values from their true mean values was found using autocorrelation techniques. By autocorrelating the raw data signal (Φ) using MATLAB®, the number of samples it took for the signal to decorrelate (N_{decorr}) was calculated. This information, the RMS and mean value from the sampled data, in addition to the total number of N samples recorded was used to estimate E from the following relationship.

$$E = \frac{\Phi_{RMS}}{\sqrt{N \cdot N_{decorr}{}^{-1}}} \tag{41}$$

Equation 41 dictates that as total sample size increased and the number of samples it took to decorrelate the signal decreased, the smaller the error estimate. This uncertainty analysis was applied to the five unique sampling locations shown in the phase Doppler profiles illustrated in figure 92. The process was executed on select phase Doppler vertical profile locations listed in table 10 for each firefighting jet nozzle pressure-flow rate combination using water and 6% AFFF as the agent. The five uncertainty estimates from each profile are averaged with the results annotated on each respective profile plot.

Table 10. Phase Doppler Profile Measurement Locations Containing Uncertainty Analysis

		Water Jet	AFFF Jet
Station No.	X-Axis Location	1-D Vertical Z-Axis Profile	1-D Vertical Z-Axis Profile
3	0.152 m (6 in.)	•	o
5	0.914 m (3 ft)	•	o
7	3.05 m (10 ft)	•	o
9	6.10 m (20 ft)	•	o

Auxiliary information regarding PDPA velocity and diameter measurement uncertainty based on hardware resolution and spatial system alignment from manufacturer experience is located in section 3.5. Information on the manufacturer's calibration certification procedure for measuring particle diameter for the PDPA used specifically for this work is in appendix D. In general, all methods of determining PDPA measurement error reported uncertainties on the order of 1% or less, which was often much less than the statistical variation in the flow parameters.

Figure 94 illustrates sample results of the five aforementioned measured flow parameters as a function of vertical profile location for the medium-flow, medium-pressure jet. All phase Doppler data shown in figure 94 are from the axial downstream x = 6.10-m (20-ft) profile location. For spatial reference, figure 48 and table 7 illustrate and outline all PDPA profile measurement locations, respectively. Figure 94(a) represents a downstream mean axial droplet velocity profile exhibiting asymmetric spread directionally biased toward the floor due to gravity. Axial AFFF droplet velocity slightly lagged axial water droplet velocity due to the presence of smaller mean AFFF droplet diameters with less momentum, which are illustrated in figure 94(c). Figure 94(b) represents a mean vertical droplet velocity profile showing symmetry about the z = 0-m plane. A negligible difference was observed between vertical AFFF and water droplet velocities. Figure 94(d) shows RMS droplet diameters similar in magnitude to the mean droplet diameters presented in figure 94(c), supporting the observations in figures 91 and 93 that a wide distribution of droplet sizes are present. AFFF RMS droplet diameter magnitudes are slightly smaller compared to the water jet RMS droplet diameters, which is likely an extended consequence of smaller mean droplet sizes. Figure 94(e) shows that the AFFF jet exhibits larger

Sauter mean droplet diameters in comparison to the water jet, but the results are noticeably more scattered and less conclusive compared to the mean droplet diameter profile results. In general, the Sauter mean diameter is larger than the mean droplet diameter. Further discussion of firefighting jet PDPA flow parameter patterns as they relate to all firefighting jet configurations is in section 6.3.3. The phase Doppler flow parameter profile data from all firefighting jet conditions examined are in appendix C.

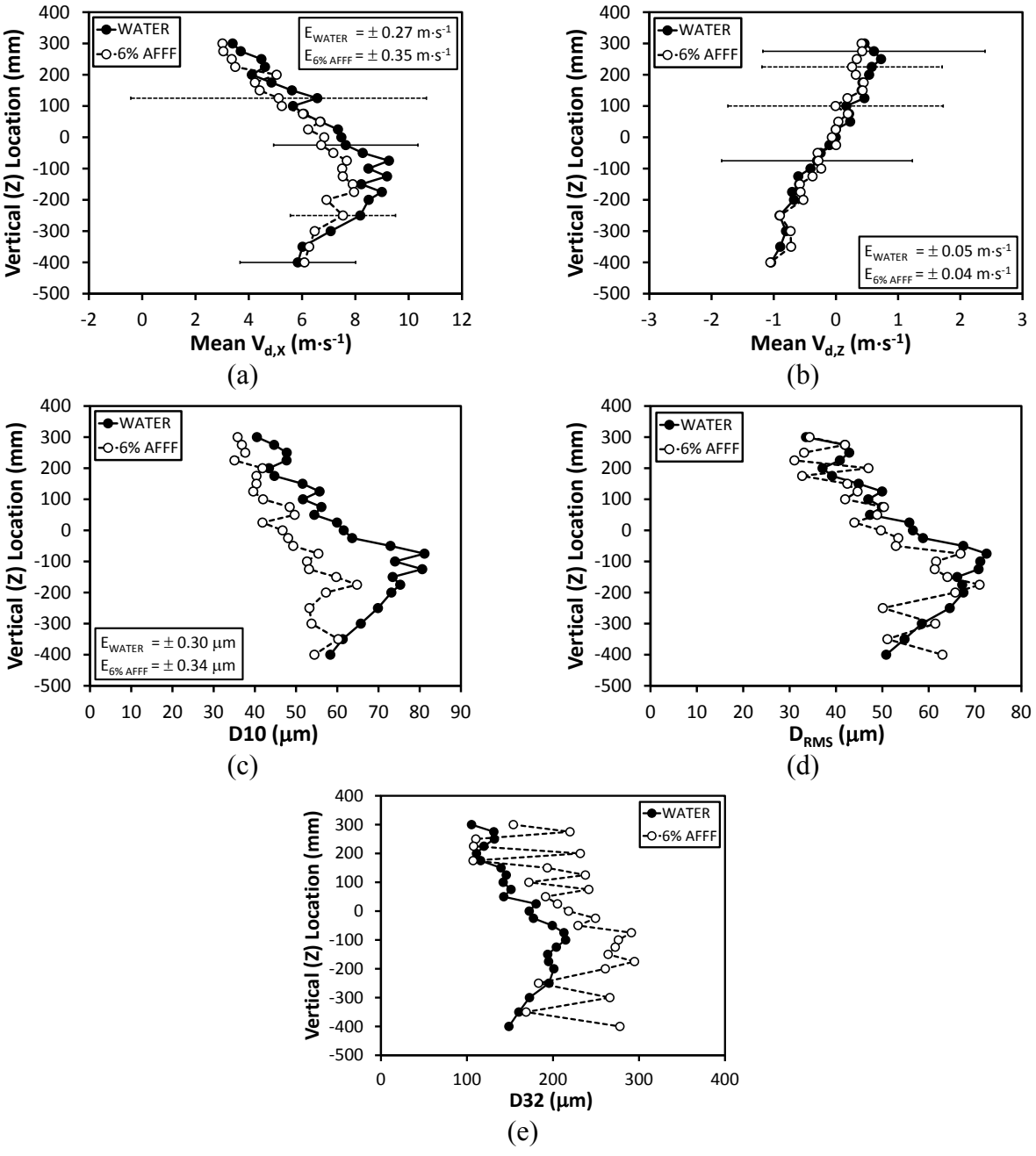

Figure 94. A Sample of Vertical, Phase Doppler Droplet Profile Data From the x = 6.10-m (20-ft) Axial Downstream Location From the Medium-Flow, Medium-Pressure Firefighting Jet

Figure 95 depicts sample axial ($V_{G,X}$) and vertical ($V_{G,Z}$) mean, gaseous (air) vertical velocity profile estimates for the medium-flow, medium-pressure jet, respectively. The horizontal bars represent the ±RMS velocity magnitude. The data are presented at the same axial downstream location used in figure 94. These values were approximated based on the phase Doppler data recorded on droplets 10 μm or less in diameter, assuming their trajectories followed air streamlines. The results are presented at the five measurement locations highlighted in figure 92. Based on the ratio of RMS to mean air velocity fluctuations, turbulence intensity values ranged from about 35% to 90%, indicating highly turbulent flow. This was a consistent observation for all firefighting jet configurations. Mean air velocity estimates are similar but slightly less in value to those shown in figure 94(a) and (b), which take the entire droplet diameter range measured into account. The similarity is due to fully entrained air flow, particularly downstream where droplet slip velocities subsequently reduced in magnitude as distance from the nozzle increased. AFFF jet, axial air velocities also slightly lagged water jet, axial air velocities similar to the trends and reasons observed in figure 94(a). More axial and vertical air velocity profile data estimates from the medium-flow, medium-pressure jet are in appendix C-3.

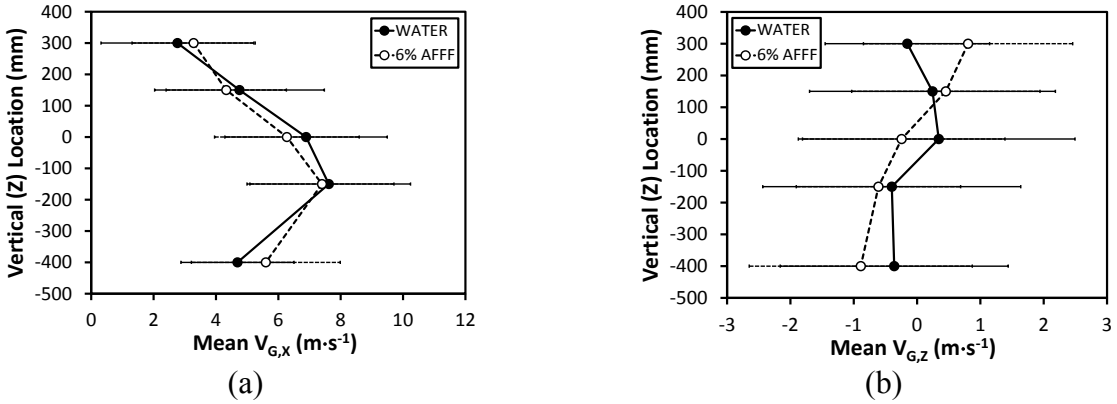

Figure 95. A Sample of Vertical, Phase Doppler Profile Estimates of Axial, Gaseous (Air) Velocity From the x = 6.10-m (20-ft) Axial Downstream Location From the Medium-Flow, Medium-Pressure Firefighting Jet

6.3.3 Firefighting Jet Phase Doppler Results Summary.

Phase Doppler results have been condensed to summarize the global patterns of each of the five main flow parameters presented for every firefighting jet configuration analyzed. All individual phase Doppler profile results are located in appendix C. Each 1-D vertical profile composed of 25 discrete locations was averaged to generate a single mean profile value for every flow parameter. Maximum mean axial and mean vertical droplet velocity values were also extracted from each profile to provide another point of comparison. Figure 96 illustrates this process.

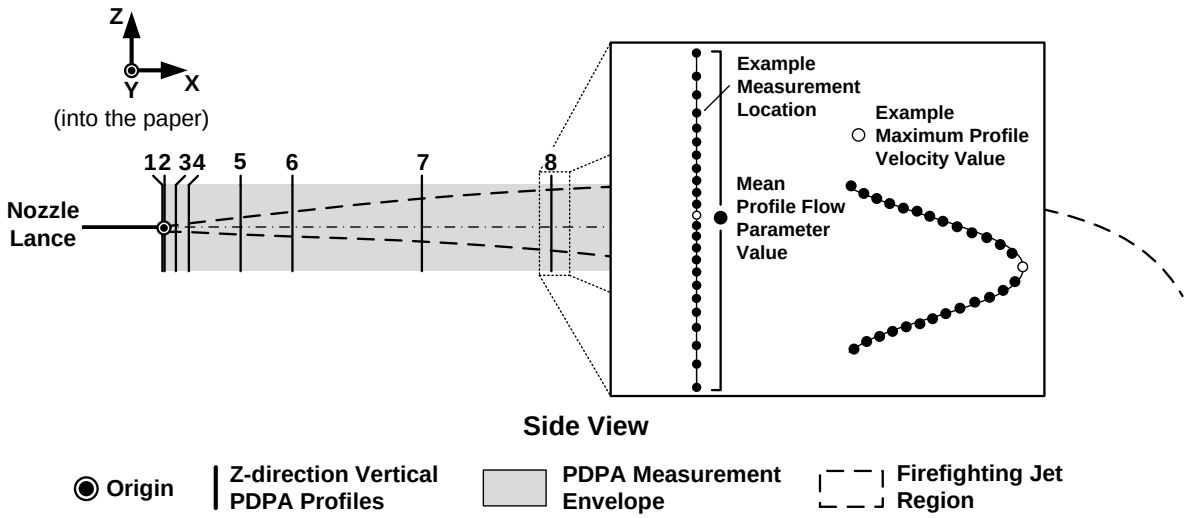

Figure 96. A Schematic Illustrating the Maximum and Mean Phase Doppler Profile Value

The data presented describe the mean or maximum profile flow parameter as a function of axial downstream jet location for each firefighting jet configuration. Profile data for each flow parameter consisted of 9 to 11 points, depending on the number of vertical profiles recorded. The downstream *x*-axis axial jet location is reported nondimensionally with respect to the nozzle diameter analogous to how 1-D agent ground pattern results are presented in sections 6.2.5 and 6.2.6.

Figure 97 summarizes the phase Doppler mean axial droplet velocity measurements for all firefighting jet configurations analyzed. Figure 97(a) illustrates the maximum profile, mean axial water droplet velocity nondimensionalized with respect to the maximum profile, mean axial water droplet velocity measured adjacent to the nozzle exit (i.e., Station 1 in figure 48 and table 7). Figure 97(c) depicts the maximum profile, mean axial water droplet velocity but in dimensional form, and figure 97(e) shows the mean profile, axial water droplet velocity. Figure 97(b), (d), and (e) illustrate the same scenarios as in figure 97(a), (c), and (e), respectively, but instead use 6% AFFF as the agent.

Maximum mean axial droplet velocity did not occur at the measurement plane adjacent to the nozzle, but rather anywhere from approximately 2- to 15-cm (0.75- to 6-in.) downstream, depending on the nozzle pressure-flow rate combination. This was due to a phenomenon referred to as vena contracta, where the fluid stream continued to contract downstream of the orifice causing the jet to further accelerate beyond the nozzle exit plane. The water jet and AFFF jet maximum mean axial droplet velocity magnitudes were similar to one another with near nozzle velocities ranging from about 45 to 138 $m \cdot s^{-1}$ for low-flow, low-pressure and low-flow, high-pressure jets, respectively. All firefighting jet axial velocities exhibited classic nonlinear decay as downstream distance increased. Mean profile, mean axial droplet velocity followed the same trend with respect to nozzle pressure and flow rate as the highest velocities ranged from approximately 35 to 85 $m \cdot s^{-1}$ near the nozzle to as low as 3 to 7 $m \cdot s^{-1}$ at the far reaches of each firefighting jet.

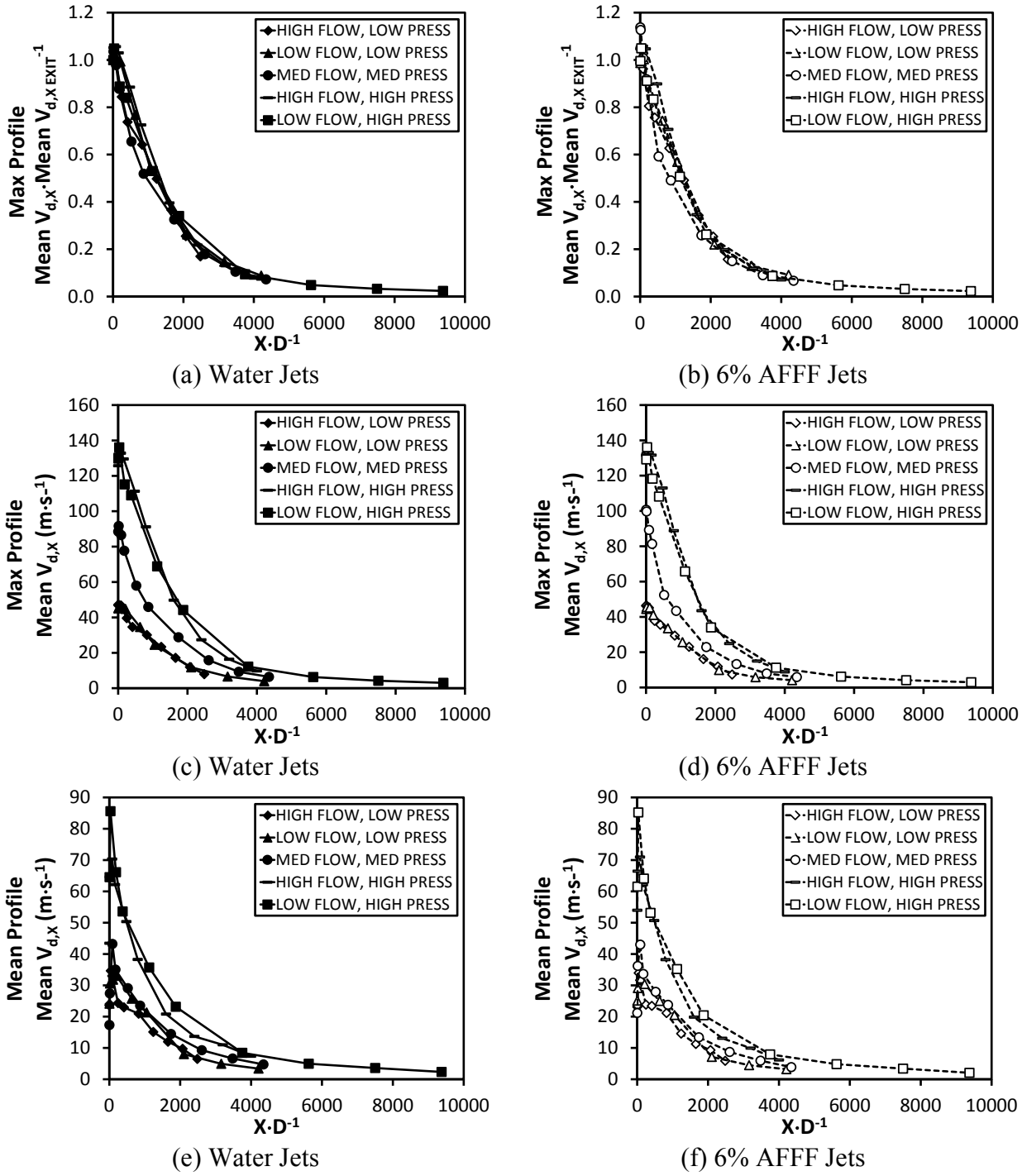

Figure 97. Firefighting Jet PDPA Summary Data in Terms of Maximum and Mean Profile, Axial Droplet Velocity

Figures 98 through 100 reproduce the same data shown in figure 97, but highlight the effect AFFF had on each nozzle pressure-flow rate combination compared to water. Figure 98 expands nondimensional, maximum profile, mean axial droplet velocities illustrated in figure 97(a) and (b). Figure 99 expands the dimensional form of the maximum profile, mean axial droplet velocities depicted in figure 97(c) and (d), and figure 100 expands mean profile, mean axial droplet velocities shown in figure 97(e) and (f). In addition to reporting mean profile, mean axial droplet velocity, figure 100 depicts the mean profile, ±RMS axial droplet velocity magnitude via vertical bars. Mean profile turbulence intensities were reported up to 40% in near-field nozzle areas and approached 0% in some locations measured furthest downstream. Individual profiles presented in appendix C commonly depict turbulence intensities approaching 100% for many cases.

Figures 98, 99, and particularly 100 more clearly illustrated vena contracta, exhibiting up to a 17% velocity increase just downstream of the nozzle for the medium-flow, medium-pressure jet. The high-flow, low-pressure jet appeared least affected by the phenomena with a near negligible increase in velocity beyond the nozzle.

Figures 98 through 100 also depict AFFF mean profile, mean axial droplet velocity equaling or slightly lagging water mean profile, mean axial droplet velocity universally for every nozzle pressure-flow rate combination by as much as 10% in certain circumstances. This observation was acknowledged in discussing figure 94(a). This is presumed due to the additional momentum loss exhibited by AFFF jets from an increase in aerodynamic drag that was caused by their enhanced breakup.

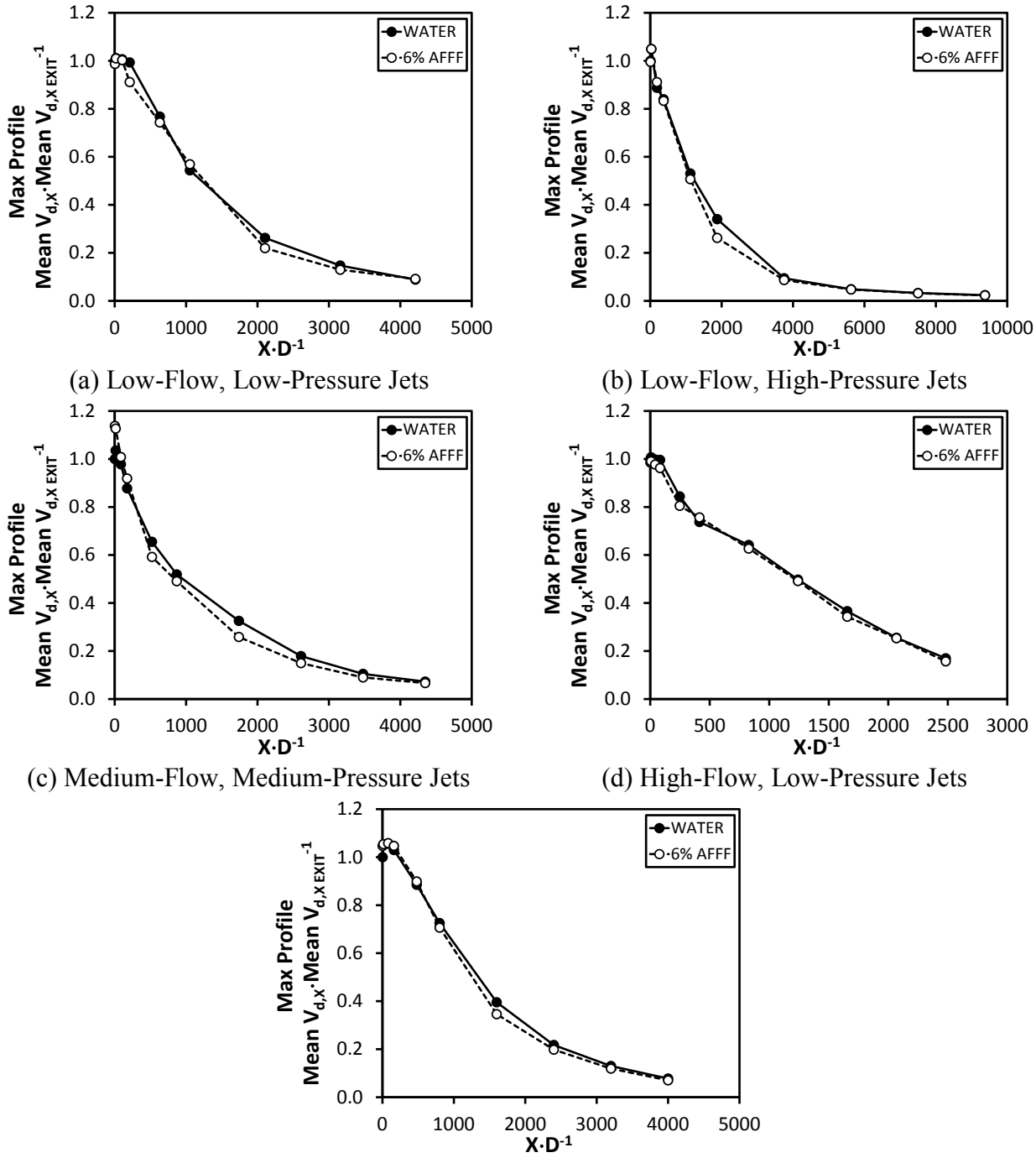

(a) Low-Flow, Low-Pressure Jets

(b) Low-Flow, High-Pressure Jets

(c) Medium-Flow, Medium-Pressure Jets

(d) High-Flow, Low-Pressure Jets

(e) High-Flow, High-Pressure Jets

Figure 98. Firefighting Jet PDPA Summary in Terms of Nondimensional Maximum Profile, Mean Axial Droplet Velocity

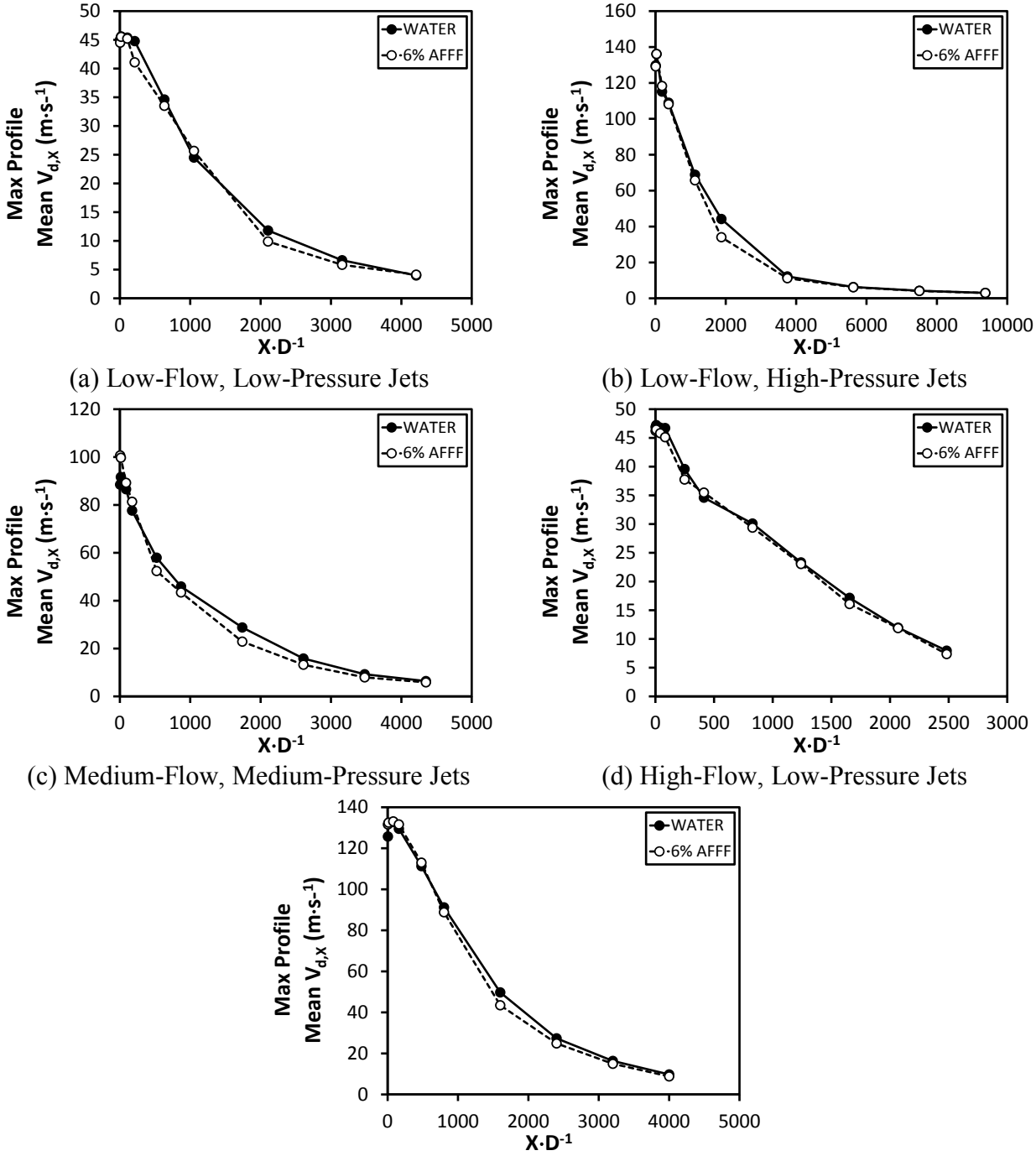

(a) Low-Flow, Low-Pressure Jets

(b) Low-Flow, High-Pressure Jets

(c) Medium-Flow, Medium-Pressure Jets

(d) High-Flow, Low-Pressure Jets

(e) High-Flow, High-Pressure Jets

Figure 99. Firefighting Jet PDPA Summary in Terms of Dimensional Maximum Profile, Mean Axial Droplet Velocity

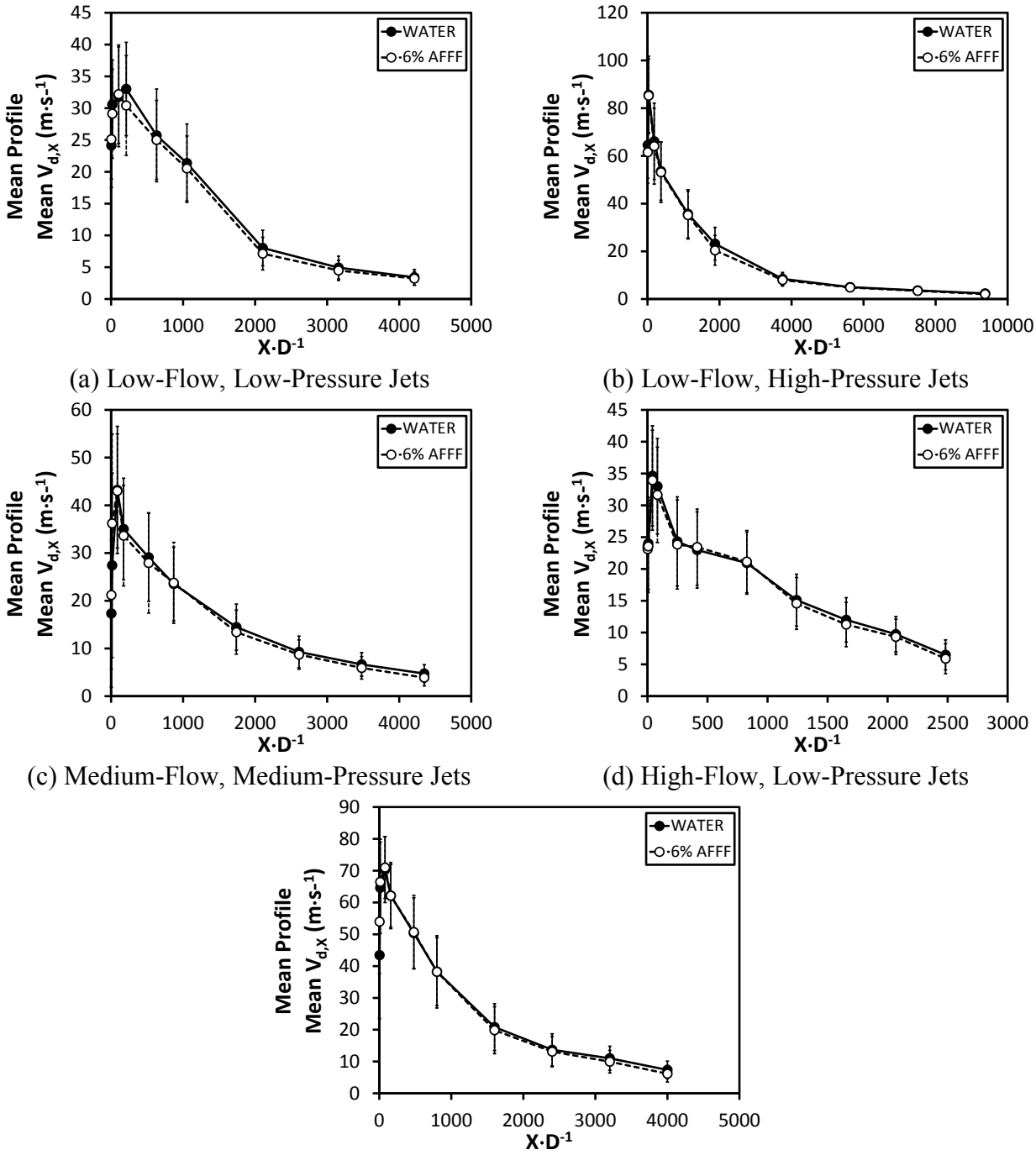

(a) Low-Flow, Low-Pressure Jets

(b) Low-Flow, High-Pressure Jets

(c) Medium-Flow, Medium-Pressure Jets

(d) High-Flow, Low-Pressure Jets

(e) High-Flow, High-Pressure Jets

Figure 100. Firefighting Jet PDPA Summary in Terms of Mean Profile, Mean Axial Droplet Velocity (Vertical bars represent mean profile, ±RMS axial droplet velocity magnitude.)

Figure 101 summarizes the phase Doppler mean vertical droplet velocity measurements for all firefighting jet configurations analyzed. Figure 101(a) illustrates the maximum profile, mean vertical water droplet velocity, and figure 101(c) depicts the mean profile, mean vertical water droplet velocity. Figure 101(b) and (d) depict the same scenarios as figure 101(a) and (c), respectively, but instead use 6% AFFF as the agent.

For all firefighting jet configurations, maximum profile, mean vertical droplet velocity magnitude increased as nozzle pressure increased, illustrating the effect pressure had on dispersion strength and overall momentum exchange in the vertical direction. Maximum profile, mean vertical droplet velocity magnitude also tended to decrease as flow rate increased, indicating the loss in vertical jet momentum as axial jet momentum increased. Maximum profile, mean vertical droplet velocity magnitudes ranged as high as 8 $m \cdot s^{-1}$ for the low-flow, high-pressure jet to as low as 2 $m \cdot s^{-1}$ for the high-flow, low-pressure jet. Mean profile, mean vertical droplet velocities followed the same trend as the maximum profile data, ranging from a high of about 1.75 $m \cdot s^{-1}$ to a low of approximately 0.75 $m \cdot s^{-1}$.

Figures 102 and 103 reproduce the same data shown in figure 101, but highlight the effect AFFF had on each nozzle pressure-flow rate combination compared to water. Figure 102 expands the maximum profile, mean vertical droplet velocities illustrated in figure 101(a) and (b), and figure 103 expands the mean profile, mean vertical droplet velocities depicted in figure 101(c) and (d), respectively. Figure 103 shows the mean profile, ±RMS vertical droplet velocity via vertical bars in addition to reporting the mean profile, mean vertical droplet velocity. Insignificant differences were observed between AFFF and water jets, mean vertical droplet velocities regardless of the nozzle pressure-flow rate combination. RMS vertical droplet velocity magnitudes with mean values typically around zero ranged as high as 5 $m \cdot s^{-1}$ in some instances, reinforcing the turbulent nature of the firefighting jet flow field.

The results presented in figure 103 also serve as a PDPA system alignment check to ensure mean profile, mean vertical droplet velocities fell at or near zero, particularly for lower-flow, higher-pressure jets with strong symmetry about the jet axial centerline. Low-flow, high-pressure and medium-flow, medium-pressure jets exhibited the best vertical symmetry as expected. High-flow, low-pressure jets showed the most significant asymmetry in figure 103(d) with the largest observed mean droplet diameters under the strongest influence of gravity over the furthest axial reach.

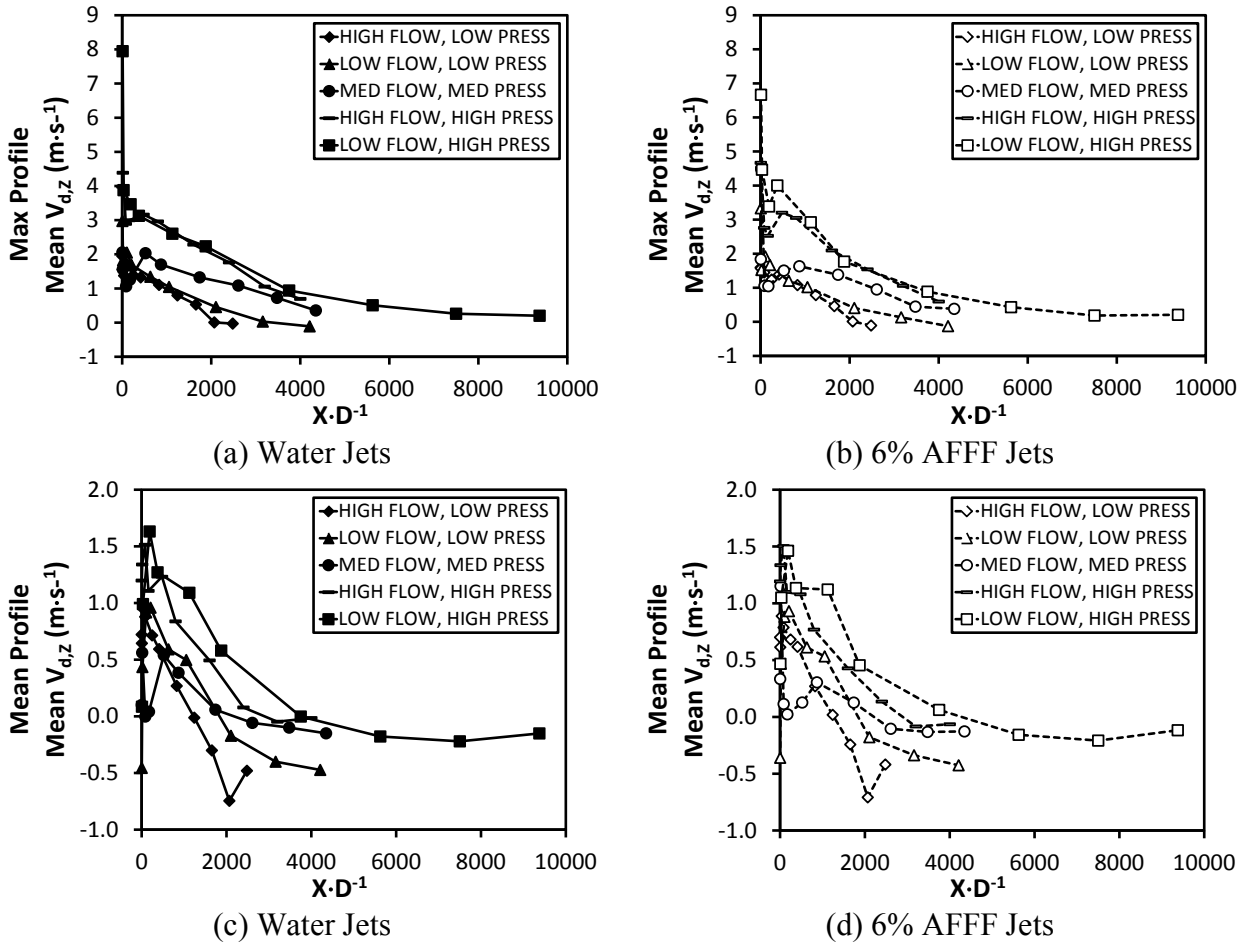

Figure 101. Firefighting Jet PDPA Summary Data in Terms of Maximum and Mean Profile, Mean Vertical Droplet Velocity

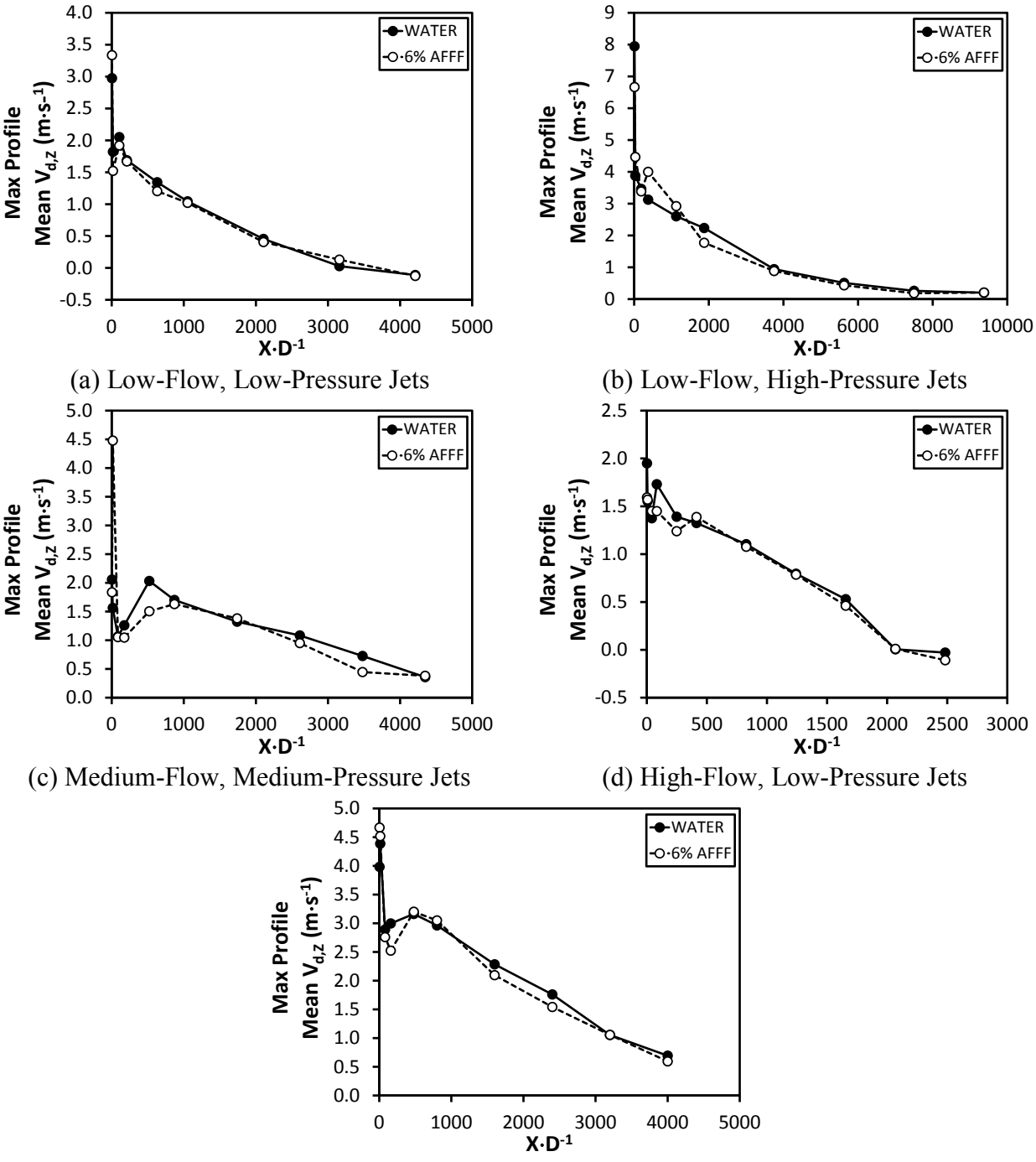

(a) Low-Flow, Low-Pressure Jets

(b) Low-Flow, High-Pressure Jets

(c) Medium-Flow, Medium-Pressure Jets

(d) High-Flow, Low-Pressure Jets

(e) High-Flow, High-Pressure Jets

Figure 102. Firefighting Jet PDPA Summary in Terms of Maximum Profile, Mean Vertical Droplet Velocity

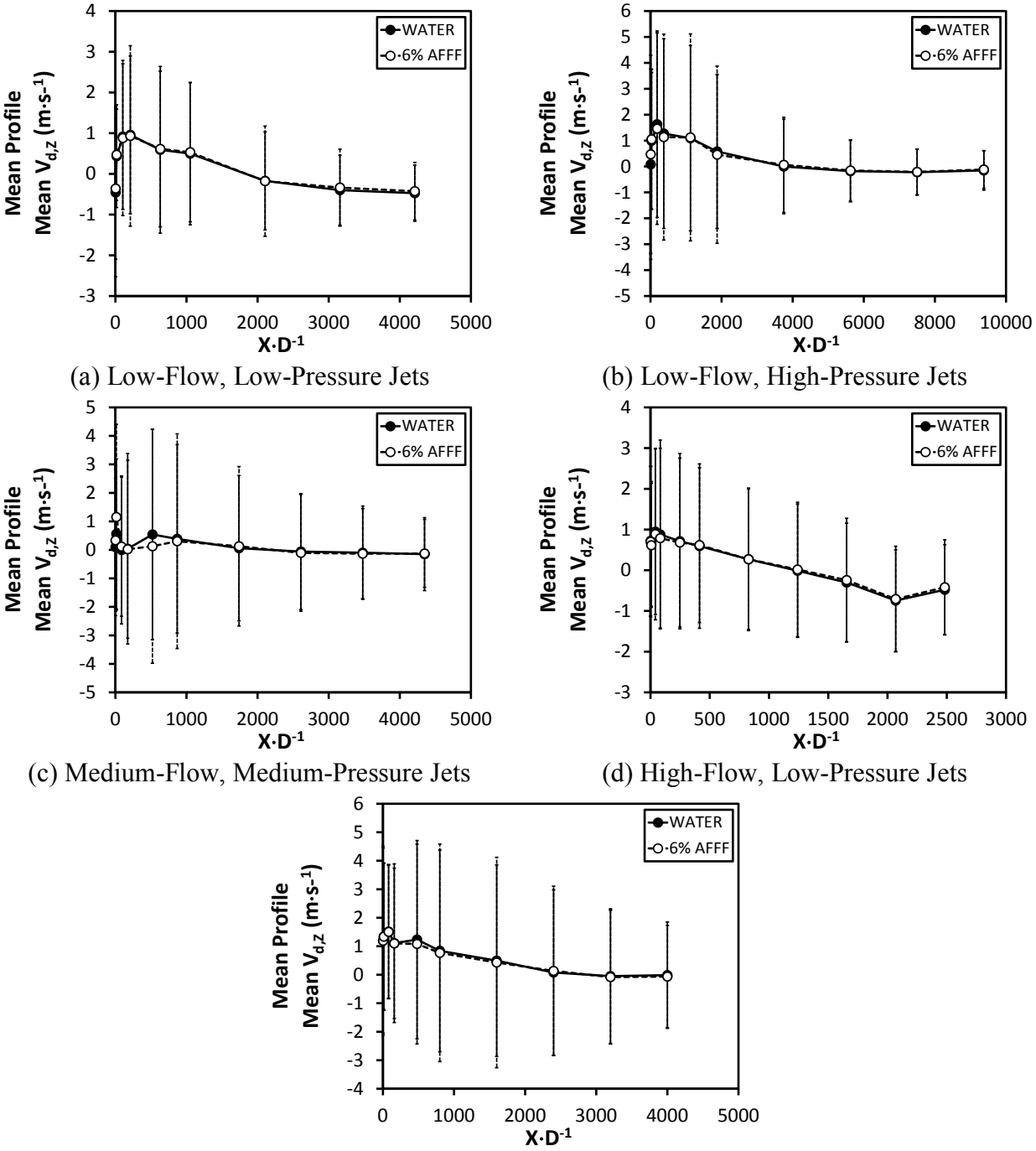

(a) Low-Flow, Low-Pressure Jets

(b) Low-Flow, High-Pressure Jets

(c) Medium-Flow, Medium-Pressure Jets

(d) High-Flow, Low-Pressure Jets

(e) High-Flow, High-Pressure Jets

Figure 103. Firefighting Jet PDPA Summary in Terms of Mean Profile, Mean Vertical Droplet Velocity (Vertical bars represent mean profile, ±RMS vertical droplet velocity magnitude.)

Figure 104 summarizes phase Doppler droplet diameter measurements for all firefighting jet configurations analyzed. Figure 104(a) shows the mean profile, mean water droplet diameter, figure 104(c) illustrates the mean profile, RMS water droplet diameter, and figure 104(e) depicts the mean profile, Sauter mean water droplet diameter. Figure 104(b), (d), and (e) illustrate the same scenarios as in figure 104(a), (c), and (e), respectively, but instead use 6% AFFF as the agent.

Mean profile, mean droplet diameters for all nozzle pressure-flow rate combinations were globally reduced by 7% to 38% with the addition of AFFF, resulting in the most definitive measure of difference between water and AFFF jets. The reduction in mean droplet size was due to the surface tension-lowering surfactant additives, which improved overall jet breakup. Mean droplet diameter increased as flow rate increased with the high-flow, low-pressure water jet registering the largest magnitude at 90 μm. Mean droplet diameter decreased as flow rate decreased with the low-flow, high-pressure AFFF jet-generated droplets recording sizes as low as 17 μm. Nozzle pressure increases also decreased mean droplet diameter, which was expected as jet atomization and secondary breakup was further enhanced.

Mean profile, RMS droplet diameter results observed the same trends as those of the mean profile, mean droplet diameter results, most notably showing a wide droplet size distribution irrespective of nozzle pressure-flow rate combination. Mean profile, RMS droplet diameter magnitudes were also consistently similar to mean profile, mean droplet diameter magnitudes, which indicated droplet distribution range was proportional to mean droplet size. This assumption was reasonable because the larger the parent droplet, the greater the opportunity for successive breakup resulting in a larger distribution of droplets.

Mean profile, Sauter mean droplet diameter results followed a similar, definitive trend to those of mean profile, mean droplet diameter results for three of the five nozzle pressure-flow rate combinations. However, the other two nozzle settings generated conflicting results. A peak magnitude of about 365 μm was exhibited by the high-flow, low-pressure water jet, and magnitudes as low as 50 μm were observed for the low-flow, high-pressure AFFF jet.

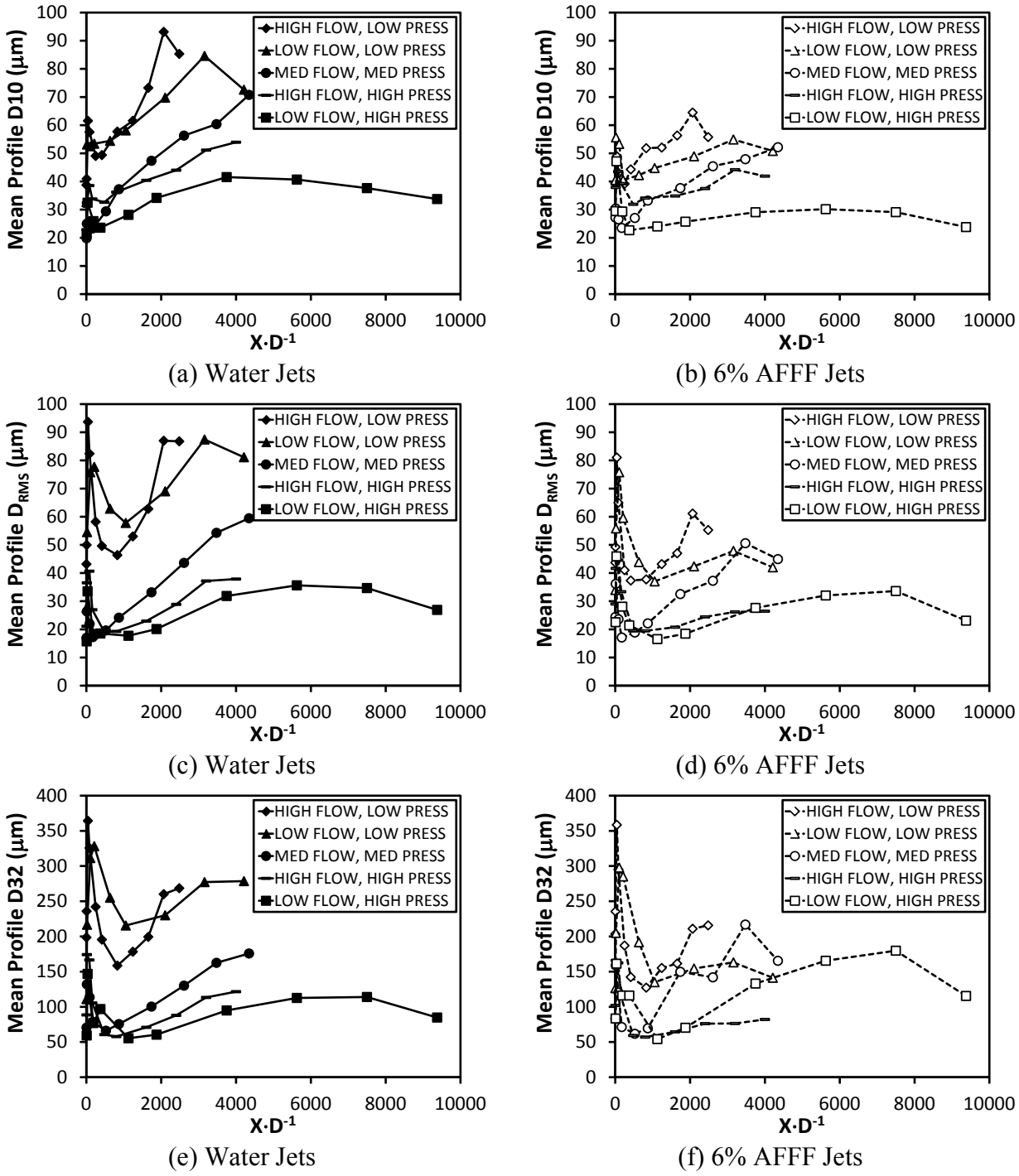

Figure 104. Firefighting Jet PDPA Summary Data in Terms of Mean Profile, Droplet Diameters

Figures 105 through 107 reproduce the same data shown in figure 104, but highlight the effect AFFF had on each nozzle pressure-flow rate combination compared to water. Figure 105 expands the mean profile, mean droplet diameters illustrated in figure 104(a) and (b), and figure 106 expands the mean profile, RMS droplet diameters shown in figure 104(c) and (d), respectively. Figure 107(a) and (b) expands the mean profile, Sauter mean diameters depicted in figure 104(e) and (f).

Figure 105 depicts the decisive reduction in mean profile, mean droplet diameter AFFF jets in comparison to water jets. The ability of AFFF to lower mean droplet diameters decreased as the flow rate increased, although the loss in efficiency was minor. This was likely due to the increased presence of jet ligaments as illustrated in figure 12(a) compared to satellite droplets where surfactant effectiveness was reduced. The change in mean droplet diameter as nozzle pressure increased was less apparent. According to figure 105, enhanced breakup due to AFFF had the greatest effect in the nozzle near field within the first 1000 nozzle diameters with its influence gradually decaying for the remainder of the effective jet length. This observation is supported by figures 10 and 11 in which AFFF has the greatest affect in lowering surface tension within the first second of droplet life.

Figure 106 shows mean profile, RMS droplet diameters are consistently lower for AFFF jets compared to water jets similar to mean droplet diameter trends, with this margin decreasing as flow rate increased. The low-flow, low-pressure jet exhibited the largest disparity with an approximate 50% reduction in RMS droplet diameter.

Figure 107 illustrates mean profile, Sauter mean droplet diameters with inconsistent results regarding the influence of AFFF. Low-flow, high-pressure jets and medium-flow, medium-pressure jets did not follow the trend of water jet mean profile, Sauter mean droplet diameters exceeding AFFF jet values as in the other three nozzle settings. A closer inspection of individual Sauter mean diameter profiles in appendix C shows a large amount of scatter between AFFF jet sampling points for the two outlying nozzle settings, particularly in the downstream region of each jet. The reason behind this contrast is not absolutely known. Based on the AFFF concentration sensitivity in section 6.3.4 on the medium-flow, medium-pressure jet, it is speculated Sauter mean diameter profile scatter was amplified as AFFF solution concentration was increased. This indicates a nonnegligible number of nonspherical, bubble-like AFFF formations much larger than water droplets may have been validated by the PDPA skewing Sauter mean droplet diameter values for these profile locations. Very few (e.g., ten or fewer) droplets measured in the upper threshold of the PDPA measurement envelope in the field of 50,000 samples were also capable of altering Sauter mean diameter by 10% or more.

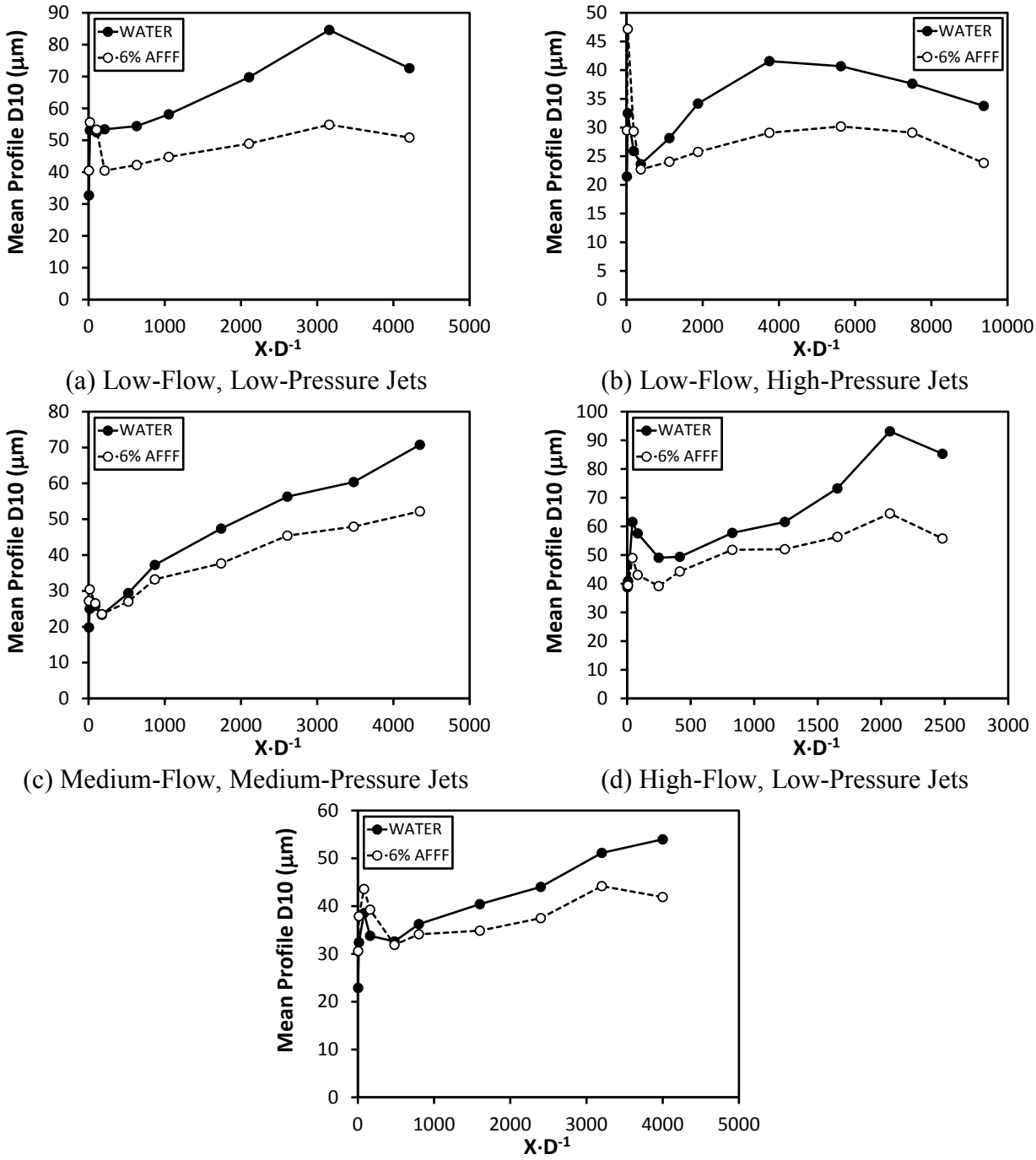

(a) Low-Flow, Low-Pressure Jets

(b) Low-Flow, High-Pressure Jets

(c) Medium-Flow, Medium-Pressure Jets

(d) High-Flow, Low-Pressure Jets

(e) High-Flow, High-Pressure Jets

Figure 105. Firefighting Jet PDPA Summary in Terms of Mean Profile, Mean Droplet Diameters

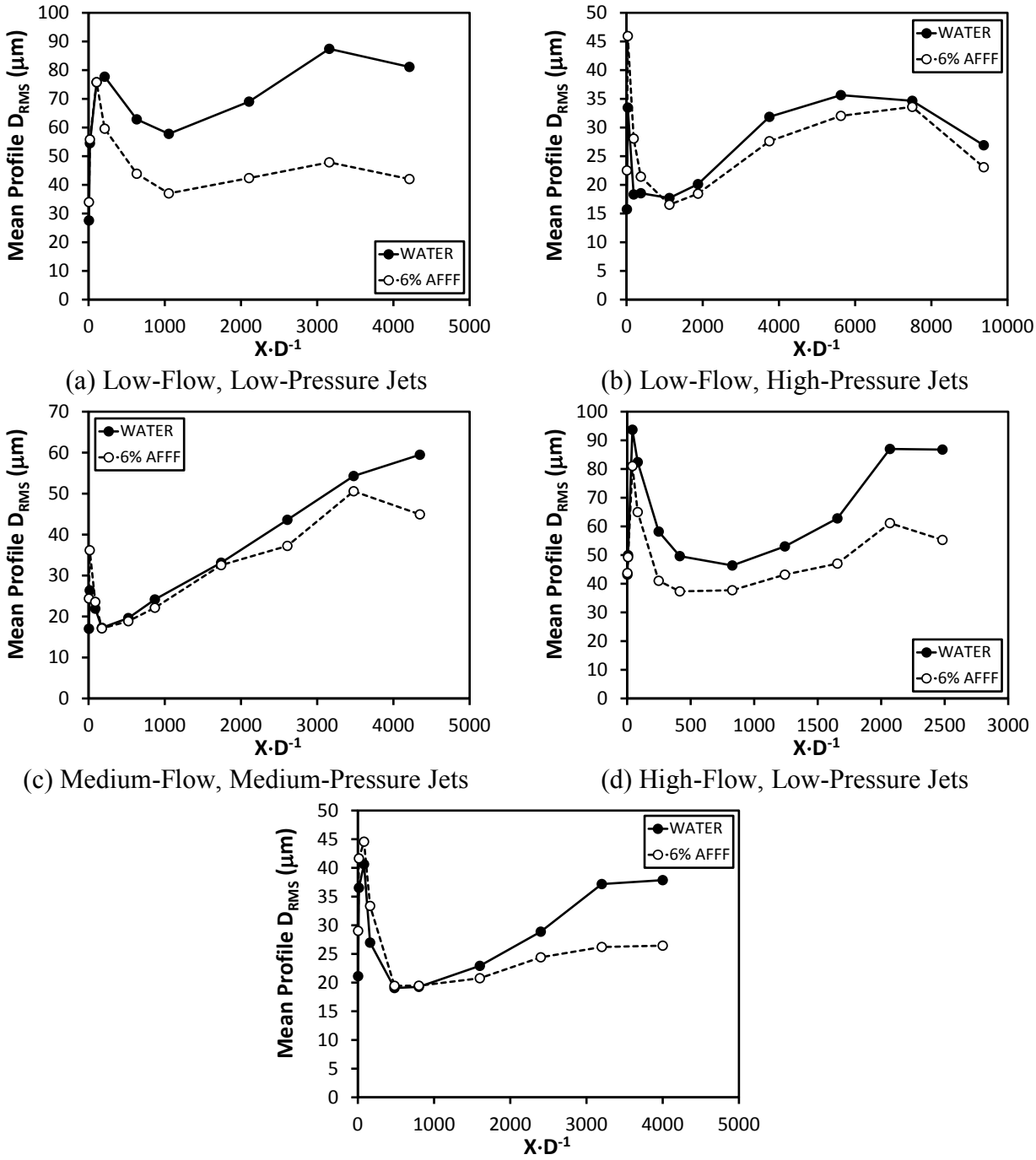

(a) Low-Flow, Low-Pressure Jets

(b) Low-Flow, High-Pressure Jets

(c) Medium-Flow, Medium-Pressure Jets

(d) High-Flow, Low-Pressure Jets

(e) High-Flow, High-Pressure Jets

Figure 106. Firefighting Jet PDPA Summary in Terms of Mean Profile, RMS Droplet Diameters

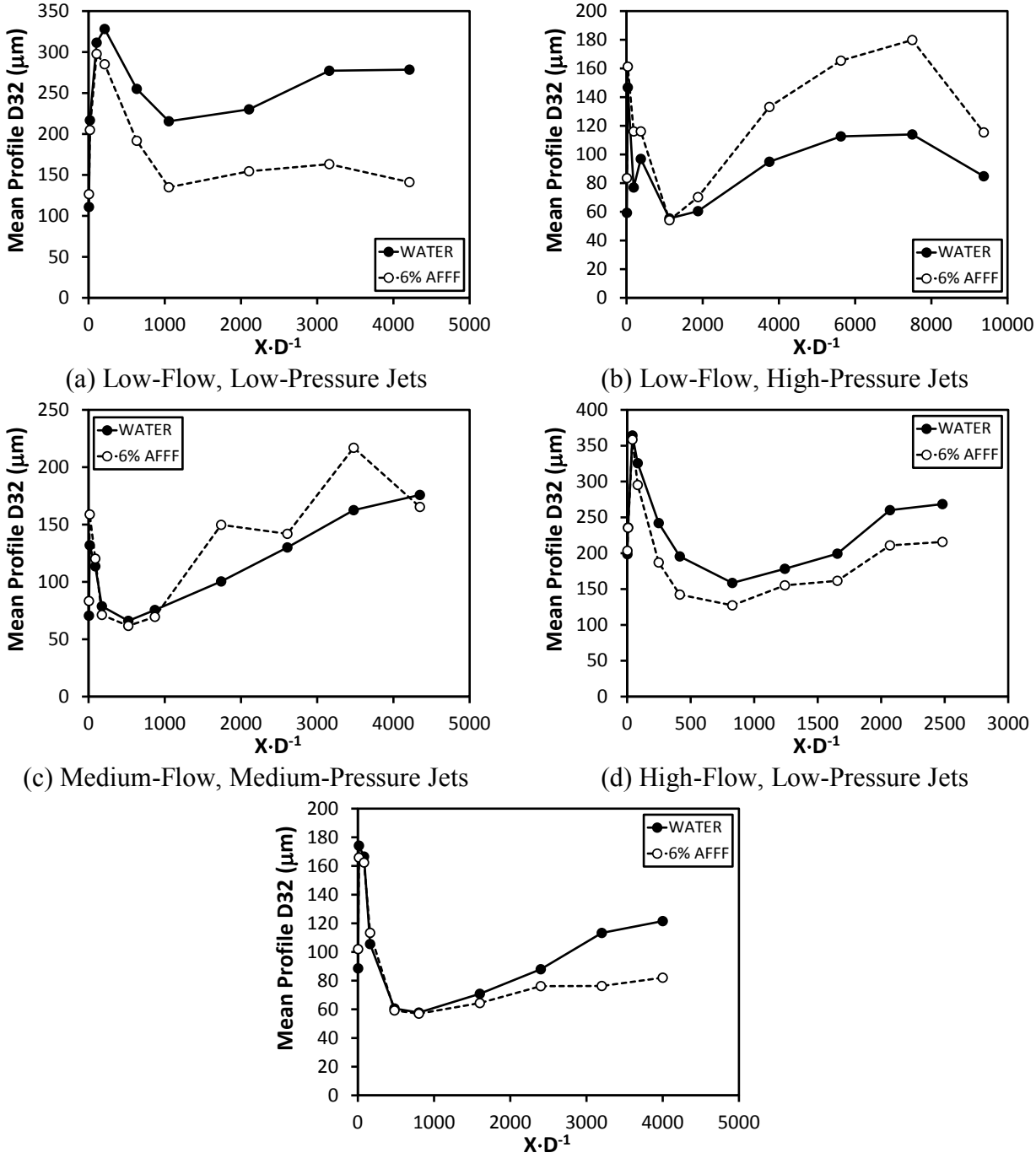

(a) Low-Flow, Low-Pressure Jets

(b) Low-Flow, High-Pressure Jets

(c) Medium-Flow, Medium-Pressure Jets

(d) High-Flow, Low-Pressure Jets

(e) High-Flow, High-Pressure Jets

Figure 107. Firefighting Jet PDPA Summary in Terms of Mean Profile, Sauter Mean Droplet Diameters

Phase Doppler sampling statistics are presented to examine broad trends in the data acquisition process. They are also investigated to determine if any bias or dependency exists in the results with respect to agent delivery pump pulsations known to affect the flow physics of certain firefighting jet configurations. These pulsations are discussed in detail in section 6.1.2. PDPA data acquisition rate and mean sample count are presented in figure 108(a) and (b), respectively. The data presented represent the mean profile value averaged for all five firefighting jet nozzle pressure-flow rate combinations. It is shown that in the nozzle near field, the mean profile data acquisition rate ranged from approximately 3000 to 4500 samples per second, but tapered to as low as 100 samples per second in the far axial reaches of each jet. Mean profile sample count followed a similar trend, totaling about 42,000 samples per measurement location in the near field of the nozzle, but dropped to about 1,000 samples in the jet far field. It should be noted that PDPA data acquisition rates and sample counts shown in figure 108 are biased towards a lower value. This is due to measurements purposefully taken up to and slightly beyond the outer boundary of each firefighting jet to ensure the flow was fully described at each profile location.

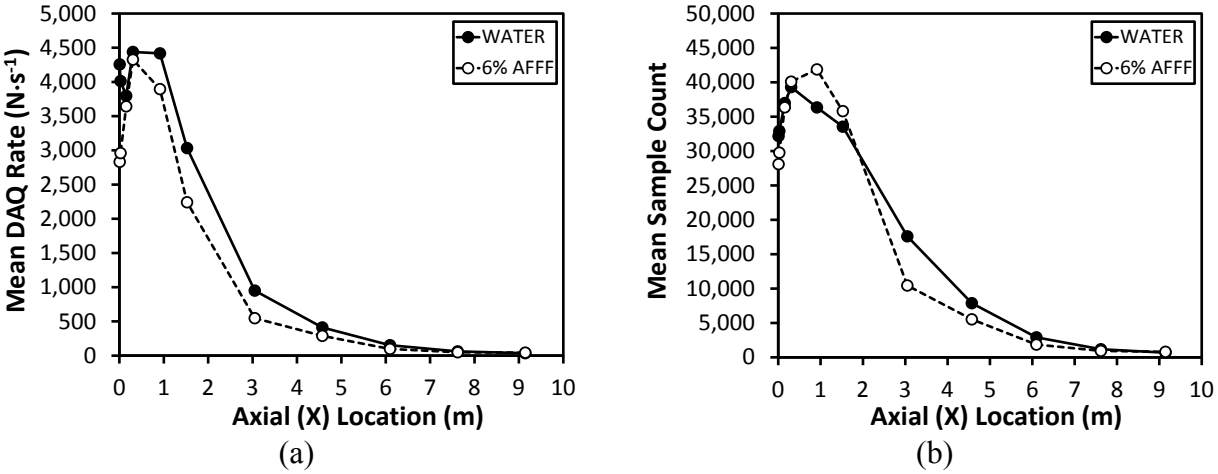

Figure 108. (a) PDPA Mean Profile Data Acquisition Rate vs Axial Measurement Location and (b) PDPA Mean Data Sample Count vs Axial Measurement Location

Based on the agent delivery pump oscillation frequency and the mean elapsed time per sampling point recorded for each firefighting jet flow configuration, the number of pump oscillations per point sampling period was calculated. The results are listed in table 11. A range of about 6,000 to 40,000 pump oscillations were generated while measuring each point from the low-flow, high-pressure jet to the high-flow, low-pressure jet, respectively. The phase Doppler data likely exhibited some bias towards recording higher-velocity versus lower-velocity droplets due to uneven time sampling of the PDPA system. Even-time sampling would have eliminated most of this bias, but it was not practical due to the reduced data acquisition rates that would have accompanied this technique coupled with the expense associated with AFFF testing.

Table 11. Calculated Pump Oscillations per Phase Doppler Data Acquisition Sampling Period

Test Case	Pump Oscillation Frequency (Hz)	Mean Elapsed Time Per Sampling Point (s)	Pump Oscillations Per Point Sampling Period (-)
Low-Flow, Low-Pressure Water Jet	389	17.53	6,819
Low-Flow, Low-Pressure 6% AFFF Jet	389	16.67	6,485
Low-Flow, High-Pressure Water Jet	389	15.34	5,967
Low-Flow, High-Pressure 6% AFFF Jet	389	17.03	6,625
Medium-Flow, Medium-Pressure Water Jet	1151	15.29	17,600
Medium-Flow, Medium-Pressure 6% AFFF Jet	1151	16.94	19,500
High-Flow, Low-Pressure Water Jet	2340	17.15	40,130
High-Flow, Low-Pressure 6% AFFF Jet	2340	15.59	36,480
High-Flow, High-Pressure Water Jet	1852	16.16	29,930
High-Flow, High-Pressure 6% AFFF Jet	1852	17.39	32,210

6.3.4 Firefighting Jet Phase Doppler AFFF Concentration Sensitivity Results.

A phase Doppler AFFF concentration sensitivity study was conducted on the medium-flow, medium-pressure jet to quantify changes in measured firefighting jet flow parameters with respect to AFFF concentration. The concentration range spanned from 3% to 9% AFFF. A fourth concentration (12% AFFF) was not tested because an interim analysis determined a negligible difference existed between the 6% and 9% AFFF phase Doppler results. Figures 109 through 113 show mean axial droplet velocity, mean vertical droplet velocity, mean droplet diameter, RMS droplet diameter, and Sauter mean droplet diameter profile results, respectively, for profile locations illustrated in figure 48 and listed in table 7. Plots are presented similarly to those in section 6.3.2.

Mean axial droplet velocity was affected by the addition of AFFF in a similar manner as discussed in section 6.3.3 with a minor (10% or less) lag observed globally from water jet to 6% AFFF profiles. However, the change in the axial velocity profile among all AFFF profiles was negligible. Mean vertical droplet velocity results behaved similarly to mean axial droplet velocity results, except differences between AFFF and water jet profiles were less significant, and the difference among AFFF results was even less indiscernible. The mean droplet diameter results exhibited the largest variation, with AFFF droplets reduced by as much as 50% compared to water droplets. The AFFF mean droplet diameter shrank as AFFF concentration increased from 3% to 6% AFFF, but negligibly decreased between 6% and 9% AFFF. The size differential between AFFF and water droplets grew as the distance downstream increased. An increase in AFFF concentration showed a distinguishable increase in RMS droplet diameter, particularly for 9% AFFF as downstream distance increased similar to the mean droplet diameter results, likely due to the early onset of enhanced breakup. The Sauter mean droplet diameter results produced analogous results to those of mean droplet diameter, except the diameter magnitudes were

amplified and the AFFF profile data had more scatter in downstream profiles consistent with the low-flow, high-pressure jet studied solely at 6% AFFF.

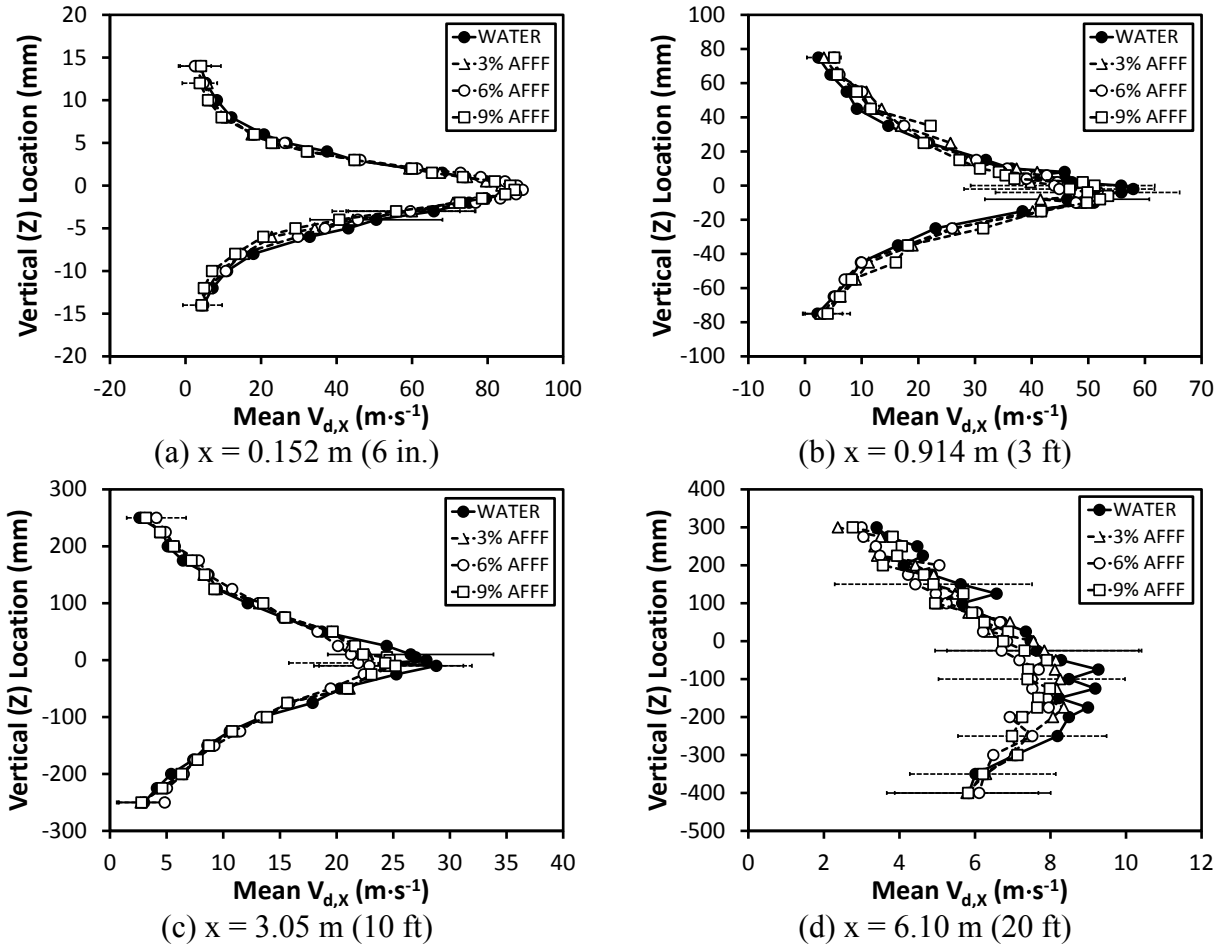

(a) x = 0.152 m (6 in.)

(b) x = 0.914 m (3 ft)

(c) x = 3.05 m (10 ft)

(d) x = 6.10 m (20 ft)

Figure 109. Medium-Flow, Medium-Pressure Jet Vertical Location vs Mean Axial Droplet Velocity With Respect to Variation in AFFF Concentration

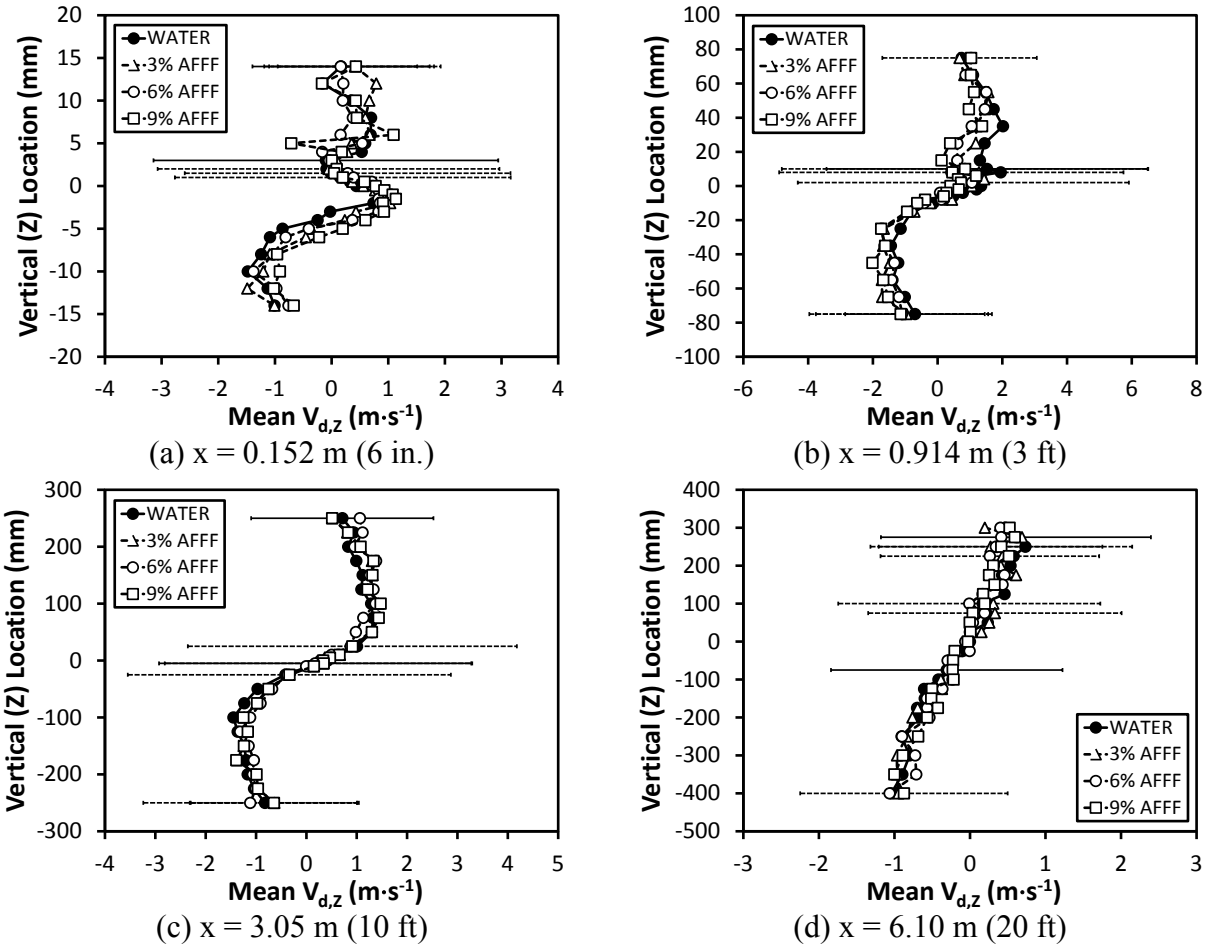

(a) x = 0.152 m (6 in.)

(b) x = 0.914 m (3 ft)

(c) x = 3.05 m (10 ft)

(d) x = 6.10 m (20 ft)

Figure 110. Medium-Flow, Medium-Pressure Jet Vertical Location vs Mean Vertical Droplet Velocity With Respect to Variation in AFFF Concentration

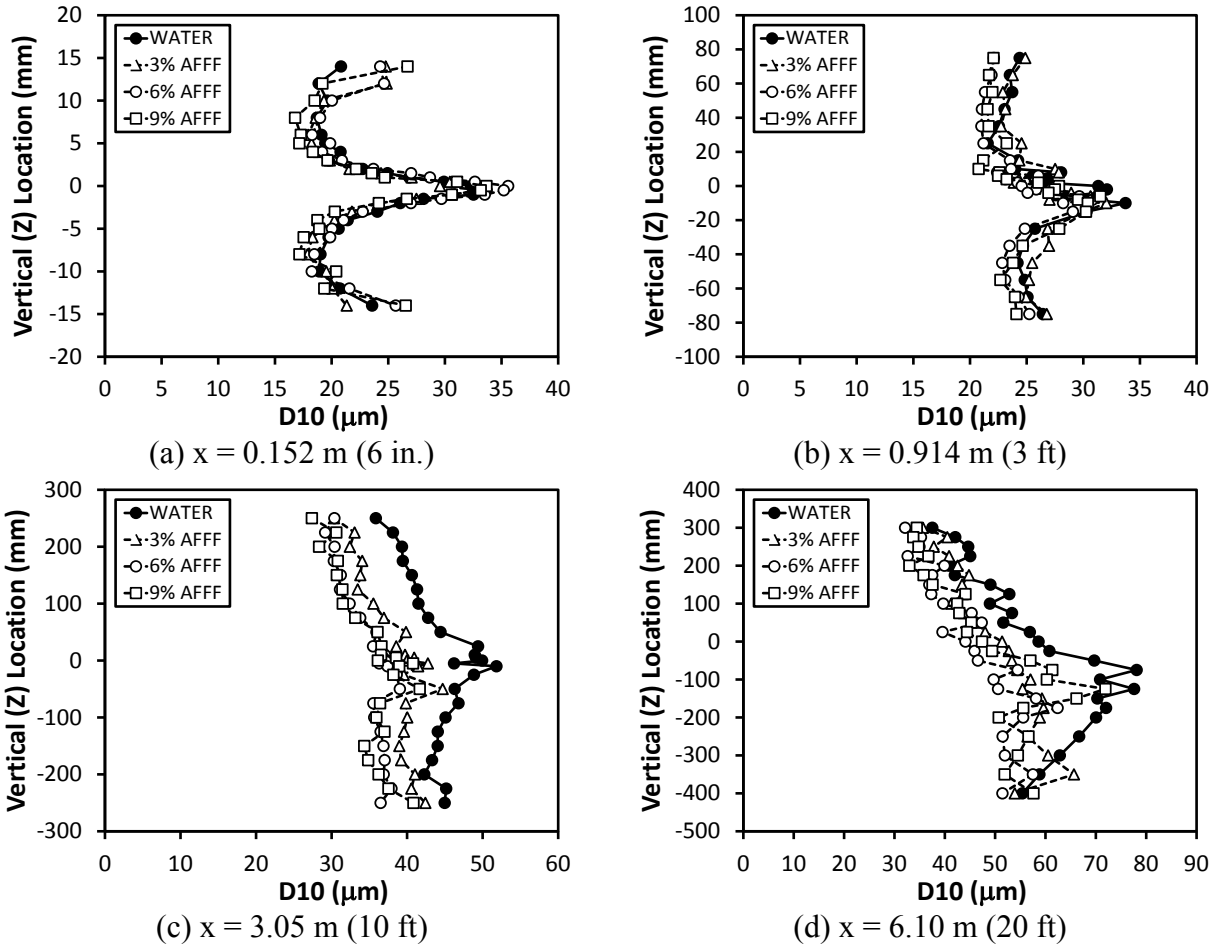

(a) x = 0.152 m (6 in.)

(b) x = 0.914 m (3 ft)

(c) x = 3.05 m (10 ft)

(d) x = 6.10 m (20 ft)

Figure 111. Medium-Flow, Medium-Pressure Jet Vertical Location vs Mean Droplet Diameter With Respect to Variation in AFFF Concentration

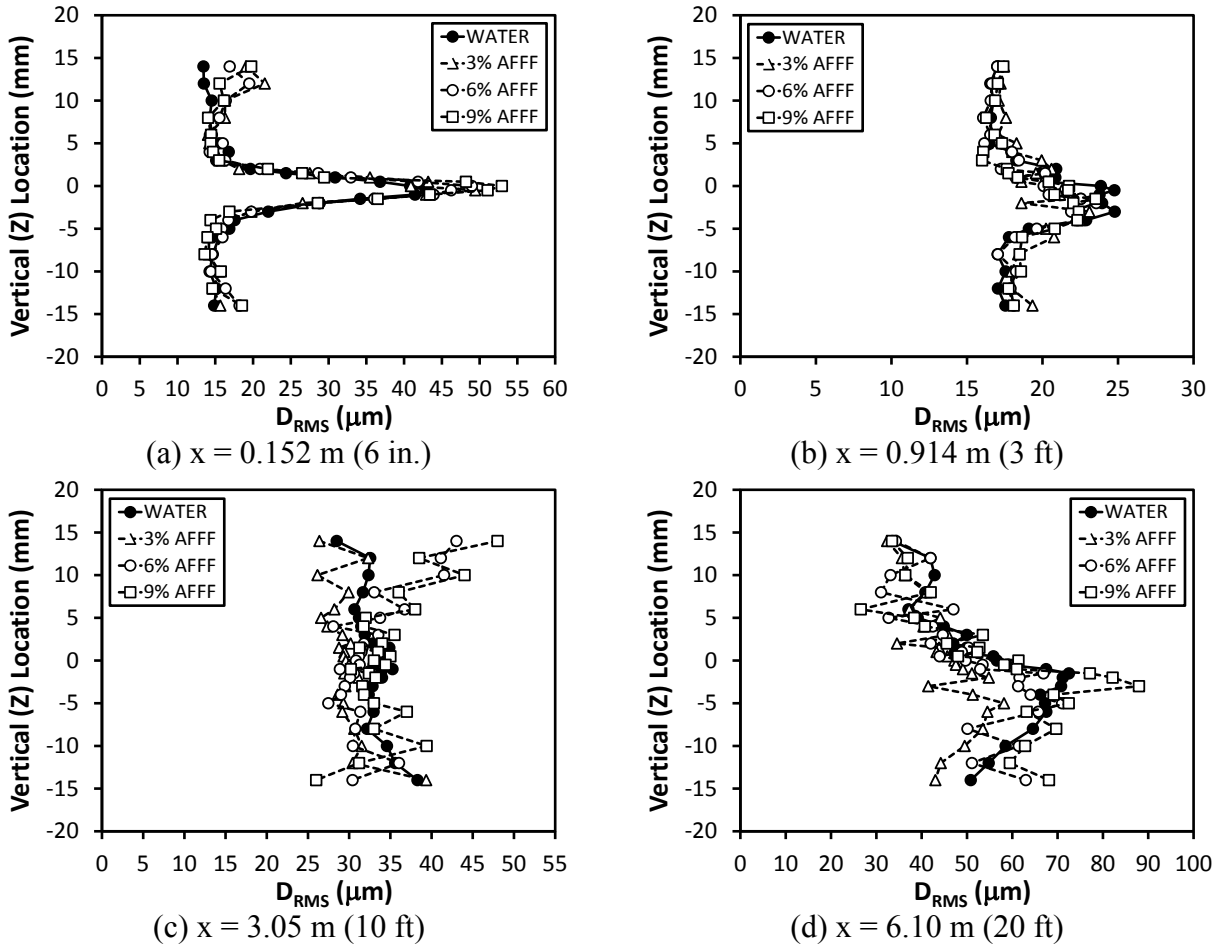

(a) x = 0.152 m (6 in.)

(b) x = 0.914 m (3 ft)

(c) x = 3.05 m (10 ft)

(d) x = 6.10 m (20 ft)

Figure 112. Medium-Flow, Medium-Pressure Jet Vertical Location vs RMS Droplet Diameter With Respect to Variation in AFFF Concentration

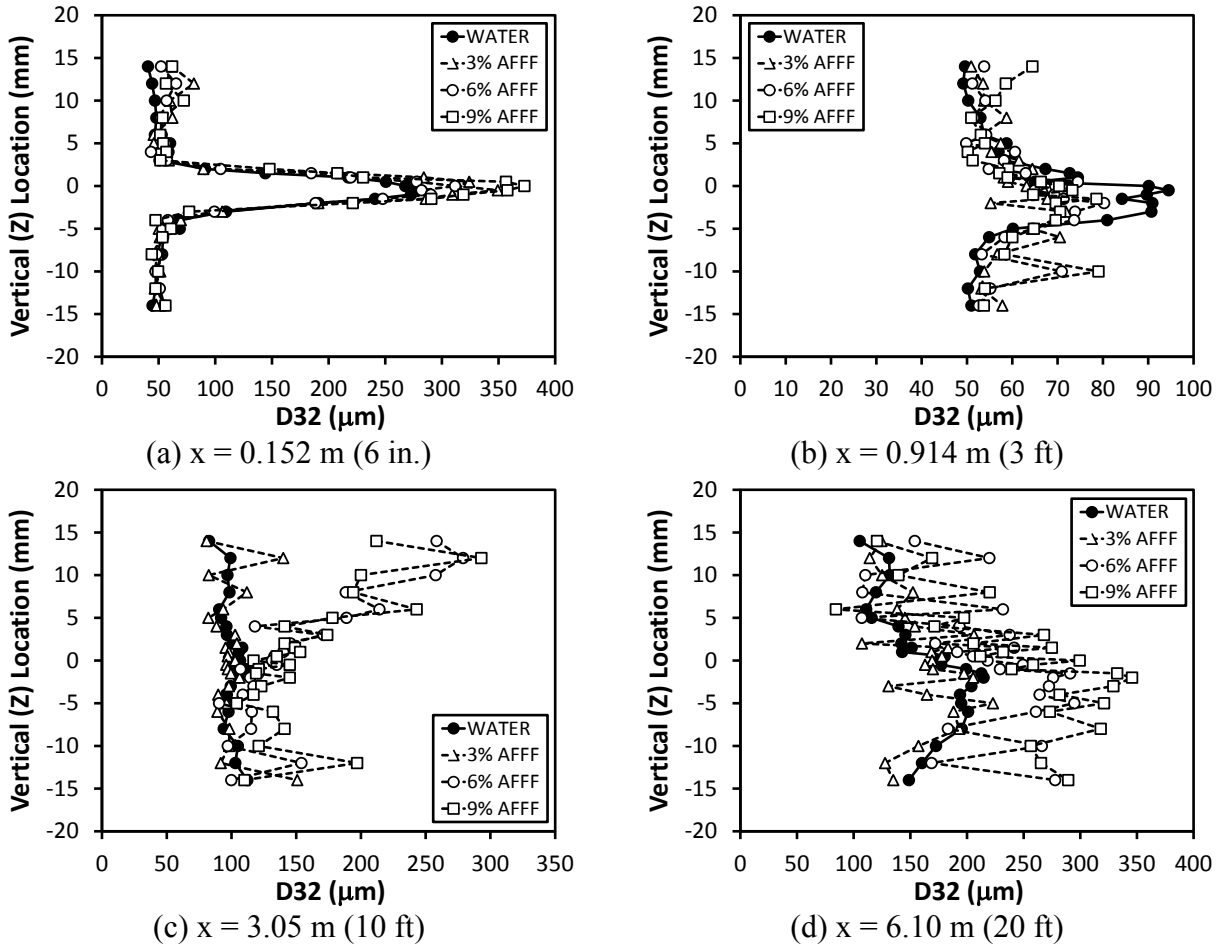

Figure 113. Medium-Flow, Medium-Pressure Jet Vertical Location vs Sauter Mean Droplet Diameter With Respect to Variation in AFFF Concentration

6.4 COMPUTATIONAL FIREFIGHTING JET MODEL RESULTS.

The CFD model results were computed for the ten firefighting jet configurations listed in table 8. The same five firefighting jet pressure-flow rate combinations investigated for flow visualization and PDPA were also modeled using water and 6% AFFF. A model parameter dependence study is presented, which helped shape the overall computational strategy. Select CFD model results are then compared to experiments in terms of qualitative flow features, select vertical flow parameter profiles similar to the presentation in section 6.3.2, and mean profile data similar to the presentation in section 6.3.3. A firefighting jet flow characterization study of all CFD model solutions is then presented illustrating various aspects of the simulated firefighting jets.

6.4.1 Computational Firefighting Jet Model Parameter Dependence Results.

A CFD model parameter dependence study was conducted to determine how variation in certain factors affected results. The key parameters examined were the DPM breakup model selection, spatial mesh resolution, temporal resolution, and the impact of the firefighting jet containment zone. Unless otherwise noted, all computational results used the TAB collision and coalescence

CFD physical submodels. Similar to sensitivity studies conducted experimentally, each analysis used the medium-flow, medium-pressure water jet condition for the baseline. Mean axial droplet velocity and mean droplet diameter data were the flow parameters used for comparison. The CFD model results represent each flow parameter averaged over the entire physical domain at a constant *x*-plane as a function of axial downstream location nondimensionalized with respect to the nozzle diameter. All parameter dependence studies followed the same solution strategy as that used in the CFD model results reported in sections 6.4.2 and 6.4.3.

Two DPM breakup models were applicable for low (< 100) gaseous Weber number jet flows within ANSYS Fluent®: the TAB model and the SSD model. Figure 114 illustrates a negligible difference in firefighting jet performance in terms of mean plane, mean axial droplet velocity and mean plane, mean droplet diameter over the entire length of the jet. The TAB model was selected versus the SSD model for the final solution strategy because speed to solution was 25% to 50% faster by comparison.

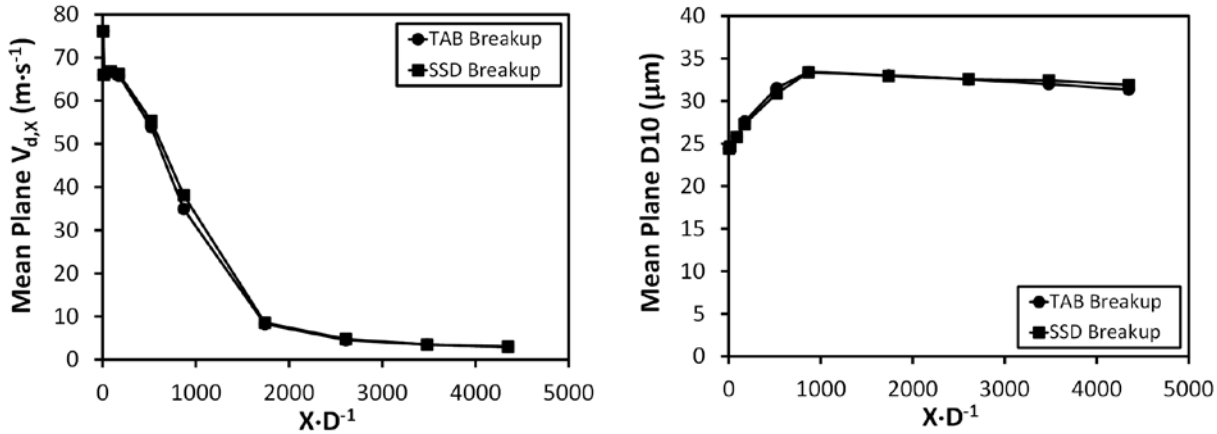

Figure 114. The CFD Model Solution Dependence on the DPM Secondary Droplet Breakup Model

Model sensitivity to coalescence was examined by comparing DPM TAB model solutions with and without the coalescence physical submodel activated. Figure 115 illustrates the results. Coalescence modeling added approximately 5% more time per iteration to the overall computation. The collision model was active for both cases presented. Mean plane, mean axial droplet velocity magnitudes depicted mild dependence, indicating coalescence modeling allowed droplet size families or parcels to enlarge and effectively alter trajectories primarily in the mid field of the firefighting jet. Mean plane, mean droplet diameter comparisons show significant divergence between model selections, illustrating the flow parameter can increase by almost 50%. The collision-only model depicted no significant growth in mean droplet diameter.

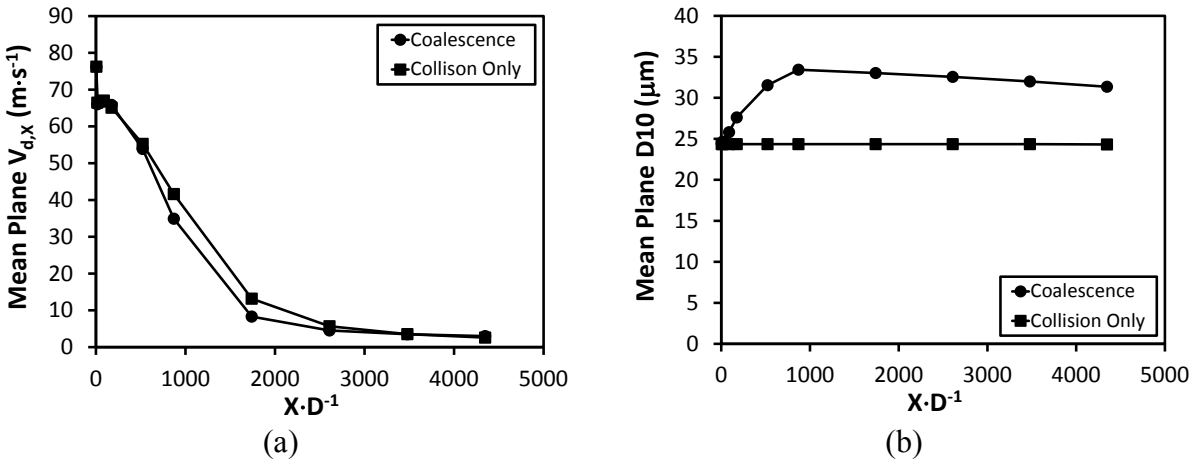

Figure 115. The CFD Model Solution Dependence on the DPM Coalescence Model

A spatial mesh resolution study was conducted to determine the solution dependence on three different grids ranging from a 254,000, 411,000, up to a 3.46 million cell grid shown in figure 116. Grid dependence studies regarding DPM flows are complex due to DPM (droplet) volume-to-cell volume ratio thresholds that must be maintained to preserve model applicability as discussed in section 5.2.1. Dimensions of the structured topology were linearly scaled to achieve all three grid sizes. Mesh resolution in the near nozzle injection field was maintained at 2 cm to maintain numerical stability. The mean plane, mean axial droplet velocity and the mean plane, mean droplet diameter results showed some dependence on the coarse mesh with values asymptoting to similar values between the regular and fine mesh. The regular mesh was employed for the resultant modeling strategy. A maximum CFD spatial discretization error of ±1.03% and ±0.67% was calculated for the mean plane, mean axial droplet velocity and the mean plane, mean droplet diameter, respectively. These errors are based on the Richardson extrapolation method and are representative of all CFD model results in the current study [73].

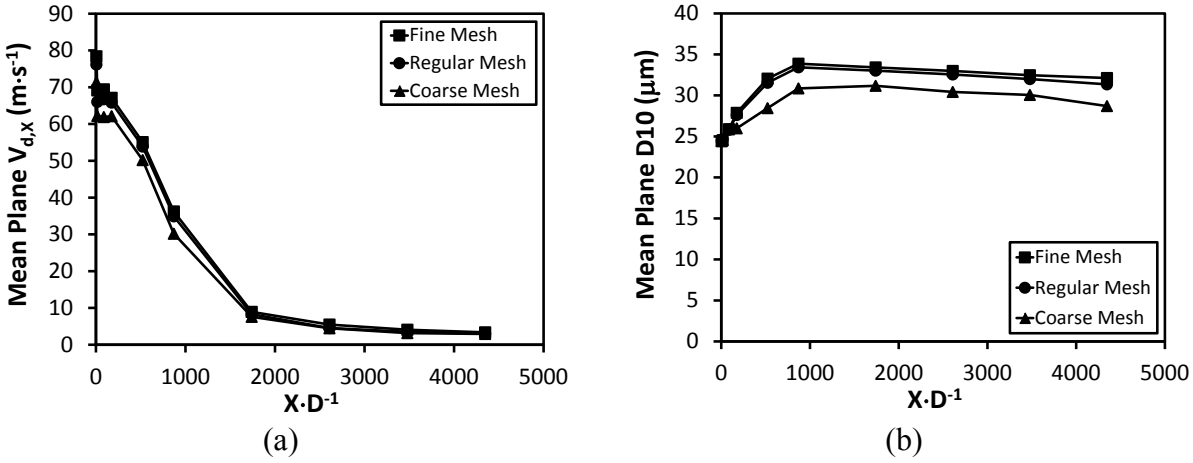

Figure 116. The CFD Model Solution Dependence on the Mesh Resolution

A temporal resolution study was executed to determine the solution dependence on the unsteady physical time step. Developing a CFD modeling strategy capable of generating reliable solutions with 1-ms time steps or larger was critical to future applications regarding integrated aircraft combustion models in which scenarios of interest may last several tens of seconds to minutes. Figure 117 shows the results.

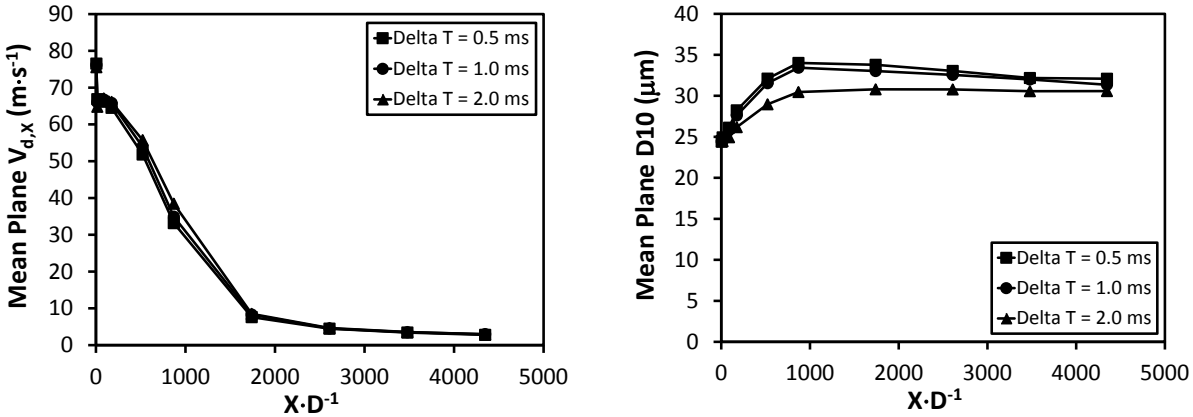

Figure 117. The CFD Model Solution Dependence on the Physical Time Step

A total of three time steps, ranging from 0.5 to 2 ms, were examined. The mean plane, mean axial droplet velocity magnitudes showed minor dependence on time step with noticeable dependence in the mean plane, mean droplet diameter results occurring for the largest time step. Negligible change was observed between the 0.5- and 1-ms time step. The 1-ms time step was employed for all firefighting jet CFD model results.

A computational study was conducted to determine the impact modeling the firefighting jet containment zone would have on the CFD model results. The containment zone was modeled as a no-slip wall similar to how the floor is modeled for all other computational results. The results are presented in figure 118. The containment bed starts at an $x \cdot D^{-1}$ of about 3500. The containment zone was shown to alter the effective mean plane, mean axial droplet velocity by as much as 12% upstream of the containment zone approximately halfway between it and the nozzle. A consistent gradual loss in firefighting jet momentum was observed as the stream approached and entered the containment zone, likely due to the flow resistance (pressure increase) imparted by the containment zone curtains. The mean plane, mean droplet diameters were reduced by as much as 10% with the addition of the containment zone due to airborne droplet lifetimes being extended within the flow domain allowing for secondary droplet breakup to continue for a longer period of time.

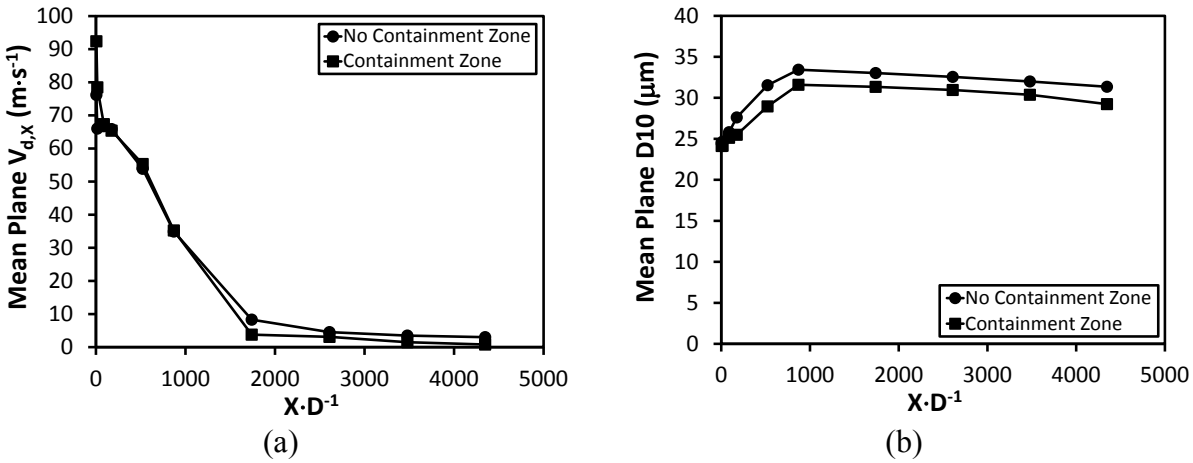

Figure 118. The CFD Model Solution Dependence on the Presence of the Firefighting Jet Containment Zone

6.4.2 Select Computational Firefighting Jet Model Results Compared to Experiments.

The CFD model, flow visualization, and phase Doppler results are compared to determine the ability of the computational solution strategy to reproduce the major firefighting jet physical features and flow parameter trends observed in experiments. Figures 119 through 121 compare the qualitative, instantaneous firefighting jet flow structure of the low-flow, low-pressure jet; the medium-flow, medium-pressure jet; and the high-flow, high-pressure jet of flow visualization (labeled Flow Viz) photography and computational (labeled CFD) model results, respectively. Flow visualization illustrations are sized such that the spatial scales between experimental and computational results are equivalent. The water jet and 6% AFFF jet results are presented showing a side and top view of each firefighting jet. Laboratory lighting and camera lens range limited full firefighting jet trajectory comparisons. Although the visual differences between these three nozzle conditions shown are significant, the firefighting jet Reynolds number range is relatively narrow, spanning from 6.9 by 10^4 to 2.47 by 10^5 and defining fully turbulent jet flow. For a summary of all case conditions examined in the present study, refer to appendix A.

Experimental firefighting jet trajectories were reproduced by the CFD model in terms of jet reach, spread, and axial centerline decay angle under the influence of gravity. Large-scale turbulent eddies were also qualitatively similar in terms of size and structure, and became more visible for medium- and high-flow, high-pressure jets operating at higher Reynolds numbers, particularly in the downstream wake region. The CFD model results also predicted the generation of more AFFF droplets compared to water droplets due to enhanced breakup from the surfactant agents, a trend consistent for every nozzle pressure-flow rate combination, which was also confirmed by photography.

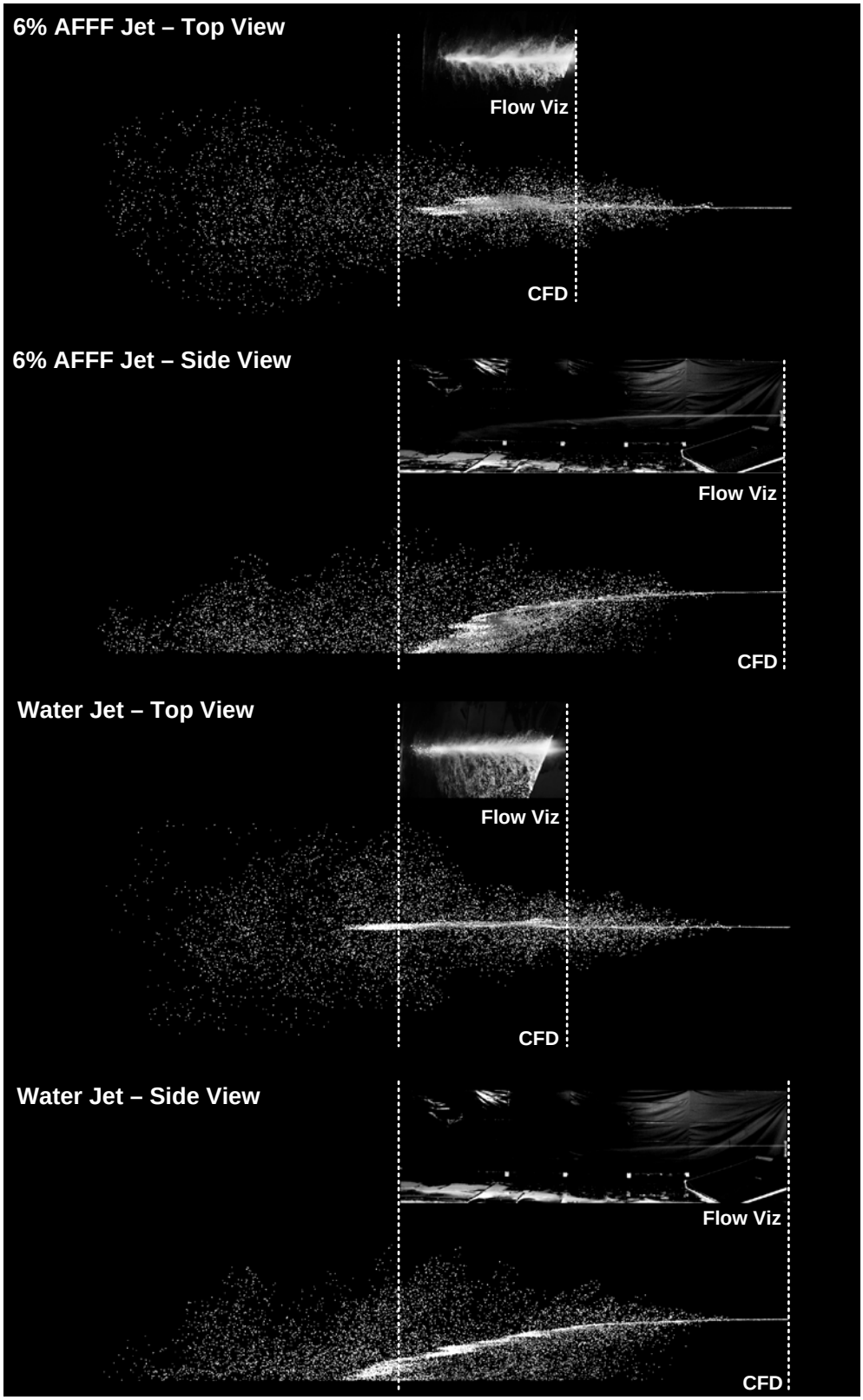

Figure 119. Qualitative Flow Structure Comparison Between CFD Model and Flow Visualization Results of the Low-Flow, Low-Pressure Jet (Flow is from right to left.)

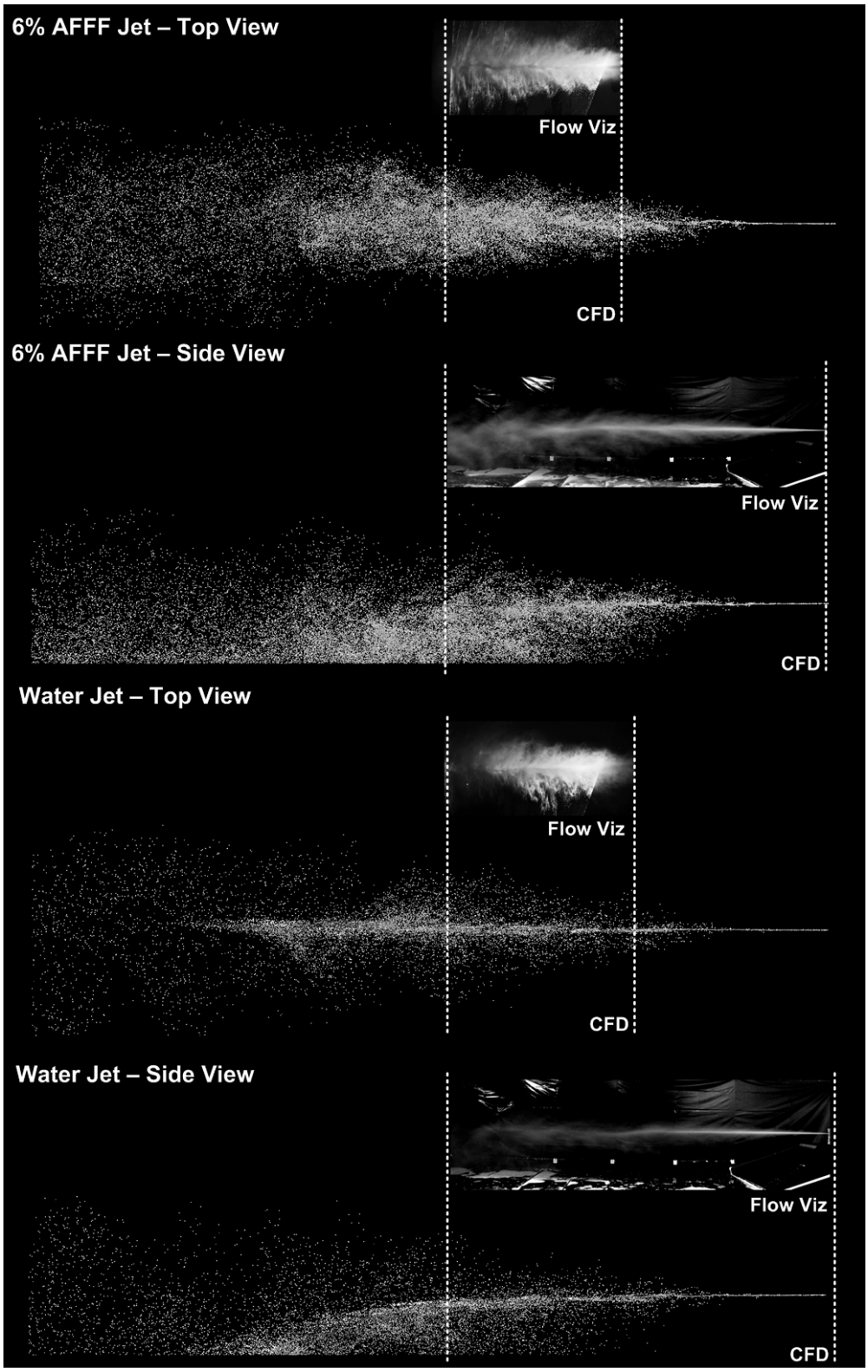

Figure 120. Qualitative Flow Structure Comparison Between CFD Model and Flow Visualization Results of the Medium-Flow, Medium-Pressure Jet (Flow is from right to left.)

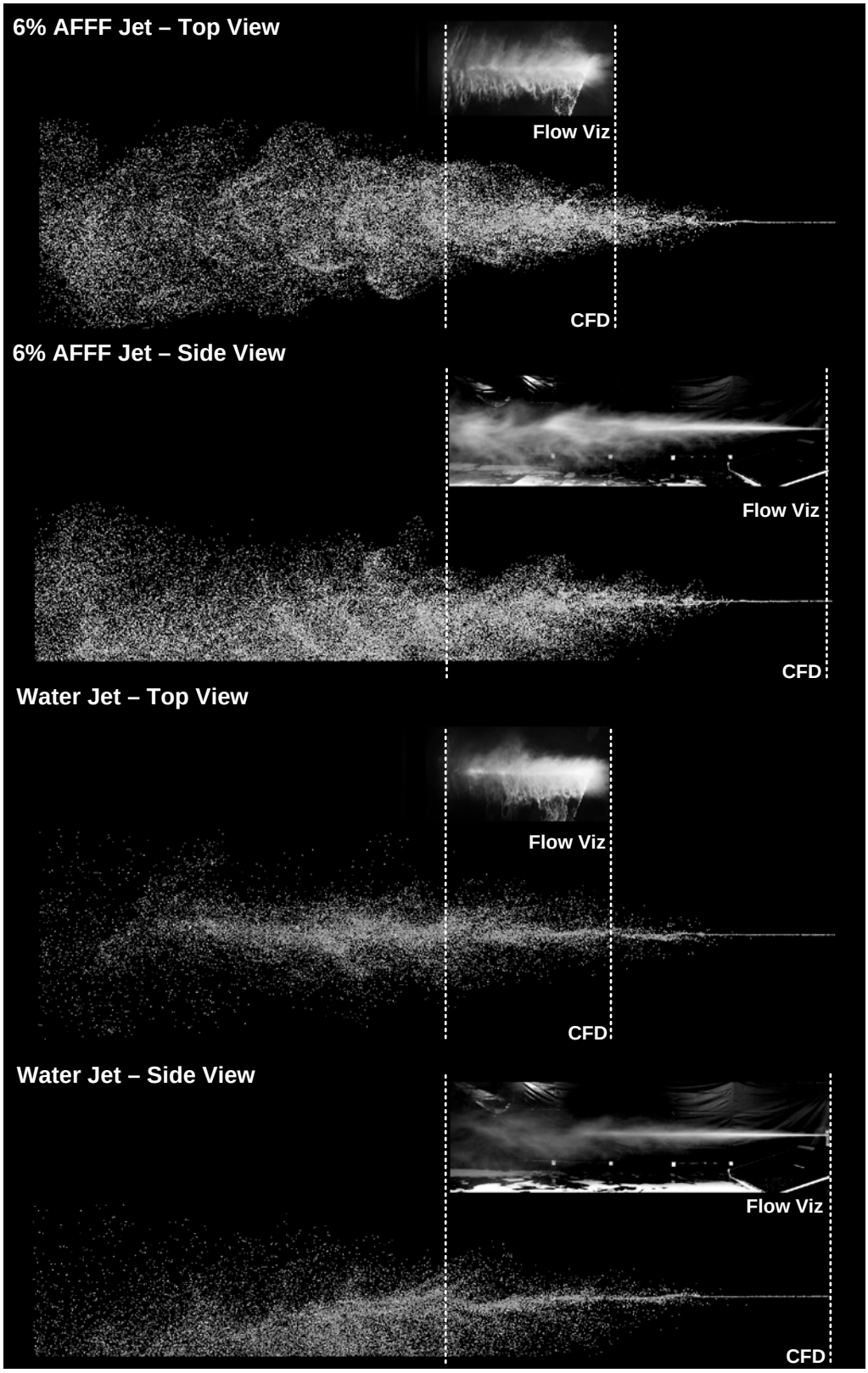

Figure 121. Qualitative Flow Structure Comparison Between CFD Model and Flow Visualization Results of the High-Flow, High-Pressure Jet (Flow is from right to left.)

Figures 122 through 124 compare the CFD model and phase Doppler, vertical profile results at select jet axial downstream locations for the medium-flow, medium-pressure jet. Water and 6% AFFF jets are presented, examining mean axial droplet velocity, mean vertical droplet velocity, and mean droplet diameter, respectively. The phase Doppler, mean droplet velocity profile results shown in figures 122 and 123 are accompanied by two horizontal bars illustrating the minimum and maximum ±RMS velocity for each profile in a similar style consistently used throughout this report. Both CFD model and phase Doppler, mean axial droplet velocity and mean droplet diameter data follow the same trend in terms of water jet values, leaving the AFFF jet values with mean profile magnitudes nearly equivalent. Mean vertical droplet velocity magnitudes are also similar, with no significant change between CFD model water jet and AFFF jet results supporting observations made in sections 6.3.2 and 6.3.3. The largest disparity is how much narrower each CFD profile is compared to the phase Doppler profile. Divergence is the worst nearest to the nozzle. This is due to simplifications and assumptions mainly related to the DPM injection condition. The DPM injection into the continuous phase is prescribed as a single, nonperturbed point injection with velocity defined exclusively in the axial direction. No horizontal or vertical velocity was considered. In reality, the agent is exiting a finite, 2-D circular area while being perturbed by a 3-D flow environment. In addition, CFD profile data are derived based on a moving average of droplets that penetrated virtual planes of finite height and width defined to represent the approximate profile window measured by the PDPA. Because a moving average was employed, CFD model profile edge data were artificially clipped. The CFD solution process did not record RMS droplet velocity data to provide another means of comparison to phase Doppler experiments. The difference between CFD model and phase Doppler profile results is lessened as axial distance downstream proportionally increases due to growing 3-D droplet-air interaction. Other limitations are placed on the comparability of CFD model and phase Doppler results, particularly for the droplet size distribution where the PDPA had a measurement envelope of about 2 to 685 μm, whereas the CFD model had no upper or lower limit on droplet size.

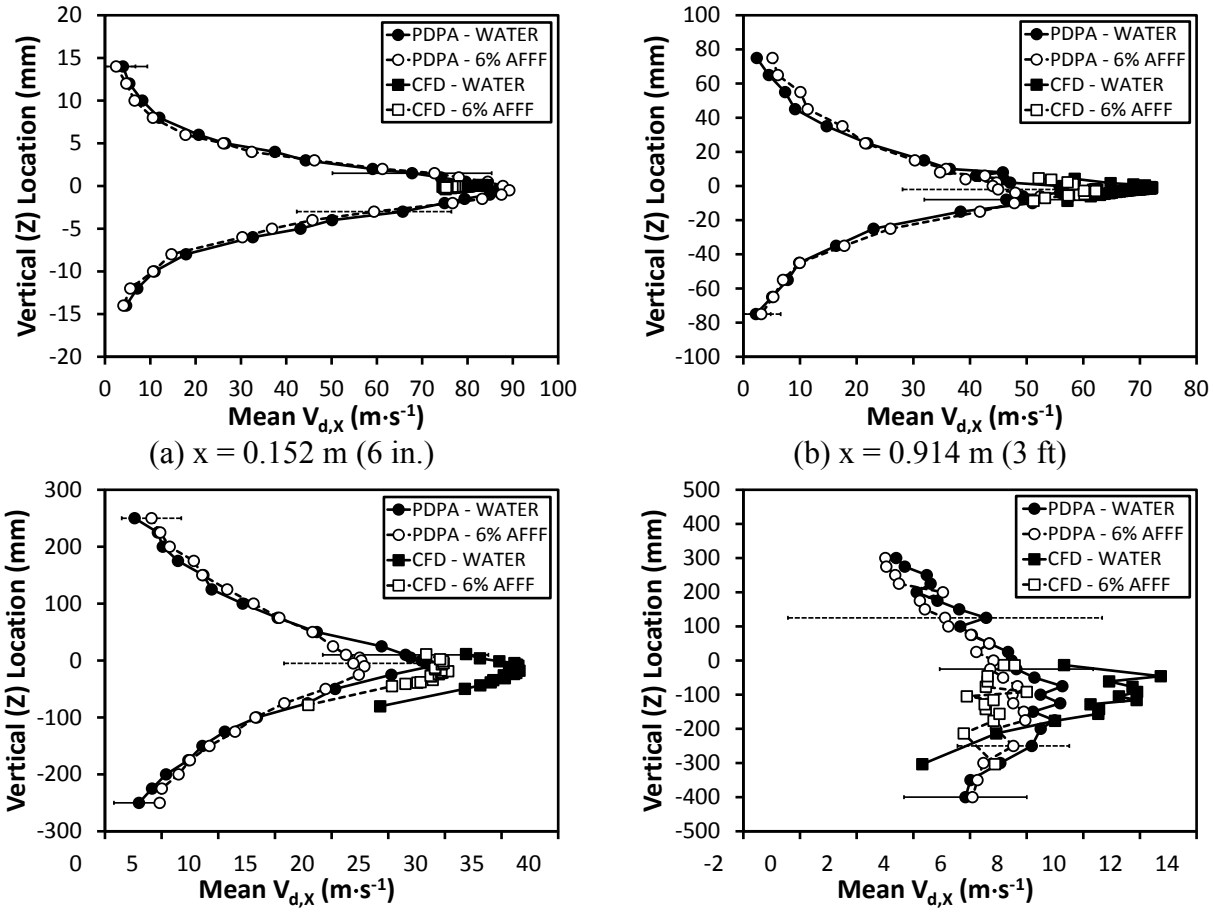

Figure 122. A Comparison of Phase Doppler and CFD Model, Mean Axial Droplet Velocity Profile Data for the Medium-Flow, Medium-Pressure Jet

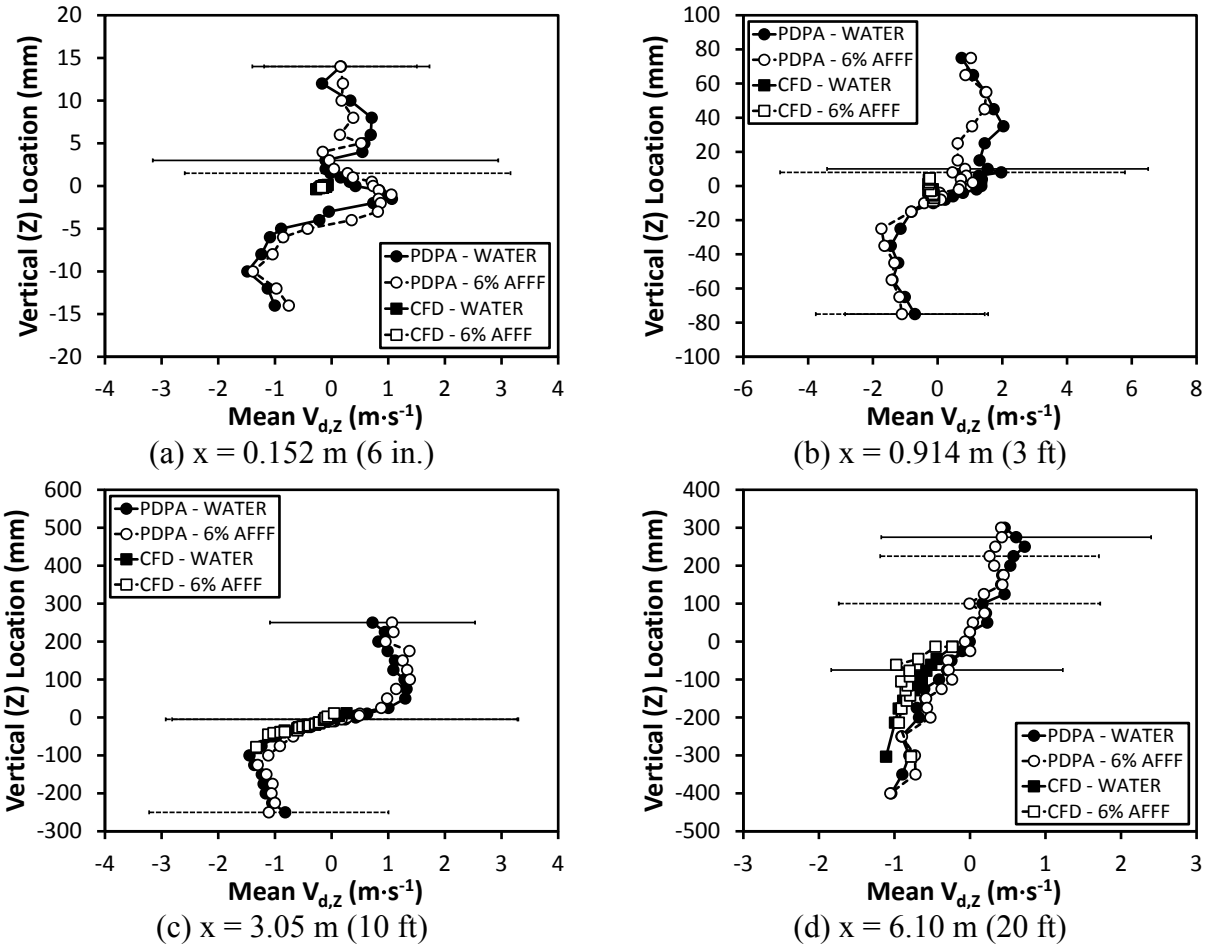

Figure 123. A Comparison of Phase Doppler and CFD Model, Mean Vertical Droplet Velocity Profile Data for the Medium-Flow, Medium-Pressure Jet

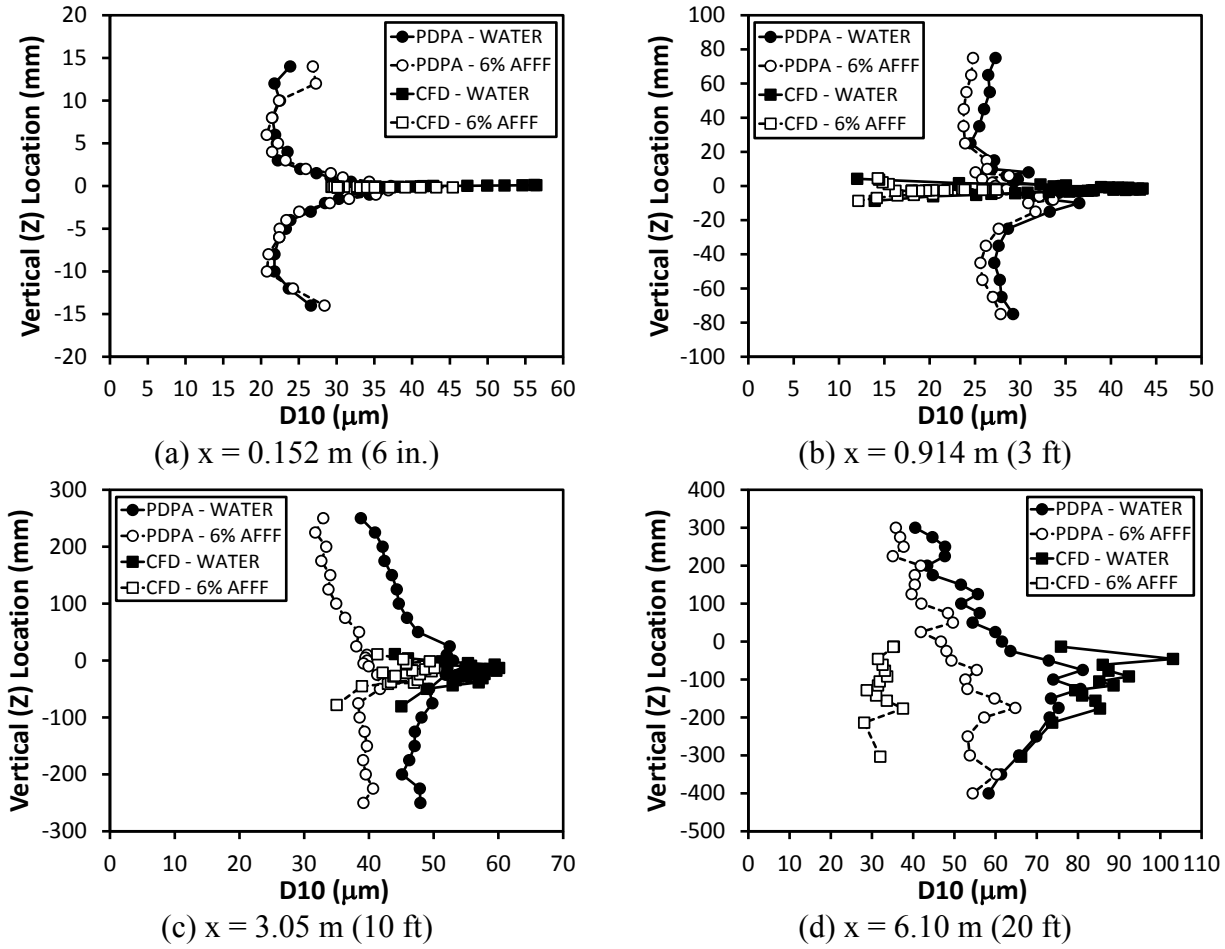

Figure 124. A Comparison of Phase Doppler and CFD Model, Mean Droplet Diameter Profile Data for the Medium-Flow, Medium-Pressure Jet

Figures 125 through 129 compare the CFD model and phase Doppler results in terms of mean and maximum vertical flow parameter profiles in order to illustrate global trends in the data. Data presentation is similar to how the phase Doppler summary results are presented in section 6.3.3. Maximum profile, mean axial droplet velocity; mean profile, mean axial droplet velocity; mean profile, mean droplet diameter; and mean profile, Sauter mean diameter are chosen for comparison. Each figure represents a firefighting jet pressure-flow rate combination analyzed.

In general, the maximum and mean profile, mean axial droplet velocity CFD model and phase Doppler results were in reasonable agreement with each other with most profile points within 10% of one another. The CFD model results not only followed experimental trends, but the relative difference in flow parameter values between water jets and AFFF jets were similar in magnitude to those reported by phase Doppler experiments. For some firefighting jet configurations, larger discrepancies were observed and believed to be the result of DPM droplet injection simplifications discussed earlier. Most of the CFD model mean profile, mean droplet diameter results drifted higher than the PDPA values. This is likely due to the PDPA being unable to record droplets larger than 685 μm, and the CFD model had no such upper limitation. Another theory for the observed differences could be the firefighting jet containment zone had a

more significant impact on results than anticipated as mean droplet diameters tended to increase when this influence was taken into account in the CFD model. Overall, firefighting jet flow parameter characteristics of interest were predicted adequately enough by the CFD model to rely on other parameter estimations predicted by flow calculations that were too difficult or impossible to quantify experimentally.

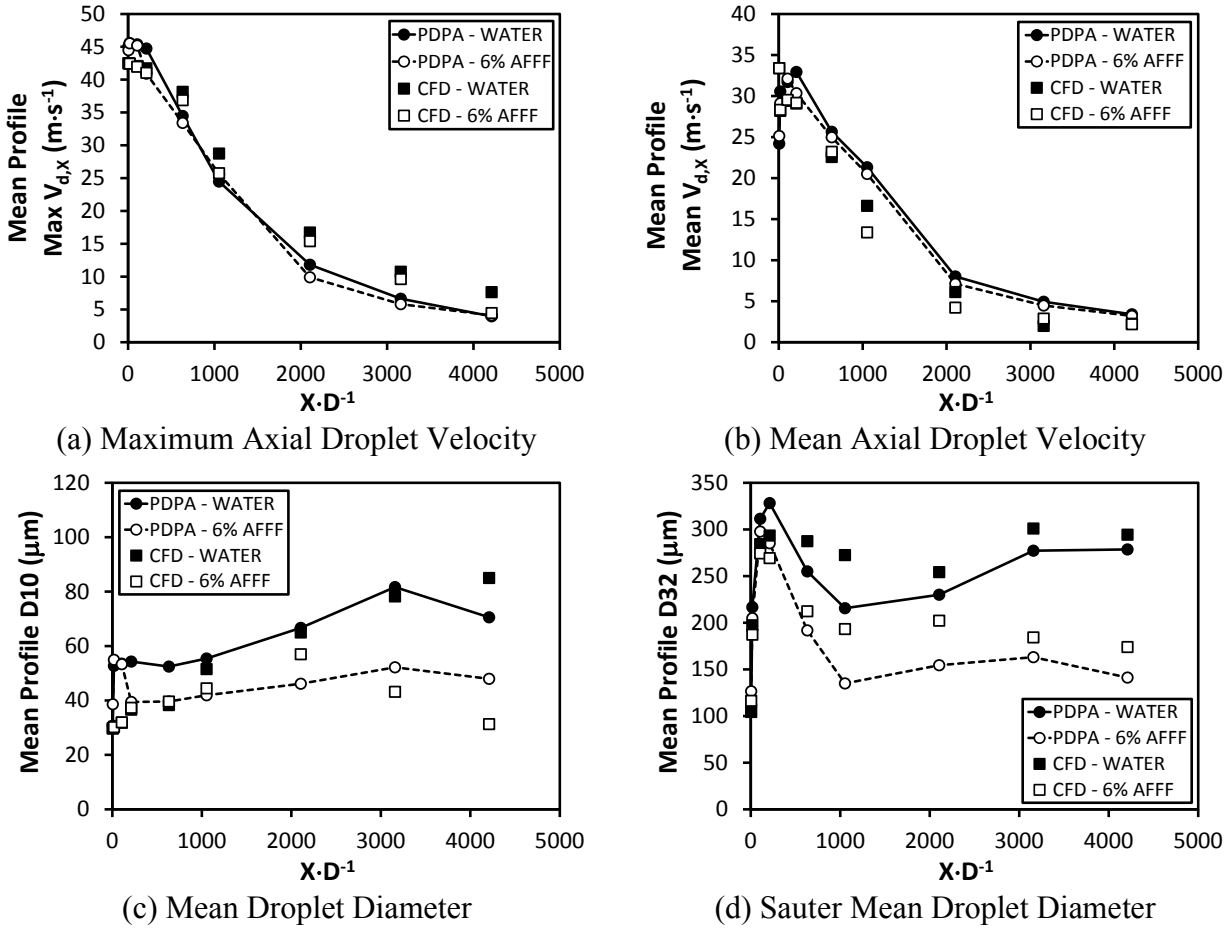

(a) Maximum Axial Droplet Velocity

(b) Mean Axial Droplet Velocity

(c) Mean Droplet Diameter

(d) Sauter Mean Droplet Diameter

Figure 125. A Comparison of PDPA and CFD Mean Vertical Profile Data for the Low-Flow, Low-Pressure Jet

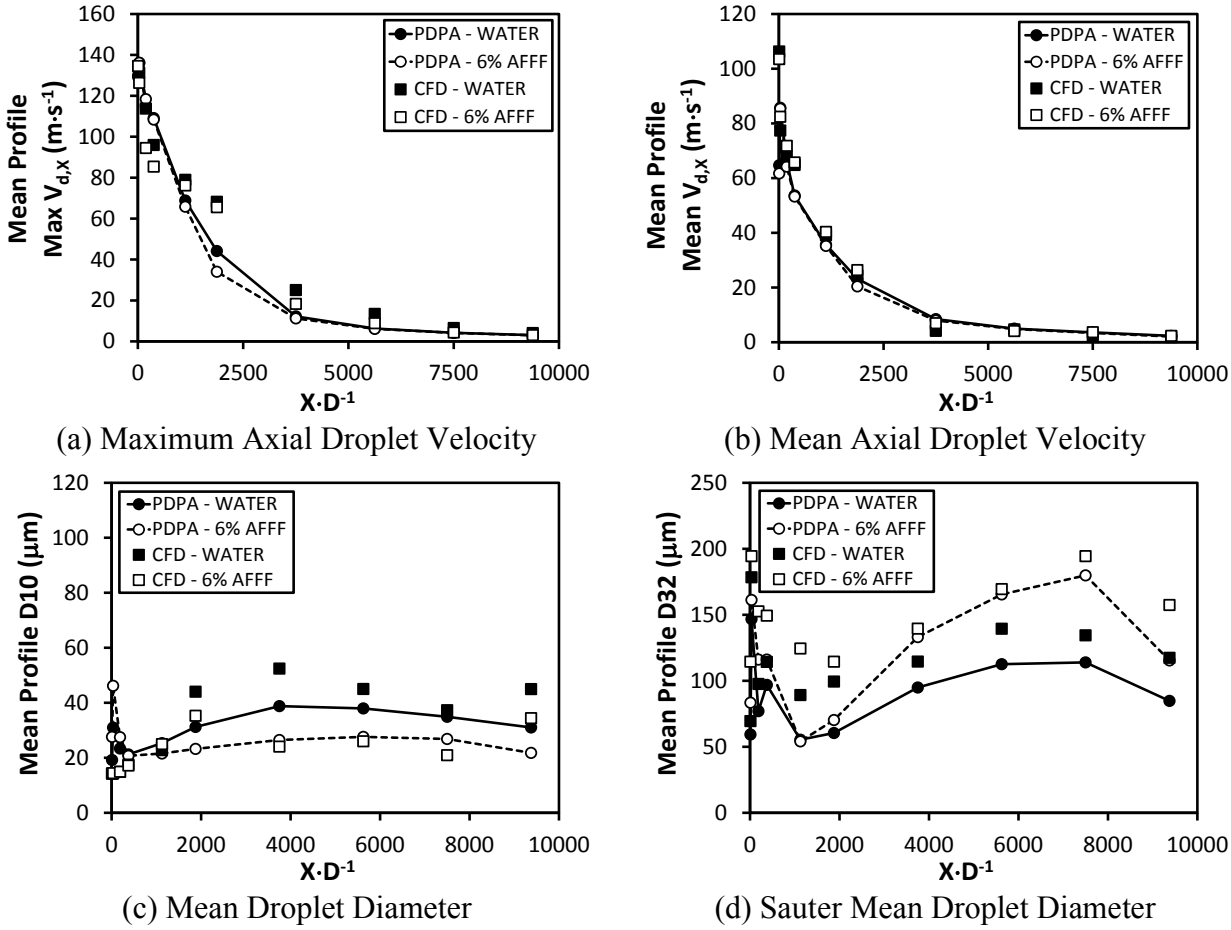

(a) Maximum Axial Droplet Velocity

(b) Mean Axial Droplet Velocity

(c) Mean Droplet Diameter

(d) Sauter Mean Droplet Diameter

Figure 126. A Comparison of PDPA and CFD Mean Vertical Profile Data for the Low-Flow, High-Pressure Jet

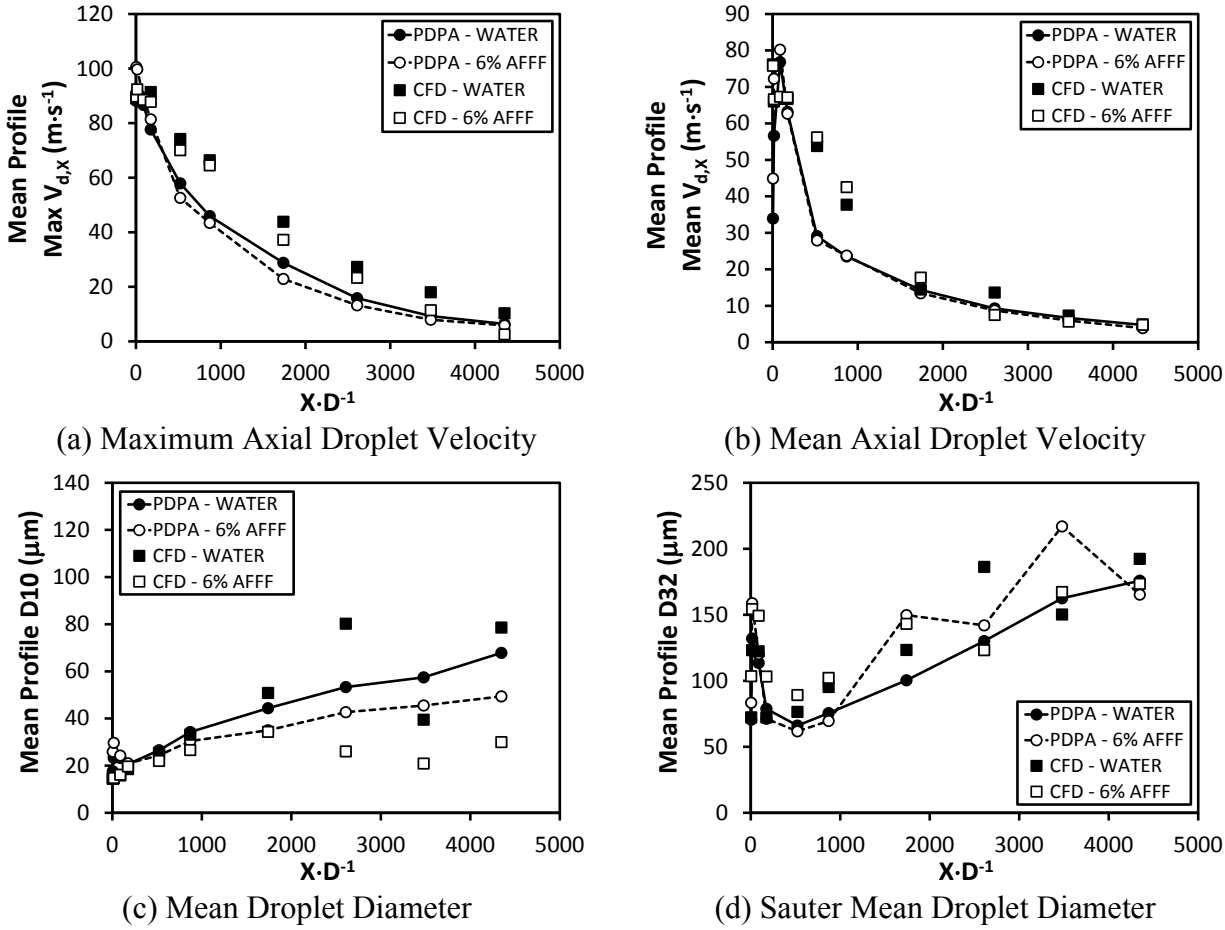

(a) Maximum Axial Droplet Velocity

(b) Mean Axial Droplet Velocity

(c) Mean Droplet Diameter

(d) Sauter Mean Droplet Diameter

Figure 127. A Comparison of PDPA and CFD Mean Vertical Profile Data for the Medium-Flow, Medium-Pressure Jet

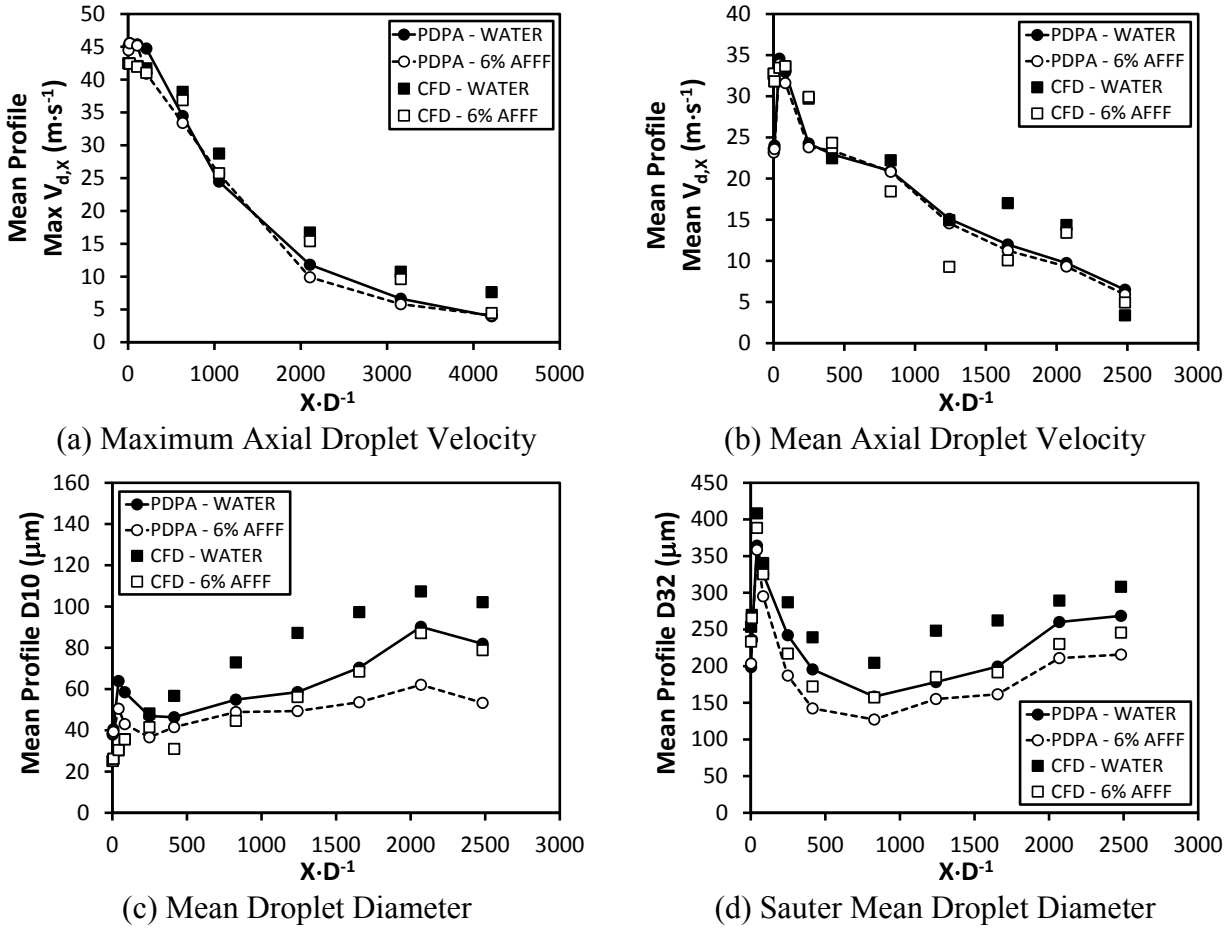

Figure 128. A Comparison of PDPA and CFD Mean Vertical Profile Data for the High-Flow, Low-Pressure Jet

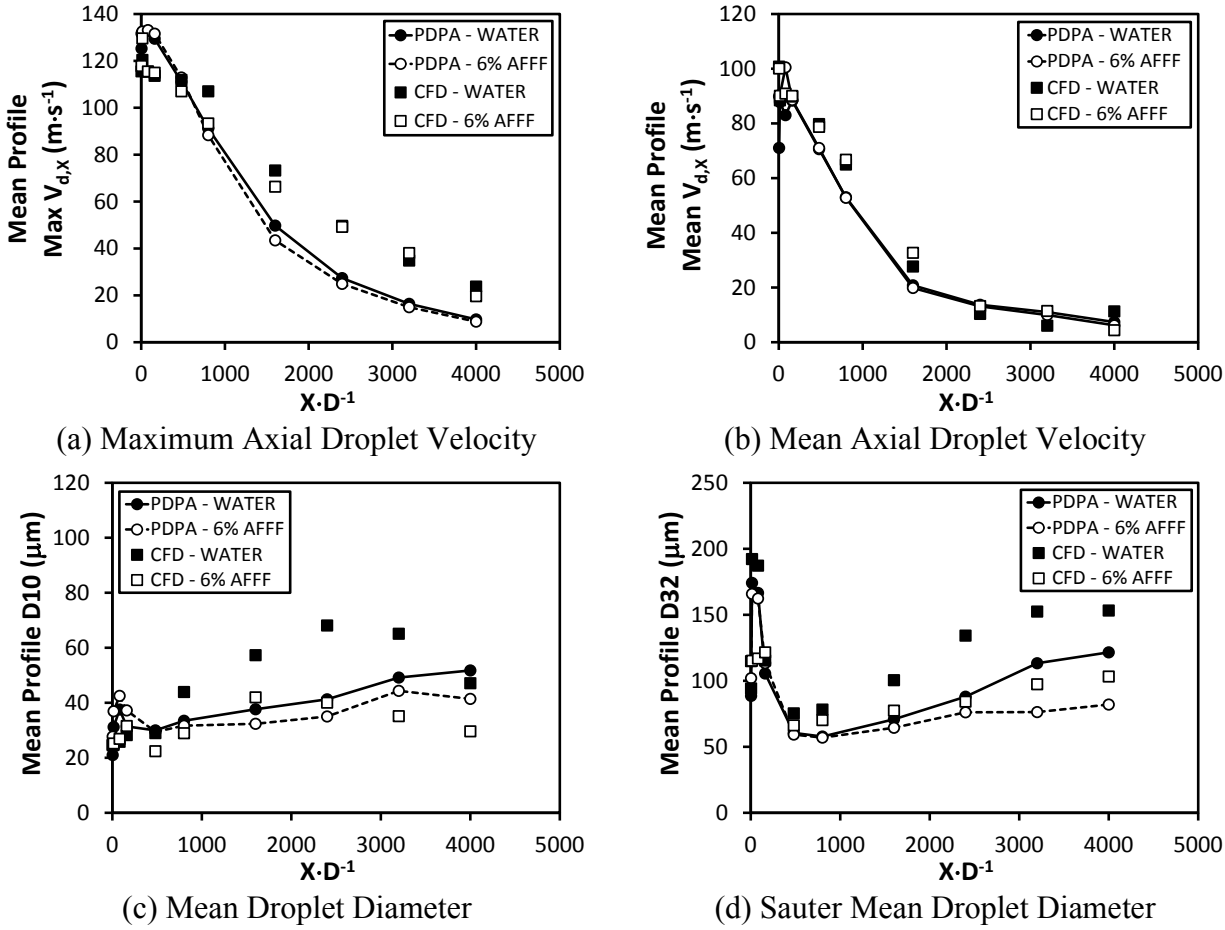

Figure 129. A Comparison of PDPA and CFD Mean Vertical Profile Data for the High-Flow, High-Pressure Jet

6.4.3 Computational Firefighting Jet Model Results Summary.

The CFD model results are presented for the five firefighting jet pressure-flow rate combinations listed in table 8. The data presented in this section describe instantaneous firefighting jet flow parameters from a fully developed flow field. Table 12 summarizes the overall, globally averaged droplet size information for each flow domain. Each droplet parcel represents a group of about 50,000 droplets. The minimum droplet diameter (d_{min}), maximum droplet diameter (d_{max}), mean droplet diameter, and Sauter mean droplet diameter are listed. For all instances, the amount of 6% AFFF jet droplet parcels were larger for every CFD model case compared to the water jet droplet parcels due to the enhanced breakup induced by the surfactants in AFFF. As expected, the low-flow, low-pressure jets generated the least amount of droplets and the high-flow, high-pressure jets created the most droplets based on each jet's respective degree of atomization. The minimum droplet diameter is the minimum droplet diameter bin for the DPM injection condition, which for all CFD model cases was 13.72 µm. The range in maximum droplet diameter followed the same trend observed in the phase Doppler data. The largest-sized droplets were generated by the high-flow, low-pressure water jet, and the smallest-sized droplets were produced by the low-flow, high-pressure 6% AFFF jet. The CFD models report a large

disparity between low-pressure water and 6% AFFF jets in terms of mean droplet diameter. The difference in some cases, particularly the low-flow jet cases, was negligible. Conversely, medium- and high-pressure jets exhibited distinct mean droplet diameter divergence by as much as 28%. Sauter mean droplet diameter comparisons between the water and 6% AFFF jets were less consistent across the nozzle pressure-flow rate combinations. Most CFD model results showed a reduction in Sauter mean diameter from the water jet to the 6% AFFF jet, a similar pattern was also observed in phase Doppler Sauter mean droplet profiles.

Table 12. Computational Firefighting Jet Flow Model Domain Droplet Summary

Model Test Case	Total No. of Droplet Parcels	d_{MIN} (μm)	d_{MAX} (mm)	$D10$ (μm)	$D32$ (μm)
Low-Flow, Low-Pressure Water Jet	19,454	13.72	4.079	20.11	154.0
Low-Flow, Low-Pressure 6% AFFF Jet	26,504	13.72	2.497	19.38	157.0
Low-Flow, High-Pressure Water Jet	22,246	13.72	1.005	28.94	93.92
Low-Flow, High-Pressure 6% AFFF Jet	28,977	13.72	0.5851	17.86	88.86
Medium-Flow, Medium-Pressure Water Jet	16,059	13.72	3.725	22.91	137.7
Medium-Flow, Medium-Pressure 6% AFFF Jet	38,916	13.72	1.988	19.81	170.0
High-Flow, Low-Pressure Water Jet	10,061	13.72	5.690	21.78	455.4
High-Flow, Low-Pressure 6% AFFF Jet	13,541	13.72	3.267	21.66	422.3
High-Flow, High-Pressure Water Jet	29,334	13.72	3.326	28.20	190.6
High-Flow, High-Pressure 6% AFFF Jet	58,722	13.72	1.547	20.27	172.7

Figure 130 shows particle traces of firefighting jet droplets colored by residence time for the medium-flow, medium-pressure firefighting jet. This figure is intended to provide an estimate of the average droplet lifetime for both water and AFFF jets. Droplet lifetimes for AFFF jets appear slightly longer compared to water jets due to the breakup and more intense dispersion of smaller, less massive droplets that are prone to stay airborne longer. The effective jet core for both agents was observed to have a lifetime on the order of 1 to 2 s with peripheral and far downstream droplets on the order of 3 to 5 s. Low-pressure jets generate droplets with lifetimes about twice as long, and high-pressure jets generate droplets with lifetimes about half as long. Figure 10 shows AFFF has approached its equilibrium surface tension value by about 1 s. This indicates that prescribing surface tension dynamically as a function of time similarly to figure 10 may impact results, particularly for high-pressure AFFF jets, but negligibly influences low-pressure AFFF jets.

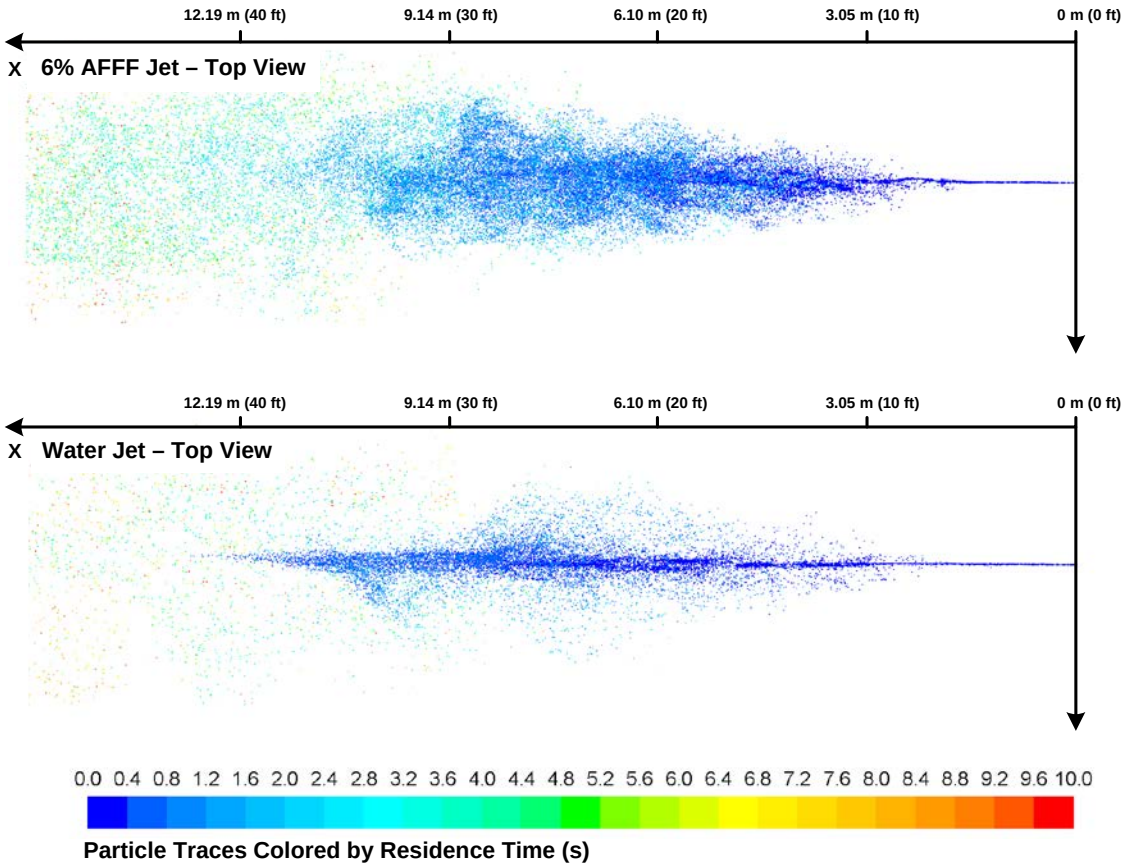

Figure 130. The CFD Model Results of Droplet Residence Time for Medium-Flow, Medium-Pressure Jets

Figures 131 through 135 illustrate particle traces of firefighting jet droplets colored by velocity magnitude for each nozzle-pressure combination modeled. The nonlinear velocity decay in the near-field region of the nozzle is best illustrated in these figures, particularly for the medium- and high-pressure jets. Nozzle exit velocity ranged from approximately 42 to 116 $m \cdot s^{-1}$. Most satellite droplets away from the jet core exhibited velocities on the order of 10 $m \cdot s^{-1}$ or much less.

Figures 136 through 140 depict particle traces of firefighting jet droplets colored by droplet diameter using a logarithmic scale. The ranges shown in each figure reflect the minimum and maximum droplet diameter ranges shown in table 12. Finer droplet diameter details were difficult to graphically resolve while illustrating the firefighting jet in its entirety with respect to the far field, especially alongside larger-diameter droplets. Hence, local average droplet diameters, particularly in areas of higher droplet concentrations, may appear skewed towards higher mean droplet diameters.

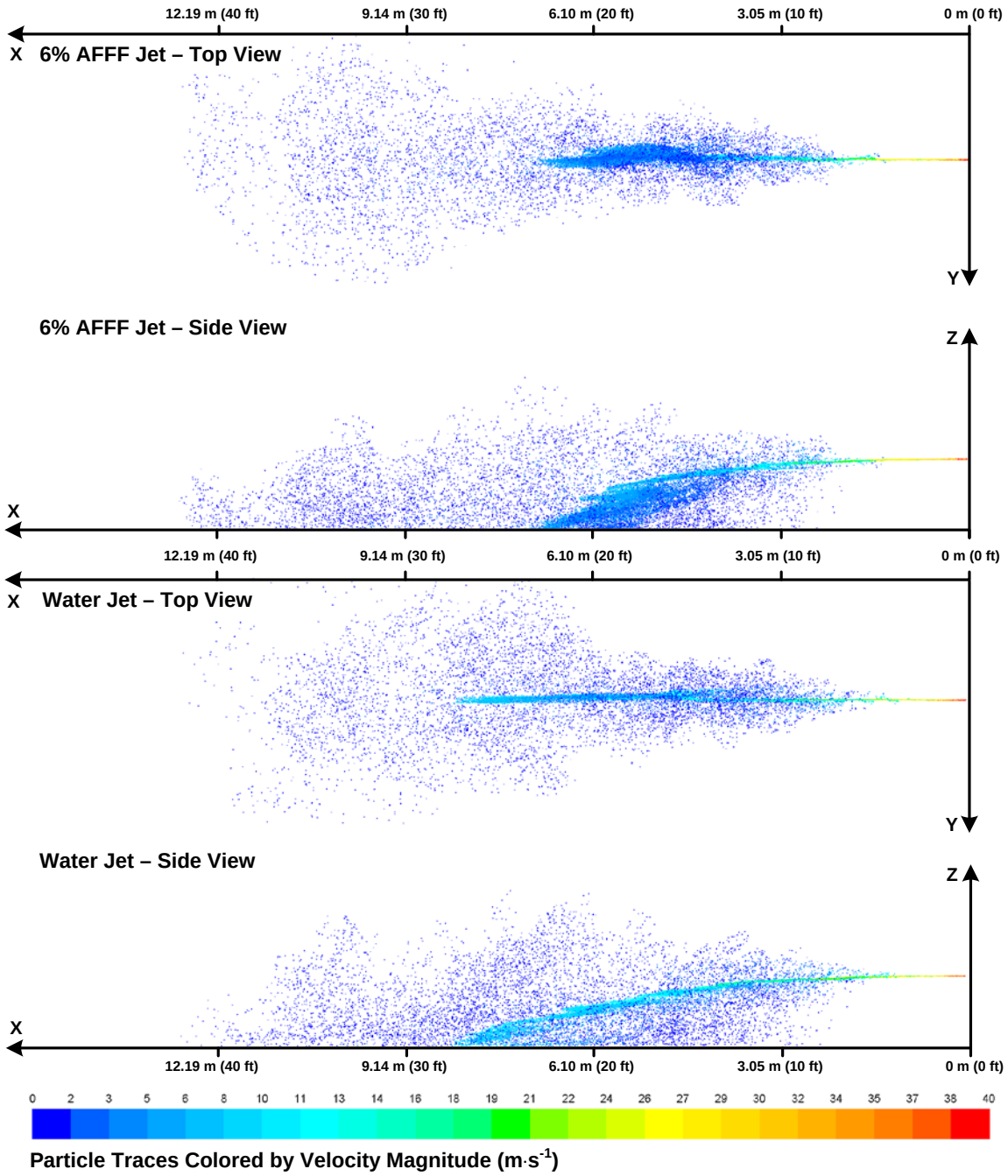

Figure 131. The CFD Model Results of Droplet Velocity Magnitude for Low-Flow, Low-Pressure Jets

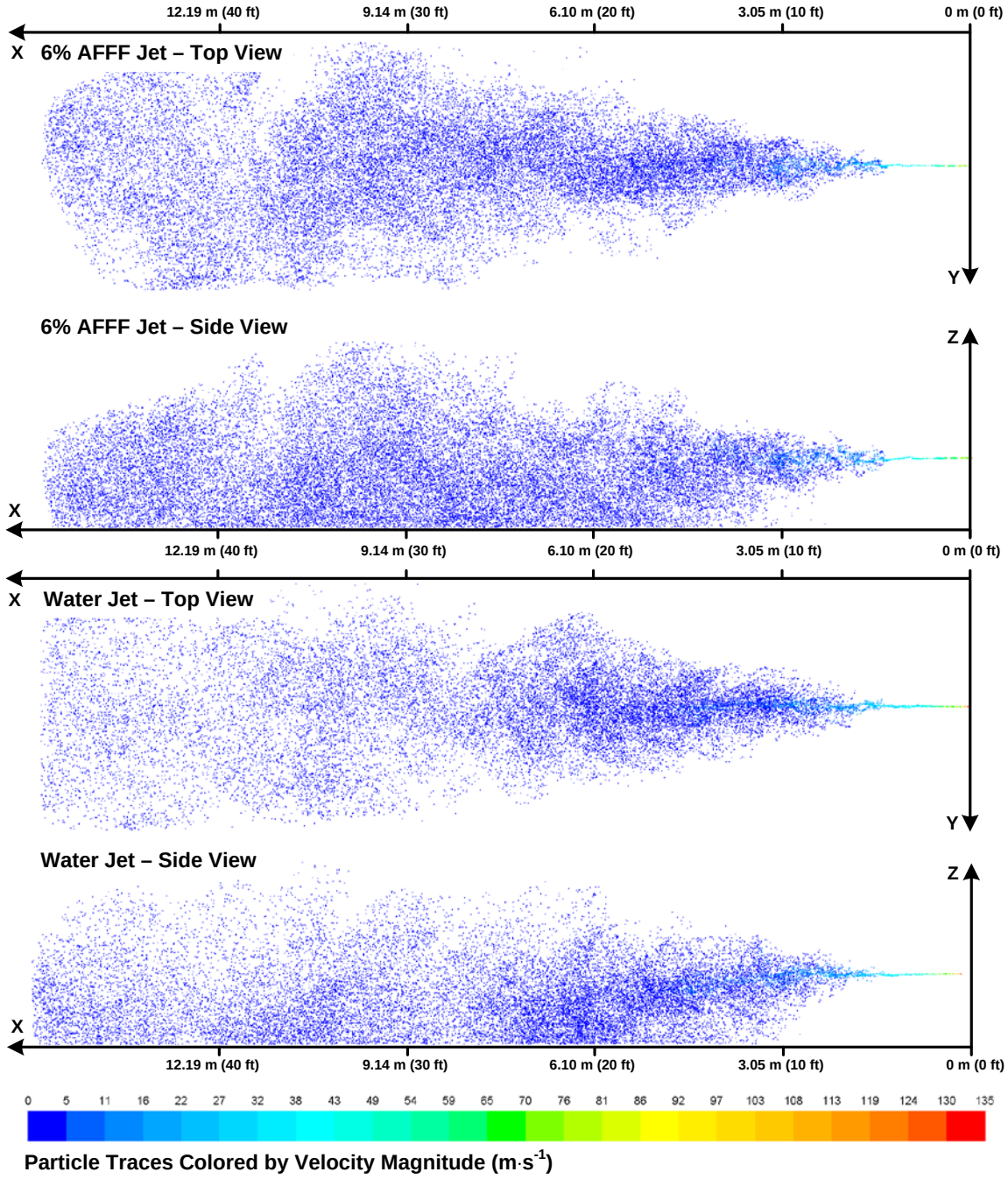

Figure 132. The CFD Model Results of Droplet Velocity Magnitude for Low-Flow, High-Pressure Jets

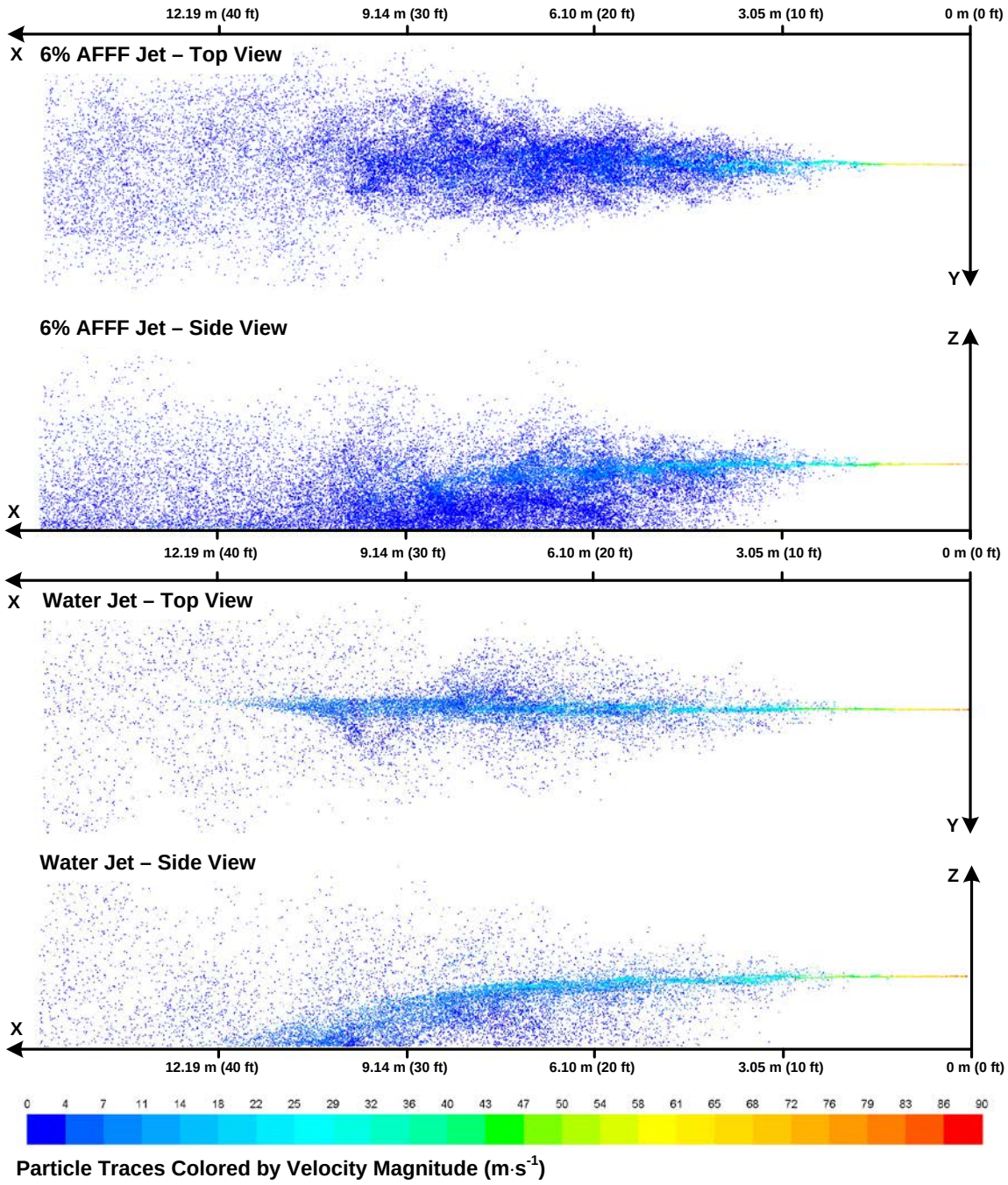

Figure 133. The CFD Model Results of Droplet Velocity Magnitude for Medium-Flow, Medium-Pressure Jets

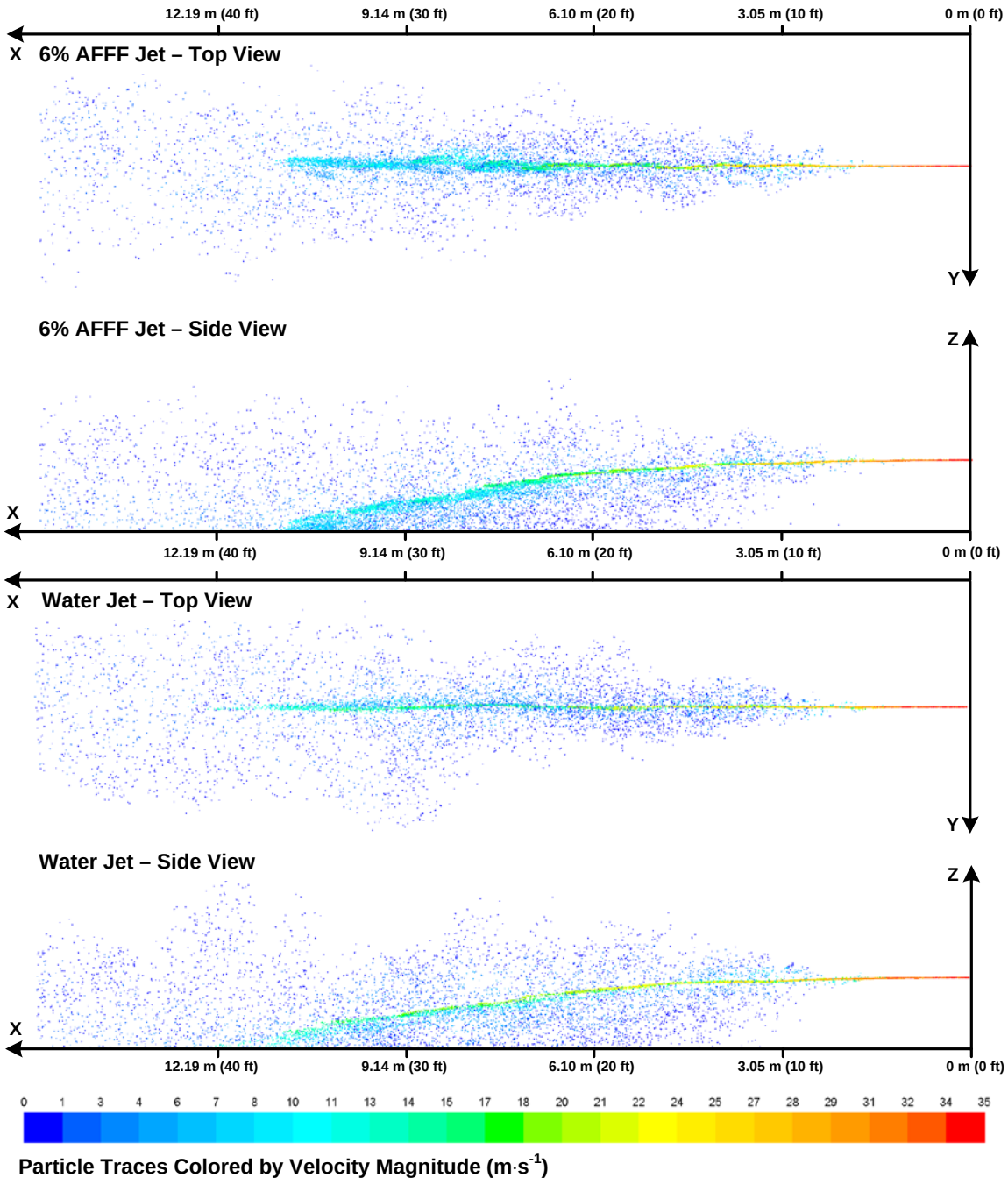

Figure 134. The CFD Model Results of Droplet Velocity Magnitude for High-Flow, Low-Pressure Jets

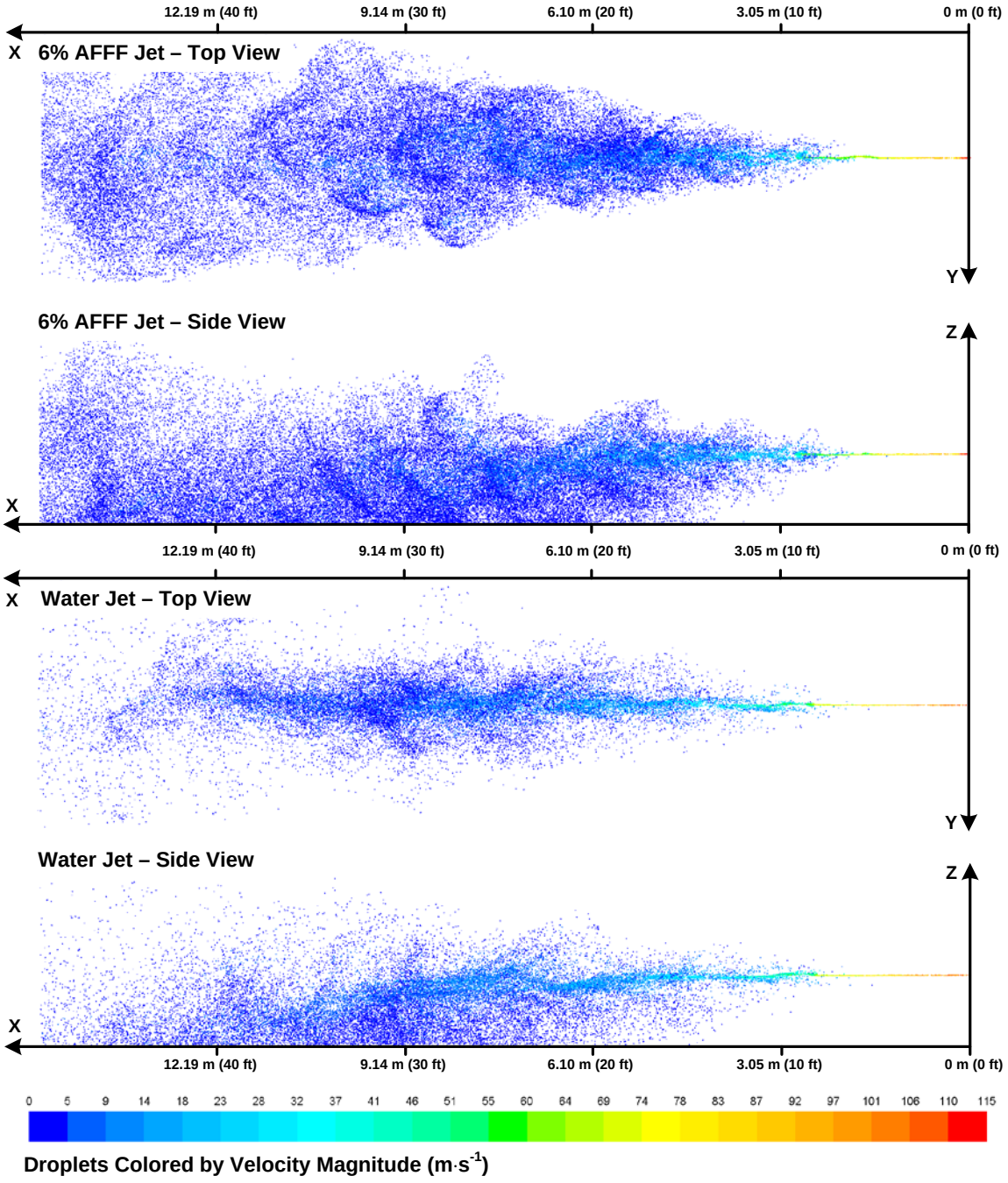

Figure 135. The CFD Model Results of Droplet Velocity Magnitude for High-Flow, High-Pressure Jets

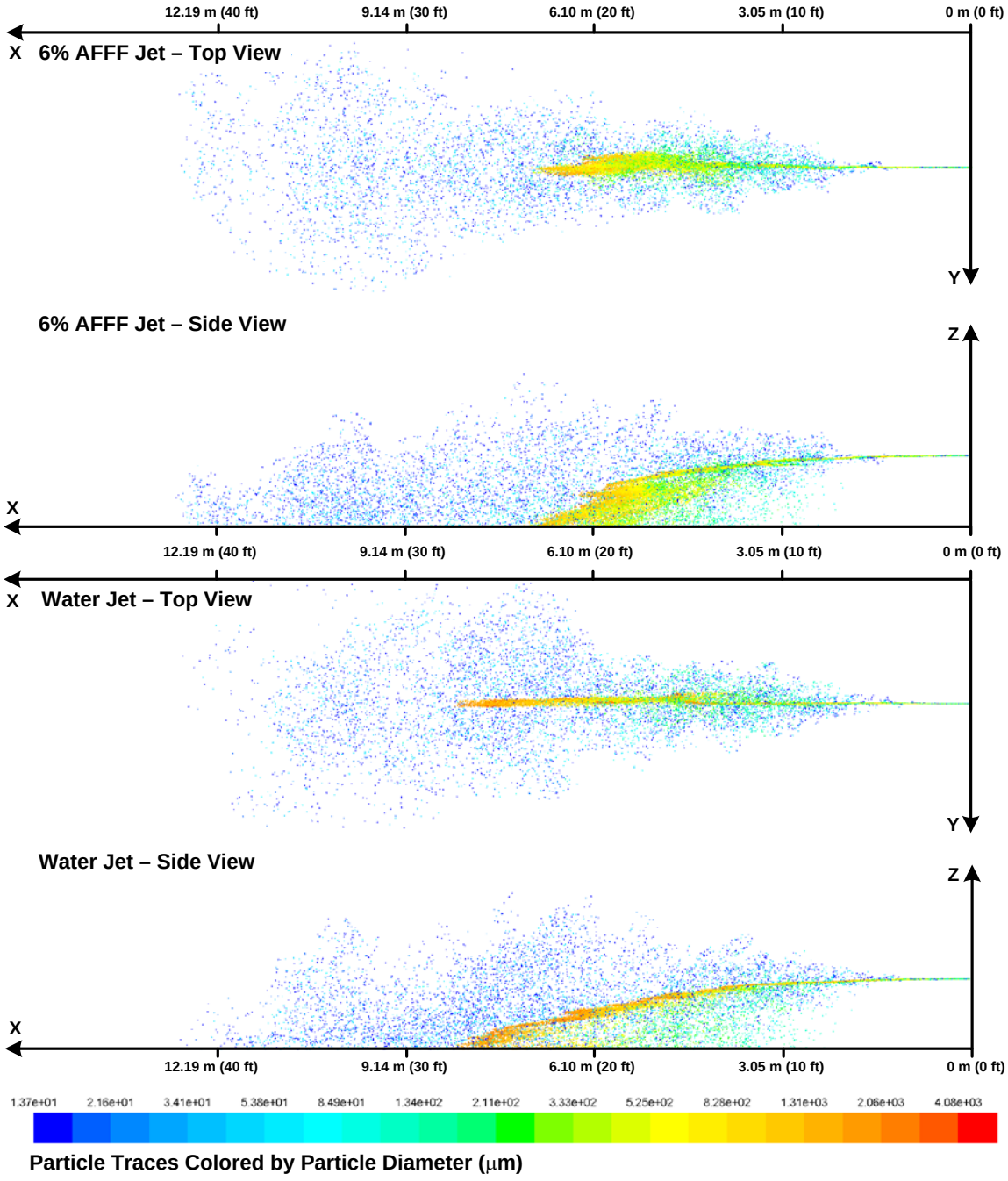

Figure 136. The CFD Model Results of Droplet Diameter for Low-Flow, Low-Pressure Jets

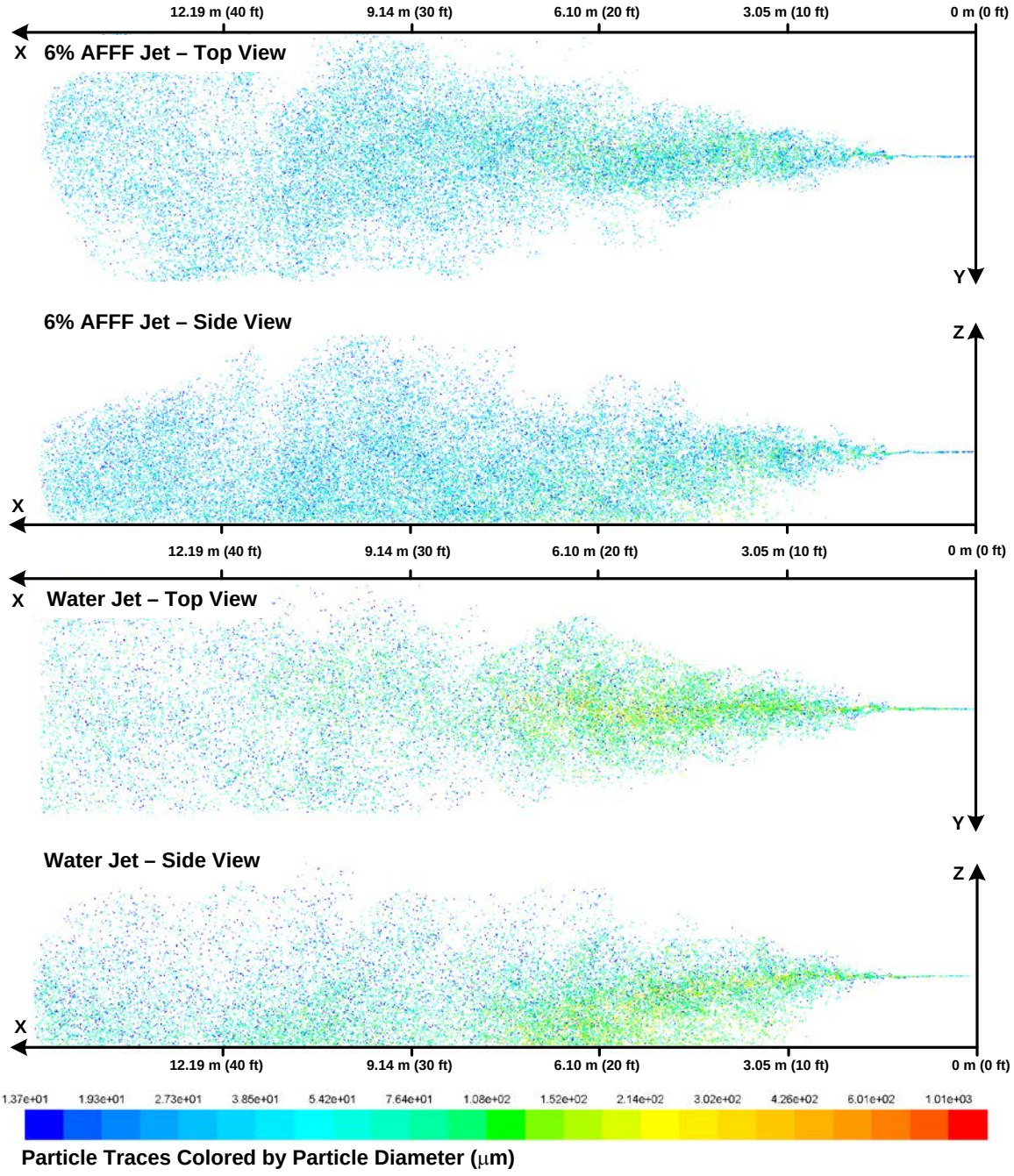

Figure 137. The CFD Model Results of Droplet Diameter for Low-Flow, High-Pressure Jets

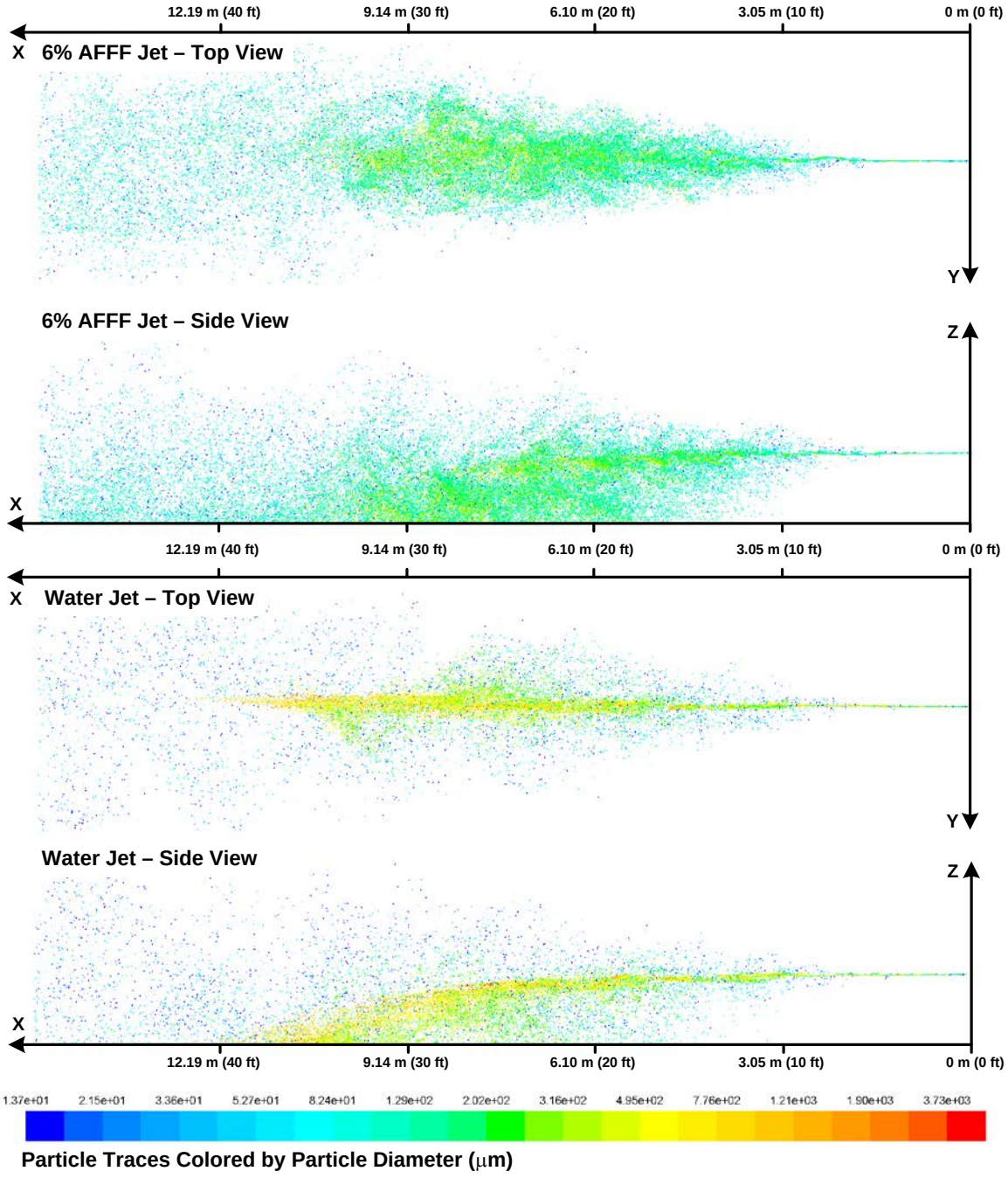

Figure 138. The CFD Model Results of Droplet Diameter for Medium-Flow, Medium-Pressure Jets

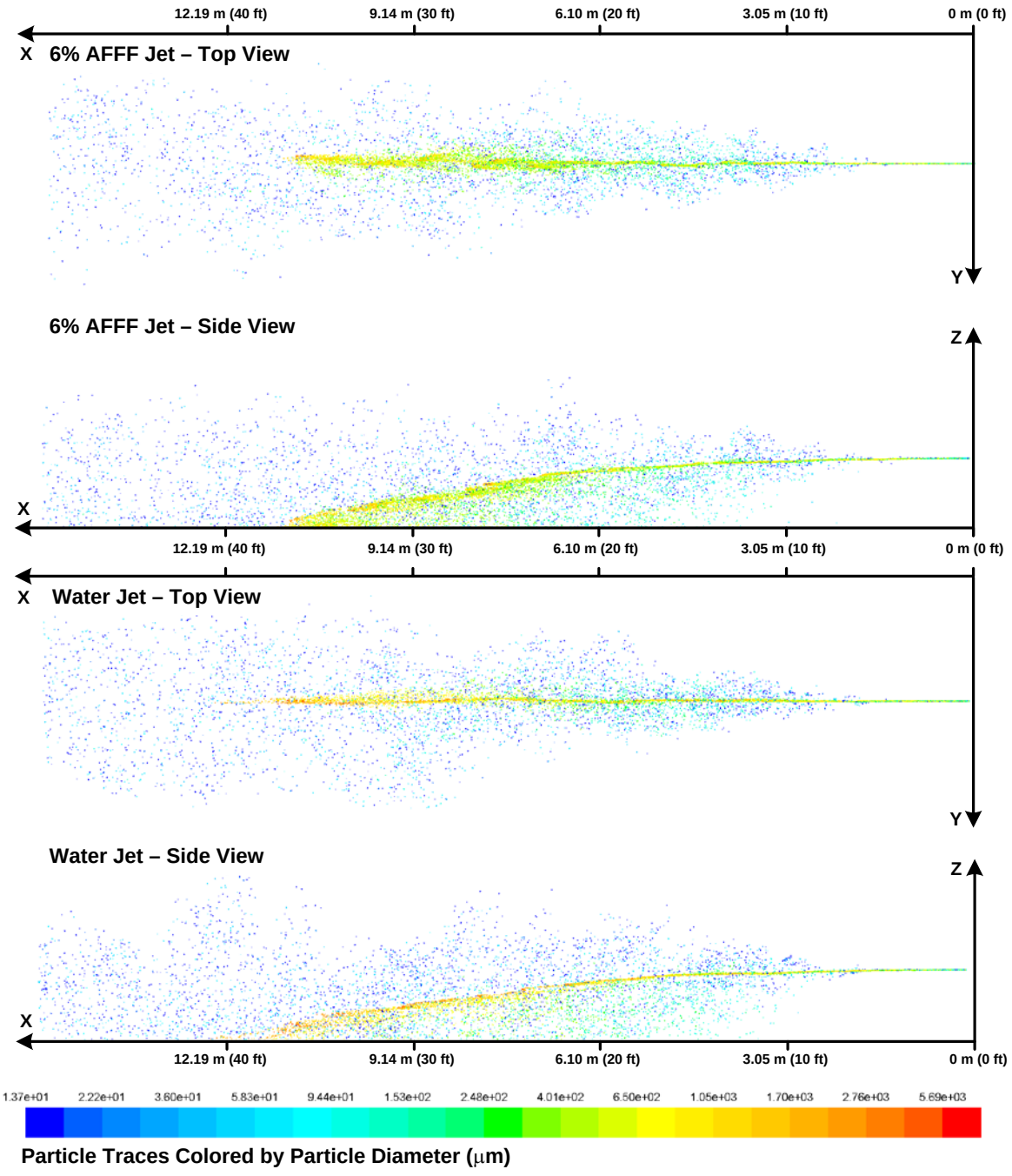

Figure 139. The CFD Model Results of Droplet Diameter for High-Flow, Low-Pressure Jets

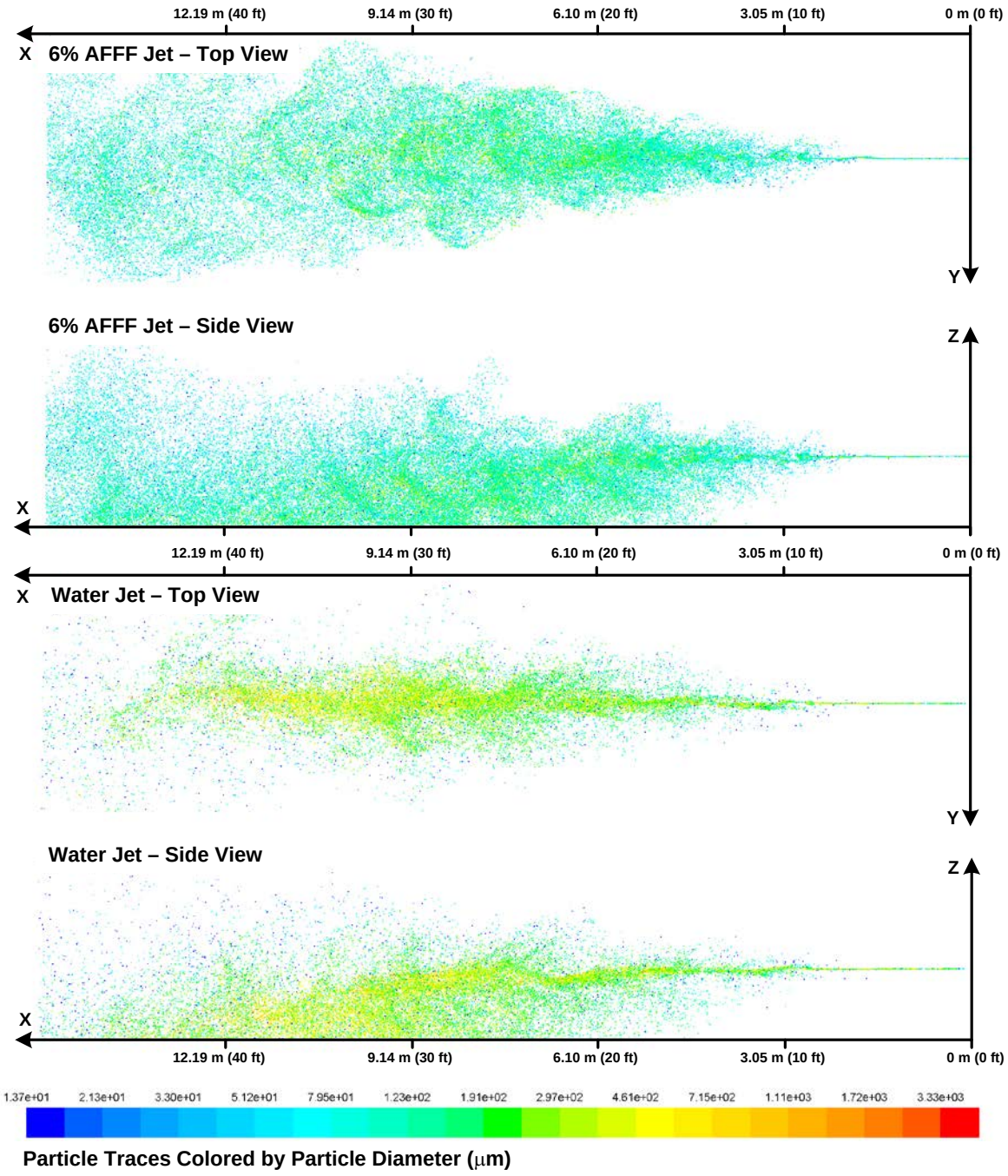

Figure 140. The CFD Model Results of Droplet Diameter for High-Flow, High-Pressure Jets

Figures 141 through 145 show particle traces of firefighting jet droplets colored by gaseous Weber number illustrating the effect droplet size and surface tension have on universal jet dynamics. The gaseous Weber number distinction between water and AFFF jets is more pronounced for some CFD model cases compared to others, with all values staying less than 100, indicating the TAB model was a good selection given nozzle exit flow physics.

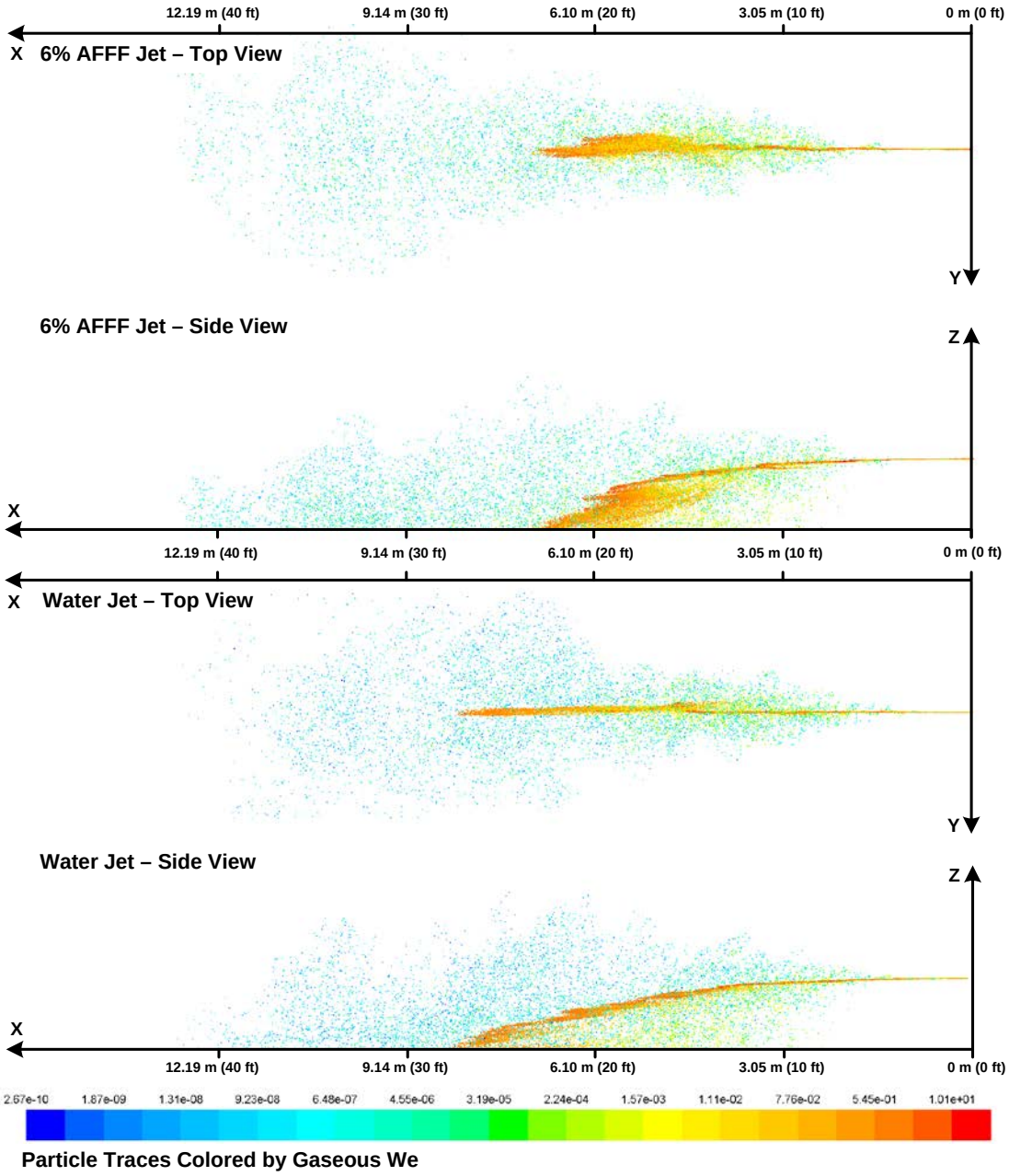

Figure 141. The CFD Model Results of Gaseous Weber Number for Low-Flow, Low-Pressure Jets

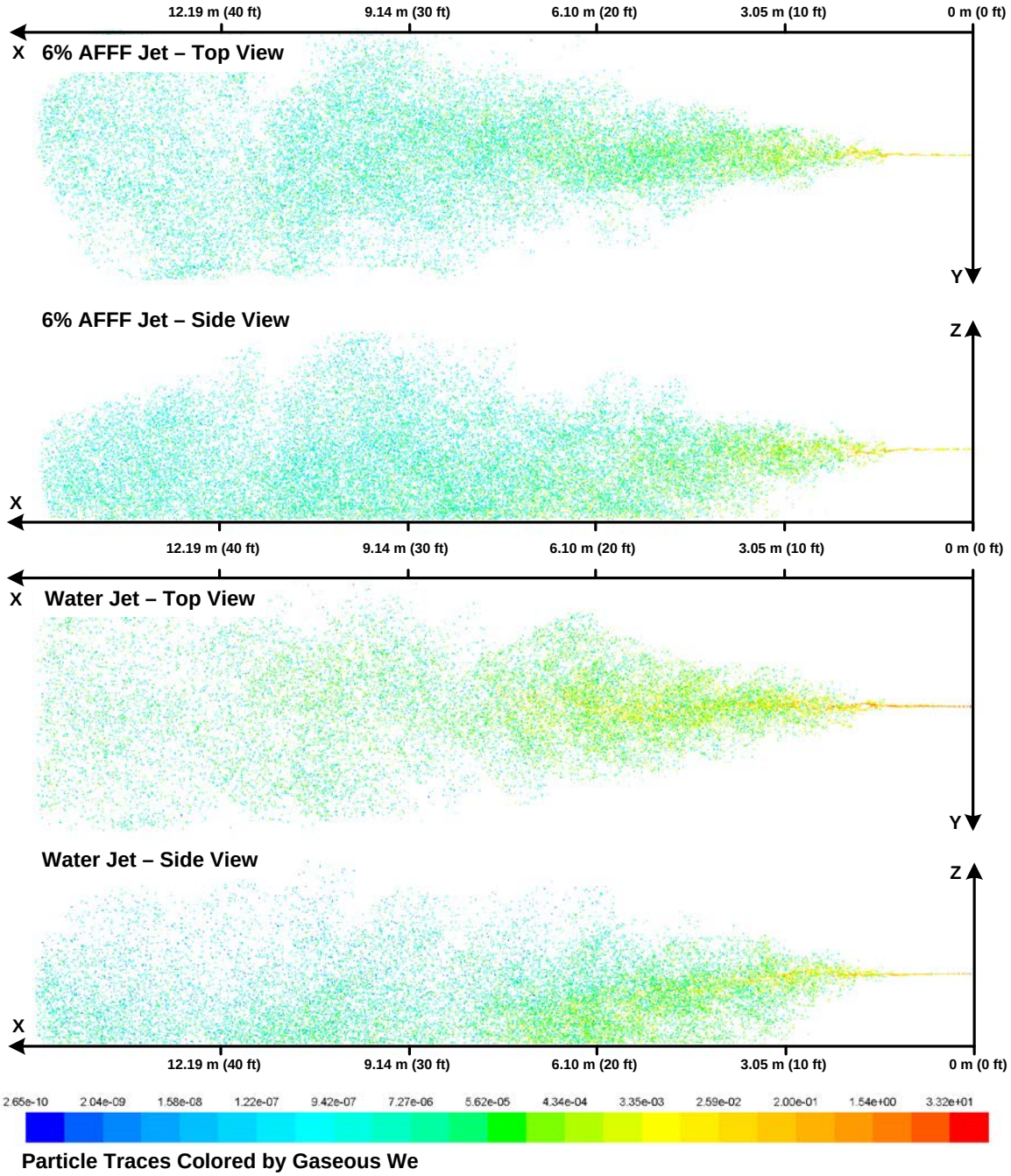

Figure 142. The CFD Model Results of Gaseous Weber Number for Low-Flow, High-Pressure Jets

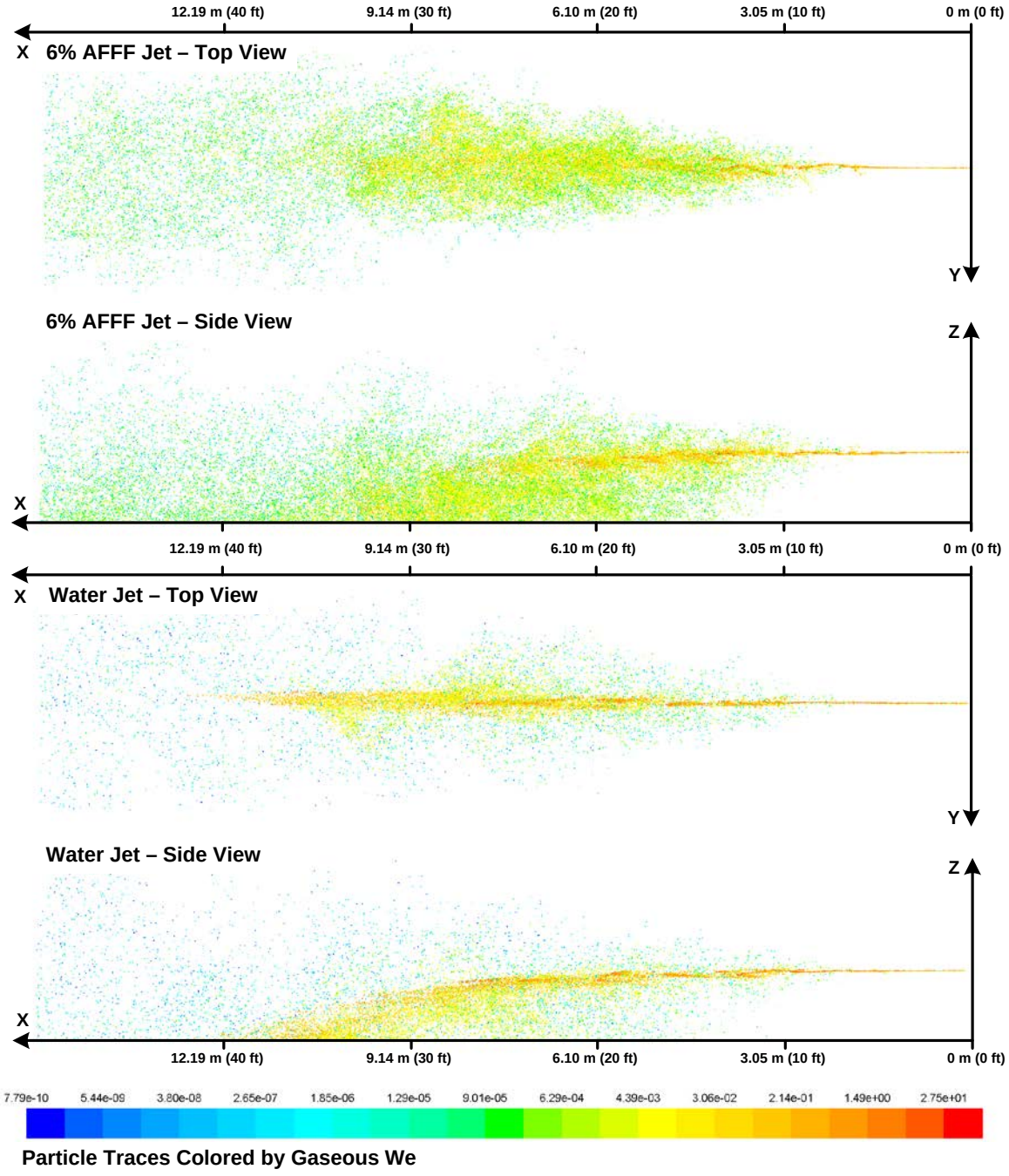

Figure 143. The CFD Model Results of Gaseous Weber Number for Medium-Flow, Medium-Pressure Jets

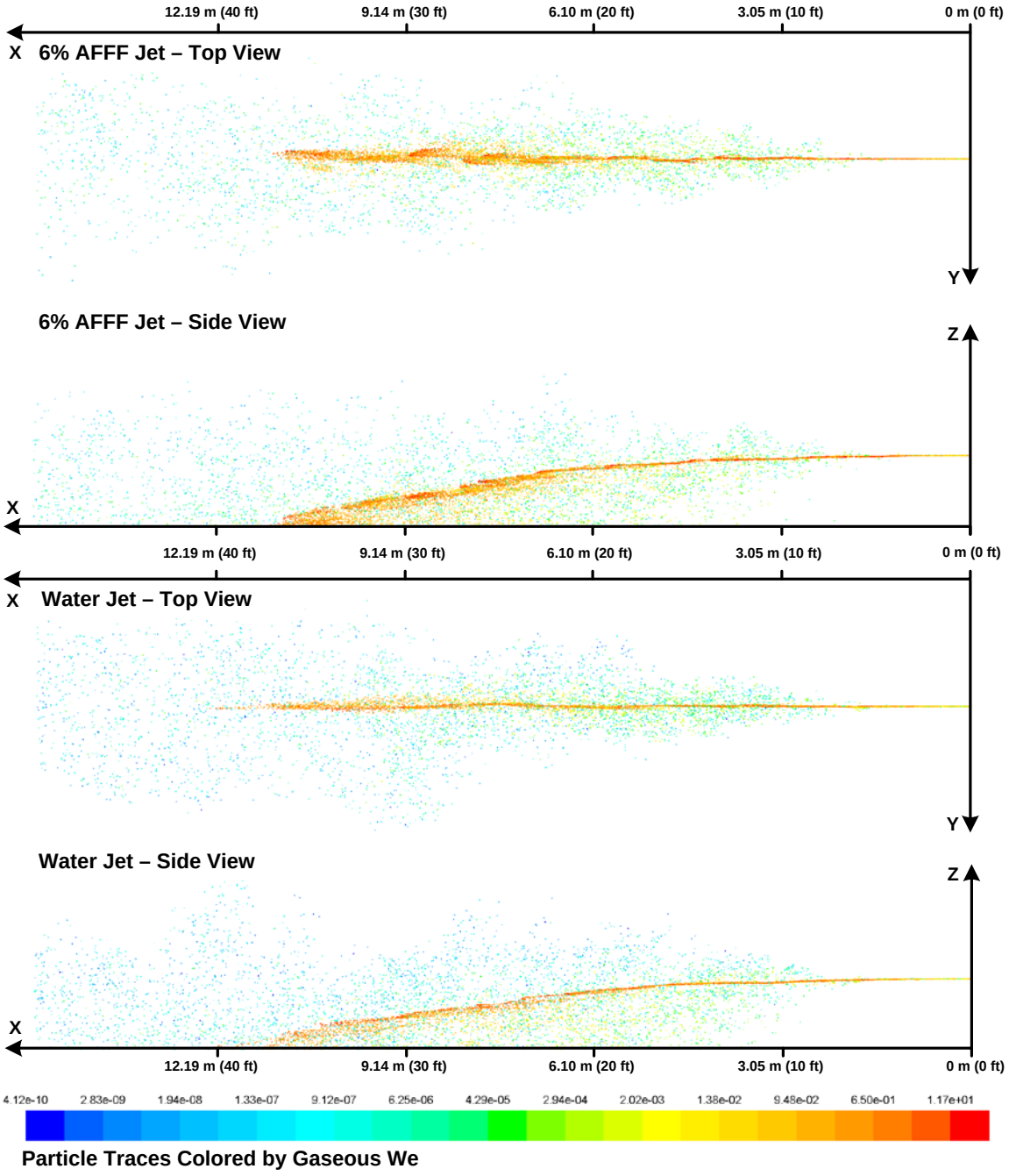

Figure 144. The CFD Model Results of Gaseous Weber Number for High-Flow, Low-Pressure Jets

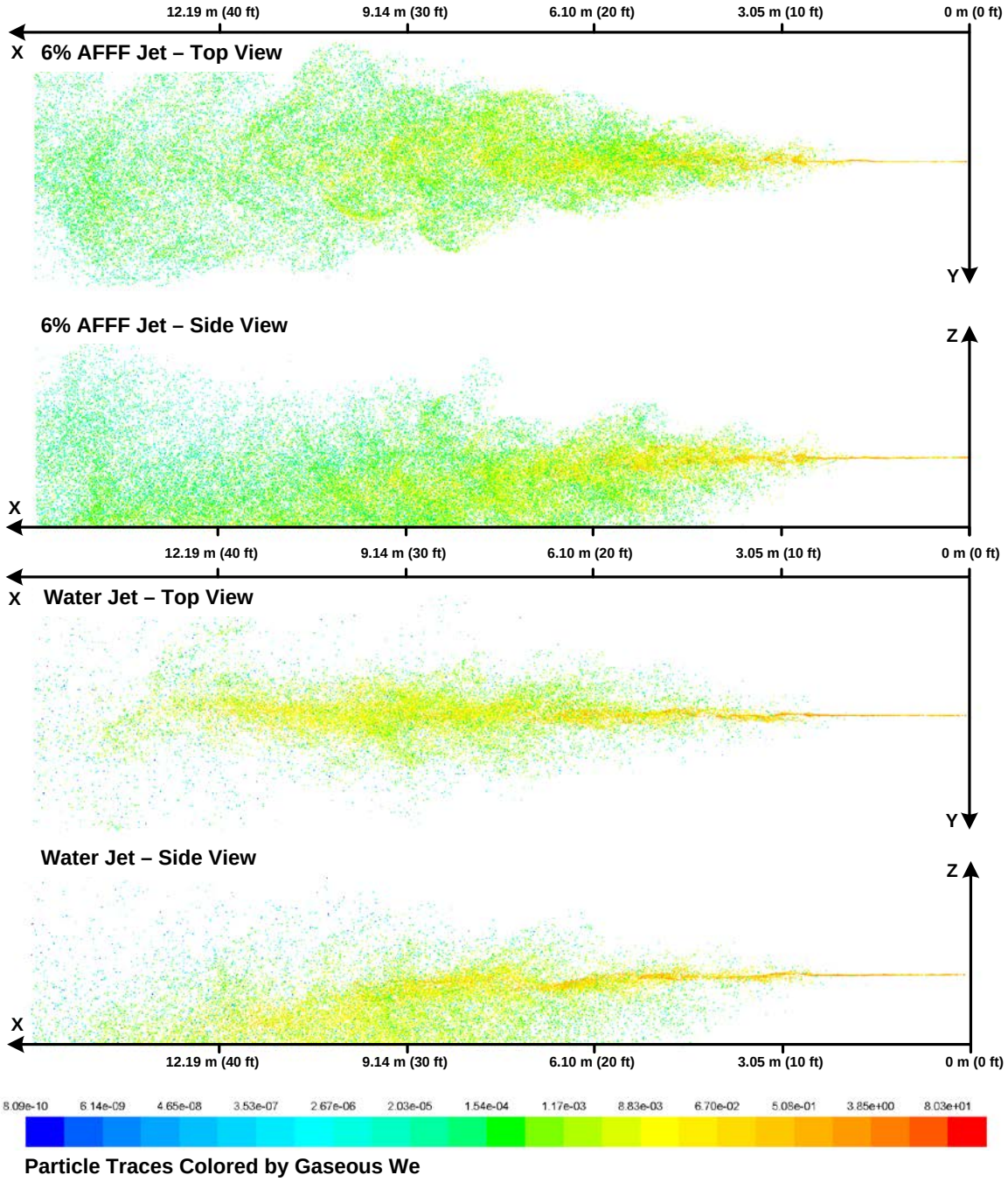

Figure 145. The CFD Model Results of Gaseous Weber Number for High-Flow, High-Pressure Jets

Figures 146 through 150 illustrate velocity magnitude of the gaseous continuous (air) phase spanning from approximately 5 $m \cdot s^{-1}$ in the jet far field up to 45 $m \cdot s^{-1}$ near the nozzle exit for high-pressure jets. This results in a firefighting jet droplet slip velocity of about 60% to 80% that of reported droplet velocities shown in figures 130 through 134. As expected, near nozzle air velocities are higher for firefighting jets with higher pressures and higher droplet velocities due to enhanced entrainment, whereas low-pressure jets exhibited lower droplet velocities and in turn lower air entrainment velocities. Large-scale, turbulent 3-D eddies are also well described in figures 146 through 150, which are also prominent in all mid- and far-field flow visualization imagery.

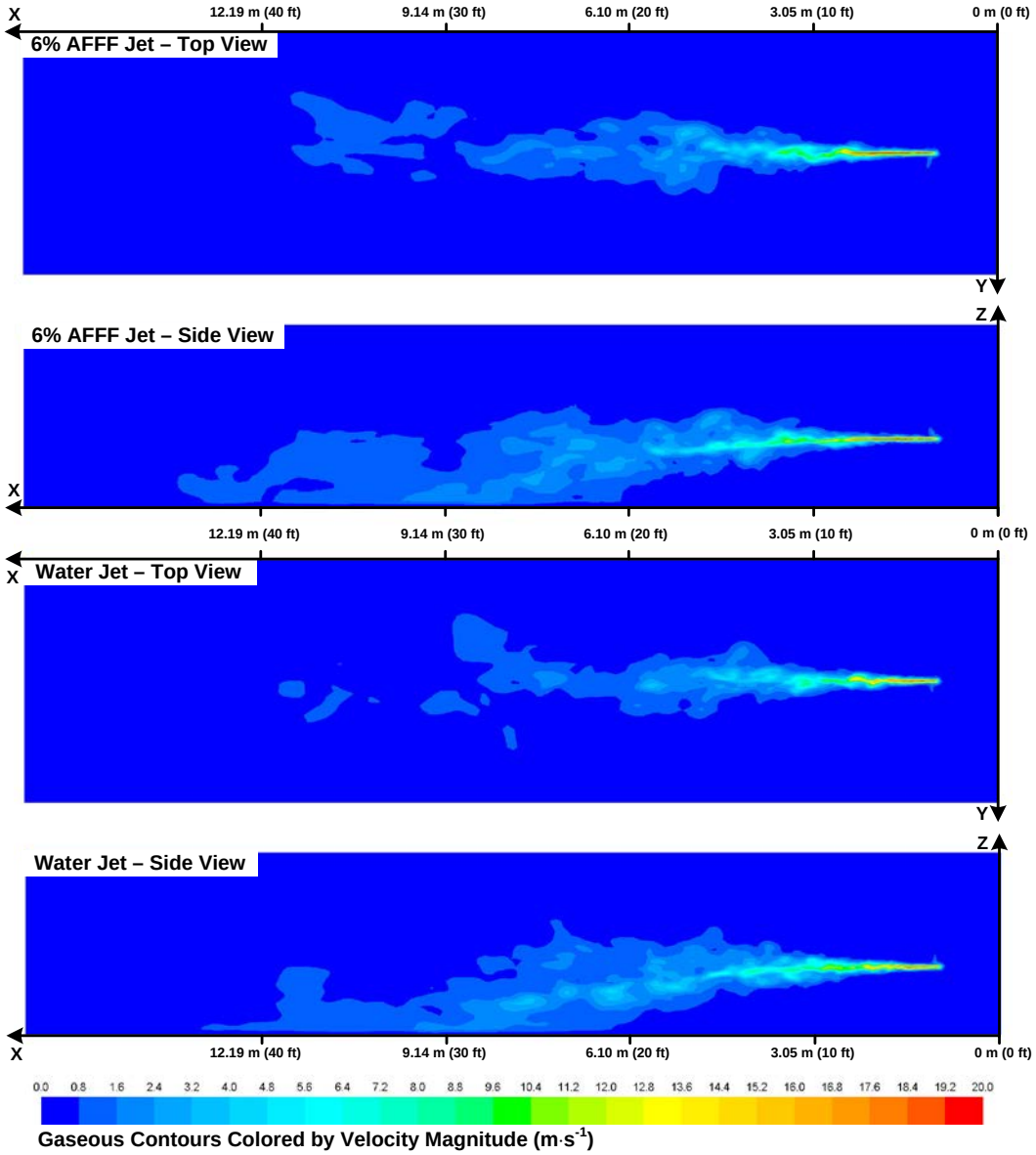

Figure 146. The CFD Model Results of the Gaseous Continuous (Air) Phase Velocity Magnitude for Low-Flow, Low-Pressure Jets

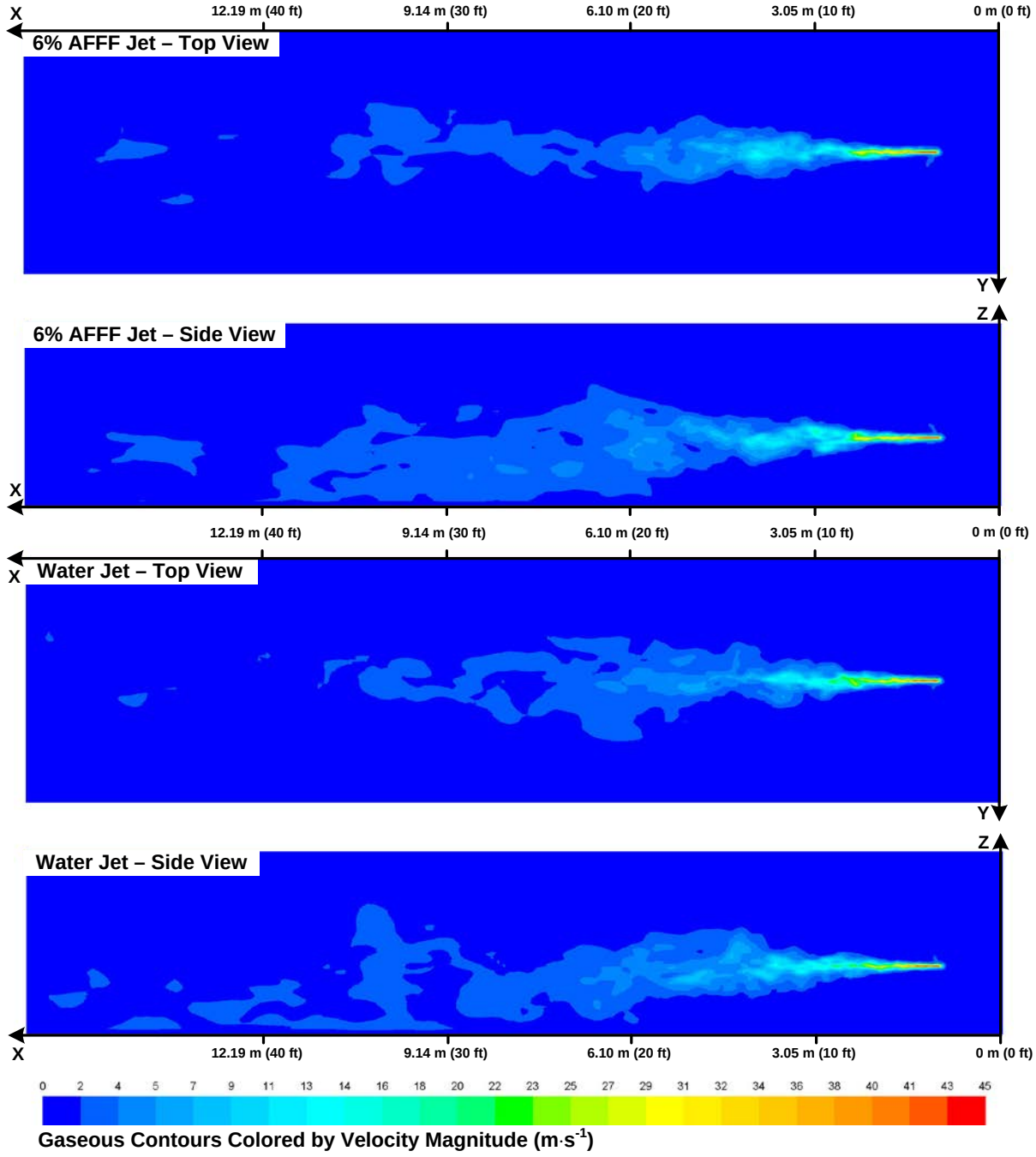

Figure 147. The CFD Model Results of the Gaseous Continuous (Air) Phase Velocity Magnitude for Low-Flow, High-Pressure Jets

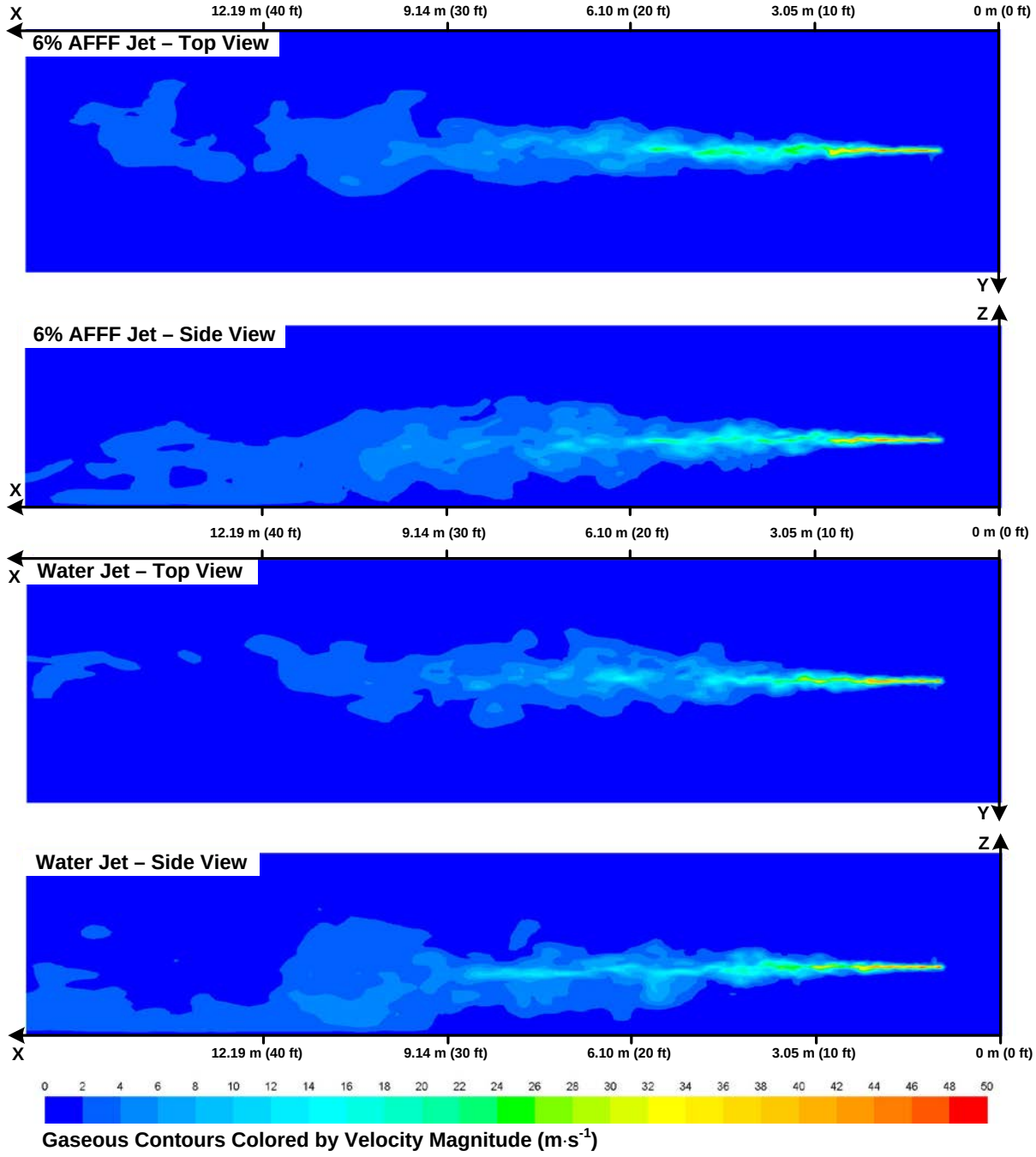

Figure 148. The CFD Model Results of the Gaseous Continuous (Air) Phase Velocity Magnitude for Medium-Flow, Medium-Pressure Jets

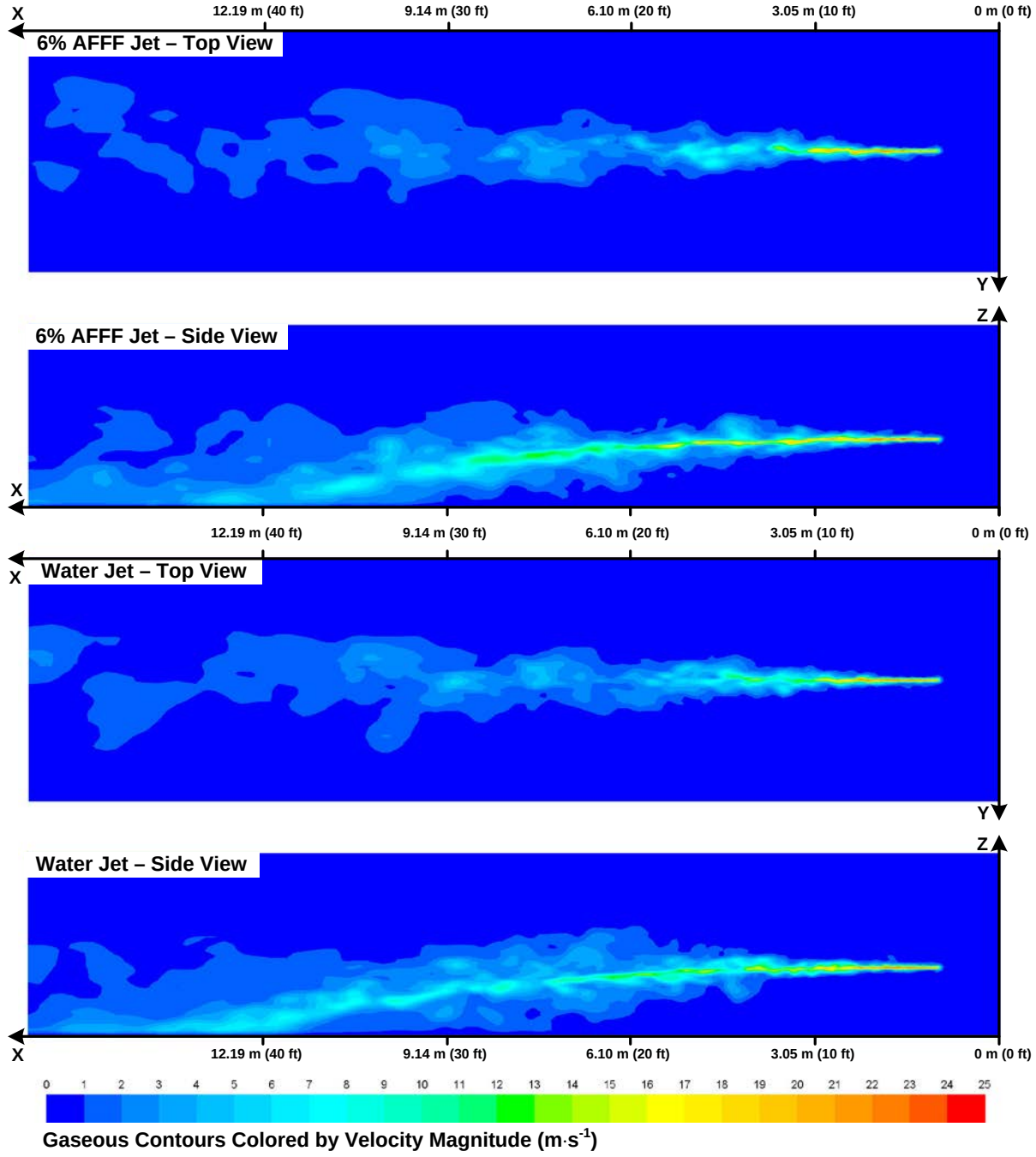

Figure 149. The CFD Model Results of the Gaseous Continuous (Air) Phase Velocity Magnitude for High-Flow, Low-Pressure Jets

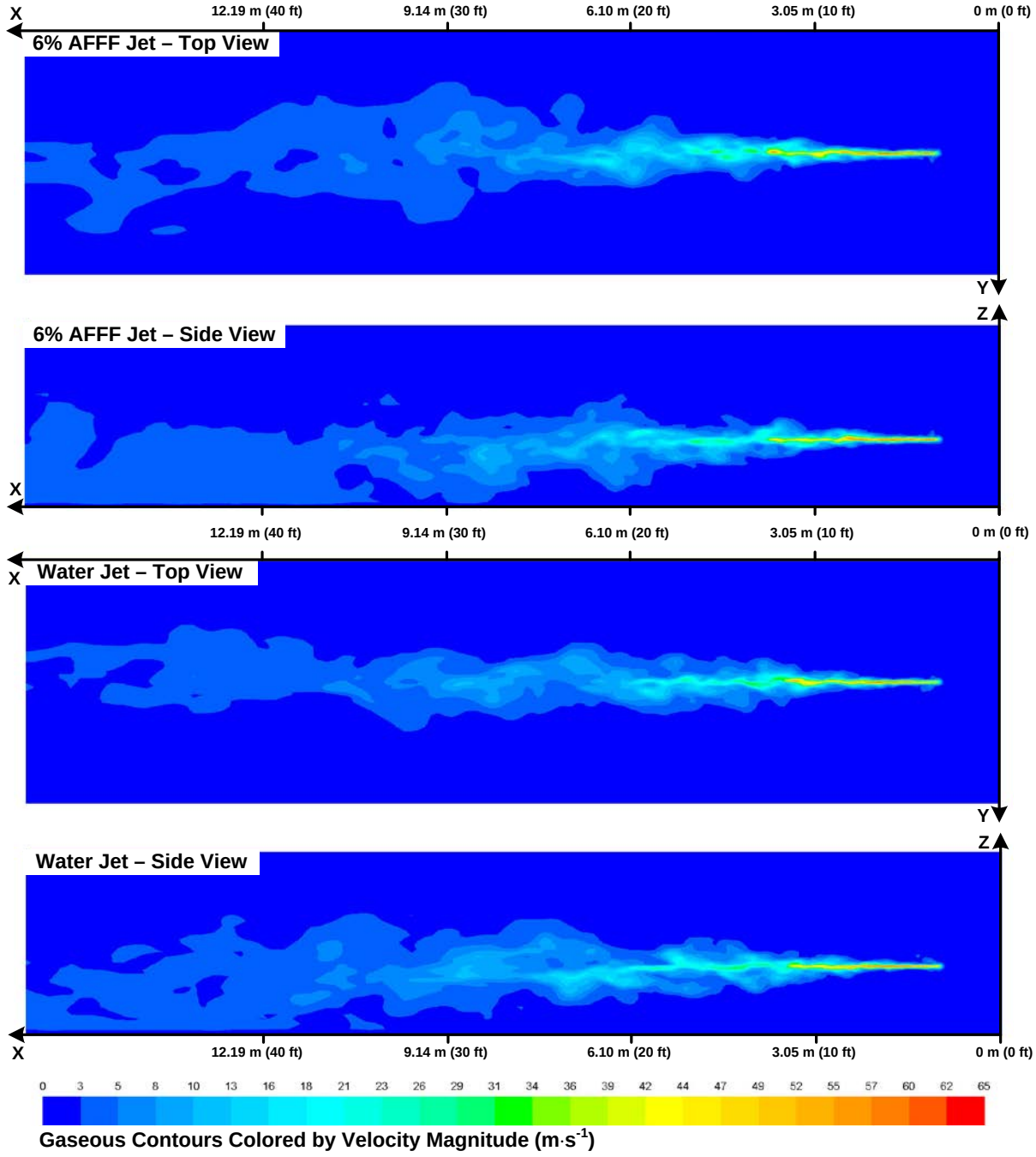

Figure 150. The CFD Model Results of the Gaseous Continuous (Air) Phase Velocity Magnitude for High-Flow, High-Pressure Jets

7. CONCLUSIONS.

All key experimental and computational research milestones defined in section 1.3 were achieved. Construction of the aqueous firefighting agent application laboratory provided the unique infrastructure necessary to achieve all of the experimental tasks, and a computational fluid dynamics (CFD) modeling strategy to predict the bulk in-flight flow characteristics of firefighting jets influenced by aqueous film forming foam (AFFF) was completed. Although the foam expansion ratio for experiments fell below the National Fire Protection Association (NFPA) recommended level of 5:1 for most applications, the AP4 nozzle family provided adequate distinction over the span of firefighting jet flow parameters analyzed to provide meaning and relevance to the results. Experimental flow visualization and phase Doppler particle analysis (PDPA) provided qualitative as well as quantitative details, respectively, on the in-flight flow features that distinguish water and AFFF jets from one another. However, measurable change between the two agents was less significant than anticipated. The CFD model results were able to reproduce the majority of flow trends observed in experiments, but comparisons were less agreeable. This was due to simplifications made in the modeling environment coupled with indirect comparisons between phase Doppler and CFD model data due to computational postprocessing limitations.

In addition to the primary objectives, determining AFFF fluid properties in liquid solution form was of high interest as available information was previously sparse at best. It was important to determine the AFFF flow properties, such as viscosity and surface tension, in order for the material properties to be well defined for the CFD firefighting jet model. It was found that AFFF solution exhibits Newtonian fluid properties over the entire shear range of interest for use in firefighting agent delivery systems, a plausible outcome based on the mild flow behavior differences recorded from phase Doppler experiments between water and AFFF jets.

7.1 EXPERIMENTAL CONCLUSIONS.

Most firefighting jet flow visualization showed unremarkable differences between water and AFFF jets in terms of global shape and structure. Enhanced photography methods provided better clarity compared to standard techniques, but fine, near-field details of the entire pressure-flow rate envelope were unable to be documented. This was due to restricted indoor lighting conditions, the physical scale and composition of the subject matter, and the lack of a well-defined focal plane downstream in high interest areas of the firefighting jet. AFFF jets underwent enhanced breakup compared to water jets due to the surface tension-lowering effect AFFF surfactants had on firefighting jet droplets. This generated greater jet atomization and caused more light to scatter, making AFFF jets appear more dense and fuller compared to water jets. Nonspherical-shaped droplets and disks were also observed in several near-field photographs. This was particularly evident with the high-flow, low-pressure AFFF jet in which bubble-like formations were observed in the downstream wake region. All other AFFF jet pressure-flow rate combinations behaved similar to water jets by exhibiting discrete, spherical droplets more suited for PDPA data acquisition and more in line with the simulation strategy employed for this study.

Agent ground pattern analysis related firefighting jet control factors (such as nozzle pressure, flow rate, and AFFF concentration) to flow performance parameters (such as foam quality,

ground coverage area, ground reach, and maximum ground span). Ground coverage area, ground reach, and maximum ground span demonstrated a mean, minor dependence on water versus AFFF jets. All flow performance parameters increased with an increase in flow rate. Ground coverage area benefited the most with a mean increase of 0.70 m^2 per liter per minute increase in flow rate. Ground reach benefited with a mean increase of 21 cm per liter per minute increase in flow rate, and maximum ground span benefited the least with a mean increase of about 5 cm per liter per minute increase in flow rate. Flow performance parameters were aided by nozzle pressure by a similar effective range, except foam quality measured on the laboratory scale showed little dependency on either nozzle pressure or flow rate. However, the full-scale agent ground pattern analysis showed definitive foam quality decline as nozzle pressure increased by as much as 50% from about 1 to 10 MPa (150 to 1500 $lbf \cdot in.^{-2}$). Foam distribution from AFFF jets also closely tracked agent accumulation patterns from water jets demonstrating higher local agent volumes generated higher foam qualities. This observation was also supported by the full-scale agent ground pattern results.

Firefighting jet mass conservation was inspected using data from the agent ground pattern analysis based on uniform agent ground accumulation. The results showed an overshoot, or a net gain in mass, by as much as 8.58% to an undershoot, or net loss in mass, by as much as 19.44%. Net losses were expected due to evaporation for most nozzle pressure-flow rate combinations, particularly for low-flow, high-pressure jets that exhibited greater atomization and exposed more droplet surface area to the air. Net gains were anticipated for high-flow, low-pressure jets where most of the firefighting jet spray volume landed exclusively in agent capture devices placed along the jet containment bed centerline. Averaging the mass balance across all firefighting jet cases resulted in a mean net loss of 4.4%. This indicated droplet evaporation was a factor, albeit not a significant one.

Although PDPA had its limitations in terms of discrete point measurements, spherical particle assumptions, and possessing a finite droplet diameter measurement range, most flow fields generated a favorable environment for the data acquisition process to be effective. All firefighting jets exhibited log-normal droplet distribution behavior consistent with pressure atomizer nozzles, and the Nukiyama-Tanasawa method provided the best fit for all nozzle pressure-flow rate combinations. Root mean square (RMS) droplet diameters consistently reflected a diameter spread of the same order of magnitude as the mean droplet diameter. PDPA reported AFFF jet, mean droplet diameters universally lower compared to water jet, mean droplet diameters by 7% to 38% in the effective range of the jet. However, the difference in mean axial droplet velocity profile measurements was minor with AFFF jets slightly lagging water jets, a result due to momentum loss from the transport of smaller, less massive AFFF droplets due to enhanced diffusion and greater turbulent mixing. For some firefighting jet profiles, the velocity lag measured was close to or equal to zero, and in others, the differential was as much as 10%. All firefighting jets exhibited large RMS velocity fluctuations, generating turbulence intensities in several cases on the order of the mean velocity, resulting in a turbulent flow classification for all flow regimes considered. Sauter mean droplet diameters followed trends consistent with mean droplet diameter measurements with relative size offsets between AFFF and water droplets also in the same quantitative range as mean droplet diameter. However, inconsistencies were reported for a minority of nozzle settings due to extensive scatter observed in a few individual profile measurements, particularly downstream in the far reaches of each jet. The PDPA system may have recorded invalid, nonspherical, and/or bubble-like spray

formations in these locations, resulting in a misrepresentative Sauter mean diameter calculation. Because Sauter mean diameter measurements weight the presence of large droplets significantly more than smaller droplets, a very few (e.g., 10 or fewer in a sample field of 50,000) droplets recorded along the upper threshold of the PDPA measurement envelope were capable of altering the Sauter mean diameter measurement on the order of 10% or more. PDPA data on the order of 500,000 samples would have to be recorded to provide good statistical convergence for this particular type of data, which was impractical due to the expense of AFFF testing.

Phase Doppler and agent ground pattern data showed unique responses to variation in AFFF solution concentration. The only flow parameter measured by the PDPA that exhibited a dependence on AFFF solution concentration was mean droplet diameter where a mean 12% magnitude reduction was measured between 3% and 6% AFFF. Above 6% AFFF, measured phase Doppler velocities and droplet sizes reported a mean negligible change of less than 1%. This outcome is plausible as AFFF compositions are designed for peak performance based on a particular water dilution level. Although these data were not collected for all nozzle settings, the results are likely indicative of all pressure-flow rate combinations. However, it is reasonable to assume that high-flow AFFF jets with relatively larger initial droplets would exhibit greater sensitivity to AFFF concentration as a wider range of droplet breakup would incur before reaching a potential low-end droplet size threshold. For agent ground pattern analysis, foam quality increased quasi-linearly, proportional with AFFF concentration up to the highest tested concentration of 12% AFFF. The AFFF jet foam expansion ratio proportionally increased by about 25% per 3% increase in AFFF solution concentration. This suggests the AFFF influence is more apparent in the presence of continuous or semicontinuous liquids with larger surface areas where surface tension forces dominate compared to the aerodynamic forces imparted on in-flight droplets. These results also suggest a more complex relationship between AFFF concentration diffusion rates and droplet size, or perhaps a loss in PDPA measurement accuracy due to the physical changes undergone by droplets at high AFFF concentration levels in terms of shape and refractive index properties.

7.2 COMPUTATIONAL FIREFIGHTING JET MODEL CONCLUSIONS.

A firefighting jet CFD flow-modeling strategy was developed based on liquid jet breakup classification from the literature, basic knowledge of the firefighting agent delivery system and nozzle, and droplet size distribution information pertaining to the nozzle near-field exit region from phase Doppler measurements. The qualitative CFD model results reproduced firefighting jet trajectory, reach, span, and spread well when compared to flow visualization results. The CFD model flow parameter results compared better to the phase Doppler results in regions further downstream in contrast to the nozzle near field due to an oversimplification of the discrete phase model (DPM) nozzle injection condition. It only accounted for the axial component of velocity in terms of a constant value at a single point in space. Nozzle perturbations and turbulent droplet dispersion was not accounted for at the injection point, and thus, firefighting jet characteristics were dependent on downstream droplet-air interactions to provide progressively more plausible flow physics as the jet flowed downstream. Despite these inconsistencies, the CFD model showed reasonable agreement with the phase Doppler results in terms of overall flow parameter trends, magnitudes, and the influence of AFFF. The employment of a constant model equilibrium surface tension value for AFFF increased droplet breakup, which was consistent with measurements made by the PDPA. Most mean profile, axial

and vertical droplet velocity CFD model and phase Doppler result comparisons were within 10% of one another with a minority of points deviating by as much as 50%. Mean droplet diameter and Sauter mean droplet diameter comparisons exhibited greater divergence with most data within 25%, with a minority of points differing by as much as 100%. The majority of CFD droplet diameters were reportedly larger than phase Doppler droplet diameters because model evaporation was neglected. Further discrepancy between the phase Doppler and CFD model results was likely due to a multitude of factors, including differences in droplet size and window range reporting, droplet shape restrictions, possible alignment inconsistency between experiments and the model environment, and droplet-air interactions unaccounted for in the physical submodels. Examples of other errors induced by physical CFD submodels include isotropic turbulence assumptions, three-dimensional liquid jet ligaments simulated as solid, discrete droplets (particles), and droplet parcel fidelity limited by the efficiency of numerical solution techniques and computational resources. CFD model droplets were also not allowed to directly interact with the nonpermeable surfaces, such as the modeled laboratory floor or the firefighting jet containment zone. Their presence was only accounted for in part via the continuous (air) phase. The ANSYS Fluent® DPM simulation strategy performs best for firefighting jets that do not have a continuous liquid core and experience-enhanced atomization either due to lower-flow rates, higher pressures, or a combination thereof based on the modeling assumptions employed. For firefighting jets with a substantial, contiguous liquid core, alternative modeling methods, such as dense discrete phase modeling, must be considered.

This work describes the first known, comprehensive effort to quantify flow characteristics and properties that differentiate water and AFFF firefighting jets using high-fidelity experimental techniques. This work also includes the first known iteration of a firefighting agent application CFD model designed for use in the aircraft rescue and firefighting (ARFF) industry that takes into account the influence of AFFF. Data collected from this study can be used to develop future, more ecofriendly alternatives to AFFF, optimize current AFFF compositions and application techniques for greater effectiveness, and aid the ongoing construction of a simulation framework to provide scientifically based risk assessment for aircraft-crash-fire suppression scenarios of interest.

8. REFERENCES.

1. Fittes, D.W., Griffiths, D.J., and Nash, P., "The Use of Light Water for Major Aircraft Fires," *Fire Technology*, vol. 5, no. 4, November 1969, pp. 284-298.

2. Enlow, M.A., Dierdorf, D.S., and Campbell, R., "Time Dependent Analysis of Hydrocarbon and Fluorocarbon Surfactant Solutions," AFRL report AFRL-RX-TY-TR-2010-0075, Air Force Research Laboratory, Tyndall Air Force Base, Florida, 2011.

3. Grove, C.S., Wise, G.E., Marsh, W.C., and Gray, J.B., "Viscosity of Fire-Fighting Foam," *Journal of Industrial & Engineering Chemistry*, vol. 43, no. 5, May 1951, pp. 1120-1122.

4. Gipe, R.L. and Peterson, H.B., "Proportioning Characteristics of Aqueous Film Forming Foam Concentrates," NRL Report 7437, Naval Research Laboratory, Washington, D.C., July 1972.

5. Geyer, G.B., "Firefighting Effectiveness of Aqueous Film-Forming Foam (AFFF) Agents," FAA report AD-774 025, National Aviation Facilities Experimental Center, Atlantic City, New Jersey, 1973.

6. Elliott, D.E. and Chiesa, Jr., P.J., "A New Foam Rheometer for Studying Fire Fighting Foams," *Fire Technology*, vol. 12, no. 1, February 1976, pp. 66-69.

7. Elliott, D.E. and Chiesa, Jr., P.J., "Rheological Properties of Fire Fighting Foams," *Fire Technology*, vol. 12, no. 2, May 1976, pp. 141-150.

8. Chiesa, P.J. and Alger, R.S., "Severe Laboratory Fire Tests for Fire Fighting Foams," *Fire Technology*, vol. 16, no. 1, February 1980, pp. 12-21.

9. U.S. Military Specification MIL-F-24385F, "Firefighting Extinguishing Agent, Aqueous Film Forming Foam (AFFF) Liquid Concentrate for Fresh and Sea Water," Naval Sea Systems Command, Washington Navy Yard, Washington, D.C., January 1992.

10. National Fire Protection Association, *NFPA 403: Standard for Aircraft Rescue and Fire-Fighting Services at Airports*, 2009 edition, NFPA, Quincy, Massachusetts, 2009.

11. National Fire Protection Association, *NFPA 412: Standard for Evaluating Aircraft Rescue and Fire-Fighting Foam Equipment*, 2009 edition, NFPA, Quincy, Massachusetts, 2009.

12. Chemguard 3% C-301MS, Material Safety Data Sheet, Chemguard, Inc., Mansfield, Texas, January 2011, available at www.chemguard.com (date last visited 4/22/15).

13. Moody, C.A. and Field, J.A., "Perfluorinated Surfactants and the Environmental Implications of Their Use in Fire-Fighting Foams," *Environmental Science & Technology*, vol. 34, no. 18, September 2000, pp. 3864-3870.

14. Vecitis, C.D., Wang, Y., Cheng, J., Park, H., Mader, B.T., and Hoffmann, M.R., "Sonochemical Degradation of Perfluorooctanesulfonate in Aqueous Film-Forming Foams," *Environmental Science & Technology*, vol. 44, no. 1, January 2010, pp. 432-438.

15. Magrabi, S.A., Dlugogorski, B.Z., and Jameson, G.J., "A Comparative Study of Drainage Characteristics in AFFF and FFFP Compressed-Air Fire-Fighting Foams," *Fire Safety Journal*, vol. 37, no. 1, February 2002, pp. 21-52.

16. Carruette, M.L., Persson, H., and Pabon, M., "New Additive for Low Viscosity of AFFF/AR Concentrates—Study of the Potential Fire Performance," *Fire Technology*, vol. 40, no.4, October 2004, pp. 367-384.

17. Walker, J.R., "The Effect of Surfactants on the Breakup of an Axisymmetric Laminar Liquid Jet," Ph.D. thesis, University of Maryland, College Park, Maryland, 2012.

18. Place, B.J. and Field, J.A., "Identification of Novel Fluorochemicals in Aqueous Film-Forming Foams (AFFF) Used by the U.S. Military," *Environmental Science & Technology*, vol. 46, no. 13, July 2012, pp. 7120-7127.

19. United States Environmental Protection Agency, "Emerging Containments—Perfluorooctane Sulfonate (PFOS) and Perfluoroctanoic Acid (PFOA): Emerging Contaminants Fact Sheet—PFOS and PFOA," Solid Waste and Emergency Response (5106P), EPA 505-F-11-002, May 2012.

20. Munson, B.R., Young, D.F., and Okishi, T.H., *Fundamentals of Fluid Mechanics*, Fifth Edition, John Wiley & Sons, Inc., Danvers, Massachusetts, 2006.

21. Figueredo, R.C.R. and Sabadini, E., "Firefighting Foam Stability: The Effect of the Drag Reducer Poly(ethylene) Oxide," *Colloids and Surfaces A: Physiochemical and Engineering Aspects*, vol. 215, no. 1, March 2003, pp. 77-86.

22. Hyland, E.K. and Williams, B.A., "Characterization of the Dynamic Surface Tension of Aqueous Film-Forming Foam," NRL report NRL/MR/6180--04-8749, Naval Technology Center for Safety and Survivability, Washington, D.C., February 2004.

23. Meissner, E., Twardochleb, B., Milchert, E., Wroblewska, A., and Szymanowski, J., "Estimation of Foam Forming Properties and Surface Tension of Fire-Extinguishing Agents," *Journal of Tensile Surfactants Detergents*, vol. 40, no. 6, 2003, pp. 353-360.

24. ASTM International, "Standard Practice for the Preparation of Substitute Ocean Water," ASTM D1141-98, ASTM International, West Conshohocken, Pennsylvania, 2013.

25. Persson, B., Lonnermark, A., and Persson, H., "FOAMSPEX: Large Scale Foam Application—Modeling of Foam Spread and Extinguishment," *Fire Technology*, vol. 39, no. 4, October 2003, pp. 347-362.

26. Lefort, G., Marshall, A.W., and Pabon, M., "Evaluation of Surfactant Enhanced Water Mist Performance," *Fire Technology*, vol. 45, no. 3, September 2009, pp. 341-354.

27. Timms, G. and Haggar, P., "Foam Concentration Measurement Techniques," *Fire Technology*, vol. 26, no. 1, February 1990, pp. 41-50.

28. Scheffey, J.L., Darwin, R.L., and Leonard, J.T., "Evaluating Firefighting Foams for Aviation Fire Protection," *Fire Technology*, vol. 31, no. 3, August 1995, pp. 224-243.

29. Gardiner, B.S., Dlugogorski, B.Z., and Jameson, G.J., "Rheology of Fire-Fighting Foams," *Fire Safety Journal*, vol. 31, no. 1, July 1998, pp. 61-75.

30. Laundess, A.J., Rayson, M.S., Dlugogorski, B.Z., and Kennedy, E.M., "Small-Scale Test Protocol for Firefighting Foams DEF(AUST) 5706: Effect of Bubble Size Distribution and Expansion Ratio," *Fire Technology*, vol. 47, no. 1, January 2011, pp. 149-162.

31. Sheinson, R.S., Williams, B.A., Green, C., Fleming, J.W., Anleitner, R., Ayers, S., and Maranghides, A., "The Future of Aqueous Film Forming Foam (AFFF): Performance Parameters and Requirements," NIST Special Publication 984, *Proceedings of the HOTWC-2002 12th Halon Options Technical Working Conference*, Albuquerque, New Mexico, April 30-May 2, 2002.

32. Grant, R.P., "Newtonian Jet Stability," Ph.D. thesis, University of Rochester, New York, University Microfilms No. 65-12006, Ann Arbor, Michigan, 1965.

33. McCarthy, M.J. and Malloy, N.A., "Review of Stability of Liquid Jets and the Influence of Nozzle Design," *The Chemical Engineering Journal*, vol. 7, no. 1, 1974, pp. 1-20.

34. Lin, S.P. and Reitz, R.D., "Drop and Spray Formation from a Liquid Jet," *Annual Review of Fluid Mechanics*, vol. 30, January 1998, pp. 85-105.

35. Phinney, R.E., "The Break-up of a Turbulent Liquid Jet in a Gaseous Atmosphere," *Journal of Fluid Mechanics*, vol. 60, no. 4, October 1973, pp. 689-701.

36. Birouk, M. and Lekic, N., "Liquid Jet Break-up in Quiescent Atmosphere: A Review," *Atomization and Sprays*, vol. 19, no. 6, 2009, pp. 501-528.

37. Chen, T.F. and Davis, J.R., "Disintegration of a Turbulent Water Jet," *Journal of the Hydraulics Division*, vol. 90, no. 1, January/February 1964, pp. 175-206.

38. Hoyt, J.W. and Taylor, J.J., "Turbulence Structure in a Water Jet Discharging in Air," *The Physics of Fluids*, vol. 20, no. 10, part II, October 1977.

39. Ruff, G.A., Sagar, A.D., and Faeth, G.M., "Structure and Mixing Properties of Pressure-Atomized Sprays," *AIAA Journal*, vol. 27, no. 7, July 1989, pp. 901-908.

40. Faeth, G.M., Hsiang, L.P., and Wu, P.K., "Structure and Breakup Properties of Sprays," *International Journal of Multiphase Flow*, vol. 21, supplement, December 1995, pp. 99-127.

41. Delteil, J., Vincent, S., Erriguible, A., and Subra-Paternault, P., "Numerical Investigations in Rayleigh Breakup of Round Liquid Jets with VOF Methods," *Computers & Fluids*, vol. 50, no. 1, November 2011, pp. 10-23.

42. Hiroyasu, H., "Spray Breakup Mechanism From the Hole-Type Nozzle and Its Applications," *Atomization and Sprays*, vol. 10, no. 3-5, 2000, pp. 511-527.

43. Joseph, D.D., Belanger, J., and Beavers, G.S., "Breakup of a Liquid Drop Suddenly Exposed to a High-Speed Airstream," *International Journal of Multiphase Flow*, vol. 25, no. 6-7, September 1999, pp. 1263-1303.

44. Wu, P.K., Miranda, R.F., and Faeth, G.M., "Effects of Initial Flow Conditions on Primary Breakup of Nonturbulent and Turbulent Liquid Jets," AIAA 94-0561, *AIAA 32nd Aerospace Sciences Meeting & Exhibit*, Reno, Nevada, January 10-13, 1994.

45. Reitz, R.D., "Atomization and Other Breakup Regimes of a Liquid Jet," Ph.D. thesis, Princeton University, Princeton, New Jersey, 1978.

46. Wu, P.K., "Liquid Surface Breakup of Nonturbulent and Turbulent Liquids," Ph.D. thesis, University of Michigan, Ann Arbor, Michigan, 1992.

47. Hatton, A.P. and Osbourne, M.J., "The Trajectories of Large Fire Fighting Jets," *International Journal of Heat and Fluid Flow*, vol. 1, no. 1, pp. 37-41, 1979.

48. Freeman, J.R., "Experiments Relating to Hydraulics of Fire Streams," *Transactions of the American Society of Civil Engineers*, vol. 21, no. 2, July 1889, pp. 303-461.

49. Rouse, H., Howe, J.W., and Metzler, D.E., "Experimental Investigation of Fire Monitors and Nozzles," *Transactions of the American Society of Civil Engineers*, vol. 117, no. 1, January 1952, pp. 1186-1188.

50. Murakami, M. and Katayama, K., "Discharge Coefficients of Fire Nozzles," *Journal of Basic Engineering*, vol. 88, no. 4, December 1966, pp. 706-716.

51. Theobald, C.R., "The Design of a General Purpose Fire-Fighting Jet and Spray Branch," *Fire Safety Journal*, vol. 7, no. 2, 1984, pp. 177-190.

52. Theobald, C.R., "The Effect of Nozzle Design on the Stability and Performance of Turbulent Water Jets," *Fire Safety Journal*, vol. 4, no. 1, August 1981, pp. 1-13.

53. Jiang, X., Siamas, G.A., Jagus, K., and Karayiannis, T.G., "Physical Modelling and Advanced Simulations of Gas-Liquid Two-Phase Jet Flows in Atomization and Sprays," *Progress in Energy and Combustion Science*, vol. 36, no. 2, April 2010, pp. 131-167.

54. Gorokhovski, M. and Herrmann, M., "Modeling Primary Atomization," *Annual Review of Fluid Mechanics*, vol. 40, January 2008, pp. 343-366.

55. Archambault, M.R., "Stochastic Spray Flow Models: A Review," *ILASS-Americas 22nd Annual Conference on Liquid Atomization and Spray Systems*, Cincinnati, Ohio, May 2010.

56. ANSYS® Fluent v.14.5 Theory Guide, available at www.ansys.com, click on "customer portal" tab (date last visited 4/22/15).

57. Menard, T., Tanguy, S., and Berlement, A., "Coupling Level Set/VOF/Ghost Fluid Methods: Validation and Application to 3D Simulation of the Primary Break-up of a

Liquid Jet," *International Journal of Multiphase Flow*, vol. 33, no. 5, May 2007, pp. 510-524.

58. Shi, H. and Kleinstreuer, C., "Simulation and Analysis of High-Speed Droplet Spray Dynamics," *Journal of Fluids Engineering*, vol. 129, no. 5, January 2007, pp. 621-633.

59. Blum, A.F., "Discharge Characteristics of Canonical Sprinkler Sprays," M.S. thesis, University of Maryland, College Park, Maryland, 2007.

60. Adiga, K.C., Hatcher, Jr., R.F., Sheinson, R.S., Williams, F.W., and Ayers, S., "A Computational and Experimental Study of Ultra Fine Water Mist as a Total Flooding Agent," *Fire Safety Journal*, vol. 42, no. 2, March 2007, pp. 150-160.

61. Yoon, S.S., Hewson, J.C., DesJardin, P.E., Glaze D.J., Black, A.R., and Skaggs, R.R., "Numerical Modeling and Experimental Measurements of a High Speed Solid-Cone Water Spray for Use in Fire Suppression Application," *International Journal of Multiphase Flow*, vol. 30, no. 11, November 2004, pp. 1369-1388.

62. Sinai, Y., Stopford, P., Edwards, M., and Watkins, S., "CFD Modeling of Fire Suppression by Water Spray: Sensitivity and Validation for a Pool Fire in a Room," *Eighth International IBPSA Conference*, Eindhoven, Netherlands, August 11-14, 2003, pp. 1217-1220.

63. Tanner, G., Kalata, W., Brown, K., and Schick, R.J., "Computational Study Effects of Drop Size Distribution in Fire Suppression Systems," *ILASS-Americas 22nd Annual Conference on Liquid Atomization and Spray Systems*, May 2010, Cincinnati, Ohio.

64. DesJardin, P.E. and Gritzo, L.A., "A Dilute Spray Model for Fire Simulations: Formulation, Usage and Benchmark Problems," SAND report SAND2002-3419, Sandia National Laboratories, October 2002.

65. Baldor Motor & Drives, Baldor Smartmotor™ Installation & Operating Manual, Print Version, P/N MN750, September 2002 Revision.

66. TSI Incorporated, Phase Doppler Particle Analyzer (PDPA)/Laser Doppler Velocimeter Operations Manual, Print Version, P/N 1990048, Revision E, 2006.

67. Albrecht, H.E., Damaschke, N., Borys, M., and Tropea, C., *Laser Doppler and Phase Doppler Measurement Techniques*, Springer-Verlag, Berlin, Germany, 2003.

68. Dantec Measurement Technology, "Principles of Phase Doppler Anemometry," available at https://www.ara.bme.hu/oktatas/tantargy/NEPTUN/BMEGEATMG19/2010-2011-II/ea/12_ea_PDA_0_DantecPDA_2011.pdf (date last visited April 8, 2013).

69. Lai, W., Shakal, J., and Troolin, D., "Accuracy, Resolution, and Repeatability of Powersight PDPA and LDV Systems," TSI Technical Note P/N 5001520 (A4), TSI Incorporated, Shoreview, Minnesota, 2013.

70. TSI Incorporated, Phase Doppler Particle Analyzer (PDPA)/Laser Doppler Velocimeter Installation Manual, Print Version, P/N 1990024, Revision B, February 2005.

71. Solidworks 2012®, available at www.solidworks.com (date last visited April 8, 2013).

72. Pointwise V17.0®, available at www.pointwise.com (date last visited April 8, 2013).

73. Celik, I.B., Ghia, U., Roache, P.J., Freitas, C.J., Coleman, H., and Raad, P.E., "Procedure for Estimating and Reporting of Uncertainty Due to Discretization in CFD Applications," *ASME Journal of Fluids Engineering (Special Publication)*, vol. 130, no. 7, July 22, 2008.

APPENDIX A—CASE STUDY SUMMARY

Table A-1 summarizes the operating parameters for both the experimental as well as the computational fluid dynamic (CFD) modeling cases executed during the present study. All cases listed in table A-1 represent all experimental case conditions. The cases highlighted in light gray were also investigated computationally. Refer to section 2 for details on how the specific Reynolds, Weber, and Ohnesorge numbers are formulated.

Table A-1. A Summary of the Firefighting Jet Nozzle Exit Conditions Examined

Case	Nozzle Diameter (mm)	Nozzle Flow Rate ($L \cdot min^{-1}$)	Nozzle Velocity ($m \cdot s^{-1}$)	Nozzle Pressure (MPa)	Re_L ($\times 10^5$)	We_L ($\times 10^5$)	We_G	We_d	Oh ($\times 10^{-3}$)
Low-Flow, Low-Pressure Water Jet	1.45	4.20	42.5	1.20	0.690	0.363	43	1.49	2.76
Low-Flow, Low-Pressure 6% AFFF Jet	1.45	4.20	42.5	1.20	0.617	1.51	178	6.16	6.30
Low-Flow, High-Pressure Water Jet	0.81	4.20	135	10.7	1.23	2.05	243	15.0	3.69
Low-Flow, High-Pressure 6% AFFF Jet	0.81	4.20	135	10.7	1.10	8.53	1007	62.0	8.41
Medium-Flow, Medium-Pressure Water Jet	1.75	12.9	88.9	5.85	1.75	1.92	228	6.50	2.51
Medium-Flow, Medium-Pressure 3% AFFF Jet	1.75	12.9	88.9	5.85	1.62	8.25	976	27.9	5.62
Medium-Flow, Medium-Pressure 6% AFFF Jet	1.75	12.9	88.9	5.85	1.56	7.98	943	26.9	5.73
Medium-Flow, Medium-Pressure 9% AFFF Jet	1.75	12.9	88.9	5.85	1.55	7.65	901	25.7	5.63
Medium-Flow, Medium-Pressure 12% AFFF Jet	1.75	12.9	88.9	5.85	1.50	7.42	873	24.9	5.73
High-Flow, Low-Pressure Water Jet	3.68	23.6	36.8	1.16	1.52	0.692	82	1.12	1.73
High-Flow, Low-Pressure 6% AFFF Jet	3.68	23.6	36.8	1.16	1.36	2.88	340	4.62	3.95
High-Flow, High-Pressure Water Jet	1.91	19.8	116	10.6	2.47	3.52	418	11.0	2.41
High-Flow, High-Pressure 6% AFFF Jet	1.91	19.8	116	10.6	2.20	14.7	1730	45.4	5.49

CFD Model Conditions

APPENDIX B—AQUEOUS FILM FORMING FOAM MATERIAL PROPERTY DATA

B.1 DENSITY.

Density (ρ) measurements of various aqueous film forming foam (AFFF) solution concentrations were conducted by the Air Force Civil Engineer Center (AFCEC) personnel at Tyndall Air Force Base, Florida, on Military Specification (MIL-SPEC) C301MS 3% AFFF manufactured by Chemguard and Williams®, a subsidiary of Tyco International. Table B-1 lists the density of each AFFF solution, and figure B-1 illustrates the relationship between the AFFF solution and its density. All measurements were taken at approximately 298 K. Density values were extrapolated by measuring the specific gravity (γ_{SG}) of each solution using a Mettler Toledo Densito 30PX with an accuracy of ±1 kg·m^{-3}. Although using this instrument involved drawing a sample of solution through a thin capillary tube, foam or bubbles did not appear to occur. AFFF density was calculated using the following equation where ρ_{H2O} is the density of water equal to 997.0 kg·m^3 at 298 K.

$$\rho = \gamma_{SG}\rho_{H2O} \tag{B-1}$$

Because AFFF concentrate has a density similar to water in conjunction with also being heavily diluted in water for standard firefighting application purposes, AFFF solution density is a nearly negligible distinguishing property in comparison to water.

Table B-1. Density of Various AFFF Solution Concentrations

Solution Description	Density - ρ (kg·m^{-3})
100% AFFF (pure concentrate)	1069.7
12% AFFF	1007.0
9% AFFF	1004.4
6% AFFF	1002.4
3% AFFF	999.9
0.3% AFFF	996.7
0.03% AFFF	996.6
Water	997.0

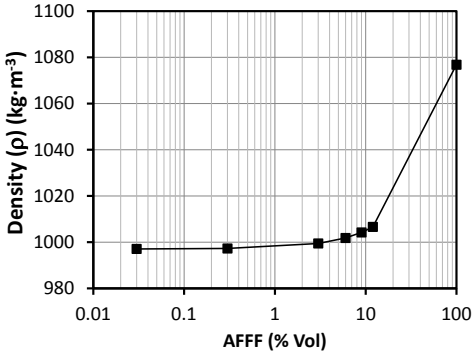

Figure B-1. The AFFF Solution Density vs AFFF Solution Concentration

B.2 VISCOSITY.

Dynamic viscosity (μ) at a constant shear rate was derived for various AFFF solution concentrations by AFCEC personnel at Tyndall Air Force Base, Florida, on MIL-SPEC C301MS 3% AFFF. Kinematic viscosity (ν) was recorded using a size 50 Canon-Fenske Routine viscometer with an effective range of 0.8 to 4 cSt. All AFFF measurements fell within this range and were carried out using ASTM Standard D445-11a with the exception that measurements were conducted at ambient solution temperatures rather than in a temperature bath [B-1]. Dynamic viscosity was calculated from the measured kinematic viscosity and the density measurement from equation B-1.

$$\mu = \rho\nu \tag{B-2}$$

Using this instrument involved allowing the solution to flow through a capillary tube of varying diameters. It was noted that for concentrations above 0.3% AFFF, varying amounts of bubbles were generated above the liquid surface. It is not known what degree of error this introduced. All measurements were taken at approximately 298 K.

Supplemental viscosity data were later provided by Brookfield Engineering Laboratories, Inc. to determine if any AFFF solutions tested by AFCEC exhibited non-Newtonian characteristics by measuring their viscous dependence on shear rate. Similar batches of AFFF solution were tested using an LVDV-III+ Ultra Brookfield Rheometer with an accuracy of ±1% of the current test data range. A CPE-40 cone spindle with a CPE-44PY sample cup with an integral temperature probe was used to analyze each batch of AFFF solution. All measurements were taken at 298 K in the absence of air to prevent foaming. Each sample was equilibrated for at least 10 minutes before the start of each run at the lowest spindle revolution per minute (RPM), incrementally ramped up to the maximum RPM, and then returned to the lowest spindle RPM to verify repeatability at each previous increment. Table B-2 and figure B-2(a) summarize and illustrate the relationship between the AFFF solution concentration and the dynamic viscosity, respectively. Figure B-2(b) depicts the relationship of AFFF solution dynamic viscosity as a function of shear rate.

Table B-2. Derived Dynamic Viscosity of Various AFFF Solution Concentrations

Solution Description	Dynamic Viscosity - μ ($MPa \cdot s^{-1}$)
100% AFFF (pure concentrate)	2.616
12% AFFF	1.043
9% AFFF	1.008
6% AFFF	1.001
3% AFFF	0.9639
0.3% AFFF	0.9394
0.03% AFFF	0.9500
Water	0.9224

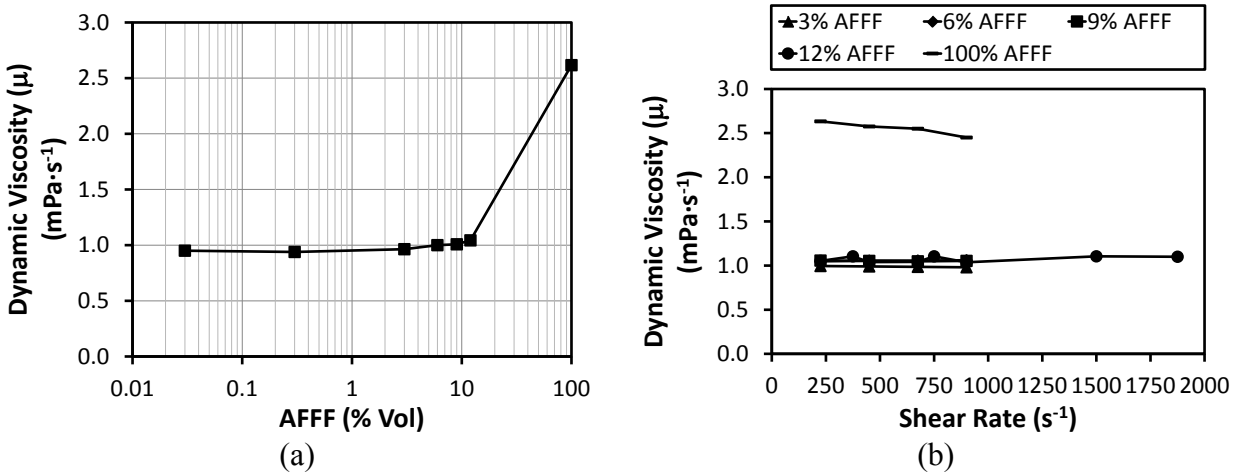

Figure B-2. (a) AFFF Solution Dynamic Viscosity vs AFFF Solution Concentration and (b) AFFF Solution Dynamic Viscosity vs Shear Rate for Various AFFF Solution Concentrations

Both AFCEC and Brookfield confirmed that AFFF solutions at practical proportions with water maintain viscosities very similar to that of water. The data collected by Brookfield also confirmed that all AFFF solutions diluted for practical aircraft rescue and firefighting (ARFF) implementation exhibited primarily Newtonian characteristics with a nearly constant viscosity with respect to shear rate. The 100% AFFF concentrate solution exhibited a very slight dependence on shear rate. The 12% AFFF solution, a composition still within an order of magnitude of the manufacturer's recommended proportion with water, was tested up to a shear of 2000 s^{-1} to ensure no significant dependencies existed at higher thresholds.

This data suggests that AFFF's non-Newtonian nature in aqueous foam form is primarily governed by the multiphase relationship that exists between the AFFF solution and the air bubbles for which it has entrained, rather than the pure liquid state of the AFFF solution.

B.3 SURFACE TENSION.

Equilibrium surface tension and dynamic surface tension measurements were conducted on various AFFF solution concentrations by AFCEC personnel at Tyndall Air Force Base, Florida, on MIL-SPEC C301MS 3% AFFF. Additional AFFF dilutions were added for relative comparison. All measurements were taken at approximately 298 K. All equilibrium surface tension data were collected using a Kruss model K10ST digital tensiometer with an accuracy of ± 0.1 $mN \cdot m^{-1}$. Equilibrium surface tension measurements were made using a platinum Wilhlemy plate at ambient temperature. Table B-3 lists the equilibrium surface tension data measured for each corresponding solution concentration. Figure B-3(a) illustrates the equilibrium surface tension as a function of AFFF solution concentration, and figure B-3(b) depicts dynamic surface tension as a function of surface age for each respective AFFF solution concentration. Dynamic surface tension measurements were conducted using a Kruss model DVT30 drop volume tensiometer using conventional operating procedures.

Table B-3. Equilibrium Surface Tension of Various AFFF Solution Concentrations

Solution Description	Equilibrium Surface Tension - σ ($mN \cdot m^{-1}$)
100% AFFF (pure concentrate)	23.6
12% AFFF	18.8
9% AFFF	18.2
6% AFFF	17.4
3% AFFF	16.8
0.3% AFFF	17.4
0.03% AFFF	37.3
Water	72.14

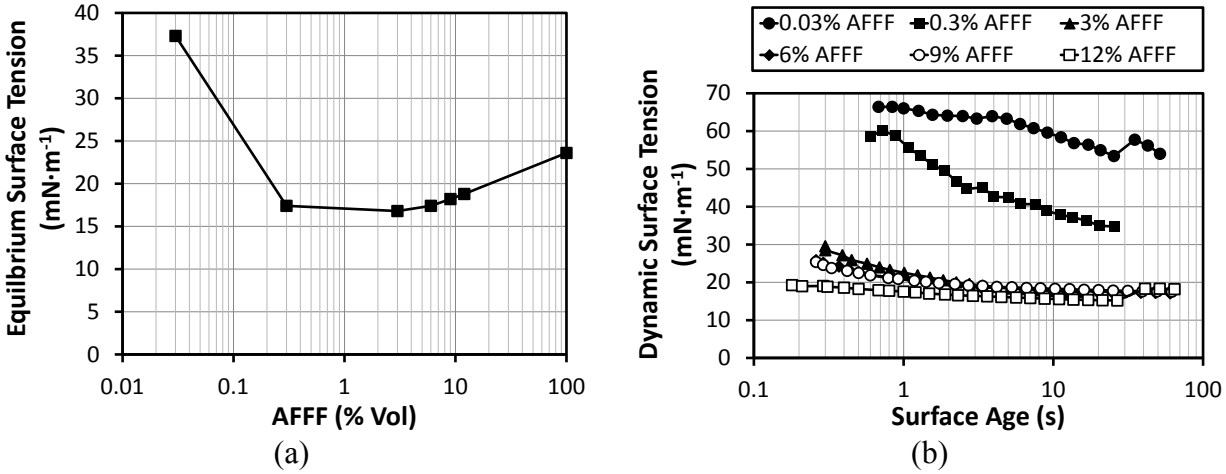

(a) (b)

Figure B-3. (a) Equilibrium Surface Tension vs AFFF Solution Concentration and (b) Dynamic Surface Tension vs Surface Age for Various AFFF Solution Concentrations

Both the equilibrium and dynamic surface tension of AFFF are important material properties that have exhibited the most divergence compared to water results due to the surfactant nature of AFFF's constituents. Surface tension can significantly affect firefighting jet breakup rate, mean droplet size distribution, and potentially other flow phenomena not characterized in the present study. For AFFF solution dilutions within the same order of magnitude of the manufacturer's recommended dilution with water, differences in equilibrium and dynamic surface tension are nearly negligible. This indicates AFFF ingredients are selectively proportioned to carefully optimize properties like surface tension, indirectly supporting evidence of past work conducted by Hyland and Williams [B-2].

B.4 INDEX OF REFRACTION.

Refractive measurements were executed on various AFFF solution concentrations by West Virginia University personnel in the aqueous firefighting agent application laboratory on MIL-SPEC C301MS 3% AFFF. All measurements were conducted at approximately 298 K. An Atago Palette PR-32 alpha digital refractometer was used to measure the degrees Brix with ±0.1% accuracy of each AFFF solution. The instrument is temperature compensated and linearly

calibrated using distilled water and a series of small AFFF solution samples representing various dilution levels. Ten measurements were taken and averaged for each solution. Brix measurements are commonly used to measure the sucrose content of liquids for the food and agriculture industry. Brix values were converted to an index of refraction based on available sucrose conversion tables [B-3]. The results are shown in figure B-4(a) for select AFFF solution concentrations mixed with tap water as well as distilled water. Index of refraction measurements with respect to AFFF solution concentration are illustrated in figure B-4(b). Table B-4 summarizes the information shown in figure B-4(a) and (b).

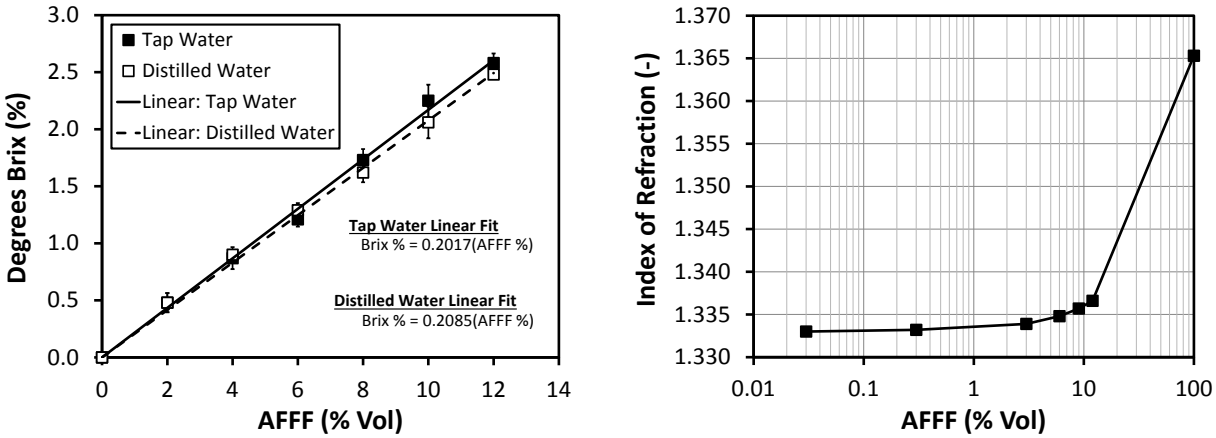

(a) (b)

Figure B-4. (a) Degrees Brix vs AFFF Solution Concentration and (b) Index of Refraction vs AFFF Solution Concentration

Table B-4. Measured Degrees Brix and the Corresponding Index of Various AFFF Solution Dilutions

Solution Description	Degrees Brix (%)	Index of Refraction (-)
100% AFFF (pure concentrate)	20.9	1.3653
12% AFFF	2.5	1.3366
9% AFFF	1.9	1.3357
6% AFFF	1.3	1.3349
3% AFFF	0.6	1.3339
0.3% AFFF	0.1	1.3334
0.03% AFFF	0.0	1.3330
Water	0.0	1.3330

The index of refraction is a key material property that must be defined before phase Doppler particle analysis can occur, as run-time algorithms used to calculate droplet size by measuring scattered light are dependent upon the amount of refraction generated by the liquid in the droplet. Figure B-4(a) and (b) as well as table B-4 show that the index of refraction varies negligibly for AFFF solution concentrations of practical interest to the ARFF community.

B.5 REFERENCES.

B-1. ASTM Standard D445-11a, 2013, Historical Standard: "ASTM D445-11a Standard Test Method for Kinematic Viscosity of Transparent and Opaque Liquids (and Calculation of Dynamic Viscosity)," ASTM International, West Conshohocken, Pennsylvania, DOI: 10.1520/D445-11a, available at www.astm.org (date last visited February 25, 2015).

B-2. Hyland, E.K. and Williams, B.A., "Characterization of the Dynamic Surface Tension of Aqueous Film Forming Foam," NRL Report NRL/MR/6180--04-8749, Naval Technology Center for Safety and Survivability, Washington, D.C., 2004.

B-3. United States Department of Agriculture, "Sucrose Conversion Table: Technical Inspection Procedures," Processed Products Branch, File Code 135-A-50, 1970.

APPENDIX C—FIREFIGHTING JET PHASE DOPPLER DATA

Phase Doppler data are presented for all five firefighting jet pressure-flow rate combinations examined in the laboratory. A case summary of data collected is illustrated in figure 43 and listed in table 6. The experimental approach is discussed in section 4.4. All profile data in this appendix compares water and 6% aqueous film forming foam (AFFF) jets. The results collected in profile form are mean axial droplet velocity, mean vertical droplet velocity; mean droplet diameter, root mean square (RMS) droplet diameter; and Sauter mean droplet diameter. Each flow parameter is defined in section 6.3.2. Plot layout and features, such as ±RMS velocity magnitude bars and references to error estimation, are also identical to those shown in figure 94.

Vertical profile measurements spanning the vertical height of each firefighting jet were recorded. A select number of horizontal profiles were also recorded for medium-flow, medium-pressure jets to measure the full jet width in areas near the nozzle, and approximate half jet widths further downstream where the phase Doppler particle analysis traverse was limited in its reach. Select axial and vertical gaseous (air) velocity estimates are also provided for this jet configuration. Droplet size distribution measurements presented similar to those in figure 91 are also presented at the end of each section highlighting phase Doppler sampling locations where the maximum profile, mean axial droplet velocity was measured.

C.1 LOW-FLOW, LOW-PRESSURE FIREFIGHTING JET DATA.

The low-flow, low-pressure firefighting jet data are shown in figures C-1 through C-11.

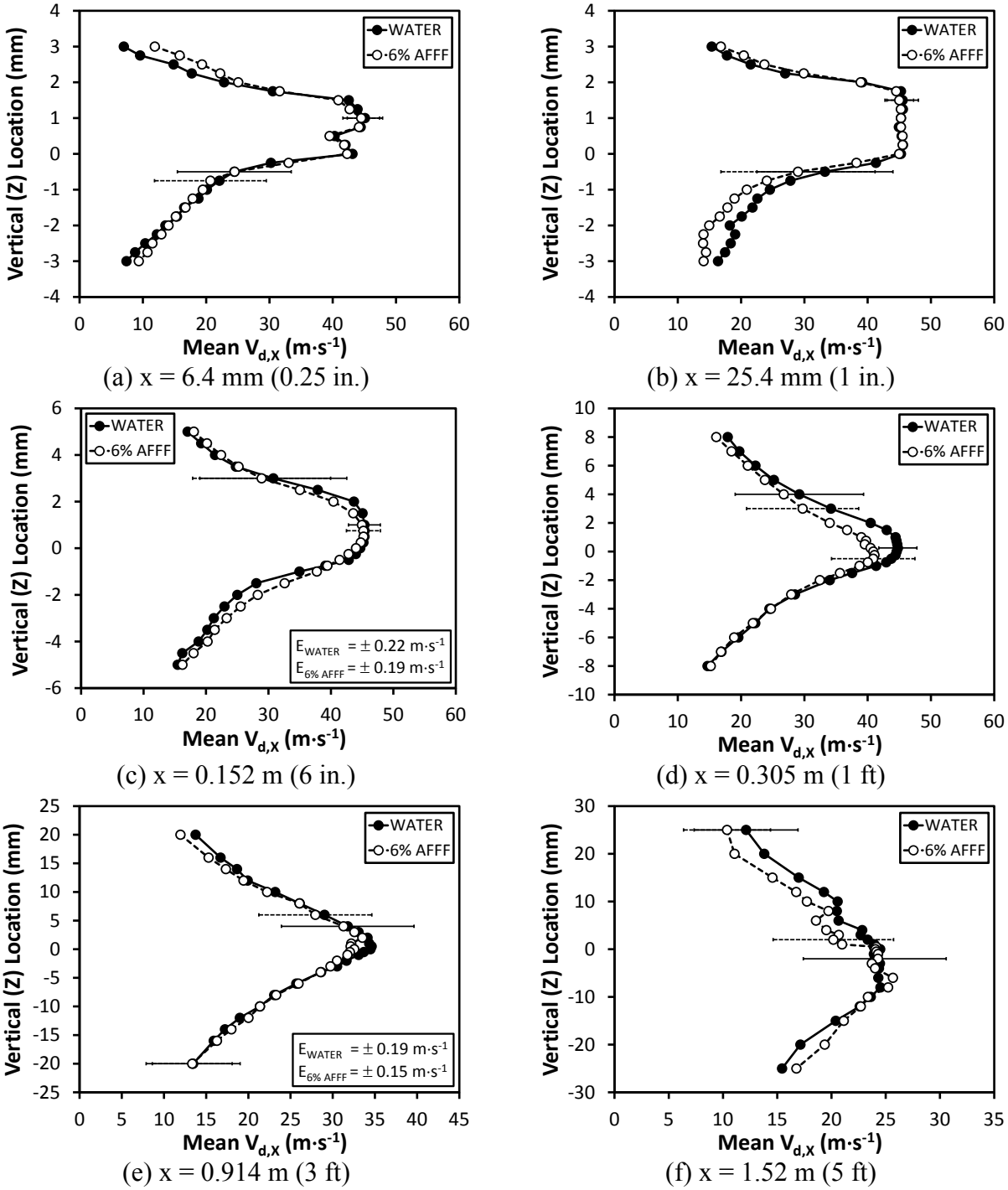

(a) x = 6.4 mm (0.25 in.)

(b) x = 25.4 mm (1 in.)

(c) x = 0.152 m (6 in.)

(d) x = 0.305 m (1 ft)

(e) x = 0.914 m (3 ft)

(f) x = 1.52 m (5 ft)

Figure C-1. Near-Field, Low-Flow, Low-Pressure Jet Vertical Profiles of Mean Axial Droplet Velocity

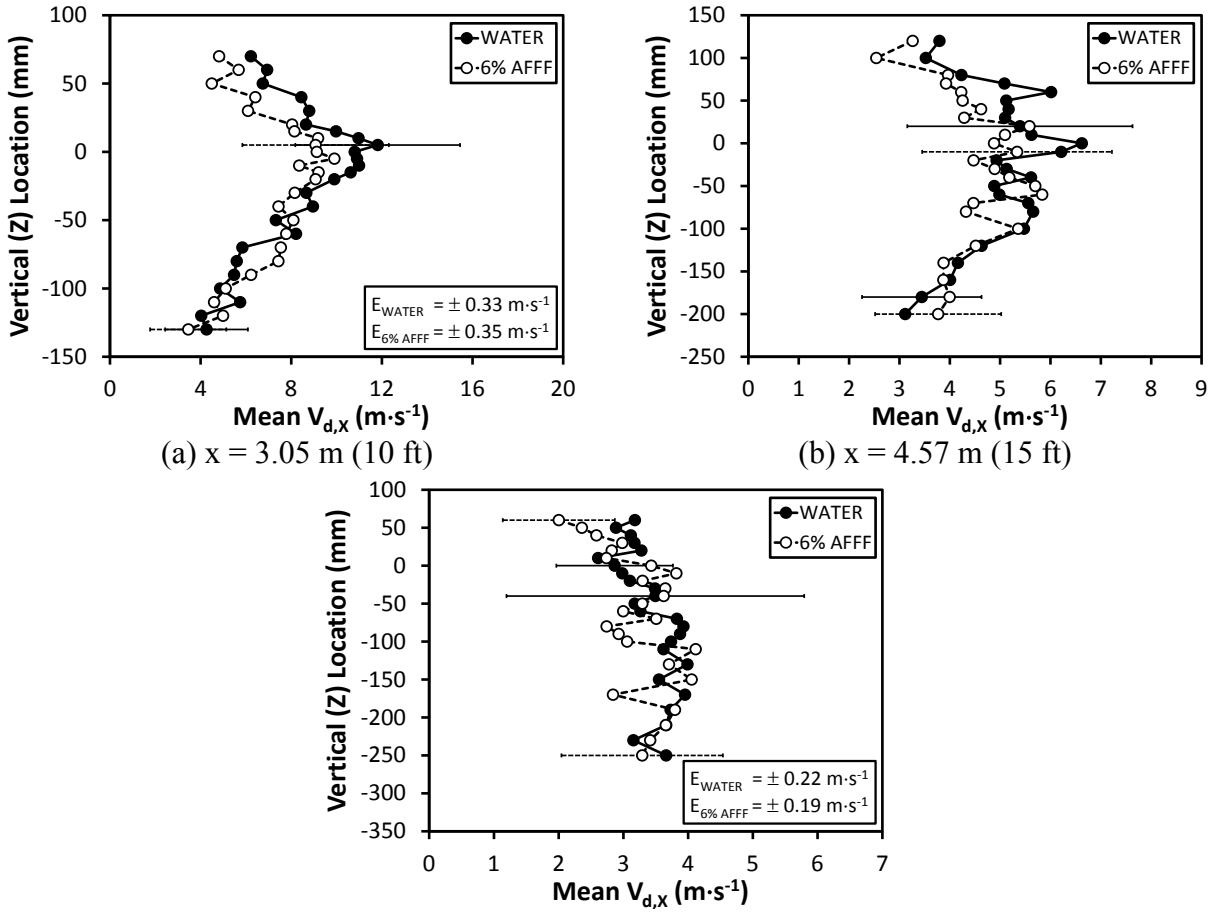

Figure C-2. Far-Field, Low-Flow, Low-Pressure Jet Vertical Profiles of Mean Axial Droplet Velocity

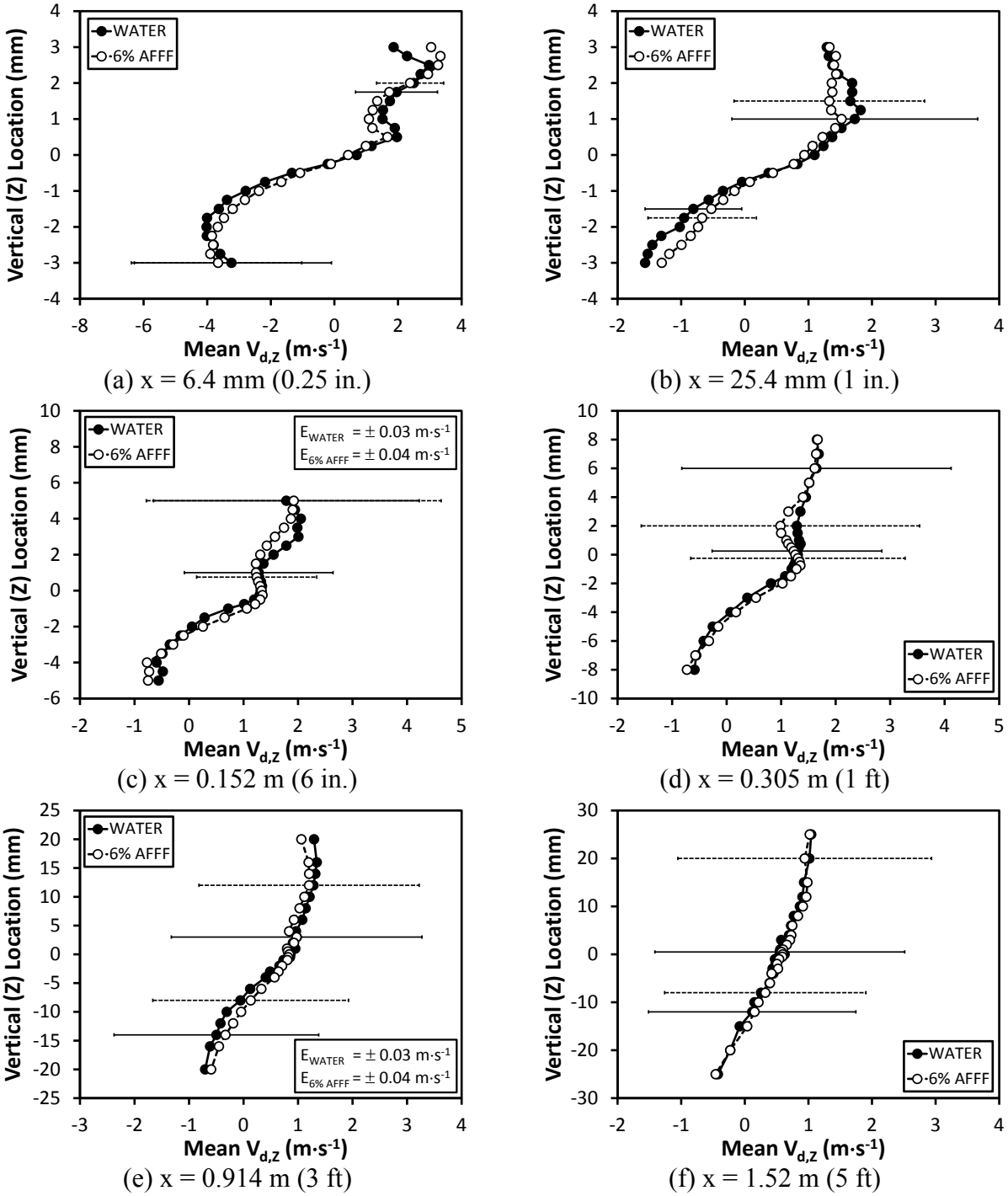

(a) x = 6.4 mm (0.25 in.)

(b) x = 25.4 mm (1 in.)

(c) x = 0.152 m (6 in.)

(d) x = 0.305 m (1 ft)

(e) x = 0.914 m (3 ft)

(f) x = 1.52 m (5 ft)

Figure C-3. Near-Field, Low-Flow, Low-Pressure Jet Vertical Profiles of Mean Vertical Droplet Velocity

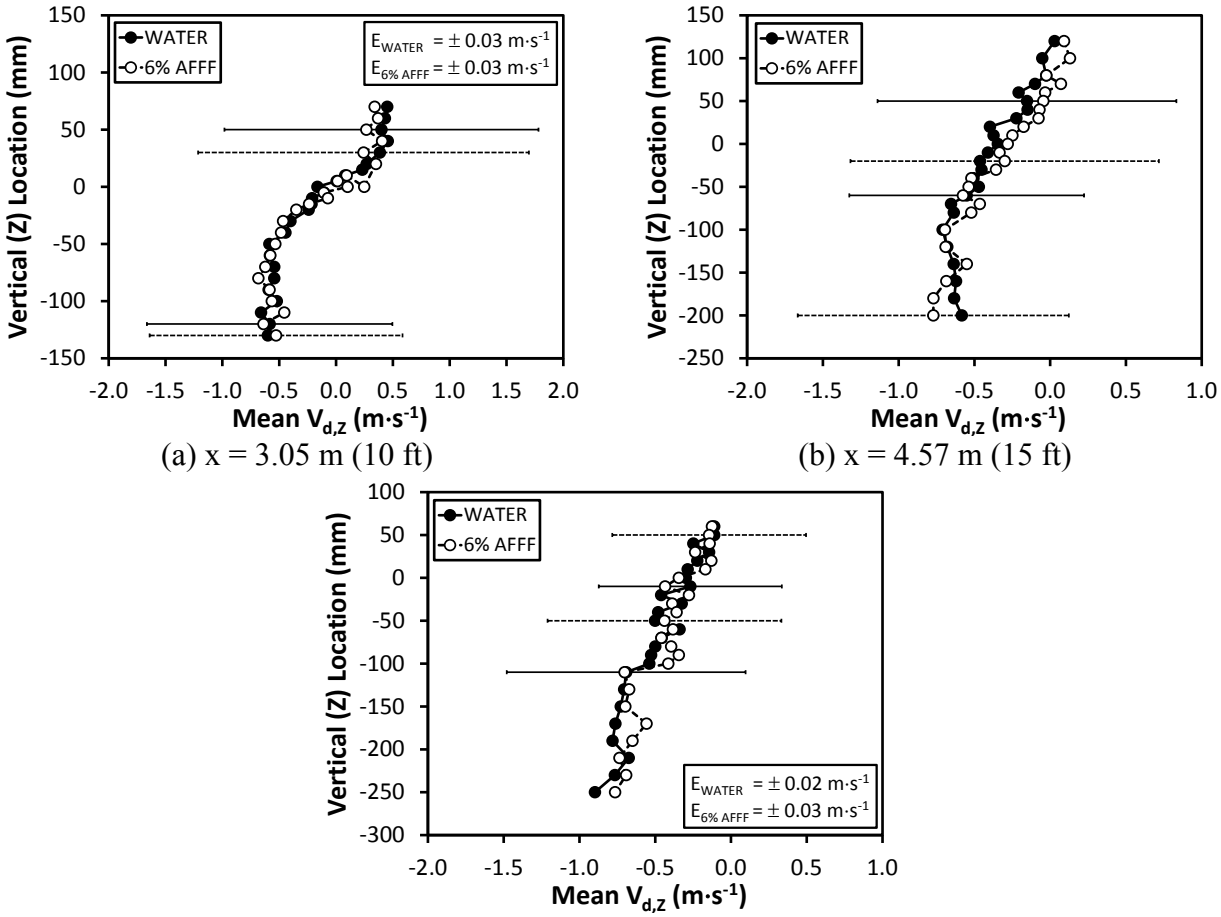

Figure C-4. Far-Field, Low-Flow, Low-Pressure Jet Vertical Profiles of Mean Vertical Droplet Velocity

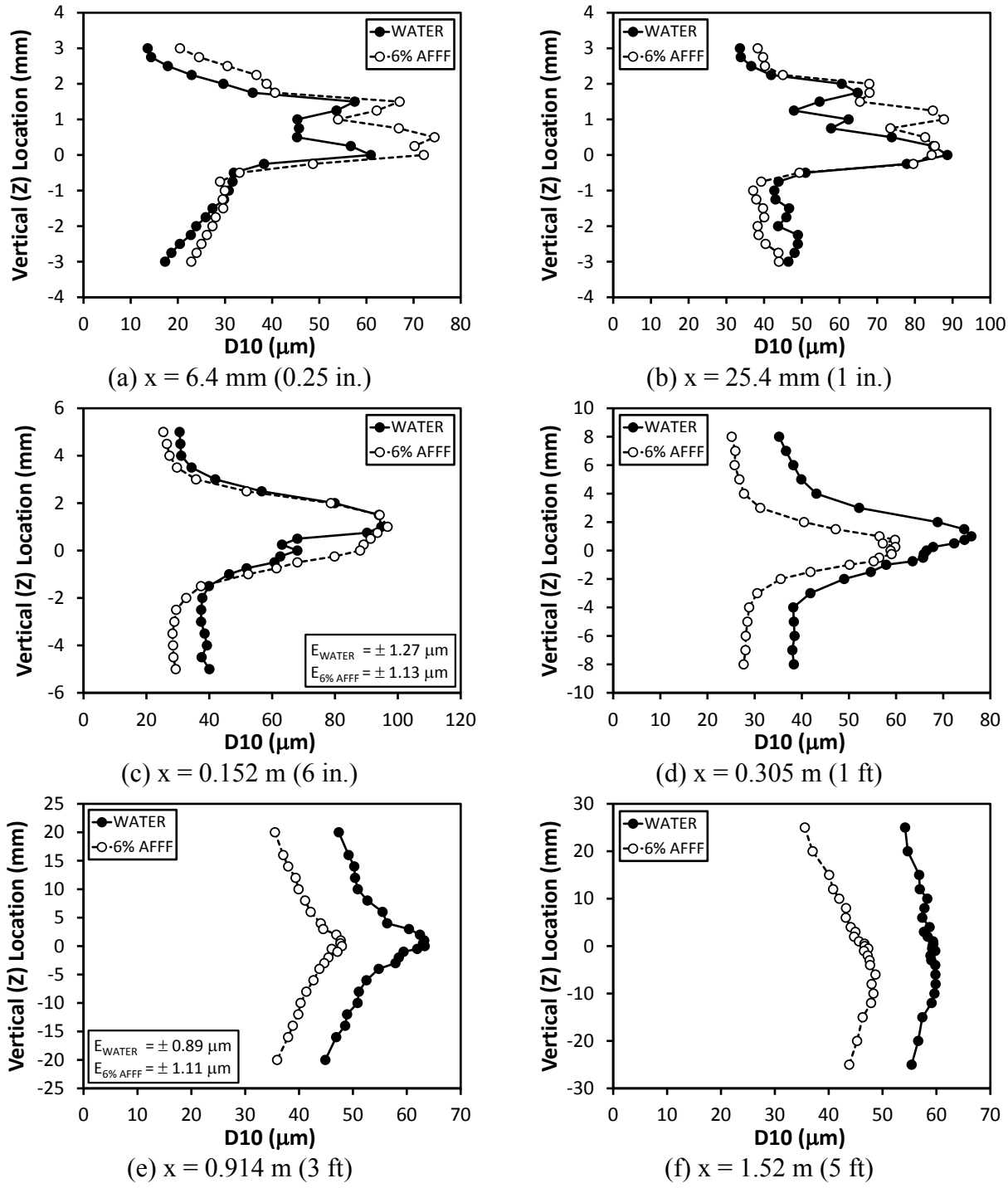

(a) x = 6.4 mm (0.25 in.)

(b) x = 25.4 mm (1 in.)

(c) x = 0.152 m (6 in.)

(d) x = 0.305 m (1 ft)

(e) x = 0.914 m (3 ft)

(f) x = 1.52 m (5 ft)

Figure C-5. Near-Field, Low-Flow, Low-Pressure Jet Vertical Profiles of Mean Droplet Diameter

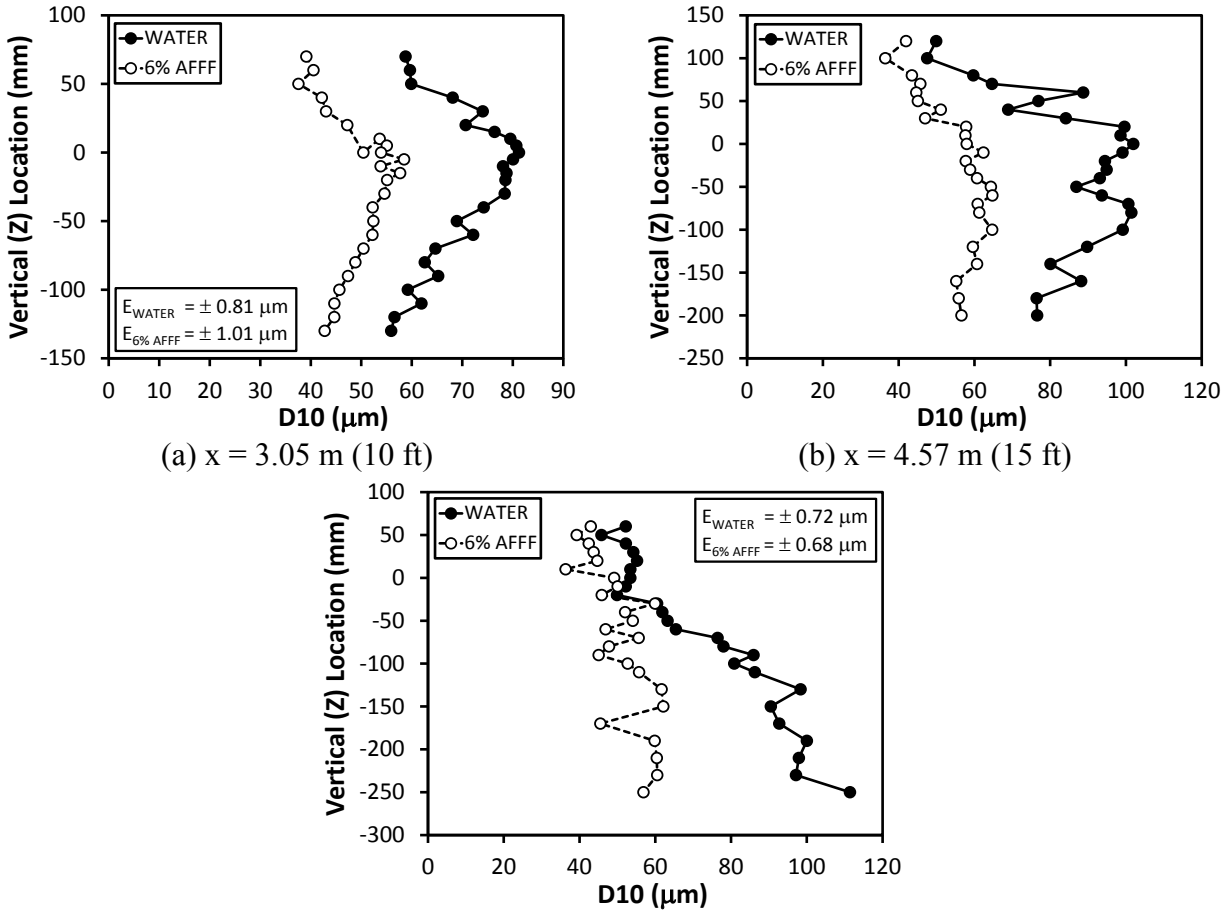

(a) x = 3.05 m (10 ft)

(b) x = 4.57 m (15 ft)

(c) x = 6.10 m (20 ft)

Figure C-6. Far-Field, Low-Flow, Low-Pressure Jet Vertical Profiles of Mean Droplet Diameter

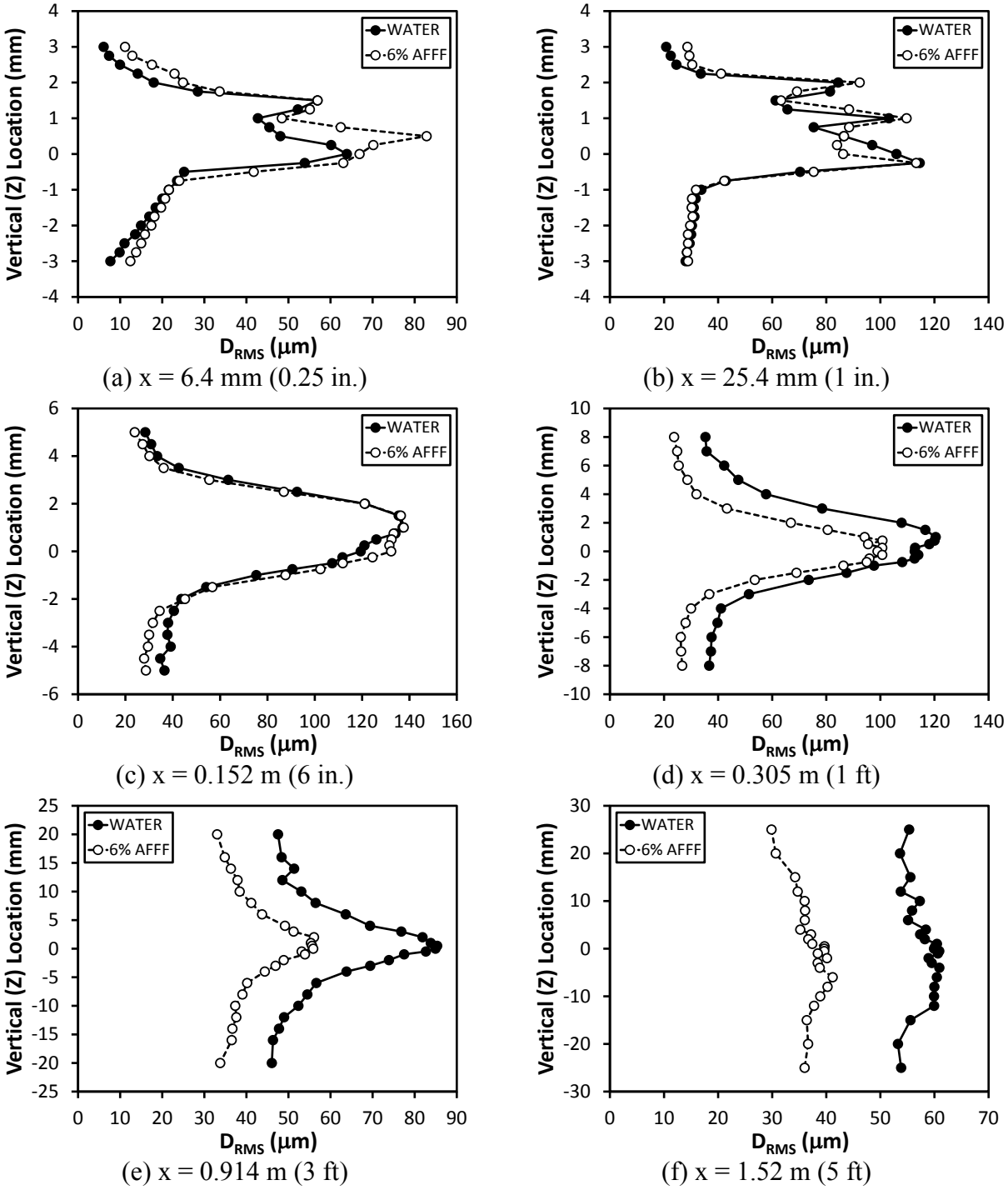

(a) x = 6.4 mm (0.25 in.)

(b) x = 25.4 mm (1 in.)

(c) x = 0.152 m (6 in.)

(d) x = 0.305 m (1 ft)

(e) x = 0.914 m (3 ft)

(f) x = 1.52 m (5 ft)

Figure C-7. Near-Field, Low-Flow, Low-Pressure Jet Vertical Profiles of RMS Droplet Diameter

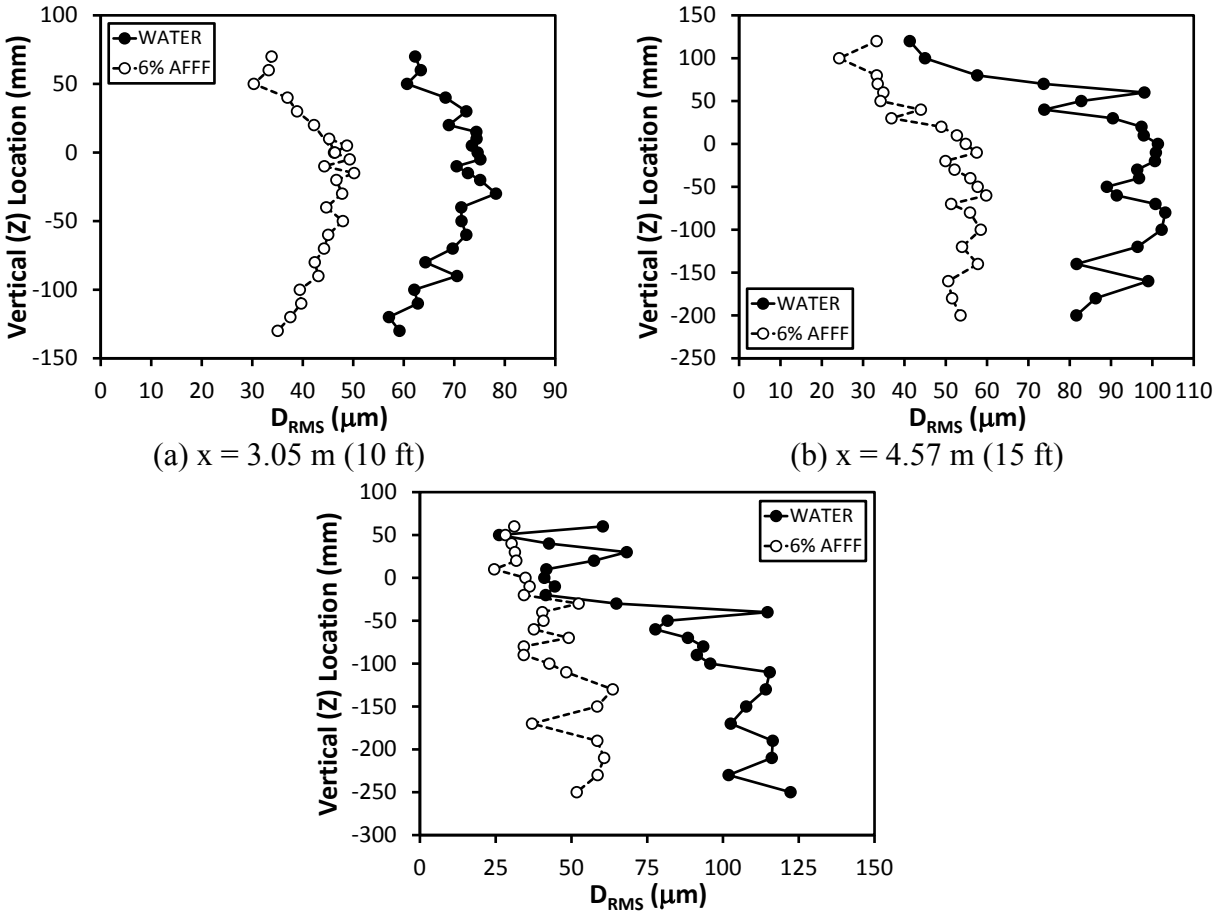

(a) x = 3.05 m (10 ft)

(b) x = 4.57 m (15 ft)

(c) x = 6.10 m (20 ft)

Figure C-8. Far-Field, Low-Flow, Low-Pressure Jet Vertical Profiles of RMS Droplet Diameter

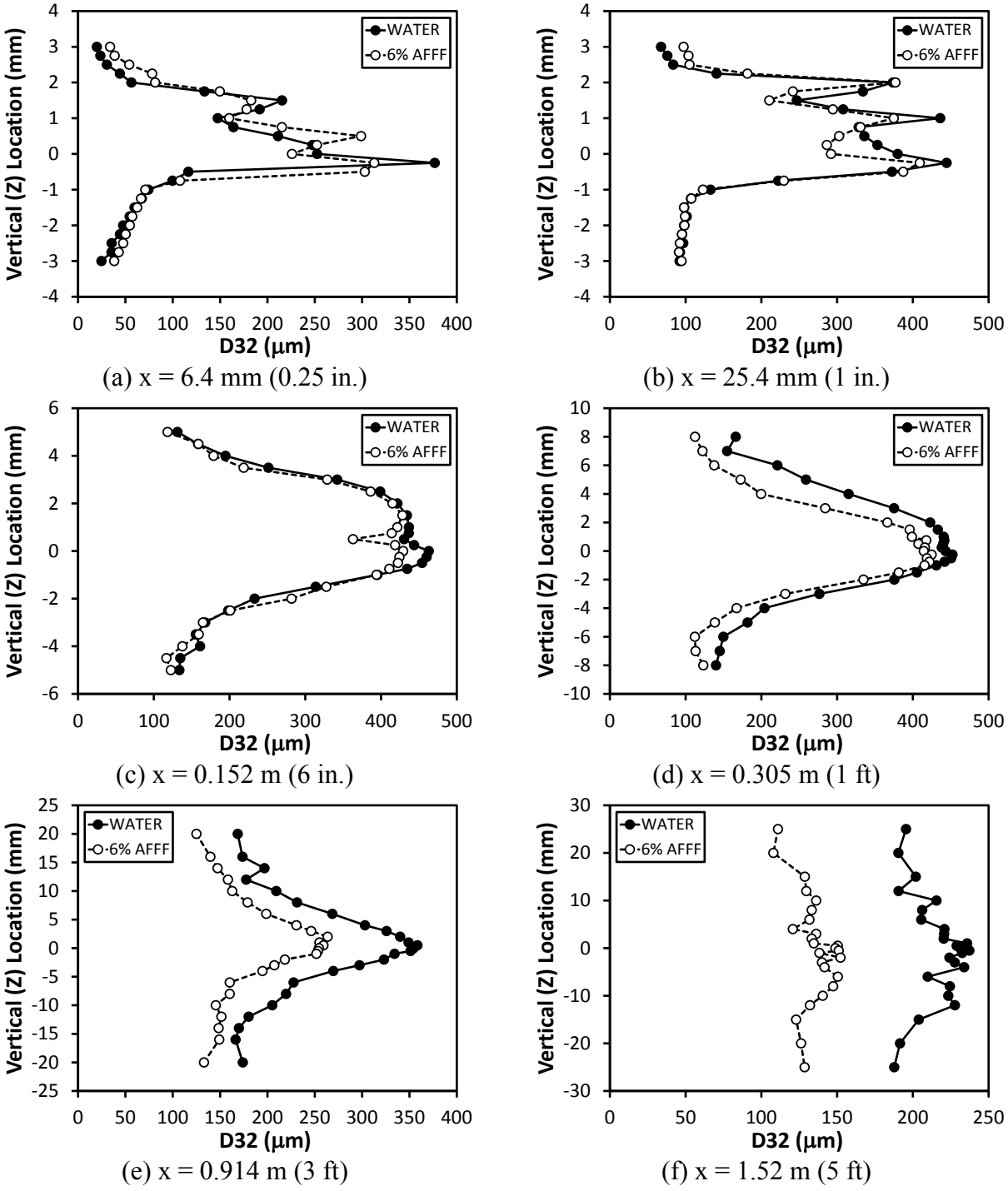

(a) x = 6.4 mm (0.25 in.)

(b) x = 25.4 mm (1 in.)

(c) x = 0.152 m (6 in.)

(d) x = 0.305 m (1 ft)

(e) x = 0.914 m (3 ft)

(f) x = 1.52 m (5 ft)

Figure C-9. Near-Field, Low-Flow, Low-Pressure Jet Vertical Profiles of Sauter Mean Droplet Diameter

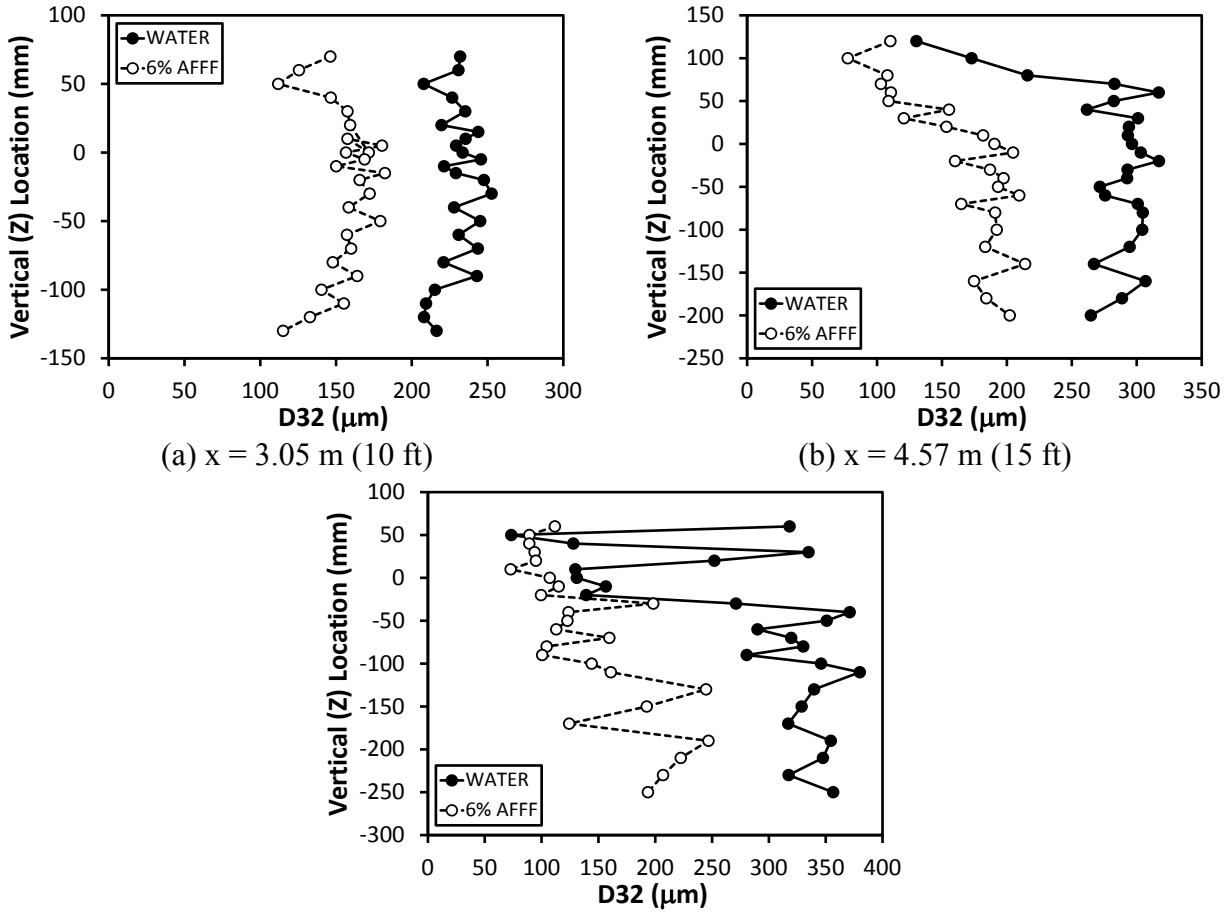

(a) x = 3.05 m (10 ft)

(b) x = 4.57 m (15 ft)

(c) x = 6.10 m (20 ft)

Figure C-10. Far-Field, Low-Flow, Low-Pressure Jet Vertical Profiles of Sauter Mean Droplet Diameter

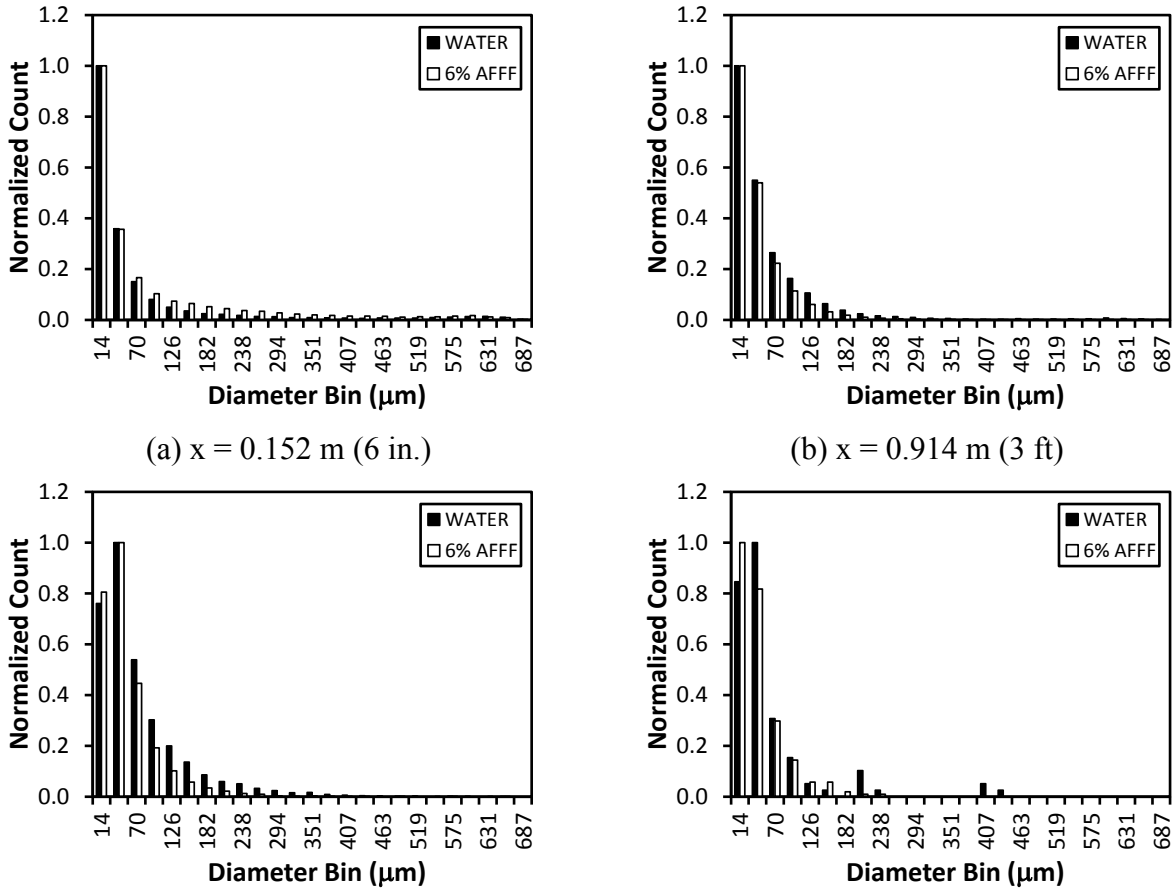

(a) x = 0.152 m (6 in.)

(b) x = 0.914 m (3 ft)

(c) x = 3.05 m (10 ft)

(d) x = 6.10 m (20 ft)

Figure C-11. Low-Flow, Low-Pressure Jet Droplet Size Distribution at the Maximum Profile, Mean Axial Droplet Velocity for Select Vertical Profiles

C.2 LOW-FLOW, HIGH-PRESSURE FIREFIGHTING JET DATA.

The low-flow, high-pressure firefighting jet data are shown in figures C-12 through C-22.

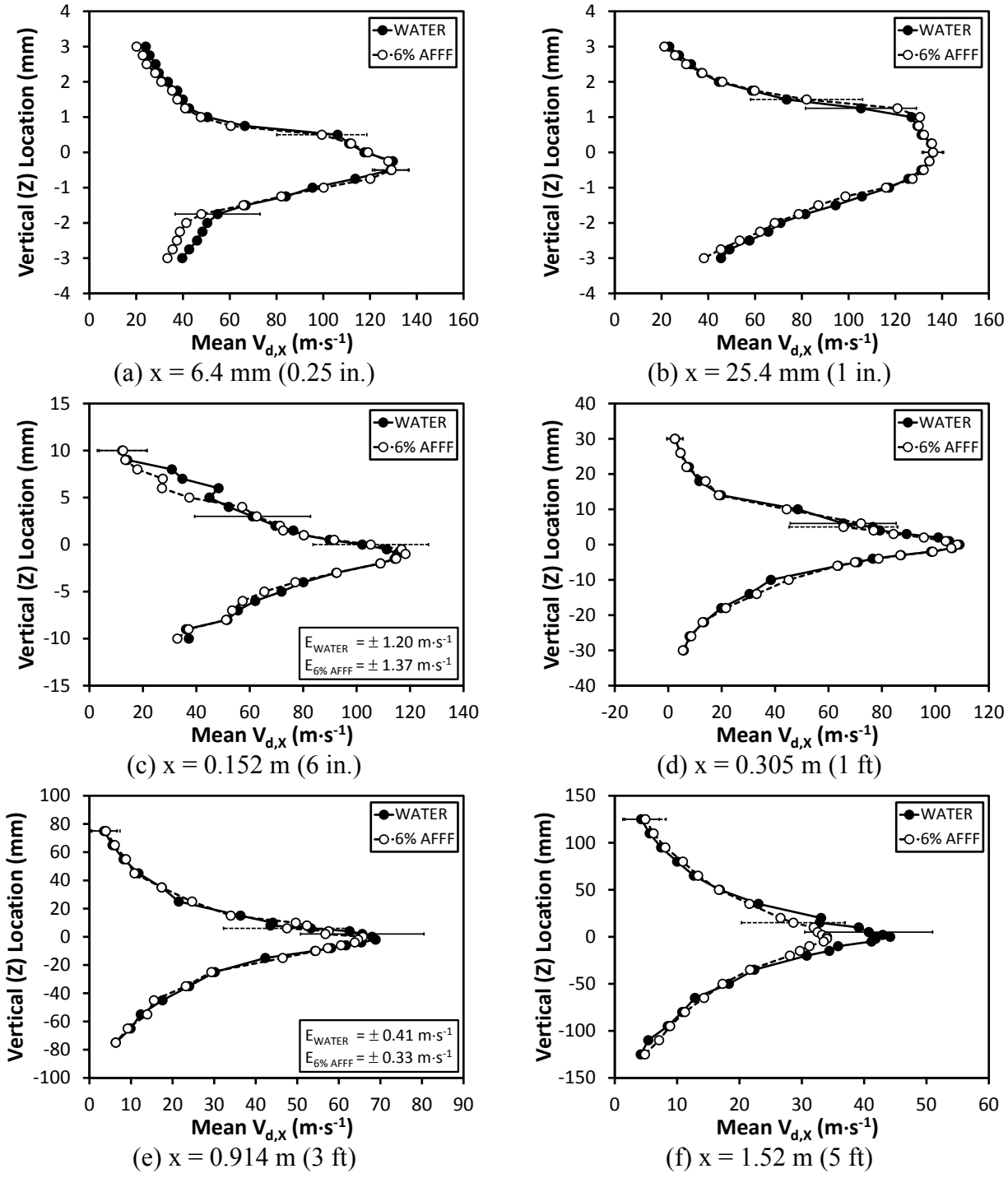

Figure C-12. Near-Field, Low-Flow, High-Pressure Jet Vertical Profiles of Mean Axial Droplet Velocity

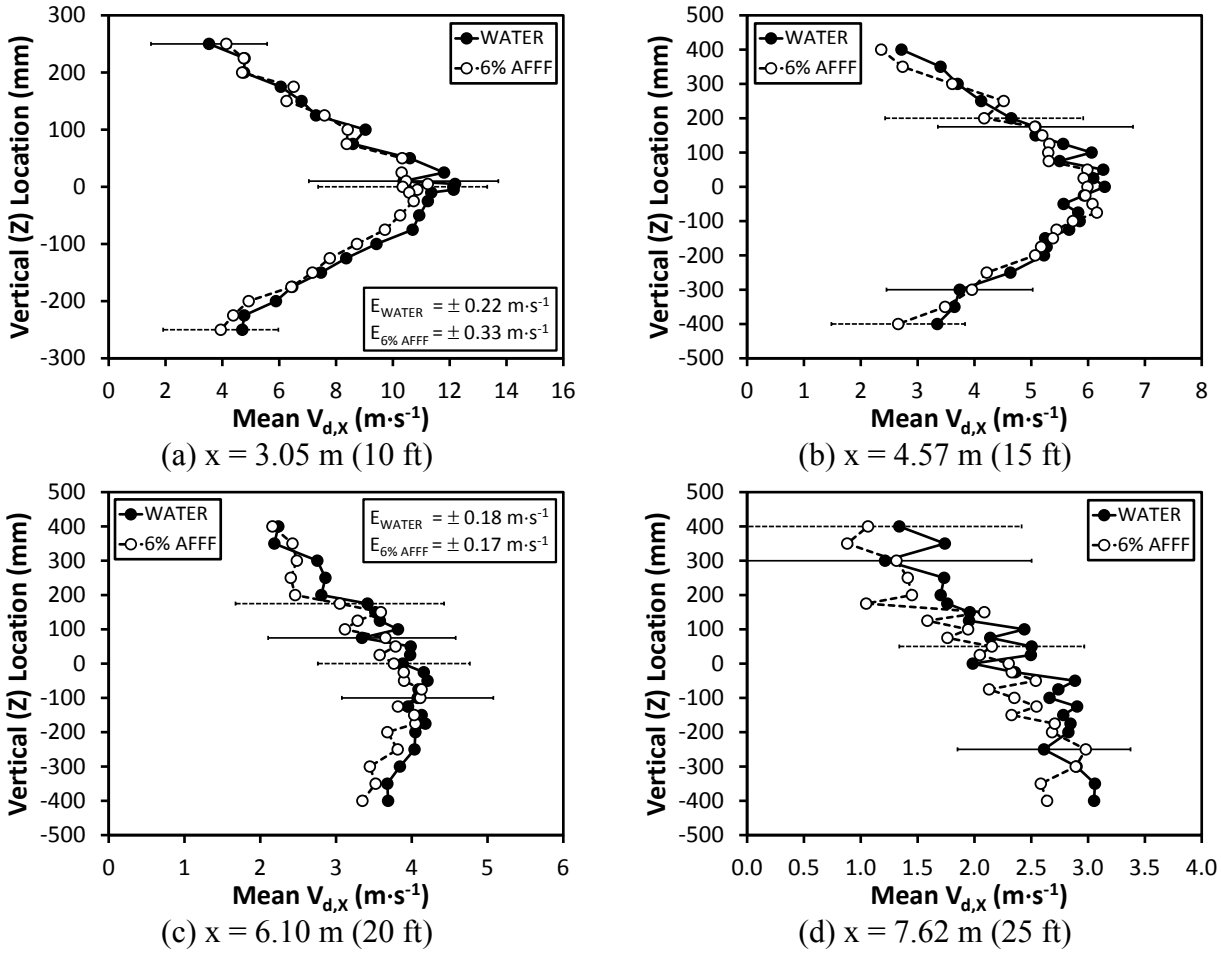

Figure C-13. Far-Field, Low-Flow, High-Pressure Jet Vertical Profiles of Mean Axial Droplet Velocity

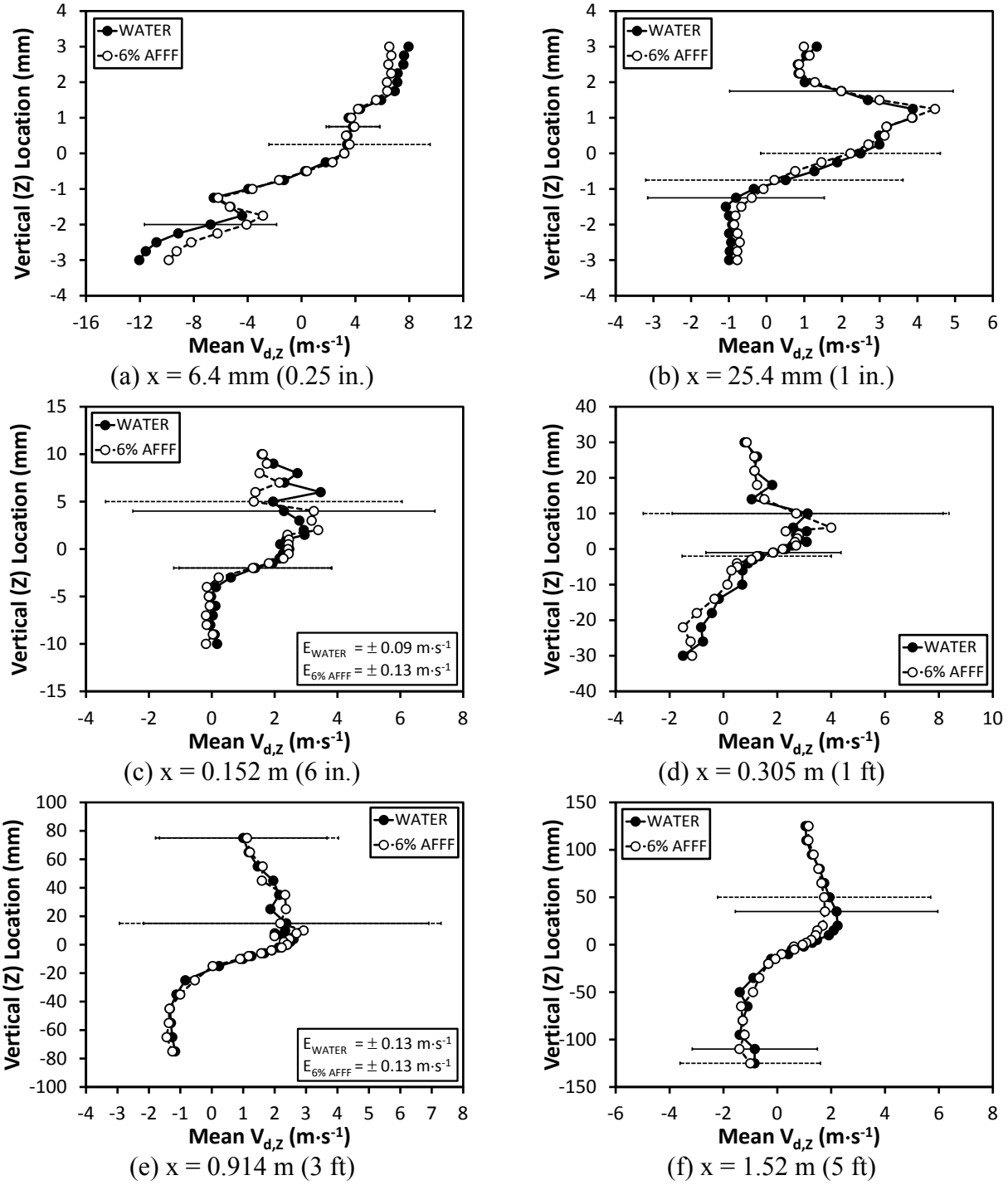

(a) x = 6.4 mm (0.25 in.)

(b) x = 25.4 mm (1 in.)

(c) x = 0.152 m (6 in.)

(d) x = 0.305 m (1 ft)

(e) x = 0.914 m (3 ft)

(f) x = 1.52 m (5 ft)

Figure C-14. Near-Field, Low-Flow, High-Pressure Jet Vertical Profiles of Mean Vertical Droplet Velocity

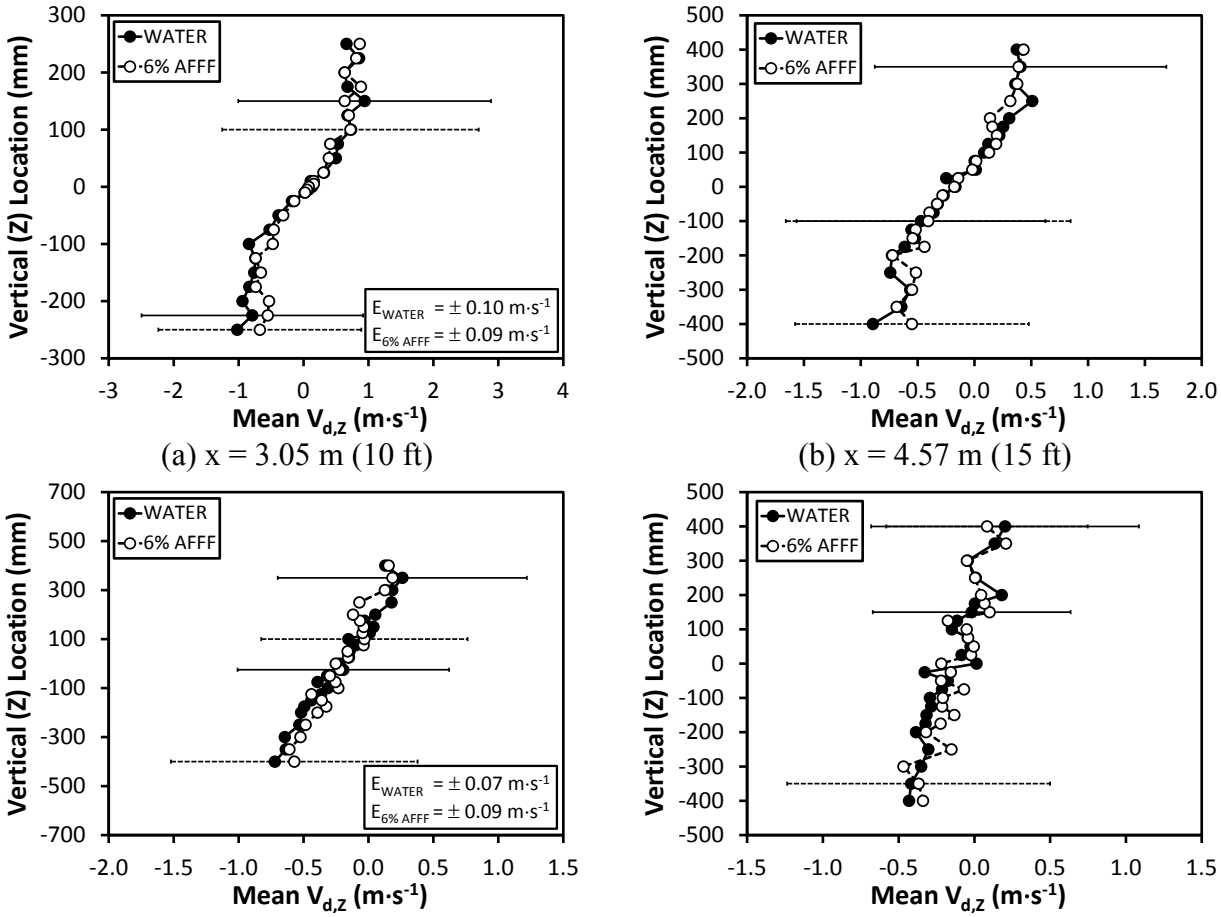

Figure C-15. Far-Field, Low-Flow, High-Pressure Jet Vertical Profiles of Mean Vertical Droplet Velocity

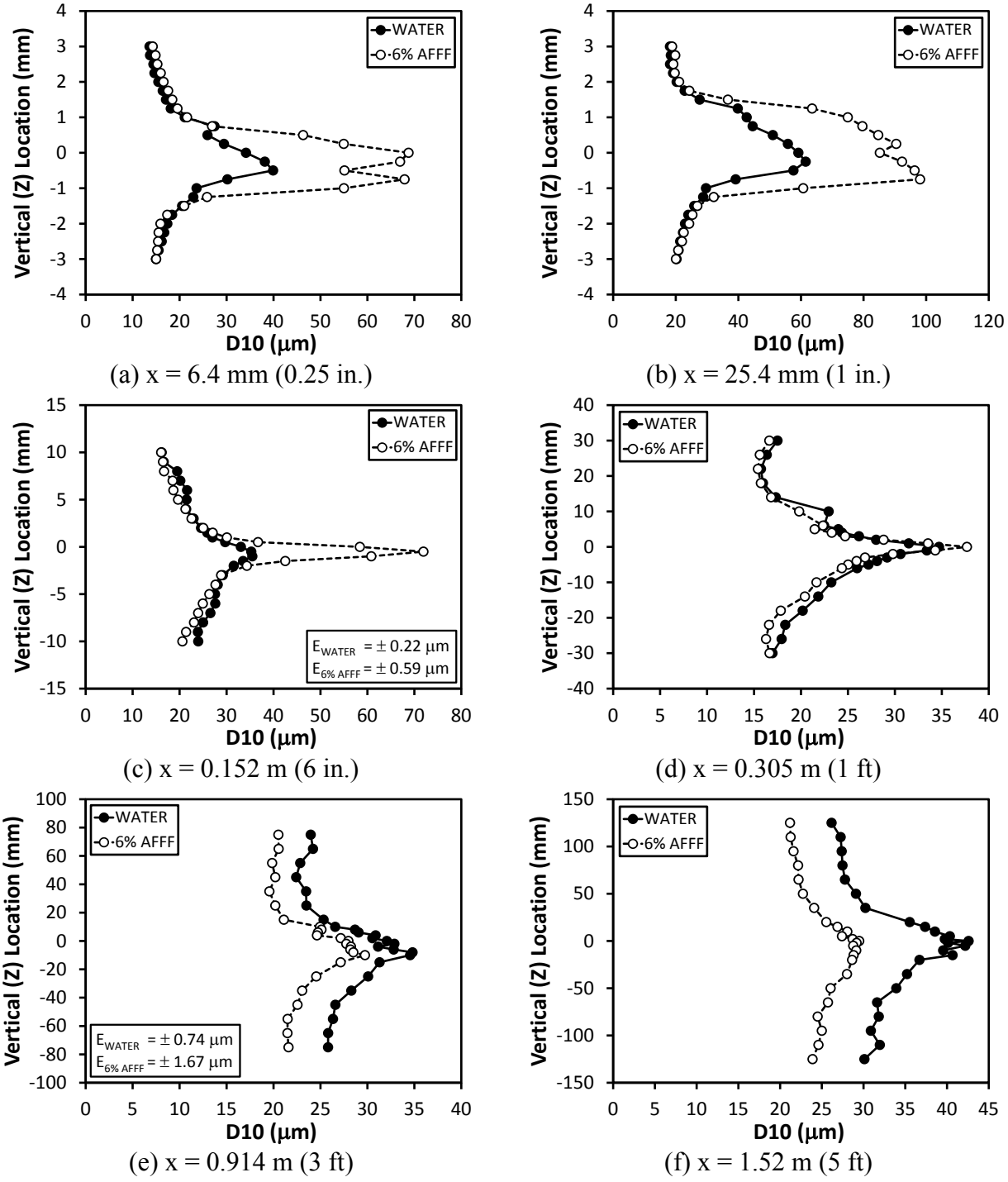

(a) x = 6.4 mm (0.25 in.)

(b) x = 25.4 mm (1 in.)

(c) x = 0.152 m (6 in.)

(d) x = 0.305 m (1 ft)

(e) x = 0.914 m (3 ft)

(f) x = 1.52 m (5 ft)

Figure C-16. Near-Field, Low-Flow, High-Pressure Jet Vertical Profiles of Mean Droplet Diameter

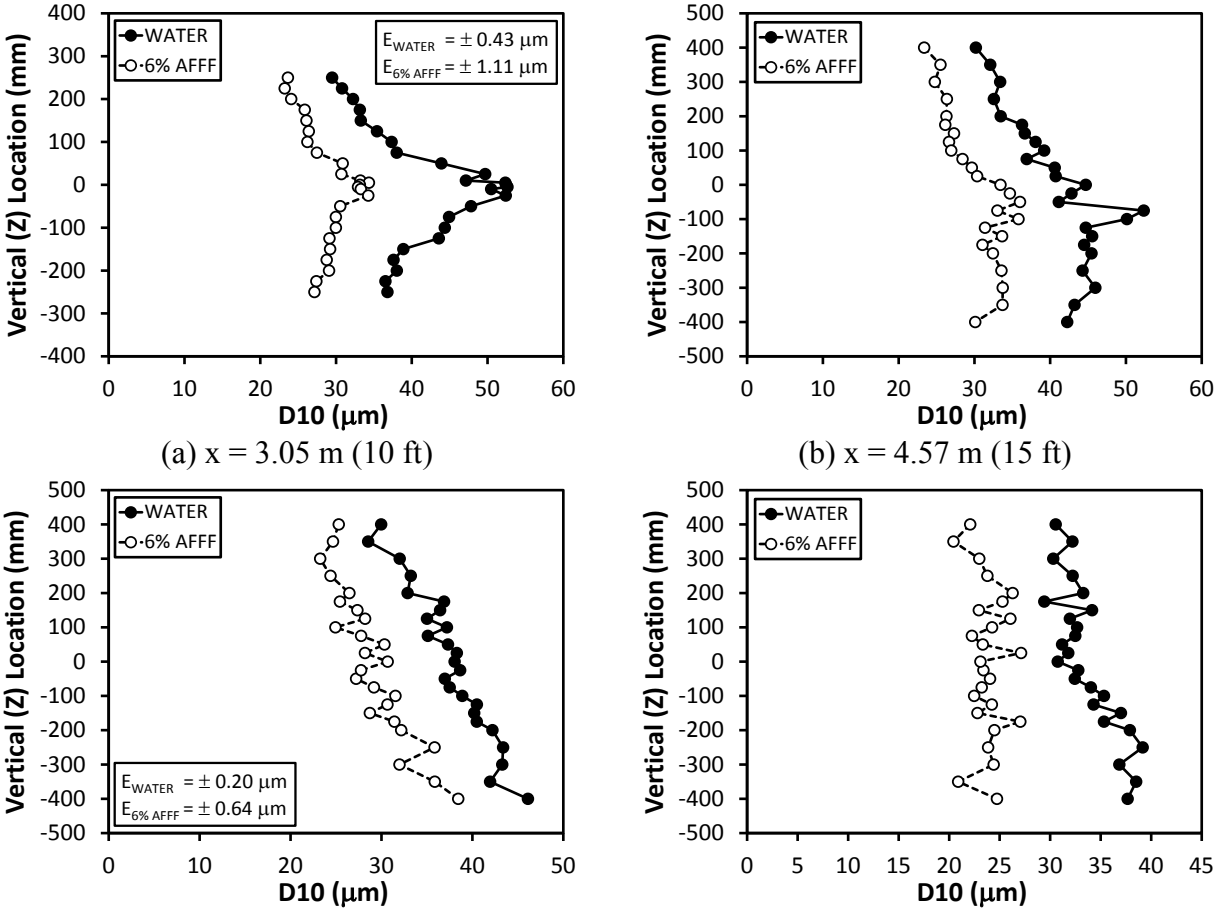

Figure C-17. Far-Field, Low-Flow, High-Pressure Jet Vertical Profiles of Mean Droplet Diameter

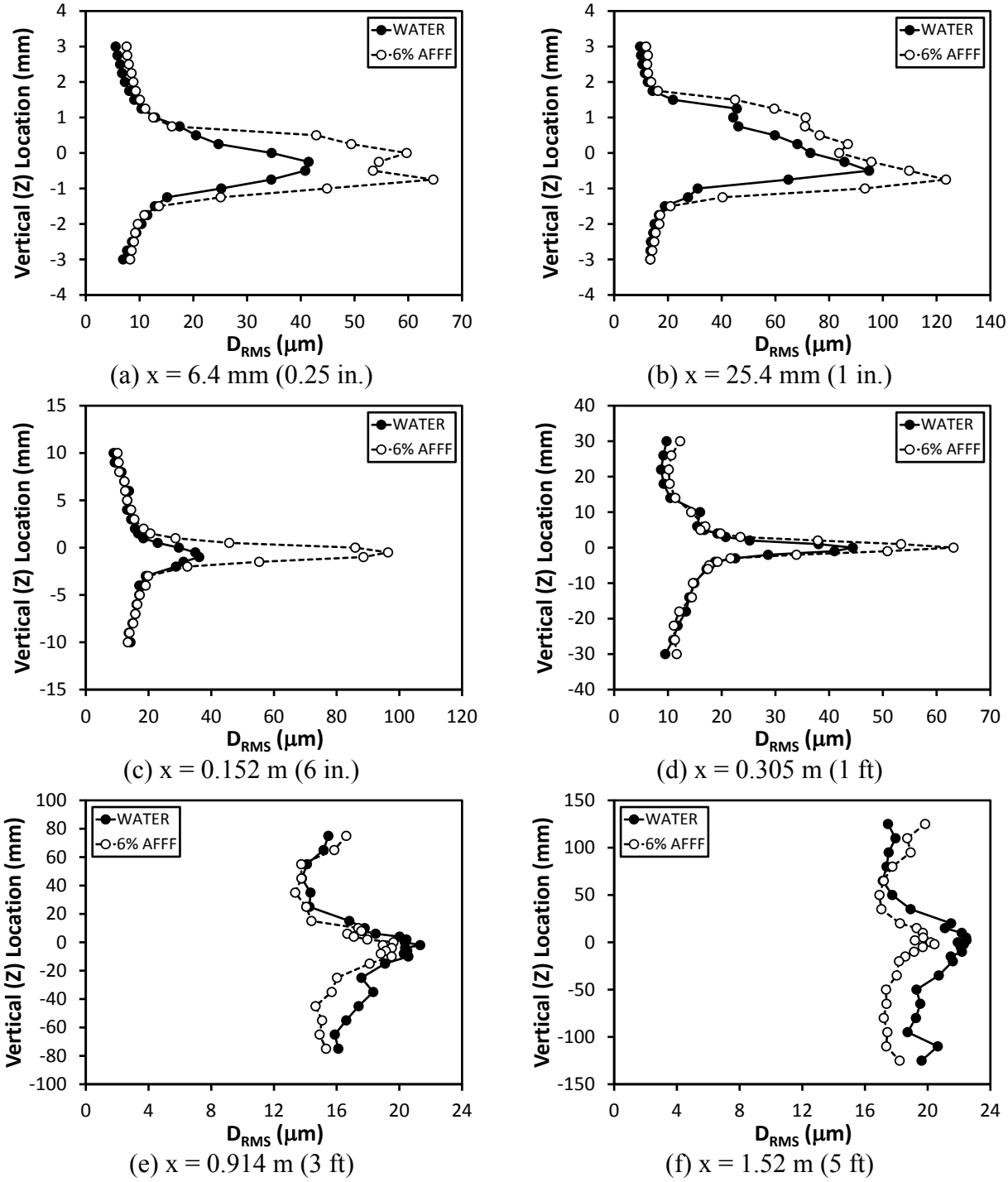

(a) x = 6.4 mm (0.25 in.)

(b) x = 25.4 mm (1 in.)

(c) x = 0.152 m (6 in.)

(d) x = 0.305 m (1 ft)

(e) x = 0.914 m (3 ft)

(f) x = 1.52 m (5 ft)

Figure C-18. Near-Field, Low-Flow, High-Pressure Jet Vertical Profiles of RMS Droplet Diameter

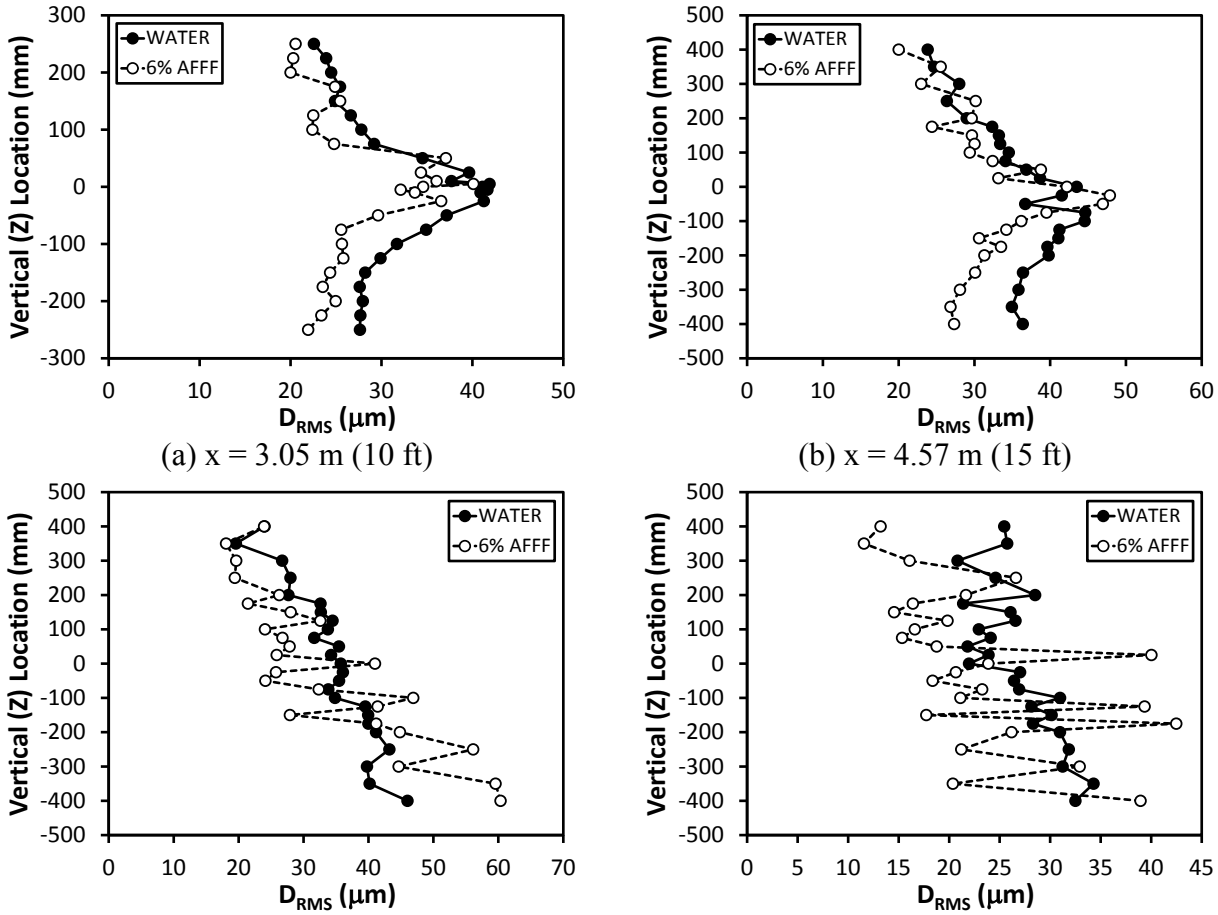

Figure C-19. Far-Field, Low-Flow, High-Pressure Jet Vertical Profiles of RMS Droplet Diameter

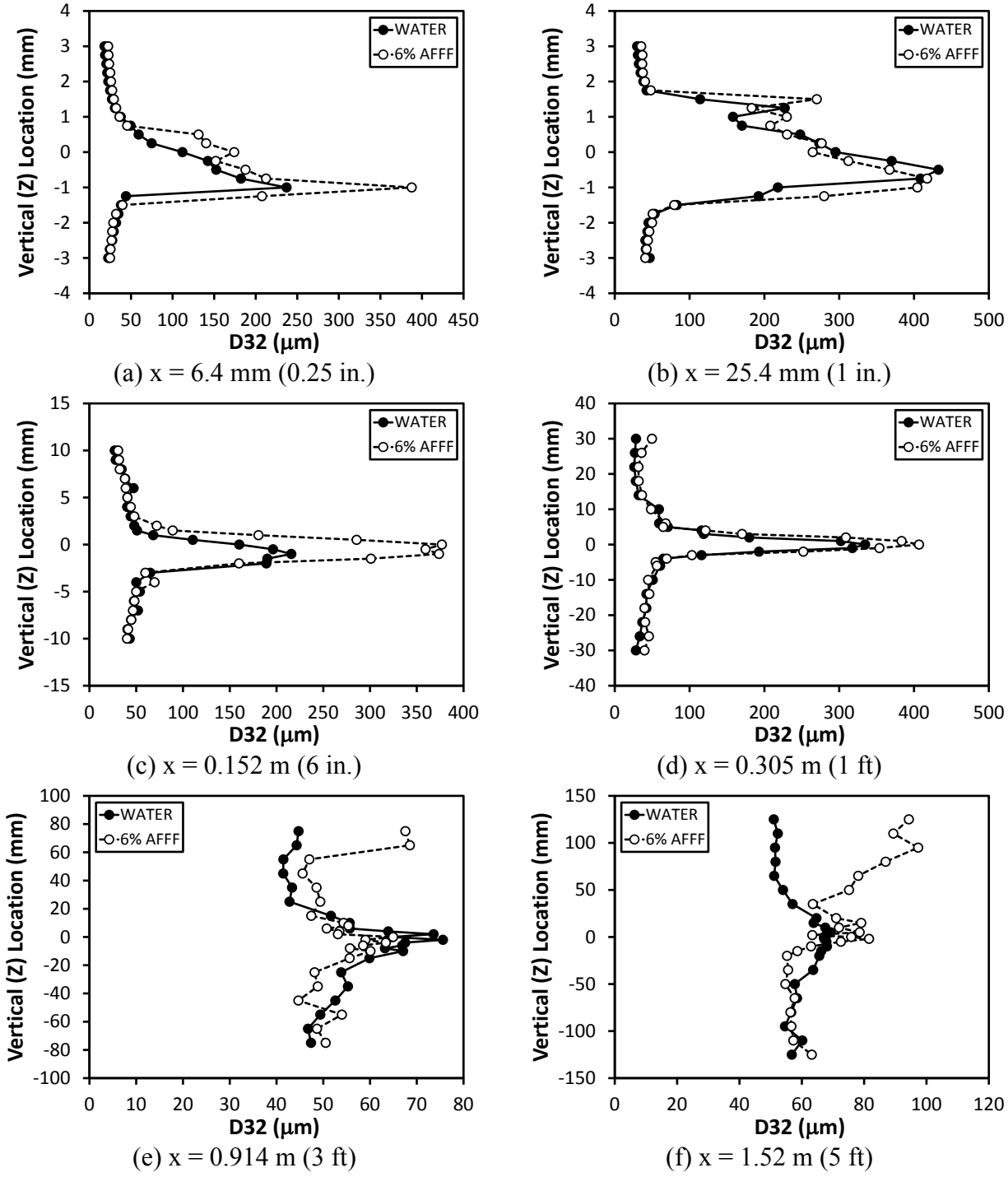

Figure C-20. Near-Field, Low-Flow, High-Pressure Jet Vertical Profiles of Sauter Mean Droplet Diameter

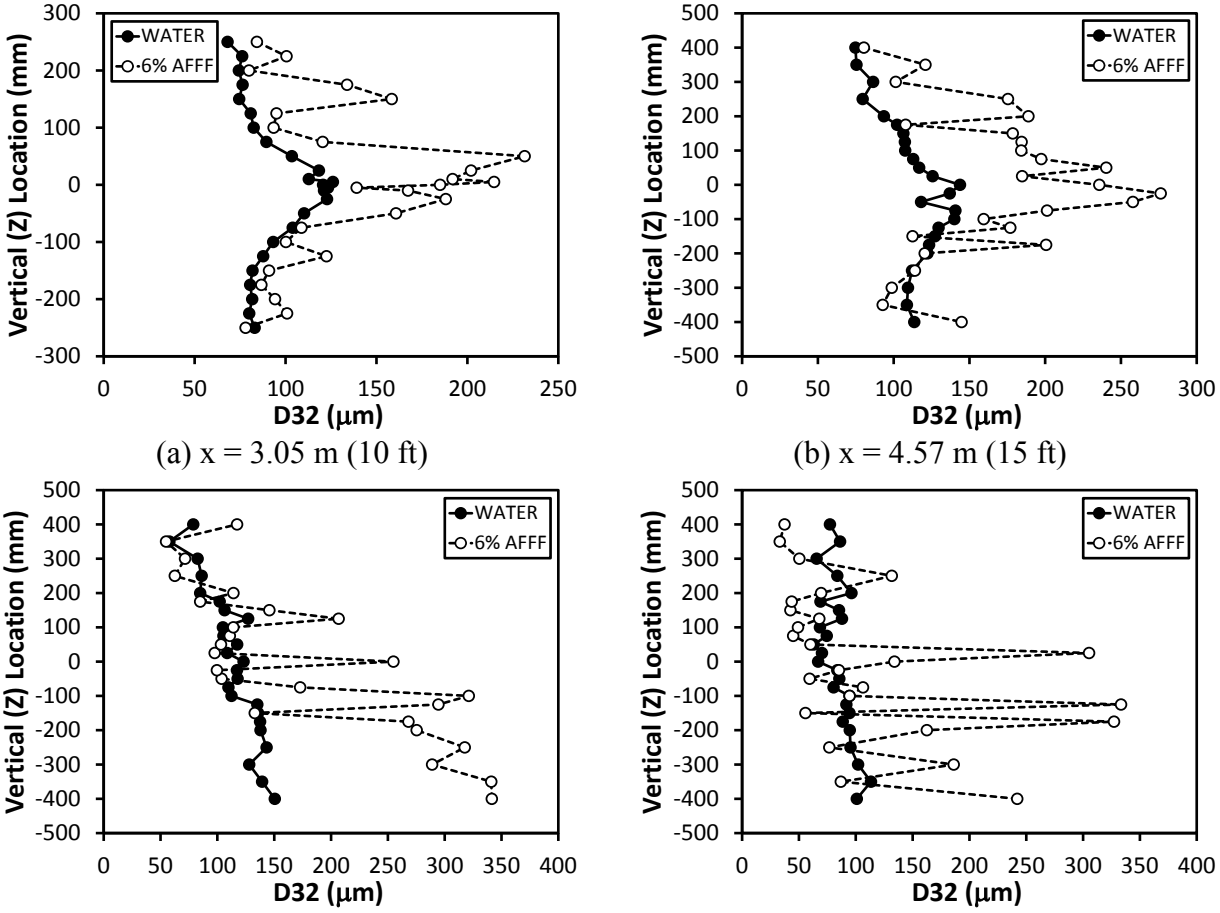

(a) x = 3.05 m (10 ft)

(b) x = 4.57 m (15 ft)

(c) x = 6.10 m (20 ft)

(d) x = 7.62 m (25 ft)

Figure C-21. Far-Field, Low-Flow, High-Pressure Jet Vertical Profiles of Sauter Mean Droplet Diameter

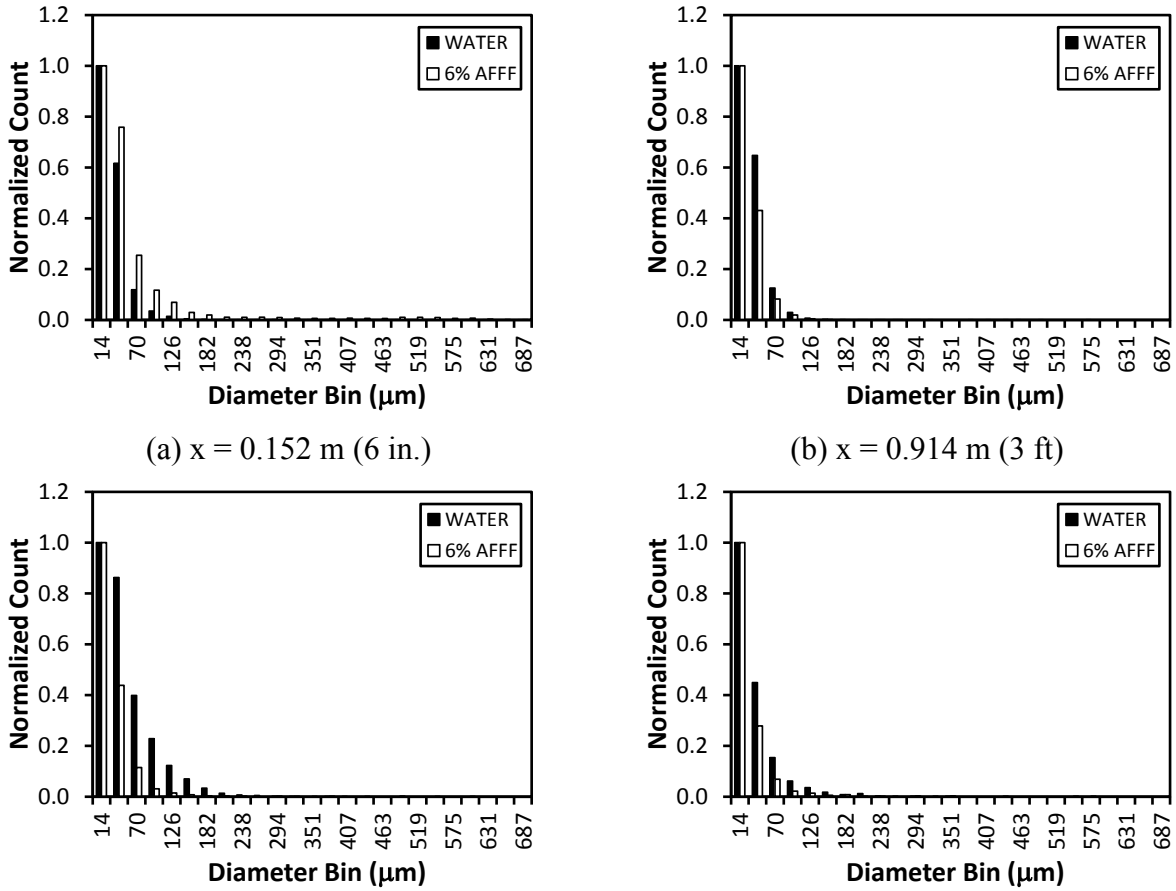

(a) x = 0.152 m (6 in.)

(b) x = 0.914 m (3 ft)

(c) x = 3.05 m (10 ft)

(d) x = 6.10 m (20 ft)

Figure C-22. Low-Flow, High-Pressure Jet Droplet Size Distribution at the Maximum Profile, Mean Axial Droplet Velocity for Select Vertical Profiles

C.3 MEDIUM-FLOW, MEDIUM-PRESSURE FIREFIGHTING JET DATA.

The medium-flow, medium-pressure firefighting jet data are shown in figures C-23 through C-40.

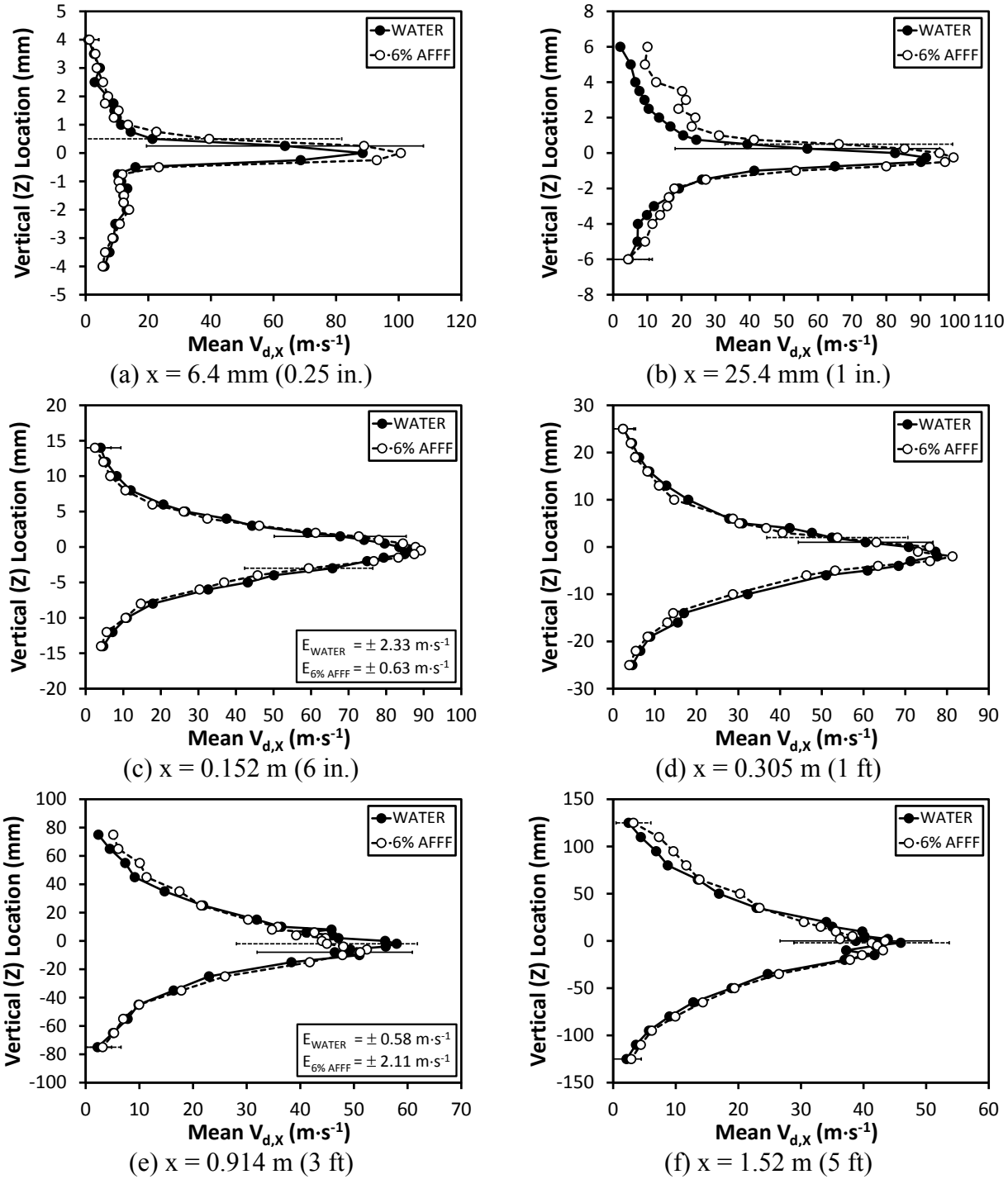

(a) x = 6.4 mm (0.25 in.)

(b) x = 25.4 mm (1 in.)

(c) x = 0.152 m (6 in.)

(d) x = 0.305 m (1 ft)

(e) x = 0.914 m (3 ft)

(f) x = 1.52 m (5 ft)

Figure C-23. Near-Field, Medium-Flow, Medium-Pressure Jet Vertical Profiles of Mean Axial Droplet Velocity

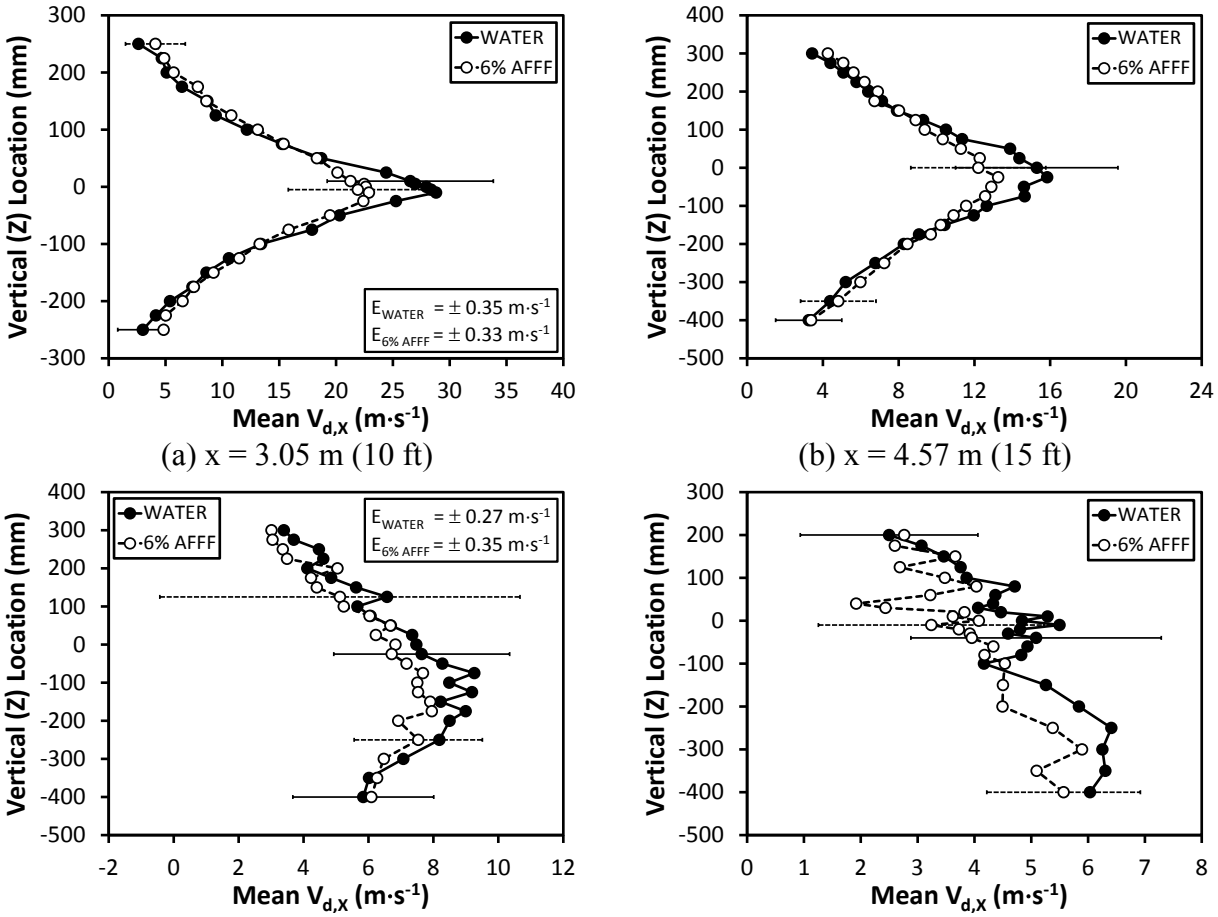

Figure C-24. Far-Field, Medium-Flow, Medium-Pressure Jet Vertical Profiles of Mean Axial Droplet Velocity

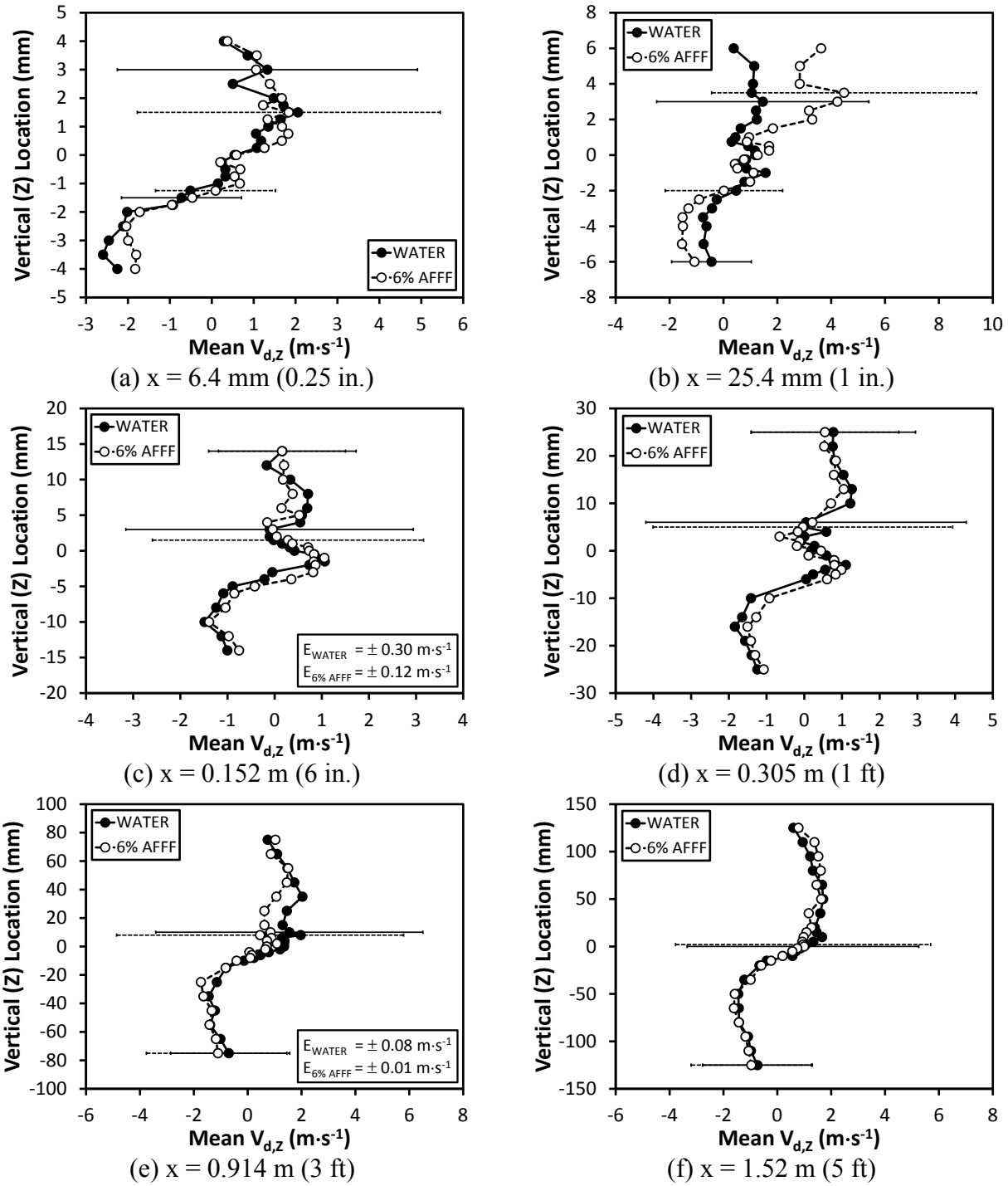

(a) x = 6.4 mm (0.25 in.)

(b) x = 25.4 mm (1 in.)

(c) x = 0.152 m (6 in.)

(d) x = 0.305 m (1 ft)

(e) x = 0.914 m (3 ft)

(f) x = 1.52 m (5 ft)

Figure C-25. Near-Field, Medium-Flow, Medium-Pressure Jet Vertical Profiles of Mean Vertical Droplet Velocity

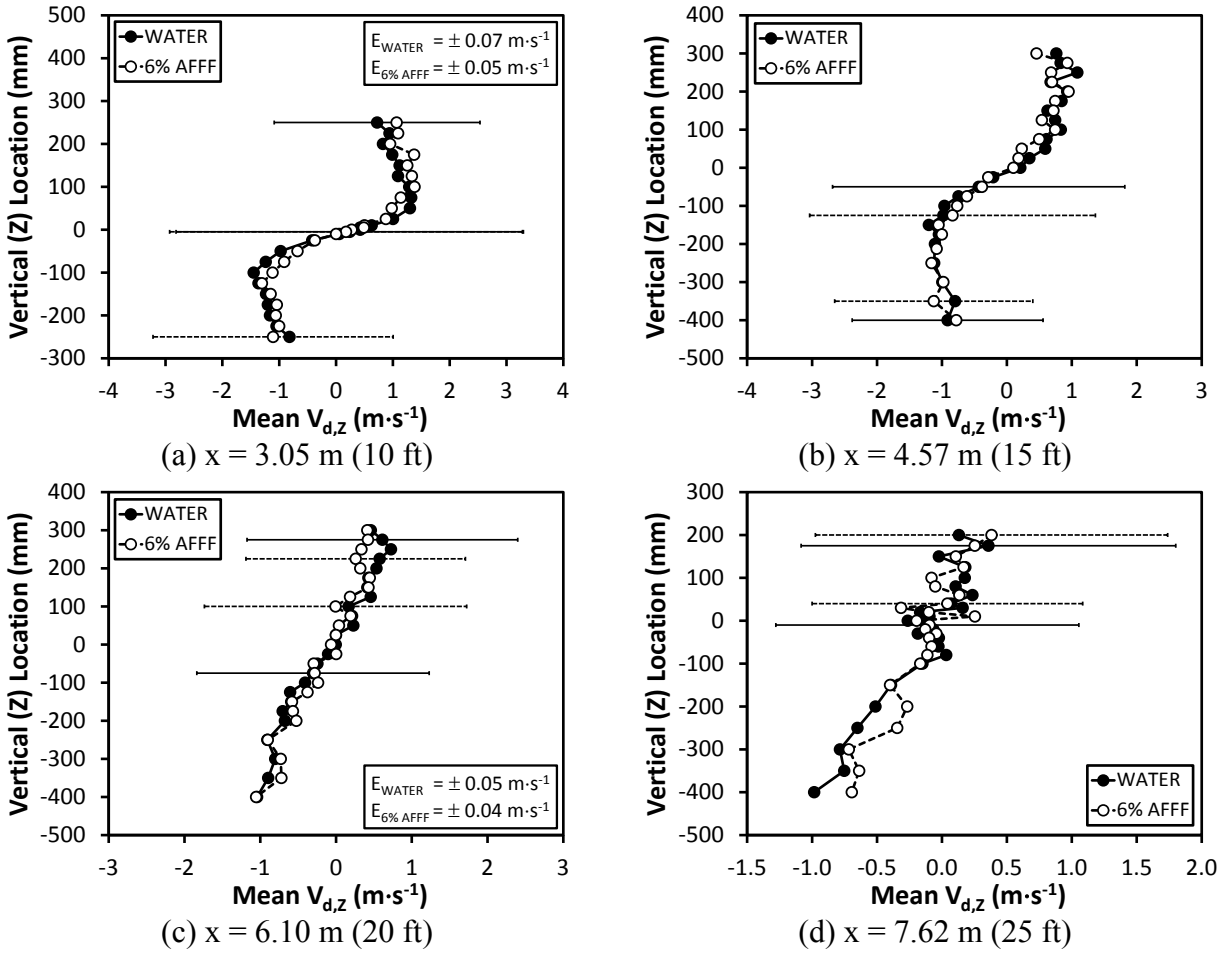

Figure C-26. Far-Field, Medium-Flow, Medium-Pressure Jet Vertical Profiles of Mean Vertical Droplet Velocity

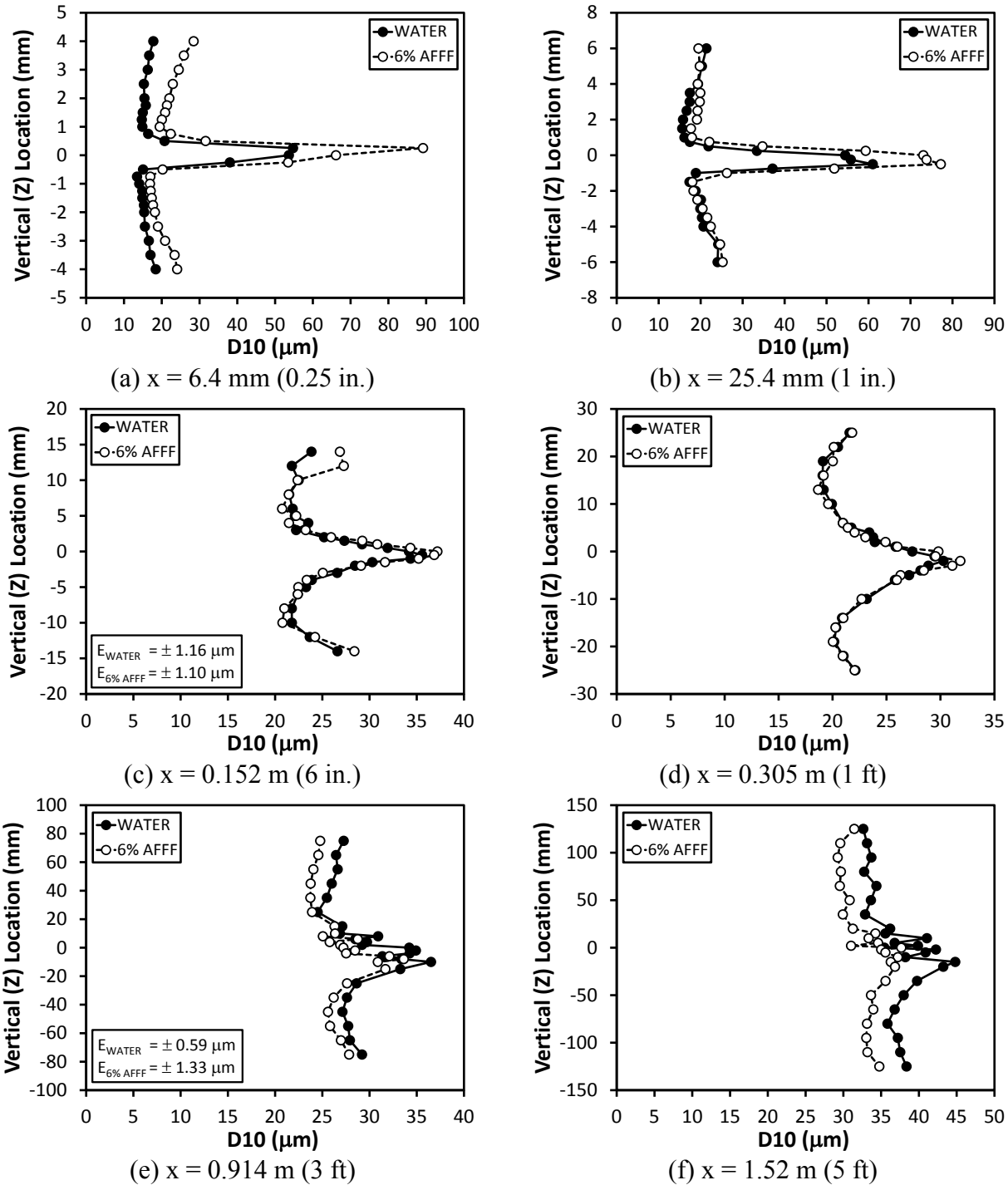

(a) x = 6.4 mm (0.25 in.)

(b) x = 25.4 mm (1 in.)

(c) x = 0.152 m (6 in.)

(d) x = 0.305 m (1 ft)

(e) x = 0.914 m (3 ft)

(f) x = 1.52 m (5 ft)

Figure C-27. Near-Field, Medium-Flow, Medium-Pressure Jet Vertical Profiles of Mean Droplet Diameter

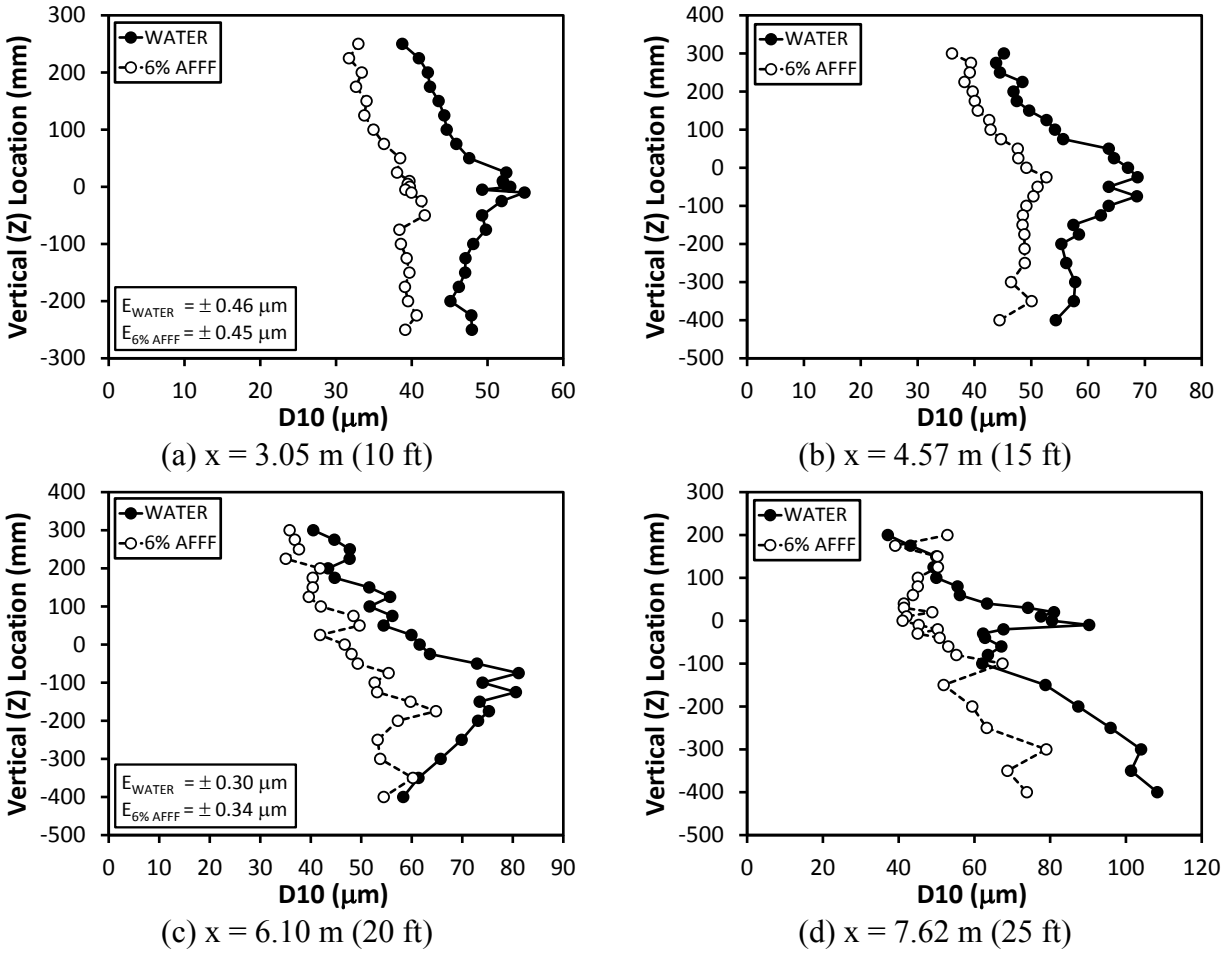

(a) x = 3.05 m (10 ft)

(b) x = 4.57 m (15 ft)

(c) x = 6.10 m (20 ft)

(d) x = 7.62 m (25 ft)

Figure C-28. Far-Field, Medium-Flow, Medium-Pressure Jet Vertical Profiles of Mean Droplet Diameter

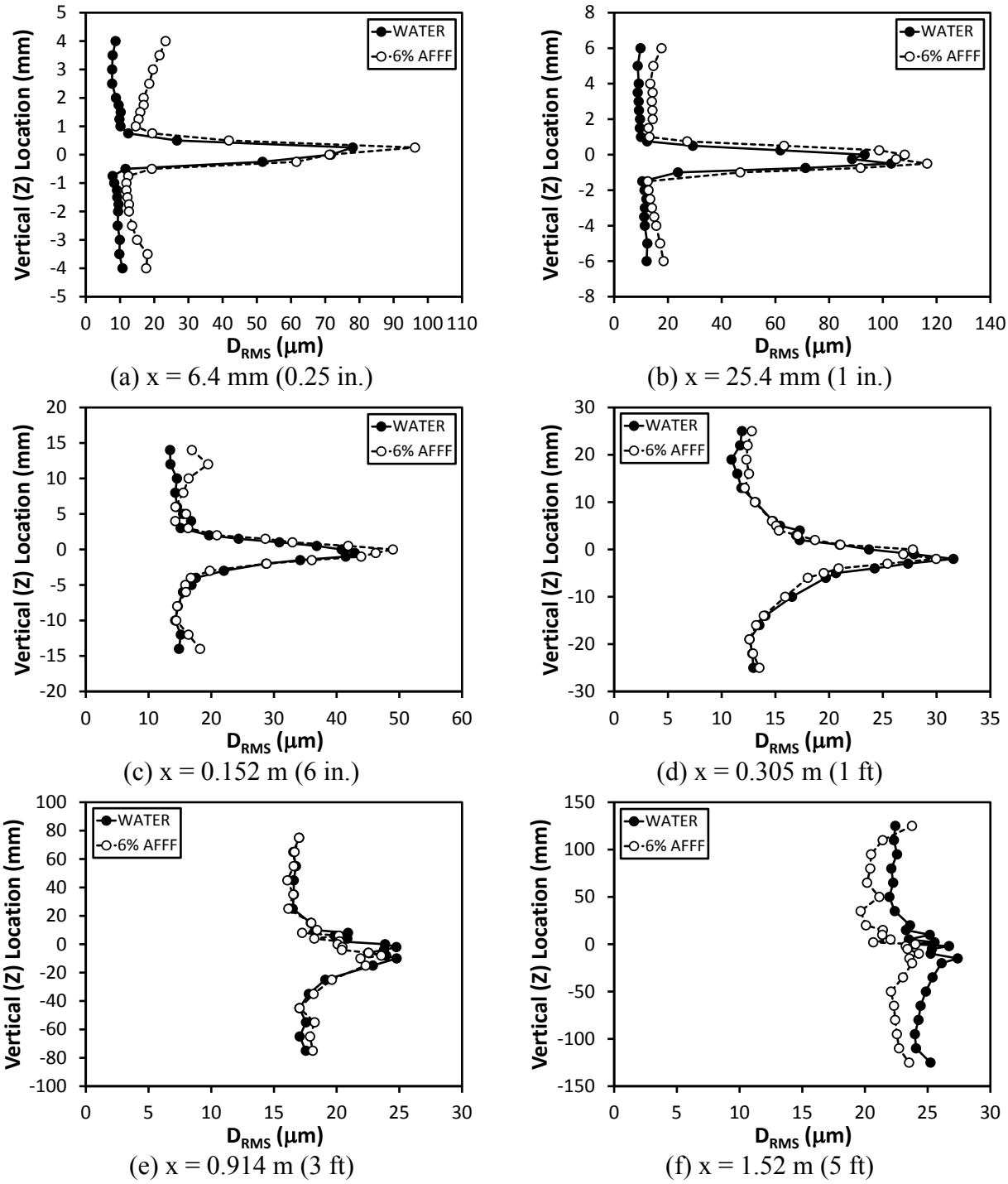

(a) x = 6.4 mm (0.25 in.)

(b) x = 25.4 mm (1 in.)

(c) x = 0.152 m (6 in.)

(d) x = 0.305 m (1 ft)

(e) x = 0.914 m (3 ft)

(f) x = 1.52 m (5 ft)

Figure C-29. Near-Field, Medium-Flow, Medium-Pressure Jet Vertical Profiles of RMS Droplet Diameter

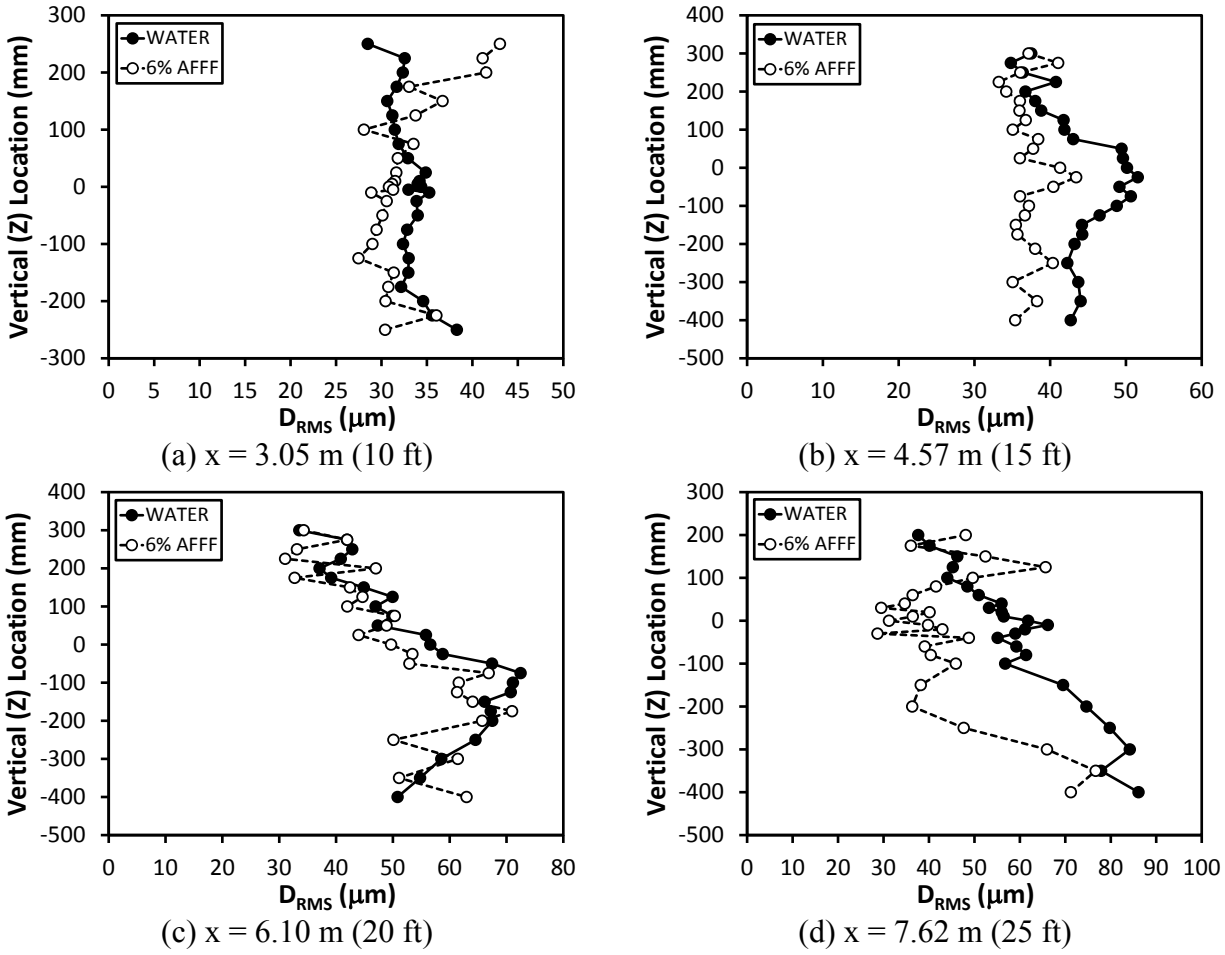

(a) x = 3.05 m (10 ft)

(b) x = 4.57 m (15 ft)

(c) x = 6.10 m (20 ft)

(d) x = 7.62 m (25 ft)

Figure C-30. Far-Field, Medium-Flow, Medium-Pressure Jet Vertical Profiles of RMS Droplet Diameter

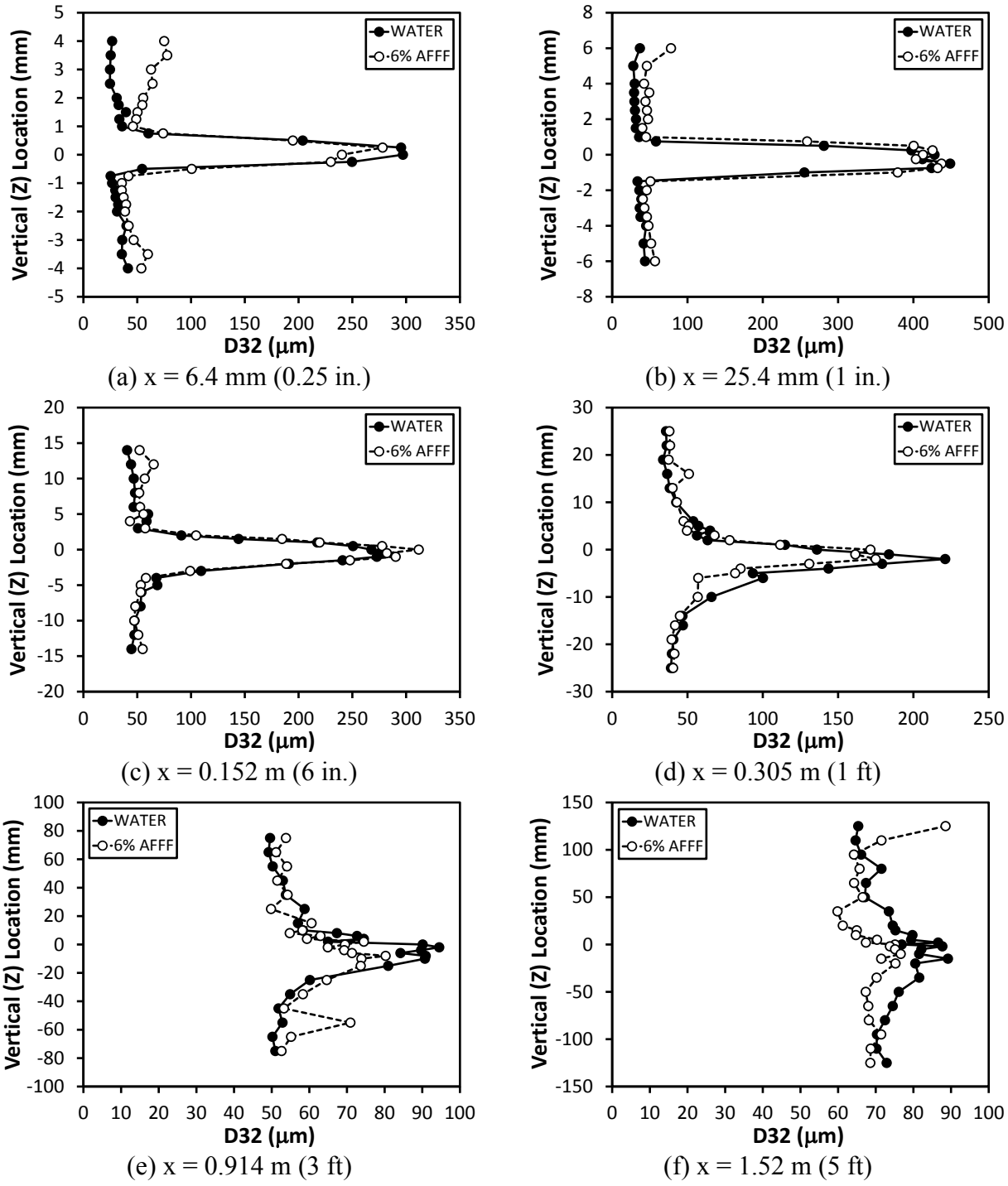

(a) x = 6.4 mm (0.25 in.)

(b) x = 25.4 mm (1 in.)

(c) x = 0.152 m (6 in.)

(d) x = 0.305 m (1 ft)

(e) x = 0.914 m (3 ft)

(f) x = 1.52 m (5 ft)

Figure C-31. Near-Field, Medium-Flow, Medium-Pressure Jet Vertical Profiles of Sauter Mean Droplet Diameter

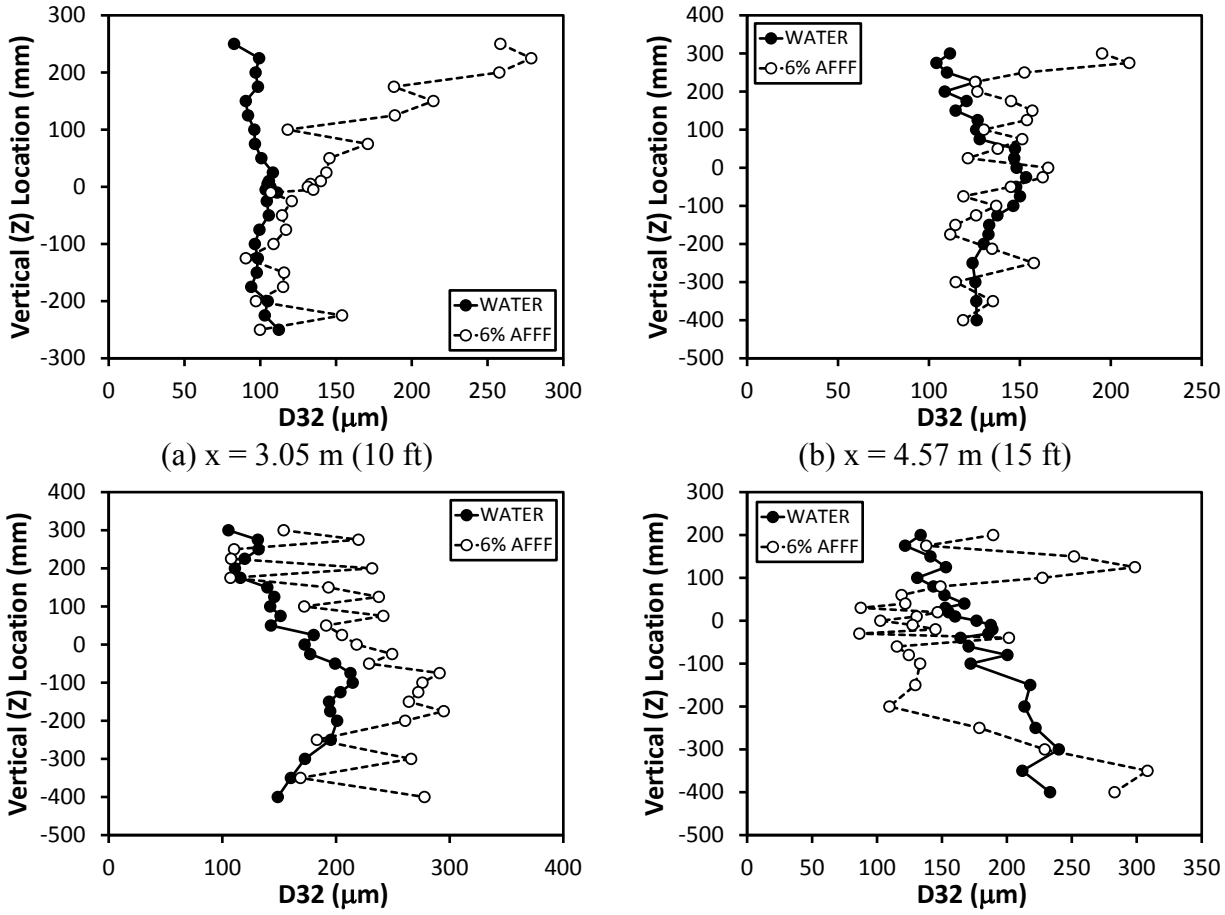

(a) x = 3.05 m (10 ft)

(b) x = 4.57 m (15 ft)

(c) x = 6.10 m (20 ft)

(d) x = 7.62 m (25 ft)

Figure C-32. Far-Field, Medium-Flow, Medium-Pressure Jet Vertical Profiles of Sauter Mean Droplet Diameter

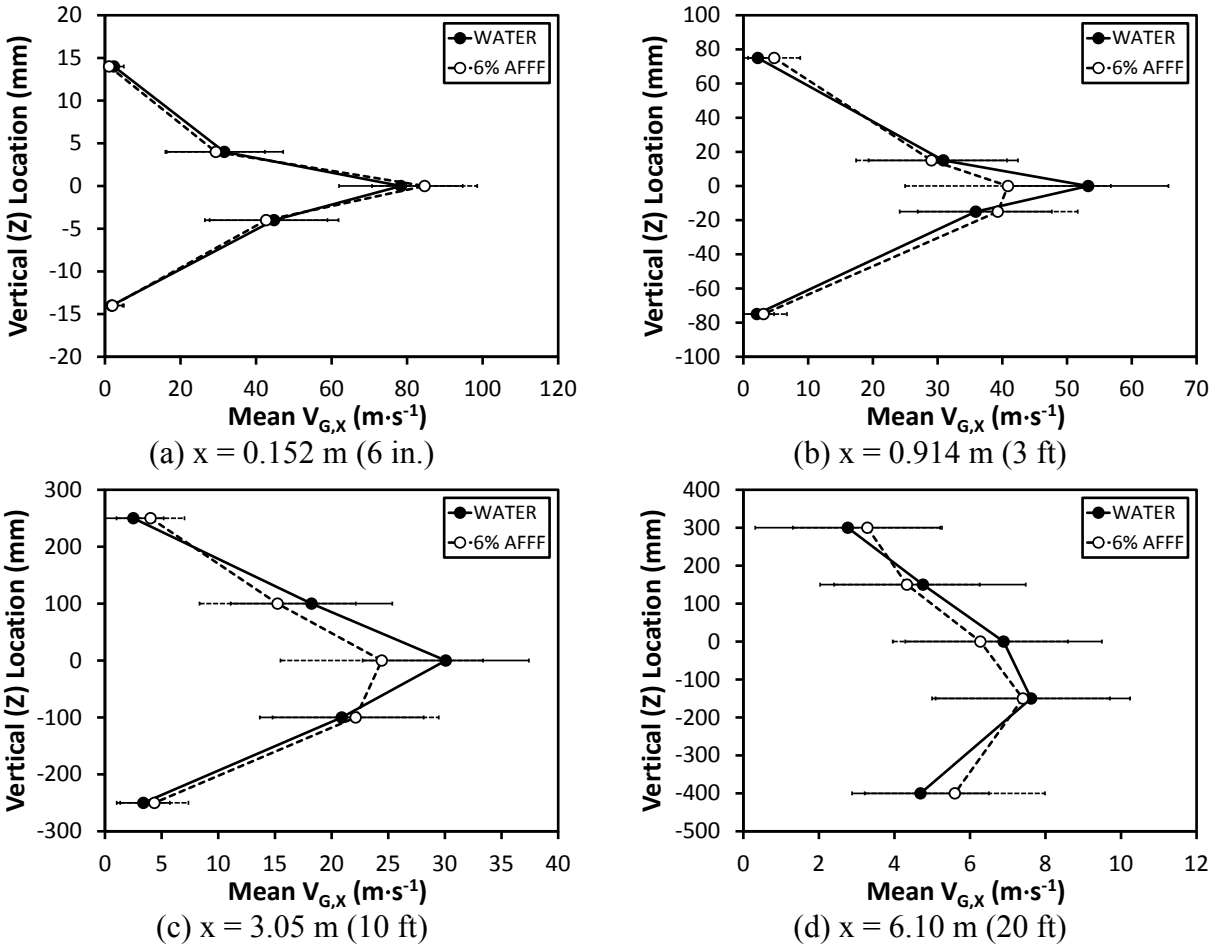

Figure C-33. Select Medium-Flow, Medium-Pressure Jet Vertical Profiles of Estimated Axial Gaseous (Air) Velocity

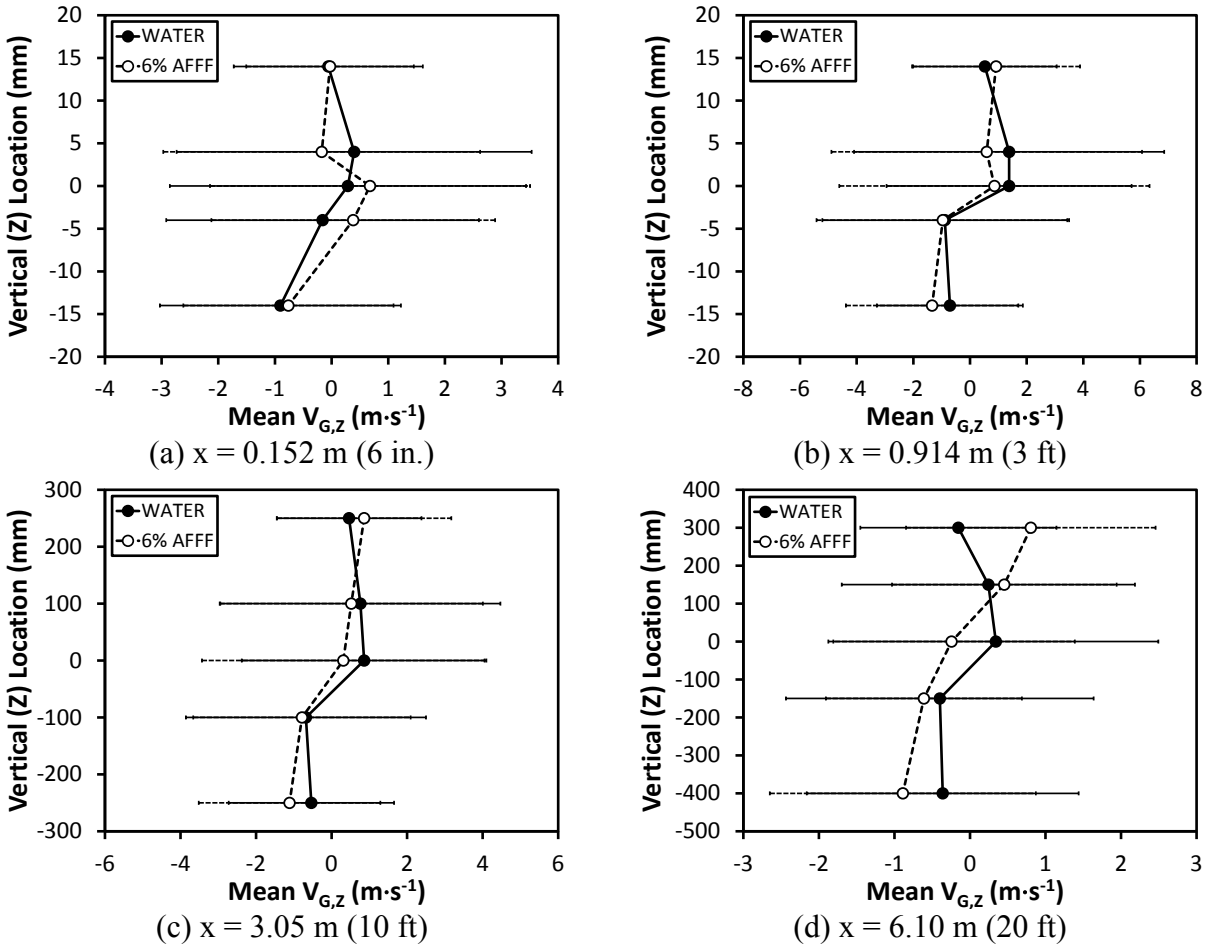

(a) x = 0.152 m (6 in.)

(b) x = 0.914 m (3 ft)

(c) x = 3.05 m (10 ft)

(d) x = 6.10 m (20 ft)

Figure C-34. Select Medium-Flow, Medium-Pressure Jet Vertical Profiles of Estimated Vertical Gaseous (Air) Velocity

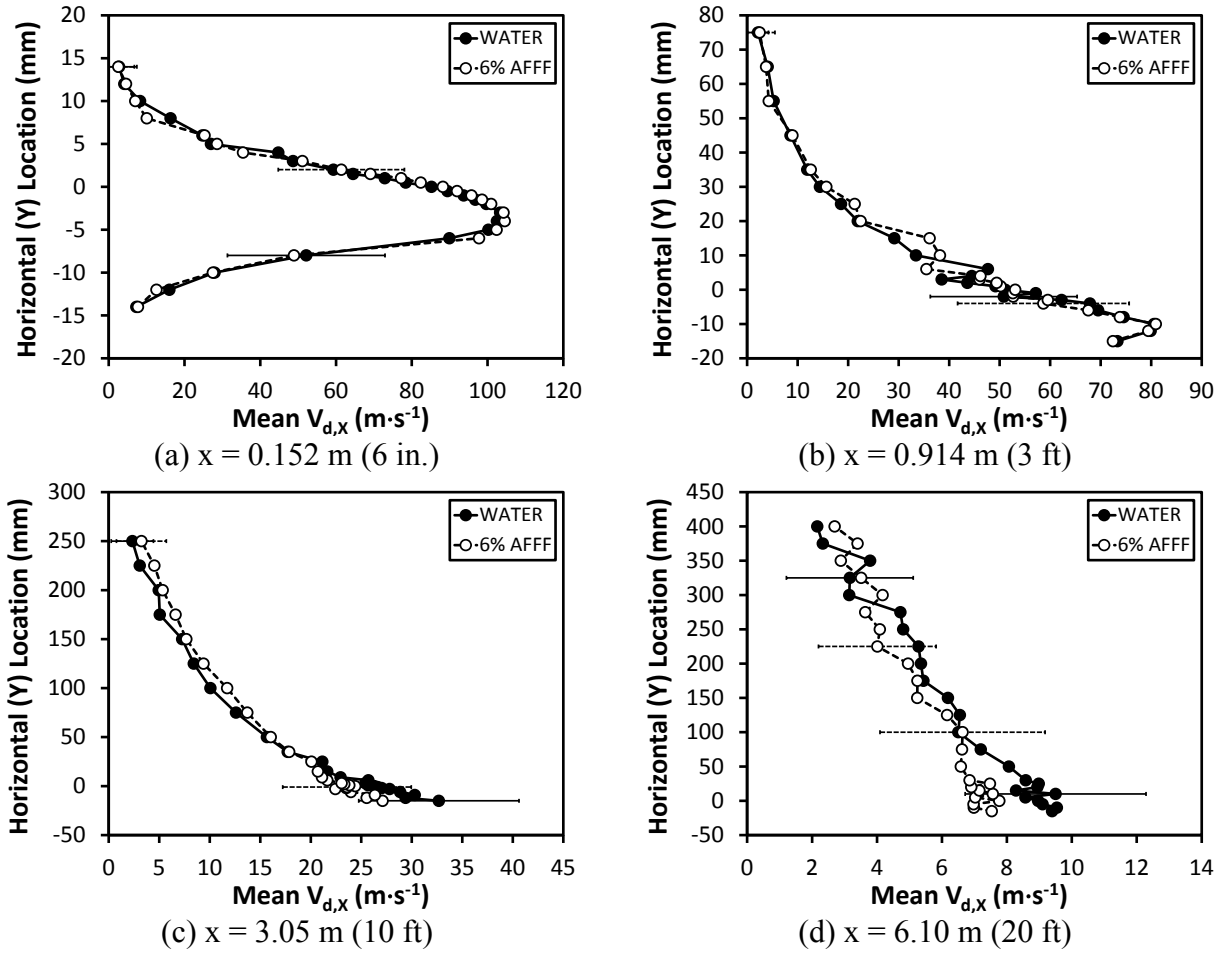

(a) x = 0.152 m (6 in.)

(b) x = 0.914 m (3 ft)

(c) x = 3.05 m (10 ft)

(d) x = 6.10 m (20 ft)

Figure C-35. Select Medium-Flow, Medium-Pressure Jet Horizontal Profiles of Mean Axial Droplet Velocity

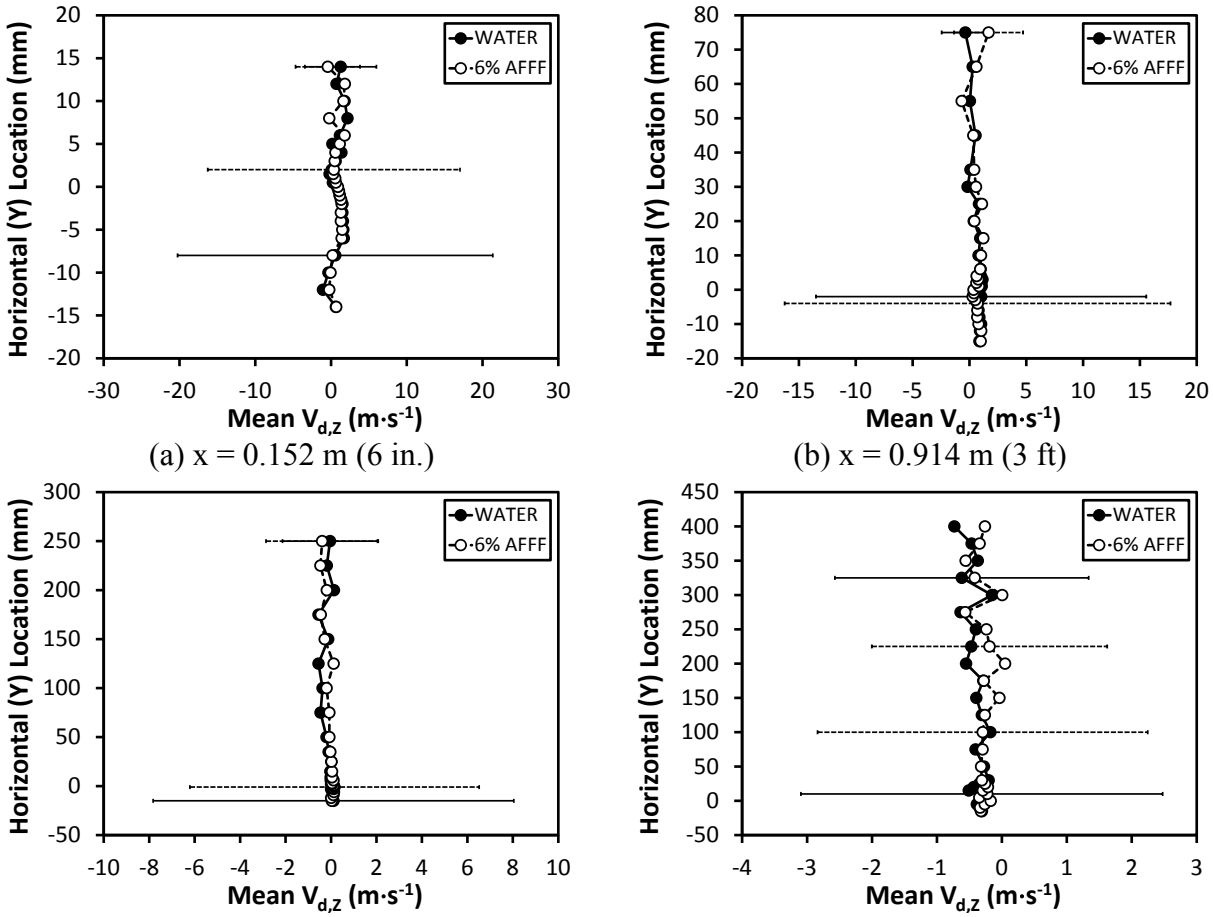

(a) x = 0.152 m (6 in.)

(b) x = 0.914 m (3 ft)

(c) x = 3.05 m (10 ft)

(d) x = 6.10 m (20 ft)

Figure C-36. Select Medium-Flow, Medium-Pressure Jet Horizontal Profiles of Mean Vertical Droplet Velocity

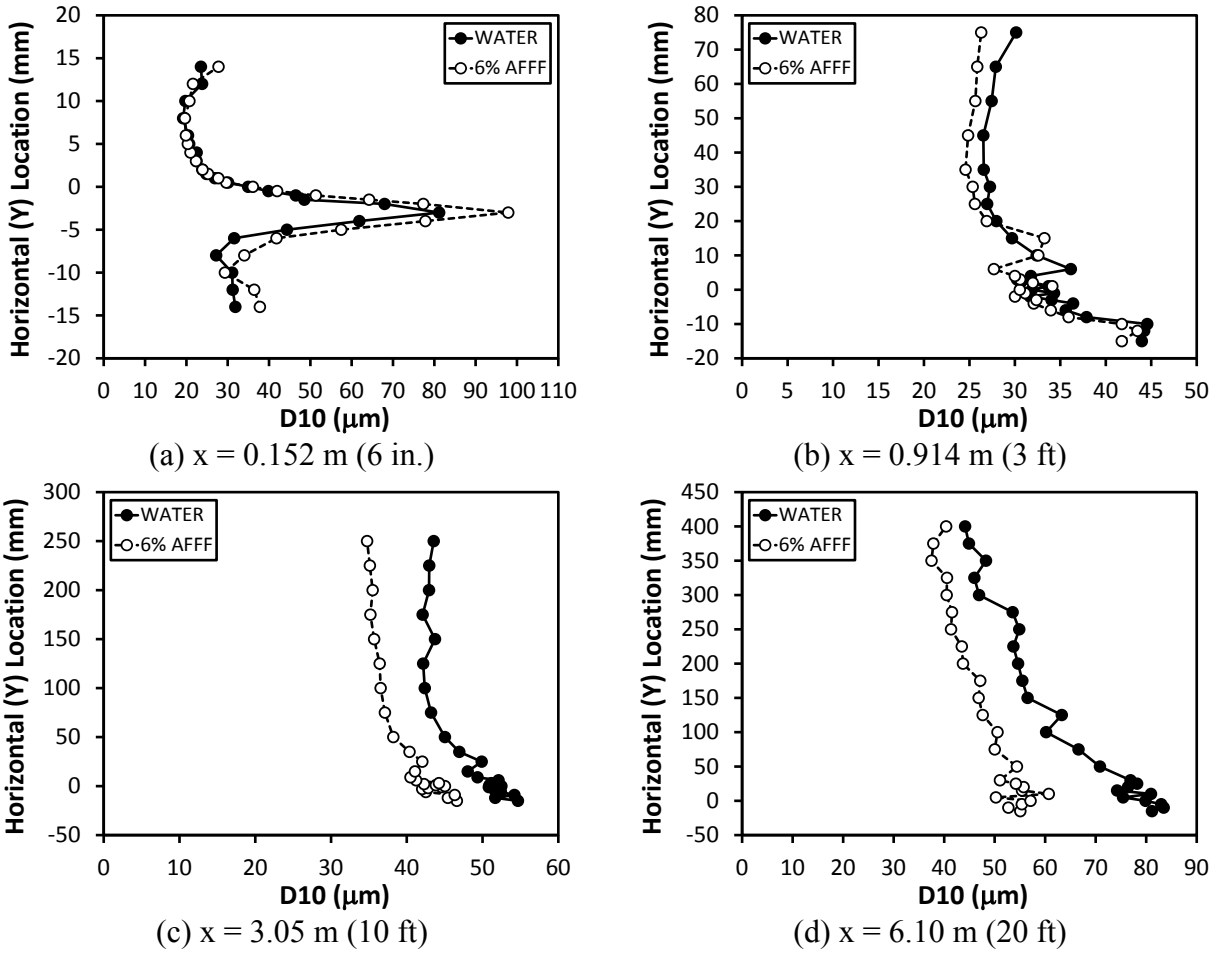

(a) x = 0.152 m (6 in.)

(b) x = 0.914 m (3 ft)

(c) x = 3.05 m (10 ft)

(d) x = 6.10 m (20 ft)

Figure C-37. Select Medium-Flow, Medium-Pressure Jet Horizontal Profiles of Mean Droplet Diameter

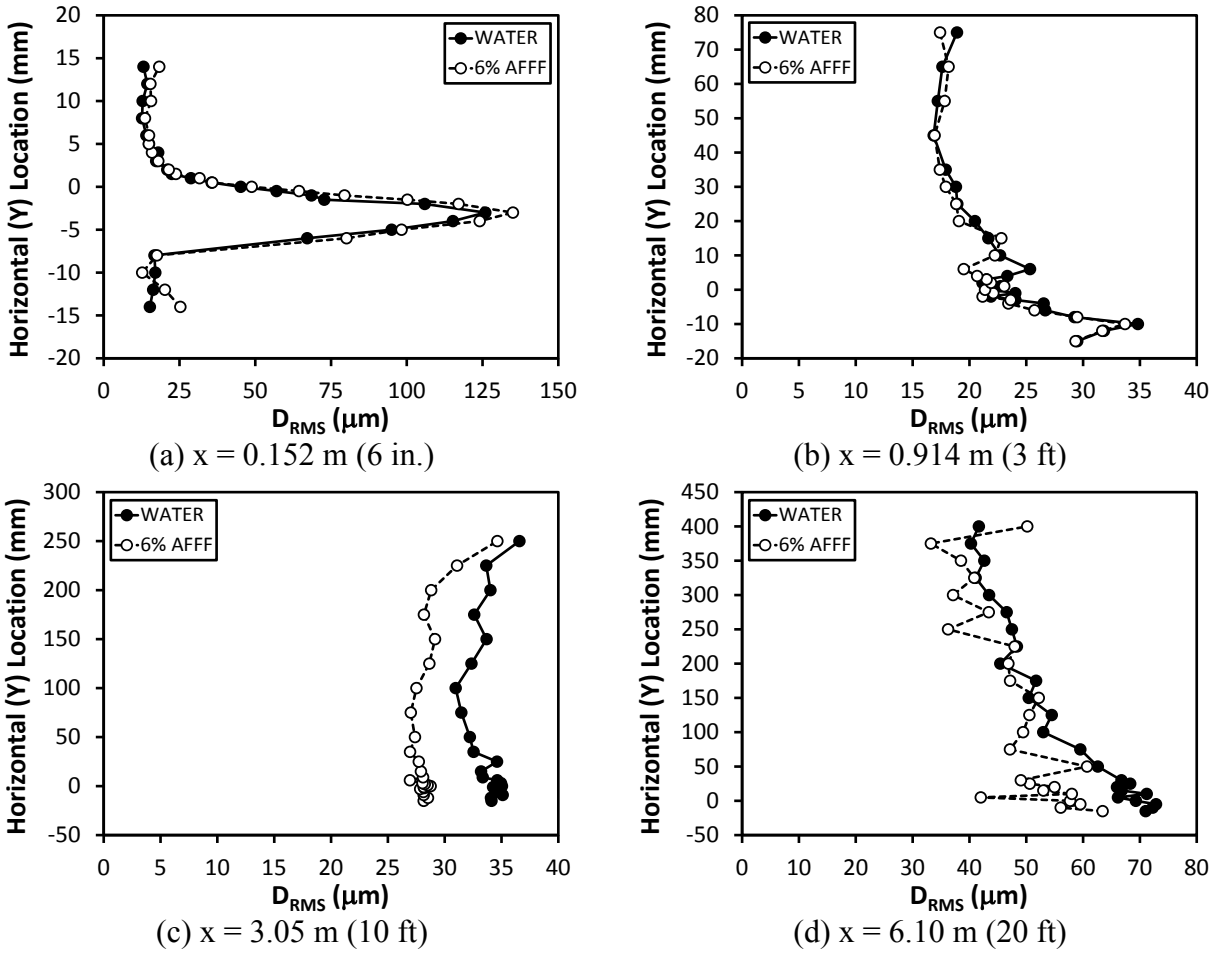

(a) x = 0.152 m (6 in.)

(b) x = 0.914 m (3 ft)

(c) x = 3.05 m (10 ft)

(d) x = 6.10 m (20 ft)

Figure C-38. Select Medium-Flow, Medium-Pressure Jet Horizontal Profiles of RMS Droplet Diameter

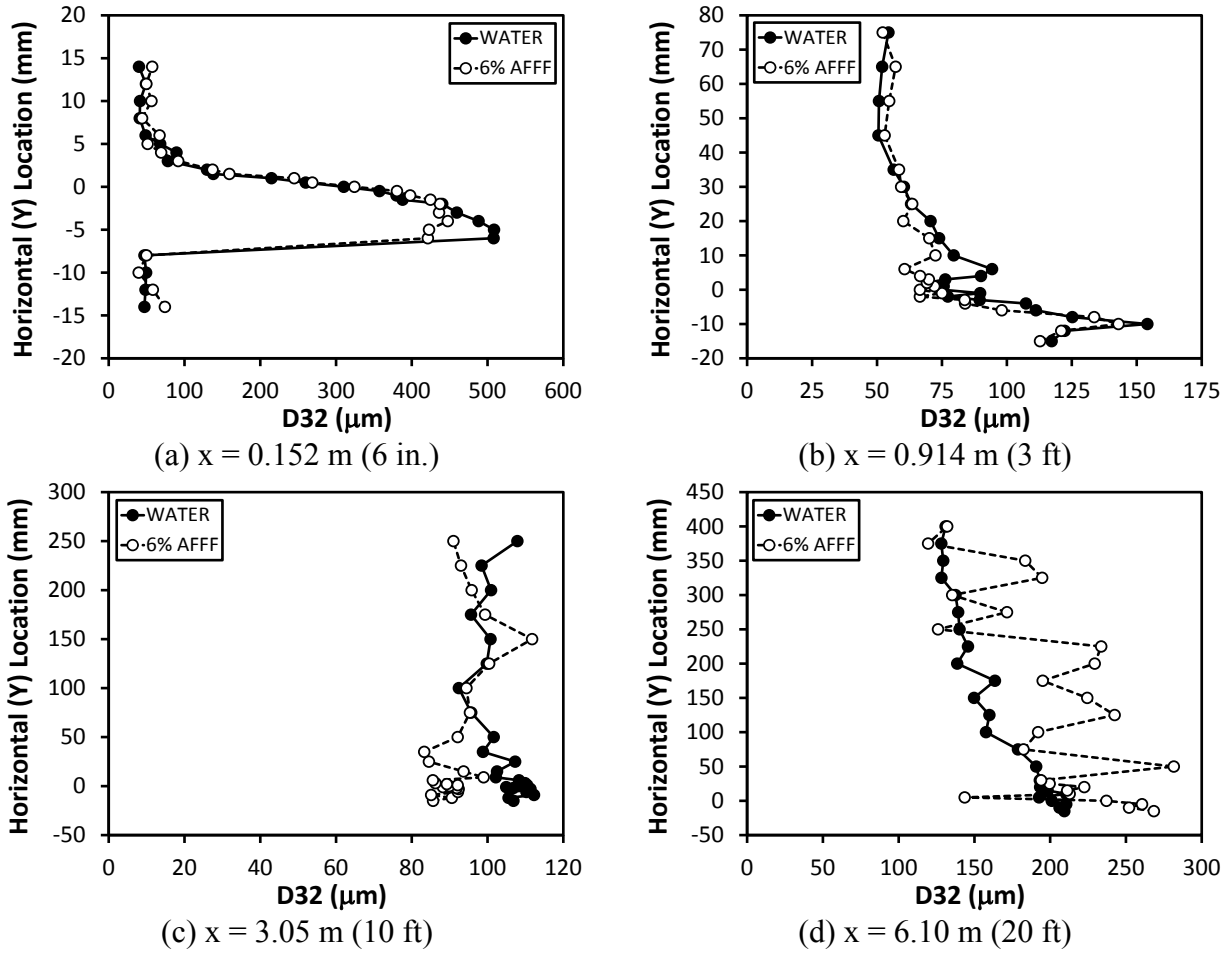

Figure C-39. Select Medium-Flow, Medium-Pressure Jet Horizontal Profiles of Sauter Mean Droplet Diameter

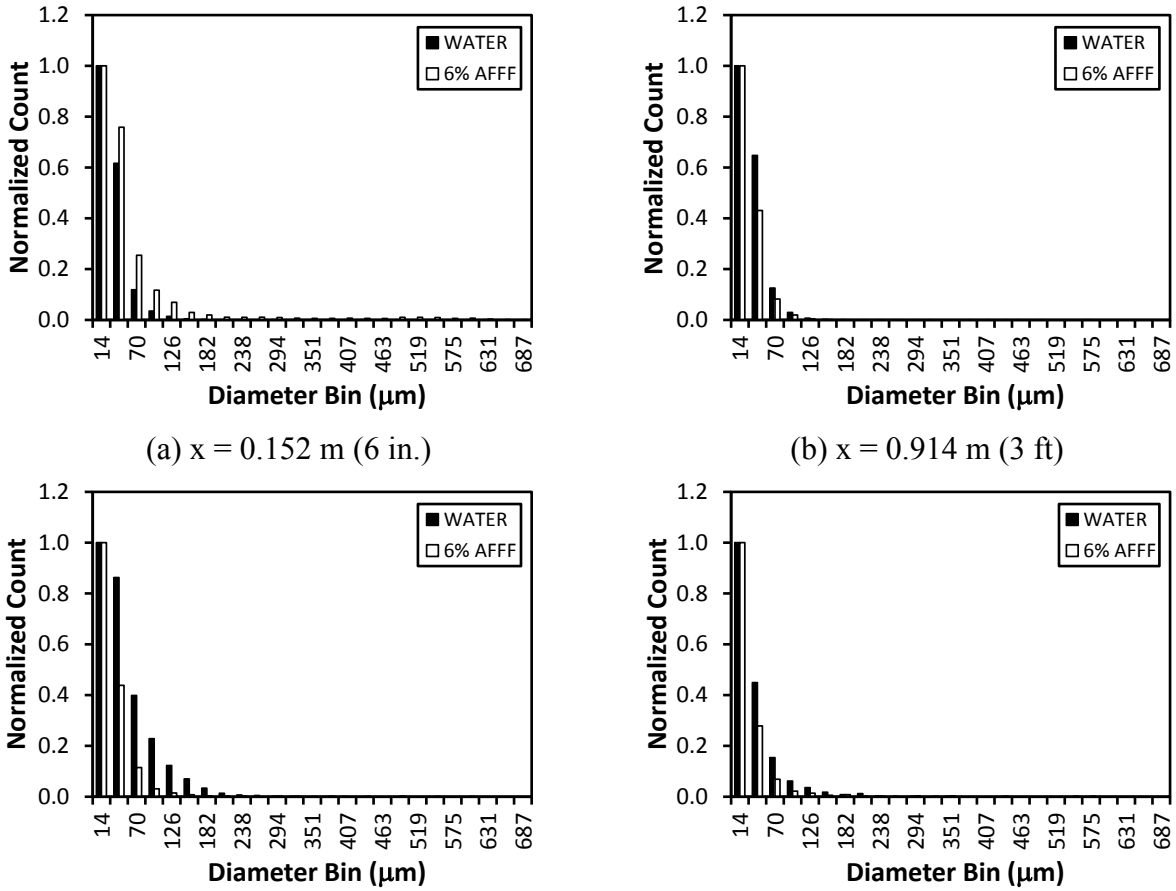

(a) x = 0.152 m (6 in.)

(b) x = 0.914 m (3 ft)

(c) x = 3.05 m (10 ft)

(d) x = 6.10 m (20 ft)

Figure C-40. Medium-Flow, Medium-Pressure Jet Droplet Size Distribution at the Maximum Profile, Mean Axial Droplet Velocity for Select Vertical Profiles

C.4 HIGH-FLOW, LOW-PRESSURE FIREFIGHTING JET DATA.

The high-flow, low-pressure firefighting jet data are shown in figures C-41 through C-51.

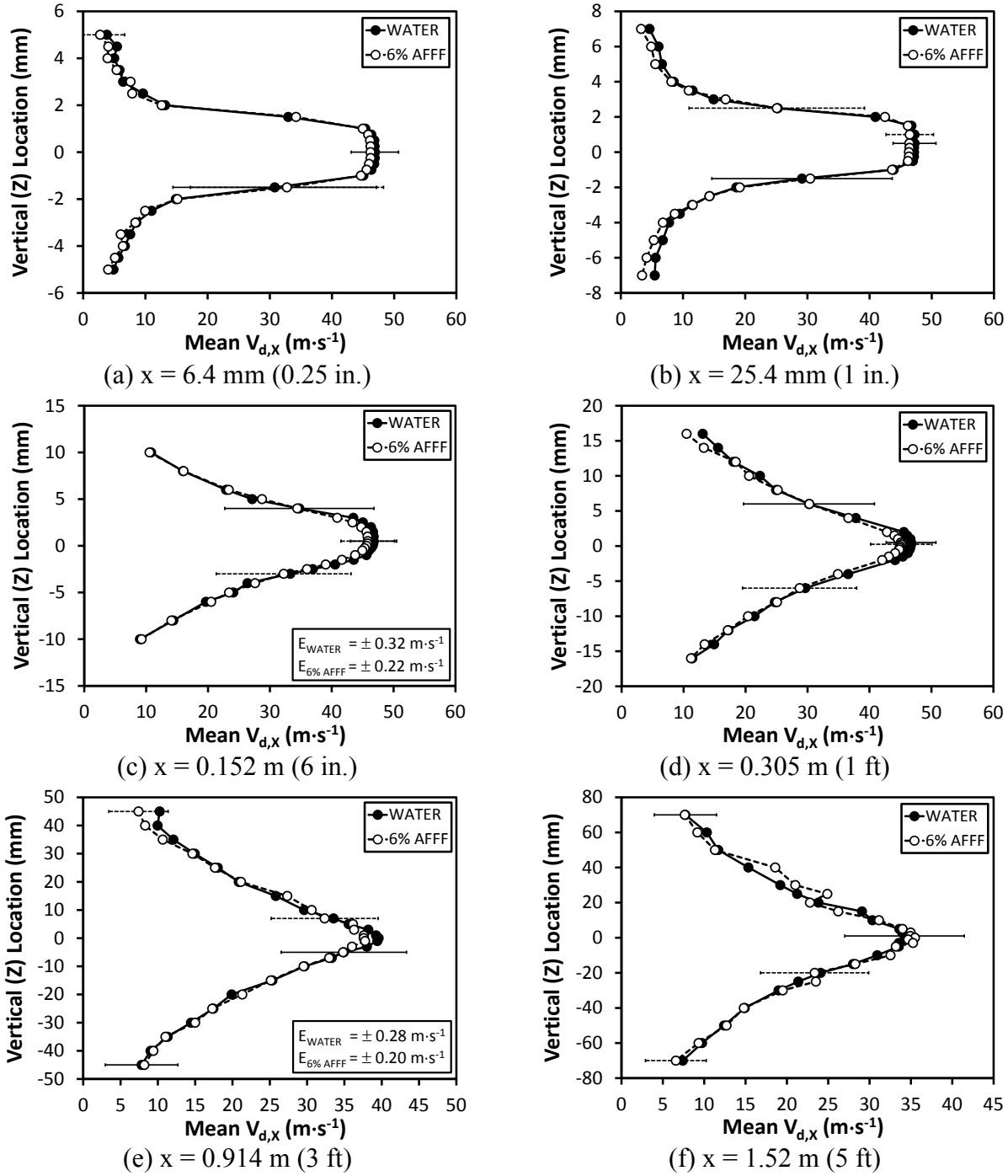

(a) x = 6.4 mm (0.25 in.)

(b) x = 25.4 mm (1 in.)

(c) x = 0.152 m (6 in.)

(d) x = 0.305 m (1 ft)

(e) x = 0.914 m (3 ft)

(f) x = 1.52 m (5 ft)

Figure C-41. Near-Field, High-Flow, Low-Pressure Jet Vertical Profiles of Mean Axial Droplet Velocity

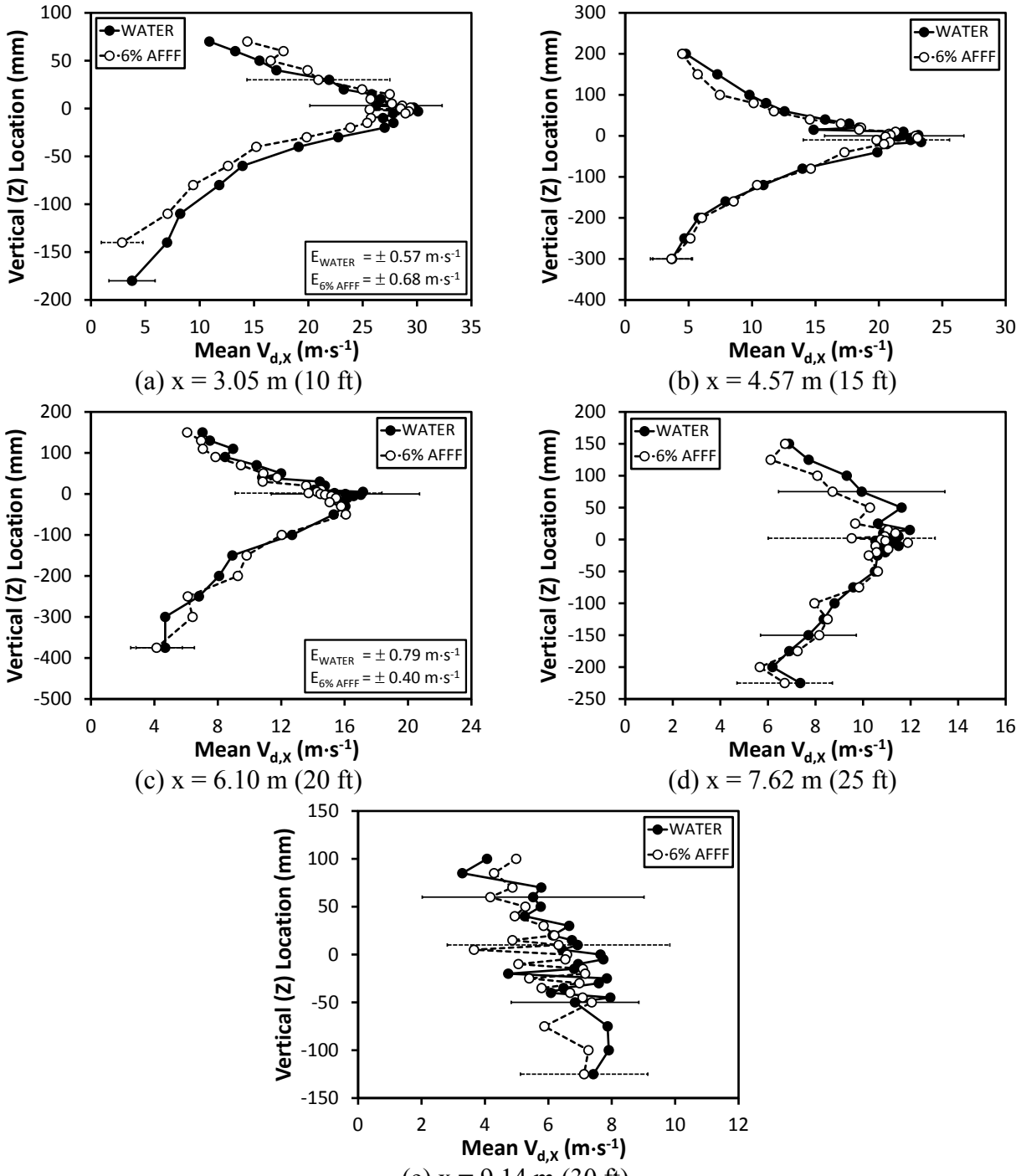

Figure C-42. Far-Field, High-Flow, Low-Pressure Jet Vertical Profiles of Mean Axial Droplet Velocity

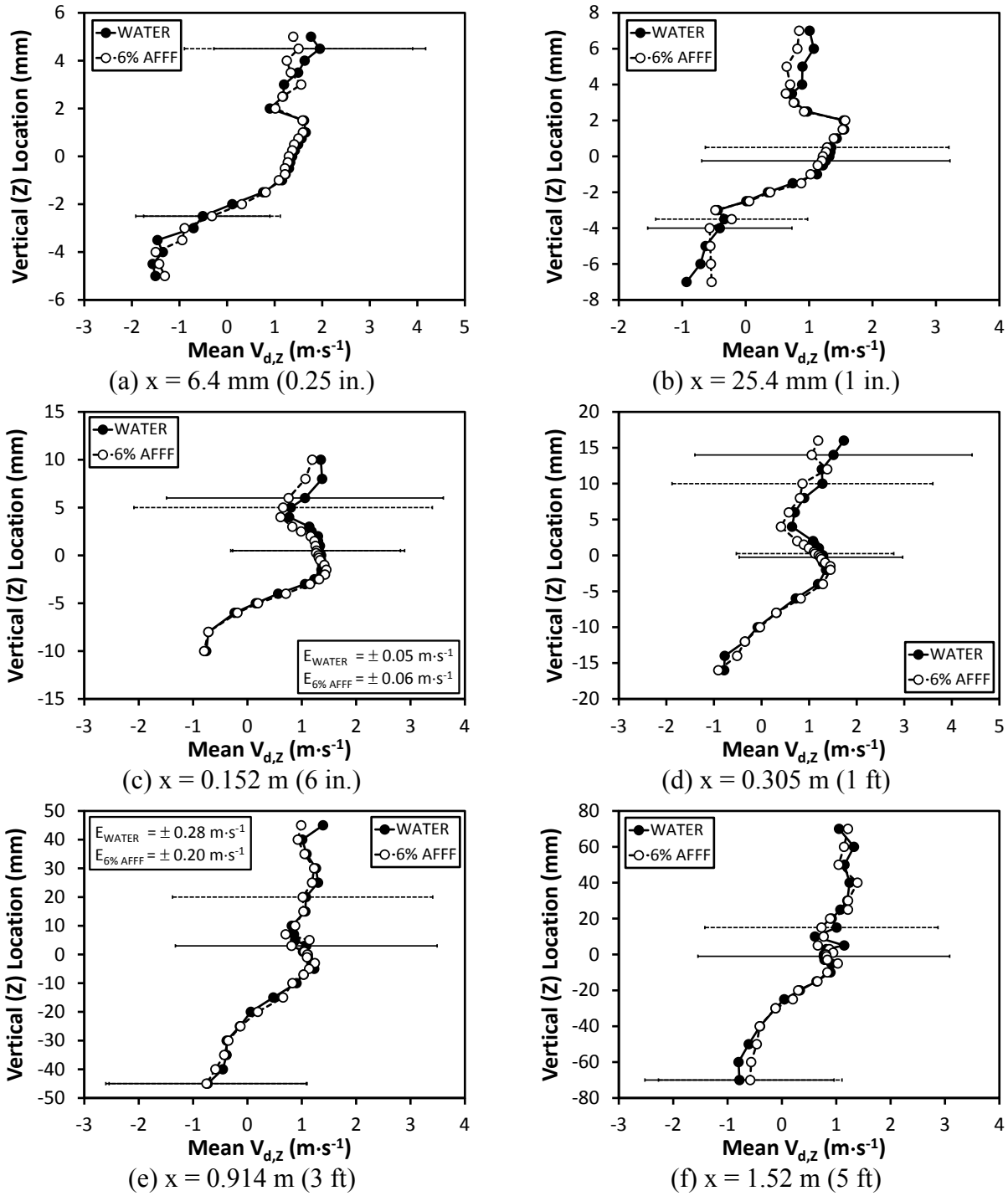

Figure C-43. Near-Field, High-Flow, Low-Pressure Jet Vertical Profiles of Mean Vertical Droplet Velocity

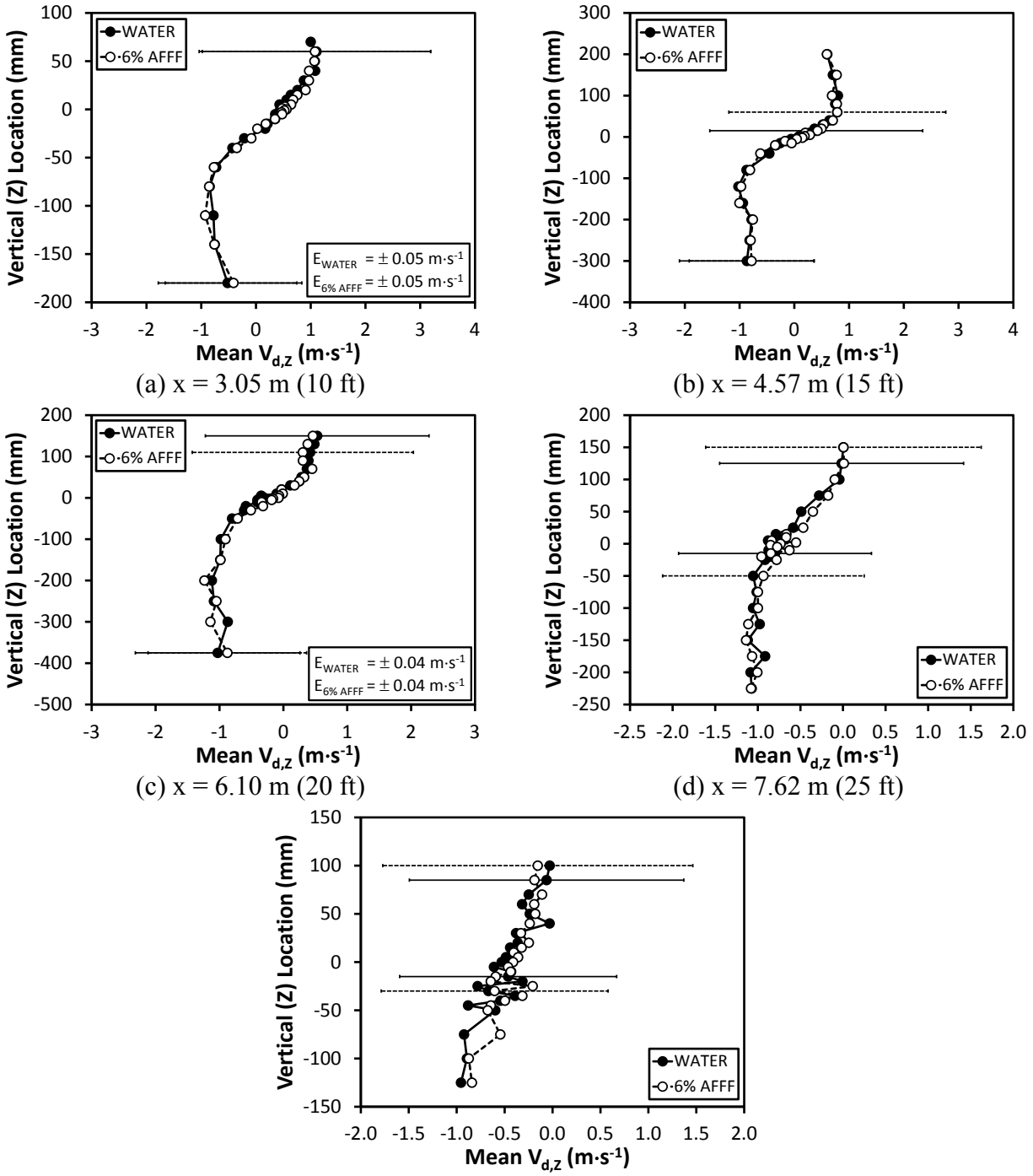

Figure C-44. Far-Field, High-Flow, Low-Pressure Jet Vertical Profiles of Mean Vertical Droplet Velocity

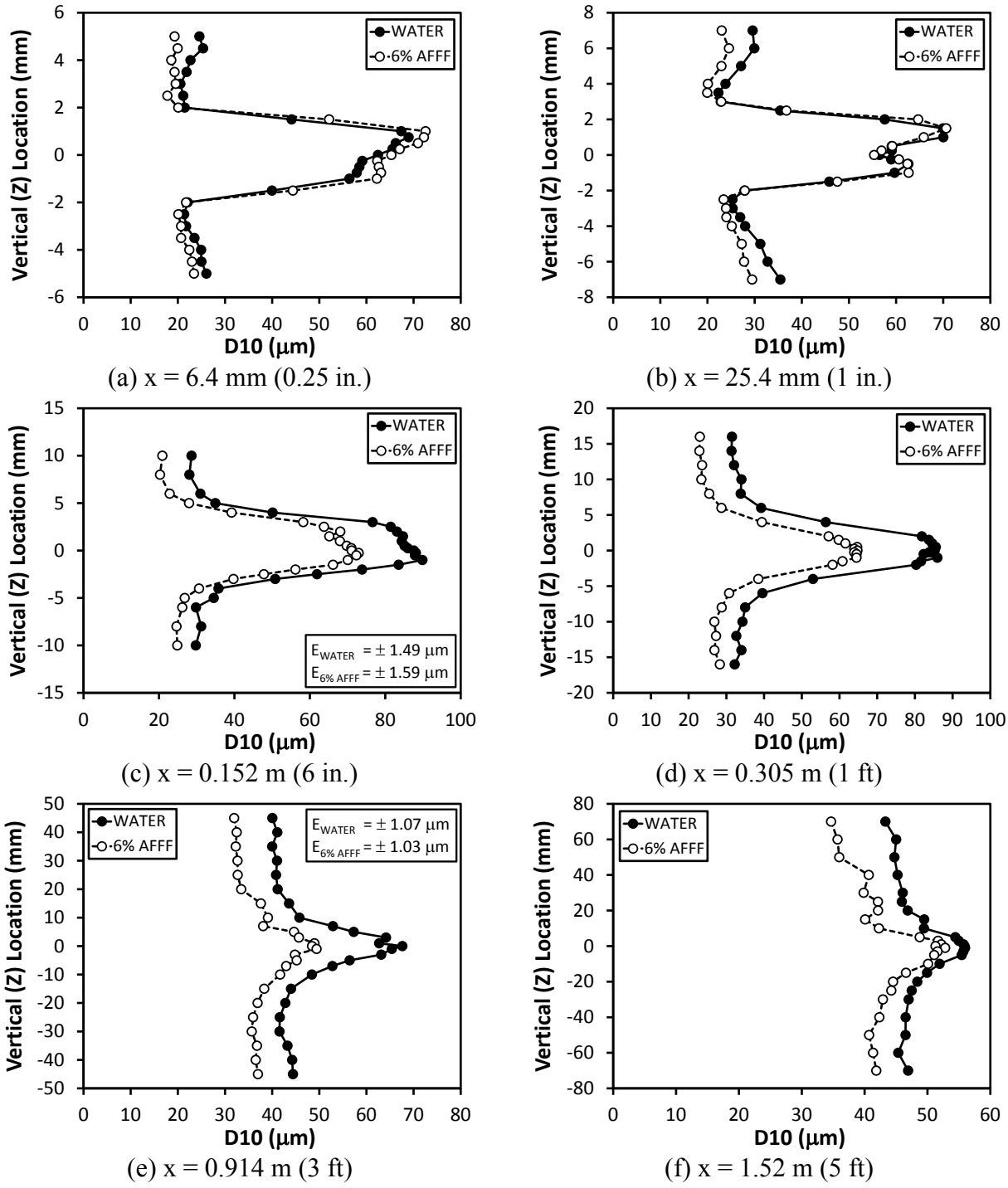

(a) x = 6.4 mm (0.25 in.)

(b) x = 25.4 mm (1 in.)

(c) x = 0.152 m (6 in.)

(d) x = 0.305 m (1 ft)

(e) x = 0.914 m (3 ft)

(f) x = 1.52 m (5 ft)

Figure C-45. Near-Field, High-Flow, Low-Pressure Jet Vertical Profiles of Mean Droplet Diameter

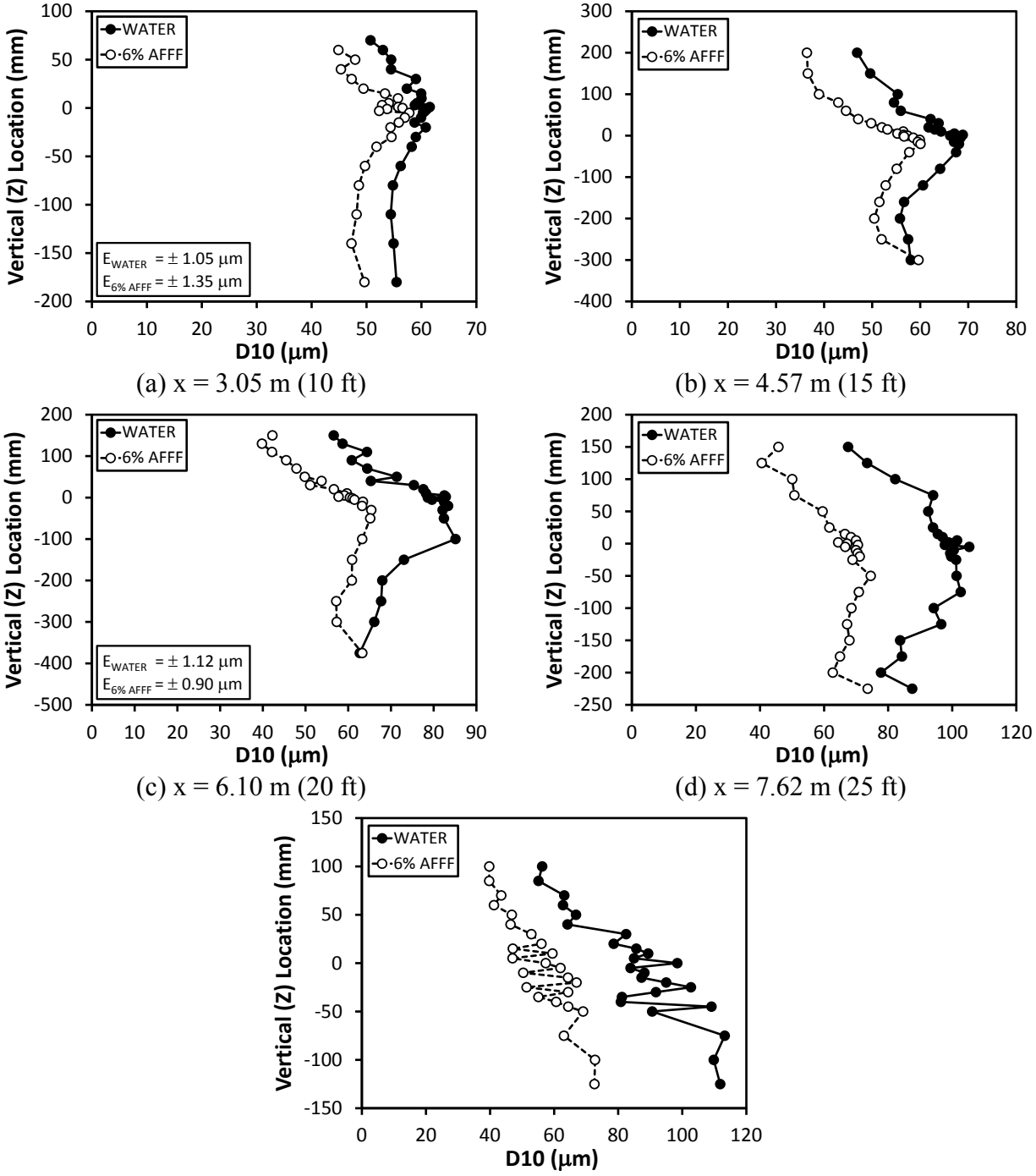

(a) x = 3.05 m (10 ft)

(b) x = 4.57 m (15 ft)

(c) x = 6.10 m (20 ft)

(d) x = 7.62 m (25 ft)

(e) x = 9.14 m (30 ft)

Figure C-46. Far-Field, High-Flow, Low-Pressure Jet Vertical Profiles of Mean Droplet Diameter

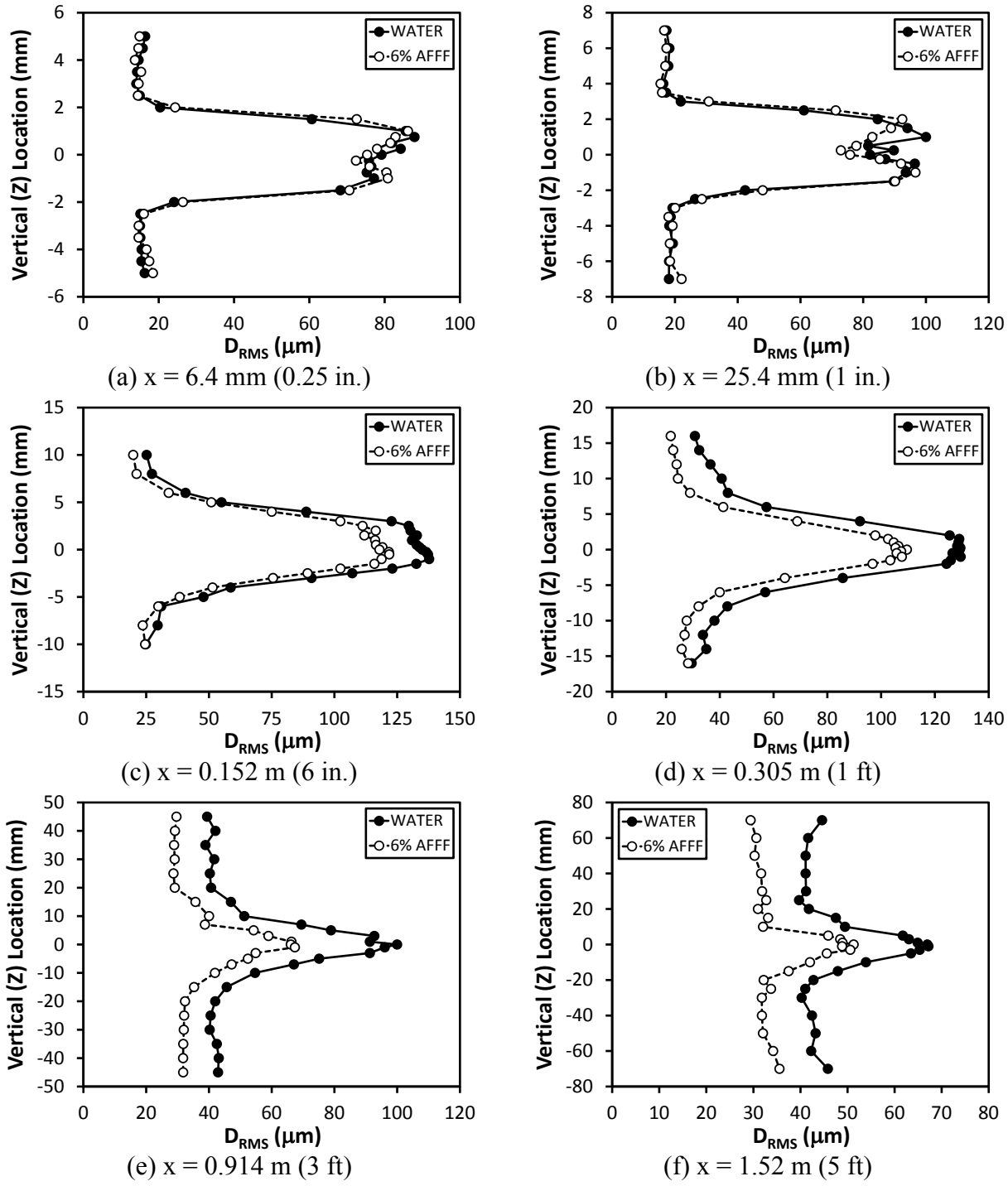

Figure C-47. Near-Field, High-Flow, Low-Pressure Jet Vertical Profiles of RMS Droplet Diameter

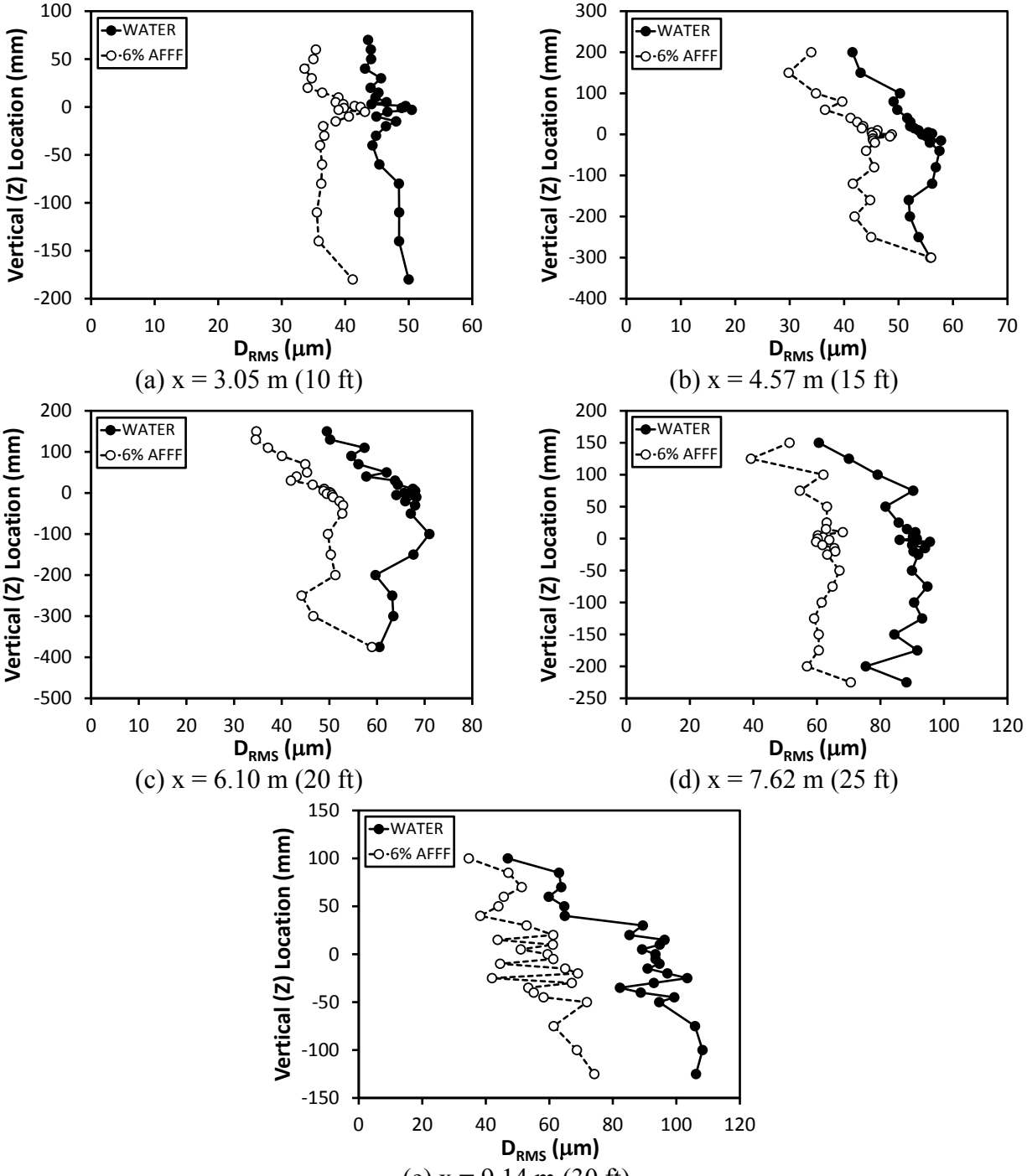

(a) x = 3.05 m (10 ft)

(b) x = 4.57 m (15 ft)

(c) x = 6.10 m (20 ft)

(d) x = 7.62 m (25 ft)

(e) x = 9.14 m (30 ft)

Figure C-48. Far-Field, High-Flow, Low-Pressure Jet Vertical Profiles of RMS Droplet Diameter

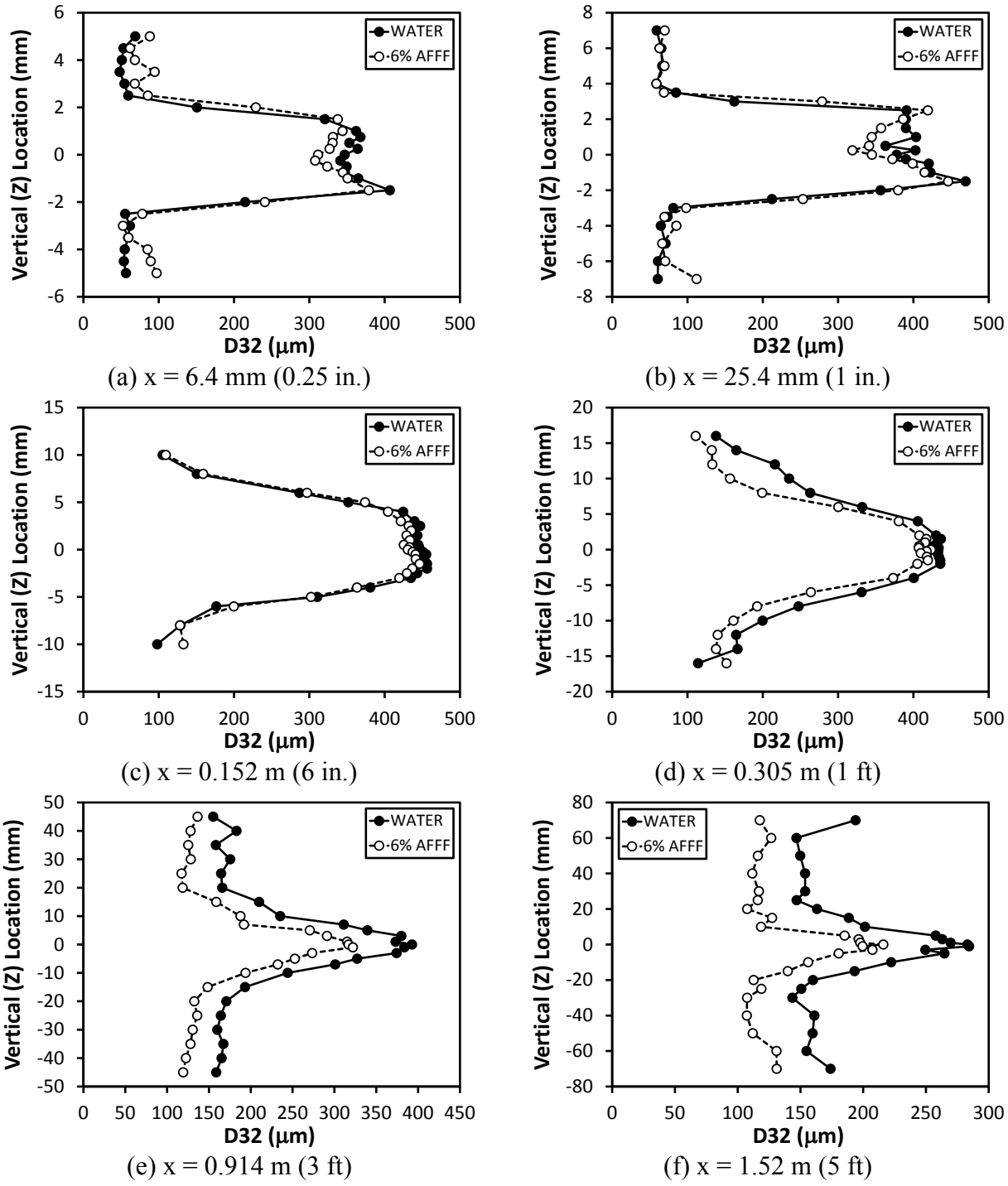

(a) x = 6.4 mm (0.25 in.)

(b) x = 25.4 mm (1 in.)

(c) x = 0.152 m (6 in.)

(d) x = 0.305 m (1 ft)

(e) x = 0.914 m (3 ft)

(f) x = 1.52 m (5 ft)

Figure C-49. Near-Field, High-Flow, Low-Pressure Jet Vertical Profiles of Sauter Mean Droplet Diameter

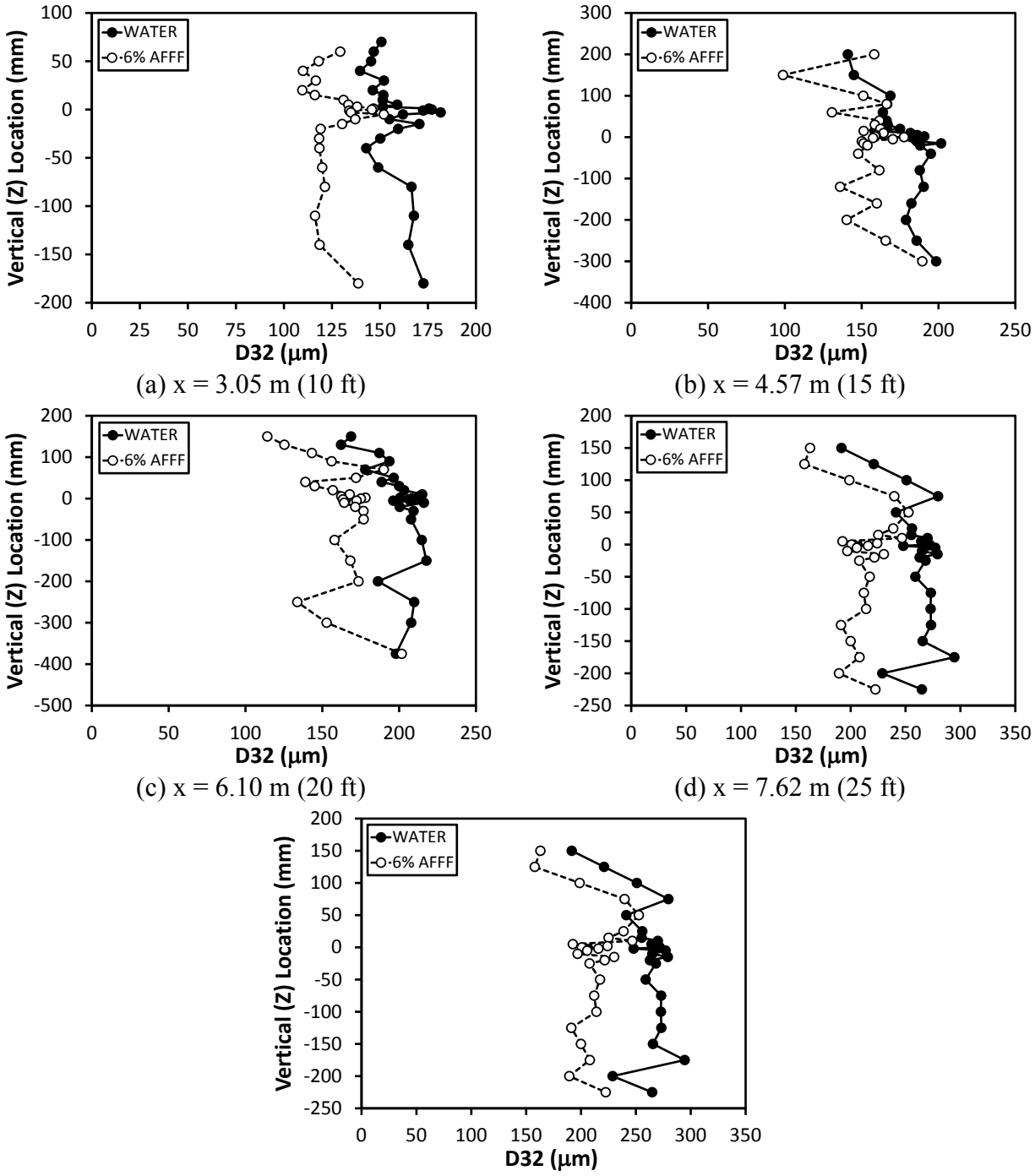

(a) x = 3.05 m (10 ft)

(b) x = 4.57 m (15 ft)

(c) x = 6.10 m (20 ft)

(d) x = 7.62 m (25 ft)

(e) x = 9.14 m (30 ft)

Figure C-50. Far-Field, High-Flow, Low-Pressure Jet Vertical Profiles of Sauter Mean Droplet Diameter

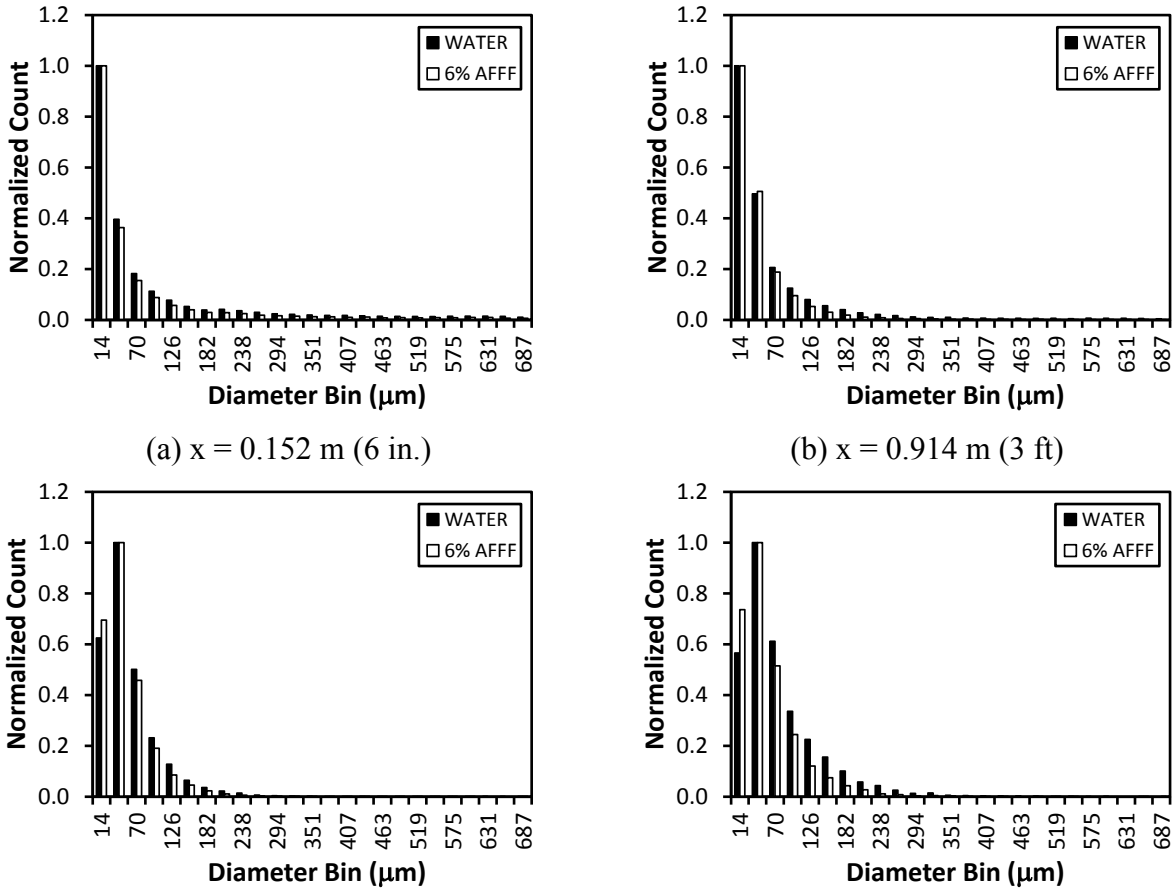

(a) x = 0.152 m (6 in.)

(b) x = 0.914 m (3 ft)

(c) x = 3.05 m (10 ft)

(d) x = 6.10 m (20 ft)

Figure C-51. High-Flow, Low-Pressure Jet Droplet Size Distribution at the Maximum Profile, Mean Axial Droplet Velocity for Select Vertical Profiles

C.5 HIGH-FLOW, HIGH-PRESSURE FIREFIGHTING JET DATA.

The high-flow, high-pressure firefighting jet data are shown in figures C-52 through C-62.

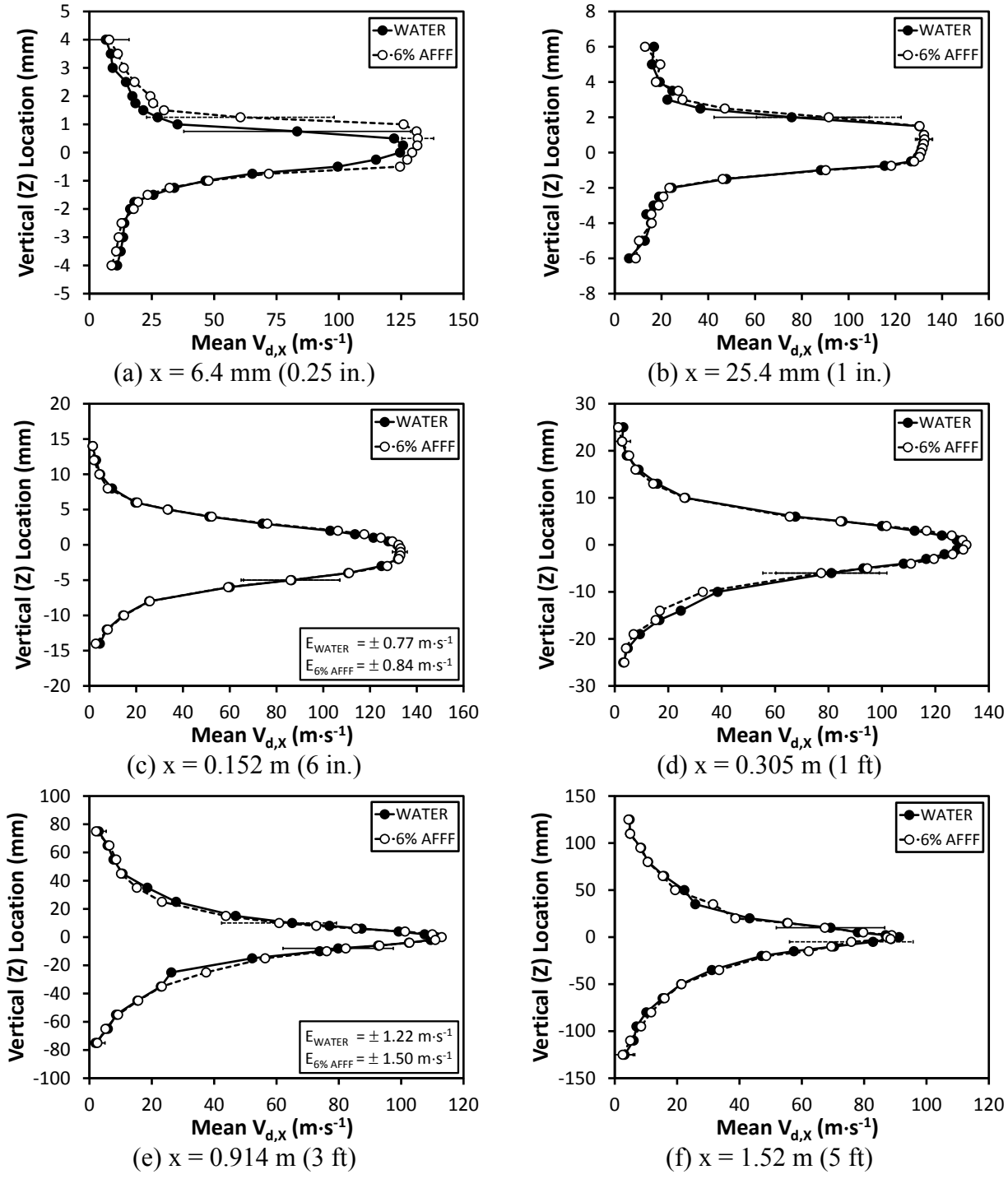

(a) x = 6.4 mm (0.25 in.)

(b) x = 25.4 mm (1 in.)

(c) x = 0.152 m (6 in.)

(d) x = 0.305 m (1 ft)

(e) x = 0.914 m (3 ft)

(f) x = 1.52 m (5 ft)

Figure C-52. Near-Field, High-Flow, High-Pressure Jet Vertical Profiles of Mean Axial Droplet Velocity

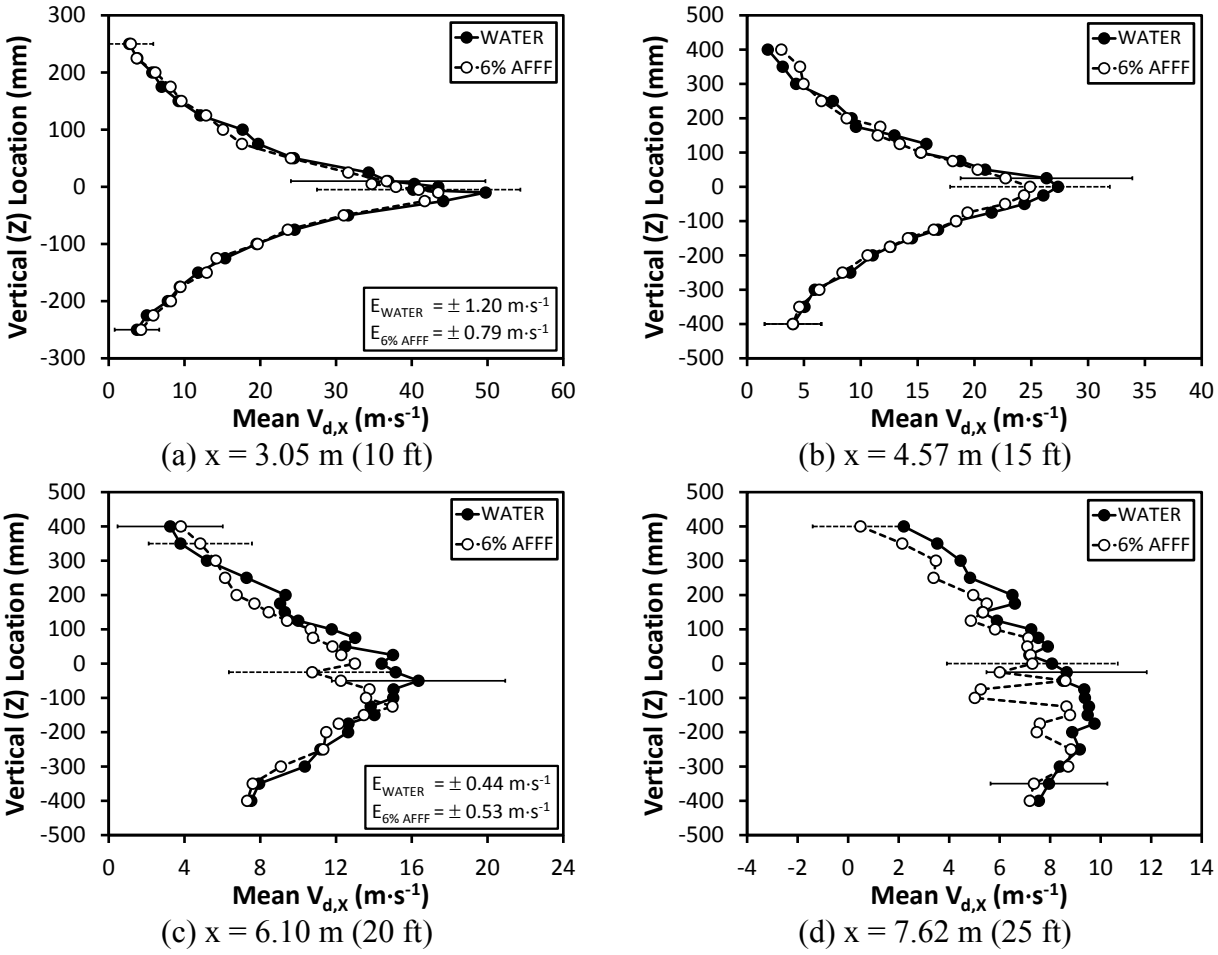

Figure C-53. Far-Field, High-Flow, High-Pressure Jet Vertical Profiles of Mean Axial Droplet Velocity

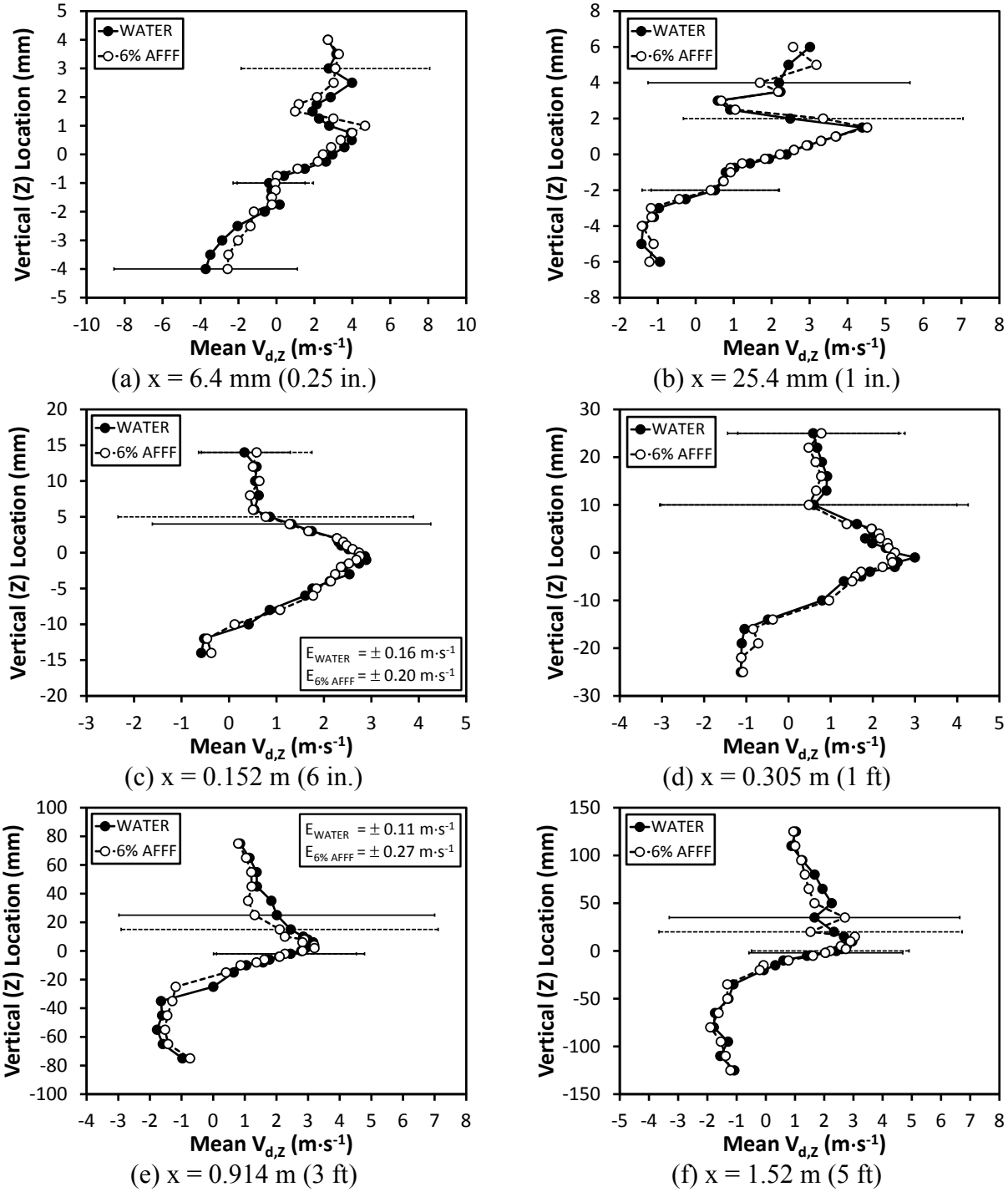

(a) x = 6.4 mm (0.25 in.)

(b) x = 25.4 mm (1 in.)

(c) x = 0.152 m (6 in.)

(d) x = 0.305 m (1 ft)

(e) x = 0.914 m (3 ft)

(f) x = 1.52 m (5 ft)

Figure C-54. Near-Field, High-Flow, High-Pressure Jet Vertical Profiles of Mean Vertical Droplet Velocity

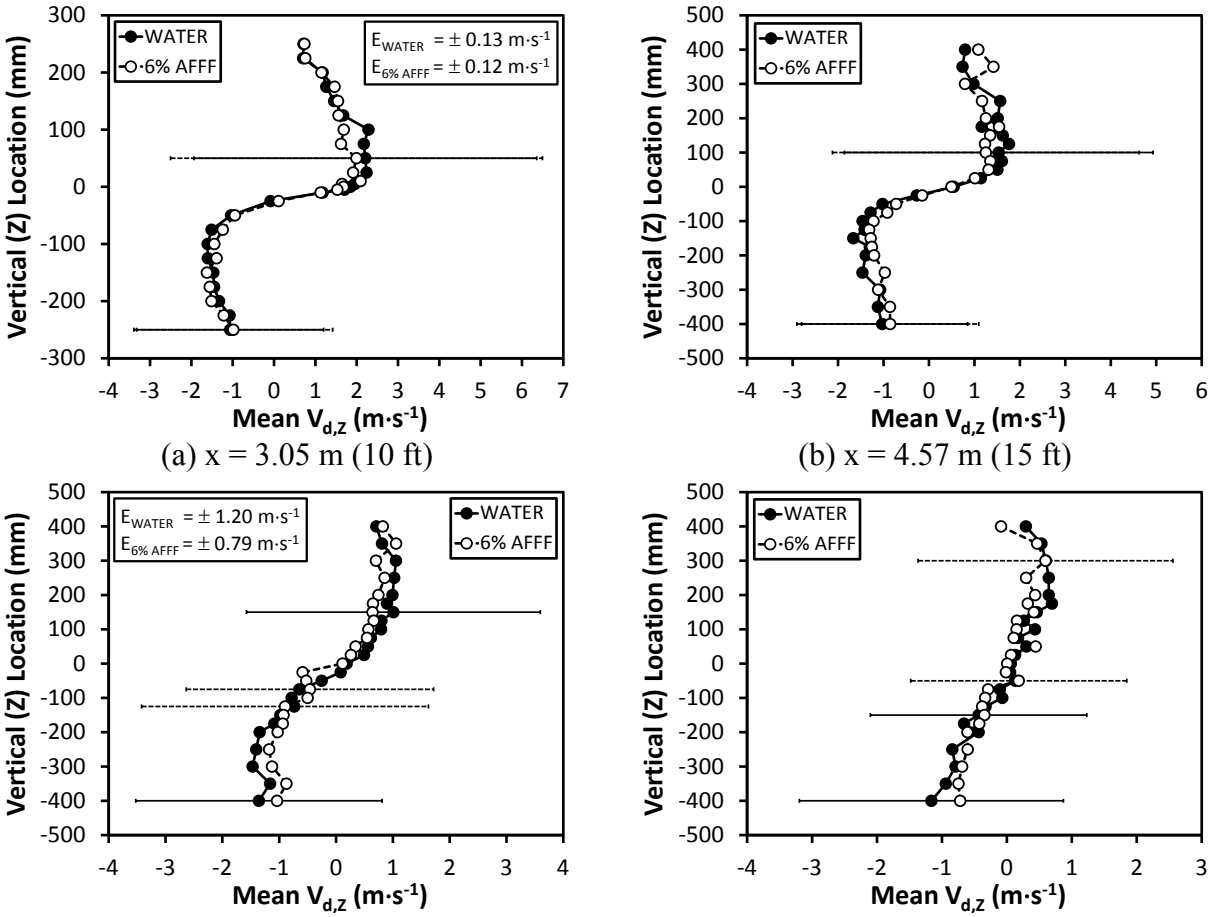

Figure C-55. Far-Field, High-Flow, High-Pressure Jet Vertical Profiles of Mean Vertical Droplet Velocity

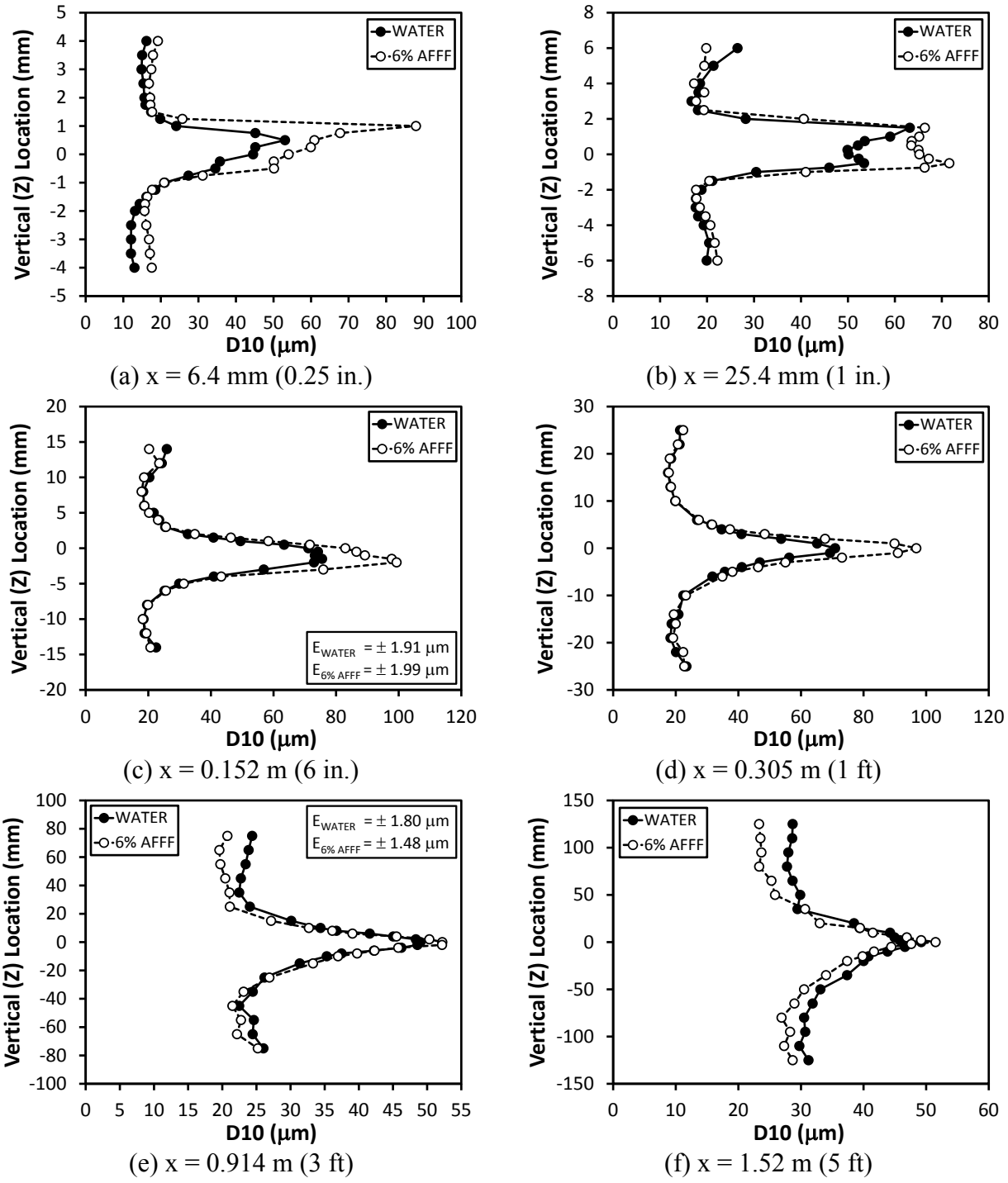

(a) x = 6.4 mm (0.25 in.)

(b) x = 25.4 mm (1 in.)

(c) x = 0.152 m (6 in.)

(d) x = 0.305 m (1 ft)

(e) x = 0.914 m (3 ft)

(f) x = 1.52 m (5 ft)

Figure C-56. Near-Field, High-Flow, High-Pressure Jet Vertical Profiles of Mean Droplet Diameter

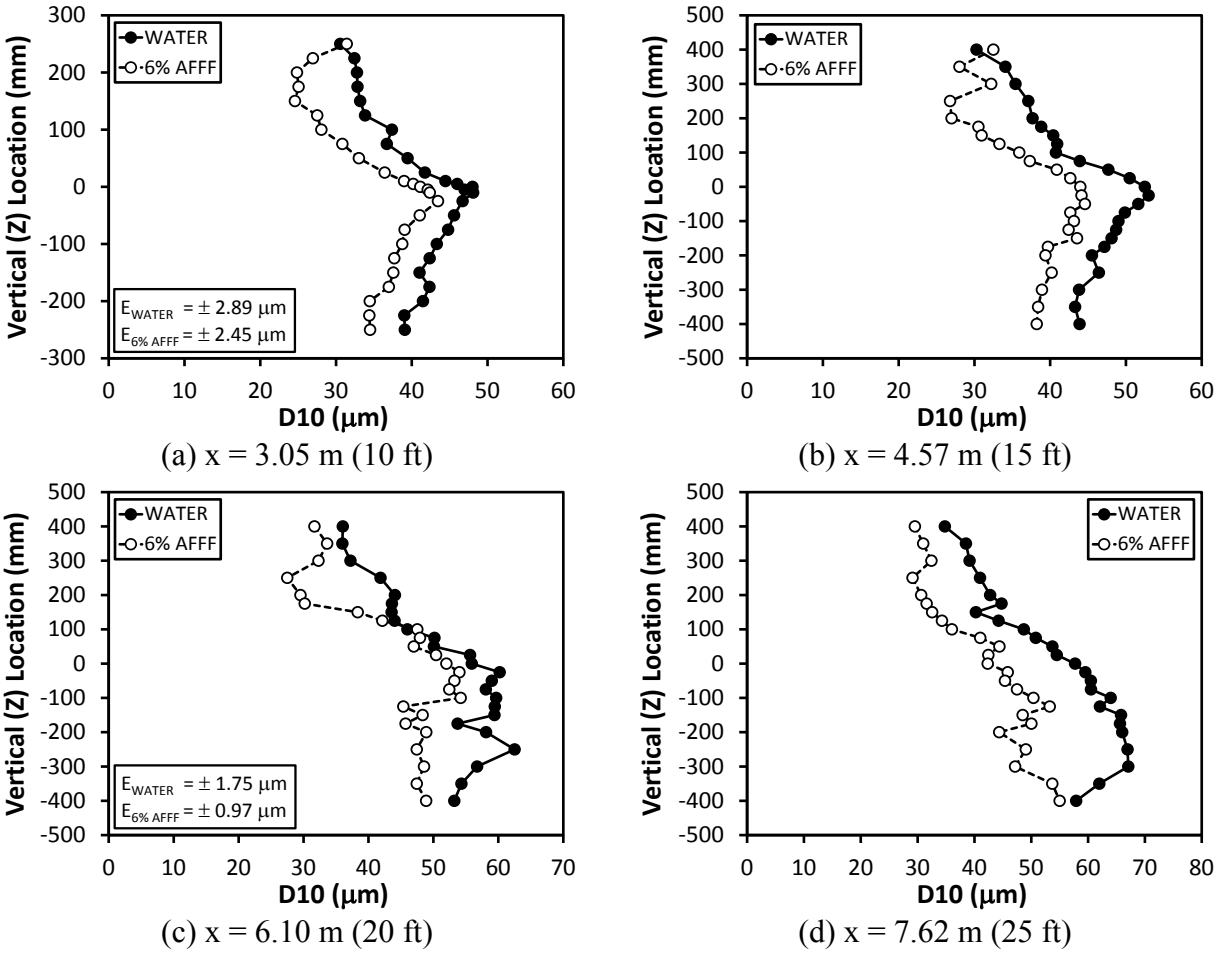

(a) x = 3.05 m (10 ft)

(b) x = 4.57 m (15 ft)

(c) x = 6.10 m (20 ft)

(d) x = 7.62 m (25 ft)

Figure C-57. Far-Field, High-Flow, High-Pressure Jet Vertical Profiles of Mean Droplet Diameter

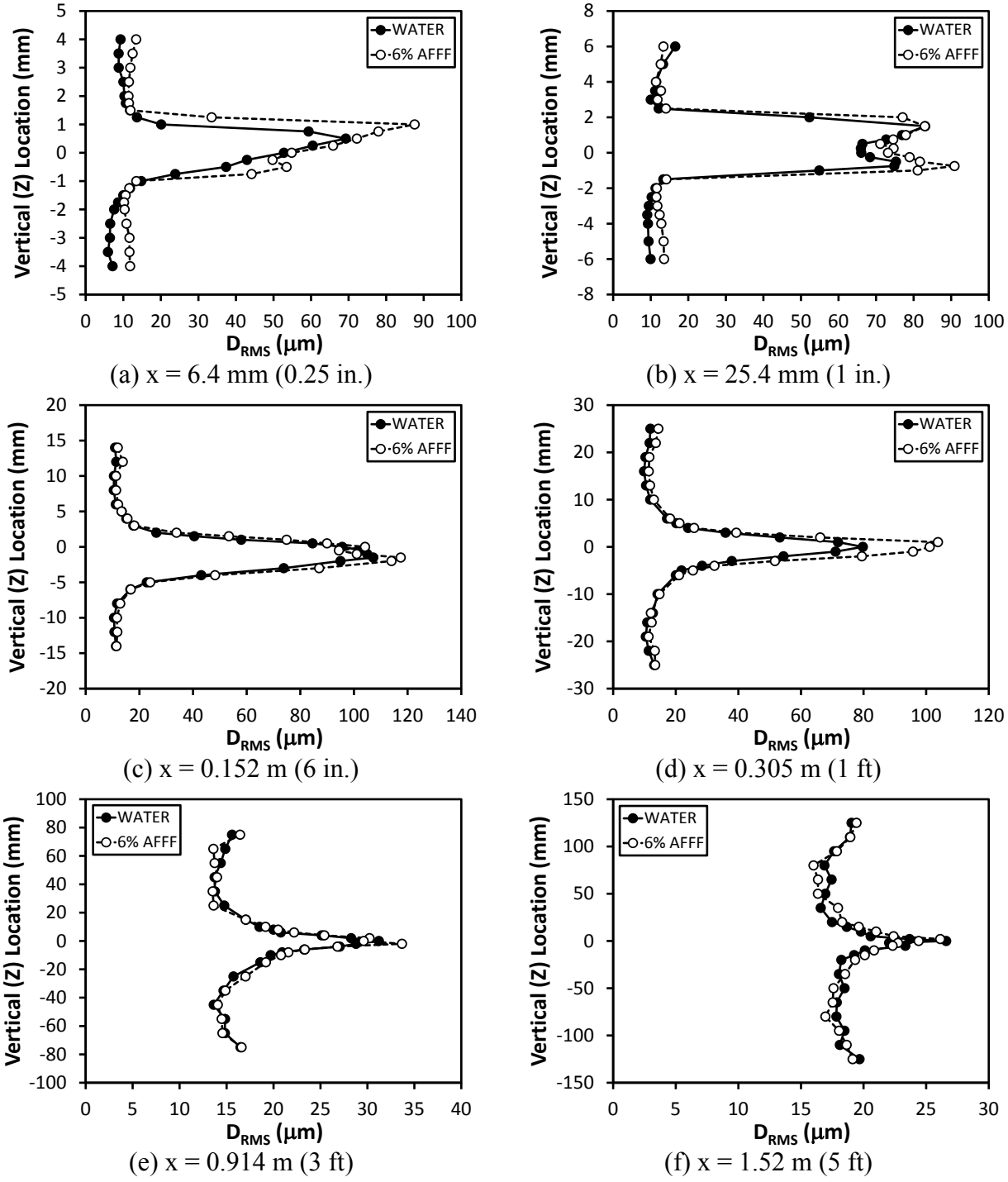

(a) x = 6.4 mm (0.25 in.)

(b) x = 25.4 mm (1 in.)

(c) x = 0.152 m (6 in.)

(d) x = 0.305 m (1 ft)

(e) x = 0.914 m (3 ft)

(f) x = 1.52 m (5 ft)

Figure C-58. Near-Field, High-Flow, High-Pressure Jet Vertical Profiles of RMS Droplet Diameter

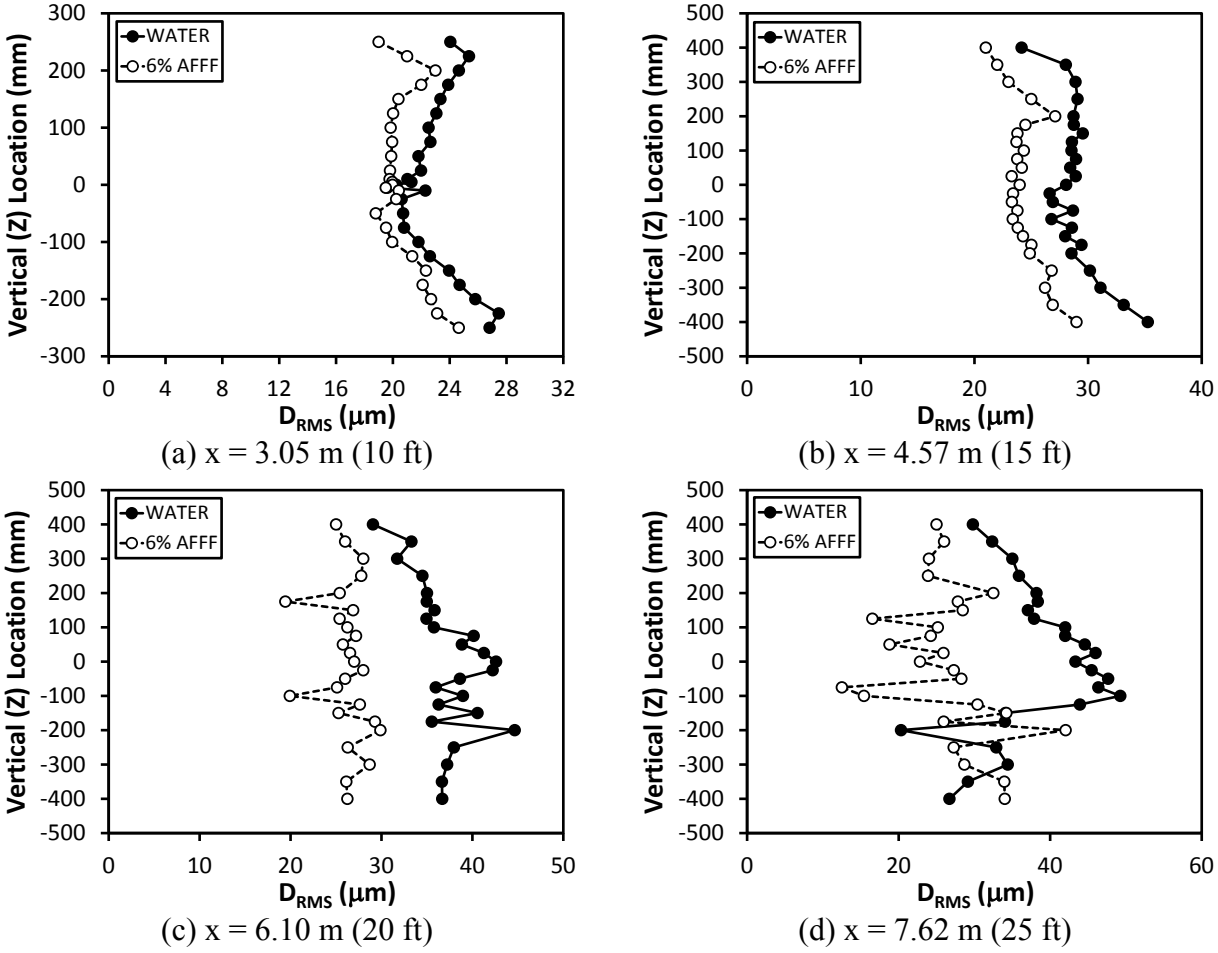

(a) x = 3.05 m (10 ft)

(b) x = 4.57 m (15 ft)

(c) x = 6.10 m (20 ft)

(d) x = 7.62 m (25 ft)

Figure C-59. Far-Field, High-Flow, High-Pressure Jet Vertical Profiles of RMS Droplet Diameter

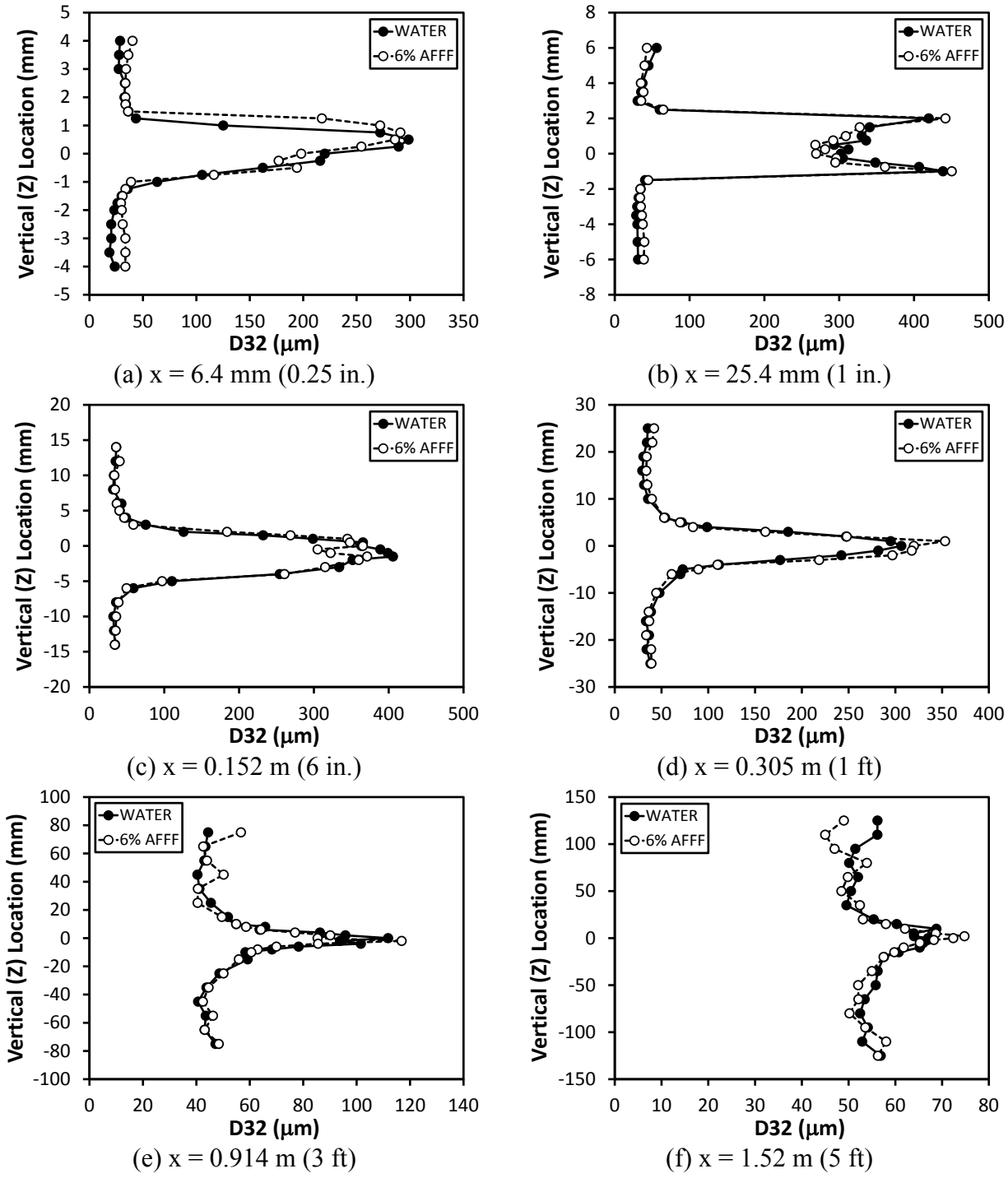

(a) x = 6.4 mm (0.25 in.)

(b) x = 25.4 mm (1 in.)

(c) x = 0.152 m (6 in.)

(d) x = 0.305 m (1 ft)

(e) x = 0.914 m (3 ft)

(f) x = 1.52 m (5 ft)

Figure C-60. Near-Field, High-Flow, High-Pressure Jet Vertical Profiles of Sauter Mean Droplet Diameter

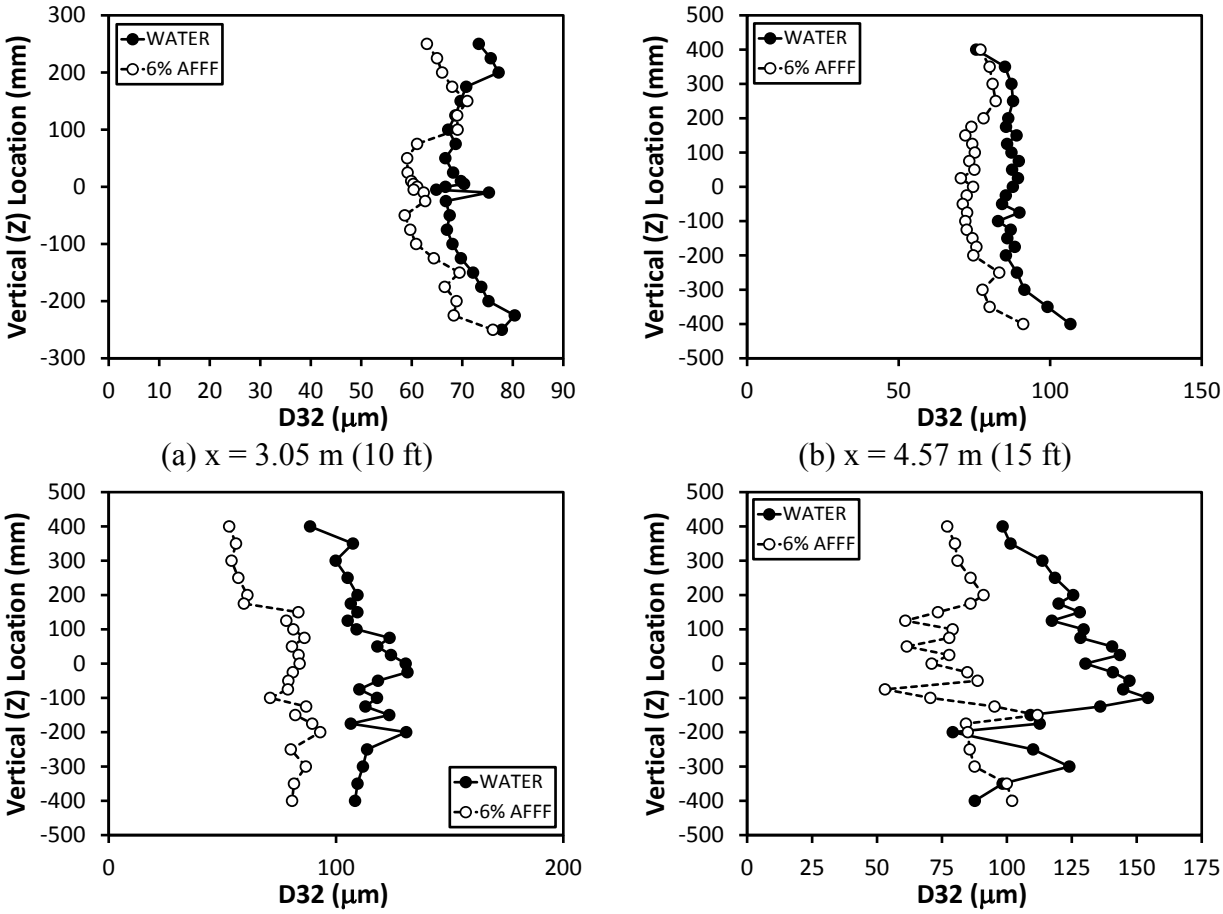

(a) x = 3.05 m (10 ft)

(b) x = 4.57 m (15 ft)

(c) x = 6.10 m (20 ft)

(d) x = 7.62 m (25 ft)

Figure C-61. Far-Field, High-Flow, High-Pressure Jet Vertical Profiles of Sauter Mean Droplet Diameter

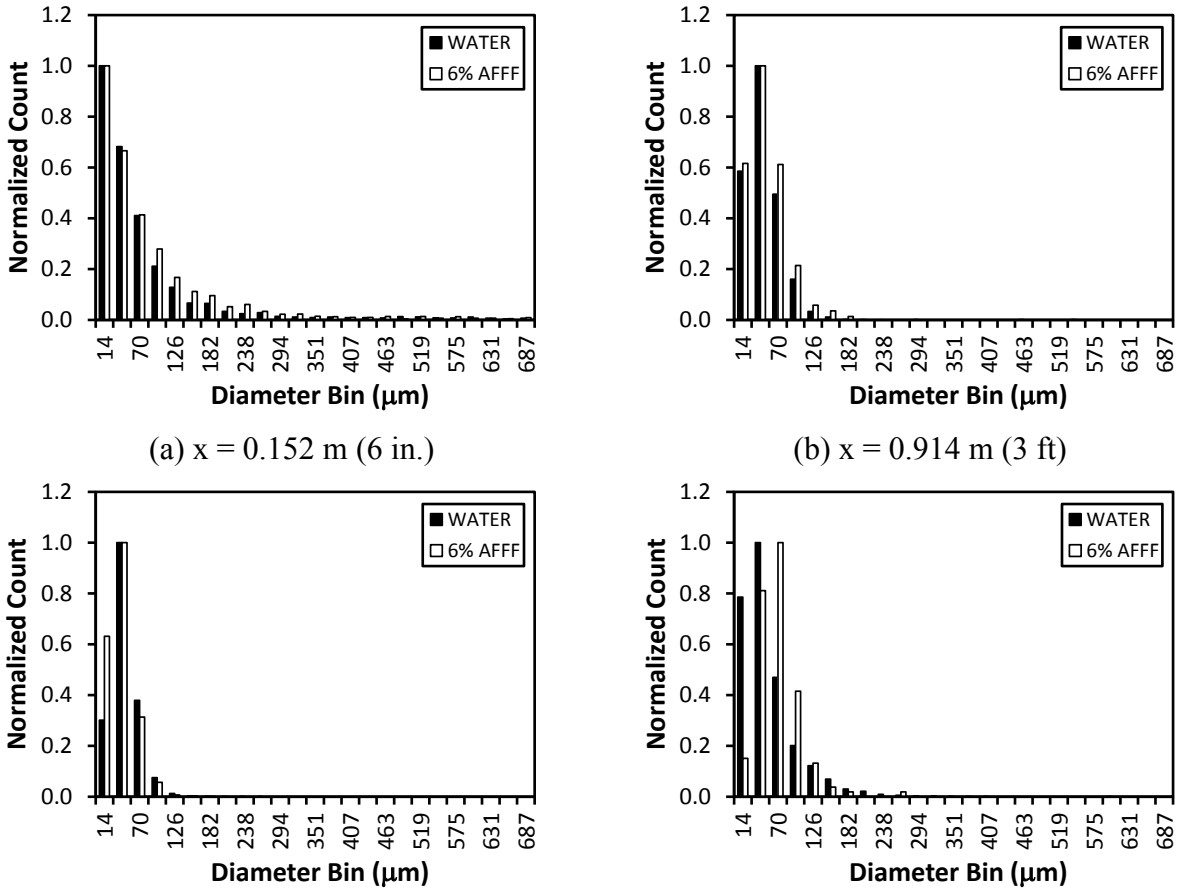

(a) x = 0.152 m (6 in.)

(b) x = 0.914 m (3 ft)

(c) x = 3.05 m (10 ft)

(d) x = 6.10 m (20 ft)

Figure C-62. High-Flow, High-Pressure Jet Droplet Size Distribution at the Maximum Profile, Mean Axial Droplet Velocity for Select Vertical Profiles

APPENDIX D—PHASE DOPPLER PARTICLE ANALYSIS CALIBRATION

An auxiliary method to quantify phase Doppler droplet size measurement uncertainty was determined via manufacturer calibration using phase Doppler particle analysis (PDPA) components specifically used in the present study. A monosize droplet generator (MDG-100 Model KD Scientific 100) was used to produce a stream of uniform, reference droplet sizes made up of distilled water in the range of approximately 100 to 175 μm with an uncertainty estimate of ±0.5%. The droplet generator relies on the principle of applying a constant periodic excitation to a laminar liquid jet, which causes surface disturbance waves to form and grow as the jet slows down. Jet breakup into a single droplet per surface wave period thus occurs. This is an established technique commonly used for fundamental droplet studies and is useful for verification and calibration checks for various instruments. The laminar liquid jet was generated by a constant flow rate pump that delivered fluid through a vibrating orifice. The orifice and column was made to vibrate by a frequency generator and piezo crystal generating one droplet per vibration cycle. The vibration rate and flow rate were controlled by the frequency generator and pump, respectively. The phase Doppler measurements were recorded using reflection light-scattering measurement techniques with the optics positioned in forward-scatter mode. A phase calibration was performed to maintain a relatively constant intensity of approximately 300 mV. Verification of the droplet generator stability was obtained by ensuring the droplet frequency generation and the phase Doppler data rates were identical. An oscilloscope was used to confirm the Doppler bursts were well formed and repeatable. Measurements were recorded for 12 droplet generation conditions. The phase Doppler measurements were found to vary between 0.01% and 0.76% with respect to the expected droplet generator diameter. Table D-1 summarizes the measurement data, and figure D-1 illustrates the droplet generator vibration frequency as a function of droplet diameter comparing the MGD-100 and mean droplet diameter reported by the PDPA. Because the PDPA and MGD-100 data are very close to one another in figure D-1, the MGD-100 data is mostly eclipsed by the PDPA data.

Table D-1. The PDPA Droplet Size Calibration Certification Check Points

MDG-100 Vibration Frequency (kHz)	MDG-100 Diameter (μm)	PDPA Mean *D*10 (μm)	Absolute Relative Error (%)
37.3	98.2	97.52	0.68
28.2	107.8	107.44	0.36
23.7	114.23	114.10	0.13
19.52	121.87	121.75	0.12
16.54	128.78	128.96	0.18
14.41	134.84	134.64	0.20
12.43	141.65	141.66	0.01
10.67	149.05	148.85	0.20
9.34	155.81	155.05	0.76
8.56	160.41	159.81	0.60
7.42	168.23	168.17	0.06
6.53	175.55	176.19	0.64

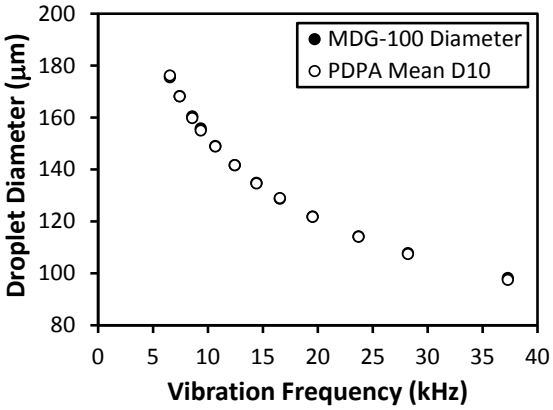

Figure D-1. The PDPA Droplet Size Calibration Certification Comparing MDG-100 Diameter and PDPA Mean *D*10